ice
Institution of Civil Engineers
publishing

Bio- and Chemo-Mechanical Processes in Geotechnical Engineering

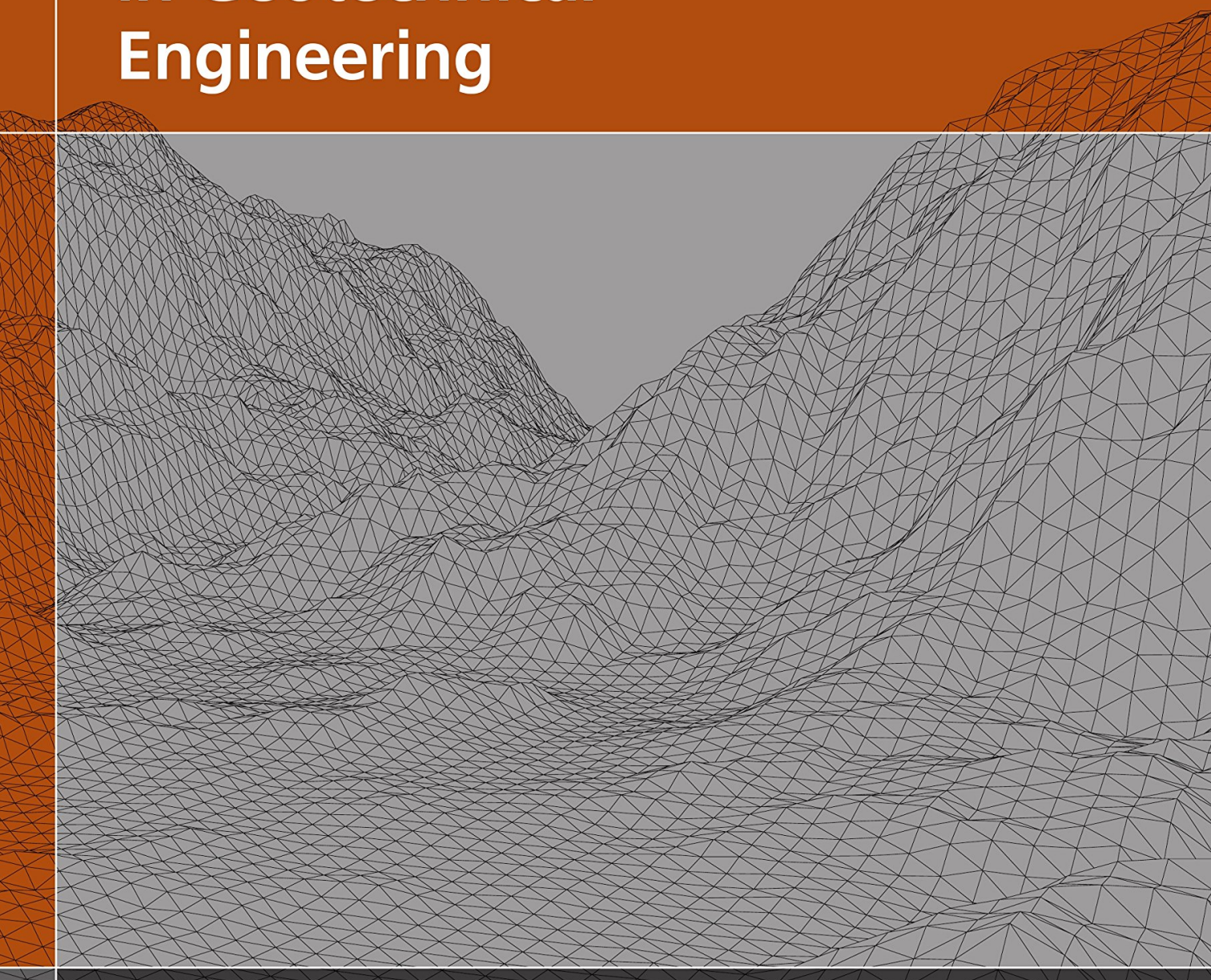

Edited by Lyesse Laloui

ice
Institution of Civil Engineers
publishing

Bio- and Chemo-Mechanical Processes in Geotechnical Engineering

Géotechnique Symposium in Print 2013

Edited by
Lyesse Laloui

Related titles from ICE Publishing:

Partial Saturation in Compacted Soils (Géotechnique Symposium in Print 2011).
D. Gallipoli (eds). ISBN 978-0-7277-5775-3

Environmental Geotechnics, Second edition.
R. Sarsby. ISBN 978-0-7277-4187-5

ICE Manual of Geotechnical Engineering.
J. Burland, T. Chapman, H. Skinner, M.J. Brown (eds). ISBN 978-0-7277-3652-9

Handbook of Geosynthetic Engineering, Second edition.
S.K. Shukla. ISBN 978-0-7277-4175-2

ISBN 978-0-7277-6053-1

Typeset by Keytec Typesetting Ltd, Bridport, Dorset
Printed and bound by Ashford Colour Press Ltd, Gosport, Hants PO13 0FW

Preface

Conventional geotechnical engineering theories do not provide a sufficient framework to fully address the new challenges that emerge due to the interactions between multi-physical phenomena. During the past two decades, advances in the study of unsaturated geo-materials including the non-isothermal conditions have been reported. A whole new framework for the characterization of the coupled thermo-hydro-mechanical processes has been set. However, the complexity of emerging energy and environmental geotechnical applications is increasing with the presence and development of chemical and biological processes. The evolution of these phenomena and their interaction with the different constituents of porous geo-materials unfold a vast new research domain, full of challenges. This is leading the global scientific interest towards new areas, far from the conventional and extensively explored ones.

The objective of this book is to present the recent developments in the study of the aforementioned phenomena and to provide readers with a handful material for addressing the uncharted chemo- and bio- mechanical couplings and their related geotechnical applications.

In recent years, substantial advances have been made in understanding the coupling between chemical and biological processes and mechanical and hydraulic behaviour in soils and rocks. At the same time, experimentation and modelling capabilities have progressed significantly, allowing effective design of geotechnical applications. The need for such analyses arises (for example) in chemical and biological soil improvement; nuclear, hazardous and municipal waste containment; petroleum and natural gas extraction; methane hydrate exploitation; carbon dioxide sequestration; and the assessment of pavement durability.

In such areas, instances of complexity and interaction are many, mainly because of the coexistence of several constituents and phases, their interactions, their reactivity, and their often non-linear behaviour. Flow involves water and gas, including the transport of chemical species and bacteria. Geomaterial deformation depends not only on classical effective stress, suction and temperature, but also on the history of chemical and bacterial activity in the material. Experimental observations are often difficult to carry out, and laboratory and in situ tests are costly challenges. An understanding of the material behaviour to be observed requires the control or measurement of many different parameters. Modelling inevitably implies numerical analyses. Coupled transient analyses are in fact a characteristic feature of this field; proper variables must be selected which can describe the behaviour of the geomaterials subjected to chemical and biological phenomena.

A challenge at hand is to quantitatively describe the reaction and transport processes that occur. In this case, more complex variables enter the field equations for the different phases since the addressed chemical and biological processes refer to solute species that can react with species either in the same or in another phase. Robust numerical techniques are therefore required in order to solve, with sufficient accuracy, the strongly coupled analytical systems. Hence, progress in coupled bio- and chemo-mechanical processes in geotechnical engineering requires advances in theoretical formulations, numerical analyses, constitutive modelling and laboratory techniques, as well as detailed examination of well-documented field cases. Another issue is the study of the micro-structure where these processes can be better investigated and interpreted in mathematical terms. The analysis at the micro-scale requires the use of testing apparatus previously employed in limited cases in testing procedures for geotechnical problems.

This book is based on the two special issues of *Géotechnique* (Volume 63 issues 3 and 4) that preceded the *Géotechnique* Symposium in Print that was held on 3rd June 2013 at the Institution of Civil Engineers (ICE) in London. The symposium offered scientists and engineers from all over the world the opportunity to learn, discuss and outline future developments in this fascinating and critically important area. To this same purpose, the content of the book is enriched with papers from subsequent issues of the journal.

A total number of twenty contributions are organized in three sections. The first two focus on couplings between chemical, biological and mechanical aspects for different geo-materials (clay, shale, bentonite and sand among others) while emphasis is laid on modelling. Experimental evidence is presented along with cases addressing these couplings for real applications such as the mitigation of the liquefaction potential of sands or the carbon dioxide sequestration in coal beds. Finally, the third section is devoted to an overview of the progress in this emerging field providing at the same time readers with an outline of future challenges and potential developments.

Lyesse Laloui
Ecole Polytechnique Fédérale de Lausanne, EPFL
May 2014

Contents

ice
Institution of Civil Engineers
publishing

Session 1. Chemo-mechanical investigations in soils

1.1 Clays

Musso, G. *et al.* (2013). *Géotechnique* **63**, No. 3, 206–220 [http://dx.doi.org/10.1680/geot.SIP13.P.011]

Double-structure effects on the chemo-hydro-mechanical behaviour of a compacted active clay

G. MUSSO*, E. ROMERO† and G. DELLA VECCHIA‡

This work presents an insight into double-structure effects on the coupled chemo-hydro-mechanical behaviour of a compacted active clay. In the first part, selected pore size distribution curves are introduced, to highlight the influence of solute concentration on the evolution of the microstructure of compacted samples. An aggregated structure with dual-pore network is induced by compaction even at relatively high water contents. This structural arrangement is enhanced by salinisation, and has a notable influence on transient volume change behaviour – that is, the occurrence of different stages of swelling upon pore water dilution and higher volume change rates upon salinisation. A coupled chemo-hydro-mechanical model, taking into consideration double-structural features from a chemo-mechanical viewpoint, is described and then used to interpret these behavioural responses and present complementary information on local transient processes. The model is designed to identify an intra-aggregate and an inter-aggregate domain, and assigns different values of hydraulic pressure and osmotic suction to each domain. Distinct constitutive laws for both domains are formulated, and the flow of salt and water between the two domains is accounted for by a physically based mass exchange term. The model is used to simulate salt diffusion tests run in an oedometer at constant vertical stress. Parameters used in the formulation are calibrated based on separate experimental evidence, both through direct test results and through back-analyses of laboratory experiments.

KEYWORDS: chemical properties; clays; constitutive relations; fabric/structure of soils; laboratory tests; suction

INTRODUCTION

The hydro-chemo-mechanical response of compacted active soils is of significant importance in geo-environmental engineering, such as for soil contamination/remediation and waste confinement at surface or at great depths using engineered clay barriers and clay liners (e.g. Delage & Romero, 2008). When designing compacted engineered clay barriers for waste repository systems, it is of primary importance to assess how hydraulic properties and the volume change response are affected by chemical changes induced by a wide range of saline concentrations and solute types.

Despite practical relevance for geo-environmental applications, not many studies have dealt with the effects of chemical changes on the volumetric behaviour of compacted and natural soils (e.g. Di Maio & Fenelli, 1997; Musso *et al.*, 2003; Rao *et al.*, 2006; Rao & Thyagaraj, 2007; Castellanos *et al.*, 2008; Siddiqua *et al.*, 2011), although chemo-mechanical interactions and pore fluid chemistry effects on reconstituted clays are a well-documented topic in the literature, and have a long research history (e.g. Bolt, 1956; Mesri & Olson, 1971a; Barbour & Fredlund, 1989; Yang & Barbour, 1992; Di Maio, 1996; Studds *et al.*, 1998).

The chemo-mechanical behaviour of slurries starting from diluted suspensions has historically been interpreted through Gouy–Chapman diffuse double layer (DDL) theory (e.g. Bolt, 1956; Warkentin *et al.*, 1957; Madsen & Muller-Vonmoos, 1985, 1989). This approach has been used to reproduce forces exchanged by particles in a system where the size of the pores is uniform (Mitchell & Soga, 2005). Despite being quite successful in explaining some features of the observed volumetric response, such as volume decrease upon salinisation, the hypothesis of a uniform pore size appears controversial when considering the behaviour of structured soils, and in general when considering hydraulic aspects.

For example, at a given void ratio, specimens saturated with saline solutions or with organic non-polar liquids show higher hydraulic conductivities than specimens saturated with distilled water (e.g. Michaels & Lin, 1954; Mesri & Olson, 1971a, 1971b; Fernandez & Quigley, 1985, Calvello *et al.*, 2005; Gajo & Maines, 2007). Hueckel *et al.* (1997) applied four different literature models to verify the impact of different mechanisms of microstructure evolution, induced by chemical changes, on the permeability of saturated active clays. They identified clusters of clay particles, saturated by immobile inter-layer water and external adsorbed water, as the fundamental microstructural unit, and concluded that the most likely cause of permeability changes as detected by Fernandez & Quigley (1988) was flocculation of particles. Mesri & Olson (1971b) hypothesised that high water salinity and/or low dielectric constant of the pore fluid causes the contraction of aggregates of clay particles, consequently decreasing the volume of the pores within the aggregates (*intra-aggregate* or *micro-voids*) and increasing the volume of voids between the aggregates (*inter-aggregate* or *macro-voids*). The increase of macro-void size could then be the dominant mechanism explaining the increase in permeability with salinity. Although an explicit hierarchy (*aggregates against clusters*) is not introduced in these different works, from Yong (1999) it follows that aggregates are made of many clusters of particles.

Manuscript received 29 February 2012; revised manuscript accepted 12 October 2012.
Discussion on this paper closes on 1 August 2013, for further details see p. ii.
* Department of Structural, Geotechnical and Building Engineering, Politecnico di Torino, Italy.
† Department of Geotechnical Engineering and Geosciences, Universitat Politècnica de Catalunya, Barcelona, Spain.
‡ Department of Structural Engineering, Politecnico di Milano, Milano, Italy.

The impact of aggregated fabric on the hydro-mechanical behaviour of compacted active clays, and jointly how this fabric is influenced by stress and suction changes, is well documented in unsaturated conditions (Romero *et al.*, 2011; Della Vecchia *et al.*, 2012). For instance, Lloret *et al.* (2003) performed an experimental study on bentonite samples compacted at different dry densities: by investigating both the pore size distribution and the water retention properties, they evidenced the advantages of modelling the microstructure of the soil through a double-porosity framework to reproduce the soil behaviour correctly.

The aim of the present paper is twofold. First, it aims at evaluating the effects of salinity changes on the fabric of compacted bentonite samples exposed to saline solutions of sodium chloride (NaCl) and calcium chloride ($CaCl_2$) ranging from null solute concentration to nearly saturated conditions. This evaluation is done by considering changes in the size of the aggregates, documented by environmental scanning electron microscopy (ESEM) photographs, and the associated changes in the size of the pore network, as measured by mercury intrusion porosimetry (MIP) tests. Experimental observations actually suggest the existence of a double-structure arrangement, which evolves upon chemical changes, and allow the introduction of a double-structure conceptual model, based on the framework proposed by Gens & Alonso (1992). Such a conceptual model foresees that the chemo-hydro-mechanical behaviour of compacted active clays upon chemical changes is governed by the interaction of two structural levels, one being related to the aggregates and their internal pore network and the other to the pore space between them. Simple laws and parameters used to give a mathematical form to the conceptual model are calibrated in a natural way using direct experimental information. For the particular case of the mass exchange terms, the interpretation of MIP results is used.

Second, the paper aims at verifying whether the double-structure model, and the way it was characterised, is actually consistent with the measured volumetric response of compacted active clays upon chemical changes. This check is done by using the conceptual model and the parameters defined in the first part to simulate a salt diffusion test, performed under well-controlled chemo-mechanical boundary value conditions. The simulation accounts for coupled transport phenomena, and handles the effects of the double structure on hydraulic processes according to the conceptual scheme of Gerke & van Genuchten (1993a). While aiming at contributing to more accurate reproduction of chemo-hydro-mechanical processes in structured materials, to be used for field geoenvironmental cases, the model also complements the experimental information of evolutionary processes at the local scale that are beyond the measurable scale of the macroscopic oedometer test performed. Thus the model should be also considered as a simulation-aided technique to better interpret and exploit the information provided by the phenomenological boundary value test.

For the sake of simplicity it was assumed that within the conditions explored during the tests, and reproduced by the model, cation exchange phenomena did not lead to relevant deformations. In order to make the model more compliant with formulations used in soil mechanics, chemical species and concentration changes were expressed in terms of variations of osmotic suction.

AN INSIGHT INTO MICROSTRUCTURAL CHANGES INDUCED BY CHEMICAL EFFECTS

The double structure of compacted active clays has been documented by several authors (e.g. Pusch, 1982; Atabek *et al.*, 1991; Lloret *et al.*, 2003; Musso *et al.*, 2003; Castellanos *et al.*, 2008; Romero *et al.*, 2011): particles of compacted active clays organise into aggregates, and pores within the aggregates are generally smaller than the pores between the aggregates.

In the present work, MIP tests and ESEM photomicrographs were performed to characterise the structure of samples of a compacted active clay (FEBEX bentonite) saturated with different saline solutions, so to provide information about the effects of chemical changes on the structural arrangement. Hydraulic conductivity measurements were also interpreted in the light of possible micro- and macroporosity changes.

FEBEX is a natural mixed bentonite (Cortijo de Archidona deposit, Almería, south-eastern Spain), proposed as an engineered barrier for radioactive waste disposal (ENRESA, 2000). It has a very high content of montmorillonite (around 90%), with small quantities of quartz, plagioclase, cristobalite, K-feldspars, trydimite and calcite. Table 1 summarises the main properties of the material.

Samples were prepared statically compacting the bentonite powder at a hygroscopic water content $w = 12\%$ (at a relative humidity of 50%), imposing an initial dry density $\rho_d = 1{\cdot}65$ Mg/m^3(void ratio $e = 0{\cdot}64$ and degree of saturation $S_r = 51\%$). Samples were subsequently loaded at constant water content up to a total vertical stress of 200 kPa, and then saturated with different saline solutions under oedometer conditions at constant vertical stress. All initially overconsolidated samples swelled upon saturation, although to different extents, depending on the solution used: so the overall final void ratios at which the microscopic analyses were performed are higher than the initial as-compacted one.

Effects detected by ESEM photomicrographs

ESEM photomicrographs were taken at different saturation conditions (as in Castellanos *et al.*, 2006), to visualise microfabric changes associated with different environmental conditions, and particularly with variations in the salinity of the pore fluid (Fig. 1). Aggregates with a size of around 100 μm, surrounded by macro-voids of comparable size, are clearly evident in the as-compacted state (Fig. 1(a)). Upon saturation, aggregates swell, reducing the volume of macro-voids between aggregates. Test results proved that the extent of aggregate swelling is noticeably influenced by the salinity of the pore fluid, since their size progressively increases from the hygroscopic state to that at saturation with 0·5 mol/l sodium chloride solution (Fig. 1(b)), and finally to the state induced by saturation with distilled water (Fig. 1(c)). In this last case, aggregates swell to such an extent that they start to merge.

Table 1. Properties of the bentonite used in the study*

Property	Value
Mineralogy	Montmorillonite (90 ± 3%)
Cation exchange complex: meq/100 g	Ca^{2+} (38%): 43 Na^{+} (23%): 25 Total CEC: 102
Liquid limit, w_L: %	102 ± 4
Plastic limit, w_P: %	53
Density of solids, ρ_S: Mg/m^3	2·70 ± 0·04
Particles < 2 μm: %	>85%
Specific surface, S_S: m^2/g	725 (total) 65 (external)

* Lloret *et al.* (2003); Musso *et al.* (2003); Villar *et al.* (2005).

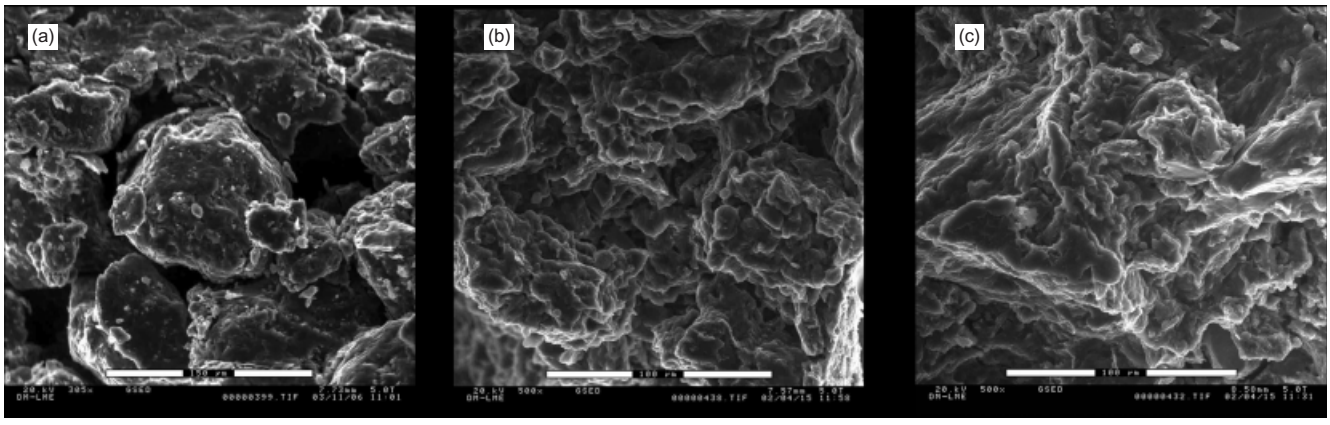

Fig. 1. ESEM pictures of statically compacted FEBEX samples (dry density 1·65 Mg/m^3): (a) as-compacted at hygroscopic water content, (b) after saturation with 0·5 mol/l sodium chloride solution; (c) after saturation with distilled water. Black bar is 150 μm in (a) and 100 μm in (b) and (c)

Effects detected by pore size distribution analyses

ESEM pictures testify that decreasing pore fluid salinities lead not only to greater aggregate size, but also to a progressive reduction of the size of macro-voids. Quantification of the evolution of the pore size was attempted by performing MIP on freeze-dried samples (Delage *et al.*, 1982) so as to obtain pore size distributions (PSDs) at different pore fluid concentrations. The device used was a Micromeritics-Autopore IV, which makes possible the intrusion of pore throats from 6 nm to 400 μm.

PSDs of the as-compacted sample at hygroscopic water content and of the overconsolidated samples saturated with different saline solutions are presented in Fig. 2. The PSD has been calculated as $-\Delta e/\Delta \log x$, where e is the intruded void ratio for each entrance pore diameter x: thus the area subtended by the PSD function represents the present void ratio. A consistent effect of salinisation on the PSD can be appreciated. The as-compacted sample shows a bimodal pore size distribution, with a peak at around 20 nm and another at around 20 μm. Upon saturation with highly saline solutions (5·5 mol/l), the overall void ratio increased from the original value $e = 0{\cdot}64$ to $e = 0{\cdot}75$ for the sodium chloride solution and to $e = 0{\cdot}74$ for the calcium chloride solution. The shape of the PSD suggests that the porosity increase upon saturation is partially related to a higher density of pores whose sizes are greater than approximately 20 μm. At lower salinities the density of this class of large pores progressively reduces, whereas the density of pores with sizes ranging from 100 nm to 10 μm increases significantly. The distribution of PSD function for salinities lower than 0·5 mol/l is such that a new peak emerges at a size of about 1000 nm, which is associated with the swelling of aggregates on saturation with a low-salinity fluid.

Measurements confirm that the microstructural effects of chemical changes on compacted soils are different from what could be expected for suspensions of active clays, where according to theories such as that of Derjaguin–Landau–Verweyd–Overbeek (e.g. Mitchell & Soga, 2005) a uniform pore size is expected, reducing upon an increase of salinity because of decreasing repulsion between single particles. MIP evidence also seems in contrast with externally measured deformations, since experimental studies record that salinisation induces an overall shrinkage of soil samples (e.g. Barbour & Fredlund, 1989; Di Maio, 1996; Gajo & Maines, 2007). A conceptual interpretation in terms of double porosity can help to explain these apparently opposite effects, provided the consequences of salt concentration changes for the micro-voids are different from the consequences of the same changes for macro-voids.

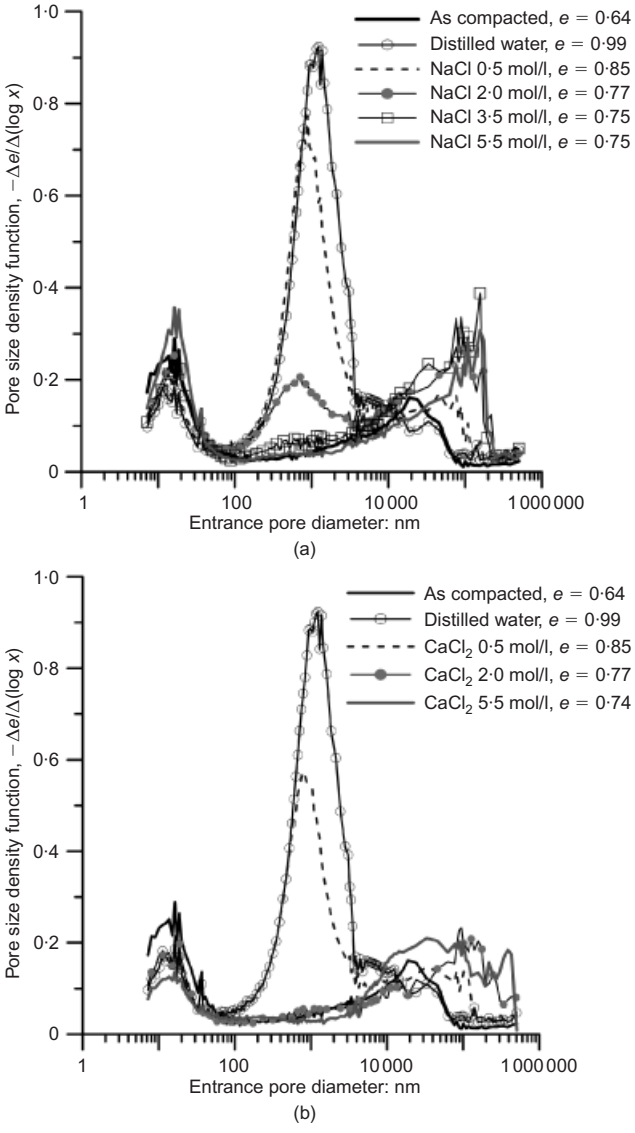

Fig. 2. MIP pore size distributions of compacted samples saturated with: (a) sodium chloride (NaCl) solution; (b) calcium chloride ($CaCl_2$) solution

Relation between salt concentration and microstructural void ratio

To put forward a quantitative interpretation in terms of double porosity, the (global) void ratio e can be split into

two components, the microstructural void ratio e_m and the macrostructural void ratio e_M, according to

$$e = e_m + e_M = \frac{V_{vm}}{V_s} + \frac{V_{vM}}{V_s} \quad (1)$$

where V_{vm} is the volume occupied by micro-voids, V_{vM} is the volume occupied by macro-voids, and V_s is the volume of solids.

It was decided to discriminate between e_m and e_M on the basis of the MIP measurements presented in the previous section, by defining a delimiting pore size that made it possible to account for the evolving size of the aggregates during chemo-hydraulic processes. As explained in Della Vecchia (2009) and Romero *et al.* (2011), the working hypothesis is that pores belonging to the microstructure can increase their size up to a limit, corresponding to the minimum size of the pores belonging to the macrostructure. So the delimiting pore size is at the same time an upper bound for the intra-aggregate porosity and a lower bound for the inter-aggregate porosity. It can be determined from MIP data referring to the condition that promotes the most significant swelling of the aggregates (in this case saturation with distilled water), since the intra-aggregate pores will have their maximum size and the inter-aggregate pores their minimum size. The delimiting pore size was then chosen in correspondence with the dominant maximum peak of the PSD of the distilled water saturated sample. According to this hypothesis, micro-voids are characterised by pores with a diameter lower than 1000 nm and macro-voids by pores with a diameter greater than 1000 nm (Fig. 2). For each solute type and salt concentration, V_{vm} was then evaluated as the volume occupied by voids whose entrance pore sizes are lower than 1000 nm. The corresponding values of e_m and e_M were obtained by equation (1).

According to the defined phenomenological framework, the sizes of the aggregates and micro-voids are different from the sizes of clusters and intra-cluster voids used in other works (e.g. Hueckel *et al.*, 1997). Since intra-cluster voids are saturated by externally adsorbed water, their size is below what is measured with the MIP technique, while the size of the elements here defined is based on the observations collected through ESEM and MIP analyses previously discussed, that is, on a broader scale. A single aggregate is regarded as composed of several clusters, so that, in accordance with Terzaghi (1956) 'the range of influence of the osmotic forces does not extend beyond the boundaries of each of the clay clusters which are scattered throughout the aggregate, but within these boundaries their influence is decisive.'

PSD changes induced by sodium chloride and calcium chloride solutions on FEBEX samples appeared comparable (Figs 2(a) and 2(b)), so that a working hypothesis that cation exchange did not induce relevant deformations was introduced, and osmotic suction π was used as a constitutive variable. According to the van't Hoff expression, osmotic suction can be written as

$$\pi = icRT \quad (2)$$

where i is the number of constituents into which the molecule separates upon dissolution ($i = 2$ for sodium chloride and $i = 3$ for calcium chloride), c is the molar concentration, R is the universal gas constant, and T is the absolute temperature.

Figure 3 shows the evolution of the microstructural void ratio e_m as a function of the osmotic suction π. Experimental data are reasonably reproduced by the expression

$$d\varepsilon_{vol}^m = \beta e^{-\alpha\pi_m} d\pi_m \quad (3)$$

being

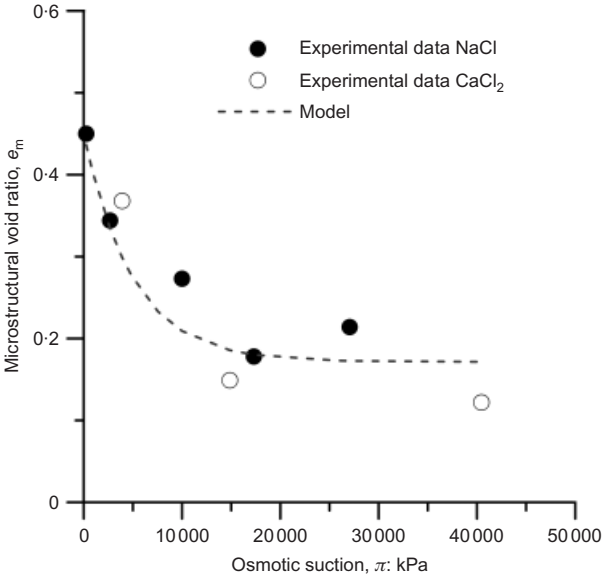

Fig. 3. Dependence of microstructural void ratio e_m on osmotic suction

$$d\varepsilon_{vol}^m = -\frac{de_m}{1+e} \quad (4)$$

where π_m is the osmotic suction of the solute in the micro-voids, ε_{vol}^m is the volumetric strain of the microstructure, and α and β are constitutive parameters of the material. The evolution of ε_{vol}^m as described by equation (3) is qualitatively similar to the predictions of the DDL theories (although the delimiting pore size of 1000 nm is well beyond the typical thickness of a double layer), and recalls the proposal of Alonso *et al.* (1994), originally formulated in terms of total suction instead of osmotic suction. Parameter calibration of equation (3) has been performed on the basis of the experimental data presented in Fig. 3, obtaining $\beta = 3{\cdot}2 \times 10^{-5}$ kPa^{-1} and $\alpha = 2{\cdot}0 \times 10^{-4}$ kPa^{-1}.

Effects of osmotic suction on hydraulic conductivity

As previously discussed, the hydraulic conductivity of bentonite samples is strongly influenced by the saline concentration of the wetting fluid (e.g. Mesri & Olson, 1971b; Calvello *et al.*, 2005; Gajo & Maines, 2007). Experimental data for the hydraulic conductivity of compacted and reconstituted FEBEX samples, saturated with saline solutions at different concentrations, are shown in Fig. 4. These values were determined by interpreting oedometer tests with Terzaghi's one-dimensional consolidation theory. Reconstituted samples were prepared by mixing FEBEX powder with saline solutions at the relevant concentration c (0·05 mol/l sodium chloride, 0·10 mol/l sodium chloride, 5·50 mol/l sodium chloride). The water content at which samples were prepared was equal to $1{\cdot}2w_L(c)$, where $w_L(c)$ is the liquid limit of the soil at a given concentration c. The pertinent values were $w_L = 105\%$ for $c = 0{\cdot}05$ mol/l, $w_L = 90\%$ for $c = 0{\cdot}10$ mol/l, and $w_L = 52\%$ for $c = 5{\cdot}5$ mol/l.

As expected, the hydraulic conductivity K increases with the global void ratio e. At a given e, K is greater the greater the saline concentration c (or the osmotic suction π). These results are in line with MIP and ESEM evidence, since the increase of the size of the inter-aggregate voids, related to higher osmotic suction, can explain the higher hydraulic conductivity. MIP evidence and the increase of K with osmotic suction (interestingly occurring also in the reconstituted samples) confirm the hypothesis of Mesri & Olson

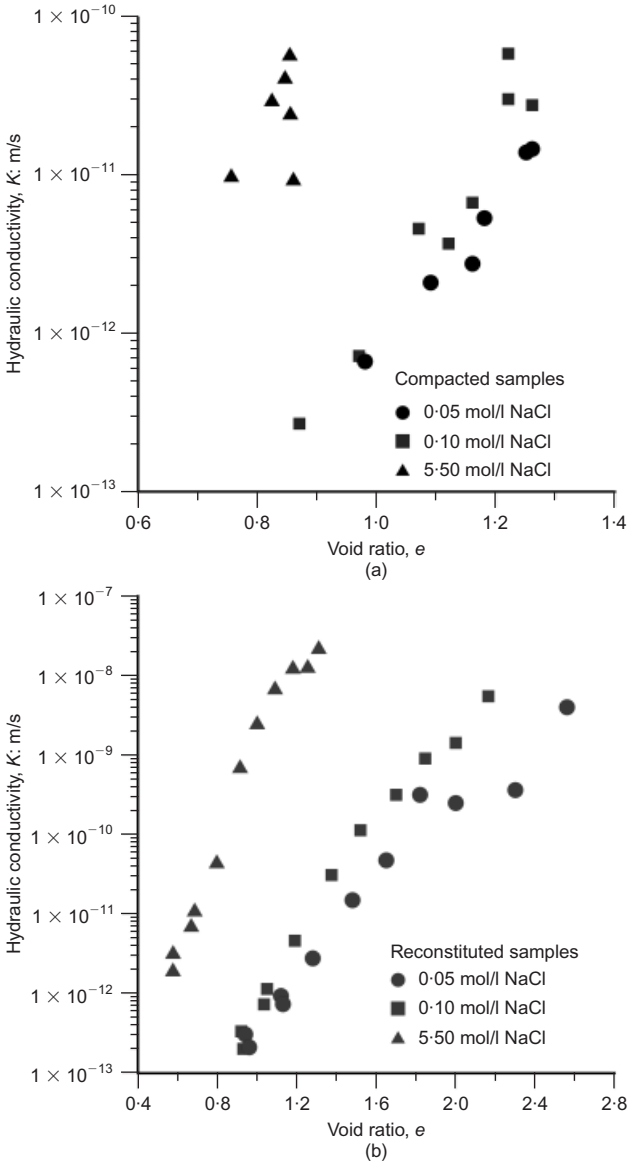

Fig. 4. Dependence of hydraulic conductivity of (a) compacted and (b) reconstituted FEBEX samples on void ratio for different salt concentrations

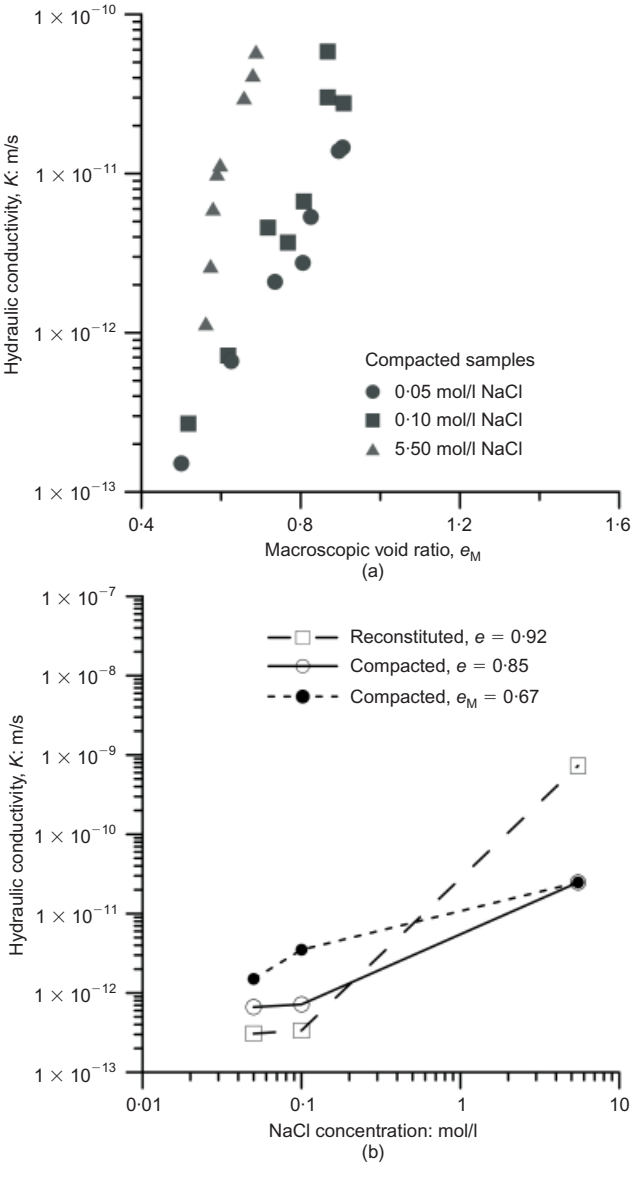

Fig. 5. Relationship between hydraulic conductivity of FEBEX samples and: (a) macrostructural void ratio e_M for different salt concentrations; (b) salt concentration at the same void ratios

(1971b) concerning the consequences of the contraction of the aggregates for permeability.

The relationship between the hydraulic conductivity and the macroscopic void ratio e_M, determined as $e_M = e - e_m$, is shown in Fig. 5(a). The microstructural void ratio e_m was assumed not to depend on the vertical effective stress applied during the test. The difference between the conductivities at different π reduces if e_M is used instead of e as a reference state variable (Fig. 5(b)).

EFFECTS OF DOUBLE STRUCTURE ON CHEMO-MECHANICAL BEHAVIOUR

Chemically induced volumetric strains

Castellanos *et al.* (2008) reported experimental data concerning the effects of salinity on the mechanical behaviour of saturated compacted FEBEX bentonite ($\rho_d = 1{\cdot}65\ \mathrm{Mg/m^3}$). Swelling tests had been performed in a conventional oedometer, soaking unsaturated samples with sodium chloride and calcium chloride solutions under a vertical total stress of 500 kPa. The results of these swelling tests provided the basis for the characterisation of the overall chemo-mechanical volumetric behaviour of compacted FEBEX bentonite, detailed in the following.

It is here assumed that the strain induced by a change of osmotic suction ($\pi_1 - \pi_0$) in a saturated sample is equal to the difference between the strains induced by saturation with fluids having osmotic suctions π_1 and π_0. The overall volumetric strain due to osmotic suction changes with respect to distilled water is thus $\varepsilon_{vol}(\pi) = \varepsilon_{sw}(\pi) - \varepsilon_{sw}(0)$, where $\varepsilon_{sw}(0)$ and $\varepsilon_{sw}(\pi)$ are the swelling strains obtained when the osmotic suction at saturation is 0 and π respectively. The experimental results organised this way are shown in Fig. 6 (closed and open symbols); the overall sensitivity to osmotic suction changes is much more pronounced at low suctions.

Interpretation of chemically induced strains in light of a double structure formulation

According to equation (1), the overall volumetric strain is the sum of the volumetric strains associated with the micro-voids and the macro-voids. Characterisation of the double-structure medium could in theory be pursued by measuring

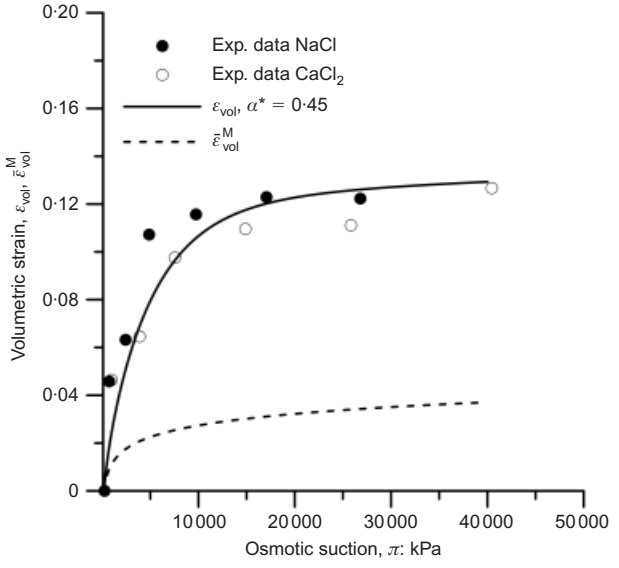

Fig. 6. Volumetric strains due to salinisation with sodium chloride (NaCl) and calcium chloride ($CaCl_2$)

the volumetric strains of the two different domains independently. In practice, this is not feasible; from external measurements it is not possible to discriminate the two different contributions. For example, during a water dilution process, both the aggregates and the soil sample swell: as a result, the volume change of the macro-voids is the difference between the volume change of the sample and that of the aggregates (micro-voids). In the limiting case of a constant-volume test, macropore volume reduction is equal and opposite to aggregate volume expansion. As a dual aspect, only a fraction α^* of aggregate strain contributes to the overall strain. The remaining fraction $(1 - \alpha^*)$ results in a reduction of the macroporosity (macro-void invasion).

In the light of the previous considerations, it is convenient to express the overall volumetric strain

$$\mathrm{d}\varepsilon_{\mathrm{vol}} = \mathrm{d}\bar{\varepsilon}^{\mathrm{M}}_{\mathrm{vol}} + \alpha^* \mathrm{d}\varepsilon^{\mathrm{m}}_{\mathrm{vol}} \tag{5}$$

where $\mathrm{d}\bar{\varepsilon}^{\mathrm{M}}_{\mathrm{vol}}$ is the volumetric strain that the macroporosity would experience at constant aggregate size. α^* can thus be interpreted as the fraction of microstructural volumetric strain that does not contribute to macropore invasion.

From a practical point of view, it is convenient to characterise the relationship between $\mathrm{d}\bar{\varepsilon}^{\mathrm{M}}_{\mathrm{vol}}$ and $\mathrm{d}\pi$ over a range of concentration where microporosity is not influenced by osmotic suction changes. Characterisation of the microstructural strains presented in equation (3) and Fig. 3 suggests that microstructural strains are negligible when π increases from 15 MPa to 40 MPa, so that characterisation of the dependence of $\mathrm{d}\bar{\varepsilon}^{\mathrm{M}}_{\mathrm{vol}}$ on π could be obtained in this range.

Under the assumption of oedometer conditions and constant vertical load, the variation of volumetric strain can be written as

$$\mathrm{d}\bar{\varepsilon}^{\mathrm{M}}_{\mathrm{vol}} = m_\pi \mathrm{d}\pi_{\mathrm{M}} \tag{6}$$

where m_π is the constitutive parameter that takes into account the compliance of the soil against osmotic suction variations. To account for non-linearity of the mechanical response, volumetric compliance has been imposed to depend on the current osmotic suction

$$m_\pi = \frac{k_\pi}{\pi_{\mathrm{M}}} \tag{7}$$

where k_π is a constant.

The value of k_π can thus be calibrated on the slope of the $\varepsilon_{\mathrm{vol}}$–$\log\pi$ data in the high-π range; as for the compacted samples, a value $k_\pi = 0{\cdot}015$ was obtained as an average value on a wider set of data available in Castellanos *et al.* (2008). In Fig. 6, the $\bar{\varepsilon}^{\mathrm{M}}_{\mathrm{vol}}$–$\pi$ curve predicted by the model is depicted by the dotted line. The difference $\alpha^* \varepsilon^{\mathrm{m}}_{\mathrm{vol}} = \varepsilon_{\mathrm{vol}} - \bar{\varepsilon}^{\mathrm{M}}_{\mathrm{vol}}$ is the fraction of microstructural swelling that contributes to the volume change of the sample.

Following Gens & Alonso (1992), it is reasonable to assume that α^* is a function of density and current stress level. If it is also assumed that the microstructural strain depends only on changes in the driving variables (i.e. in this case the osmotic suction acting within the micro-voids), once the values of k_π, α and β are known, the value of α^* for the given applied stress and initial density can be calibrated based on experimental data at low values of π. The continuous line in Fig. 6 was obtained with equation (5), using $\alpha^* = 0{\cdot}45$. An overall good reproduction of experimental data is evident.

EFFECTS OF DOUBLE STRUCTURE ON HYDRO-CHEMICAL TRANSPORT

The mechanical characterisation presented in the previous sections was pursued under well-equilibrated conditions. Stationary conditions of the deformation before experimental analyses were assumed, so as to assume that water pressure and osmotic suction in the inter-aggregate and in the intra-aggregate domain were in equilibrium.

Engineering structures are exposed to transient flux conditions, which in a double-porosity medium can easily lead to disequilibrium between the two structural levels. Under varying chemical and hydraulic conditions, a comprehensive analysis of deformation processes must then take into account the overall transport of water and salt in the medium, and how mass is exchanged between the micro- and macro-domains.

In the following, transport phenomena are modelled considering the inter-aggregate and the intra-aggregate domains as homogeneous media with different hydraulic and solute transport properties (Barrenblatt *et al.*, 1960; Warren & Root, 1963; Wilson & Aifantis, 1981). The dual-porosity medium is considered to be a superposition of these two systems over the same volume (Gerke & van Genuchten, 1993a). Microporosity ϕ_{m} and macroporosity ϕ_{M} are then defined as the volume of the corresponding pores divided by the overall volume V_{tot}.

$$\begin{aligned} \phi_{\mathrm{m}} &= \frac{V_{\mathrm{vm}}}{V_{\mathrm{tot}}} = \frac{e_{\mathrm{m}}}{1+e} \\ \phi_{\mathrm{M}} &= \frac{V_{\mathrm{vM}}}{V_{\mathrm{tot}}} = \frac{e_{\mathrm{M}}}{1+e} \end{aligned} \tag{8}$$

At each point, the hydraulic and osmotic potentials in the two continua may be different, so that salt and water can be exchanged between them. Deformation in the two domains follows from equations (3), (5) and (6).

Mass fluxes occurring completely within the microporosity are hypothesised to be negligible, so that mass of water and of solute can move from the intra-aggregate pores only towards (or from) the macroporosity. The mass balance of water for the microporosity (m) and for the macroporosity (M) is then given by

$$\frac{\partial \rho_{\mathrm{w}} \phi_{\mathrm{m}}}{\partial t} - q^{\mathrm{EX}}_{\mathrm{w}} = 0 \tag{9a}$$

$$\frac{\partial \rho_{\mathrm{w}} \phi_{\mathrm{M}}}{\partial t} + \nabla \cdot (\rho_{\mathrm{w}} v) + q^{\mathrm{EX}}_{\mathrm{w}} = 0 \tag{9b}$$

where ρ_w is the density of water, $\boldsymbol{v}$ is the volumetric flow of water relative to the solid skeleton, and q_w^{EX} is the water mass transfer term between micro- and macropores.

Similarly, the mass balance equations for the solute are

$$\frac{\partial c_m \phi_m}{\partial t} - q_s^{EX} = 0 \tag{10a}$$

$$\frac{\partial c_M \phi_M}{\partial t} + \nabla \cdot (\boldsymbol{j}) + q_s^{EX} = 0 \tag{10b}$$

where c_m and c_M are the saline concentrations in the micro- and macropores, $\boldsymbol{j}$ is the total flux of solute mass, and q_s^{EX} is the salt mass transfer term. Both q_s^{EX} and q_w^{EX} are positive when the mass exchanged is directed towards the microporosity. The exchange and transport terms used are briefly discussed in the following.

Mass exchange terms

The water and solute mass transfer terms are related to each other, being transfer of solute due to both advection and diffusion contributions. From equation (9a) with incompressible water and equation (10a) it follows that

$$\frac{\partial \phi_m}{\partial t} - \frac{q_w^{EX}}{\rho_w} = 0 \tag{11a}$$

$$\phi_m \frac{\partial c_m}{\partial t} + c_m \frac{\partial \phi_m}{\partial t} - q_s^{EX} = 0 \tag{11b}$$

and thus for consistency

$$q_w^{EX} = \frac{\rho_w q_s^{EX}}{c_m} - \frac{\rho_w \phi_m}{c_m} \frac{\partial c_m}{\partial t} \tag{12}$$

It is generally assumed that mass exchange terms are proportional to the difference between the driving potentials in the two structural levels (e.g. Gerke & van Genuchten, 1993b). In this work it was assumed that salt mass transfer is a diffusion-like phenomenon, and q_s^{EX} was defined as

$$q_s^{EX} = \chi (c_M - c_m) \tag{13}$$

where χ is a first-order transfer coefficient.

In the study of flow in saturated media with limited deformability, the first-order transfer coefficient χ is often expressed as a function of the hydraulic conductivity K (Warren & Root, 1963), through a relationship of the form

$$\chi = \chi^* \cdot K \tag{14}$$

where χ^* is a function of the geometry of the aggregates.

Figure 7 presents a conceptual scheme of the transport and exchange mechanism for different aggregate sizes (larger aggregates enhance mass exchanges between the two domains, as shown in Fig. 7(b), reducing the inter-aggregate pores and consequently the transport across the macrostructural domain). P_M and p_m represent the water pressure in the macro- and micro-structural domain, respectively.

Gerke & van Genuchten (1993a) extended the formulation to the case of unsaturated porous media, associating K to the permeability of the microporosity domain, which is a function of the degree of saturation. This observation was extended to the present case by considering that concentration changes affect the size of the microporosity domain, so that concentration was used instead of the degree of saturation. According to Romero *et al.* (1999), relative permeability is related to the size and distribution of the interconnected pores, and thus predictive equations based on PSDs make it possible to reflect this dependence. Starting

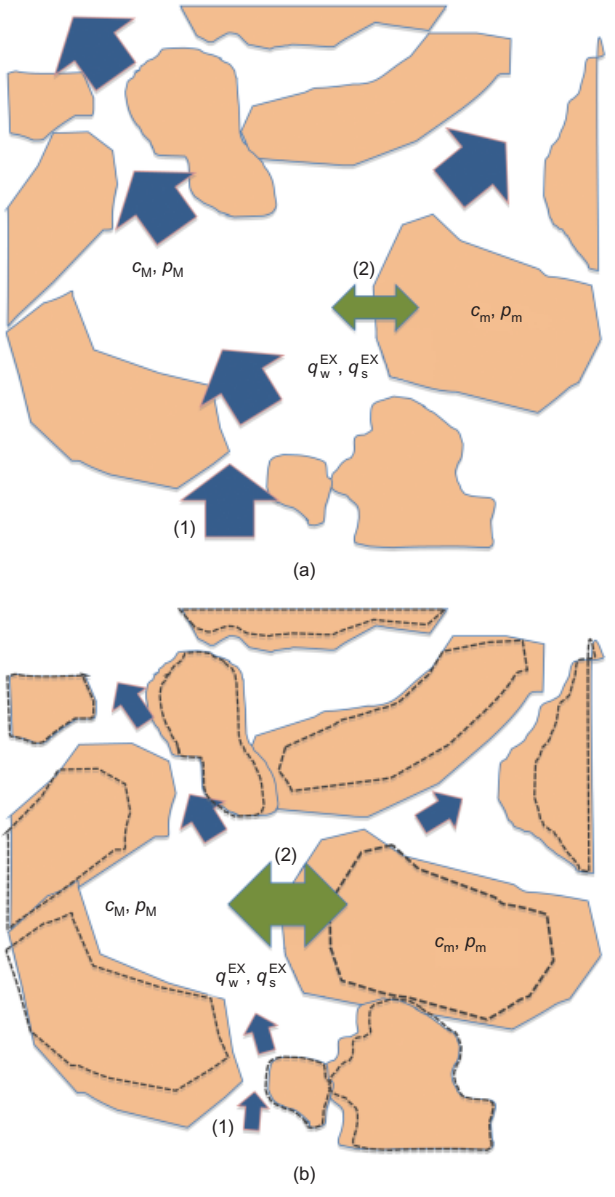

Fig. 7. Conceptual scheme of transport mechanism: (1) mass fluxes within inter-aggregate space; (2) mass exchange between inter-aggregate and intra-aggregate spaces. (a) High-suction range: aggregates have smaller dimensions; larger inter-aggregate pores enhance transport across macroscopic domain. (b) Low-suction range: larger aggregates enhance mass exchange between the two domains

from Leong & Rahardjo (1997), the role of evolving aggregates in equation (14) can be taken into account as

$$K \propto -\int_0^{x_{lim}} x^2 \frac{\partial e}{\partial x} \mathrm{d}x = f(c) \tag{15}$$

where x_{lim} is the diameter representing the threshold between microporosity and macroporosity, which earlier was set equal to 1000 nm, and $f(c)$ is a function of salt concentration. The ratio $f(c)/f(c=0)$ was evaluated for all the available PSDs, and its evolution is presented in Fig. 8. A possible mathematical equation for the transfer coefficient χ is then

$$\chi = \hat{\alpha} \exp(-\hat{\gamma} c_M) \tag{16}$$

where $\hat{\alpha}$ and $\hat{\gamma}$ are two parameters to be calibrated on the phenomenological response of the material.

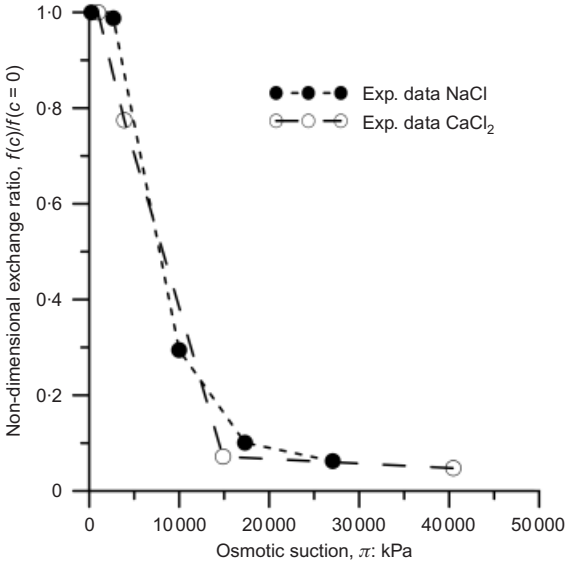

Fig. 8. Normalisation of transfer term at given concentration with respect to null concentration condition. Transfer terms are hypothesised to depend on permeability of microstructure, reconstructed on MIP measurements

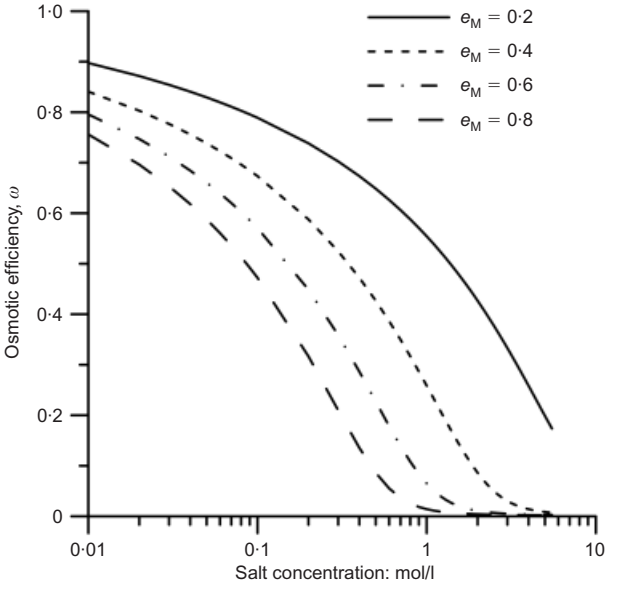

Fig. 9. Dependence of osmotic efficiency ω on salt concentration (two monovalent species) and on macroscopic void ratio for FEBEX bentonite. Interpretation based on data of Bresler (1973), using external specific surface of soil

Fluxes of water and solute

Water and salt flow through the macrostructure was formulated following the theory of irreversible thermodynamics, introducing a number of coupled flows (e.g. Yeung & Mitchell, 1993; Manassero & Dominijanni, 2003; Lu *et al.*, 2004). Neglecting the presence of electrical gradients, water flow is driven by the gradients of both hydraulic and osmotic potentials

$$\boldsymbol{v} = -\frac{K_{\mathrm{M}}}{\rho_{\mathrm{w}}\boldsymbol{g}}\nabla(p_{\mathrm{M}} + \rho_{\mathrm{w}}\boldsymbol{g}z) + \frac{K_{\pi}}{\rho_{\mathrm{w}}\boldsymbol{g}}\nabla(\pi_{\mathrm{M}}) \tag{17}$$

where $\boldsymbol{g}$ is gravitational acceleration, K_{M} is macrostructural hydraulic conductivity, and K_{π} is osmotic permeability. The latter is related to the former by the coefficient of osmotic efficiency, ω (e.g. Mitchell & Soga, 2005), so that $K_{\pi} = \omega K_{\mathrm{M}}$.

The experimental data of Bresler (1973) concerning the dependence of osmotic efficiency ω on salt concentration in the macro-voids c_{M} were expressed through a suitable fitting expression

$$\log\omega = B - \arctan\left\{A\left[\log\left(10b\sqrt{c_{\mathrm{M}}}\right) + C\right]\right\} \tag{18}$$

where b is the half-distance between soil particles. If b is expressed in nm and c_{M} in normality (for dominant monovalent cations, equivalent to mol/l), it follows that $A = 5{\cdot}5$, $B = -1{\cdot}5$ and $C = -1{\cdot}3$ for salts with monovalent cations. Since in this work the osmotic flow is assumed to occur only through the macropores, b was estimated from the specific surface of the solid particle S_{S} and the void ratio of the macropores e_{M} (Mitchell & Soga, 2005) according to

$$b = \frac{1}{2}\frac{e_{\mathrm{M}}}{S_{\mathrm{S}}\rho_{\mathrm{S}}} \tag{19}$$

where ρ_{S} is the density of the solid particles; then b is here the average half-distance between aggregates. Fig. 9 shows the evolution of the osmotic coefficient as a function of salt concentration in the macropores, for different void ratios.

The salt flow in the macropores, $\boldsymbol{j}$, is due to both advection and diffusion. Neglecting the movement of the solid phase with respect to the reference configuration, it can be written as

$$\boldsymbol{j} = c_{\mathrm{M}}(1-\omega)\boldsymbol{v} - D_{\mathrm{M}}\nabla c_{\mathrm{M}} \tag{20}$$

where D_{M} is the effective diffusion coefficient, accounting for the effects of porosity, tortuosity, osmotic efficiency and retardation. In the following the term D_{M} will be expressed as $D_{\mathrm{M}} = (1-\omega)D_{\mathrm{M0}}$, where D_{M0} is the effective diffusion coefficient in the absence of osmotic effects.

APPLICATION OF THE FRAMEWORK

The double-porosity framework was applied to simulate a salt diffusion test run in an oedometer at constant vertical stress. The aim of the simulation was to verify the capabilities of the framework in capturing the main features of the mechanical and transport processes induced by desalinisation and subsequent salinisation. The simulated test was performed in a modified oedometer cell, which connects each porous stone with a reservoir aimed at hosting small quantities of solution (Fig. 10). Concentration evolution in the reservoirs was estimated on the basis of electrical conductivity measurements, by converting electrical conductivity into equivalent concentrations of sodium chloride (e.g. Shackelford *et al.*, 1999).

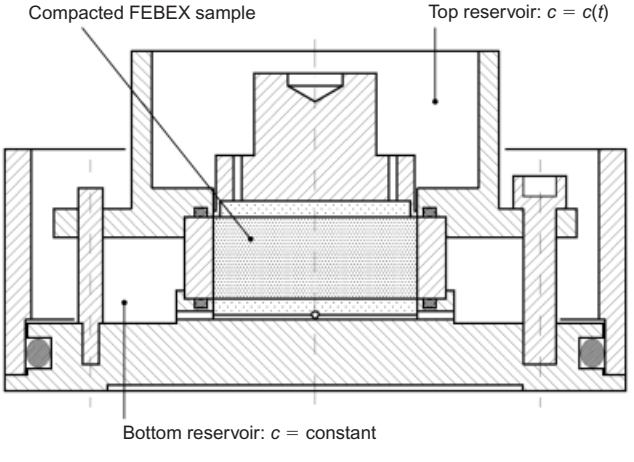

Fig. 10. Modified oedometer cell used for desalinisation–salinisation test

A sample 10·5 mm high was prepared by statically compacting the FEBEX material to a dry density $\rho_d = 1{\cdot}68$ Mg/m^3 at hygroscopic water content $w = 12\%$. The sample was placed in the oedometer and loaded (total vertical stress $\sigma_v = 200$ kPa). Saturation was induced by pouring into the two reservoirs a 5·5 mol/l sodium chloride solution and letting the sample swell accordingly. Once strain equilibrium was achieved, the saline solution was removed from the bottom reservoir, and replaced with distilled water. To ensure constant concentration conditions, this operation was repeated daily. As a consequence of the induced water and salt fluxes, salt concentration diminished in the sample and in the upper reservoir. This was evidenced by chemo-mechanical swelling, and by a progressive drop of the electrical conductivity in the top reservoir. To compensate for the volume of water lost upon evaporation, the original volume of the solution in the reservoir was maintained constant by adding distilled water. Once swelling and electrical conductivity drop had stopped, the bottom reservoir was filled with a 5·5 mol/l sodium chloride solution to revert the process. The test lasted about 1 year.

Simulation of the test was performed by way of finite-element solution of the balance equations (equations (9) and (10)). One-dimensional parabolic elements for both the salt and water mass balances were used. The physical evidence adopted as a reference for the verification of the framework comprised the evolution of the vertical displacement and of the sodium chloride concentration in the top reservoir. As for the latter, the volume of the reservoir influences the concentration and transport of salt, so that to track concentration evolution the reservoir was also simulated as a porous medium with very high hydraulic conductivity and a diffusion coefficient equal to the free diffusion coefficient of sodium chloride in water ($D = 1{\cdot}9 \times 10^{-9}$ m^2/s). The porosity of the dummy porous medium was selected in order to have a volume of voids equal to the volume of the reservoir. At the contact between the reservoir and the sample, a no-jump condition in terms of the normal component of the total flux of the salt and water was imposed (Bear & Cheng, 2010). At the upper boundary of the reservoir a no-flux condition for both water and salt was imposed. The scheme of the media and boundary conditions introduced is given in Fig. 11.

Time zero of the simulation was the end of saturation. The initial total and microstructural void ratios were set equal to $e_0 = 0{\cdot}72$ (corresponding to the initial dry density) and $e_{m0} = 0{\cdot}17$ (according to the MIP interpretation of Fig. 3). Consequently, the macroscopic void ratio was calculated as $e_{M0} = e_0 - e_{m0} = 0{\cdot}55$. In both the microstructural and macrostructural domain, the initial chemical condition was $c_{m0} = c_{M0} = 5{\cdot}5$ mol/l, and atmospheric hydraulic pressure was imposed.

The parameter values used for the simulation are presented in Table 2. The hydraulic and mechanical parameters were directly derived from the analysis given in the previous sections, which refer to independent tests performed on the same material. This holds for: the hydraulic conductivity K_M (a constant average value for the porosity of interest was chosen; see Fig. 5); the parameters describing the evolution

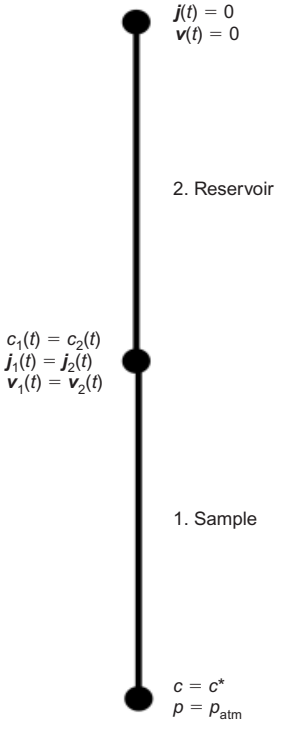

Fig. 11. Boundary condition for simulation of desalinisation–salinisation test

of the microstructural void ratio upon osmotic suction changes, α and β (Fig. 3 and equation (3)); the parameter describing the mechanical interaction between the micro- and macrostructure, α^* (Fig. 6 and equation (5)); and the compressibility of the macrostructure, k_π (Fig. 6 and equation (6)). The effective diffusion coefficient of the macrostructure, D_{M0}, was chosen according to literature data for this type of material and density (Bourg *et al.*, 2006), and the osmotic efficiency ω was set to depend on the macrostructural void ratio and concentration, as in equations (18) and (19). The parameters of the first-order transfer function (equation (16)), $\hat{\alpha}$ and $\hat{\gamma}$, were instead calibrated through back-analysis on the recorded displacement evolution along desalinisation.

Good agreement between the simulated and measured vertical displacements of the sample upon chemical cycling was obtained (Fig. 12). Consistent results were also obtained in terms of the time evolution of the measured and simulated salt concentrations in the upper reservoir (Fig. 13).

DISCUSSION

The results of the simulation can be used to outline the main effects imparted by the structural arrangement to the history of concentrations and strains.

The histories of vertical displacements and the salt concentration measured within the top reservoir appear to depend strongly on the direction of chemical loading. Both

Table 2. Parameters used in the simulation

Mechanical parameters				Transport parameters			
Microstructure compressibility: kPa^{-1}		Macrostructure logarithmic osmotic compliance, k_π	Interaction function, α^*	Hydraulic conductivity, k_M: m/s	Effective diffusion, D_{M0}: m^2/s	Transfer function	
α	β					$\hat{\alpha}$: s^{-1}	$\hat{\gamma}$: l/mol
$2{\cdot}0 \times 10^{-4}$	$3{\cdot}2 \times 10^{-5}$	0·015	0·45	5×10^{-12}	9×10^{-11}	0·8	8

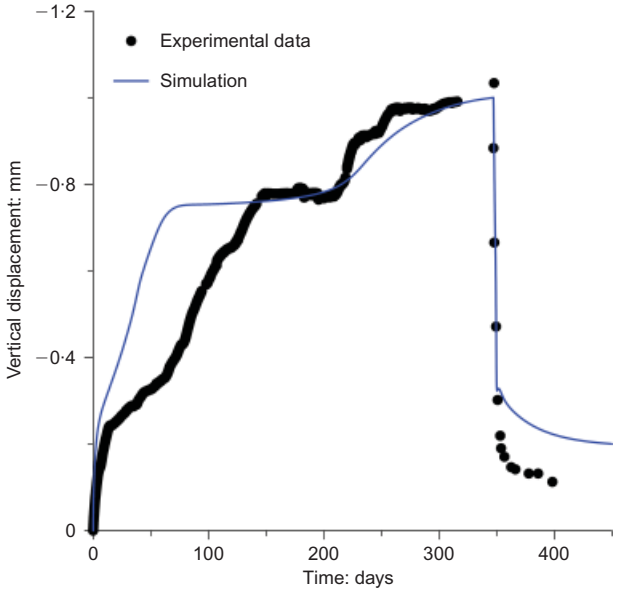

Fig. 12. History of vertical displacements during salinisation–desalinisation test (negative displacements mean sample swelling)

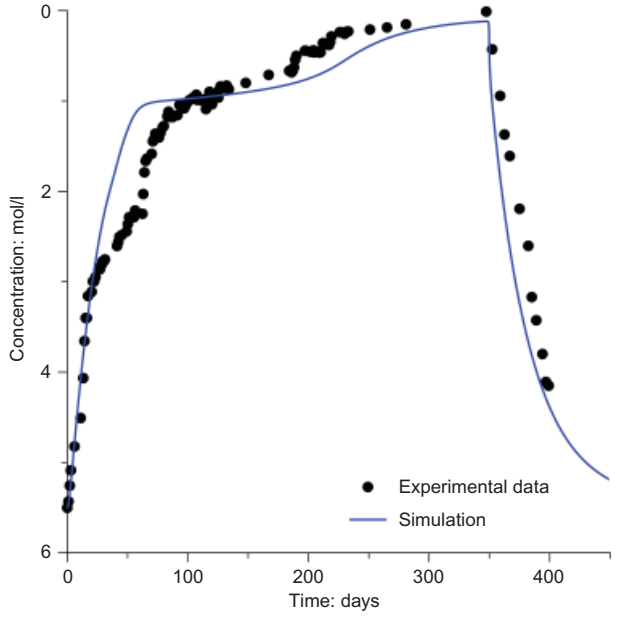

Fig. 13. History of sodium chloride concentration in upper (free) reservoir during salinisation–desalinisation test

deformations and concentration evolve more rapidly upon salinisation than upon desalinisation. This is especially evident for the history of deformations, with a difference in timescales of about 1/10. Similar evidence has been previously noted by several authors working on reconstituted specimens of different active clays (e.g. Barbour & Fredlund, 1989; Di Maio, 1996; Gajo & Maines, 2007). The fact that deformation proceeds quite continuously in a single stage during salinisation (shrinkage), and very discontinuously in different stages upon desalinisation (swelling), as shown in Fig. 12, is also remarkable. This aspect does not pertain to reconstituted soils, but is reported in previous experimental works on compacted FEBEX samples (Musso *et al.*, 2003). An analogous phenomenon has been documented by Rao & Thyagaraj (2007), who performed a series of tests on Indian active clay: specimens were prepared at different saline contents, compacted in unsaturated conditions and then saturated with distilled water under a small seating load. In their work, Rao & Thyagaraj (2007) identified two swelling stages for specimens prepared at low salt contents, and a third swelling stage emerging at longer times for specimens prepared at high salt content. Since the first swelling stage was due to the dissipation of matric suction, in Rao & Thyagaraj (2007) chemical swelling also occurs in a single stage when the initial salt content is low, and in two or more stages when the initial salt content is high.

Tracking of the deformation and of concentration induced by changes in the chemical boundary conditions is complicated by the several coupled transport processes, and by the different ways through which deformation can arise. Strains can arise because of osmotic suction changes (*osmotic consolidation* according to Barbour & Fredlund, 1989), and because of transient water flow caused by osmotic gradients (*osmotically induced consolidation* according to Barbour & Fredlund, 1989). Darcian flow associated with pore pressure variations, due to constrictions caused by the low permeability, and advective flow of the dissolved chemical further influence the deformation pattern (Kaczmarek & Hueckel, 1998; Peters & Smith, 2004).

Profiles of e_M and e_m at different times can be useful in understanding the evolution of the deformation process, and possibly the structural arrangement, as foreseen by the model. During the first 5 days, displacement progresses at a relatively fast rate (Fig. 12). The dominant role of e_M, whose increment is more noticeable in the lower part of the sample, although also appreciable at the upper side, is evidenced in Fig. 14(a). By contrast, the increase of e_m is limited to the bottom 3 mm of the sample (Fig. 14(b)). Taking as a reference the time interval between 2·5 and 5 days, the model predicts that, in the bottom part of the sample, e_M will progressively reduce while e_m increases; swelling aggregates are progressively invading the inter-aggregate porosity (as depicted in the conceptual scheme in Fig. 7(a)). The delayed deformation of the microstructure is associated with a slow release of salt towards the macrostructure, or, in other words, with values of microstructural osmotic suction remaining high, compared with the macrostructural values (Fig. 15). Indeed, since the salt concentration is initially high, the density of pores with size smaller than 1000 nm is low, and the transfer term χ is very small. Therefore, despite significant differences in suction, transfer of mass between the inter-aggregate and the intra-aggregate pore space occurs very slowly.

After 45 days, the macrostructural and microstructural suctions have about the same value (Fig. 15); this occurs while χ attains higher values, so that mass can be transferred more easily between the two structural levels. Between $t = 90$ days and $t = 240$ days, vertical displacements are about stable. Vertical displacements increase again significantly when t is greater than 240 days, clearly as a consequence of the higher sensitivity of both microstructural and macrostructural deformations to suction changes in the low-suction range (see Figs 3 and 6). Macroporosity is further invaded by swelling aggregates, and e_M globally reduces to values smaller than the initial ones (Fig. 14). Also, the salt concentration in the upper reservoir first attains a quasi-constant value and then starts to increase again (after approximately 200 days; Fig. 12). In the light of the hypothesis concerning the mass transfer coefficient, the increase in concentration occurring after 200 days could correspond to an easier release of mass from the microporosity to the macroporosity, and then from the latter to the reservoir (refer to the conceptual scheme of Fig. 7).

According to the analysis, hydraulic pressure within the macrostructure is not constant in space and time (Fig. 16), but nevertheless remains limited between −20 kPa and

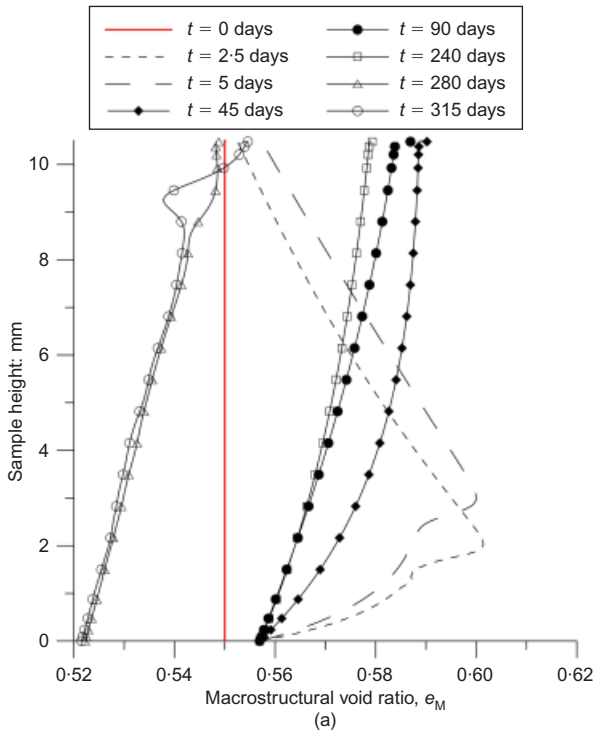

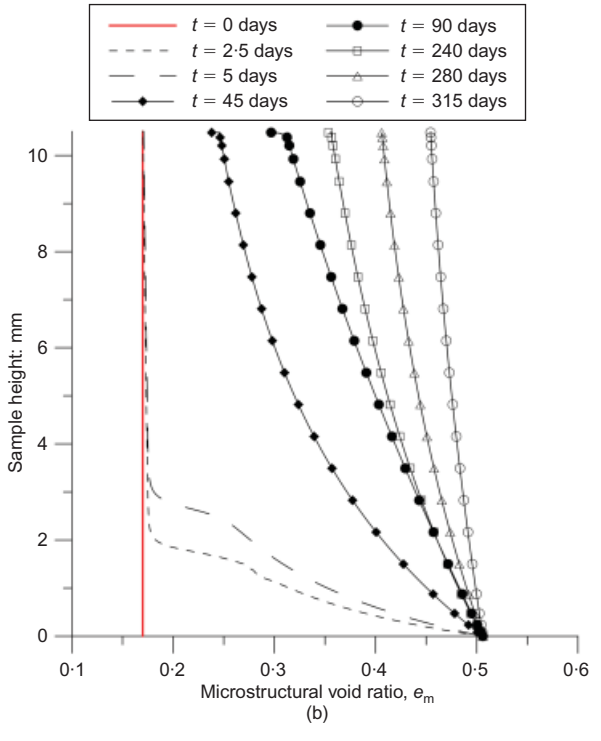

Fig. 14. Evolution of void ratios during desalinisation: (a) macrostructural, e_M; (b) microstructural, e_m

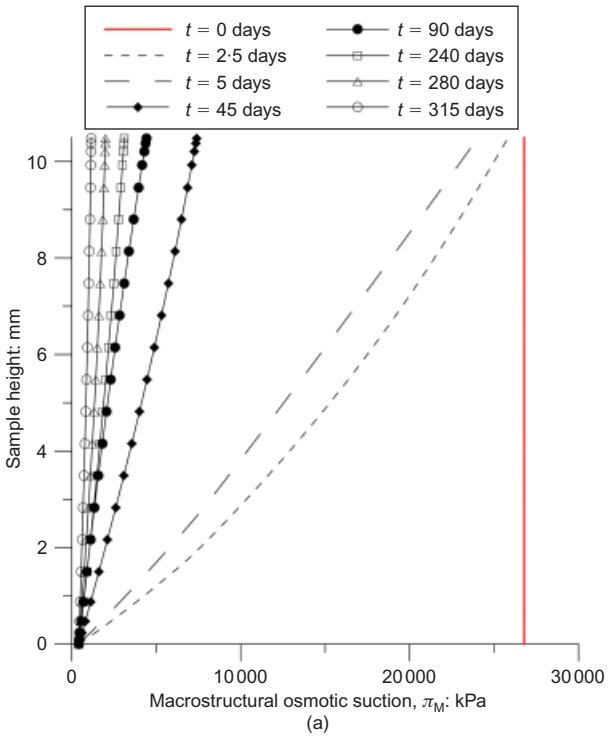

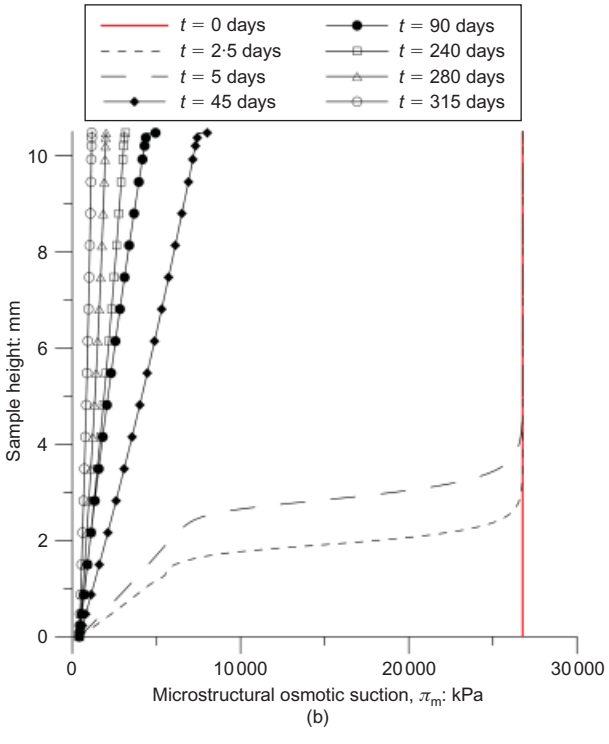

Fig. 15. Evolution of osmotic suction during desalinisation: (a) macrostructural, π_M; (b) microstructural, π_m

20 kPa. Notwithstanding the small pressure gradient developed, the Darcian and osmotic flow at the centre of the sample (at an elevation of 5 mm) would be of about the same magnitude. Indeed, although the osmotic gradients are quite high, the osmotic flow is nevertheless small, by virtue of the very low values of the predicted osmotic efficiency (Fig. 17(a)). As a whole, despite the existence of other transport forces, at the centre of the sample diffusion remains the dominant transport mechanism (Fig. 17(b)).

After 350 days, on the basis of the external measurements, swelling and transport were assumed to have come to an end, although according to the simulation small concentration gradients still existed. A 5·5 mol/l sodium chloride solution was then poured into the bottom reservoir, favouring osmotic and osmotically induced consolidation: as commented, shrinkage was faster than swelling. This is explained both by the steeper relationship between volumetric strain and osmotic suction at moderate suction values (Fig. 6) and by the shape of the first-order exchange function, which allows exchanges of mass to occur at a faster rate at low suctions (conceptual scheme of Fig. 7). In a short time e_m would reduce noticeably (see curves referring to days 351 and 352 in Fig. 18); e_M would initially increase, and then reduce at longer times. The microstructural osmotic suction

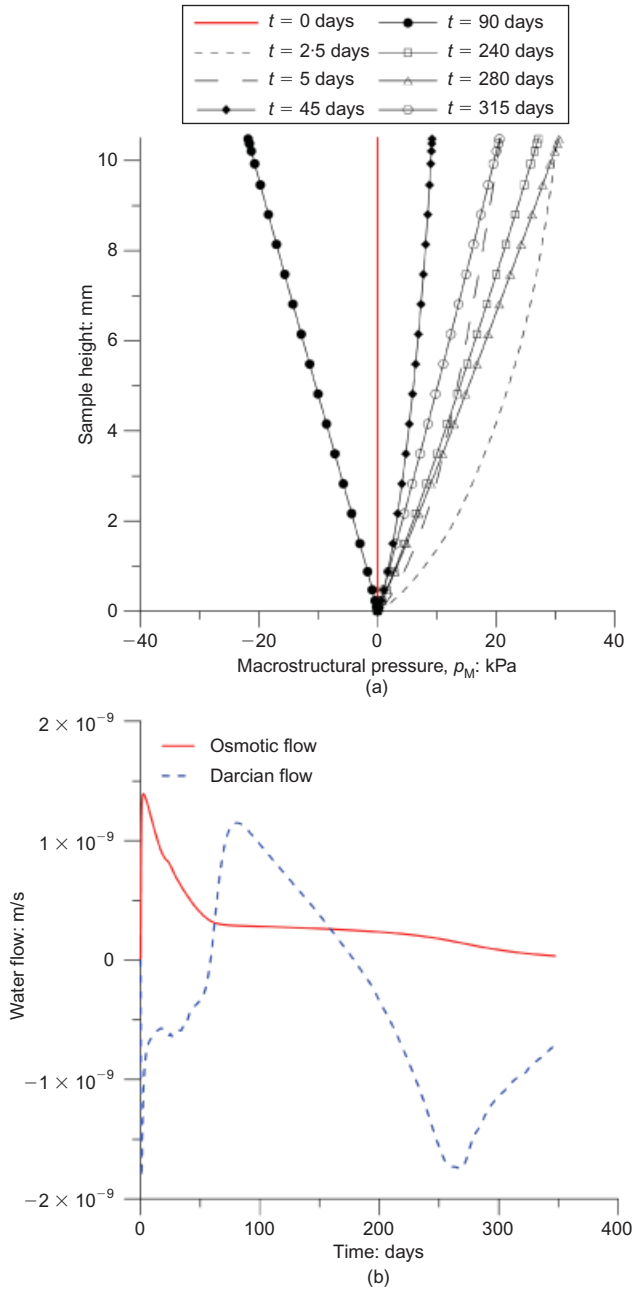

Fig. 16. Profiles of (a) macrostructural water pressure and (b) water flow in macrostructure at centre of specimen (height 5 mm)

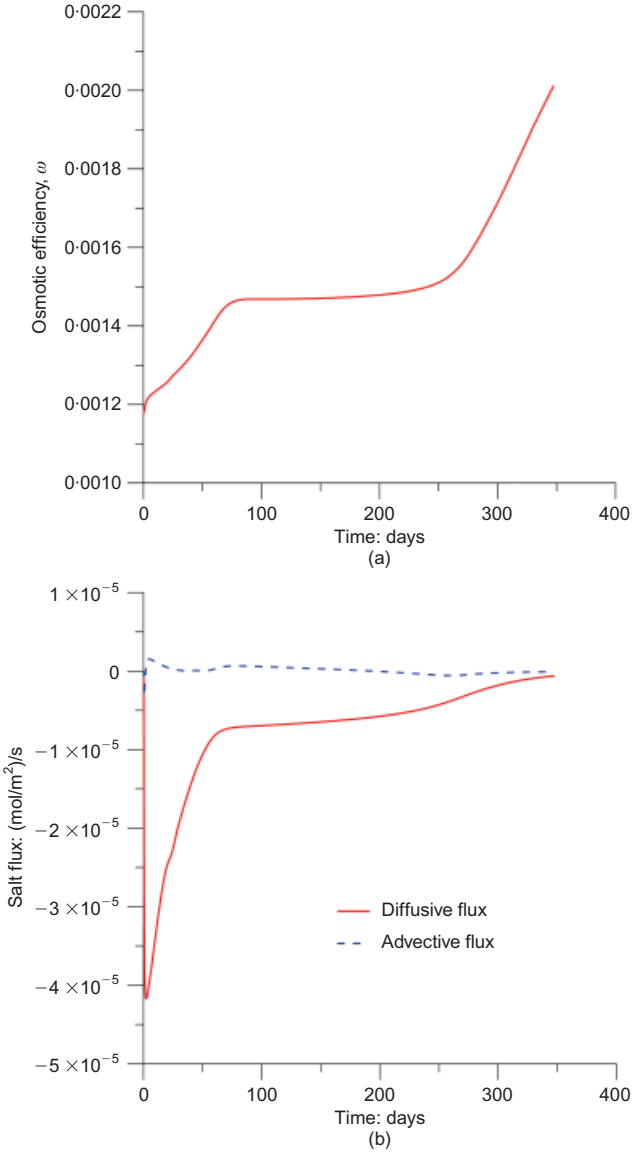

Fig. 17. History of (a) osmotic efficiency ω and (b) salt fluxes at centre of specimen (height 5 mm)

π_m increases quite significantly within the first 5 days from the beginning of salinisation (Fig. 19), giving rise to a significant reduction of microporosity. It appears that the faster transfer of mass between the structural levels, and the marked dependence on suction of the void ratios, favour deformations proceeding continuously and without jumps. Vertical displacements foreseen by the simulation are in good agreement with experimental data between 350 and 360 days, but are smaller at longer times (Fig. 12). According to the simulation, shrinkage of the aggregates would be more difficult after 360 days, and the predicted microstructural void ratio would remain roughly constant between 360 and 400 days. Despite the fact that after 400 days the displacements seem to have ceased, the values of the osmotic suction provided by the numerical simulation would suggest that equilibrium between pressures in the microporosity and in the macroporosity had not been reached yet, so that further aggregate shrinkage and positive displacements could have occurred for longer testing times. Although not perfectly reproduced by the simulation, the actual final height of the specimen was greater than the initial one, a phenomenon that could be associated with residual salt in the micro-voids.

Very interestingly, the history of concentrations also shows different timescales depending on the direction of the salinisation process. This hydro-geochemical hysteresis, as documented by van Genuchten & Cleary (1982), can also be attributed to double-structure effects, related to the existence of soil aggregates.

CONCLUSIONS

Microstructural evidence, collected after exposing compacted samples to saline solutions with increasing concentrations, suggests that a double-structure frame could be used to reproduce the chemo-hydro-mechanical behaviour of compacted active clays. After introducing a simple criterion to discriminate between microporosity and macroporosity, pore size distribution data were used to calibrate a relationship between osmotic suction and microstructural void ratio. Swelling under load testing was used instead to relate osmotic suction to the overall void ratio.

An associated double-structure transport model was identi-

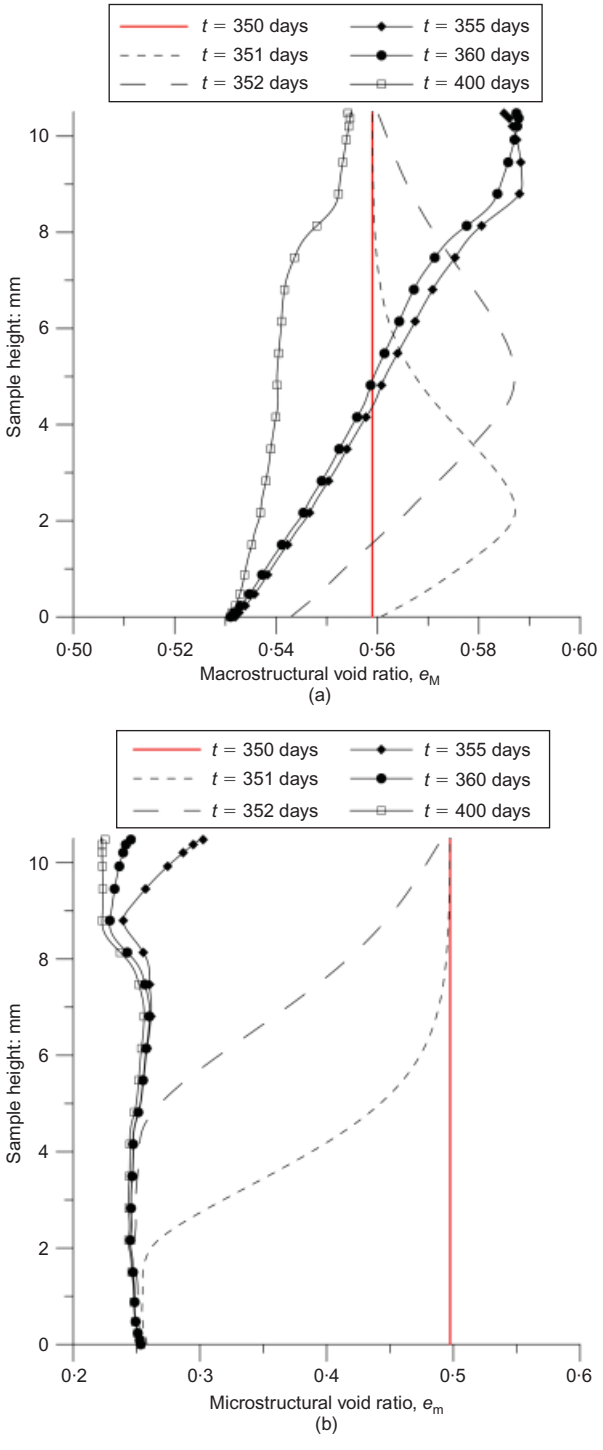

Fig. 18. Evolution of void ratios during salinisation: (a) macrostructural, e_M; (b) microstructural, e_m

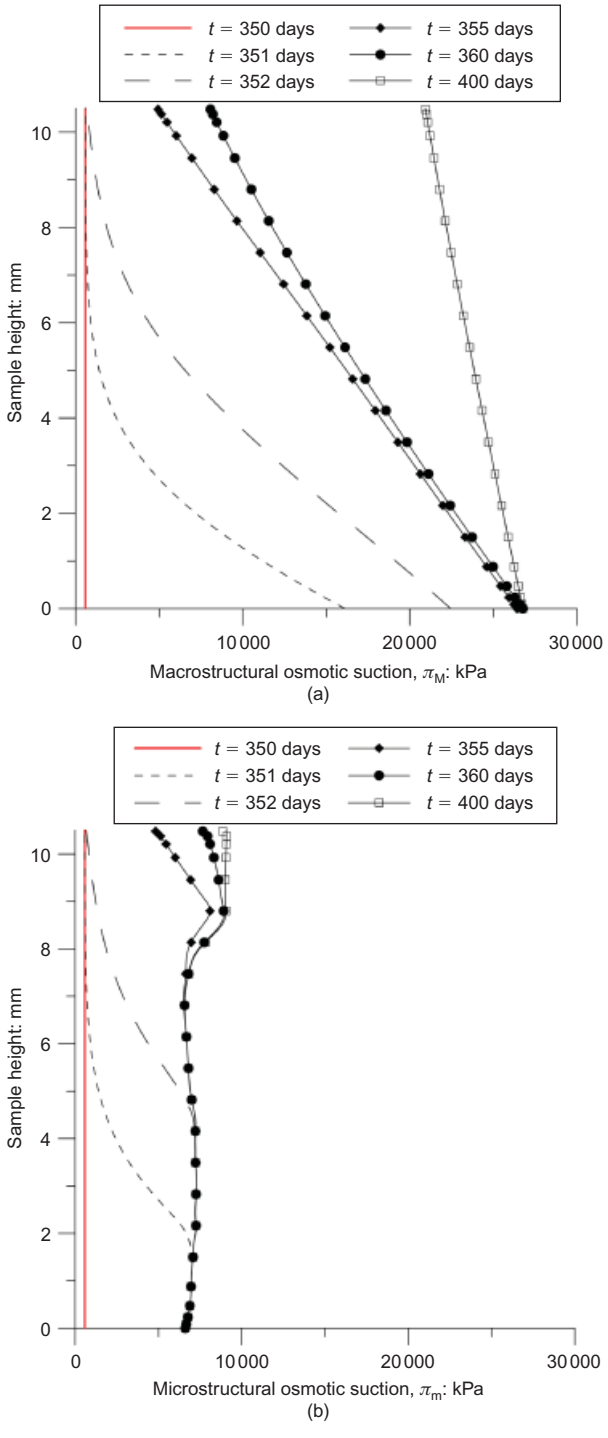

Fig. 19. Evolution of osmotic suction during salinisation: (a) macrostructural, π_M; (b) microstructural, π_m

fied and calibrated on the same microscopic data, introducing the working assumption that aggregates do not communicate one with another. The model was used to simulate the results of a salinisation–desalinisation test, during which both displacements and concentrations were recorded. Both concentration and displacement histories appear to be well reproduced by the simulation.

Simulation results support the hypothesis that effects induced by an evolving double structure take place when compacted active clays are exposed to transient chemical changes. The framework shows that, even though the overall void ratio increases upon decrease of the osmotic suction, the macroscopic void ratio can reduce. This could justify the observed decrease in water permeability. As for the history of displacement upon salinisation cycles, double-structure effects can explain both the occurrence of the development of swelling in the different stages and of the significantly different times required to complete the swelling and shrinkage processes. The consistency between the mechanical and hydraulic features of the model also ensures the reproduction of similar hysteretic aspects associated with the transport mechanisms, as documented by histories of concentrations recorded during the test.

Double-structure features, whose effects on the behaviour of compacted active clays in unsaturated conditions had already been documented, appear to have a similar influence on the chemo-mechanical behaviour. These results suggest

that problems where chemical and saturation changes are expected could be analysed by adopting a unique framework.

As a final point, the model has also allowed complementing and better exploitation of information on the evolutionary processes at the local scale that are beyond the measurable experimental scale of the macroscopic oedometer test performed.

ACKNOWLEDGEMENTS

The authors acknowledge the support of the Ministero dell'Università, dell'Istruzione e della Ricerca through research grant Prin 2008B5T829. Travel expenses were also covered, with research grant HI2008-0038/IT09D4L2L1 (Azione Integrata Italia Spagna 2009 of the Ministerio de Ciencia e Innovación and of the Ministero dell'Università, dell'Istruzione e della Ricerca). The authors acknowledge the contribution of Ernesto Castellanos for carrying out the mercury intrusion tests on compacted FEBEX bentonite.

NOTATION

b half-distance between soil particles/aggregates
c molar concentration
c_M molar concentration in macropores
c_{M0} initial molar concentration in macropores
c_m molar concentration in micropores
c_{m0} initial molar concentration in micropores
D diffusion coefficient
D_M effective diffusion coefficient in the macropores
D_{M0} effective diffusion coefficient in the macropores in the absence of osmotic effects
e total void ratio
e_0 initial total void ratio
e_M macrostructural void ratio
e_{M0} initial macrostructural void ratio
e_m microstructural void ratio
e_{m0} initial microstructural void ratio
$f(c)$ function of salt concentration
$\boldsymbol{g}$ gravitational acceleration
i number of constituents into which molecule separates upon dissolution
$\boldsymbol{j}$ total flux of solute mass
K hydraulic conductivity
K_M macrostructural hydraulic conductivity
K_π osmotic permeability
k_π macrostructural logarithmic compliance against osmotic suction changes
m_π macrostructural osmotic compressibility
p water pressure
p_{atm} atmospheric pressure
p_M macrostructural water pressure
p_m microstructural water pressure
q_s^{EX} salt mass transfer term
q_w^{EX} water mass transfer term
R universal gas constant
S_r degree of saturation
S_S specific surface
T absolute temperature
t time
V_s volume of solids
V_{tot} overall volume
V_{vM} volume occupied by macro-voids
V_{vm} volume occupied by micro-voids
υ volumetric flow of water relative to solid skeleton
w water content
w_L liquid limit of soil
$w_L(c)$ liquid limit of soil at concentration c
w_P plastic limit of soil
x entrance pore diameter
x_{lim} diameter representing threshold between microporosity and macroporosity
α, β constitutive material parameters
α^* fraction of aggregate strain not contributing to macropores invasion
$\varepsilon_{sw}(\pi)$ swelling strain when osmotic suction at saturation $= \pi$
$\varepsilon_{sw}(0)$ swelling strain when osmotic suction at saturation $= 0$
ε_{vol} overall volumetric strain
ε_{vol}^m volumetric strain of microstructure
$d\bar{\varepsilon}_{vol}^M$ volumetric strain that macroporosity would experience at constant aggregate size
π_M osmotic suction of solute in macro-voids
π_m osmotic suction of solute in micro-voids
ρ_d dry density
ρ_S density of solid particles
ρ_w density of water
σ_v total vertical stress
ϕ_M macroporosity
ϕ_m microporosity
χ first-order transfer coefficient
ω osmotic efficiency

REFERENCES

Alonso, E. E., Gens, A. & Gehling, W. (1994). Elastoplastic model for unsaturated expansive soils. *Proc. 3rd Eur. Conf. on Numer. Methods Geotech. Engng, Manchester*, 11–18.

Atabek, R., Felix, B., Robinet, J.-C. & Lahlou, R. (1991). Rheological behaviour of saturated expansive clay materials. *Proceedings of the workshop on stress partitioning in engineered clay barriers*, Durham, NC, pp. 1–12

Barbour, S. L. & Fredlund, D. G. (1989). Mechanisms of osmotic flow and volume change in clay soils. *Can. Geotech. J.* **26**, No. 4, 551–562.

Barrenblatt, G. I., Zheltov, I. P. & Kochina, I. N. (1960). Basic concepts in the theory of seepage of homogeneous liquids in fissured rocks. *J. Appl. Math. Mech*. **24**, No. 5, 1286–1303.

Bear, J. & Cheng, A. H. D. (2010). *Modeling groundwater flow and contaminant transport*. Dordrecht, the Netherlands: Springer.

Bolt, G. H. (1956). Physico-chemical analysis of the compressibility of pure clays. *Géotechnique* **6**, No. 2, 86–93.

Bourg, I. C., Sposito, G. & Bourg, A. C. M. (2006). Tracer diffusion in compacted, water-saturated bentonite. *Clays Clay Miner.* **54**, No. 3, 363–374.

Bresler, E. (1973). Anion exclusion and coupling effects in nonsteady transport through unsaturated soils. I: Theory. *Soil Sci. Soc. Am. Proc*. **37**, No. 5, 663–669.

Calvello, M., Lasco, M., Vassallo, R. & Di Maio, C. (2005). Compressibility and residual shear strength of smectitic clays: influence of pore aqueous solutions and organic solvents. *Riv. Ital. Geotec*. **39**, No. 1, 34–46.

Castellanos, E., Gens, A., Lloret, A. & Romero, E. (2006). Influence of water chemistry on the swelling capacity of a high-density bentonite. *Proc. 4th Int. Conf. on Unsaturated Soils, Carefree, AZ*, 962–972.

Castellanos, E., Villar, M. V., Romero, E., Lloret, A. & Gens, A. (2008). Chemical impact on the hydro-mechanical behavior of high-density FEBEX bentonite. *Phys. Chem. Earth* **33**, Supplement 1, S516–S526.

Delage, P., Tessier, D. & Audiguier, M. M. (1982). Use of the cryoscan apparatus for observation of freeze-fractured planes of a sensitive Quebec clay in scanning electron microscopy. *Can. Geotech. J.* **19**, No. 1, 111–114.

Delage, P. & Romero, E. (2008). Geoenvironmental testing. *Geotech. Geol. Engng* **26**, No. 6, 729–749.

Della Vecchia, G. (2009). *Coupled hydro-mechanical behaviour of compacted clayey soils*. PhD thesis, Politecnico di Milano, Italy.

Della Vecchia, G., Jommi, C. & Romero, E. (2012). A fully coupled elastic–plastic hydromechanical model for compacted soils accounting for clay activity. *Int. J. Numer. Anal. Methods Geomech*. http://dx.doi.org/10.1002/nag.1116.

Di Maio, C. (1996). Exposure of bentonite to salt solution: osmotic and mechanical effects. *Géotechnique* **46**, No. 4, 695–707, http://dx.doi.org/10.1680/geot.1996.46.4.695.

Di Maio, C. & Fenelli, G. B. (1997). Influenza delle interazioni chimico-fisiche sulla deformabilità di alcuni terreni argillosi. *Riv. Ital. Geotec*., No. 1, 44–57 (in Italian).

ENRESA (2000). *FEBEX Project: Full-scale engineered barriers experiment for a deep geological repository for high level radioactive waste in crystalline host rock: Final report*, Technical Publication ENRESA 1/2000. Madrid, Spain: ENRESA.

Fernandez, F. & Quigley, R. M. (1985). Hydraulic conductivity of natural clays permeated with simple liquid hydrocarbons. *Can. Geotech. J.* **22**, No. 2, 205–214.

Fernandez, F. & Quigley, R. M. (1988). Viscosity and dielectric constant controls on the hydraulic conductivity of clayey soils permeated with water-soluble organics. *Can. Geotech. J.* **25**, No. 3, 582–589.

Gajo, A. & Maines, M. (2007). Mechanical effects of aqueous solutions of inorganic acids and bases on a natural active clay. *Géotechnique* **57**, No. 8, 687–699, http://dx.doi.org/10.1680/geot.2007.57.8.687.

Gens, A. & Alonso, E. E. (1992). A framework for the behaviour of unsaturated expansive clays. *Can. Geotech. J.* **29**, No. 6, 1013–1032.

Gerke, H. H. & van Genuchten, M. T. (1993a). A dual-porosity model for simulating the preferential movement of water and solutes in structured porous media. *Water Resour. Res*. **29**, No. 2, 305–319.

Gerke, H. H. & van Genuchten, M. T. (1993b). Evaluation of a first-order water transfer term for variably saturated dual-porosity flow models. *Water Resour. Res*. **29**, No. 4, 1225–1238.

Hueckel, T., Kaczmarek, M. & Caramuscio, P. (1997). Theoretical assessment of fabric and permeability changes in clays affected by organic contaminants. *Can. Geotech. J.* **34**, No. 4, 588–603.

Kaczmarek, M. & Hueckel, T. (1998). Chemo-mechanical consolidation of clays: analytical solutions for a linearized one-dimensional problem. *Transp. Porous Media* **32**, No. 1, 49–74.

Leong, E. C. & Rahardjo, H. (1997). Permeability functions for unsaturated soils. *J. Geotech. Engng* **123**, No. 12, 1118–1126.

Lloret, A., Villar, M. V., Sànchez, M., Gens, A., Pintado, X. & Alonso, E. E. (2003). Mechanical behaviour of heavily compacted bentonite under high suction changes. *Géotechnique* **53**, No. 1, 27–40, http://dx.doi.org/10.1680/geot.2003.53.1.27.

Lu, N., Olsen, H. W. & Likos, W. J. (2004). Appropriate material properties for advective–diffusive solute flux in membrane soil. *J. Geotech. Geoenviron. Engng* **130**, No. 12, 1341–1346.

Madsen, F. T. & Muller-Vonmoos, M. (1985). Swelling pressure calculated from mineralogical properties of a Jurassic opalinum shale, Switzerland. *Clays Clay Miner.* **33**, No. 6, 501–509.

Madsen, F. T. & Muller-Vonmoos, M. (1989). The swelling behaviour of clays. *Appl. Clay Sci*. **4**, No. 2, 143–156.

Manassero, M. & Dominijanni, A. (2003). Modelling the osmosis effects on solute migration through porous media. *Géotechnique* **53**, No. 5, 481–492, http://dx.doi.org/10.1680/geot.2003.53.5.481.

Mesri, G. & Olson, R. E. (1971a). Consolidation characteristics of montmorillonite. *Géotechnique* **21**, No. 4, 341–352, http://dx.doi.org/10.1680/geot.1971.21.4.341.

Mesri, G. & Olson, R. E. (1971b). Mechanisms controlling the permeability of clays. *Clays Clay Miner.* **19**, No. 3, 151–158.

Michaels, A. S. & Lin, C. S. (1954). The permeability of kaolinite. *Ind. Engng Chem*. **46**, No. 6, 1239–1246.

Mitchell, J. K. & Soga, K. (2005). *Fundamentals of soil behavior*, 3rd edn. New York, NY, USA: John Wiley & Sons.

Musso, G., Romero, E., Gens, A. & Castellanos, E. (2003). The role of structure in the chemically induced deformations of FEBEX bentonite. *Appl. Clay Sci*. **23**, No. 1–4, 229–237.

Peters, G. P. & Smith, D. W. (2004). The influence of advective transport on coupled chemical and mechanical consolidation of clays. *Mech. Mater*. **36**, No. 5–6, 467–486.

Pusch, R. (1982). Mineral-water interactions and their influence on the physical behaviour of highly compacted Na bentonite. *Can. Geotech. J.* **19**, No. 3, 381–387.

Rao, S. M., Thyagaraj, T. & Thomas, H. R. (2006). Swelling of compacted clay under osmotic gradients. *Géotechnique* **56**, No. 10, 707–713, http://dx.doi.org/10.1680/geot.2006.56.10.707.

Rao, S. M. & Thyagaraj, T. (2007). Swell-compression behaviour of compacted clays under chemical gradients. *Can. Geotech. J.* **44**, No. 5, 520–532.

Romero, E., Gens, A. & Lloret, A. (1999). Water permeability, water retention and microstructure of unsaturated compacted Boom clay. *Engng Geol*. **54**, No. 1–2, 117–127.

Romero, E., Della Vecchia, G. & Jommi, C. (2011). An insight into the water retention properties of compacted clayey soils. *Géotechnique* **61**, No. 4, 313–328, http://dx.doi.org/10.1680/geot.2011.61.4.313.

Shackelford, C. D., Malusis, M. A., Majeski, M. J. & Stern, R. T. (1999). Electrical conductivity breakthrough curves. *J. Geotech. Geoenviron. Engng* **125**, No. 4, 260–270.

Siddiqua, S., Blatz, J. & Siemens, G. (2011). Evaluation of the impact of pore fluid chemistry on the hydromechanical behaviour of clay-based sealing materials. *Can. Geotech. J.* **48**, No. 2, 199–213.

Studds, P. G., Stewart, D. I. & Cousens, T. W. (1998). The effects of salt solutions on the properties of bentonite-sand mixtures. *Clay Miner*. **33**, No. 4, 651–660.

Terzaghi, K. (1956). Discussion: 'Physico-chemical analysis of the compressibility of pure clays'. *Géotechnique* **6**, No. 4, 191–192, http://dx.doi.org/10.1680/geot.1956.6.4.191.

van Genuchten, M. Th. & Cleary, R. W. (1982). Movement of solutes in soils: computer simulated and laboratory results. In *Soil chemistry, B. Physico chemical models* (ed. G. H. Bolt), pp. 349–386. Amsterdam, the Netherlands: Elsevier Scientific.

Villar, M. V., Sánchez, M., Lloret, A., Gens, A. & Romero, E. (2005). Experimental and numerical study of the THM behaviour of compacted FEBEX bentonite in small-scale tests. In *Advances in understanding engineered clay barriers*. (eds E. E. Alonso and A. Ledesma), pp. 323–335. Leiden, the Netherlands: A. A. Balkema.

Yang, N. & Barbour, S. L. (1992). The impact of soil structure and confining stress on the hydraulic conductivity of clays in brine environments. *Can. Geotech. J.* **29**, No. 5, 730–739.

Yeung, A. T. & Mitchell, J. K. (1993). Coupled fluid, electrical and chemical flows in soil. *Géotechnique* **43**, No. 1, 121–134, http://dx.doi.org/10.1680/geot.1993.43.1.121.

Yong, R. N. (1999). Overview of modeling of clay microstructure and interactions for prediction of waste isolation barrier performance. *Engng Geol*. **54**, No. 1–2, 83–91.

Warkentin, B.P., Bolt, G. H. & Miller, R. D. (1957). Swelling pressures of montmorillonite. *Soil Sci. Soc. Am. Proc*. **21**, No. 5, 495–497.

Warren, J. E. & Root, P. J. (1963). The behavior of naturally fractured reservoirs. *Soc. Petrol. Engrs J.* **3**, No. 3, 245–255.

Wilson, R. K. & Aifantis, E. C. (1981). The skin effect in double porosity media. In *Mechanics of structured media* (ed. A. P. S. Selvadurai), pp. 335–341. Amsterdam, the Netherlands: Elsevier.

Guimarães, L. Do N. *et al.* (2013). *Géotechnique* **63**, No. 3, 221–234 [http://dx.doi.org/10.1680/geot.SIP13.P.012]

A chemo-mechanical constitutive model accounting for cation exchange in expansive clays

L. DO N. GUIMARÃES*, A. GENS†, M. SÁNCHEZ‡ and S. OLIVELLA†

The paper presents a chemo-mechanical model for expansive clays that takes into account the effects of cation content and cation exchange. These factors play a key role in the mechanical behaviour of very active clays, particularly with regard to volumetric behaviour. The model is based on an existing double-structure formulation that distinguishes specifically between microstructure and macrostructure. Chemical effects are defined at the microstructural level, the seat of the basic physico-chemical phenomena affecting highly swelling clays. The microstructural model accounts for changes in both osmotic suction and in cation content. Microstructural strains are considered to be reversible; material irreversibility arises from the interaction between the two structural levels. The formulation is developed for general unsaturated conditions; saturation is considered as a limiting case. The model is successfully applied to the reproduction of experimental behaviour observed in oedometer tests on saturated bentonite subjected to chemo-mechanical loadings, and in hydration tests of unsaturated bentonite performed using different solute concentrations.

KEYWORDS: chemical properties; clays; constitutive relations; environmental engineering; expansive soils; partial saturation

INTRODUCTION

It has long been recognised that the mechanical and hydraulic behaviour of very active clays is significantly affected by their geochemical environment (e.g. Salas & Serratosa, 1953; Mesri & Olsen, 1970, 1971; Sridharan *et al.*, 1986; Moore, 1991). These interactions are coupled at different scales, making the resulting behaviour quite complex (Hueckel & Bo Hu, 2009). Interest in the interaction between hydromechanical clay behaviour and chemical variables has been recently reinforced by the potential use of these materials as part of containment systems for hazardous wastes, notably radioactive waste. A characteristic feature of these materials is their sensitivity to the solutes present in the pore water, and to the nature of the cations in their exchange sites (e.g. Pusch, 1982; Barbour & Yang, 1993; Komine & Ogata, 1996; Di Maio, 1996, 1998; Di Maio *et al.*, 2004). More recently, the effect of pH on mechanical behaviour has been highlighted (Gajo & Maines, 2007; Gajo & Loret, 2007), but this particular aspect is not dealt with herein.

A proper consideration of the chemo-mechanical effects in expansive clays requires the development of appropriate constitutive models (Gens, 2010). Hueckel (1992, 1997) published a number of seminal works in this area; subsequently, Loret *et al.* (2002), Gajo *et al.* (2002) and Gajo & Loret (2003) proposed models to describe the elasto-plastic behaviour of saturated expansive clays in the framework of thermodynamics of multiphase, multi-species porous media. Chemically sensitive clays are viewed as two-phase media, with the solid phase including clay particles, adsorbed water and ions. Independently, a chemo-mechanical model combining the Hueckel (1992) formulation with the conventional Barcelona Basic Model (BBM) has been put forward (Liu *et al.*, 2005).

In this paper a phenomenologically based chemo-mechanical model is presented, based on the double-structure framework for unsaturated expansive clays described in Gens & Alonso (1992). The aim is to obtain a constitutive model that is simple enough to be used in coupled analyses of engineering problems, but which incorporates the relevant chemical variables (Guimarães *et al.*, 2007). The chemical variables selected for modelling are the equivalent fractions of exchangeable cations and the osmotic suction. The model considers explicitly the phenomenon of cation exchange, which plays a key role in the mechanical behaviour of expansive clays. The constitutive model is developed for unsaturated soils; saturated behaviour is obtained as a limiting case. In this paper, only the volumetric part of the model – the core of the formulation – is described. The performance of the model is finally examined in relation to experimental results on saturated and unsaturated clays.

FORMULATION OF CHEMO-MECHANICAL CONSTITUTIVE MODEL

General

As stated above, the chemo-mechanical constitutive model presented here has been developed in the context of a double-structure conceptual model devised to reproduce the behaviour of unsaturated, highly swelling clays (Gens & Alonso, 1992). The main feature of this conceptual model is the distinction between two structural levels: a microstructural level and a macrostructural level. The total void ratio, e, is simply the sum of the macrostructural void ratio, e_M, and the microstructural void ratio, e_m. The macrostructural level is made up of the ensemble of particle aggregates and macropores, which can be viewed as forming a granular-like fabric. Other macrofabrics are possible, however, depending on the type of material considered, and on the way it was generated. The behaviour of the macrostructure

Manuscript received 1 March 2012; revised manuscript accepted 15 October 2012.
Discussion on this paper closes on 1 August 2013, for further details see p. ii.
* Departamento de Engenharia Civil, Universidade Federal de Pernambuco, Recife, Brazil.
† Department of Geotechnical Engineering and Geosciences, Universitat Politècnica de Catalunya, Barcelona, Spain.
‡ Zachry Department of Civil Engineering, Texas A&M University, College Station, TX, USA.

can be described by concepts and models developed for conventional soils. The microstructural level is defined by the basic physico-chemical phenomena occurring at clay-particle level. The complete expansive soil model requires, in addition, specification of the interaction between the two structural levels. A basic assumption is that the microstructural behaviour is not influenced by the macrostructure. This is reasonable, as it is unlikely that the basic physico-chemical processes will be affected by non-local variables such as macrostructural fabric. In contrast, microstructural deformations may modify or disrupt the macrostructural fabric, causing irreversible deformations. Interaction functions provide the required link between the two levels.

It has long been noted that the consideration of two structural levels provides a convenient way to model time-dependent deformation of soils, if it is assumed that the exchanges between the two levels are not instantaneous, but follow a diffusion-type process (Alonso *et al.*, 1991; Gens *et al.*, 1993; Wilson & Aifantis, 1982). This aspect is not considered in this paper; an extension of the double-structure model to incorporate local non-equilibrium in hydraulic conditions is presented in Gens *et al.* (2011). Here it is assumed that there is local hydraulic equilibrium between microstructure and macrostructure at all times. This equilibrium assumption implies that the total suction in the macrostructure is the same as that in the microstructure,

$$s_m = s_M = s + s_o \tag{1}$$

where s_m is the total microstructural suction, s_M is the total macrostructural suction, s is the macrostructural matric suction and s_o is the macrostructural osmotic suction.

The osmotic suction is given by

$$s_o = -10^{-6}\frac{RT}{v_w}\ln(a_w) \quad \text{(MPa)} \tag{2}$$

where R is the gas constant (8·3143 J/(mol K)), T is the absolute temperature (in K), v_w is the molar volume of water (in m^3/mol) and a_w is the activity of liquid water. In electrolyte solutions (both dilute and concentrated), a_w depends on the concentration of dissolved salts, and can be computed from the geochemical model. When dealing with saturated materials, it will be assumed that the matric suction is zero. However, osmotic suction is present even in saturated conditions, and depends on the solute content of the liquid phase in accordance with equation (2).

In the following, the formulation of the model for expansive clays, extended to incorporate chemical effects (BExCM), is described. In addition to the hydraulic equilibrium mentioned above, it is assumed that there is also mechanical and chemical local equilibrium between the two structural levels. Although only the volumetric part of the model is presented, extensions to general stress conditions are relatively straightforward, following the mathematical formulations described in Alonso *et al.* (1999) and Sánchez *et al.* (2005).

Macrostructural model

The inclusion of the macrostructural level in the model allows the consideration of phenomena that affect the skeleton of the material, and are relevant to the macroscopic response of expansive materials. It is possible to use conventional models to describe the behaviour of the macrostructure. As in the original proposal of Gens & Alonso (1992), macrostructural behaviour is simulated using the BBM presented in Alonso *et al.* (1990).

It is, however, necessary to incorporate a modification regarding the evolution of expansive clay compressibility with applied stress. Examining, for instance, the results of Fig. 1 (Marcial *et al.*, 2002), it is apparent that there is a distinct break in the relationship between void ratio and vertical stress; compressibility (in log terms) severely reduces when the void ratio reaches a threshold value. The same behaviour has been observed by Di Maio (1996), testing a sodium bentonite. This characteristic behaviour can be accounted for by using the following relationships for the slopes of consolidation and swelling lines.

$$\lambda_0(e_M) = \begin{cases} \lambda_0 & \text{if } e_M > e_p \\ \lambda_0 \cdot \dfrac{e_M}{e_p} & \text{otherwise} \end{cases} \tag{3a}$$

$$\kappa(e_M) = \begin{cases} \kappa & \text{if } e_M > e_p \\ \kappa \cdot \dfrac{e_M}{e_p} & \text{otherwise} \end{cases} \tag{3b}$$

$$\kappa_s(e_M) = \begin{cases} \kappa_s & \text{if } e_M > e_p \\ \kappa_s \cdot \dfrac{e_M}{e_p} & \text{otherwise} \end{cases} \tag{3c}$$

where λ_0 is the slope of the virgin consolidation line under saturated conditions, κ is the slope of the elastic swelling line, κ_s is the slope of elastic void ratio changes due to suction variations, e_M is the macrostructural void ratio and e_p, a model parameter, is the threshold void ratio where the change of slope occurs. This formulation has the additional advantage that the macrostructural void ratio can never become negative.

Microstructural model

Solid–liquid interaction in the proximity of a clay particle is a complex combination of phenomena (e.g. Coulomb attraction, Van der Waals forces, ion–dipole interaction, hydrogen bridges, and cation hydration) that molecular dynamics has only recently started to unravel in a systematic way (e.g. Katti *et al.*, 2007). Traditionally, for highly expansive smectitic clays, the diffuse double layer (DDL) theory (suitably modified to take into account the actual size of hydrated ions) provides a useful background (Mitchell & Soga, 2005). Although, for a highly compacted clay, the role of the DDL theory may be limited (Karnland, 1997), it is used here as the reference model for microstructural behaviour. Of course, there is no conceptual difficulty in updating

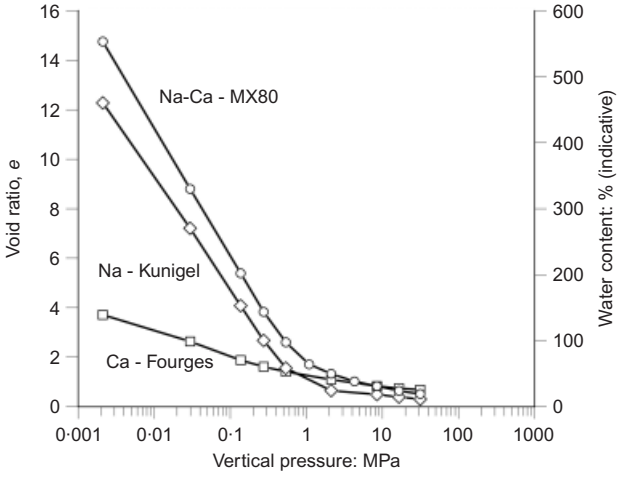

Fig. 1. Compression curves for calcium (Ca) and sodium (Na) expansive clays (MX80 clay, Kunigel clay and Fourges clay) (after Marcial *et al.*, 2002)

the microstructural law with a more sophisticated theory if the need arises.

In accordance with the general framework proposed in Gens & Alonso (1992), it is assumed that microstructural behaviour is only volumetric and reversible. Reversibility of the microstructural hydromechanical behaviour stems from the fact that basic physico-chemical phenomena at particle level are generally largely reversible.

An effective mean stress that controls microstructural behaviour is defined as

$$\hat{p} = p + \chi s_{\mathrm{m}} \tag{4}$$

where p is the mean net stress, and χ may take values between 0 and 1. This is a generalisation of the original proposal

$$\hat{p} = p + s_{\mathrm{m}} \tag{5}$$

to take into account the possibility that, under some circumstances, the microstructure may become unsaturated. Alonso *et al.* (1999) proposed $\chi = S_{\mathrm{r}}^{n}$, where S_{r} is the microstructure degree of saturation and n is a parameter. When $n = 0$ the classical effective stress definition is recovered.

A mathematically convenient way to express the dependence of the elastic microstructural volumetric strain on the chemical and mechanical variables is

$$\varepsilon_{\mathrm{m}}^{\mathrm{e}} = -\frac{\beta_{\mathrm{m}}}{\alpha_{\mathrm{m}}} \mathrm{e}^{-\alpha_{\mathrm{m}}\hat{p}} \tag{6}$$

as suggested by the theories that, based on DDL theory, describe the interparticle distance as a function of effective stress. To incorporate the influence of geochemical variables on the behaviour of the microstructure, it is assumed that the material parameter α_{m} is constant, and that the variable β_{m} depends on the exchangeable cation concentrations as

$$\beta_{\mathrm{m}} = \sum_i \beta_{\mathrm{m}}^{i} x_i \tag{7}$$

where x_i is the equivalent fraction of the exchangeable cation i, defined as

$$x_i = \frac{\text{concentration of exchangeable cation}}{\text{CEC}} \tag{8}$$

and CEC is the cation exchange capacity of the clay. The equivalent fractions, x_i, are subjected to the restrictions

$$\sum_i x_i = 1; \; 0 \leqslant x_i \leqslant 1 \tag{9}$$

The β_{m}^{i} values control microstructure stiffness, and should be defined for each of the potential exchangeable cations. Based on DDL theory, the value of β_{m}^{i} for exchangeable cation i is proportional to the ionic hydrated radius, and inversely proportional to its valence. Table 1 lists the hydrated radii of various cations. Consequently, the values of β_{m}^{i} will be ordered as $\beta_{\mathrm{m}}^{\mathrm{Li}} > \beta_{\mathrm{m}}^{\mathrm{Na}} > \beta_{\mathrm{m}}^{\mathrm{K}}$ and, in general, as $\beta_{\mathrm{m}}^{\text{monovalent cation}} > \beta_{\mathrm{m}}^{\text{divalent cation}}$. These assumptions are clearly supported by the results of Fig. 2, where it can be seen that the compressibility of homoionised (i.e. containing a single cation species) bentonite reduces as the cation valence increases, and becomes larger with an increase in hydrated radius.

Table 1. Hydrated radii of cations (after Mitchell & Soga, 2005)

Cation	Hydrated radius: Å
Li^+	7·3–10·0
Na^+	5·6–7·9
K^+	3·8–5·3
NH^+	5·4
Rb^+	3·6–5·1
Cs^+	3·6–5·0
Mg^{2+}	10·8
Ca^{2+}	9·6
Sr^{2+}	9·6
Ba^{2+}	8·8

Full differentiation of equation (6) yields the incremental form for the elastic microstructural volumetric strain

$$\mathrm{d}\varepsilon_{\mathrm{m}}^{\mathrm{e}} = \beta_{\mathrm{m}} e^{-\alpha_{\mathrm{m}}\hat{p}} \mathrm{d}\hat{p} - \frac{1}{\alpha_{\mathrm{m}}} \mathrm{e}^{-\alpha_{\mathrm{m}}\hat{p}} \mathrm{d}\beta_{\mathrm{m}} \tag{10}$$

Naturally, osmotic suction is incorporated in the value of the effective stress. Equation (10) shows an important feature of this model: cation exchange not only affects the stiffness of the microstructure to changes in effective stress (first term), but also contributes separately to the microstructural volumetric strains (second term). An important consequence of the formulation is therefore that microstructural strains due to a geochemical change depend not only on the variation of osmotic suction, but also on the nature of the cations present in the clay.

To illustrate the microstructural behaviour proposed here, a series of oedometer tests on remoulded samples of a sodium

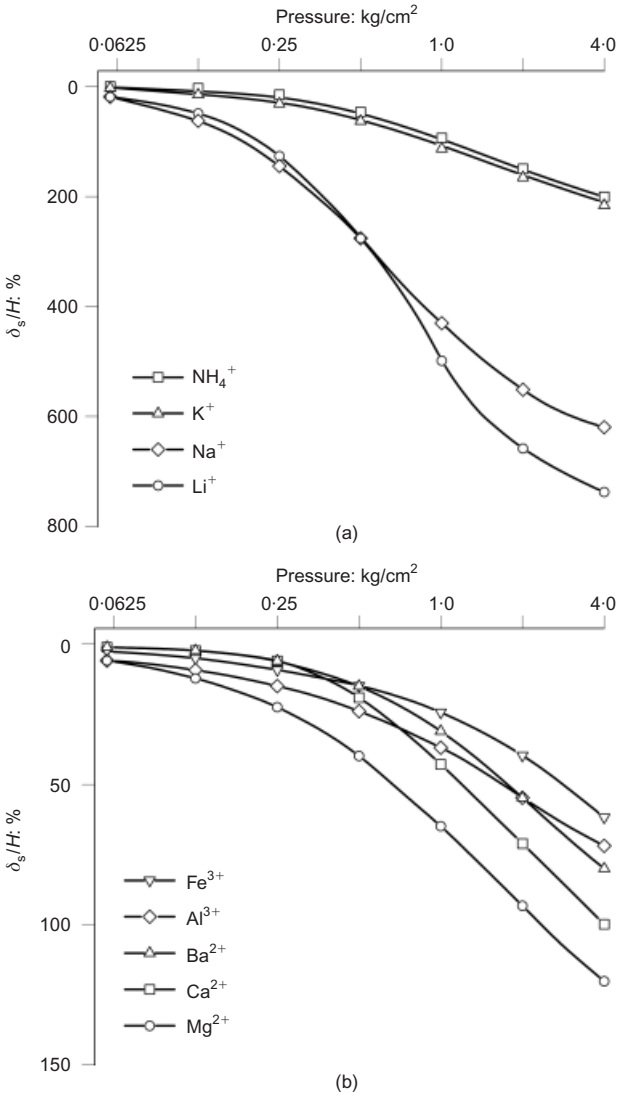

Fig. 2. Results of oedometer tests on homoionised bentonite (after Sridharan *et al.*, 1986): (a) monovalent bentonites; (b) heterovalent bentonites

montmorillonite (Di Maio, 1996) are shown in Fig. 3. In these tests, three bentonite samples were initially consolidated to 640 kPa, and then were exposed to saturated solutions of sodium chloride (NaCl), potassium chloride (KCl) and calcium chloride ($CaCl_2$). The osmotic suctions of these solutions are 39 MPa, 24 MPa and 185 MPa respectively. The values of osmotic suction have been obtained from equation (2) for a temperature of 25°C. For these tests, the observed differences are due to the microstructural behaviour – the dominant deformation mechanism. It can be seen that the sample exposed to calcium chloride compresses only slightly more, in spite of the large osmotic suction applied. When the sodium bentonite is exposed to the saturated solution of calcium chloride, the Ca^{2+} cations in the solution will tend to replace the Na^{+} and the other cations in the exchange complex. As the value of β_m^{Ca} is lower than the values for the other cations, the specimen exhibits a higher stiffness, and the effects of osmotic suction variation are more muted. It is also interesting to note that, in spite of the fact that the osmotic suction of the sodium chloride solution is higher than that of the potassium chloride solution, the deformation is very similar. The effect of the change in osmotic suction effect is compensated for by the cation exchange and the associated differences in microstructural stiffness ($\beta_m^{Na} > \beta_m^{K}$) that occur in the test. As a matter of fact, the potassium chloride sample compresses marginally more. It is apparent, therefore, that changes in osmotic suction alone do not explain fully the volumetric behaviour of the material; the effect of individual cations must be considered as well.

For the development and implementation of the model, a more convenient way to express the elastic microstructural volumetric strain given in equation (6) is

$$\begin{aligned}\varepsilon_m^e &= -\frac{\beta_m}{\alpha_m}e^{-\alpha_m \hat{p}} \\ &= -\frac{1}{\alpha_m}e^{-\alpha_m \psi}\end{aligned} \tag{11}$$

where the variable ψ is defined as

$$\begin{aligned}\psi &= \hat{p} - \frac{1}{\alpha_m}\ln\beta_m \\ &= p + \chi s_m - \frac{1}{\alpha_m}\ln\beta_m\end{aligned} \tag{12}$$

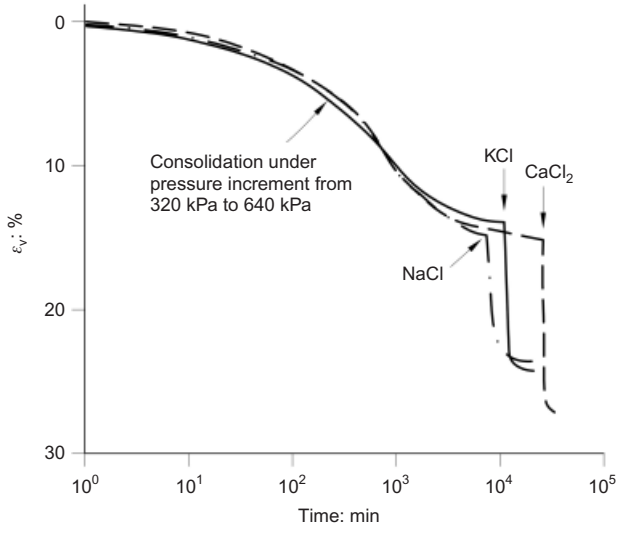

Fig. 3. Volume change of sodium bentonite due to loading and exposure to different saturated solutions (after Di Maio, 1996). Osmotic suctions of solutions: 39 MPa, 24 MPa and 185 MPa for sodium chloride (NaCl), potassium chloride (KCl) and calcium chloride ($CaCl_2$) respectively

This variable will be called the *chemically modified effective stress* of the microstructure. This term reflects the fact that the microstructural volumetric strain depends only on changes of ψ, according to

$$d\varepsilon_m^e = e^{-\alpha_m \psi} d\psi \tag{13}$$

It is possible to write equation (13) as

$$d\varepsilon_m^e = \frac{d\psi}{K_m} \tag{14}$$

where K_m is the microstructural volumetric stiffness, given by

$$K_m = e^{\alpha_m \psi} \tag{15}$$

To simplify the notation, equation (12) is written as

$$\psi = p + \chi s_m + \psi_c \tag{16}$$

where

$$\psi_c = -\frac{1}{\alpha_m}\ln\beta_m \tag{17}$$

Therefore the variable ψ_c depends on the microstructural material parameters α_m and β_m^i, and on the equivalent fractions of exchangeable cations. Based on the previous discussion, a cation exchange process that causes an increase in β_m (e.g. the replacement of Ca^{2+} by Na^{+} in the exchange sites of the clay) will result in a reduction of ψ_c and an expansion of the microstructure. Indeed, reductions in p, s_m or ψ_c will all cause a microstructural expansion. Hence a reduction of ψ will be associated with microstructural wetting. Conversely, when the net effect of changes in microstructural variables p, s_m and ψ_c is an increase of ψ, there will be shrinkage of the microstructure, and it will be associated with microstructural drying.

In Gens & Alonso (1992), a neutral line was defined as the locus where the increment of microstructural volumetric strain was zero. In the present model, this implies that

$$\begin{aligned}&d\varepsilon_m^e = 0 \\ &\Rightarrow d\psi = d(p + \chi s_m + \psi_c) = 0\end{aligned} \tag{18}$$

and it corresponds to the plane of equal ψ that contains the current stress state in the space p–s_m–ψ_c (Fig. 4(a)). While the generalised stress state remains in this plane of constant ψ, there will be no microstructural deformations. By analogy to the neutral line, this plane is called the neutral plane (NP), separating stress paths that cause either drying or wetting of the microstructure. When there is no cation exchange, the original concept of the neutral line is recovered.

Coupling between microstructure and macrostructure

The deformation of the microstructure may cause a rearrangement of the macrostructure, leading to irreversible volumetric strains, which will be reflected in a variation of the macrostructural yield surface via a change in the hardening parameter p_0^*, the saturated yield stress. For this plastic mechanism, it is possible to envisage an elastic domain where microstructural deformations do not affect the macrostructure in an irreversible manner. Since it is assumed that the microstructural strains are reversible and depend only on the chemically modified effective stress (ψ), the elastic domain can be defined by providing bounds for ψ, leading to two yield surfaces that depend on microstructural variables only.

SI:

$$F_{SI} = \psi_I^* - \psi \leqslant 0 \tag{19}$$

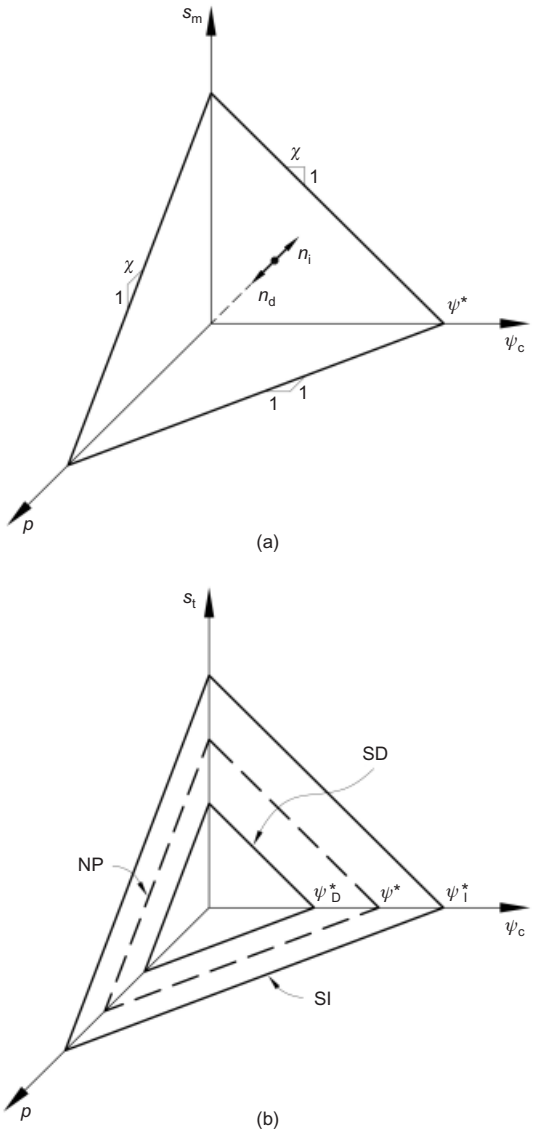

Fig. 4. Representations in p–s_m–ψ_c space of: (a) neutral plane (NP); (b) yield surfaces SI and SD, and of NP

SD:

$$F_{SD} = \psi - \psi_D^* \leqslant 0 \tag{20}$$

The names of these surfaces, SI (suction increase) and SD (suction decrease), coincide with those used in the original BExM. ψ_I^* and ψ_D^* ($\psi_I^* \geqslant \psi_D^*$) are the maximum and minimum values that ψ may have without causing macrostructural plastic strains starting from the present configuration. These history variables define the planes representing the SI and SD surfaces in the space p–s_m–ψ_c (Fig. 4(b)). The NP contains the present stress state, and is located between SI and SD. A particular form of this formulation consists in assuming that the planes SI, SD and NP coincide: that is, $\psi^* = \psi_I^* = \psi_D^*$. In this case, microstructural deformations always bring about some plastic macrostructural strains and the elastic domain is reduced to the NP only. This particular form of the model yields itself naturally to a generalised plasticity formulation as described in Sánchez *et al.* (2005).

In Gens & Alonso (1992), it was postulated that the effect of microstructural strains on the macrostructure depended on p/p_0, where p_0 is the yield stress for the value of matric suction acting on the soil. p/p_0 represents a measure of the degree of openness of the macrostructure in relation to the particular stress applied. Values of p/p_0 close to 1 indicate a macrostructure that is open, and potentially collapsible. Small values of p/p_0 are associated with a close packing of the soil. It therefore appears reasonable to assume that the nature and magnitude of the effect of microstructural strains on macrostructure depend on the p/p_0 variable.

Alonso *et al.* (1999) proposed the following expressions to define the link between microstructural and macrostructural volumetric strains (ε_m^e and ε_M^p respectively)

$$d\varepsilon_M^p = f_D d\varepsilon_m^e \tag{21}$$

when the SD is activated (microstructural expansion) and

$$d\varepsilon_M^p = f_I d\varepsilon_m^e \tag{22}$$

when the SI is activated (microstructural shrinking).

The interaction functions f_D and f_I depend on p/p_0 (Fig. 5). The plastic volumetric strains of the macrostructure caused by the coupling with the microstructure can be computed from the combination of equations (14), (21) and (22) to give

$$d\varepsilon_{M\beta}^p = f_\beta d\varepsilon_m^e = f_\beta \frac{d\psi}{K_m}, \ \beta = \text{I, D} \tag{23}$$

where the symbol β indicates the mechanism currently active, I or D.

The history variable associated with the mechanism β is ψ_β^* ($\beta = $ I, D) and the hardening law for this mechanism, in accordance with equation (23), is

$$d\psi_\beta^* = \frac{K_m}{f_\beta} d\varepsilon_{M\beta}^p, \ \beta = \text{I, D} \tag{24}$$

A basic component of the BBM model is the loading-collapse (LC) curve, which expresses the variation of apparent consolidation pressure with suction for a given value of plastic volumetric strain. The coupling between mechanism β and the macrostructural model establishes that when there is a plastic macrostructural densification, the LC surface expands (moving to the right). On the other hand, when there is a plastic opening of the macrostructure, the LC surface shrinks (moving to the left). This is automatically achieved by using the hardening law for the BBM, where, now, the plastic volumetric strain is the sum of the contributions of the two plastic mechanisms LC ($d\varepsilon_{MLC}^p$) and β ($d\varepsilon_{M\beta}^p$),

$$\frac{dp_0^*}{p_0^*} = \frac{1 + e_M}{\lambda_0 - \kappa} \left(d\varepsilon_{MLC}^p + d\varepsilon_{M\beta}^p \right) \tag{25}$$

where λ_0 is the slope of the saturated virgin consolidation

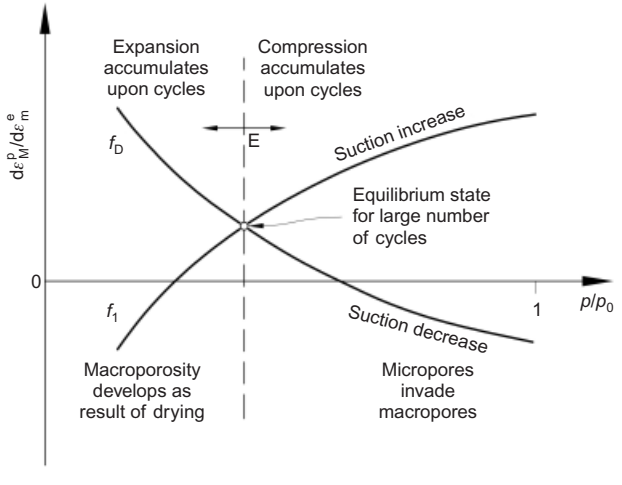

Fig. 5. Schematic representation of interaction functions f_I and f_D (after Alonso *et al.*, 1999)

line and κ is the slope of the swelling line (both in semi-log space). They are the same parameters as used in the BBM. Note that, in the plastic regime, the two mechanisms can be active simultaneously, but situations in which only one of them operates are equally possible.

APPLICATIONS

In this section, the proposed model is verified by reproducing qualitatively a number of tests on expansive clays in which chemical and mechanical actions have been applied. The basic aim is to capture the main phenomena related to the dependence of volume change on the nature of dissolved salts and exchangeable cation content. Tests under saturated conditions are considered first, followed by some unsaturated soil applications. As only oedometer tests are available, the usual assumption is made that the formulation developed using mean stresses is also applicable in terms of applied vertical stresses. In the tests, there is a time evolution of the measured strains before reaching equilibrium, because of the delay required for pore pressure and chemical concentration equilibration throughout the specimen. However, the soil response at constitutive level is instantaneous. Despite this, model computations have been plotted against time for presentation purposes only, so that comparisons with experiments can be more readily made.

Reference soil

A quantitative analysis of the hydro-chemo-mechanical problem requires a detailed geochemical characterisation of the particular expansive clay being examined. The equilibrium constants of the cation exchange reactions are especially significant, as they control the proportion of cations occupying the exchange sites. The presence of secondary minerals such as calcite, dolomite, gypsum or anhydrite has a significant influence on the chemistry of the pore water of natural clays (Guimarães, 2002). They account for the buffering of the system with respect to changes in chemical variables such as pH, and also restrict the concentration of aqueous species in equilibrium with them.

Since the information required for complete physico-chemical modelling of the tests on natural clays reported in the literature is generally not available, computations have been made using a reference soil with appropriate parameters. Therefore only qualitative comparisons are possible. The relevant parameters for the volumetric component of the model are collected in Table 2. They are representative of a chemically active expansive clay with an initial high void ratio and a large volume change potential due to variations in matric suction or chemical actions, but they are not intended to apply to a specific soil. At high confining pressures stiffness increases considerably, and expansion potential is much reduced. This agrees with the behaviour of sodium montmorillonites typically found in the literature. In accordance with the discussion above, the β_m^i values of Table 2 are consistent with DDL theory, as $\beta_m^{Na} > \beta_m^K$, $\beta_m^{Mg} > \beta_m^{Ca}$ and, in general, $\beta_m^{monovalent} > \beta_m^{divalent}$.

In this type of material microstructural behaviour is dominant, so the model results and experimental observations address mainly the performance of the microstructural component of the model. It will be shown, however, that the macrostructural component and its interaction with the microstructure are required to describe the observed behaviour fully. To obtain the desired shape for the interaction functions, the following equations are adopted.

$$f_I = 0{\cdot}075 \tanh\left[30(p/p_0 - 0{\cdot}2)\right] \tag{26a}$$

$$f_D = -0{\cdot}075 \tanh\left[30(p/p_0 - 0{\cdot}2)\right] \tag{26b}$$

In all the examples it is assumed that there is no elastic domain for the interaction mechanism, and the SI, SD and NP planes coincide. Therefore any microstructural strain will cause at least some macrostructural plastic strain, although the microstructural behaviour will of course remain reversible. The internal variables of the model are the macro- and micro-void ratios e_M and e_m, and the history variable p_0^*. In the simulations, it is assumed that the soil is initially in a normally consolidated state ($p/p_0 = 1$), consistent with the procedure used for sample preparation.

For the constitutive law computations, the simplified geochemical model of the clay summarised in Table 3 is assumed. The cation exchange reactions shown follow the Gaines–Thomas convention (Appelo & Postma, 1993). It is necessary to adopt a convention of this kind because of the lack of consensus over the computation of the chemical activity of the cations adsorbed in the clay. Here, an approximate thermodynamical formulation is used in which chemical activities are equated to their equivalent fractions. The constants of equilibrium of those reactions, called selectivity constants, are not really thermodynamic constants, as their value depends on the experimental conditions and type of soil. According to the convention adopted, the mass action law for the Table 3 exchange reactions can be written as

$$K_{Na/K} = \frac{x_{Na} a_{K^+}}{x_K a_{Na^+}} \tag{27}$$

$$K_{Na/Mg} = \frac{x_{Na} a_{Mg^{2+}}^{0{\cdot}5}}{x_{Mg}^{0{\cdot}5} a_{Na^+}} \tag{28}$$

$$K_{Na/Ca} = \frac{x_{Na} a_{Ca^{2+}}^{0{\cdot}5}}{x_{Ca}^{0{\cdot}5} a_{Na^+}} \tag{29}$$

where x_{Na}, x_K, x_{Mg} and x_{Ca} are the equivalent fractions of exchangeable cations NaX, KX, MgX_2 and CaX_2 as defined in equation (8). a_{Na^+}, a_{K^+}, $a_{Mg^{2+}}$ and $a_{Ca^{2+}}$ are the chemical activities for the cations in solution. These chemical activities are a measure of the effective concentration, and they may differ from the actual concentration because of interactions in the solution. For the selectivity constants of these reactions, the mean values compiled by Appelo & Postma (1993) have been adopted: $K_{Na/K} = 0{\cdot}2$, $K_{Na/Mg} = 0{\cdot}5$ and $K_{Na/Ca} = 0{\cdot}4$, taking Na^+ as the reference cation.

Table 2. Main parameters of volumetric component of elasto-plastic constitutive law for chemically active soil (reference soil)

Macrostructure parameters (modified BBM)						
$\lambda_0 = 1{\cdot}2$	$\kappa = 0{\cdot}4$	$\kappa_s = 0{\cdot}04$	$p_c = 0{\cdot}001$ MPa	$r = 0{\cdot}9$	$\beta = 5$ MPa^{-1}	$e_p = 2$
Microstructure parameters (BExCM)						
$\chi = 1{\cdot}0$	$\alpha_m = 2{\cdot}5$ MPa^{-1}	$\beta_m^{Na} = 5$	$\beta_m^K = 1{\cdot}5$		$\beta_m^{Mg} = 1{\cdot}0$	$\beta_m^{Ca} = 0{\cdot}5$

Table 3. Species present in system, and reactions considered in geochemical model for reference soil

Species in liquid phase				
Na^+	K^+	Mg^{2+}	Ca^{2+}	Cl^-
Species in solid phase				
NaX	KX	MgX_2		CaX_2
Chemical reactions (cation exchange)				
$Na^+ + KX \leftrightarrow NaX + K^+$				
$Na^+ + \frac{1}{2}MgX_2 \leftrightarrow NaX + \frac{1}{2}Mg^{2+}$				
$Na^+ + \frac{1}{2}CaX_2 \leftrightarrow NaX + \frac{1}{2}Ca^{2+}$				

Note: species NaX, KX, CaX_2 and MgX_2 are the exchangeable cations of sodium, potassium, calcium and magnesium present in the exchange complex of the clay. X^- represents the negatively charged clay mineral surface.

To compute the chemical activities of the aqueous species, the Harvie & Weare (1980) model was used. It belongs to the family of Pitzer models valid for very concentrated saline solutions. In most tests considered here, the solutions were saturated by the salts sodium chloride, calcium chloride and potassium chloride. As the osmotic suction and the equivalent fractions of the exchangeable cations required by the model are computed from the activities of the aqueous species, it is important to use a chemical model appropriate for high solute concentrations.

The initial geochemical conditions used in the computations are listed in Table 4. Initially, it was considered that the pore water contains only sodium chloride in relatively diluted concentrations (0·1 M). The osmotic suction for this solution is 0·46 MPa (obtained from equation (2)). From the equilibrium of the clay–water system, the sodium cation predominates in the exchangeable sites of the clay. So, initially, the reference soil is initially a homoionic sodium-clay.

Single-cation oedometer tests on saturated clay

Di Maio (1996) carried out a series of oedometer tests on reconstituted samples of Ponza bentonite. This is a natural bentonite with 80% clay fraction, composed mostly of sodium montmorillonite, and a plasticity index of 320%. Reconstituted specimens were prepared by mixing powdered clay with distilled water to a slurry at about the liquid limit. The tests were performed in conventional oedometers on specimens 2 cm thick. They were first consolidated to several axial stresses, and then exposed to different saturated solutions (sodium chloride, potassium chloride and calcium chloride). Other more complex combinations of load and chemical solutions were also applied in some cases.

The results of a set of tests performed by Di Maio (1996), combining chemical and mechanical effects, are presented in Fig. 6. It can be seen (dotted lines) that very different volumetric behaviours are measured between samples formed with distilled water and those formed with a saturated solution of sodium chloride. Additional tests in which a cycle of sodium chloride solution/distilled water was applied to the samples (under different loads) indicated that, for this set of tests, the volumetric behaviour was independent of the generalised chemo-mechanical stress path, since the final states of the specimens are practically the same irrespective of their previous history. However, irreversible behaviour is evident, with a final void ratio significantly below the initial one.

Examining Fig. 7, it is apparent that the model is capable of providing a satisfactory reproduction of this behaviour, including stress path independence. The reason for this agreement is that the samples have been loaded to a vertical stress sufficiently high (10 MPa) that the virgin consolidation lines converge. Thereby, the two specimens reach the same values of history variables, e and p_0^*, although the stress paths have been different (one has undergone a sodium chloride solution/distilled water cycle and the other has not). Irreversible behaviour is also captured; it is associated with the plastic behaviour of the macrostructure, since microstructural behaviour is considered reversible. This can be illustrated by computing the evolution of the void ratios of the two structural levels during the tests (Fig. 8). It can be seen that the microstructural strain cycle is closed, whereas the macrostructural void ratio exhibits a degree of irreversible behaviour.

Figure 9 shows the results of another set of tests carried out by Di Maio (1996) where bentonite samples, after consolidation to different stress levels, were initially exposed to a saturated solution of sodium chloride and, subsequently, to distilled water. These actions result in some permanent

Table 4. Geochemical initial conditions for reference soil used in constitutive law computations

Aqueous species (molality)				
Na^+ 0·10 M	K^+ 0·00 M	Mg^{2+} 0·00 M	Ca^{2+} 0·00 M	Cl^- 0·10 M
Exchangeable cations (equivalent fractions)				
NaX 1·00	KX 0·00	MgX_2 0·00		CaX_2 0·00

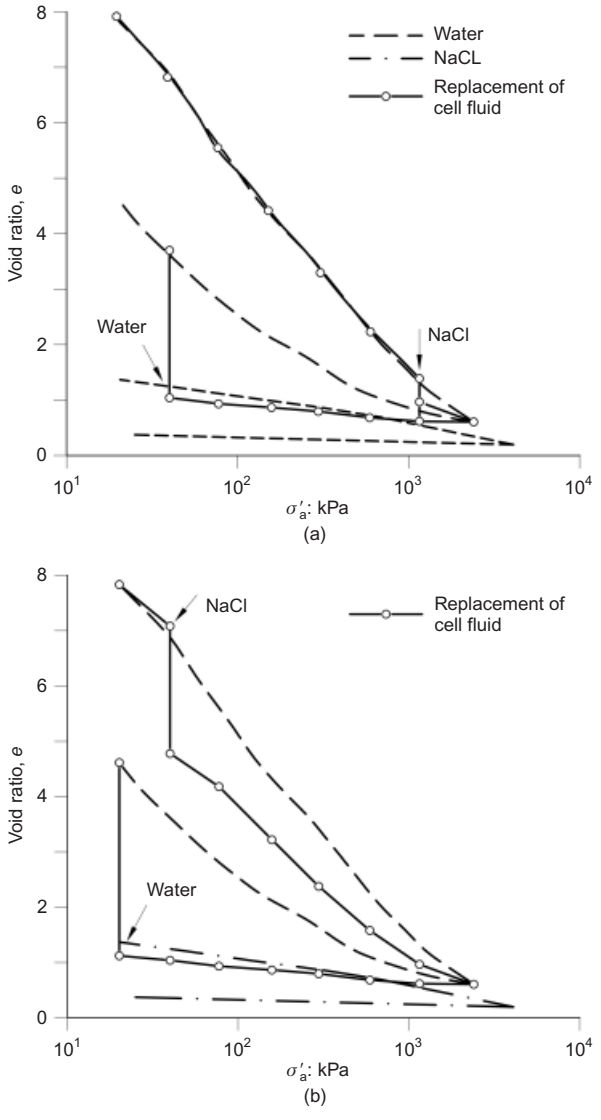

Fig. 6. Volume change of sodium bentonite subjected to consolidation and swelling with and without fluid replacement (after Di Maio, 1996). Volume change curves without fluid replacement indicated by dotted lines. Samples exposed to saline solutions under: (a) 1·2 MPa stress; (b) 0·04 MPa stress

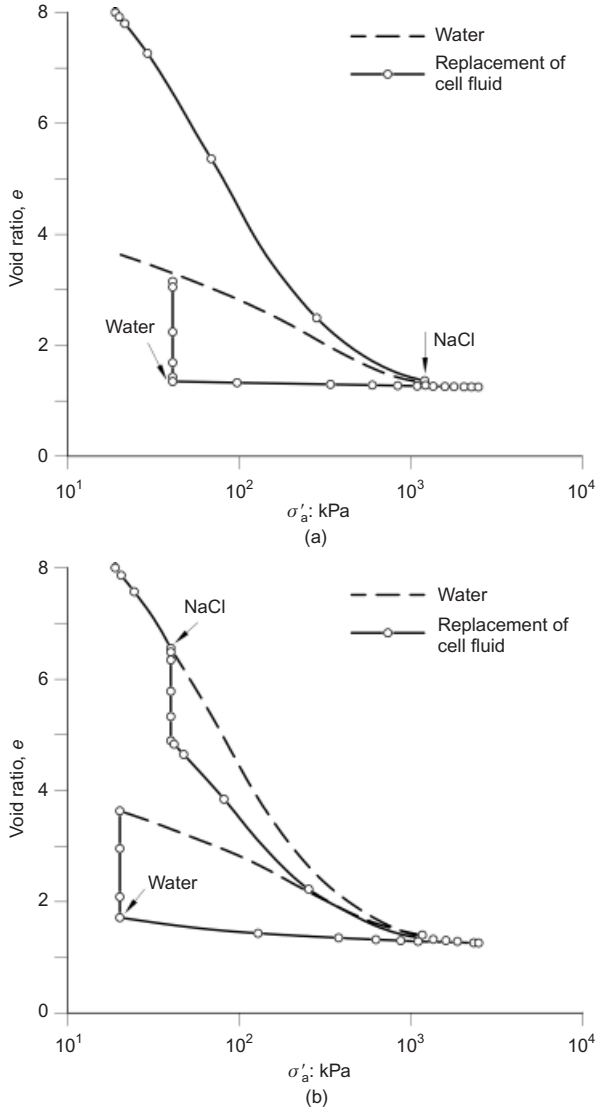

Fig. 7. Model responses for samples exposed to saline solutions under: (a) 1·2 MPa stress; (b) 0·04 MPa stress

deformations, since the initial shrinking is not totally recovered by the subsequent expansion. It is also noticeable that strains are larger under low stresses. As Fig. 10 shows, the model reproduces the same type of behaviour: the larger the load applied, the smaller the deformations computed. This is a consequence of the increase of microstructural stiffness with applied stress (equation (14)). There is also a measure of volumetric irreversible behaviour due to the interaction between micro- and macrostructures, although the degree of irreversibility is underestimated by the model.

Multiple-cation oedometer tests on saturated clay

A more stringent test of the model arises when different chemical species are used, and cation exchange occurs. Fig. 11(a) shows the results of a test reported in Di Maio (1998), where the Ponza bentonite has been subjected to cycles of exposure to different saline solutions of sodium chloride and potassium chloride under an effective vertical stress of 40 kPa. Fig. 11(b) shows the satisfactory reproduction of the behaviour by the model using the reference soil. In this test, the observed behaviour of the clay is explained by the model through the effects of the osmotic suction (s_o) and of the exchangeable cations (variable β_m in equation (6)) on the microstructural model. Now, in addition to the effect on microstructural stiffness (equation (15)), deformations are also induced by cation change.

To illustrate further the performance of the model, the evolutions of the computed total, macro- and micro-void ratios are plotted in Fig. 12(a), together with the variables that control the behaviour: osmotic suction (s_o) and β_m (Fig. 12(b)). It can be seen that the behaviour of the material is basically controlled by the microstructure, and only a slight irreversible behaviour is generated in the macrostructure in this case. In fact, the macrostructural void ratio becomes constant after a few sodium chloride-water cycles.

Initially, in the various cycles of exposure to sodium chloride-water, the clay remains an Na-clay, and the only variable that causes deformations is the osmotic suction. It can be seen (Fig. 11(a)) that, in the experiment, there is a slight increase of swelling strains as the test cycles progress that is not reproduced by the model (Fig. 11(b)). This behaviour is attributed by Di Maio (1998) to a progressive replacement of other cations present in the natural bentonite, a feature not accounted for in a time-independent model that assumes chemical equilibrium throughout.

Subsequently, the specimen is subjected to cycles of potassium chloride-water and the deformations become smaller

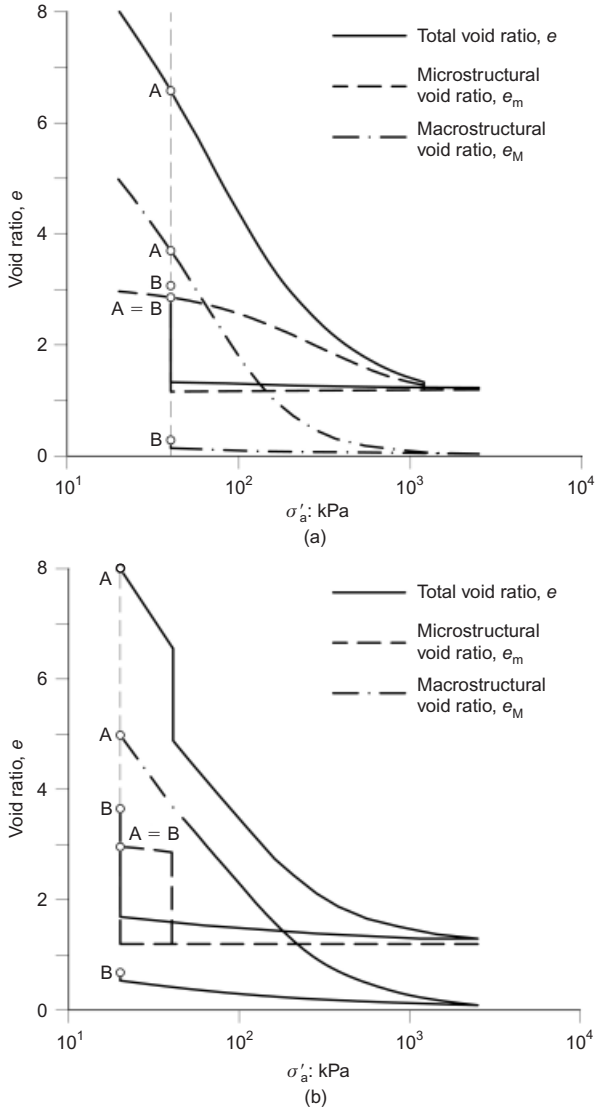

Fig. 8. Computed micro-, macro- and total void ratios for samples exposed to saline solutions under different loads (A and B indicate start and end of a closed chemo-mechanical cycle): (a) 1·2 MPa stress; (b) 0·04 MPa stress

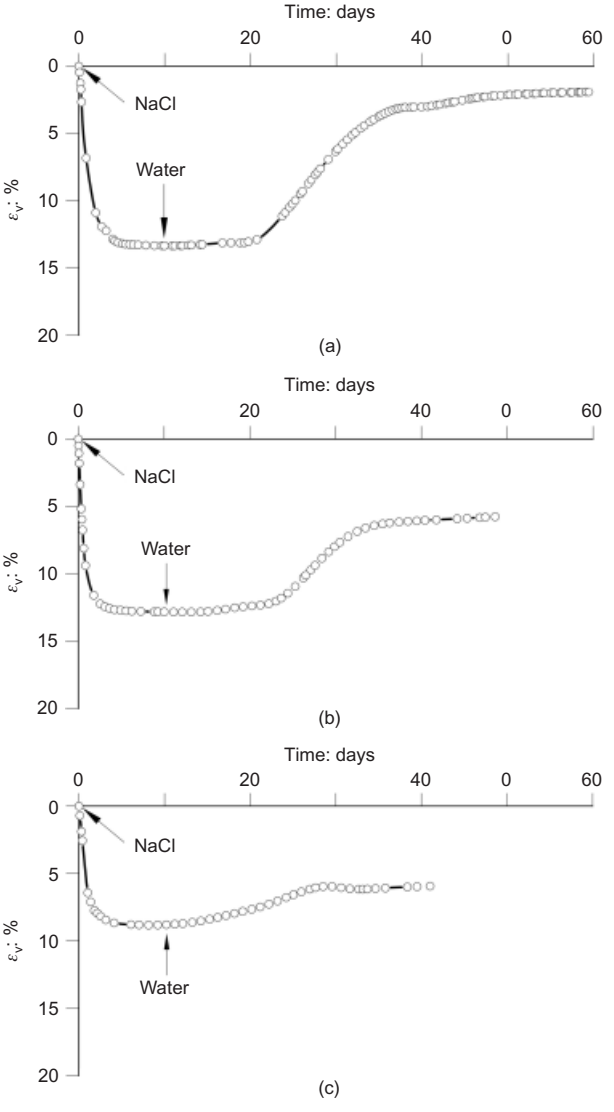

Fig. 9. Volume change of a sodium bentonite due to exposure to sodium chloride (NaCl) solution and water under different applied stresses, σ_a (after Di Maio, 1996): (a) $\sigma_a = 160$ kPa; (b) $\sigma_a = 320$ kPa; (c) $\sigma_a = 640$ kPa

(see Fig. 11(a) for experimental results and Fig. 11(b) for model results). One reason is that the potassium chloride-water cycles apply variations of osmotic suction of 24 kPa, smaller than the variations of 39 MPa applied by the sodium chloride-water cycles. However, the main contribution to the difference arises from cation exchange. When the sample is exposed to the potassium chloride solution for the first time, the following reaction takes place

$$\mathrm{NaX} + \mathrm{K}^+ \rightarrow \mathrm{Na}^+ + \mathrm{KX} \tag{30}$$

and the clay becomes potassic (K-clay). In this equation, X represents the clay mineral surface. As $\beta_m^{Na} > \beta_m^{K}$, the microstructure becomes stiffer, and the potassium chloride-water cycles exhibit compressive and swelling strains much smaller than those observed in the sodium chloride-water cycles.

Figure 11 also illustrates the largely reversible behaviour of the Ponza bentonite when, after the potassium chloride-water cycles, it is again exposed to a saturated solution of sodium chloride. In this case, the exposure to sodium chloride produces a cation exchange reaction in the opposite direction to reaction (30). The bentonite becomes a Na-clay again, and it recovers the highly expansive behaviour observed in the initial stages of the test. Finally, the sample is exposed to a saturated solution of calcium chloride, and a contraction ensues that is also reproduced by the model.

The effect of calcium on the chemo-mechanical behaviour of Ponza bentonite is explored further in Fig. 13(a) (Di Maio, 1998). A large compressive deformation is observed when the sample is put in contact with the calcium chloride solution. Subsequently, on exposure to water, the sample does not expand in spite of the large variation of osmotic suction (185 MPa) applied by the process. When the specimen is exposed to sodium chloride and later to water, it exhibits a large swelling associated with a much smaller osmotic suction variation (39 MPa).

The explanation naturally lies in the effect of exchangeable cations on the clay microstructure. The exposure to calcium chloride causes the Ca^{2+} of the solution to replace the other cations in the exchange complex of the clay, which becomes a stiffer Ca-clay. This is reflected in the low β_m value for calcium (β_m^{Ca}). Therefore subsequent exposure of the sample to water causes only a small expansion (Fig. 13(b)). Subsequent exposure of the specimen to sodium chloride brings about the reaction

$$\mathrm{Na}^+ + \tfrac{1}{2}\mathrm{CaX}_2 \rightarrow \mathrm{NaX} + \tfrac{1}{2}\mathrm{Ca}^{2+} \tag{31}$$

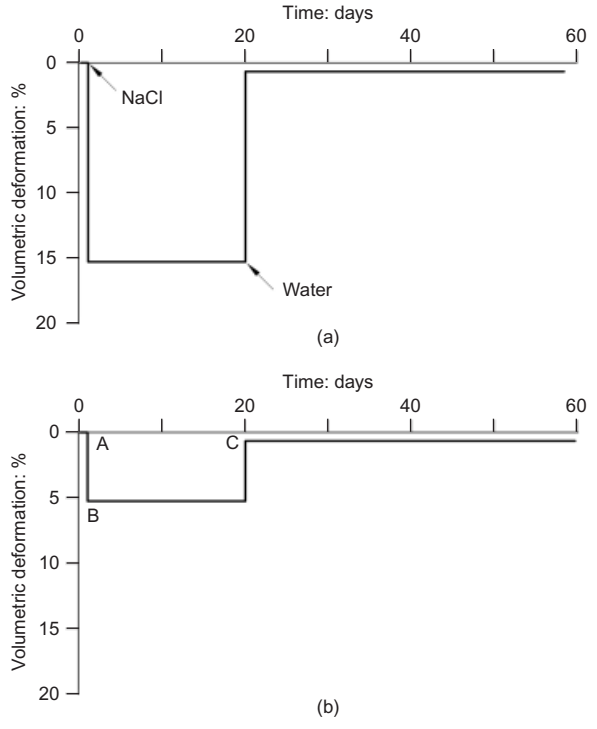

Fig. 10. Model response to exposure to sodium chloride (NaCl) solution and water under: (a) 160 kPa applied stress; (b) 640 kPa applied stress

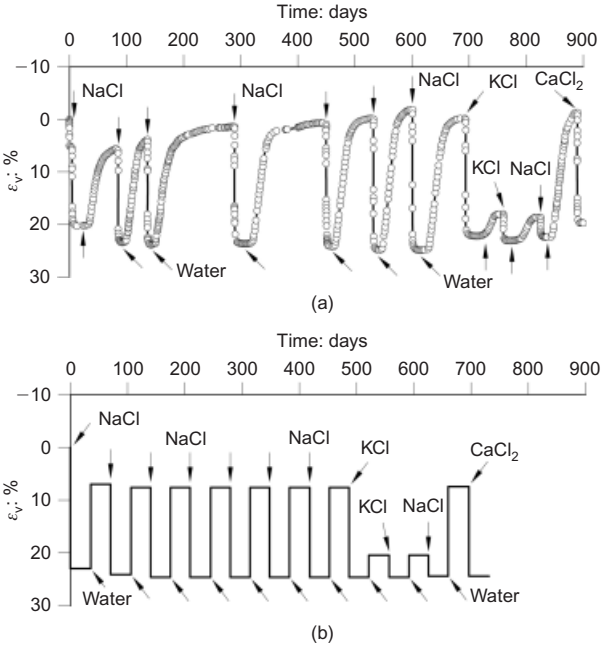

Fig. 11. Cyclic exposure of sodium bentonite to saturated solutions of sodium chloride (NaCl), potassium chloride (KCl) and calcium chloride ($CaCl_2$) under axial stress of 40 kPa: (a) experimental results (after Di Maio, 1998); (b) computed model response

resulting in an Na-clay that is therefore more expansive when in contact with water, as can be observed both in the test (Fig. 13(a)) and in the model response (Fig. 13(b)).

A test that is not satisfactorily reproduced by the model is depicted in Fig. 14(a). It involves exposure of the sample to a calcium chloride solution at high stress levels. As shown in Fig. 14(b), the model predicts a higher degree of reversibility than observed. The same effect was observed when

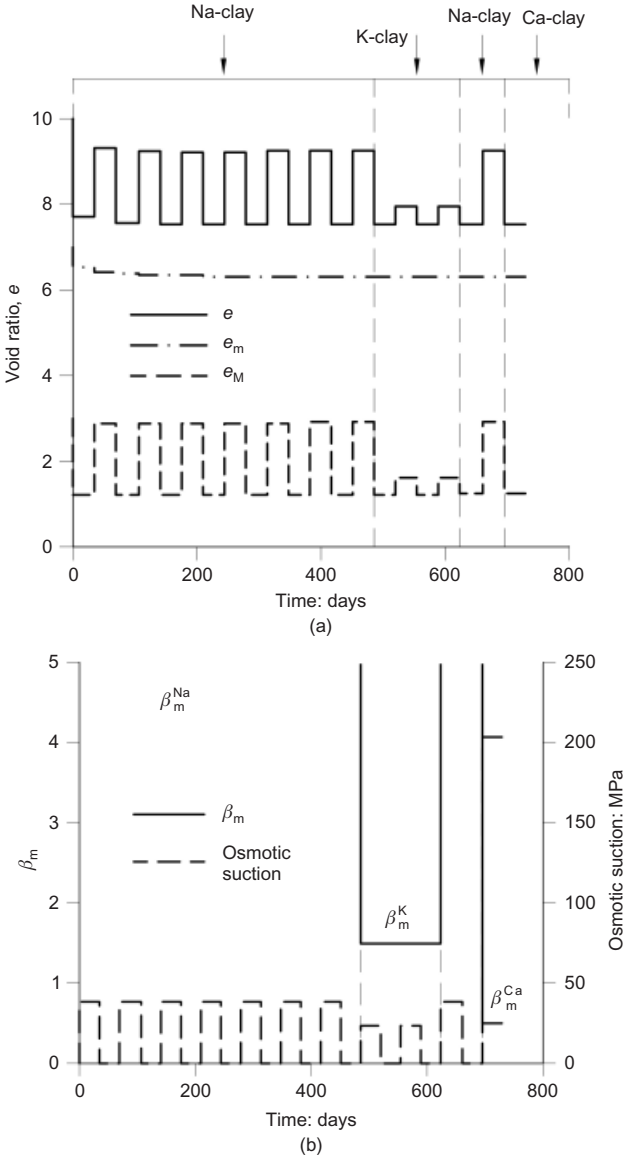

Fig. 12. Cyclic exposure of sodium bentonite to saturated solutions of sodium chloride, potassium chloride and calcium chloride under axial stress of 40 kPa: (a) model response in terms of total, macro- and micro-void ratios; (b) evolution of osmotic suction and variable β_m as a function of cation exchange reactions

using a saturated potassium chloride solution. As shown above, this difference between model predictions and test results does not arise at low stresses. An updated version of the model would require a refinement of the formulation to include the effect of applied stresses on reaction reversibility. Note, however, that reaction irreversibility is still compatible with the assumption of reversible microstructural strains.

Unsaturated clays

Although fewer swelling tests on unsaturated soils with chemo-mechanical loading have been reported, two cases are considered in this section. Now, in addition to osmotic suction effects, matric suction s also plays a role in the behaviour of both macrostructure (BBM model) and microstructure (equations (1) and (13)).

The first case involves the tests presented by Studds *et al.* (1998), who studied the swelling behaviour of Wyoming sodium bentonite. Samples of bentonite powder were placed in an oedometer ring, subjected to vertical stress, and either

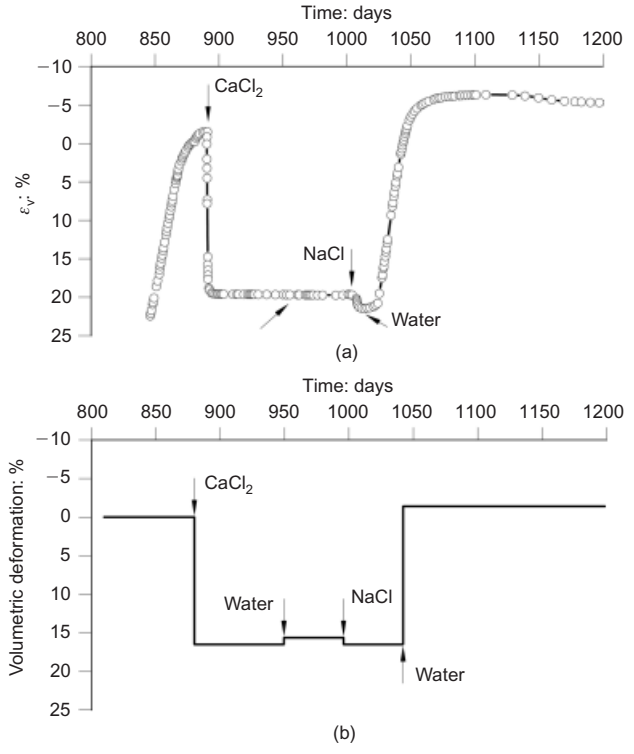

Fig. 13. Volume change of sodium bentonite exposed to caclium chloride ($CaCl_2$) and sodium chloride (NaCl) saturated solutions under axial stress of 40 kPa: (a) experimental results (after Di Maio, 1998); (b) computed model response

distilled water or one of the chloride salt solutions was allowed access to the sample. The sample height was monitored until swelling ceased, at which point the final void ratio was calculated. Fig. 15 shows the observed swelling of the bentonite hydrated with distilled water and with chloride salt solutions at concentrations of 0·001, 0·1 and 1 mol/l under different stress levels. The specimens were initially unsaturated, with an estimated matric suction (from water content) of 1 MPa. In Fig. 15(a) it can be seen that the swelling with distilled water becomes larger as the applied stress is reduced; in fact, above a confining stress of 200 kPa the specimens exhibit practically no expansion when placed in contact with the water. Fig. 15(b) shows that the swelling of the samples reduces as the saline concentration of the hydration water increases.

These swelling tests have been simulated using the reference soil parameters. As shown in Fig. 16, the model results are consistent with experimental observations for the two types of test: hydration with distilled water (Fig. 16(a)) and hydration with sodium chloride saline water (Fig. 16(b)). Here exchangeable cations have no effect; the model explains observed behaviour simply from the variations of osmotic and matric suctions. Hydration with distilled water causes a reduction of matric and osmotic suction, and the sample swells. When hydrating with a saline solution, swelling is smaller because of the combined effects of an applied larger osmotic suction and an increase in the clay microstructural stiffness.

A second case of the chemo-mechanical effects on unsaturated compacted soil has been reported by Alawaji (1999). In this case the material tested was a mixture of sand and bentonite, the proportion of bentonite being 20% by weight. To prepare the oedometer test specimens, bentonite was added to the dry sand and initially mixed with a spoon. This was followed by adding distilled water in several stages until the desired water content of 8% was reached. A 24 h curing period followed. Specimens were finally prepared by statically compacting the soil directly in the confining oedometer ring to a dry density of 18 kN/m^3. The specimens were then hydrated with aqueous solutions of calcium nitrates at different concentration values and different applied stresses.

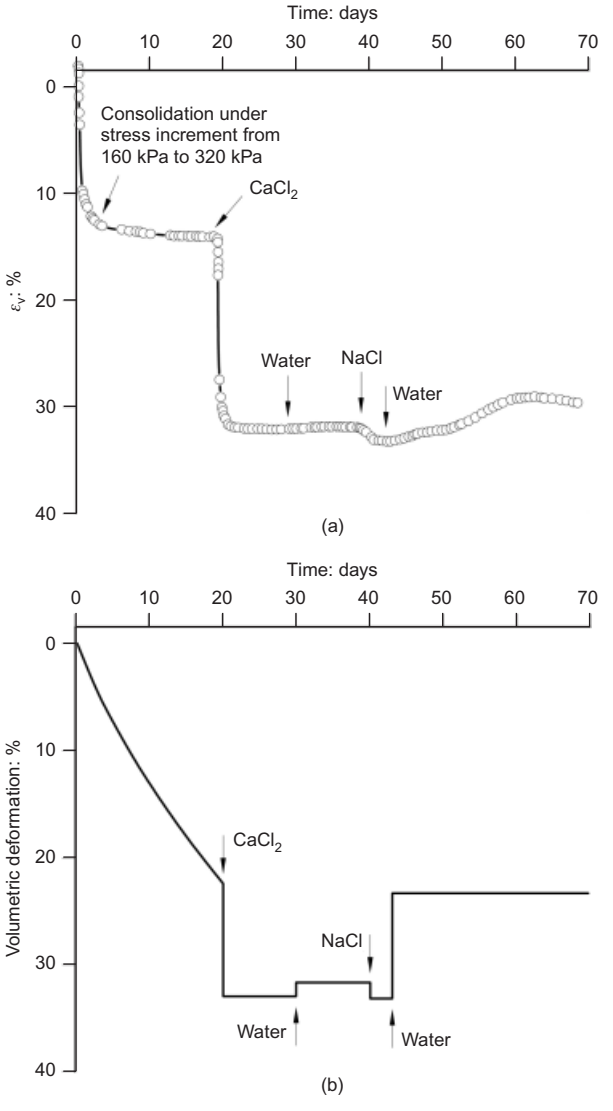

Fig. 14. Volume change of sodium bentonite exposed to calcium chloride ($CaCl_2$) and sodium chloride (NaCl) saturated solutions under axial stress of 320 kPa: (a) experimental results (after Di Maio, 1996); (b) computed model response

Figure 17(a) shows the observed swelling under load as a function of calcium nitrate concentrations. It can be seen that, for the different values of applied load, the swelling potential reduces drastically for concentrations above 0·3N. For a qualitative comparison, the results of model simulations are represented in a plot of void ratio against concentration for the various applied loads (Fig. 17(b)). It can be seen that the model results for the reference soil exhibit the same trends as those observed in the tests. Apart from some potential precipitation phenomena, Alawaji (1999) identified two main causes for the observed behaviour: the change in the electrolyte concentration (i.e. osmotic suction), and replacement of monovalent ions by divalent ones such as calcium – the two main mechanisms considered in the model.

CONCLUDING REMARKS

A constitutive model has been described that incorporates the effect of geochemical variables on the volumetric behaviour of expansive clays. The relevant geochemical variables

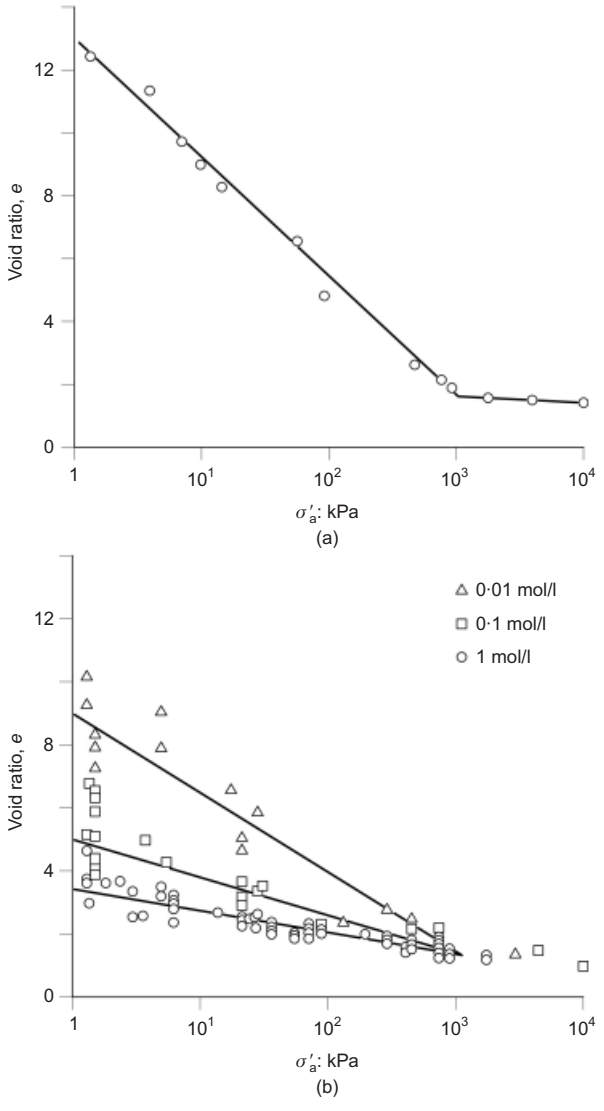

Fig. 15. Swelling of unsaturated bentonite powder as a function of vertical stress (after Studds *et al.*, 1998). Hydration performed with: (a) distilled water; (b) different-strength chloride salt solutions

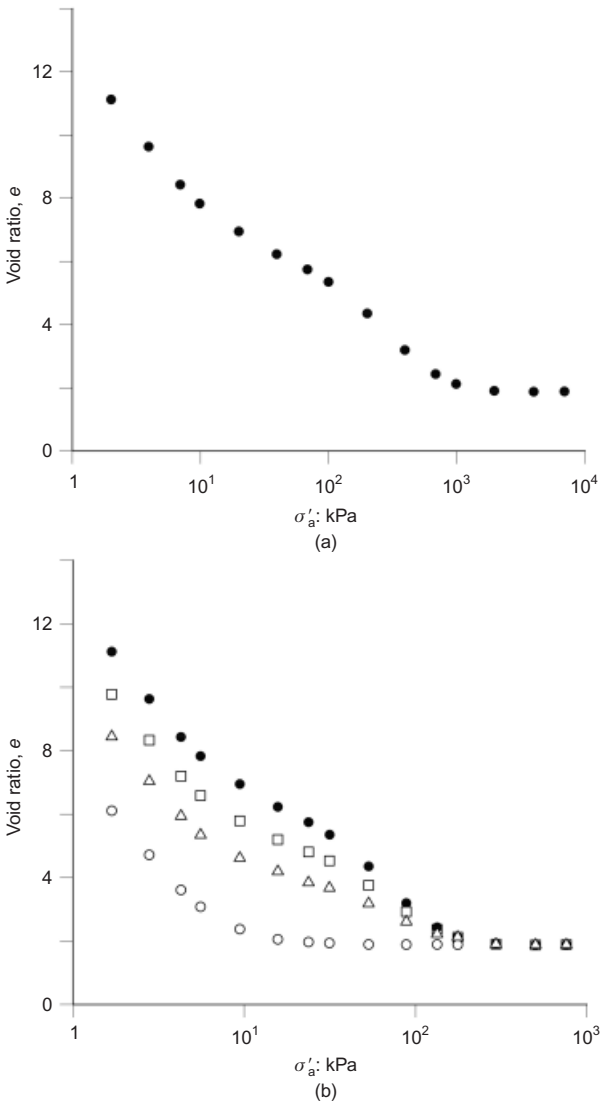

Fig. 16. Computed model response of swelling as a function of vertical stress. Hydration performed with: (a) distilled water; (b) different-strength sodium chloride solutions

selected for model development are osmotic suction and the distribution of cations over the exchange sites of the clay. In this way, the influence of cation exchange and osmotic suction can be explicitly considered.

The model has been developed within the framework of an existing double-structure model. This framework provides a microstructural level where the chemical effects can be incorporated in a natural manner. Microstructural strains are considered reversible, and volume change irreversibility arises from the interaction between the two structural levels. The capabilities of the model have been demonstrated with a series of applications addressing the simulation of experimental behaviour observed in oedometer tests on saturated bentonite subjected to chemo-mechanical loading, and in hydration tests of unsaturated bentonite performed with different solute concentrations. Although some limitations have been identified that may require further developments (e.g. the assumption of local equilibrium for chemical reactions, and the potential existence of irreversible chemical reactions at large stresses), the constitutive model presented is able to reproduce a wide range of features of the chemo-mechanical behaviour of saturated and unsaturated expansive soils.

ACKNOWLEDGEMENTS

The authors are grateful to the European Commission and ENRESA for their financial support of this work. The first author has been supported by a CAPES Scholarship from Brazil. The assistance of the Ministerio de Economía and Competitividad through grant BIA2011-27217 is gratefully acknowledged.

NOTATION

a_w	activity of liquid water
a_{Na^+}, a_{K^+}, $a_{Mg^{2+}}$, $a_{Ca^{2+}}$	chemical activities for cations in solution
CEC	cation exchange capacity of clay
e	total void ratio
e_M	macrostructural void ratio
e_m	microstructural void ratio
e_p	threshold void ratio where change of slope occurs
F_{SD}	yield function for suction decrease
F_{SI}	yield function for suction increase
f_D, f_I	interaction functions
H	sample height
K_m	microstructural volumetric stiffness

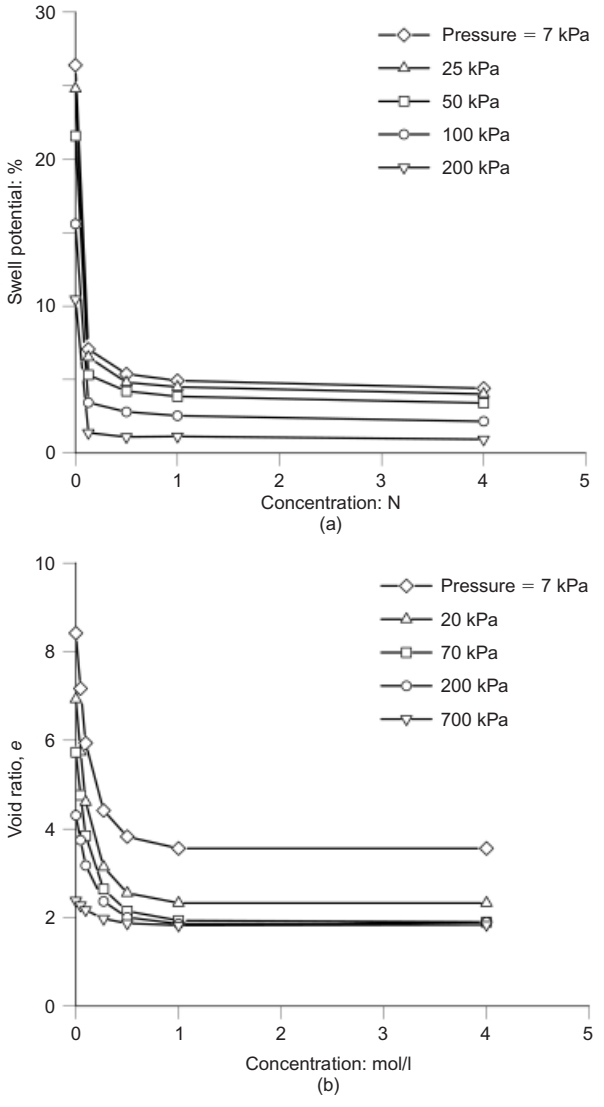

Fig. 17. Swelling of unsaturated sand–bentonite mixture as a function of calcium nitrate concentrations under different stress levels: (a) experimental results (after Alawaji, 1999); (b) computed model response

n parameter
n_d normal to the neutral plane, suction decrease
n_i normal to the neutral plane, suction increase
p mean net stress
p_0 yield stress for value of matric suction acting on soil
$\hat{p}$ effective mean stress
p_0^* saturated yield stress
R gas constant
r parameter of the LC yield surface
S_r microstructure degree of saturation
s macrostructural matric suction
s_M total macrostructural suction
s_m total microstructural suction
s_o macrostructural osmotic suction
s_t total suction
T absolute temperature
v_w molar volume of water
x_i equivalent fraction of exchangeable cation i
α_m material parameter
β_m model variable
δ_s vertical displacement
ε_M^p plastic macrostructural volumetric strain
ε_{MLC}^p plastic macrostructural volumetric strain due to LC yield function
$d\varepsilon_{M\beta}^p$ plastic macrostrucural volumetric strain due to the active I or D mechanism
ε_m^e microstructural volumetric strain
ε_v volumetric strain
κ slope of elastic swelling line
κ_s slope of elastic void ratio changes due to suction variations
λ_0 slope of the saturated virgin consolidation line
σ_a applied total vertical stress
σ_a' applied effective vertical stress
χ Bishop parameter
ψ chemically modified effective stress of the microstructure
ψ^* hardening parameter if SI and SD yield surfaces coincide
ψ_D^* hardening parameter for the SD yield surface
ψ_I^* hardening parameter for the SI yield surface
ψ_c chemical component of chemically modified effective stress of the microstructure

REFERENCES

Alawaji, H. A. (1999). Swell and compressibility characteristics of sand–bentonite mixtures inundated with liquids. *Appl. Clay Sci*. **15**, No. 3–4, 411–430.

Alonso, E. E., Gens, A. & Josa, A. (1990). A constitutive model for partially saturated soils. *Géotechnique* **40**, No. 3, 405–430, http://dx.doi.org/10.1680/geot.1990.40.3.405.

Alonso, E. E., Gens, A. & Lloret, A. (1991). Double structure model for the prediction of long-term movements in expansive materials. In *Computer methods and advances in geomechanics* (eds G. Beer, J. R. Booker and J. P. Carter), vol. 1, pp. 541–548. Rotterdam, the Netherlands: Balkema.

Alonso, E. E., Vaunat, J. & Gens, A. (1999). Modelling the mechanical behaviour of expansive clays. *Engng Geol*. **54**, No. 1–2, 173–183.

Appelo, C. & Postma, D. (1993). *Geochemistry, groundwater and pollution*. Rotterdam, the Netherlands: Balkema.

Barbour, S. L. & Yang, N. (1993). A review of the influence of clay-brine interactions on the geotechnical properties of Ca-montmorillonitic clayey soils from western Canada. *Can. Geotech. J.*, **30**, No. 6, 920–934.

Di Maio, C. (1996). Exposure of bentonite to salt solution: osmotic and mechanical effects. *Géotechnique* **46**, No. 4, 695–707, http://dx.doi.org/10.1680/geot.1996.46.4.695.

Di Maio, C. (1998). Discussion: 'Exposure of bentonite to salt solution: osmotic and mechanical effects'. *Géotechnique* **48**, No. 3, 433–436, http://dx.doi.org/10.1680/geot.1998.48.3.433.

Di Maio, C., Santoli, L. & Schiavone, P. (2004). Volume change behavior of clays: the influence of mineral composition, pore fluid composition and stress state. *Mech. Mater.* **36**, No. 5–6, 435–451.

Gajo, A. & Loret, B. (2003). Finite element simulations of chemo-mechanical coupling in elastic-plastic homoionic expansive clays. *Comp. Methods Appl. Mech. Engng* **192**, No. 31–32, 3489–3530.

Gajo, A. & Loret, B. (2007). The mechanics of active clays circulated by salts, acids and bases. *J. Mech. Phys. Solids* **55**, No. 8, 1762–1801.

Gajo, A. & Maines, M. (2007). Mechanical effects of aqueous solutions of inorganic acids and bases on a natural active clay. *Géotechnique* **57**, No. 8, 687–699, http://dx.doi.org/10.1680/geot.2007.57.8.687.

Gajo, A., Loret, B. & Hueckel, T. (2002). Electro-chemo-mechanical couplings in saturated porous media: elasto-plastic behaviour of heteroionic expansive clays. *Int. J. Solids Struct*. **39**, No. 16, 4327–4362.

Gens, A. (2010). Soil-environment interactions in geotechnical

engineering. 47th Rankine Lecture. *Géotechnique* **60**, No. 1, 3–74, http://dx.doi.org/10.1680/geot.9.P.109.

Gens, A. & Alonso, E. E. (1992). A framework for the behaviour of unsaturated expansive clays. *Can. Geotech. J.* **29**, No. 6, 1013–1032.

Gens, A., Alonso, E. E., Lloret, A. & Battle, F. (1993). Prediction of long term swelling of expansive soft rocks: a double-structure approach. In *Geotechnical engineering of hard soils – soft rocks* (eds A. Anagnostopoulos, F. Schlosser, N. Kalteziotis and R. Frank), vol. 1, pp. 495–500. Rotterdam, the Netherlands: Balkema.

Gens, A., Valleján, B., Sánchez, M., Imbert, C., Villar, M. V. & Van Geet, M. (2011). Hydromechanical behaviour of a heterogeneous compacted soil: experimental observations and modelling. *Géotechnique* **61**, No. 5, 367–386, http://dx.doi.org/10.1680/geot.SIP11.P.015.

Guimarães, L. do N. (2002). *Análisis multi-componente no isotermo en medio poroso deformable no saturado*. PhD thesis, Universitat Politècnica de Catalunya, Spain.

Guimarães, L. do N., Gens, A. & Olivella, S. (2007). Coupled thermo-hydro-mechanical and chemical analysis of expansive clay subjected to heating and hydration. *Transp. Porous Media* **66**, No. 3, 341–372.

Harvie, C. & Weare, J. (1980). The prediction of mineral solubilities in natural waters: the Na-K-Mg-Ca-Cl-SO_4-H_2O system from zero to high concentration at 25°C. *Geochim. Cosmochim. Acta* **44**, No. 7, 981–997.

Hueckel, T. (1992). Water-mineral interaction in hygro-mechanics of clays exposed to environmental loads: a mixture approach. *Can. Geotech. J.* **29**, No. 6, 1071–1086.

Hueckel, T. (1997). Chemo-plasticity of clays subjected to stress and flow of a single contaminant. *Int. J. Numer. Anal. Methods Geomech*. **21**, No. 1, 43–72.

Hueckel, T. & Bo Hu, L. (2009). Feedback mechanisms in chemo-mechanical multi-stage modelling of soil and sediment compaction. *Comput. Geotech*. **36**, No. 6, 934–943.

Karnland, O. (1997). *Bentonite swelling pressure in strong NaCl solutions. Correlation between model calculations and experimentally determined data*, Technical report 97-31. Stockholm, Sweden: Swedish Nuclear Fuel and Waste Management Company (SKB).

Katti, D. R., Schmidt, S. R., Ghosh, P. & Katti, K. S. (2007). Molecular modelling of the mechanical behavior and interactions in dry and slightly hydrated sodium montmorillonite interlayer. *Can. Geotech. J.* **44**, No. 4, 425–435.

Komine, H. & Ogata, N. (1996). Prediction for swelling characteristics of compacted bentonite. *Can. Geotech. J.* **33**, No. 1, 11–22.

Liu, Z., Boukpeti, N., Li, X., Collin, F., Radu, J.-P., Hueckel, T. & Charlier, R. (2005). Modelling chemo-hydro-mechanical behaviour of unsaturated clays: a feasibility study. *Int. J. Numer. Anal. Methods Geomech*. **29**, No. 9, 919–940.

Loret, B., Hueckel, T. & Gajo, A. (2002). Chemo-mechanical coupling in saturated porous media: elasto-plastic behaviour of homoionic expansive clays. *Int. J. Solids Struct*. **39**, No. 10, 2773–2806.

Marcial, D., Delage, P. & Cui, Y-F. (2002). On the high stress compression of bentonites. *Can. Geotech. J.* **39**, No. 4, 812–820.

Mesri, G. & Olsen, R. (1970). Shear strength of montmorillonite. *Géotechnique* **20**, No. 3, 261–270, http://dx.doi.org/10.1680/geot.1970.20.3.261.

Mesri, G. & Olsen, R. (1971). Consolidation characteristics of montmorillonite. *Géotechnique* **21**, No. 4, 341–352, http://dx.doi.org/10.1680/geot.1971.21.4.341.

Mitchell, J. K. & Soga, K. (2005). *Fundamentals of soil behaviour*, 3rd edn. Hoboken, NJ, USA: Wiley.

Moore, R. (1991). The chemical and mineralogical controls upon the residual strength of pure and natural clays. *Géotechnique* **41**, No. 1, 35–47, http://dx.doi.org/10.1680/geot.1991.41.1.35.

Pusch, R. (1982). Mineral-water interactions and their influence on the physical behaviour of highly compacted Na bentonite. *Can. Geotech. J.* **19**, No. 3, 381–387.

Salas, J. & Serratosa, J. (1953). Compressibility of clays. *Proc. 3rd Int. Conf. Soil Mech. Found. Engng, Zurich* **1**, 192–198.

Sánchez, M., Gens, A., Guimarães, L. do N. & Olivella, S. (2005). A double structure generalized plasticity model for expansive materials. *Int. J. Numer. Anal. Methods Geomech*. **29**, No. 8, 751–787.

Sridharan, A., Rao, S. & Murthy, N. (1986). Compressibility behaviour of homoionized bentonites. *Géotechnique* **36**, No. 4, 551–564, http://dx.doi.org/10.1680/geot.1986.36.4.551.

Studds, P. G., Stewart, D. I. & Cousens, T. W. (1998). The effects of salt solutions on the properties of bentonite-sand mixtures. *Clay Miner*. **33**, No. 4, 651–660.

Wilson, R. & Aifantis, E. (1982). On the theory of consolidation with double porosity. *Int. J. Engng Sci*. **20**, No. 9, 1009–1035.

Witteveen, P. *et al.* (2013). *Géotechnique* **63**, No. 3, 244–255 [http://dx.doi.org/10.1680/geot.SIP13.P.027]

An experimental and constitutive investigation on the chemo-mechanical behaviour of a clay

P. WITTEVEEN*, A. FERRARI* and L. LALOUI*

Engineering issues for which the understanding of the chemo-mechanical behaviour of soils is relevant include wellbore stability problems, the salinification of groundwater, and nuclear waste storage. However, despite the vast number of situations in which couplings between chemistry and mechanics occur, the available constitutive models rely on limited experimental evidence. This paper presents the results of an experimental programme on the chemo-mechanical behaviour of a non-swelling illite. The osmotic suction is controlled through the ion concentration of sodium chloride in the pore water. Stress paths include mechanical loading at a constant osmotic suction, and an increasing osmotic suction at a constant mechanical stress. The experimental results point out a correlation between the osmotic suction and initial oedometric modulus, as well as between the osmotic suction and yield stress. A constitutive framework for soils is extended to take the observed chemo-mechanical couplings into account. The numerical model has been calibrated for the illite using the parameters obtained through the tests under mechanical loading at a constant concentration, and validated using more elaborate stress paths. The presented experimental and constitutive investigation builds a basis for the assessment of engineering issues in which pore liquid chemistry plays a major role.

KEYWORDS: chemical properties; clays; constitutive relations; laboratory tests; suction

INTRODUCTION

Understanding couplings between the chemical composition of the pore liquid and the mechanical behaviour in clayey soils is becoming essential in the practice of civil, energy and environmental engineering. While the applications were previously limited to groundwater pollution problems (e.g. for drinking water, or with respect to plant growth), the relevance of knowledge on the behaviour of clay soils subject to influences of a chemical type is now significant in many fields, including the storage of nuclear waste (degradation of concrete liners), oil and gas wellbore stability (entrance of drill fluid in soil), and/or soil stabilisation.

The effects of electrolytes in contact with the clay soil's pore liquid have been researched since the 1950s. Early contributions, such as Bolt (1956) and Bolt & Miller (1955), focused mainly on soil compressibility. In the 1970s and 1980s, chemically induced consolidation, permeability and shear strength variations, and osmosis and osmotic effects were extensively studied (e.g. Mesri & Olson, 1970, 1971; Mitchell *et al.*, 1973; Sridharan & Venkatappa Rao, 1973, 1979; Marine & Fritz, 1981; Fritz, 1986; Barbour & Fredlund, 1989). The late 1990s and 2000s brought forth coupled chemo-mechanical models, in which the concentration or mass fraction of certain species in the pore liquid played a major role (e.g. Loret *et al.*, 2002; Gajo & Loret, 2003; Gens, 2010; Guimarães *et al.*, 2007).

This study aimed to extend the experimental database on the subject of one-dimensional consolidation induced by a change in the chemical composition of the pore liquid, with a focus on electrolytes. A laboratory programme was carried out, under which the experimental results were modelled within a new constitutive framework.

Manuscript received 5 March 2012; revised manuscript accepted 17 October 2012.
Discussion on this paper closes on 1 August 2013, for further details see p. ii.
* Laboratory for Soil Mechanics, Swiss Federal Institute of Technology Lausanne, Switzerland.

THEORIES AND EVIDENCE

It is widely acknowledged that clays exhibit a negative electrical charge at their platy particle surface (e.g. Mitchell & Soga, 2005). Thus their aggregates, the groups of parallel-arranged platelets, exhibit this negative electrical charge all along their outer boundaries, leading clays to attract positively charged ions from the pore liquid, and the diffuse double layer to be constructed (Gouy, 1910; Chapman, 1913; Verwey & Overbeek, 1948). The high concentration of cations and the low concentration of anions at the clay boundary result in a high electrical potential, which decreases as the distance from the aggregate increases. This potential causes the clay to act as a non-ideal, semi-permeable membrane, reducing the migration of electrically charged ions but allowing electrically neutral water molecules to move freely. The so-called 'osmotic processes' resulting from these properties have been widely described in the literature (e.g. Marine & Fritz, 1981; Fritz, 1986; Barbour & Fredlund, 1989; Loret *et al.*, 2002).

The migration of ions or water may alter the pore liquid composition in two distinct ways. First, a chemical concentration gradient can lead to the entry of ions into the pores, where the negatively charged clay aggregate boundaries will attract the positively charged cations. Thus the interaggregate repulsive forces decrease, leading the modal pore diameter and therefore the overall volume to decrease. This phenomenon is referred to as *chemical consolidation*. Second, if there is a chemical concentration gradient and the higher concentration is on the outside of the considered soil mass, water flows out of the soil owing to the osmotic effects occurring in clays with thick, diffuse double layers (or high electrical potential along their particle surfaces) with respect to the pore diameter. This outflow increases the negative pore liquid pressure and thus the effective stress (total stress minus pore water pressure), leading to an overall volume reduction. This phenomenon is referred to as *osmotic consolidation*.

These two main phenomena may occur in parallel, because the semi-permeable properties of the clay are not

ideal. Various authors use different terminology for these phenomena: Barbour & Fredlund (1989) mention *osmotic consolidation* and *osmotically induced consolidation*, whereas Kaczmarek & Hueckel (1998) discuss *chemical consolidation* and *chemico-osmotic consolidation*.

Barbour & Fredlund (1989) interpreted the results of a series of four experiments conducted by Mesri & Olson (1971), and presented additional experimental results on two different types of soil to quantify 'osmotic compressibility and permeability'. The main conclusion of their work was that the dominant mechanism of volume change was osmotic consolidation, referred to as chemical consolidation here.

Consolidation due to a difference in chemical composition of the pore water was investigated by Fernandez & Quigley (1985, 1991) and later by Hueckel (1997) and Boukpeti *et al.* (2004). They studied the influence of a single organic contaminant on the compressibility properties of Sarnia clay, which is an Na-montmorillonite with traces of Ca-smectite. Hueckel (1997) and Boukpeti *et al.* (2004) modelled mainly the evolution of the yield limit stress. They proposed a logarithmic evolution law, under which the yield stress decreases as the contaminant concentration increases, defined as the 'chemical softening function'.

Di Maio (1996), Di Maio & Fenelli (1997) and Di Maio & Onorati (1999) described a series of experiments with the aim of evidencing and quantifying the aforementioned consolidation phenomena without naming them. The main part of their research was focused on a bentonite, yielding large deformations (up to 15% due to a change in pore liquid only). Constitutive models based on these results were proposed by Loret *et al.* (2002), Gajo & Loret (2003), and Gajo *et al.* (2002) under one framework, and by Gens (2010) and Guimarães *et al.* (2007) under a different framework.

The former framework (Loret *et al.*, 2002; Gajo & Loret, 2003) consists of an elasto-plastic model in which the chemical part is governed by the mass fractions and mass balance of all of the species in the soil sample. In contrast, the latter framework (Gens, 2010; Guimarães *et al.*, 2007) consists of a double-structured model in which the chemical part is represented by osmotic suction. This osmotic suction works at the microscopic level, and all of the strains it produces are considered completely reversible.

A chemo-poro-elasticity model for shales was presented by Bunger (2010) and Sarout & Detournay (2011). The model is an extension of classic Biot poro-elasticity (Biot, 1941, 1956a, 1956b, 1973), including the evolution of pore pressures through a sample due to the presence and transport of ions in the pore liquid. Based on the work of Sherwood (1993, 1994), Heidug & Wong (1996) and Coussy (2004), the joint papers described the effects of mechanical perturbations (due to a pore liquid *pressure* gradient) and chemical perturbations (due to a pore liquid *concentration* gradient) in a pore pressure transmission experiment. Sarout & Detournay (2011) presented a fully described elastic model. These models for shales are defined in terms of the chemical composition of the pore liquid, taking the quantities of different species or components in the pore water into account.

With increasing interest in geomechanical applications in which the chemistry of the pore liquid plays a major role, advanced chemo-mechanical frameworks are increasingly important. This paper proposes a coupled elasto-plastic, chemo-mechanical model. In contrast to previous studies, where the (ion) concentration was considered as the governing variable, the present model is defined for changes in osmotic suction, which allows the results to be presented and discussed independently of the pore liquid components.

EXPERIMENTAL PROGRAMME

A comprehensive laboratory programme was conducted with the aim of providing additional experimental evidence on: (a) a 'chemical softening function', an evolution law for the yield limit stress with respect to the pore liquid chemistry; and (b) deformation due to chemical loading. The programme involved a series of chemo-mechanical experiments in which the osmotic suction was controlled through the sodium chloride concentration in the pore water.

Materials

Solutions of sodium chloride (NaCl) in distilled water at different ion concentrations, ranging from 0·0 M (distilled water) to 6·0 M (practically saturated sodium chloride solution), were mixed with a non-swelling illite powder. The mineralogy, Atterberg limits and initial conditions of the illite powder and its grain size distribution are presented in Table 1. Because of the fairly low activity of the illite, the chemo-mechanical behaviour is quite different from that in other studies reported in the literature.

During preparation, a mass of illite powder was mixed with the appropriate amount of solution. The mixture was cured in a sealed plastic chamber for a minimum of 24 h to guarantee the internal redistribution of the pore liquid.

Suction measurements

Osmotic suction is a function of the ion concentration, and for dilute solutions (ion concentrations up to approx. 2·0 M), it can be approximated by the Van't Hoff equation as

$$\pi = \nu RTc \tag{1}$$

where π is the osmotic suction (kPa), ν is the number of constituent ions, R is the universal gas constant (J/(mol K)), T is the absolute temperature (K), and c is the ion concentration of the electrolyte. A first series of experiments was performed to obtain a correlation between the osmotic suction and ion concentration that was valid for the entire range of applied sodium chloride concentrations. The matric and total suction of the clay powder–pore liquid mixtures were

Table 1. Mineralogy, Atterberg limits, grain size distribution and physical data of soil used in experiments

Mineralogy	
Illite: %	77
Kaolinite: %	10
Calcite: %	12
Quartz:	Traces
Feldspar	Traces
Atterberg limits	
Liquid limit: %	54
Plastic limit: %	30
Plasticity index: %	24
Grain-size distribution	
Sand fraction: %	12
Silt fraction: %	21
Clay fraction: %	67
Physical data	
Hygroscopic water content: % (at 40% RH)	5
Grain density: g/cm^3	2·65
Specific surface: m^2/g	170–180

first determined by the filter paper method, using Schleicher and Schuell no. 589/2 40·5 mm dia. filter papers. The suction values of the filter paper were calibrated with respect to the water content for the matric suction (difference between pore air and pore water pressures) and the total suction (matric suction plus osmotic suction) separately. The calibration involved use of the axis-translation technique to control the matric suction, and the vapour equilibrium technique to control the total suction of the filter paper.

Five of the mixtures were prepared with distilled water at different water contents; four additional mixtures were prepared with a 4·0 M solution at different water contents. Additionally, the total suction of clay powder-pore liquid mixtures prepared at different sodium chloride target concentrations (distilled water, 0·5, 1·0, 2·0, 4·0 and 6·0 M) and at different water contents was determined using a chilled-mirror dew-point psychrometer (Leong *et al.*, 2003; Cardoso *et al.*, 2007). The water content of all mixtures was determined after the tests by oven-drying at 105°C until no mass change occurred in the last 24 h.

Chemo-mechanical oedometric tests

Chemo-mechanical oedometric tests were conducted involving changes in the vertically applied mechanical stress and osmotic suction. The goal of this research programme was to highlight changes in the yield stress and elasto-plastic parameters of the clay material.

The specimens were prepared by compacting a clay powder–pore liquid mixture directly in the oedometer rings (60 mm in diameter and 10 mm high), targeting an initial void ratio of $e_0 = 0{\cdot}95 \pm 0{\cdot}02$. The compaction energy was kept constant for all samples. With the density of the solutions in the range $\rho_{solution} = 1{\cdot}10 \pm 0{\cdot}10$ Mg/m^3, this resulted in an initial water content of $w_0 = 0{\cdot}39 \pm 0{\cdot}05$, corresponding to fully saturated conditions. The typical loading time for mechanical increments was 24 h.

The osmotic suction and vertically applied mechanical stress (corresponding to the vertical effective stress) were the independent driving variables. Therefore there were two types of stress increment, mechanical and chemical, which allowed the elaborate stress paths to be defined.

The experimental programme was designed such that the influence of osmotic suction on the mechanical behaviour could be researched first. To this end, a series of seven oedometer tests were conducted at different but constant values of osmotic suction of the pore liquid. Two of the samples were prepared with distilled water; the five others were prepared with one of the aforementioned solutions.

The influence of changes in osmotic suction was then investigated through two experiments in which there was an incremental concentration change at different but constant mechanical stress levels. Two oedometric samples were prepared with distilled water and loaded mechanically up to different vertical stress levels ($\sigma_v = 30$ kPa and $\sigma_v = 77$ kPa). The chemical loading was achieved by replacing the oedometer cell fluid with an electrolyte of higher osmotic suction and monitoring the deformation of the sample until it stabilised after 2–4 days. The surrounding solution was frequently renewed to ensure the ion concentration in the sample. The incremental approach meant that this procedure was repeated for different osmotic suctions, until a saturated sodium chloride solution was applied in the last step. Afterwards, these chemically loaded samples were subjected to the remaining loading increments of the conventional mechanical oedometric test.

The previously described stress paths are quantitatively represented in Figs 1 and 2. In both the mechanical and the chemical loading increments, secondary compression is not taken into account.

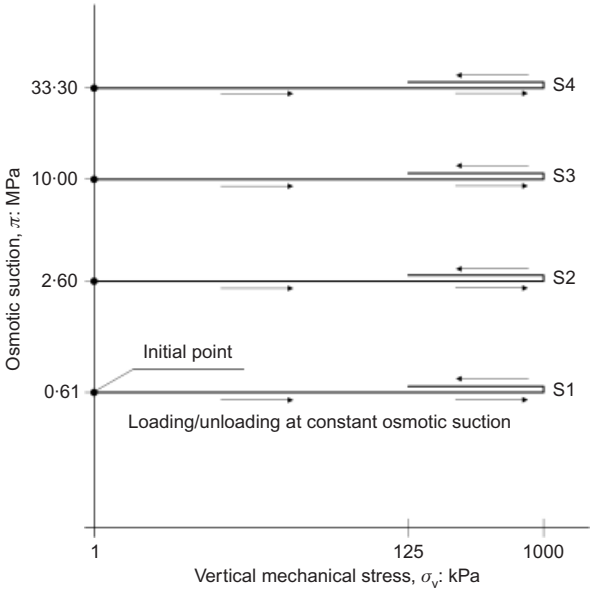

Fig. 1. Applied stress paths for oedometer samples under mechanical loading only

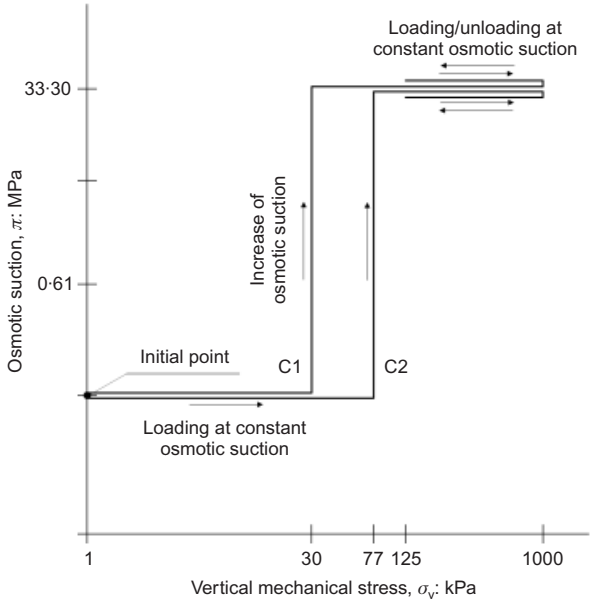

Fig. 2. Applied stress paths for oedometer samples under mechanical and chemical loading

Table 2 provides an overview of all the tests performed.

EXPERIMENTAL RESULTS

Suction measurements

Figure 3 depicts the results of the filter paper method and the psychrometric readings for the mixtures prepared with distilled water and with the 4·0 M solution. The total suction ψ (MPa) and matric suction s_m (MPa) are plotted against the water content of the mixtures of illite powder with either distilled water or a 4·0 M sodium chloride solution. In the distilled water mixtures, the matric suction is two orders of magnitude smaller than the total suction. This effect is even larger (three to four orders of magnitude) for the mixtures prepared with the salt solution, because the presence of salt increases the osmotic component of the suction, while the

Table 2. Overview of all tests performed

	Tested material		
	Solutions of sodium chloride in distilled water	Mixtures of clay powder with distilled water	Mixtures of clay powder with solutions of sodium chloride
Suction measurement	Total suction determination by psychrometric readings for different concentrations of solution	Matric and total suction determination by filter paper method and psychrometric readings for different water content values	
Mechanical oedometer tests		Two loading–unloading tests	Five loading–unloading tests at concentrations of 0·5, 1·0, 2·0, 4·0 and 6·0 M
Chemo-mechanical oedometer tests		Two loading–unloading tests with chemical loading at constant vertical stress	

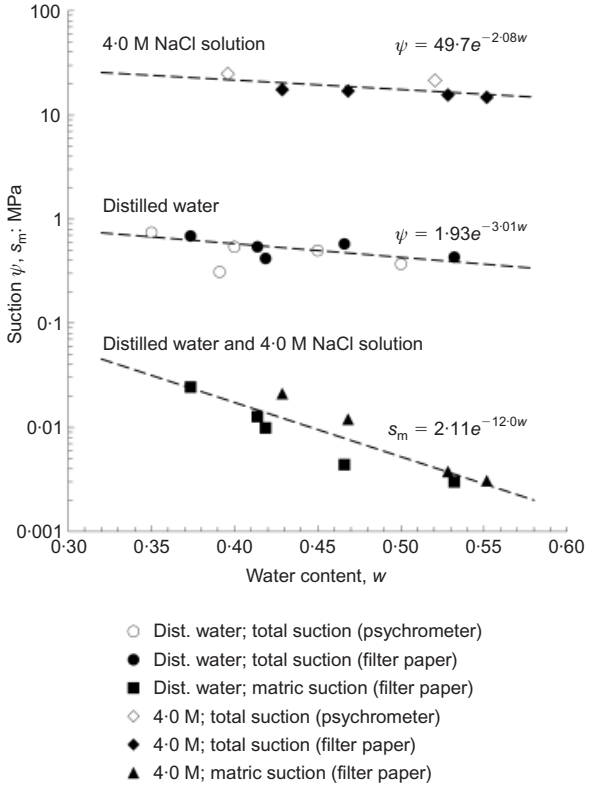

Fig. 3. Total and matric suction measurements on mixtures of illite powder and either distilled water or 4·0 M sodium chloride (NaCl) solution

matric suction remains fairly constant. These results indicate that the presence of salt in the pore water does not significantly influence the matric suction. Thus the measurements in terms of total suction are subsequently assumed to be representative of the osmotic component, and in the following the matric suction will be neglected. However, this assumption might be different for other types of clay and salt, because the interaction between clay and salt might be of a different nature.

Figure 3 also shows the marginal influence of the water content on the osmotic suction for the considered range. Within the range of initial water contents for the oedometric specimens, the osmotic suctions are of the same order of magnitude. Therefore the influence of the water content in this range can be neglected.

The test results show that the osmotic suction measured for the specimens prepared with distilled water is greater than zero. This measurement can be explained by the dissolution of ions from the clay powder, as the illite can exchange cations. This finding allowed an average initial osmotic suction $\pi_0 = 0{\cdot}61$ MPa for the average initial water content $w_0 = 0{\cdot}39$ to be determined. This value will be the intercept in the correlation between the ion concentration and osmotic suction.

Finally, the results of the total suction measurements with both the filter paper method and dew-point psychrometer are plotted in Fig. 4 as a function of the sodium chloride concentration. Psychrometer readings for sodium chloride solutions prepared at different concentrations are also reported.

The graph shows a monotonic dependence of increasing suction with increasing ion concentration that can be appropriately described with a polynomial of the second order. The fact that the suction values for both the solutions and mixtures lie on the same line confirms that the influence of the matrix on the osmotic suction, as well as the influence of the presence of salt on the matric suction, is negligible.

The regression line in Fig. 4 provides an empirical relationship for the osmotic suction (in MPa) in a mixture of illite and a sodium chloride solution as a function of the ion

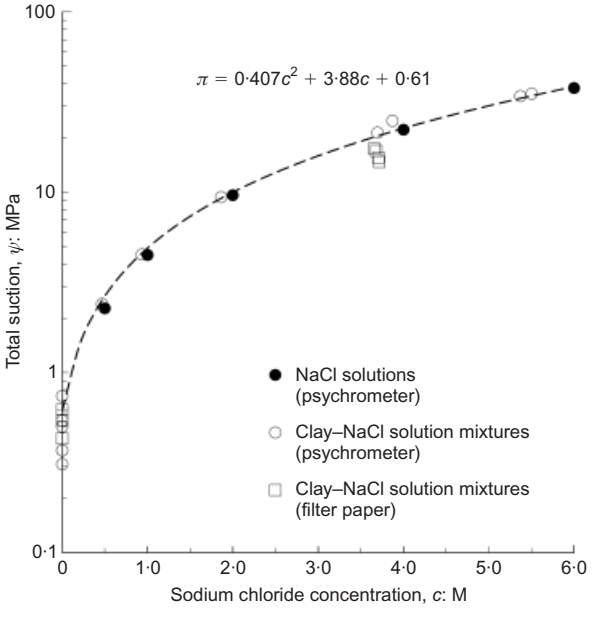

Fig. 4. Empirical relationship between osmotic suction of clay samples and sodium chloride (NaCl) concentration of pore water

concentration of that solution for the applied range of ion concentrations. The relationship is described with the function

$$\pi = f(c) = 0{\cdot}407c^2 + 3{\cdot}888c + 0{\cdot}61 \quad (2)$$

Chemo-mechanical oedometric tests

For clarity, the results of only four of the tests under mechanical loading are plotted in Fig. 5. Three major observations follow from these oedometric curves.

(*a*) The initial stiffness of the material decreases as the osmotic suction increases.
(*b*) The yield stress (the stress at the transition point from the elastic into the elasto-plastic behaviour) decreases as the osmotic suction increases.
(*c*) The slopes of the normal consolidation line (NCL) and unloading–reloading line (URL) do not change significantly with respect to the osmotic suction.

Observation (a) is confirmed when plotting the initial oedometric modulus (the applied stress increment from 1 to 15 kPa, divided by the occurring strain difference) against the osmotic suction, as shown in Fig. 6. There is a power trend, where the oedometric modulus decreases as the osmotic suction increases.

Observation (b) is confirmed by plotting the yield stress against the osmotic suction, as shown in Fig. 7. There is a logarithmic correlation, whereby the mechanical yield stress decreases as the osmotic suction increases. This conclusion corresponds to the proposed correlation between the preconsolidation pressure and concentration of one (organic) contaminant by Hueckel (1997) and Boukpeti *et al.* (2004). A new mathematical form is proposed in the present study for the evolution of the yield limit stress with respect to the osmotic suction of the pore water, as

$$\sigma_c = \left(1 - \gamma_\pi \log\frac{\pi}{\pi_0}\right)\sigma_{c0} \quad (3)$$

where σ_c is the vertical yield stress (kPa), γ_π is the chemical evolution factor, π is the current osmotic suction (MPa), $\pi_0 = 0{\cdot}61$ MPa is the osmotic suction for the samples prepared with distilled water, and σ_{c0} is the vertical yield stress at π_0.

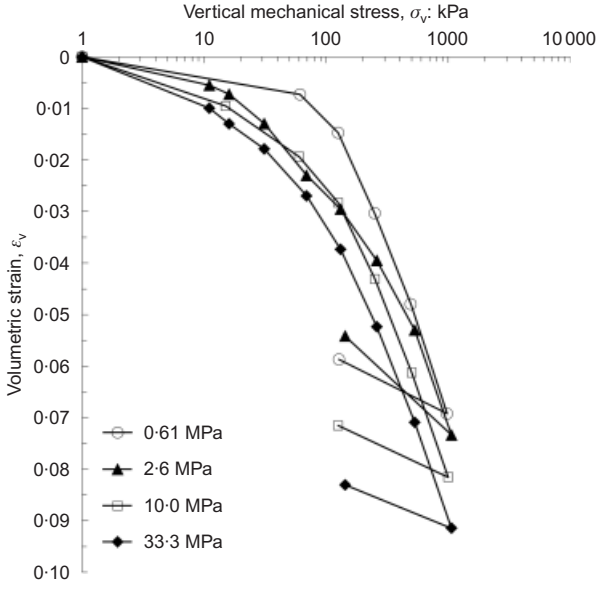

Fig. 5. Oedometric curves of four of the oedometric tests under mechanical loading only with different osmotic suctions

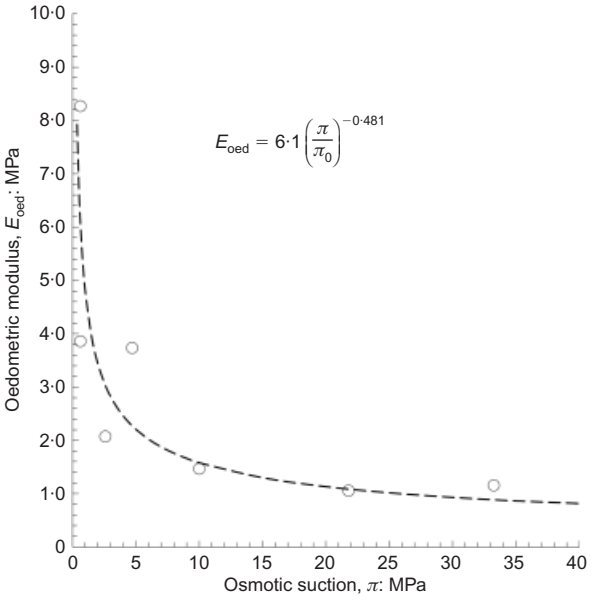

Fig. 6. Empirical correlation between initial oedometric modulus upon first loading (vertical stress 1–15 kPa) and osmotic suction of mixtures of illite powder and sodium chloride solutions at different osmotic suctions

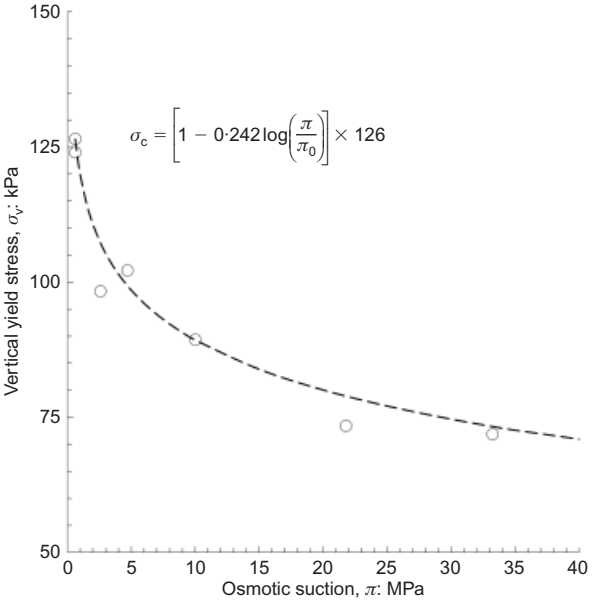

Fig. 7. Correlation between vertical mechanical yield stress and osmotic suction of mixtures of illite powder and sodium chloride solutions at different osmotic suctions

Observation (c) is confirmed when the compression and swelling indices are plotted against the osmotic suction, as shown in Fig. 8. The diagram shows that the slopes of the NCL and URL remain almost constant. However, the high swelling index for the sample at $\pi = 2{\cdot}6$ MPa is clearly distinguished.

The results of the two tests including chemical loading increments (stress paths C1 and C2 in Fig. 2) are presented in Fig. 9. In both cases, the clay underwent consolidation due to a change in the osmotic suction. From the incremental approach, it shows that this volumetric strain ε_v follows a straight line in the ε_v–$\log\pi$ diagram (Fig. 10). This rate of consolidation due to chemical loading does not change significantly within the applied void ratio and vertical mechanical stress ranges.

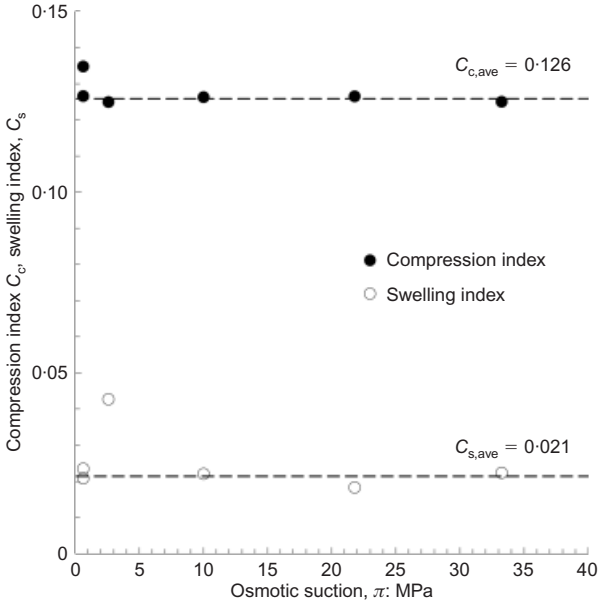

Fig. 8. Compression and swelling indices against osmotic suction of mixtures of illite powder and sodium chloride solutions at different osmotic suctions

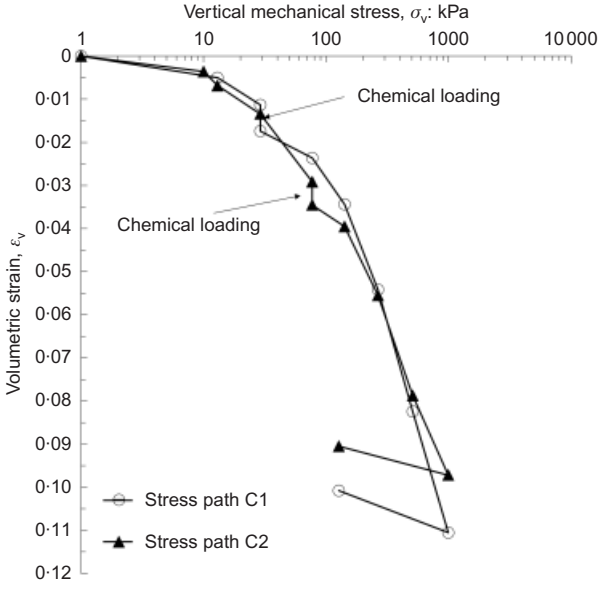

Fig. 9. Oedometric curves of the two tests under mechanical and chemical loading

CONSTITUTIVE FRAMEWORK

The results of the oedometric tests under mechanical loading allowed an innovative extension of a constitutive framework to be developed, with the aim of reproducing and quantitatively predicting the observed chemo-mechanical behaviour. This framework is based on the Hujeux model (Hujeux, 1979). Existing extensions of it are known under the name ACMEG (advanced constitutive model for environmental geomechanics; Laloui *et al.*, 2010). They can cope with partial saturation (Laloui & Nuth, 2009), thermoplasticity for saturated soil (Laloui & François, 2009) and unsaturated soils (François & Laloui, 2008), and double-structured geomaterials (Koliji *et al.*, 2010), among other variables.

The current extension, ACMEG-C (chemical effect), is able to account for changes in osmotic suction as well as the evolution of the elastic and plastic material parameters and the plastic deformation induced by these changes.

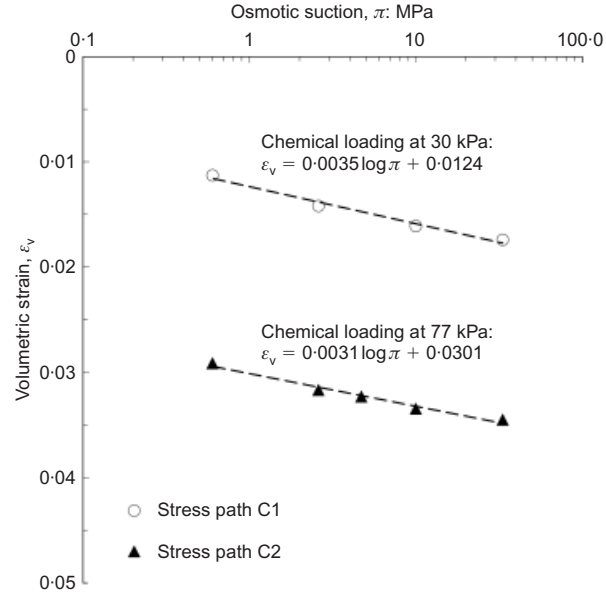

Fig. 10. Consolidation due to an incremental increase in osmotic suction with respect to osmotic suction

ACMEG-C is a soil-plasticity-based model for chemo-mechanical formulations. To take the loading history of the soil into account, ACMEG-C is defined in terms of infinitesimal increments. Elasto-plasticity implies the existence of a loading surface in both mechanical stress and osmotic suction that defines an elastic region in which only reversible deformations occur. The concept of elasto-plasticity allows the total strain increment, $d\varepsilon_{ij}$, to be divided into chemo-elastic, $d\varepsilon^e_{ij}$, and chemo-plastic components, $d\varepsilon^p_{ij}$,

$$d\varepsilon_{ij} = d\varepsilon^e_{ij} + d\varepsilon^p_{ij} \tag{4}$$

The constitutive model is conceived in terms of the following conjugate stress–strain variables

$$p' = \tfrac{1}{3}\mathrm{tr}(\boldsymbol{\sigma}') \text{ and } \varepsilon_v = \mathrm{tr}(\boldsymbol{\varepsilon}) \tag{5a}$$

$$q = \sqrt{3J_{2D}} \text{ and } \varepsilon_d = \frac{2}{\sqrt{3}}\sqrt{I_{2D}} \tag{5b}$$

where p' is the mean effective stress, q is the deviatoric stress, ε_v is the volumetric strain, ε_d is the deviatoric strain, and J_{2D} and I_{2D} are the second invariants of the strain and stress tensor respectively.

Chemo-hypo-elasticity

The elastic strains $d\varepsilon^e_{ij}$ are reversible, and do not affect the hardening state of the material. The elastic strain can be decomposed into chemo-elastic volumetric ($d\varepsilon^e_v$) and deviatoric ($d\varepsilon^e_d$) strains. They are computed as

$$d\varepsilon^e_v = \frac{dp'}{K} \tag{6a}$$

$$d\varepsilon^e_d = \frac{dq}{3G} \tag{6b}$$

The hypo-elastic moduli K and G are given by

$$K = K_{ref}\left(\frac{p'}{p'_{ref}}\right)^{n^e} \tag{7a}$$

$$G = G_{ref}\left(\frac{p'}{p'_{ref}}\right)^{n^e} \tag{7b}$$

where K_{ref} and G_{ref} are the reference bulk and shear moduli of the material respectively, determined at a reference mean effective stress p'_{ref}, and n^e is a material parameter.

According to the experimental findings on the evolution of the initial stiffness with respect to the osmotic suction (Fig. 6), the reference bulk modulus K_{ref} is assumed to evolve with the osmotic suction following the power function

$$K_{ref} = K_{ref,0}\left(\frac{\pi}{\pi_0}\right)^{-\delta} \tag{8}$$

where $K_{ref,0}$ is the reference bulk modulus for a test at a reference osmotic suction.

Chemo-plasticity

The plastic strain increment can be expressed as the unrecoverable part of the total strain increment.

The particularity of the Hujeux model's plasticity framework is the fact that this total plastic strain increment is a linear combination of two irreversible processes: isotropic and deviatoric mechanisms. Each mechanism has its own yield function, f_{iso} and f_{dev} respectively. Therefore the total plastic strain increment is the sum of the 'partial' plastic strain increments, $d\varepsilon_{ij}^{p,k}$, for each mechanism's k

$$d\varepsilon_{ij}^{p} = \sum_{k=1}^{2} d\varepsilon_{ij}^{p,k} \tag{9}$$

These considerations arise from the theory of multi-mechanism plasticity (Koiter, 1960; Mandel, 1965; Hujeux, 1979). Once the stress state reaches one of the yield functions, the corresponding evolution law is activated. Both irreversible processes depend on their respective dissipative potentials and plastic multipliers (Rizzi *et al.*, 1996). This relationship can be expressed as

$$d\varepsilon_{ij}^{p} = \sum_{k=1}^{2} \lambda_k^{p} \frac{\partial g_k}{\partial \sigma'_{ij}} \tag{10}$$

where g_k is the plastic potential and λ_k^{p} is the increment of the plastic multiplier of mechanism k. The latter is positive when the corresponding process is activated, and null otherwise. According to the multi-mechanism approach, these two yield functions form a closed domain in the effective stress and chemistry space, inside which the strains are reversible.

Isotropic chemo-plastic mechanism. The isotropic chemo-plastic mechanism is defined in the π–p'-plane, where π is the osmotic suction of the material, and is expressed by

$$f_{iso} = p' - p'_c r_{iso} \tag{11}$$

where p' is the current effective stress, p'_c is the mean yield stress, and r_{iso} is the degree of plastification (mobilised hardening) of the isotropic yield limit. Using this expression, the conceptual bilinearity of the elasto-plastic behaviour has been evened out, so that a smooth transition curvature can be represented. This implies a progressive evolution of the activated plastic strain according to the bonding surface theory, as presented by Dafalias & Herrmann (1980) and François & Laloui (2008).

During loading, r_{iso} is a hyperbolic function of the volumetric plastic strain induced by the isotropic mechanism $\varepsilon_v^{p,iso}$ (Hujeux, 1979), and is expressed as

$$r_{iso} = r_{iso}^{e} + \frac{\varepsilon_v^{p,iso}}{c_r + \varepsilon_v^{p,iso}} \tag{12}$$

$$dr_{iso} = \frac{(1 - r_{iso})^2}{c_r} d\varepsilon_v^{p,iso} \tag{13}$$

where c_r is a material parameter.

The yield limit stress is a function of the activated volumetric plastic strain and osmotic suction. Inserting the empirical relationship (equation (3)), and assuming that the functions for the vertical effective yield stress and the mean effective yield stress are of the same form, the yield limit is defined by the apparent preconsolidation stress as

$$p'_c = p'_{c0} \exp\left(\beta \varepsilon_v^{p}\right)\left(1 - \gamma_\pi \log\frac{\pi}{\pi_0}\right) \tag{14}$$

where p'_{c0} is the preconsolidation stress at a reference osmotic suction π_0, β is the plastic stiffness modulus, ε_v^{p} is the total plastic volumetric strain (produced by the two mechanisms), γ_π is the material parameter defining the shape of the isotropic yield limit with respect to the osmotic suction, and π is the current osmotic suction.

As the elastic stiffness is dependent on osmotic suction, and the normal compression line was observed experimentally to be constant, the plastic stiffness modulus β (the inverse of the slope of the linear function ε_v^{p}–$\log p'_c$) was assumed dependent on the osmotic suction. A logarithmic correlation is proposed of the form

$$\beta = \left(1 + \gamma_\beta \log\frac{\pi}{\pi_0}\right)\beta_0 \tag{15}$$

where γ_β is the chemical evolution factor, π is the current osmotic suction (MPa), π_0 is a reference osmotic suction, and β_0 is the plastic modulus at π_0.

Therefore, inserting equations (15) and (14) into equation (11), the detailed expression for the isotropic yield function becomes

$$\begin{aligned} f_{iso} &= p' - p'_{c0} \exp\left[\left(1 + \gamma_\beta \log\frac{\pi}{\pi_0}\right)\beta_0 \varepsilon_v^{p}\right] \\ &\quad \times \left(1 - \gamma_\pi \log\frac{\pi}{\pi_0}\right) r_{iso} \\ &= 0 \end{aligned} \tag{16}$$

where the material parameters β_0 and c_r (within the expression for r_{iso}) express the evolution of mechanical hardening, and γ_π and γ_β express the evolution of chemical hardening.

The isotropic behaviour is modelled with an associated flow rule as

$$f_{iso} = g_{iso} \tag{17}$$

$$\begin{aligned} d\varepsilon_{ij}^{p,iso} &= \lambda_{iso}^{p} \frac{\partial g_{iso}}{\partial \sigma'_{ij}} \\ &= \frac{\lambda_{iso}^{p}}{3} \end{aligned} \tag{18}$$

Deviatoric chemo-plastic mechanism. The deviatoric chemo-plastic mechanism is an extension of the original Cam-clay model, as presented by Roscoe & Burland (1968) and Hujeux (1979). It is defined in the q–p' plane as

$$f_{dev} = q - Mp'\left(1 - b \ln\frac{p}{p'_c}\right) r_{dev} \tag{19}$$

where M is the critical state parameter, b is a material parameter defining the shape of the deviatoric yield limit, d is the ratio between the yield and critical state mean effec-

tive stresses, and r_{dev} is the degree of mobilisation of the deviatoric yield limit.

The critical state parameter M depends on the shear strength angle at the critical state, ϕ', according to

$$M = \frac{6\sin\phi'}{3-\sin\phi'} \tag{20}$$

The progressive evolution of r_{dev} is defined by (Hujeux, 1979)

$$r_{dev} = r^{e}_{dev} + \frac{\varepsilon^{p}_{d}}{a+\varepsilon^{p}_{d}} \tag{21}$$

$$dr_{dev} = \frac{(1-r_{dev})^2}{a} d\varepsilon^{p}_{d} \tag{22}$$

where r^{e}_{dev} and a are material parameters defining the size of the elastic nuclei, and ε^{p}_{d} is the deviatoric plastic strain.

Therefore, inserting equations (14) and (15) into equation (19), the expression for the deviatoric yield function becomes

$$\begin{aligned} f_{dev} = {} & q \\ & - Mp' \left[1 - b\ln \frac{p'd}{p'_{c0}\exp\left\{\left[1+\gamma_\beta \log(\pi/\pi_0)\right]\beta_0 \varepsilon^{p}_{v}\right\}} \right. \\ & \left. \times \left[1-\gamma_\pi \log(\pi/\pi_0)\right] \right] r_{dev} \\ = {} & 0 \end{aligned} \tag{23}$$

The hardening and dilatancy rules are as follows.

$$\begin{aligned} d\varepsilon^{p,dev}_{ij} &= \lambda^{p}_{dev} \frac{\partial g_{dev}}{\partial \sigma'_{ij}} \\ &= \lambda^{p}_{dev} \frac{1}{Mp'} \left[\frac{\partial q}{\partial \sigma'_{ij}} + \alpha \left(M - \frac{q}{p'} \right) \frac{\delta_{ij}}{3} \right] \end{aligned} \tag{24}$$

with

$$\frac{\partial q}{\partial \sigma'_{ij}} = \begin{cases} \dfrac{3}{2q}\left(\sigma'_{ij} - p'\right) & \text{for } i = j \\ \dfrac{3\sigma'_{ij}}{2q} & \text{for } i \neq j \end{cases} \tag{25}$$

$$\begin{aligned} d\varepsilon^{p,dev}_{v} &= \lambda^{p}_{dev} \frac{\partial g_{dev}}{\partial p'} \\ &= \lambda^{p}_{dev} \frac{\alpha}{Mp'} \left(M - \frac{q}{p'} \right) \end{aligned} \tag{26}$$

$$\begin{aligned} d\varepsilon^{p}_{d} &= \lambda^{p}_{dev} \frac{\partial g_{dev}}{\partial q} \\ &= \lambda^{p}_{dev} \frac{1}{Mp'} \end{aligned} \tag{27}$$

where α is a material parameter introducing the non-associative behaviour.

Coupling. The two mechanisms are linked through the hardening variable ε^{p}_{v}. Therefore, a fully coupled behaviour can be represented. The yield stress limit depends on this parameter, and it appears in both expressions for the yield functions. This causes the isotropic yield surface to stretch when the deviatoric yield surface is expanded, and vice versa, as shown in Fig. 11.

When the two mechanisms are activated simultaneously, the volumetric plastic strain is the sum of the components corresponding to both processes, according to

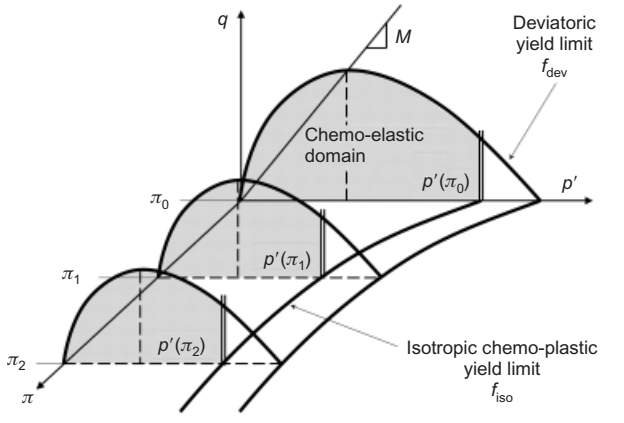

Fig. 11. Coupling of isotropic and deviatoric mechanisms of chemo-mechanical constitutive model ACMEG-C

$$\begin{aligned} d\varepsilon^{p}_{v} &= \lambda^{p}_{dev} \frac{\partial g_{dev}}{\partial p'} + \lambda^{p}_{iso} \frac{\partial g_{iso}}{\partial p'} \\ &= \lambda^{p}_{dev} \frac{\alpha}{Mp'} \left(M - \frac{q}{p'} \right) + \lambda^{p}_{iso} \end{aligned} \tag{28}$$

The two consistency equations must be met simultaneously, resulting in the need to solve the following set of two equations with two unknowns.

$$\begin{aligned} d\boldsymbol{F} &= \frac{\partial \boldsymbol{F}}{\partial \boldsymbol{\sigma}'} : d\boldsymbol{\sigma}' + \frac{\partial \boldsymbol{F}}{\partial \pi} d\pi + \frac{\partial \boldsymbol{F}}{\partial \boldsymbol{\omega}} \cdot \frac{\partial \boldsymbol{\omega}}{\partial \boldsymbol{\lambda}^{p}} \cdot \boldsymbol{\lambda}^{p} \\ &= \boldsymbol{s} : d\boldsymbol{\sigma}' + \boldsymbol{\Pi} d\pi - \mathbf{H} \cdot \boldsymbol{\lambda}^{p} \\ &\leqslant 0 \end{aligned} \tag{29}$$

$$\boldsymbol{\lambda}^{p} \geqslant 0 \tag{30}$$

$$d\boldsymbol{F} \cdot \boldsymbol{\lambda}^{p} \geqslant 0 \tag{31}$$

where $\boldsymbol{\sigma}'$ is the stress tensor, $\boldsymbol{\omega}$ is the internal variable vector, $\boldsymbol{s}$ collects the stress gradients and $\boldsymbol{\Pi}$ is the derivative of the loading functions $\boldsymbol{F}$ with respect to the osmotic suction. $\mathbf{H}$ is the matrix of the hardening moduli, with $H_{\alpha\beta} = -\partial f_\alpha / \partial \lambda^{p}_{\beta}$, $\boldsymbol{\lambda}^{p}$ is the plastic multiplier vector, and $d\boldsymbol{F} \leqslant \mathbf{0}$ expresses Prager's consistency condition extended for multi-dissipative processes.

NUMERICAL MODELLING

Calibration

Mechanical behaviour. The results of one of the mechanical oedometric tests on a sample prepared with distilled water allowed the reference elastic bulk modulus, the reference shear modulus and the plastic potential parameter to be determined as

$$K_{ref,0} = 2{\cdot}303 \frac{1+e_0}{C_{s0}} p'_{ref} \tag{32}$$

$$G_{ref} = \frac{3K_{ref,0}(1-K_0)}{2+4K_0} \tag{33}$$

Assuming that $K_0 = 1 - \sin\phi'$

$$\beta_0 = 2{\cdot}303 \frac{1+e_0}{C_c - C_{s0}} \tag{34}$$

where $p'_{ref} = 1$ MPa is the reference mean effective stress, e_0 is the initial void ratio, C_c is the compression index, C_{s0} is

the slope of the oedometric curve upon first loading, and K_0 is the lateral stress ratio for one-dimensional strain. The shear strength angle of the tested illite is $\phi' = 25°$ (obtained from complementary triaxial tests). The other parameters of the mechanical part of the model were determined by fitting the curve of the test results. These parameters can be found in Table 3. The results of the simulation are presented in Fig. 12.

Chemo-mechanical behaviour. The parameters defining the chemo-mechanical behaviour of the model are determined through curve-fitting processes on the results of the oedometric tests under mechanical loading. The chemical form factors δ, γ_π and γ_β are determined using plots of the oedometric modulus, yield stress and plastic stiffness modulus respectively against the osmotic suction. The values of the three parameters are presented in Table 3. These parameters were used to simulate three of the other oedometric tests under mechanical loading. The results of the simulation are plotted in Fig. 13. The model results correspond well with the experimental results.

Table 3. Model parameters for simulation of mechanical response of illite mixed with distilled water and for simulation of chemo-mechanical response of illite–sodium chloride solution mixtures

Elastic parameters	
$K_{ref,0}$: MPa	560
G_{ref}: MPa	165
n^e	1
Isotropic plastic parameters	
β_0	37·7
c	0·002
r^e_{iso}	0·2
Deviatoric plastic parameters	
b	0·6
d	1
ϕ': degrees	25
α	1
a	0·02
r^e_{dev}	0·5
Chemo-mechanical parameters	
δ	0·229
γ_π	0·242
γ_β	0·056

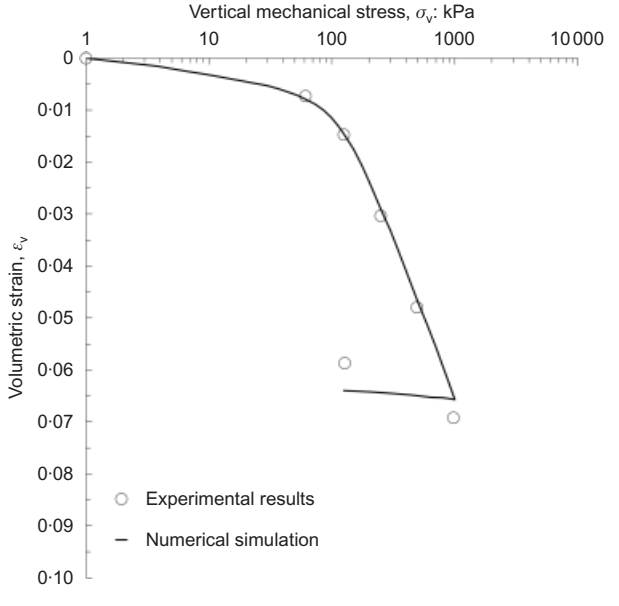

Fig. 12. Simulation of one oedometric test under mechanical loading only using chemo-mechanical constitutive model ACMEG-C

Verification

The calibration of the numerical model has been verified with two tests under both mechanical and chemical loading. These tests were conducted at a higher initial void ratio, $e_0 = 1{\cdot}03$. To take this difference into account, p'_{c0}, the representative initial yield stress at a reference osmotic suction π_0, and its evolution were calculated through the results of the oedometer tests at $\pi = 0{\cdot}61$ MPa and the vertical yield stress–osmotic suction plot (Fig. 5). The simulations were then run for stress paths C1 and C2, including a chemical loading step at approximately 30 kPa and 80 kPa in the first and second cases respectively. Their stress paths are presented in Figs 14 and 16 respectively, and the simulations are presented in Figs 15 and 17 respectively. The model and experimental results correspond well, at least until the chemical loading. The discrepancies between the experimental and the modelling results can be addressed separately for the two stress paths. For test C1, the reduction in volume associated with the chemical loading is well reproduced. The analysis of the stress path in Fig. 14 and the experimental points in Fig. 15 would suggest that the vertical yield stress moved further than the value of vertical stress at which the chemical loading occurred. In this sense, during the subsequent increment of the vertical load, a more pronounced transition from an elastic to an elasto-plastic response should have been observed. For a better prediction of this trend with the numerical simulation, a refinement of the selection of the r_{iso} value (equations (12) and (13)) could be considered. For stress path C2, the vertical deformation associated with the chemical loading is slightly overestimated. It is worth mentioning that this deformation is modelled solely through the dependence functions of the oedometric modulus, yield stress and plastic stiffness

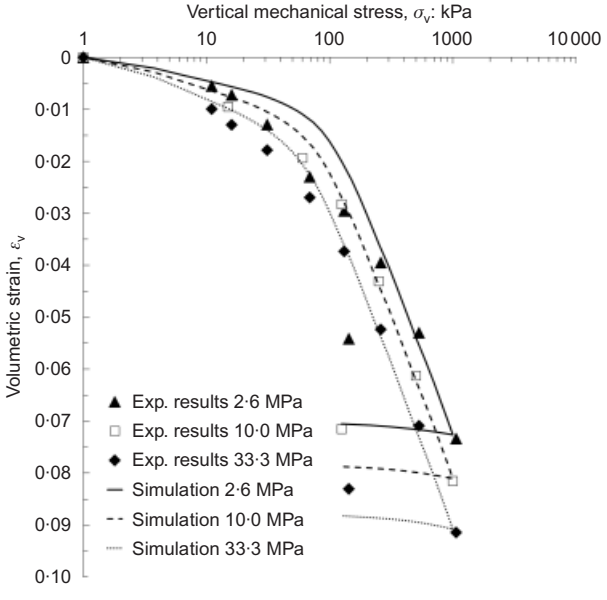

Fig. 13. Simulation of three of the oedometric tests under mechanical loading only using constitutive model ACMEG-C

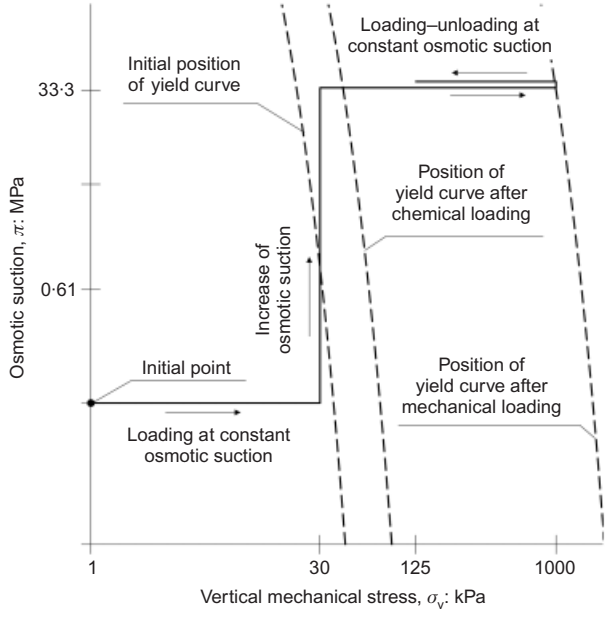

Fig. 14. Stress paths of oedometric test including chemical loading step at vertical stress of approximately 30 kPa, including evolution of yield curve

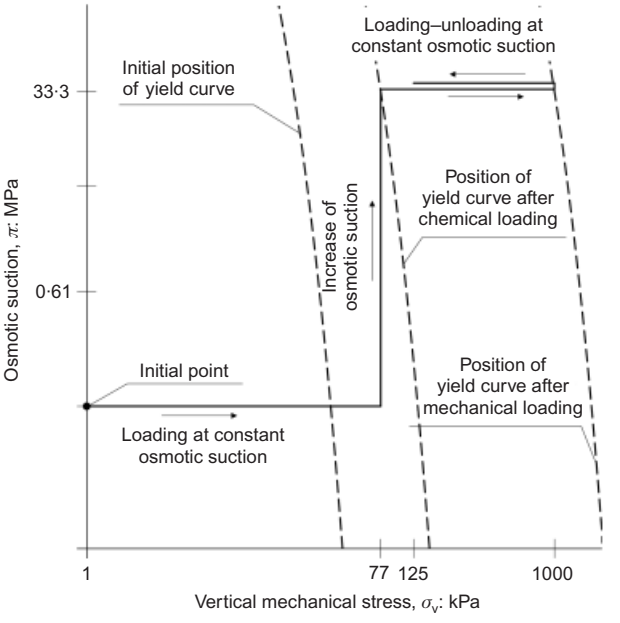

Fig. 16. Stress paths of oedometric test with chemical loading step at vertical stress of approximately 80 kPa, including evolution of yield curve

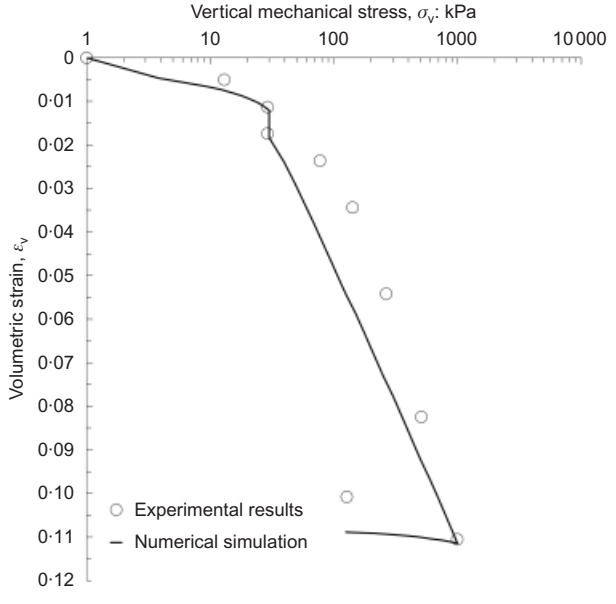

Fig. 15. Simulation of oedometric tests under mechanical loading and chemical loading step at vertical mechanical stress of approximately 30 kPa using chemo-mechanical constitutive model ACMEG-C

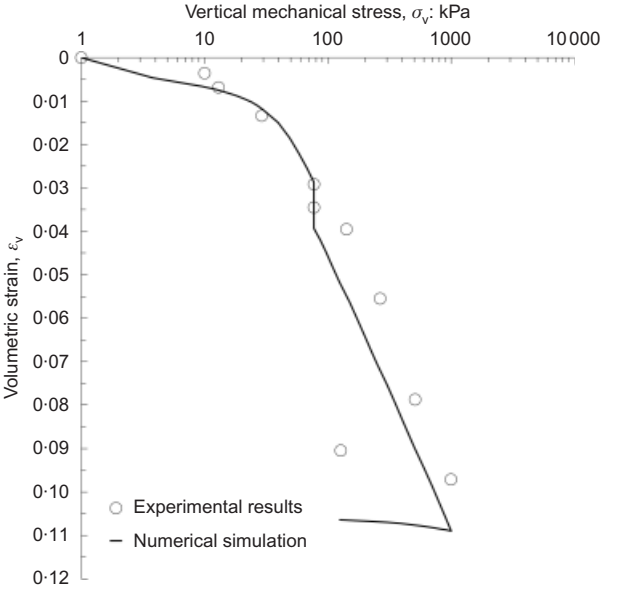

Fig. 17. Simulation of oedometric tests under mechanical loading and chemical loading step at vertical mechanical stress of approximately 80 kPa using chemo-mechanical constitutive model ACMEG-C

modulus. The slope of the plastic deformation and its order of magnitude are well predicted.

CONCLUSIONS

Despite the vast number of situations in which couplings between chemistry and mechanics occur, the available constitutive models rely on limited experimental evidence. This study extends the experimental database on the subject of one-dimensional consolidation induced by a change in the chemical composition in the pore liquid. In contrast to earlier contributions, the osmotic suction, controlled through the sodium chloride concentration in the pore water, is considered to be the governing variable.

A laboratory programme was conducted. The total, matric and osmotic suctions of the clay mixtures of illite powder and distilled water or sodium chloride solutions were determined. Mixtures of the same composition were then subjected to conventional oedometric tests. Furthermore, two clay mixtures prepared with distilled water were subjected to a conventional oedometric test including a chemical loading path performed with incremental increases in the osmotic suction.

From the suction determination, an empirical relationship was determined for the osmotic suction as a function of the sodium chloride concentration of the pore liquid. This relationship followed a polynomial of the second order. Subsequently, oedometric test results showed that the oedometric modulus upon first loading and the vertical yield stress decreased as the osmotic suction increased, whereas

the compression and swelling indices were independent of the suction. Finally, the rate of consolidation due to chemical solicitation was shown to follow a straight line in the $\varepsilon_v - \log \pi$ diagram, and its slope did not change significantly within the applied void ratio and vertical mechanical stress ranges.

The findings allowed an extension of the ACMEG constitutive framework to be developed. ACMEG-C (chemical effect) is able to take changes in osmotic suction into account, as well as the evolution of elastic and plastic material parameters and the plastic deformation induced by these changes. The mechanical behaviour was calibrated with one oedometric test on a sample prepared with distilled water, whereas the chemo-mechanical behaviour was calibrated with the oedometric test results under mechanical loading. In all cases, the model results corresponded well with the test results. The model was validated through the two tests, including a chemical loading path. These stress paths show that a large part of the chemo-mechanical oedometric test can be predicted well. Improvements could be made by taking into account the evolution of the oedometric modulus and the compression indices, as well as by researching the elastic behaviour after changing the direction of the loading.

Further study should also include the investigation of different kinds of salt and clay powder, to verify the proposed independence of the materials. Only then can previous results used, such as those by Di Maio and coworkers (Di Maio, 1996; Di Maio & Fenelli, 1997; Di Maio & Onorati, 1999), be properly compared.

ACKNOWLEDGEMENTS

The authors would like to thank the Mont Terri Project and NAGRA for their support.

NOTATION

a	material parameter defining size of elastic nuclei
b	material parameter defining shape of deviatoric yield limit
C_c	compression index
C_s	swelling index
C_{s0}	slope of oedometric curve upon first loading
c	sodium chloride concentration
c_r	material parameter
d	ratio between yield and critical-state mean effective stresses
E_{oed}	oedometric modulus
e_0	initial void ratio
$\boldsymbol{F}$	vector containing the loading functions
f_{dev}	yield function for deviatoric mechanism
f_{iso}	yield function for isotropic mechanism
G	hypoelastic shear modulus
G_{ref}	reference shear modulus
g_k	plastic potential
$\mathbf{H}$	matrix of hardening moduli
K	hypoelastic bulk modulus
K_{ref}	reference bulk modulus
$K_{ref,0}$	reference bulk modulus at reference osmotic suction
K_0	lateral stress ratio for one-dimensional strain
M	critical state parameter
n_e	material parameter
p'	mean effective stress
p'_c	mean yield stress
p'_{c0}	mean effective yield stress at reference osmotic suction
p'_{ref}	reference mean effective stress
q	deviatoric stress
R	universal gas constant
r_{dev}	degree of mobilisation of deviatoric yield limit
r^e_{dev}	material parameter defining size of elastic nuclei
r_{iso}	degree of mobilisation of isotropic yield limit
r^e_{iso}	material parameter defining size of elastic nuclei
$\boldsymbol{s}$	stress gradient vector
s_m	matric suction
T	absolute temperature
w_0	initial water content
α	material parameter introducing non-associative behaviour
β	plastic stiffness modulus
β_0	plastic stiffness modulus at reference osmotic suction
γ_β	chemical evolution factor
γ_π	chemical evolution factor for yield stress
δ	material parameter
$\boldsymbol{\varepsilon}$	strain tensor
$d\varepsilon_{ij}$	total strain increment
ε^e_{ij}	chemo-elastic strain tensor
ε^p_{ij}	chemo-plastic strain tensor
$d\varepsilon^{p,k}_{ij}$	'partial' plastic strain increment for mechanism k
ε^e_d	chemo-elastic deviatoric strain
ε^p_d	deviatoric plastic strain
ε_v	volumetric strain
ε^e_v	chemo-elastic volumetric strain
ε^p_v	plastic volumetric strain
$\varepsilon^{p,iso}_v$	volumetric plastic strain induced by isotropic mechanism
λ^p_k	plastic multiplier for mechanism k
$\boldsymbol{\lambda}^p$	plastic multiplier vector
ν	number of constituent ions
π	osmotic suction
π_0	initial osmotic suction
$\rho_{solution}$	density of solution
$\boldsymbol{\sigma}'$	effective stress tensor
σ'_{ij}	effective stress tensor
σ_c	vertical yield stress
σ_{c0}	vertical yield stress at π_0
σ_v	vertical stress
ϕ'	shear strength angle at critical state
ψ	total suction
$\boldsymbol{\omega}$	internal variable vector

REFERENCES

Barbour, S. L. & Fredlund, D. G. (1989). Mechanisms of osmotic flow and volume change in clay soils. *Can. Geotech. J.* **26**, No. 4, 551–562.

Biot, M. A. (1941). General theory of three-dimensional consolidation. *J. Appl. Phys.* **12**, No. 2, 155–164.

Biot, M. A. (1956a). Thermoelasticity and irreversible thermodynamics. *J. Appl. Phys.* **27**, No. 3, 240–253.

Biot, M. A. (1956b). Theory of deformation of a porous viscoelastic anisotropic solid. *J. Appl. Phys.* **27**, No. 5, 459–467.

Biot, M. A. (1973). Nonlinear and semilinear rheology of porous solids. *J. Geophys. Res.* **78**, No. 23, 4924–4937.

Bolt, G. H. (1956). Physico-chemical analysis of the compressibility of pure clays. *Géotechnique* **6**, No. 2, 86–93, http://dx.doi.org/10.1680/geot.1956.6.2.86.

Bolt, G. H. & Miller, R. D. (1955). Compression studies of illite suspensions. *Soc. Soil Sci. Am. J.* **19**, No. 3, 285–288.

Boukpeti, N., Charlier, R. & Hueckel, T. (2004). Modelling contamination of clays. In *Coupled thermo-hydro-mechanical-chemical processes in geo-systems: Fundamentals, modelling, experiments and applications* (ed. O. Stephansson), Vol. 2, pp. 523–528. Amsterdam, the Netherlands: Elsevier.

Bunger, A. P. (2010). The Mandel–Cryer effect in chemoporoelasticity. *Int. J. Numer. Anal. Methods Geomech.* **34**, No. 14, 1479–1511.

Cardoso, R., Romero, E., Lima, A. & Ferrari, A. (2007). A comparative study of soil suction measurement using two different high-range psychrometers. *Proc. 2nd Int. Conf. on Mechanics of Unsaturated Soils, Weimar*, pp. 79–93.

Chapman, D. L. (1913). A contribution to the theory of electrocapillarity. *Phil. Mag. Ser.* 6, **25**, No. 148, 475–481.

Coussy, O. (2004). *Poromechanics*. Hoboken, NJ, USA: John Wiley & Sons.

Dafalias, Y. & Herrmann, L. (1980). A bounding surface soil plasticity model. *Proceedings of the international symposium on soils under cyclic and transient loading*, Swansea, pp. 335–345.

Di Maio, C. (1996). Exposure of bentonite to salt solution: osmotic

and mechanical effects. *Géotechnique* **46**, No. 4, 695–707, http://dx.doi.org/10.1680/geot.1996.46.4.695.
Di Maio, C. & Fenelli, G. B. (1997). Influenza delle interazioni chimico-fisiche sulla deformabilità di alcuni terreni argillosi. *Riv. Ital. Geotec*., No. 1, 695–707.
Di Maio, C. & Onorati, R. (1999). Prove di laboratorio: Influenza della composizione del liquido di cella. *Rendiconti del XX Convegno Nazionale di Geotecnica, Parma*, 87–94.
Fernandez, F. & Quigley, R. M. (1985). Hydraulic conductivity of natural clays permeated with simple liquid hydrocarbons. *Can. Geotech. J.* **22**, No. 2, 205–214.
Fernandez, F. & Quigley, R. M. (1991). Controlling the destructive effect of clay–organic liquid interactions by application of effective stresses. *Can. Geotech. J.* **28**, No. 3, 388–398.
François, B. & Laloui, L. (2008). ACMEG-TS: a constitutive model for unsaturated soils under non-isothermal conditions. *Int. J. Numer. Anal. Methods Geomech*. **32**, No. 16, 1955–1988.
Fritz, S. J. (1986). Ideality of clay membranes in osmotic processes: a review. *Clays Clay Miner.* **34**, No. 2, 214–223.
Gajo, A. & Loret, B. (2003). Finite element simulations of chemo-mechanical coupling in elastic-plastic homoionic expansive clays. *Comput. Methods Appl. Mech. Engng* **192**, No. 31–32, 3489–3530.
Gajo, A., Loret, B. & Hueckel, T. (2002). Electro-chemo-mechanical couplings in saturated porous media: elastic-plastic behaviour of heteroionic expansive clays. *Int. J. Solids Struct*. **39**, No. 16, 4327–4362.
Gens, A. (2010). Soil–environment interactions in geotechnical engineering. *Géotechnique* **60**, No. 1, 3–74, http://dx.doi.org/10.1680/geot.9.P.109.
Guimarães, L. Do N., Gens, A. & Olivella, S. (2007). Coupled thermo-hydro-mechanical and chemical analysis of expansive clay subjected to heating and hydration. *Transp. Porous Media* **66**, No. 3, 341–372.
Gouy, G. (1910). Constitution of the electric charge at the surface of an electrolyte. *J. Physique* **9**, No. 4, 457–467.
Heidug, W. & Wong, S. W. (1996). Hydration swelling of water-absorbing rocks: a constitutive model. *Int. J. Numer. Anal. Methods Geomech*. **20**, No. 6, 403–430.
Hueckel, T. (1997). Chemo-plasticity of clays subjected to stress and flow of a single contaminant. *Int. J. Numer. Anal. Methods Geomech*. **21**, No. 1, 43–72.
Hujeux, J. C. (1979). *Calcul numérique de problèmes de consolidation élastoplastique*. PhD thesis, Ecole Centrale de Paris, Paris, France.
Kaczmarek, M. & Hueckel, T. (1998). Chemo-mechanical consolidation of clays: analytical solutions for a linearized one-dimensional problem. *Transp. Porous Media* **32**, No. 1, 49–74.
Koiter, W. T. (1960). General theorems for elastic-plastic solids. In *Progress in solid mechanics* (eds I. N. Sneddon and R. Hill), pp. 167–221. Amsterdam, the Netherlands: North-Holland.
Koliji, A., Laloui, L. & Vulliet, L. (2010). Constitutive modeling of unsaturated aggregated soils. *Int. J. Numer. Anal. Methods Geomech*. **34**, No. 17, 1846–1876.
Laloui, L. & François, B. (2009). ACMEG-T: soil thermoplasticity model. *J. Engng Mech*. **135**, No. 9, 932–944.
Laloui, L. & Nuth, M. (2009). On the use of the generalised effective stress in the constitutive modelling of unsaturated soils. *Comput. Geotech*. **36**, No. 1–2, 20–23.
Laloui, L., Nuth, M. & François, B. (2010). Mechanics of unsaturated soils In *Mechanics of unsaturated geomaterials* (ed. L. Laloui), pp. 29–51. Hoboken, NJ, USA: John Wiley & Sons.
Leong, E.-C., Tripathy, S. & Rahardjo, H. (2003). Total suction measurement of unsaturated soils with a device using the chilled-mirror dew point technique. *Géotechnique* **53**, No. 2, 173–182, http://dx.doi.org/10.1680/geot.2003.53.2.173.
Loret, B., Hueckel, T. & Gajo, A. (2002). Chemo-mechanical coupling in saturated porous media: elastic-plastic behaviour of homoionic expansive clays. *Int. J. Solids Struct*. **39**, No. 10, 2773–2806.
Mandel, W. (1965). Généralisation de la théorie de Koiter. *Int. J. Solids Struct*. **1**, No. 3, 273–295.
Marine, I. W. & Fritz, S. J. (1981). Osmotic model to explain anomalous hydraulic heads. *Water Resour. Res*. **17**, No. 1, 73–82.
Mesri, G. & Olson, R. E. (1970). Shear strength of montmorillonite. *Géotechnique* **20**, No. 3, 261–270, http://dx.doi.org/10.1680/geot.1970.20.3.261.
Mesri, G. & Olson, R. E. (1971). Consolidation characteristics of montmorillonite. *Géotechnique* **21**, No. 4, 341–352, http://dx.doi.org/10.1680/geot.1971.21.4.341.
Mitchell, J. K. & Soga, K. (2005). *Fundamentals of soil behavior*. Hoboken, NJ, USA: John Wiley & Sons.
Mitchell, J. K., Greenberg, J. A. & Witherspoon, P. A. (1973). Chemico-osmotic effects in fine-grained soils. In *Selected Papers of James K. Mitchell* (eds J. K. Mitchell and I. M. Idriss), pp. 398–413. Reston, VA, USA: ASCE.
Rizzi, E., Maier, G., & Willam, K. (1996). On failure indicators in multi-dissipative materials. *Int. J. Solids Struct*. **33**, No. 20–22, 3187–3214.
Roscoe, K. H. & Burland, J. B. (1968). On the generalized stress–strain behaviour of 'wet' clay. In *Engineering plasticity* (eds J. Heyman and F. A. Leckie), pp. 535–609. Cambridge, UK: Cambridge University Press.
Sarout, J. & Detournay, E. (2011). Chemoporoelastic analysis and experimental validation of the pore pressure transmission test for reactive shales. *Int. J. Rock Mech. Mining Sci*. **48**, No. 5, 759–772.
Sherwood, J. D. (1993). Biot poroelasticity of a chemically active shale. *Proc. R. Soc. London Ser. A* **440**, No. 1909, 365–377.
Sherwood, J. D. (1994). A model of hindered solute transport in a poroelastic shale. *Proc. R. Soc. London Ser. A* **445**, No. 1925, 679–692.
Sridharan, A. & Venkatappa Rao, G. (1973). Mechanisms controlling volume change of saturated clays and the role of the effective stress concept. *Géotechnique* **23**, No. 3, 359–382, http://dx.doi.org/10.1680/geot.1973.23.3.359.
Sridharan, A. & Venkatappa Rao, G. (1979). Shear strength behaviour of saturated clays and the role of the effective stress concept. *Géotechnique* **29**, No. 2, 177–193, http://dx.doi.org/10.1680/geot.1979.29.2.177.
Verwey, E. J. W. & Overbeek, J. Th. G. (1948). *Theory of the stability of lyophobic colloids*. New York, NY, USA: Elsevier.

Zumsteg, R. *et al.* (2013). *Géotechnique* **63**, No. 4, 276–286 [http://dx.doi.org/10.1680/geot.SIP13.P.005]

Reduction of the clogging potential of clays: new chemical applications and novel quantification approaches

R. ZUMSTEG*, M. PLÖTZE* and A. PUZRIN*

Earth pressure balance machines are increasingly being used for tunnelling in difficult soils and ground conditions. In clayey soils, clogging of the working tools is among the main hazards. Attempts to reduce this risk by adding anti-clogging chemicals do not always produce the desired effect. In this paper, the limited efficiency of the existing conditioning chemicals is quantified and explained, and an enhanced interaction mechanism is proposed. This mechanism is based on sealing the clay aggregates against the penetration of water; it requires the addition of polyamine chemicals, as a newly patented application. These chemicals have been shown to dramatically reduce the clogging potential of different clay pastes over a broad range of water contents, using novel approaches for quantifying the clogging behaviour of clays in general. These methods also establish important correlations between empirical stickiness and more fundamental soil parameters, and in particular the ratio between adhesion and strength. Together with microscopic investigations and adsorption measurements, this provides insight into the working mechanism of the new chemicals at the particle level; it also highlights the differences between this mechanism and that of commercially used foams and polymers.

KEYWORDS: chemical properties; clays; ground improvement; particle-scale behaviour; shear strength; soil/structure interaction

INTRODUCTION

Tunnelling excavations with earth pressure balance (EPB) machines use the excavated soil to support the tunnel face, and to facilitate installation of the permanent support system. The boundaries of soil conditions for the use of this tunnelling method are constantly expanded, not least thanks to the application of new chemical additives. The injection of foams and polymers at the cutter head, in the pressure chamber and in the screw conveyor can enhance the soil properties and offer various benefits. In general, a deformable paste of soft consistency, with well-defined compressibility, small adhesion and low clogging potential, is regarded as the optimum supporting soil mass (Milligan, 2000; EFNARC, 2005).

One of the main hazard scenarios when excavating in clayey soils is clogging of the working tools or, in the worst case, of the whole machine. For conditioning of these soils, the application of relatively high amounts of dispersing foams and polymers is recommended (EFNARC, 2005). Although this was helpful in several reported cases (Langmaack, 2000; Feng, 2004), full elimination of clogging problems cannot always be guaranteed on the construction site (Borghi, 2006). Alternative clogging prevention methods for tunnel boring machines (TBMs), such as electro-osmosis (van Baalen, 1999), have not shown adequate success either.

Quantification of the benefits of injecting chemicals for clogging reduction and their relation to adhesion and strength properties is a difficult task, with no reliable established methods presented in the literature. An attempt has been made by Zumsteg & Puzrin (2012) to overcome these difficulties by developing new devices and procedures, which demonstrated mainly a lubrication mechanism of commercial foams and polymers, with limited effect on stickiness reduction of soft clay pastes.

Manuscript received 28 February 2012; revised manuscript accepted 16 October 2012.
Discussion on this paper closes on 1 August 2013, for further details see p. ii.
* ETH Zurich, Zurich, Switzerland.

Objectives

Based on the analysis of limited efficiency of commercial chemicals, the main objectives of the present work are

(*a*) to introduce for tunnelling application newly patented chemicals whose enhanced interaction mechanism with clays leads to a dramatic stickiness reduction of soft soils
(*b*) to use the testing devices and procedures developed in Zumsteg & Puzrin (2012) to quantify the beneficial effects of the new chemicals in terms of mechanical parameters
(*c*) to obtain insight into the behaviour of the new chemicals at the particle level using adsorption measurements and microscopic observations, and to show the validity of the proposed mechanism based on chemical coating of the clay aggregates
(*d*) to provide further verification of the proposed mechanism by varying different mixture parameters (mixture water content, molecular weight of the chemical, clay aggregate size), and to demonstrate the potential of the patented chemicals for practical applications.

DEFINITIONS

Clogging of TBM

Numerous problems can occur during TBM excavation in clayey soils, with openings in the cutter head being plugged and steel surfaces covered by the excavated material (Braun, 1997; Weh *et al.*, 2010). These phenomena are called 'clogging', and lead to hindered material transport, standstills, and the necessity for expensive cleaning works. So far, evaluation of the clogging potential of an in situ soil for machine tunnelling has been based mostly on the index properties of the soil, such as the plasticity index I_p and the soil-consistency index I_c,

$$I_c = \frac{w_l - w}{w_l - w_p} \quad (1)$$

where w is the actual soil water content, w_l is the liquid limit and w_p is the plastic limit. The consistency index corresponds to $1 - \mathrm{LI}$, where LI is the liquidity index after Mitchell & Soga, 2005)

$$\mathrm{LI} = \frac{w - w_p}{w_l - w_p} \quad (2)$$

The most widely used diagram was developed by Thewes (1999), based on construction-site reports and laboratory measurements. The clogging potential is divided into three zones: the highest potential is attributed to in situ soils with a plasticity index $I_p > 0{\cdot}2$ and a stiff-to-hard consistency I_c between 0·75 and 1·25. Often the transformation of the in situ soil from stiff to soft consistency for an optimum EPB operation cannot prevent the addition of a certain amount of water, leading to serious clogging problems. The problem, however, is that the benefits of the different conditioners on this transformation process and clogging potential cannot be quantified with the existing index parameter classification.

Stickiness of clay pastes

To describe the tendency of soil to adhere to different surfaces in general, often the term 'stickiness' is used. Stickiness is rooted in the attractive forces on clay surfaces, and in the amount and availability of water between these charged surfaces. Mechanical crushing of a compacted, low-water-content clayey soil (e.g. during the excavation process) leads to the creation of clay aggregates with a high internal strength due to cohesion forces, but low adhesion and stickiness when the aggregates are brought into contact with a steel surface (Fig. 1(a)). The addition of a sufficient amount of water to these aggregates makes the clay sticky. The water molecules are attracted by the single clay platelets inside the aggregate, facilitating the entry of water, which in turn leads to a weakening of the bonds and to disintegration of the aggregate boundaries (Fig. 1(b)). The behaviour of the matrix is therefore determined at the micro scale by the weakened forces between the individual clay particles. As a result, the shear strength of the material decreases. Furthermore, the relatively weakly bonded water in the vicinity of the single clay platelets can also interact with other material surfaces via van der Waals and capillary forces (Mitchell & Soga, 2005), thus creating adhesion between clay and steel. Consequently, the reduction of shear strength and the increase of adhesion bring these two values into the same order-of-magnitude range and lead to stickiness.

The α ratio

The above processes can be described with the help of a ratio between adhesion and strength for different states of the clayey material. Considering a soil mass with average shear strength s_c and average tangential adhesion between soil and a steel plate of a_c, the following adhesion-to-cohesion ratio can be proposed (Fig. 2)

$$\alpha = \frac{a_c}{s_c} \quad (3)$$

Naturally, the material properties vary, following a certain probability distribution. If, however, the ratio α (calculated from average values) is low, then the strength is higher than the adhesion, and it is possible to separate almost all the clay particles from the steel surface. If the ratio α approaches unity, more of the material will remain sticking to the steel surface. Apart from these limiting cases, however, attempts to use the parameter α for universal quantification of stickiness for different types of clay, either pure or mixed with conventional clay dispersing chemicals, have not been successful (Zumsteg & Puzrin, 2012): that is, for a different composition and structure of the clay minerals, smaller values of the ratio α do not necessarily imply that the paste is less sticky.

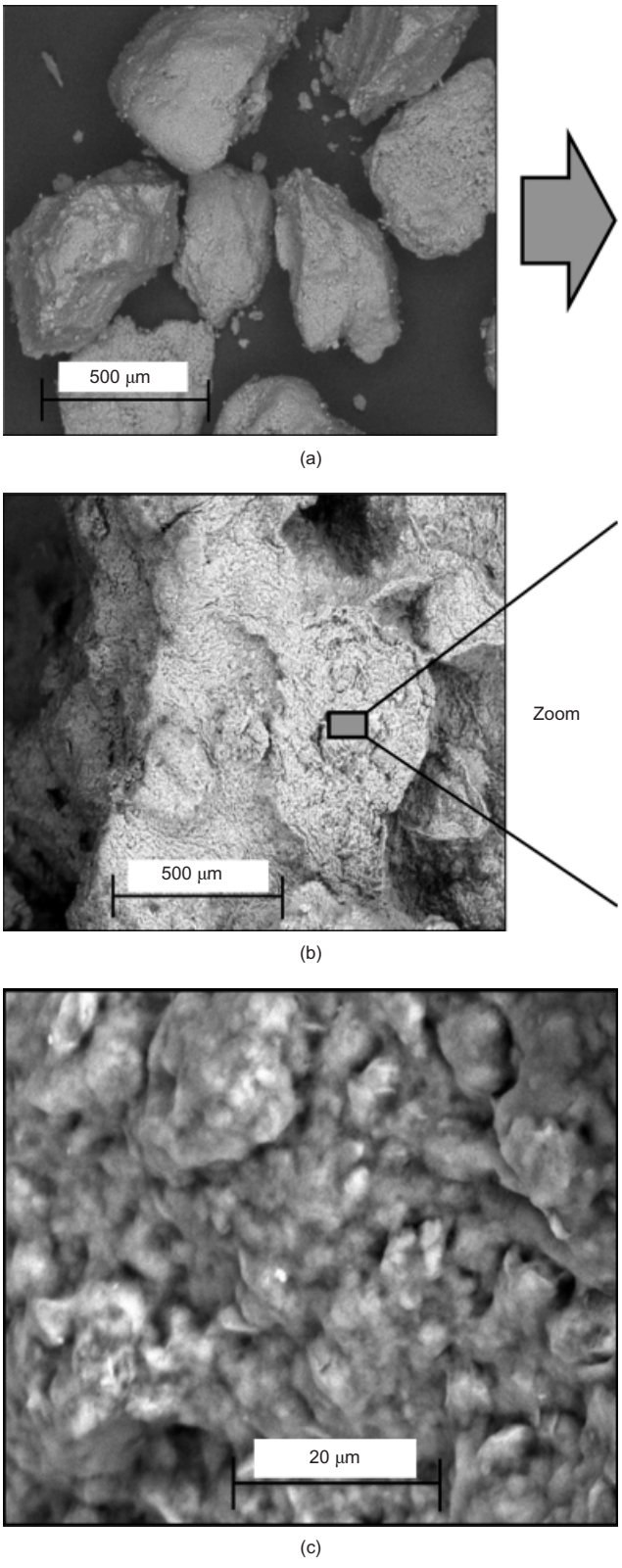

Fig. 1. Disintegration of clay aggregates through addition of water (environmental scanning electron microscope (ESEM) images): (a) base material, dry illite aggregates; (b) addition of water; (c) disintegration of aggregates

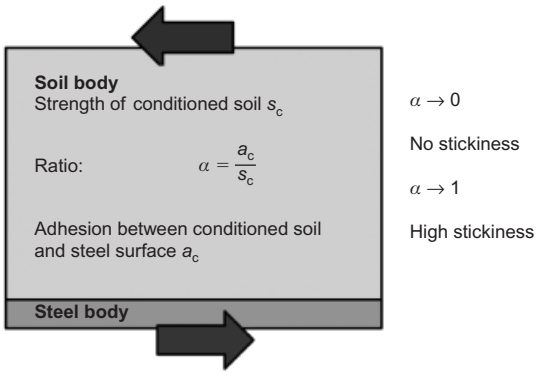

Fig. 2. Concept of α ratio and its relation to stickiness

The λ ratio

Although the ratio α allows for a qualitative description of stickiness, no standard test for the evaluation and definition of this property exists. To overcome this lack for tunnelling application, Zumsteg & Puzrin (2012) introduced a new approach based on the existing and widely used mixing test. The resulting empirical stickiness ratio λ is defined as the ratio between the weight of soil sticking to the mixing tool (G_{MT}) and the total weight of soil involved in the mixing process (G_{TOT})

$$\lambda = \frac{G_{MT}}{G_{TOT}} \tag{4}$$

The relevance of the ratio λ is demonstrated in Fig. 3. When the empirical stickiness ratios at different water contents (in the consistency range from $I_c = 0$ to 1·2) for two highly plastic clays are plotted against the consistency indices of the mixtures, good agreement between these numbers and the categorisation of Thewes (1999) can be found (left-hand diagram in Fig. 3). This allows for the quantification of low, medium and high clogging potential by assigning the corresponding ranges of parameter λ (see the table in Fig. 3).

Effects of clay-dispersing chemicals

The study by Zumsteg & Puzrin (2012) clearly showed that commercial chemicals reduce strength both between the soil particles and in the clay/steel interface, leading to decreased maximum and residual shear strength of the soil, and to a decreased tangential adhesion and sliding resistance (Fig. 4(a)). In addition, a logarithmic correlation between adhesion and empirical stickiness ratio has been established (Fig. 4(b)) for a variety of conditioning agents (pure water, foam and polymer) and clays (kaolin, illite, bentonite). This implies that although the stickiness can in principle be reduced by decreasing the soil resistance, the extent of this reduction is rather limited. Considering the stickiness behaviour at different consistencies (water contents) of the investigated soil, a higher reducing effect can be seen at higher water contents, with the polymer influence becoming negligible at stiffer soil consistencies (Fig. 4(c)). As a result, the soil is still sticky in the operation range of the TBM, and the clogging potential is not significantly reduced in the consistency range, where the highest risk of clogging is expected.

MATERIALS AND METHODS

Testing procedures

Evaluation of stickiness: empirical mixing test. The Hobart mortar mixer is often used in the mixing test, to determine the influence of different conditioning agents on soil behaviour in the mixing process, and to create a homogeneous clay–chemical paste (Fig. 5). The performance, however, is mostly judged intuitively. In order to quantify the clogging potential of soft soil mixtures empirically, this method was expanded by measuring the weight of soil sticking to the mixing tool after mixture preparation in the mortar mixer. The resulting empirical stickiness ratio λ (equation (4)) quantifies the tendency of the conditioned soil paste to remain sticking on a mixing tool after a mixing process in a mortar mixer.

Although this test is empirical, and cannot fully represent the complex conditions during excavation, it is a very simple measure of the interaction between soil and steel tools in a rotational operation mode similar to TBM excavation.

Adhesion measurement: plate shear test. Adhesion is regarded as the main cause of clogging in tunnelling, and is expected to decrease after the injection of soil conditioners. Because of the lack of reliable and established laboratory methods for quantification of tangential adhesion, a new measurement device was developed, allowing measurement of both the tangential adhesion and the sliding resistance between conditioned soft pastes and steel surfaces at different applied pressures as they occur in the pressure chamber of an EPB-TBM. The concept of the apparatus is very simple, as shown in Fig. 6; a detailed description can be found in Zumsteg & Puzrin (2012). The upper part of the apparatus consists of a soil box, which can be filled with the conditioned soil, and allows the installation of a steel plate

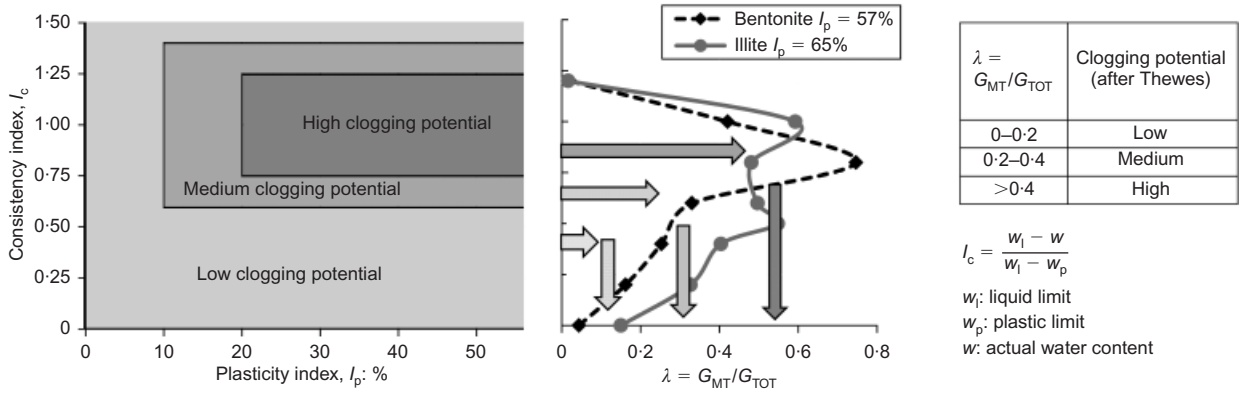

$\lambda = G_{MT}/G_{TOT}$	Clogging potential (after Thewes)
0–0·2	Low
0·2–0·4	Medium
>0·4	High

$$I_c = \frac{w_l - w}{w_l - w_p}$$

w_l: liquid limit
w_p: plastic limit
w: actual water content

Fig. 3. Evaluation of clogging potential (after Thewes, 1999) and correlation with empirical stickiness ratio for illite and bentonite at different clay consistencies

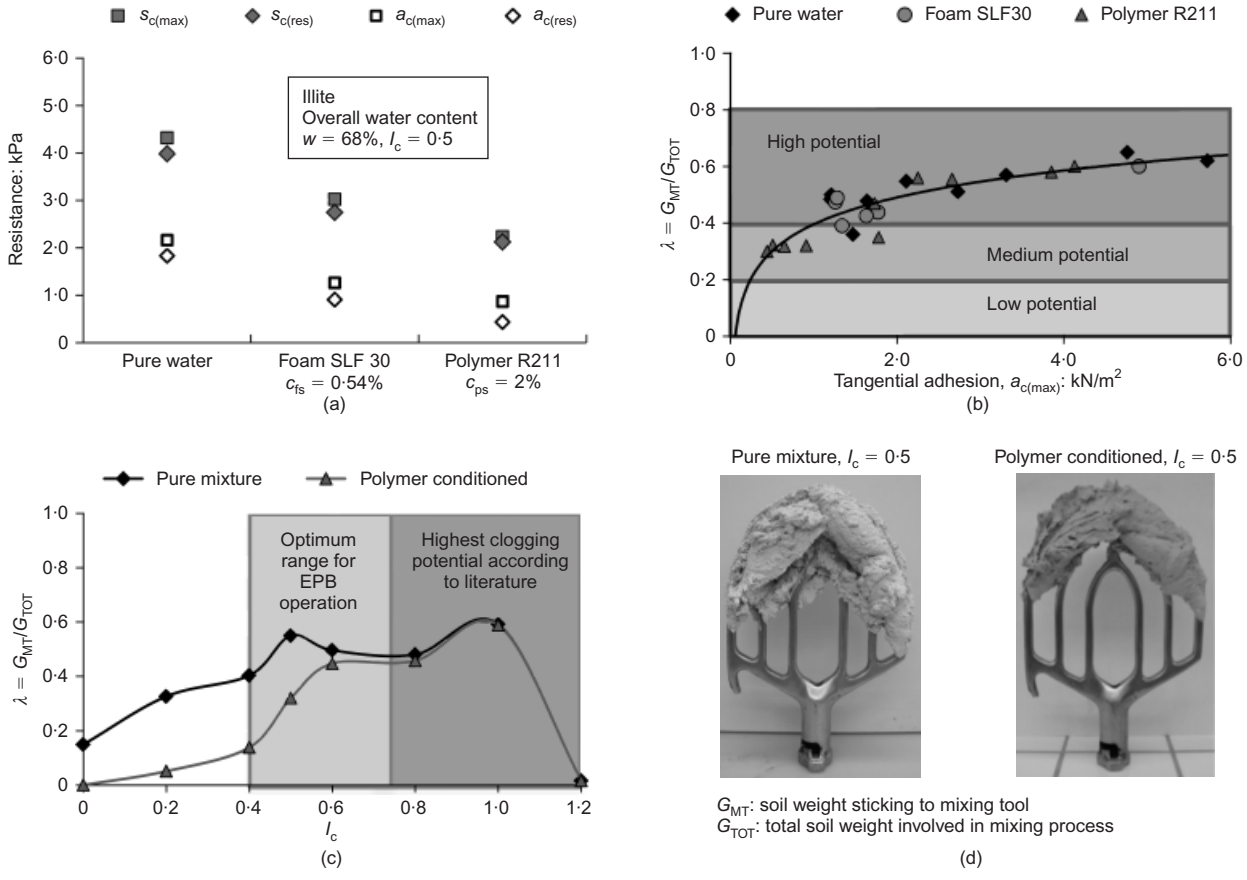

Fig. 4. (a) Influence of commercial soil conditioners on strength and adhesion of illite pastes; (b) correlation between empirical stickiness and adhesion for different mixtures*; (c) effect of dispersing polymer on stickiness behaviour of illite at different soil consistencies*; (d) mixing paddle after test with illite at consistency $I_c = 0{\cdot}5$. *Reprinted from Zumsteg & Puzrin (2012), with permission from Elsevier

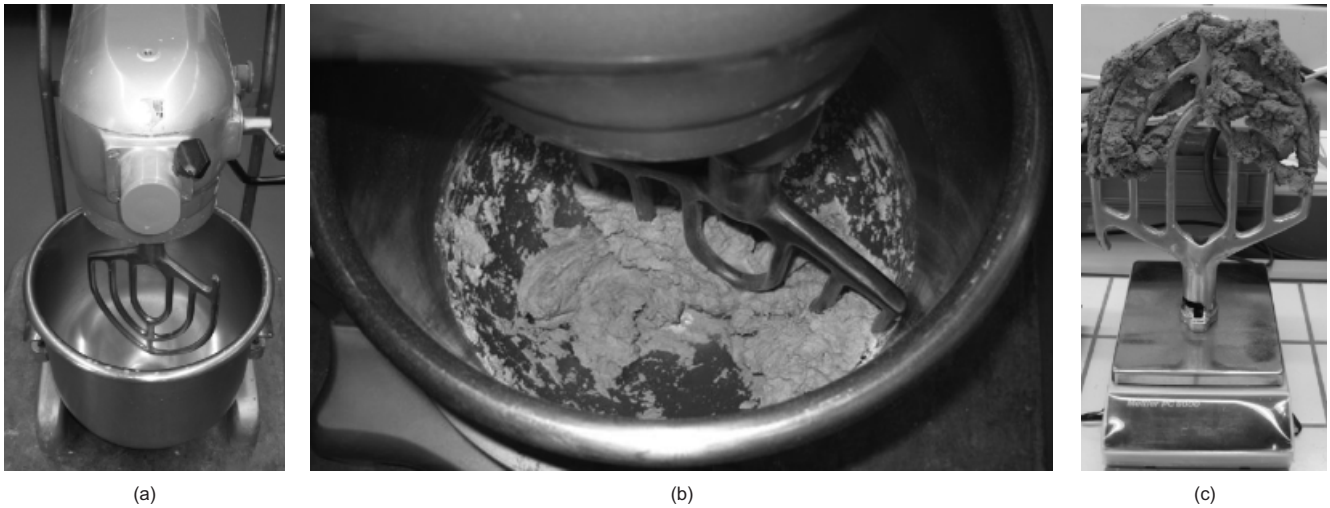

Fig. 5. (a) Photograph of mixer used, with mixing tool; (b) mixing process; (c) mixing tool after mixing process (reprinted from Zumsteg & Puzrin, 2012, with permission from Elsevier)

(with desired surface roughness) at its mid height. After application of the desired pressure at the bottom plate of the box, the plate can be rotated at the desired velocity with a continuous record of the torque moment. Assuming a constant shear stress at every point of the plate, the tangential adhesion $a_{c(max)}$ can be calculated using the maximum torque moment and the sliding resistance $a_{c(res)}$ from the average residual torque moment (Fig. 6).

For determination of the maximum conditioned shear strength $s_{c(max)}$ and the residual conditioned shear strength $s_{c(res)}$ of the mixtures, the new pressurised vane shear-test apparatus was used. This apparatus was also developed for soil-conditioning purposes, to the measure strength properties of conditioned pastes under EPB conditions, namely different applied pressures and rotation rates of the vane. It is described in detail in Messerklinger *et al.* (2011). General measurement results for different clays with different conditioning can be found in Zumsteg *et al.* (2012).

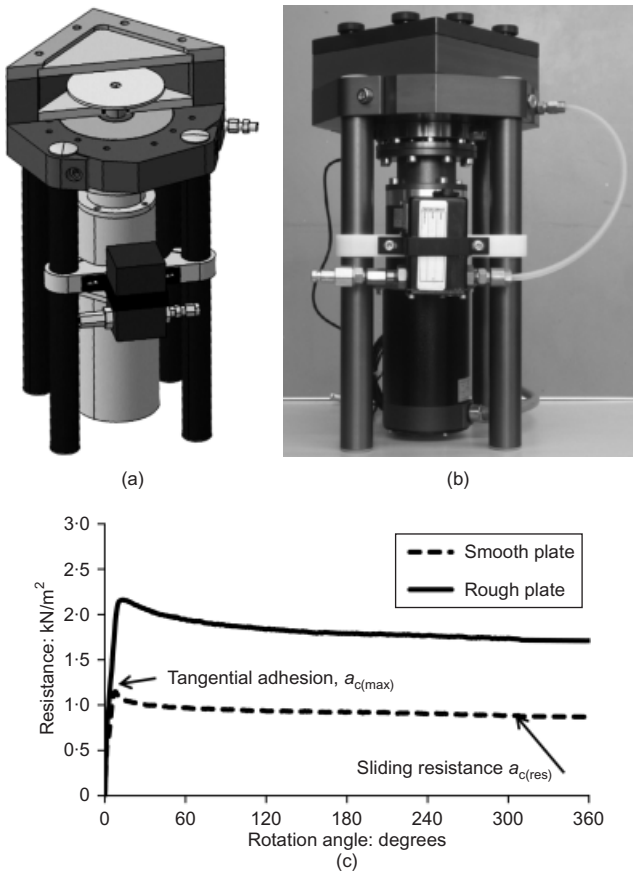

Fig. 6. Shear-plate apparatus: (a) three-dimensional schematic; (b) photograph; (c) typical test results (reprinted from Zumsteg & Puzrin, 2012, with permission from Elsevier)

Chemicals and soils used

New chemicals used. Polyamines in general are widely used as additives in drilling fluids (Jarrett & Dye, 2005), where they act mainly as hydration suppressants. Their proposed use in this study as a conditioner with the aim to change properties of soft clays in general, and for tunnelling application specifically, is novel. Polyamines used in this study are summarised in Table 1.

Clays used. Three different clays – kaolin, illite and bentonite – were used in this study, each with a predominant specific clay mineral (kaolinite, illite and montmorillonite respectively). The properties of these clays are summarised in Table 2. The kaolin and bentonite were delivered in powdered form; the illite was delivered in larger pieces and then milled to smaller-sized aggregates, allowing for the study of the effects of the aggregate size. The standard grain size of the illite material for this study was smaller than 0·5 mm. To investigate the influence of aggregate size on the chemical efficiency of the amines, one base material with smaller and one with larger average grain size was produced and tested (Table 3). The detailed grain-size distributions of all the clays can be found in Appendix 2.

Mixture preparation and composition

Production of the clay pastes for determining the mechanical parameters of the mixtures followed the described procedure. For the non-treated mixtures, 1500 g of dry clay was weighed in the mixing bowl of a Hobart mortar mixer. Depending on the desired final water content of the mixture, demineralised water was added and the mixing process was started. For the amine-treated mixtures, the desired concentration of amine (c_A, always expressed as weight of amine per weight of dry soil) was added to the demineralised water. This water–chemical mixture was added to 1500 g clay and moulded in the mortar mixer for a defined time period of 3 min.

RESULTS AND DISCUSSION

Effect of new chemicals: drastic stickiness reduction

The mixing test and determination of the empirical stickiness ratio for all three clays revealed a dramatic effect of amine addition (even in modest concentrations) on the stickiness behaviour of the mixtures (Fig. 7). Whereas after preparation of an illite paste with pure water at a soft consistency the mixing tool is completely clogged, it remains almost clean after the mixing process of the same clay at the same overall water content with the addition of 1% of pentaethylenehexamine (PEHA) only, with the empirical stickiness ratio λ dropping from 0·55 to almost zero. Conducting tests at different water contents and paste consistencies demonstrates that this effect persists over the whole range of water contents, and particularly at problematic stiff consistencies (Fig. 7(a)). A similar result is obtained for bentonite clay (Fig. 7(b)), where the clogging potential can be reduced from high ($\lambda > 0{\cdot}4$) and medium ($0{\cdot}2 < \lambda < 0{\cdot}4$) to low ($\lambda < 0{\cdot}2$) over the whole range of water contents, with the empirical stickiness ratio never exceeding 0·1. Although for kaolin the dependence of this ratio on the paste consistency is different, in this case also λ is reduced to very low values over the whole range of practical interest (Fig. 7(c)). These results clearly demonstrate the main and most important benefit of the newly patented applications of the polyamine chemicals.

Adhesion and strength

The study of the influence of different polyamines on adhesion and strength values (Fig. 8) reveals important

Table 1. Polyamines used in the present study

Polyamine	Code	Structure	Formula
Diethylenetriamine	DETA	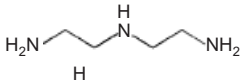	$C_4H_{13}N_3$
Triethylenetetramine	TETA	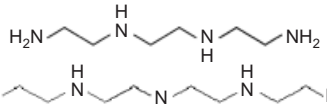	$C_6H_{18}N_4$
Tetraethlyenepentamine	TEPA	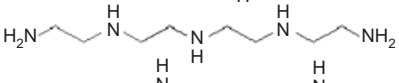	$C_8H_{23}N_5$
Pentaethylenehexamine	PEHA	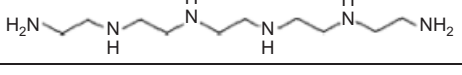	$C_{10}H_{28}N_6$

Table 2. Clays used for artificial laboratory mixtures

Clay	Specification, delivery	Mineralogical composition (X-ray diffraction, Rietveld analysis): wt %	Cation exchange capacity (Cu-complex method*): meq/100g	Surface area (N_2-BET): m^2/g	Water adsorption under free swelling (Enslin-Neff†): %	Plastic limit, w_p: %	Liquid limit, w_l: %	Plasticity index, I_p: %
Kaolin	Polwhite, China Clay, Imerys, UK, 2003	Kaolinite (69·6), K-feldspar (17·6), muscovite (10·9), quartz (1·9)	–	9·2	–	31	51	20
Illite	Sarospatakite extra, interILI, Füzérradvány, Hungary, 2007	illite (64·2), K-feldspar (27·1), quartz (8·7)	9	34	116	36	101	65
Bentonite	Calcigel, Südchemie AG, Germany, 2007	Ca-montmorillonite (71), muscovite (11·1), quartz (9·9), plagioclase (3·1), chlorite (2·8), calcite (1·6), dolomite (0·3)	65	67	120	45	102	57

* Determination after Meier & Kahr (1999).
† Determination after Kaufhold *et al.* (2010).

Table 3. Different illite base materials (Sarospatakite extra, Füzérradvány, Hungary, 2007)

Clay	Preparation/ grinding/grain size
Illite, fine-grained	Pebble mill (1 h)
Illite, medium-grained	Jaw breaker $< 0{\cdot}5$ mm
Illite, coarse-grained	Jaw breaker < 4 mm

information about the different effects of these chemicals. Clear tendencies for increasing polyamine molecular size can be observed. Whereas tangential adhesion $a_{c(max)}$ and sliding resistance $a_{c(res)}$ are slightly larger for DETA, for amines with higher molecular weight they remain close to the values for the non-treated paste. The residual hear-strength value $s_{c(res)}$ follows the same trend, and even approaches the adhesion value for PEHA. Of critical importance, however, is the behaviour of the maximum shear strength $s_{c(max)}$, which increases continuously with the molecular length of the amines used: for PEHA, it reaches a value three times higher than for a mixture at the same overall water content without chemical treatment.

Influence of chemicals on α ratio

The changes in strength and adhesion after commercial foam and polymer treatment (Fig. 4) clearly demonstrate that the lubricants used are capable of decreasing adhesion, but at the same time they also reduce the shear strength of the mixture to a similar extent. This inevitably results in a limited reduction of the α ratio. In this case low stickiness is achieved mainly by reducing the strength and adhesion to very low values, which is possible only at liquid consistencies. This is not a desired conditioning effect.

Attempts to find a general correlation between the parameter α and the empirical stickiness parameter λ for different types of clay mixed at the same overall water content with conventional clay-dispersing chemicals were not successful (Fig. 9(a)). Apparently, because of the different composition and structure of the clay minerals used, they have to be considered separately. What all types of clay have in common, however, is that chemical treatment with commercial products leads to a rather small change of the ratio α, when compared with the non-treated paste of the same clay at the same water content. The biggest effect in Fig. 9(a) is evident for illite, where polymer application in particular manages to a certain extent to reduce both α and the stickiness λ. The data points for illite indicate a possible correlation between α ratio and stickiness ratio λ, although the trend is not very clear.

Plotting the α ratios for these illite mixtures treated with amines against their empirical stickiness ratio λ displays a good correlation (Fig. 9(b)), clearly supporting the hypothesis that the reduced α ratio is mainly responsible for the decreased stickiness. When these results are plotted as λ against adhesion, together with the results for non-treated and commercially treated pastes (Fig. 10), it becomes clear that in the case of polyamines a different interaction mechanism is at work; the polyamine- treated pastes do not follow the general logarithmic correlation seen in (and limiting the stickiness-reduction capacity of) commercial chemicals.

Interaction mechanism of commercial products: lubrication

When water is added together with the commercially tested polymers and foams, their chemical interaction mechanism is based on reducing the attractive potential in the

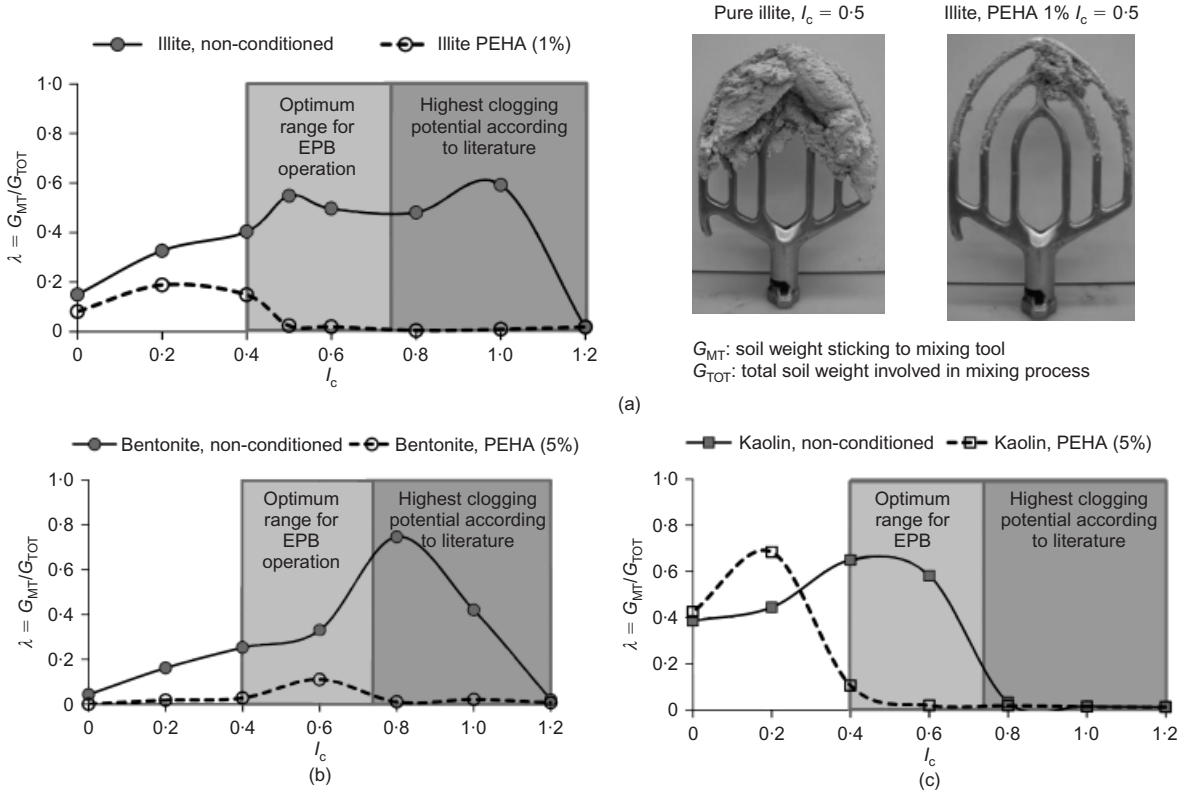

Fig. 7. Beneficial effect of PEHA on clogging behaviour in mixing test plotted against different water contents of soil (consistency index) for: (a) illite; (b) bentonite; (c) kaolin

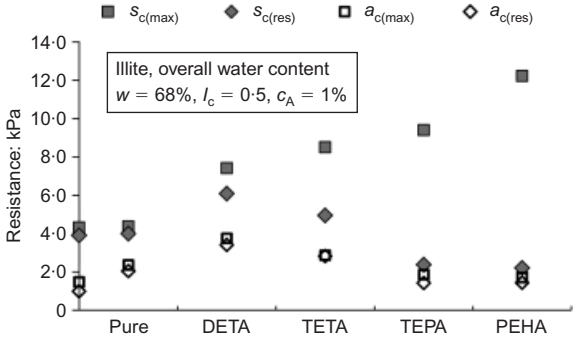

Fig. 8. Effect of different amines on strength and adhesion values for illite

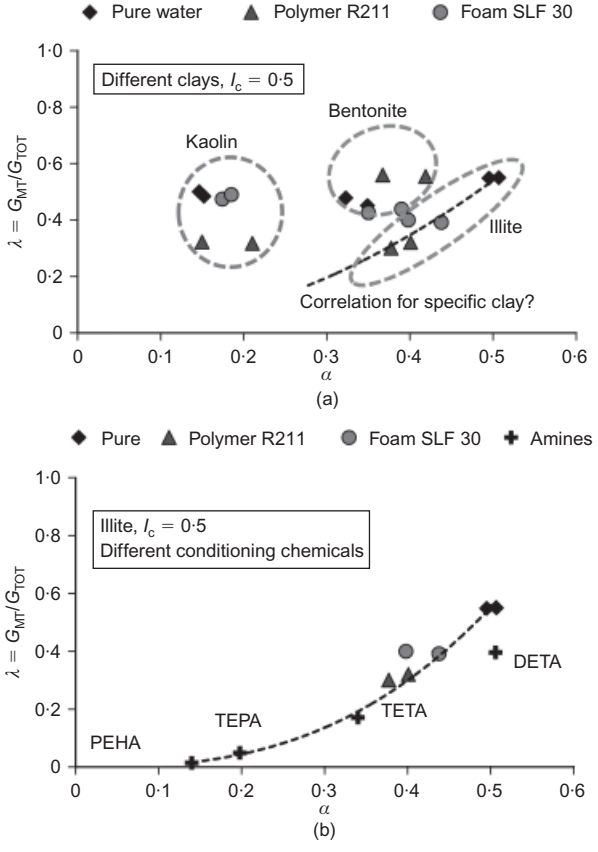

Fig. 9. α ratios for different treated and non-treated clay pastes and relation to stickiness at same consistency: (a) for different clays, and commercial foam and polymer (after Zumsteg & Puzrin, 2012); (b) for illite and different amines

water films around the individual clay particles in their immediate proximity. Ion exchange and complexation reactions between clays and chemicals lead to decreased electrostatic forces, and therefore to enhanced mobility of water molecules between clay particles and at the clay/steel interface (lubrication). With respect to the resulting soil structure, there is no principal difference between adding pure water or aqueous lubricant solutions. Together with the water, the chemicals enter the clay aggregates, dissolve the boundaries and enhance lubrication at the contact points between particles. Mechanically this leads to decreased adhesion, but also to decreased strength. As a result, the α ratio and also the stickiness can be reduced, but only to a very limited extent.

Interaction mechanism of polyamines: sealing of aggregates

The polyamines used increase the difference between adhesion and shear strength, causing a reduction in the α

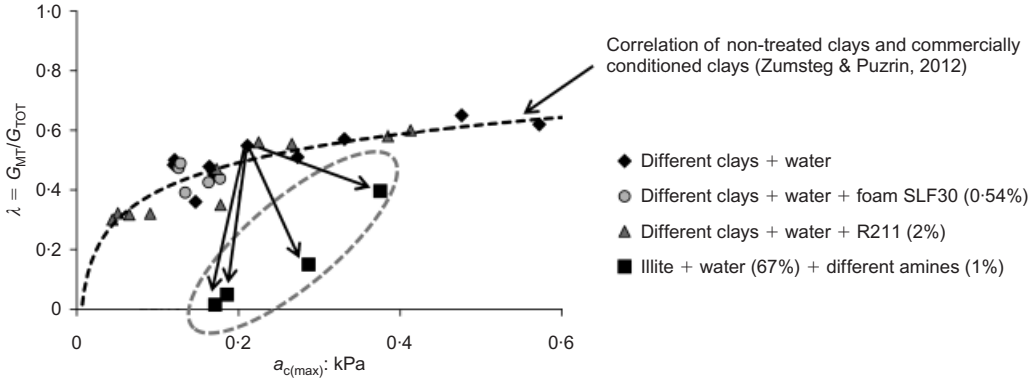

Fig. 10. Change in correlation between stickiness and adhesion for commercially conditioned and amine-treated soils

ratio. This is assumed to be achieved by partially maintaining the aggregate structure (and the shear strength) of the clay during the addition of water, preventing destruction of the clay aggregates. This inhibition of water entrance is based on adsorption of the applied amines (which have a high affinity to clay surfaces) on aggregate surfaces. As a result, the chemicals seal the clay/aggregate surface and hold the water in thick layers around the aggregates. Evidence for this mechanism is also given in the following sections, based on a number of alternative investigations.

Microscopic investigations: ESEM. The mechanism of sealing by the applied chemicals is clearly visible at the aggregate scale in micrographs taken with an environmental scanning electron microscope (ESEM). Fig. 11 confirms the different soil structure of the amine-conditioned paste, if compared with a paste at the same water content but without the addition of any chemicals (Fig. 1). The aggregate boundaries are still easily visible, clearly indicating that the water is attracted around the particles, but is not able to dissolve the agglomerates. The mechanical behaviour of this matrix is to a large extent determined by the properties of the aggregate, and not by the single-particle contacts inside the aggregates, as is the case for the addition both of pure water and of commercial conditioners.

Adsorption measurement. One necessary condition for the sealing mechanism is chemical coating of the clay aggregates, and therefore adsorption of the chemicals on the clay surface. A simple procedure was developed to determine amine adsorption for the three different clays and two types of amine. Details of the procedure and results are described in Appendix 1. In all cases the results clearly confirm a strong amine adsorption on the clay/aggregate surfaces, with the adsorbed quantity depending strongly on the available concentration of amines and on the type of clay. Amines with higher molecular weight adsorbed in bigger quantities on the same type of clay, directly supporting the model of increased efficiency through increased amine size.

Water content. The mixing test clearly showed the beneficial anti-sticking behaviour of amines over a large range of paste consistency (Fig. 7). For a consistency of $I_c = 0{\cdot}5$, it has been shown (Fig. 9) that this effect was linked to a decrease of the ratio between adhesion and strength. Fig. 12 shows shear strength and adhesion measurements for a range of paste consistencies, for both non-treated and amine-treated illite pastes at four different water contents. Although the amine treatment does reduce adhesion to some limited extent (Fig. 12(b)), the main effect is as expected, based on the shear behaviour (Fig. 12(a)), with reduced residual and increased maximum shear strength, compared with the strength values

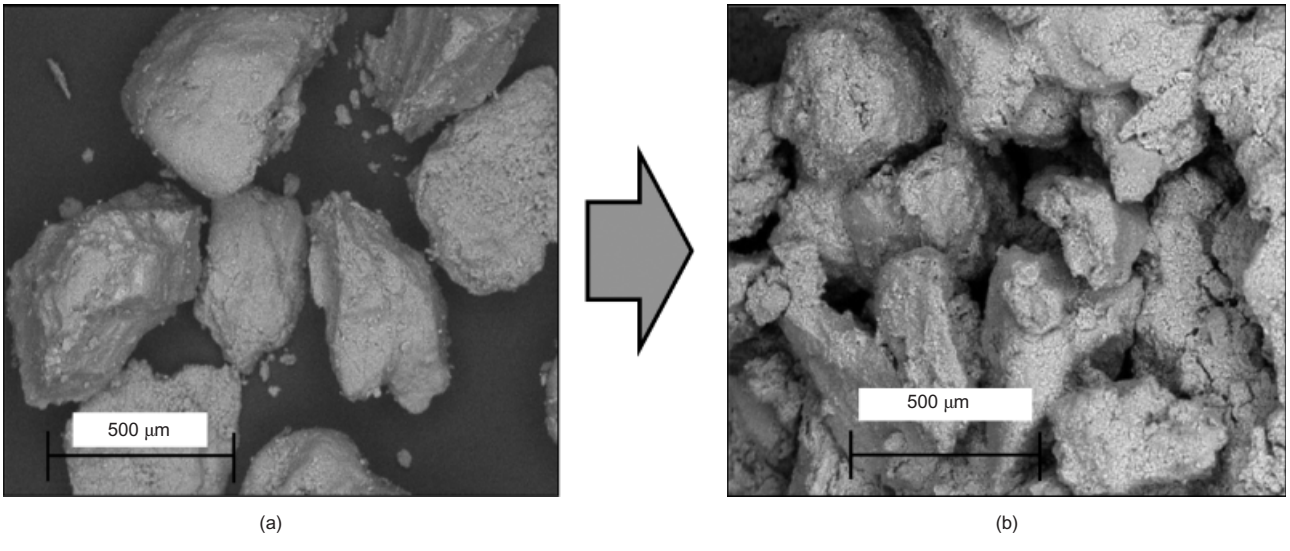

Fig. 11. Effect of water and amine addition on structure of clay (ESEM images): (a) base material, dry illite aggregates; (b) addition of water and 1% PEHA (no disintegration of clay agregates)

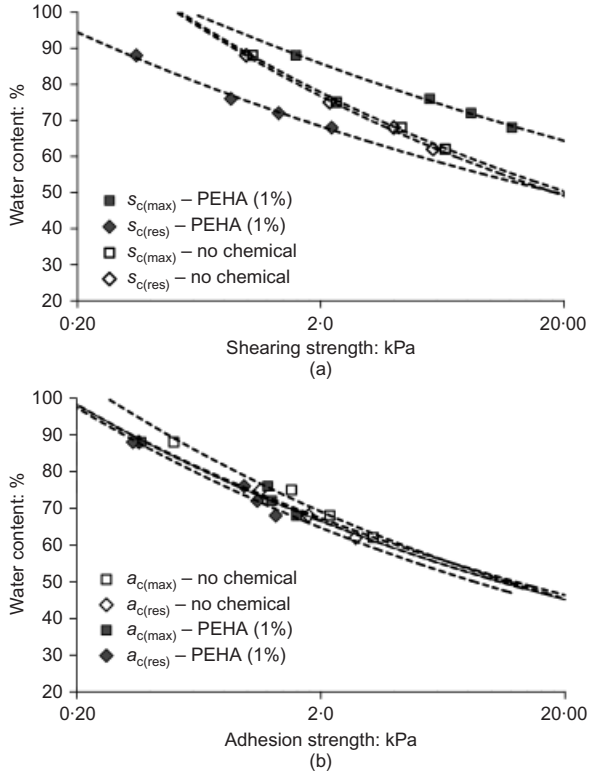

Fig. 12. Effect of water content on (a) strength and (b) adhesion behaviour of non-treated illite and illite treated with 1% PEHA

for non-treated pastes. Another, indirect validation of the sealing mechanism comes from analysis of the slopes of the fitted strength curves (power-law trend lines in Fig. 12(a)). For amine-treated pastes the slope is flatter, which means that less water is needed to reduce the strength by the same amount as in a non-treated paste. This can be explained by assuming that in the case of amine treatment the added water is distributed around the clay aggregates, producing a thicker water film than in non-treated pastes, where water is distributed inside the aggregate around the individual clay particles with much larger specific surface. The thicker water film in the amine-treated pastes leads to the faster strength reduction.

Particle grain size. The assumed aggregate-sealing mechanism suggests that for a smaller average aggregate size, because of the larger surface area, a larger concentration of amines is needed to achieve the same sealing effect. To validate this assumption, three illite base materials with different aggregate size, different water contents but comparable maximum conditioned shear strengths were tested (Fig. 13). Indeed, in order to achieve a clearly reduced stickiness ratio λ, small aggregates (fine-grained illite) require a higher amount of amine addition (4%), whereas for coarse aggregates (coarse-grained illite) only a small concentration (0·5%) is needed to produce the desired effect. Moreover, for small aggregates, even when a higher concentration of amines is used, the reductions in both the α ratio and the correlated stickiness ratio λ are smaller than in the coarse base material. This is a further confirmation of the mechanism of aggregate sealing, which becomes, as expected, less efficient as the aggregate size approaches the size of the single clay platelet.

CONCLUSIONS

Quantification of the stickiness-reducing effects of commercially available clay-dispersing foams and polymers and their relation to the more fundamental parameters of shear strength and adhesion was carried out in a previous study, using novel devices and characterisation methods. The established logarithmic correlation between the empirical stickiness ratio and both adhesion and shear strength for different types of clay and chemicals used indicated a limited efficiency of the commercial products for reducing stickiness and clogging potential.

This limited efficiency of the commercial chemicals can be attributed to their lubrication mechanism, and can be quantified in terms of adhesion, shear strength, their ratio α and the stickiness parameter λ (Fig. 14). In fact, during the tunnel excavation process the problem of clogging occurs after the penetration of added water into the crushed clay agglomerates. This leads to destruction of the aggregate structure, reduction of its internal strength, and the development of adhesion stresses between the single clay platelets and the steel surfaces. Once the adhesion and strength values are in the same range, both the ratio between them (α ratio) and the stickiness (λ ratio) become significant. The main effect of commercial products is lubrication between clay particles and between the clay and steel at their interface, leading not only to reduced adhesion but also to decreased shear strength. As a result, the α ratio is not significantly reduced, and a large reduction in stickiness can be achieved only at liquid consistency, which is not feasible for TBM operation.

This indicates the need for an enhanced chemical interaction mechanism for stickiness reduction. The proposed mechanism is based on adsorption of the chemicals on the clay surface, leading to coating and sealing of the clay aggregates, preventing the entrance of water and maintaining their shape and internal strength. As a result, the intact clay aggregates maintain a certain structure with a higher strength compared with clays mixed only with water or with water and commercial conditioners. At the same time, as the water is prevented from entering the aggregates, it accumulates

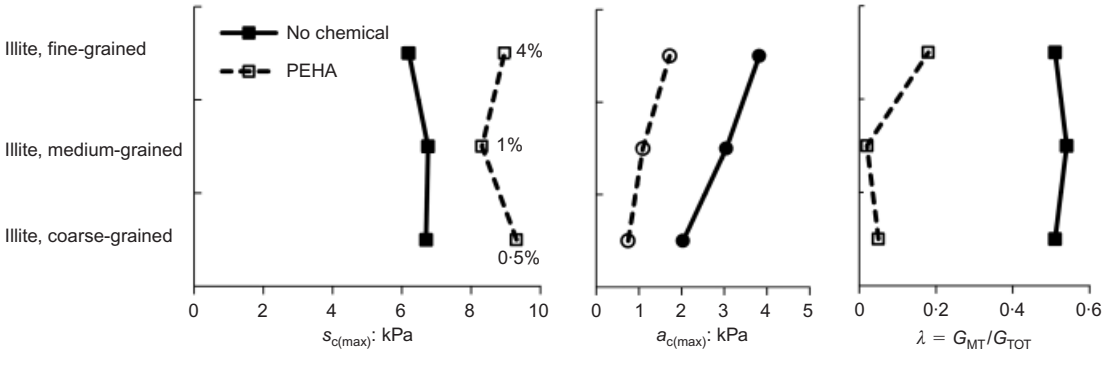

Fig. 13. Influence of grain size on efficiency of the amines

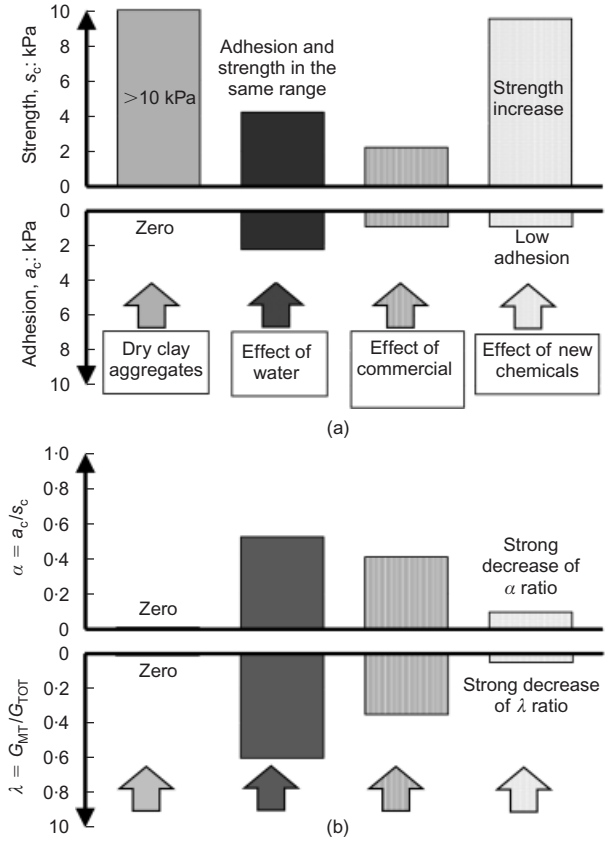

Fig. 14. Effects of commercial lubricants and new chemicals on: (a) strength and adhesion values; (b) adhesion to strength and stickiness ratios

around the aggregates in thicker water films, ensuring that the adhesion stays low. This guarantees a low α ratio, resulting in a low empirical stickiness ratio λ (Fig. 14).

The proposed sealing mechanism has been realised with the help of polyamine chemicals (which is a novel patented application), and has been validated in electron microscopy observations, adsorption tests and parametric studies varying the molecular weight of the chemicals, clay minerals, clay aggregate size and water content of the mixtures. The presented results clearly show the great potential of the polyamines for reducing the stickiness of all types of clay tested over the entire consistency range. The study also confirms the applicability of the recently developed characterisation procedures and devices for stickiness and clogging problems, and the proposed sealing mechanism is expected to contribute to the development of new conditioning products to reduce potential risks for tunnelling in clay soils.

ACKNOWLEDGEMENTS

The presented work is a by-product of a research project between ETH Zurich and BASF Construction Chemicals Europe Ltd, MEYCO Global Underground Construction, Zurich, represented by Dr A. Walliser and H. Egli. The project has been supported by the Swiss Confederations Innovation Promotion Agency (CTI; Grant No. 8554.2 EPRP-IW). The support of the staff of the IGT Claylab of ETH Zurich (B. Hornung, A. Röthlisberger) and the contribution of Dr L. P. Meier are greatly appreciated.

APPENDIX 1: ADSORPTION MEASUREMENTS

Amines in general are reactive substances, and are known to form stable complexes, especially with divalent cations (Ca^{2+}, Mg^{2+}, Cu^{2+}). This fact is used, for example, for determination of the cation exchange capacity (CEC) of clays with the copper complex method (Meier & Kahr, 1999), where the amine–Cu^{2+} complexes are responsible for the exchange reaction. Because the complexes are violet-blue in colour, their concentration can be easily determined photometrically.

Procedure

The measurement method used is based on the above reaction, and was adopted in this case for determination of the adsorbed amount of amine on the clay particles. Water–amine solution (40 ml) at five different amine concentrations (0 g, 0·0125 g, 0·0475 g, 0·2 g, 1 g) was mixed with 10 g of clay. Constant, slow turnover shaking of the suspension bins for 30 min allowed an equilibrium state to be reached. In a second step, the suspensions were centrifuged for 20 min at 2000 rev/min. After that, 0·5 ml of the clear supernatant solution of each sample was removed and mixed with 0·5 ml copper sulphate (0·2 mol/l), leading to the formation of Cu^{2+} complexes with the non-adsorbed amines. Extinction measurement of these solutions at 610 nm in a 10 mm cuvette (Dr Lange CADAS 100 photometer) enabled the solution colour depth to be determined. Extinction values at the same amine concentrations without any addition of clay served as a control, showing linear dependence on concentration. This allowed back-calculation of the supernatant and adsorbed concentration in the clay samples.

Results

The results in Fig. 15 clearly show that the suggested amines adsorb on the clay particles. The amount of adsorbed TEPA is dependent on the equilibrium concentration in solution and, to a high degree, on the type of clay (Fig. 15(a)). For bentonite, for example, a few percentages (wt% of clay) can be adsorbed; for kaolin the adsorption is much lower ($< 1\%$). Adsorption increases with increasing molecular weight of the amines used, indicated by a stronger adsorption for TEPA compared with TETA on illite clay (Fig. 15(b)).

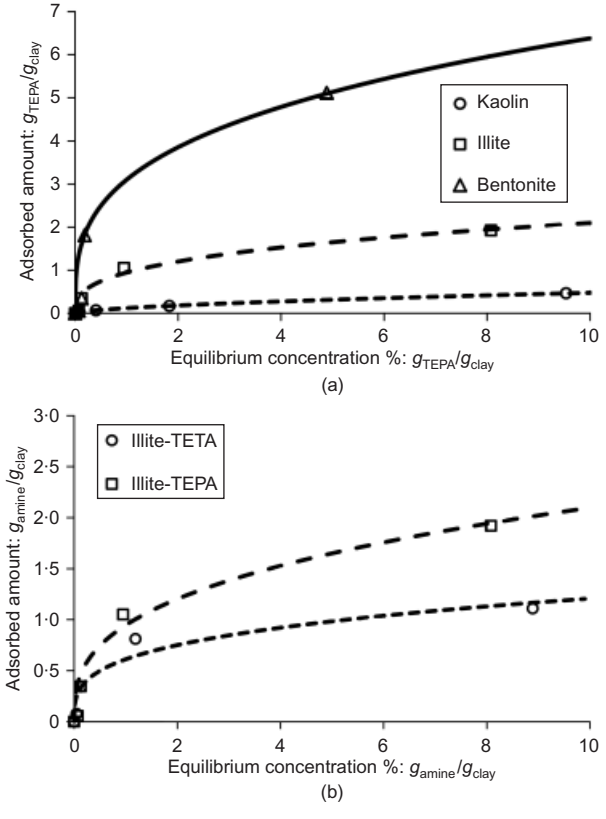

Fig. 15. (a) Adsorption of TEPA on different clays (fitted with Freundlich isotherms); (b) adsorption of TEPA and TETA on illite clay

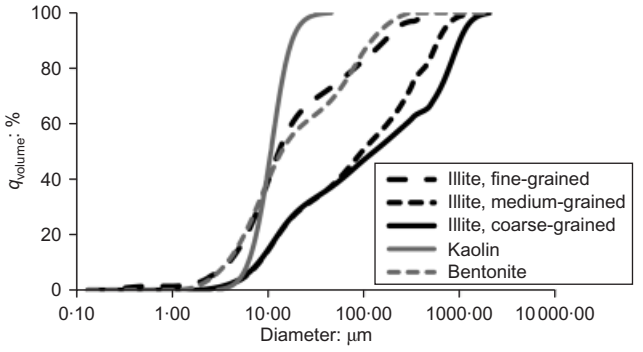

Fig. 16. Grading curves of the different clays and fractions used

APPENDIX 2: GRADING CURVES

The grading curves for the different materials were determined with particle-size analysis (Horiba LA 950, laser particle sizer), and are given in Fig. 16.

NOTATION

a_c	average resistance between conditioned soil and steel plate
$a_{c(max)}$	tangential adhesion
$a_{c(res)}$	sliding resistance
c_A	concentration of amine (wt% of dry clay)
G_{MT}	weight of soil sticking to mixing tool
G_{TOT}	total weight of soil sample
I_c	soil consistency index
I_p	plasticity index
LI	liquidity index
s_c	average shear strength of conditioned soil
$s_{c(max)}$	maximum conditioned shear strength
$s_{c(res)}$	residual conditioned shear strength
w	soil water content
w_l	liquid limit
w_p	plastic limit
α	ratio of adhesion to shear strength
λ	empirical stickiness ratio

REFERENCES

Borghi, F. X. (2006). *Soil conditioning for pipe jacking and tunnelling*. Dissertation, Department of Engineering, University of Cambridge, UK.

Braun, M. (1997). *Verklebungen von Tunnelbohrschilden und Schneidrädern im Zusammenhang mit adhäsiven Böden*. Diplomarbeit, Institut für Maschinenwesen im Baubetrieb, Universität Karlsruhe, Germany (in German).

EFNARC (2005). *Specification and guidelines for the use of specialist products for soft ground tunnelling*. Farnham, UK: European Federation for Specialist Construction Chemicals and Concrete Systems. See http://www.efnarc.org/pdf/SGTSpec.pdf (accessed 3 February 2012).

Feng, Q. L. (2004). Soil conditioning for modern EPBM drives. *Tunnels Tunnelling Int*. **36**, No. 12, 18–20.

Jarrett, M. & Dye, B. (2005). Organo-amine surfactant as hydration suppressants for reactive clay. *Proc. AADE National Technical Conference and Exhibition*, Houston, TX.

Kaufhold, S., Dohrmann, R. & Klinkenberg, M. (2010). Water-uptake capacity of bentonite. *Clays Clay Miner.* **58**, No. 1, 37–43.

Langmaack, L. (2000). Advanced technology of soil conditioning in EPB shield tunnelling. *Proc. North American Tunnelling 2000 Conf., Boston, MA*, 525–542.

Meier, L. P. & Kahr, G. (1999). Determination of the cation exchange capacity (CEC) of clay minerals using the complexes of copper(II) ion with triethylenetetramine and tetraethylenepentamine. *Clays Clay Miner.* **47**, No. 3, 386–388.

Messerklinger, S., Zumsteg, R. & Puzrin, A. M. (2011). A new pressurized vane shear apparatus. *Geotech. Test. J.* **34**, No. 2, GTJ103175.

Milligan, G. W. E. (2000). *Lubrication and soil conditioning in tunnelling, pipe jacking and micro-tunnelling: A state-of-the-art review.* London, UK: Geotechnical Consulting Group. See http://www.civil.eng.ox.ac.uk/research/pipejack/pdf/soilcond.pdf (accessed 10 January 2013).

Mitchell, J. K. & Soga, K. (2005). *Fundamentals of soil behavior*, 3rd edn. Hoboken, NJ, USA: John Wiley & Sons.

Thewes, M. (1999). *Adhäsion von Tonböden beim Tunnelvortrieb mit Flüssigkeitsschilden*. Bericht Nr. 21, Bergische Universität Gesamthochschule, Wuppertal, Germany (in German).

van Baalen, L. R. (1999). Reduction of clay adherence by electro-osmosis. *Memoirs of the Centre of Engineering Geology in the Netherlands*, No. 189.

Weh, M., Ziegler, M. & Zwick, O. (2010). Verklebungen bei EPB-Vortrieben in wechselndem Baugrund: Eintrittsbedingungen und Gegenmassnahmen. *Proc. STUVA-Tagung 2009, Hamburg*, 185–189 (in German).

Zumsteg, R. & Puzrin, A. M. (2012). Stickiness and adhesion of conditioned clay pastes. *Tunnelling Underground Space Technol*. **31**, September, 86–96.

Zumsteg, R., Plötze, M. & Puzrin, A. M. (2012). Effect of soil conditioners on the pressure and rate dependent shear strength of conditioned clays. *J. Geotech. Geoenviron. Engng* **138**, No. 9, 1138–1146.

ice
Institution of Civil Engineers
publishing

Session 1. Chemo-mechanical investigations in soils

1.2 Other geo-materials

Dominijanni, A. *et al.* (2013). *Géotechnique* **63**, No. 3, 191–205 [http://dx.doi.org/10.1680/geot.SIP13.P.010]

Coupled chemical-hydraulic-mechanical behaviour of bentonites

A. DOMINIJANNI*, M. MANASSERO* and S. PUMA*

Bentonites are clay soils characterised by a high specific surface and a permanent negative electric charge on their solid skeleton. Their common use as hydraulic and contaminant barriers for landfill and soil remediation applications, including the final disposal of nuclear waste, needs to be supported by adequate theoretical modelling of their mechanical behaviour and transport properties, in order to assess the expected performance in the long term. To this end, a theoretical approach has been proposed in order to derive constitutive equations for their coupled chemical-hydraulic-mechanical behaviour. The phenomenological parameters that govern the transport of electrolyte solutions through bentonites – that is, the hydraulic conductivity, the reflection coefficient (which is also called the chemico-osmotic efficiency coefficient), and the osmotic effective diffusion coefficient – have been measured through laboratory tests on a bentonite with porosity of 0·81, over a range of sodium chloride concentrations in the pore solution that varied from 5 mM to 100 mM. The relevance of the osmotic phenomena has been shown to decrease when the salt concentration increases. The obtained results have been interpreted by assuming that the microscopic deviations of the pore solution state variables from their average values are negligible. In this way, it is possible to interpret the macroscopic behaviour on the basis of the physical and chemical properties of the bentonite mineralogical components.

KEYWORDS: chemical properties; clays; constitutive relations; expansive soils; laboratory tests; pore pressures

INTRODUCTION

The term ‘bentonite’ is commonly used to indicate a clay soil with a high content ($> 70\%$) of montmorillonite, a mineral of the smectite group. Montmorillonite particles are thin lamellae that are characterised by a high specific surface (defined as the surface per unit weight) and a permanent negative electric charge. Bentonite is used in hydraulic and contaminant barriers, because of its low hydraulic conductivity, k, to permeation with water and dilute aqueous solutions (k typically $\leqslant 3 \times 10^{-11}$ m/s). Geosynthetic clay liners (GCLs), which consist of a thin layer of bentonite (~5–10 mm thick) sandwiched between two geotextiles, are examples of such barriers. GCLs are currently used in bottom and cover landfill barriers to limit water infiltration and contaminant migration.

Owing to its physical and chemical properties, bentonite’s macroscopic mechanical behaviour and transport properties cannot be modelled through classical soil mechanics approaches (Manassero & Dominijanni, 2003). In fact, bentonite swells or shrinks in response to changes in the chemical composition of the pore solution. Moreover, when a hydraulic pressure gradient, or a solute concentration gradient, is applied to it, both a volumetric flux and a diffusive solute mass flux occur, as in semi-permeable membranes. For this reason, a theoretical approach that accounts for the electric interaction that occurs between the solid skeleton of the bentonite and the ions contained in the pore solution is proposed in the first part of this paper. The experimental determination of the swelling pressure and the transport properties of a natural sodium bentonite is described in the second part. The obtained results have been interpreted with the proposed theoretical model, in which the microscopic properties of the bentonite have been linked to the observed macroscopic behaviour.

Manuscript received 29 February 2012; revised manuscript accepted 22 October 2012.
Discussion on this paper closes on 1 August 2013, for further details see p. ii.
* Department of Structural, Geotechnical and Building Engineering, Politecnico di Torino, Torino, Italy.

THEORY

Montmorillonite lamellae are characterised by a negative electric charge, owing to the isomorphic substitution of a portion of the tetravalent silicon (Si^{4+}) and the trivalent aluminium (Al^{3+}) in their crystalline structure, with metals, such as magnesium (Mg^{2+}), which have a lower valence. This electric charge per unit solid volume can be expressed as $F \cdot \bar{c}_{sk,0}$, where F is Faraday’s constant (96 485 C/mol) and $\bar{c}_{sk,0}$ is the molar concentration per unit solid volume of the solid skeleton electric charge, which is assumed to have unit valence (i.e. $z_{sk} = -1$). $\bar{c}_{sk,0}$ represents the moles of solid skeleton electric charge per volume of solids and, in order to be compared with the ion concentrations of the pore solution, it needs to be divided by the void ratio, e, which represents the pore volume per volume of solids. Dominijanni & Manassero (2012b) have shown that $\bar{c}_{sk,0}$ is proportional to the effective specific surface of the solid particles, and decreases when the montmorillonite lamellae aggregate to form the so-called *tactoids*.

If the pore solution contains a single salt that is completely dissociated with the stoichiometric reaction

$$(\text{Cation})_{z_1}^{\nu_1}(\text{Anion})_{z_2}^{\nu_2} \rightarrow \nu_1(\text{Cation})^{z_1} + \nu_2(\text{Anion})^{z_2}$$

where z_1 and z_2 are the electrochemical valences of the cation and the anion, and ν_1 and ν_2 are the stoichiometric coefficients of the cation and the anion respectively, then the following condition has to be satisfied in order to preserve electroneutrality within a saturated porous medium, even in the presence of the solid skeleton electric charge

$$z_1\bar{c}_1 + z_2\bar{c}_2 = \frac{\bar{c}_{sk,0}}{e} \quad (1)$$

where $\bar{c}_1$ and $\bar{c}_2$ are the molar concentrations of the cation and the anion respectively, and e is the void ratio.

As a consequence, the solid skeleton electric charge influences the distribution of the ions contained in the pore solution. This phenomenon is known as the *ion partition effect*, and is expected to be more relevant for porous media characterised by higher solid skeleton charge concentrations.

Equilibrium conditions

When an electrically charged porous medium is placed in contact with an external bulk solution that contains the same ions as are present in the pore solution, a thermodynamic equilibrium condition is reached, after a certain period of time, in which the water chemical potential and the ion electrochemical potentials between the two solutions are equal. The external bulk solution can be considered as a 'chemical thermometer' in order to evaluate the equilibrium conditions of the porous medium (Coussy, 2004). The electroneutrality condition in the external solution is given by

$$z_1 c_1 + z_2 c_2 = 0 \tag{2}$$

where c_1 and c_2 are the molar concentrations of the cation and the anion that are contained in the bulk solution.

It is convenient to define the salt concentration, c_s, of the external solution as

$$c_s = \frac{c_1}{\nu_1} = \frac{c_2}{\nu_2} \tag{3}$$

Using equation (3), the electroneutrality condition, equation (2), provides the relation between the electrochemical valences and the stoichiometric coefficients as

$$z_1 \nu_1 + z_2 \nu_2 = 0 \tag{4}$$

As a result, the equilibrium condition can be characterised by the following state variables of the external bulk solution: the absolute temperature, T; the hydraulic pressure (referenced to the atmospheric pressure, as is usual in soil mechanics), u; and the salt concentration, c_s. The corresponding variables of the pore solution can be evaluated from the following conditions

$$\bar{T} = T \tag{5}$$

$$\bar{\mu}_w = \mu_w \tag{6}$$

$$\bar{\mu}_i^{ec} = \mu_i^{ec} \quad i = 1, 2 \tag{7}$$

where $\bar{T}$ and T are the absolute temperature in the pore solution and in the external bulk solution respectively; $\bar{\mu}_w$ and μ_w are the water chemical potential in the pore solution and in the external bulk solution respectively; and $\bar{\mu}_i^{ec}$ and μ_i^{ec} are the electrochemical potentials of the ith ion in the pore solution and in the external bulk solution respectively.

The water chemical potential, μ_w, and the ion electrochemical potentials, μ_i^{ec}, of the external solution can be related to the hydraulic pressure, u, and the salt concentration, c_s, for a dilute solution according to (Katchalsky & Curran, 1965; Dominijanni & Manassero, 2012a)

$$\mu_w = \mu_w^0(T) + \frac{u - \Pi}{c_w} \tag{8}$$

$$\mu_i^{ec} = \mu_i + z_i F \phi = \mu_i^0(T) + RT \ln(\nu_i c_s) + z_i F \phi \quad i = 1, 2 \tag{9}$$

where μ_w^0 and μ_i^0 are integration constants that only depend on the absolute temperature T; c_w is the water molar concentration; $\Pi = RT \sum_{i=1}^{2} \nu_i c_s$ is the osmotic pressure; μ_i is the chemical potential of the ith ion; R is the universal gas constant ($= 8{\cdot}314$ J/(mol K)); and ϕ is the electric potential.

The state variables in the external bulk solution can be measured easily, whereas it is very difficult to determine the corresponding variables in the pore solution. Moreover, the relations obtained by linking the chemical potentials to the state variables of the pore solution are more uncertain, owing to the interaction with the solid skeleton charge, which alters the ion concentration distribution near the solid particles. The simplest assumption that can be adopted involves using relations analogous to equations (8) and (9), as they are also considered valid for the pore solution. This assumption, which was first proposed by Donnan (1911), neglects the microscopic deviations of the ion concentrations from their average values that are induced by the electric potential distribution within the pores. If this approximation is accepted, then the water chemical potential, $\bar{\mu}_w$, and the ion electrochemical potentials, $\bar{\mu}_i^{ec}$, of the pore solution can be expressed as

$$\bar{\mu}_w = \bar{\mu}_w^0(T) + \frac{\bar{u} - \bar{\Pi}}{\bar{c}_w} \tag{10}$$

$$\bar{\mu}_i^{ec} = \bar{\mu}_i + z_i F \bar{\phi} = \bar{\mu}_i^0(T) + RT \ln(\bar{c}_i) + z_i F \bar{\phi} \quad i = 1, 2 \tag{11}$$

where $\bar{\mu}_w^0$ and $\bar{\mu}_i^0$ are integration constants that depend only on the absolute temperature, T; $\bar{c}_w$ is the molar concentration of the water in the pore solution, which can be taken equal to the molar concentration of the water in the external bulk solution, that is, $\bar{c}_w \cong c_w$; $\bar{\Pi} = RT \sum_{i=1}^{2} \bar{c}_i$ is the osmotic pressure of the pore solution; $\bar{\mu}_i$ is the chemical potential of the ith ion in the pore solution; and $\bar{\phi}$ is the electric potential in the pore solution.

The hydraulic pressure of the pore solution, $\bar{u}$, and the ion partition factor, Γ_i, defined as the ratio between the ion concentration of the pore solution and the ion concentration of the external bulk solution, can therefore be expressed on the basis of equations (6) and (7), and using equations (8)–(11)

$$\bar{u} = u + (\bar{\Pi} - \Pi) \tag{12}$$

$$\Gamma_i = \frac{\bar{c}_i}{c_i} = \frac{\bar{c}_i}{\nu_i c_s} = \exp\left(-z_i \frac{F}{RT} \bar{\psi}\right) \quad i = 1, 2 \tag{13}$$

where $\bar{\psi} = \bar{\phi} - \phi$ is the electric potential of the porous medium, which is also called Donnan's potential.

On the basis of this approach, the hydraulic pressure of the pore solution is different from the hydraulic pressure of the external solution that is in equilibrium with it. The pressure difference between the pore solution and the external solution is called the swelling pressure, u_{sw}, and is given by

$$u_{sw} = \bar{\Pi} - \Pi \tag{14}$$

Equations (12) and (13) for $i = 1, 2$, together with equation (1), constitute a set of four equations that can be solved to find the four unknown variables: the hydraulic pressure, $\bar{u}$, the ion concentrations, $\bar{c}_i$ for $i = 1, 2$, and the electric potential, $\bar{\psi}$.

When the ion electrochemical valences are both unitary, such as for soidium chloride, equation (13) implies that

$$\Gamma_1 = \Gamma_2^{-1} \tag{15}$$

Inserting equation (15) into equation (1) results in the equation

$$\Gamma_2^{-1} - \Gamma_2 - \frac{\bar{c}_{sk,0}}{e c_s} = 0 \tag{16}$$

which has a positive solution of the form

$$\Gamma_2 = -\frac{\bar{c}_{\mathrm{sk},0}}{2ec_\mathrm{s}} + \sqrt{\left(\frac{\bar{c}_{\mathrm{sk},0}}{2ec_\mathrm{s}}\right)^2 + 1} \tag{17}$$

and

$$\Gamma_1 = \Gamma_2^{-1} = \frac{\bar{c}_{\mathrm{sk},0}}{2ec_\mathrm{s}} + \sqrt{\left(\frac{\bar{c}_{\mathrm{sk},0}}{2ec_\mathrm{s}}\right)^2 + 1} \tag{18}$$

On the basis of equations (17) and (18), the swelling pressure can be expressed as

$$\begin{aligned} u_\mathrm{sw} &= RTc_\mathrm{s}(\Gamma_1 + \Gamma_2 - 2) \\ &= 2RTc_\mathrm{s}\left[\sqrt{\left(\frac{\bar{c}_{\mathrm{sk},0}}{2ec_\mathrm{s}}\right)^2 + 1} - 1\right] \end{aligned} \tag{19}$$

Change in equilibrium

When the hydraulic pressure and/or the salt concentration are changed in the external bulk solution, a new equilibrium condition is restored in the porous medium after a sufficiently long period of time. In order to evaluate this new condition, the change in the free energy per unit initial (undeformed) volume of the porous medium, $\Im_\mathrm{V}$, can be determined by assuming that it is a function of the macroscopic strain tensor, $\boldsymbol{\varepsilon}$, and the concentration of each fluid component (Dormieux *et al.*, 2003). A second assumption that can be made refers to the reversible mechanical behaviour of the solid constituents: in such a case, the intrinsic dissipation, due to the solid skeleton strains, is zero (Dormieux *et al.*, 2003; Dominijanni & Manassero, 2012a). On the basis of these assumptions, the increment in free energy per unit initial volume, under isothermal conditions, can be expressed as

$$\mathrm{d}\Im_\mathrm{V} = \boldsymbol{\sigma} : \mathrm{d}\boldsymbol{\varepsilon} + \sum_{k=\mathrm{w},1}^{2} \bar{\mu}_k \frac{\mathrm{d}(e\bar{c}_k)}{1+e_0} \tag{20}$$

where $\boldsymbol{\sigma}$ is the total stress tensor and e_0 is the initial void ratio.

In equation (20), the chemical potentials of the pore solution, $\bar{\mu}_i$, can be substituted by the electrochemical potentials, $\bar{\mu}_i^\mathrm{ec}$, since the adding term given by

$$F\bar{\phi}\left\{\frac{\mathrm{d}[e(z_1\bar{c}_1 + z_2\bar{c}_2)]}{1+e_0}\right\} = F\bar{\phi}\frac{\mathrm{d}\bar{c}_{\mathrm{sk},0}}{1+e_0}$$

is null, if the solid skeleton charge, $\bar{c}_{\mathrm{sk},0}$, is assumed constant.

Then, applying equations (6) and (7), the water chemical potential and the ion electrochemical potentials in the pore solution can be substituted by the corresponding potentials in the external solution. If the electroneutrality condition, equation (2), is taken into account, the ion electrochemical potentials of the bulk solution can be substituted by the ion chemical potentials. As a result, $\mathrm{d}\Im_\mathrm{V}$ can be expressed using the readily available chemical potentials of the external bulk solution, instead of the chemical potentials of the pore solution. If the analysis is restricted to a unidimensional geometry, equation (20) becomes

$$\mathrm{d}\Im_\mathrm{V} = \sigma\,\mathrm{d}\varepsilon + \sum_{k=\mathrm{w},1}^{2} \mu_k \frac{d(e\bar{c}_k)}{1+e_0} \tag{21}$$

The free energy of the solid skeleton, which accounts for the interaction with the fluid phase, $\Im_\mathrm{V}^\mathrm{sk}$, can be derived by subtracting, from $\Im_\mathrm{V}$, the free energy of the fluid phase that is given as a function of the specific free energies of the components of the external bulk solution, F_k ($k = w$, 1, 2), to give

$$\Im_\mathrm{V}^\mathrm{sk} = \Im_\mathrm{V} - \frac{e}{1+e_0}\sum_{k=\mathrm{w},1}^{2}(\bar{c}_k F_k) \tag{22}$$

The free energy change, due to the interaction between the solid skeleton charge and the ions in the pore solution, is included in $\Im_\mathrm{V}^\mathrm{sk}$ because the specific free energy of the equilibrium bulk solution is subtracted from $\Im_\mathrm{V}$, instead of the specific free energy of the pore solution.

Using the thermodynamic relations

$$\mu_k = F_k + \frac{u_k}{c_k} \quad k = \mathrm{w},\ 1,\ 2 \tag{23}$$

$$\mathrm{d}\mu_k = \frac{\mathrm{d}u_k}{c_k} \quad k = \mathrm{w},\ 1,\ 2 \tag{24}$$

$$\mathrm{d}F_k = -u_k\mathrm{d}\left(\frac{1}{c_k}\right) \quad k = \mathrm{w},\ 1,\ 2 \tag{25}$$

where u_k represents the partial pressure of the kth component of the bulk solution, the change in $\Im_\mathrm{V}^\mathrm{sk}$ can be expressed as

$$\mathrm{d}\Im_\mathrm{V}^\mathrm{sk} = \sigma\,\mathrm{d}\varepsilon + \sum_{k=w,1}^{2}\frac{u_k}{1+e_0}\mathrm{d}\left(\frac{e\bar{c}_k}{c_k}\right) \tag{26}$$

Observing that $\bar{c}_\mathrm{w} \cong c_\mathrm{w}$ and

$$u_\mathrm{w} = u - \Pi \tag{27}$$

where the osmotic pressure represents the sum of the ion partial pressures

$$\Pi = \sum_{i=1}^{2} u_i \tag{28}$$

the increment $\mathrm{d}\Im_\mathrm{V}^\mathrm{sk}$ can be expressed as

$$\mathrm{d}\Im_\mathrm{V}^\mathrm{sk} = \sigma\,\mathrm{d}\varepsilon + (u-\Pi)\frac{\mathrm{d}e}{1+e_0} + \sum_{i=1}^{2}\frac{u_i}{1+e_0}\mathrm{d}\left(\frac{e\bar{c}_i}{c_i}\right) \tag{29}$$

For infinitesimal strains, assuming that the solid component is incompressible

$$\mathrm{d}\varepsilon = -\frac{\mathrm{d}e}{1+e_0} \tag{30}$$

and, as a consequence, equation (29) can be expressed as

$$\mathrm{d}\Im_\mathrm{V}^\mathrm{sk} = [\sigma - (u-\Pi)]\mathrm{d}\varepsilon + \sum_{i=1}^{2}\frac{u_i}{1+e_0}\mathrm{d}\left(\frac{e\bar{c}_i}{c_i}\right) \tag{31}$$

In order to derive the mechanical constitutive equations, it is convenient to work with the Gibbs free energy, $\mathrm{G}_\mathrm{V}^\mathrm{sk}$, which is the following Legendre transform of $\Im_\mathrm{V}^\mathrm{sk}$

$$\mathrm{G}_\mathrm{V}^\mathrm{sk} = [\sigma - (u-\Pi)]\varepsilon + \sum_{i=1}^{2}\frac{e}{1+e_0}u_i\frac{\bar{c}_i}{c_i} - \Im_\mathrm{V}^\mathrm{sk} \tag{32}$$

Taking into account equations (31) and (24), the infinitesimal increment in $\mathrm{G}_\mathrm{V}^\mathrm{sk}$ is given by

$$\begin{aligned} \mathrm{dG}_\mathrm{V}^\mathrm{sk} &= \varepsilon[\mathrm{d}\sigma - (\mathrm{d}u - \mathrm{d}\Pi)] + \sum_{i=1}^{2}\frac{e\bar{c}_i}{1+e_0}\mathrm{d}\mu_i \\ &= \varepsilon[\mathrm{d}\sigma - (\mathrm{d}u - \mathrm{d}\Pi)] + \left[\frac{e(\bar{c}_1+\bar{c}_2)}{1+e_0}\right]\frac{1}{\nu_1+\nu_2}\mathrm{d}\mu_\mathrm{s} \end{aligned} \tag{33}$$

where $d\mu_s$ is the salt chemical potential increment, which is defined as

$$\begin{aligned} d\mu_s &= \nu_1 d\mu_1 + \nu_2 d\mu_2 \\ &= \frac{1}{c_s} d\Pi \end{aligned} \tag{34}$$

The function G_V^{sk} can be considered to depend on the variables $[\sigma - (u - \Pi)]$ and μ_s: therefore the simplest constitutive equations that can be inferred are

$$d\varepsilon = \beta_{vv}[d\sigma - (du - d\Pi)] + \beta_{vs} d\mu_s \tag{35}$$

$$\frac{d[e(\bar{c}_1 + \bar{c}_2)]}{(\nu_1 + \nu_2)(1 + e_0)} = \beta_{sv}[d\sigma - (du - d\Pi)] + \beta_{ss} d\mu_s \tag{36}$$

Symmetry of the coefficients (i.e. $\beta_{vs} = \beta_{sv}$) can be demonstrated by considering G_V^{sk} as a continuous function of the variables $[\sigma - (u - \Pi)]$ and μ_s (Dominijanni & Manassero, 2012a).

Equation (35) can also be expressed in the form

$$d\sigma - du - du_{sw} = M d\varepsilon \tag{37}$$

where $M = 1/\beta_{vv}$ is the unidimensional elastic modulus of the porous medium and du_{sw} represents the swelling pressure increment, which is given by

$$du_{sw} = -\varpi d\Pi \tag{38}$$

where $\varpi = 1 + (\beta_{vs}/\beta_{vv} c_s)$ is the swelling coefficient (Dominijanni & Manassero, 2012a).

Since it is known, from experimental observations, that the swelling pressure tends to zero when $c_s \to \infty$, the swelling pressure, u_{sw}, can be obtained as

$$u_{sw} = \int_{\Pi}^{\infty} \varpi d\Pi \tag{39}$$

The effective stress principle can be restored, on the basis of equation (37), if the effective stress increment, $d\sigma'$, is defined as

$$d\sigma' = d\sigma - du - du_{sw} \tag{40}$$

The classical definition of effective stress, $d\sigma' = d\sigma - du$, corresponds to the particular case for which $du_{sw} = 0$, that is, $\varpi = 0$ and $\beta_{vs} = -\beta_{vv} c_s$.

Adopting Donnan's assumptions and using equation (14), the swelling coefficient can be expressed as

$$\varpi = 1 - \frac{d\bar{\Pi}}{d\Pi} \tag{41}$$

Dominijanni & Manassero (2012b) have demonstrated that equation (41) can also be expressed in the form

$$\begin{aligned} \varpi &= 1 - \frac{d\bar{\Pi}}{d\Pi} \\ &= 1 - \frac{\nu_1 + \nu_2}{\nu_1 \Gamma_2 + \nu_2 \Gamma_1} \Gamma_1 \Gamma_2 \end{aligned} \tag{42}$$

Transport equations

If clay is interposed between two reservoirs with different hydraulic pressures or ion concentrations, a pore solution volumetric flux, q, and an ion mass flux, J_i, relative to the solid skeleton, are generated. In order to derive appropriate flux equations, the linear momentum balance equations of the fluid components can be developed on the basis of a number of assumptions. If only unidimensional problems are considered and inertial effects are neglected, these equations can be expressed as (Ehlers, 2002; Dominijanni & Manassero, 2010)

$$-\frac{\partial(n\bar{u}_w)}{\partial x} + f_w = m_w \tag{43}$$

$$-\frac{\partial(n\bar{u}_i)}{\partial x} + f_i = m_i \quad i = 1, 2 \tag{44}$$

where n is the porosity, x is the spatial coordinate, f_w is the external force per unit volume acting on the water, m_w is the momentum supply of water, f_i is the external force per unit volume acting on the ith ion, and m_i is the momentum supply of the ith ion.

The external forces are gravity, which can be considered only to act on the solvent (i.e. water) in the x direction, and the electric force, which is proportional to the electric potential gradient.

$$f_w = n\rho_w \boldsymbol{g} \tag{45}$$

$$f_i = -n\bar{c}_i z_i F \frac{\partial \bar{\phi}}{\partial x} \quad i = 1, 2 \tag{46}$$

where ρ_w is the water density and $\boldsymbol{g}$ is the gravitational acceleration.

The momentum supply of the fluid components can be expressed as

$$m_k = -\bar{u}_k \nabla n + m_k^E \quad k = w, 1, 2 \tag{47}$$

where m_k^E represents the extra-momentum supply of the kth fluid component, which can be associated with the friction between the porous medium components that move with different velocities.

If the extra-momentum supply is associated with the frictional force per unit volume exchanged with the other components of the porous medium, it can be assumed to be equal to the sum of the binary interactions

$$m_w^E = m_{w,sk}^E + \sum_{i=1}^{2} m_{w,i}^E \tag{48}$$

$$m_i^E = m_{i,w}^E + m_{i,j}^E + m_{i,sk}^E \quad i, j = 1, 2;\ i \neq j \tag{49}$$

where w is the water, sk the solid skeleton, and i and j are the ith and jth ions. The friction between the ions and between the ions and the solid skeleton can be considered negligible for a dilute solution compared with the friction between the ions and the solvent

$$\begin{aligned} &m_{i,j}^E;\ m_{i,sk}^E \ll m_{i,w}^E \quad i, j = 1, 2;\ i \neq j \\ &m_i^E \cong m_{i,w}^E \quad i = 1, 2 \end{aligned} \tag{50}$$

Moreover, on the basis of the assumption of binary interaction, it can be assumed that

$$m_{w,i}^E = -m_{i,w}^E \quad i = 1, 2 \tag{51}$$

For the friction forces per unit volume, the following constitutive equations can be adopted.

$$m_{w,sk}^E = \alpha n(v_w - v_{sk}) = \alpha q \tag{52}$$

$$m_{i,w}^E = -m_{w,i}^E = \beta_i n\bar{c}_i(v_i - v_w) \quad i = 1, 2 \tag{53}$$

where α and β_i are friction coefficients, and v_w, v_{sk} and v_i are the water, solid skeleton and ith ion velocities respectively.

The factors n and $(v_w - v_{sk})$ in equation (52), as well as $n\bar{c}_i$ and $(v_i - v_w)$ in equation (53), have been picked out as an indication of the fact that $m_{w,sk}^E = 0$ if $n = 0$ or

$(v_w - v_{sk}) = 0$, and $m^E_{i,w} = 0$ if $n\bar{c}_i = 0$ or $(v_i - v_w) = 0$. However, this does not mean that the friction coefficients α and β_i are independent of n, $\bar{c}_i$ and the relative velocities.

Taking into account these constitutive assumptions, and using the thermodynamic relation that relates the chemical potentials to the partial pressure

$$d\bar{\mu}_k = \frac{d\bar{u}_k}{\bar{c}_k} \quad k = w, 1, 2 \tag{54}$$

the following flux equations can be derived from equations (43) and (44).

$$\begin{aligned} q &= n(v_w - v_{sk}) \\ &= -\frac{n}{\alpha}\left(\bar{c}_w \frac{\partial \bar{\mu}_w}{\partial x} - \rho_w g + \sum_{i=1}^{2} \bar{c}_i \frac{\partial \bar{\mu}_i^{ec}}{\partial x}\right) \end{aligned} \tag{55}$$

$$\begin{aligned} J_i &= n\bar{c}_i(v_i - v_{sk}) \\ &= q\bar{c}_i - n\frac{D_i}{RT}\bar{c}_i \frac{\partial \bar{\mu}_i^{ec}}{\partial x} \quad i = 1, 2 \end{aligned} \tag{56}$$

where $D_i = RT/\beta_i$ represents the macroscopic diffusion coefficient of the ith ion.

At this point, it is convenient to introduce the concept of a virtual external bulk solution that is in thermodynamic equilibrium with the pore solution at the generic position x within the porous medium (Dormieux *et al.*, 1995; Yaroshchuk, 1995). The virtual solution coincides with the real bulk solutions in contact with the porous medium at the boundaries. The thermodynamic potentials in equations (55) and (56) can be substituted with the corresponding potentials of this virtual solution, using equations (6) and (7). This leads to a formulation that does not depend on the determination of the pore solution variables. Therefore, equations (55) and (56) can be expressed as

$$q = -\frac{n}{\alpha}\left(\frac{\partial u}{\partial x} - \frac{\partial \Pi}{\partial x} - \rho_w g + RT\sum_{i=1}^{2}\Gamma_i \frac{\partial c_i}{\partial x} + F\frac{\bar{c}_{sk,0}}{e}\frac{\partial \phi}{\partial x}\right) \tag{57}$$

$$J_i = q\Gamma_i c_i - nD_i\Gamma_i \frac{\partial c_i}{\partial x} - z_i\Gamma_i c_i \frac{nD_i}{RT}F\frac{\partial \phi}{\partial x} \quad i = 1, 2 \tag{58}$$

If an external electric current is not applied to the porous medium, the electric potential derivative in equations (57) and (58) can be eliminated by means of the condition of electric current, I_e, equal to zero.

$$I_e = F\sum_{i=1}^{2} z_i J_i = 0 \tag{59}$$

The resulting flux equations can be expressed as follows

$$q = -\frac{k}{\gamma_w}\left(\frac{\partial u}{\partial x} - \omega\frac{\partial \Pi}{\partial x}\right) \tag{60}$$

$$J_s = (1-\omega)qc_s - nD^*_\omega \frac{\partial c_s}{\partial x} \tag{61}$$

where

$$k = \frac{n\gamma_w}{\alpha\left[1 + \frac{RT}{\alpha}\frac{(\Gamma_1 - \Gamma_2)^2 \nu_1\nu_2 c_s}{\nu_1\Gamma_2 D_2 + \nu_2\Gamma_1 D_1}\right]} \tag{62}$$

$$\omega = 1 - \frac{\nu_1 D_2 + \nu_2 D_1}{\nu_1\Gamma_2 D_2 + \nu_2\Gamma_1 D_1}\Gamma_1\Gamma_2 \tag{63}$$

$$J_s = \frac{J_1}{\nu_1} = \frac{J_2}{\nu_2} \tag{64}$$

$$D^*_\omega = (1-\omega)D_s \tag{65}$$

$$D_s = \frac{(\nu_1 + \nu_2)D_1 D_2}{\nu_1 D_2 + \nu_2 D_1} \tag{66}$$

where k is the hydraulic conductivity, ω is the reflection coefficient, J_s is the salt molar flux, D^*_ω is the osmotic effective diffusion coefficient, and D_s is the macroscopic salt diffusion coefficient.

Dominijanni & Manassero (2012b) have demonstrated that, if the microscopic deviations of the variables from their average values are assumed to be negligible, the macroscopic ion diffusion coefficients, D_i, are equal to the ion effective diffusion coefficients, D^*_i

$$D_i = D^*_i = \tau_m D_{i,0} \quad i = 1, 2 \tag{67}$$

$$\begin{aligned} D_s = D^*_s &= \frac{(\nu_1 + \nu_2)D^*_1 D^*_2}{\nu_1 D^*_2 + \nu_2 D^*_1} \\ &= \tau_m \frac{(\nu_1 + \nu_2)D_{1,0}D_{2,0}}{\nu_1 D_{2,0} + \nu_2 D_{1,0}} \\ &= \tau_m D_{s,0} \end{aligned} \tag{68}$$

where τ_m is the dimensionless matrix tortuosity factor, which accounts for the tortuous nature of the actual diffusive pathway through the porous medium (Malusis & Shackelford, 2002b); $D_{i,0}$ is the free (aqueous) solution diffusion coefficient of the ith ion; D^*_s is the salt effective diffusion coefficient; and $D_{s,0}$ is the free-solution diffusion coefficient of the salt.

An interesting observation is that the reflection coefficient, ω, results as equal to the swelling pressure coefficient, ϖ, when the ion free-solution diffusion coefficients are equal.

When the solid skeleton electric charge is equal to zero, the ion partition coefficients, Γ_i, are equal to 1, and equations (60) and (61) reduce to the Darcy equation and the classical advective diffusion equation respectively.

The osmotic effective diffusion coefficient, D^*_ω, results as related to the reflection coefficient, ω, through equation (65), so that $D^*_\omega = 0$ when $\omega = 1$. As a result, the condition $\omega = 1$ implies a null salt flux through the porous medium, which in this case can be said to act as a 'perfect' or 'ideal' barrier.

If equation (65) is compared with the expression for D^*_ω proposed by Malusis & Shackelford (2002b) and Malusis *et al.* (2012)

$$D^*_\omega = \tau_r D^*_s \tag{69}$$

where τ_r is the restrictive tortuosity factor, the result is that τ_r is given by

$$\tau_r = (1-\omega)\frac{D_s}{D^*_s} \tag{70}$$

Moreover, if the hypotheses implied by equation (68) are adopted, the expression for τ_r reduces to

$$\tau_r = 1 - \omega \tag{71}$$

The coefficient k can be measured, under steady-state conditions, using traditional permeameters. Malusis *et al.* (2001) developed a testing apparatus to determine ω and D^*_ω. This apparatus is able to impose the condition of no volumetric flux ($q = 0$) through a soil sample in contact with two external solutions, maintained at constant salt concentrations, so that the global or averaged values of the coefficients can be measured. The global values of ω and D^*_ω are defined as (Auclair *et al.*, 2002)

$$\omega_g = \frac{1}{\Delta c_s}\int_{c_b}^{c_t} \omega \mathrm{d}c_s \tag{72}$$

$$D^*_{\omega g} = \frac{1}{\Delta c_s}\int_{c_b}^{c_t} D^*_{\omega} \mathrm{d}c_s \tag{73}$$

where c_t and c_b represent the salt concentration at the top and the bottom boundaries of the clay sample respectively, and $\Delta c_s = c_t - c_b$ is their difference. These coefficients can be determined by means of the following relations under steady-state conditions.

$$\omega_g = \left(\frac{\Delta u}{\Delta \Pi}\right)_{q=0} \tag{74}$$

$$D^*_{\omega g} = \frac{L}{n}\left(\frac{J_s}{\Delta c_s}\right)_{q=0} \tag{75}$$

where $\Delta u = u_t - u_b$ and $\Delta \Pi = \Pi_t - \Pi_b$ represent the differences between the hydraulic pressure and the osmotic pressure at the boundaries of the clay sample, and L is the length of the sample.

It is interesting to observe that the relationship between D^*_{ω} and ω is also maintained between their corresponding global values; in fact, inserting equation (65) into equation (73) with $D_s = D^*_s$ leads to

$$\begin{aligned} D^*_{\omega g} &= (1-\omega_g) D^*_s \\ &= (1-\omega_g)\tau_m D_{s,0} \end{aligned} \tag{76}$$

For a salt constituted by monovalent ions, inserting equation (63) into equation (72) and using equations (17) and (18), the following expression for ω_g is obtained

$$\omega_g = 1 + \frac{\bar{c}_{sk,0}}{2\Delta c_s e}\left[Z_2 - Z_1 - (2t_1 - 1)\ln\left(\frac{Z_2 + 2t_1 - 1}{Z_1 + 2t_1 - 1}\right)\right] \tag{77}$$

where

$$t_1 = \frac{D_{1,0}}{D_{1,0} + D_{2,0}} \tag{78}$$

$$Z_1 = \sqrt{1 + \left(\frac{2c_t e}{\bar{c}_{sk,0}}\right)^2} \tag{79}$$

$$Z_2 = \sqrt{1 + \left(\frac{2c_b e}{\bar{c}_{sk,0}}\right)^2} \tag{80}$$

and t_1 is the cation transport number.

MATERIALS AND METHODS

Materials

The powdered bentonite tested in this study is an Indian sodium bentonite that is used for the production of a needle-punched GCL. The bentonite is characterised by a cation exchange capacity (CEC, measured using the methylene blue adsorption method) of 105 meq/100 g. The mineralogical composition, evaluated through X-ray diffraction analysis, indicates a bentonite that is composed primarily of smectite (> 98%), with traces of calcite, quartz, mica and gypsum.

The bentonite is characterised by a liquid limit (LL) of 525% and a hydraulic conductivity of 8×10^{-12} m/s, measured at a 27·5 kPa confining effective stress using de-ionised water (DW) as the permeant liquid.

Sodium solutions were prepared with sodium chloride (ACS reagent, purity ⩾ 99%) and DW. The sodium solutions were prepared at different molarity values in the range 5–100 mM, with the aim of investigating the effect of the monovalent cations on the osmotic behaviour of the bentonite. The DW (pH = 6·95; electrical conductivity (EC) at 20°C = 0·6 mS/m) consisted of tapwater processed through a series of activated carbon filters, a reverse osmosis process and, finally, an ultraviolet (UV) lamp (Elix Water Purification system). Moreover, the DW was de-aerated prior to use. The EC measured at 20°C for the sodium chloride solutions ranged from 60·5 mS/m to 1·1 mS/m.

Bentonite preparation. Prior to the osmotic property determination, the bentonite was submitted to a process with the aim of removing the soluble salts (mainly sodium) that are naturally present inside the material, owing to its marine origin. The treatment prevents soluble salts from interfering with the determination of the osmotic properties.

Previous studies (Malusis *et al.*, 2001; Malusis & Shackelford, 2002a, 2002b; Shackelford & Lee, 2003; Yeo *et al.*, 2005; Kang & Shackelford, 2009; Di Emidio, 2010) have used the 'flushing' method to remove soluble salts. This method consists of an initial permeation phase, performed under back-pressure, which requires a long period of time (i.e. from months to a year), because of the low bentonite hydraulic conductivity.

In this study the 'squeezing' method has been used, with the aim of reducing the salt removal time. The squeezing method consists of a series of consecutive phases of powder bentonite hydration with DW, at a higher water content than the LL, and drained consolidation, performed in a consolidometer under a maximum load of 500 kPa. Moreover, the drained solution is sampled daily, and the EC is monitored to evaluate the soluble salt concentration in the bentonite pore water. After the squeezing process, the material is oven-dried at 105°C and pulverised once again. When a 5 l consolidometer is used, the above procedure can produce about 500 g of squeezed dry powder bentonite, characterised by an EC value lower than 50 mS/m, in 40–50 days. The results of the EC monitoring during the squeezing process are reported in Fig. 1.

The specimen for the chemico-osmotic test is prepared by rehydrating the squeezed bentonite with DW at a lower water content than the LL value, and then by statically compacting the material in a compaction mould, while allowing the excess water to be released.

Dry powder bentonite is required for the swelling pressure test.

Testing apparatus and procedures

Chemico-osmotic test. The testing apparatus used to measure the global reflection coefficient and the global osmotic effective diffusion coefficient is described in detail in Malusis *et al.* (2001). The main components of the apparatus, shown in Fig. 2, are the osmotic cell, the flow pump system, the pressure transducer, which is used to measure the differential pressure that develops across the specimen during the test, and the data acquisition system.

The cell consists of a modified rigid-wall permeameter, in which the top piston and the bottom pedestal are equipped with three ports each: two enable the different solutions to circulate through the top (sodium chloride solution) and the bottom (DW) porous stones, with the aim of establishing a constant concentration gradient across the specimen. The third port is installed in both the top piston and the bottom pedestal to allow the differential pressure across the specimen to be measured.

The flow pump system, which consists of a dual-carriage

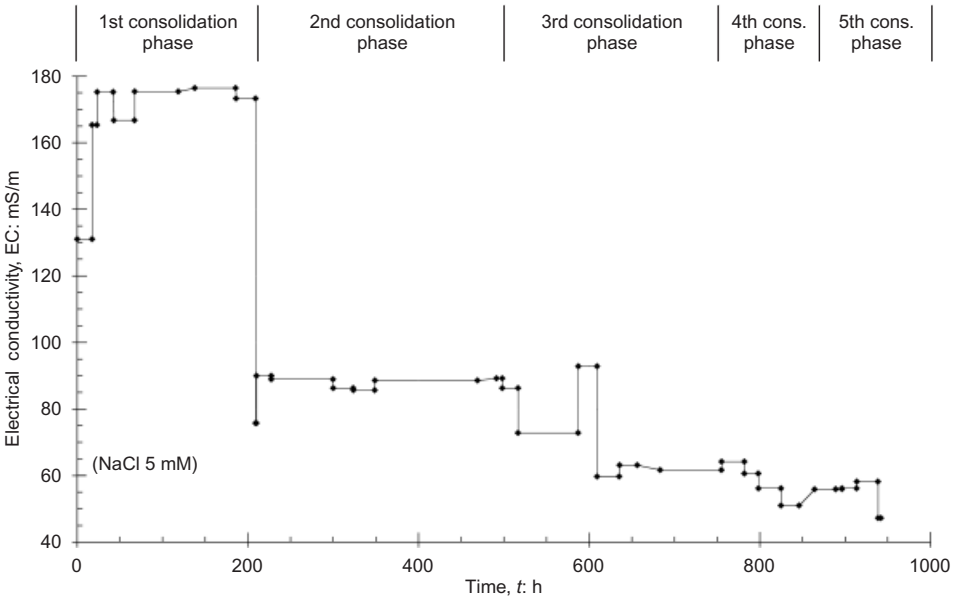

Fig. 1. Electrical conductivity as a function of time during squeezing process

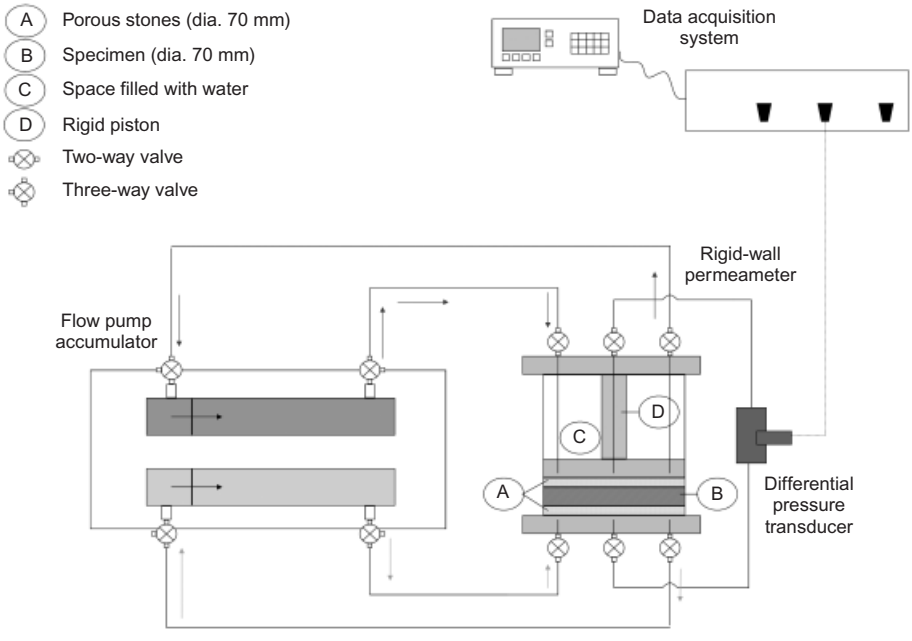

Fig. 2. Schematic view of chemico-osmotic test apparatus. More details on this apparatus can be found in Malusis *et al.* (2001)

syringe pump and two stainless steel accumulators (Model 33 twin syringe pump, produced by Harvard, Holliston, MA), prevents volumetric flux through the specimen by simultaneously injecting into and withdrawing from the porous stones the same volume of solution. In order to obtain this result, the syringes have to move at the same rate.

The test was performed according to the procedure proposed by Malusis *et al.* (2001): a solution containing a known electrolyte concentration (sodium chloride) was circulated in the top porous stone, while DW was circulated in the bottom porous stone. The concentration difference across the specimen was maintained constant by continuously infusing the two liquids at the boundaries of the specimen.

As the specimen was first squeezed with DW to remove the soluble salts, the EC of the electrolyte solutions in the flux exiting from the porous stones at the steady state was induced solely by the contributions of Cl^- and Na^+ ions. Moreover, the calibration reported in Fig. 3 shows that the relation between the EC and solution molarity was linear over the concentration range examined in the study. As a consequence, the EC of the withdrawn fluxes (i.e. from the top and bottom porous stones) was monitored by sampling the solution contained in the pistons, and the sodium chloride molar concentration was derived using a linear relation. Since the volumetric flux through the specimen was hindered, the global reflection coefficient could be calculated using equation (74).

The diffusive solute flux through the specimen was calculated for the nth sampling interval according to

$$J_s^n = \frac{\sum_{m=1}^{n} (c_s^m \Delta V^m)}{A_S \Delta t^n} = \frac{\Delta Q^n}{\Delta t^n} \tag{81}$$

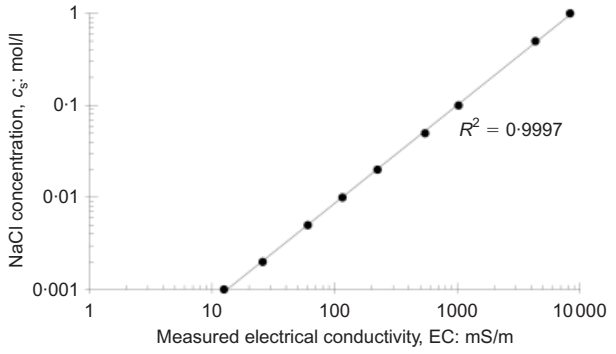

Fig. 3. Calibration of sodium chloride (NaCl) concentration with electrical conductivity. R^2 is coefficient of determination of regression line

where c_s^n is the solute molar concentration measured by sampling the solution coming out from the bottom porous stone, ΔV^m is the volume of the solution circulating in the porous stones in the interval Δt^m, A_S is the cross-section of the specimen, and ΔQ^n is the cumulative salt molar mass per unit area that passed through the specimen. The global osmotic effective diffusion coefficient, $D^*_{\omega g}$, is calculated at the steady state as

$$D^*_{\omega g} = \frac{\Delta Q}{\Delta t} \frac{L}{n(c_{t,avg} - c_{b,avg})} \quad (82)$$

where $c_{t,avg}$ and $c_{b,avg}$ are the average top and bottom salt concentrations respectively.

Swelling pressure test. The swelling pressure apparatus, shown in Fig. 4, consists primarily of a stainless steel oedometer cell, a sodium chloride solution supply tank placed above the pressure panel, a displacement transducer connected to the cell top piston, which is used to measure the axial strains of the specimen, a load cell, and a data acquisition system.

The swelling pressure apparatus consists of a rigid cell that confines the sample (i.e. the oedometer), which allows access to the water through both porous stones. The cell is connected to a pressure panel that allows the specimen to be back-pressurised. The rigid piston above the upper porous stone is connected to the load cell, which measures the pressure that has to be applied in order to hinder the axial strain of the specimen.

The test procedure requires a known amount of dry material to be dusted inside the oedometer ring, the cell to be assembled, and a sodium chloride solution to be supplied. The specimen, which is characterised by an initial dry height of 5 mm, is allowed to swell to 10 mm. The piston is then blocked, the sample is back-pressurised, and the steady-state swelling pressure is recorded after a short transitional phase.

Since the bentonite that is initially dusted inside the oedometer is dry, the pressure increases for a number of days during the hydration phase, and the steady-state swelling pressure is reached when hydration has been completed.

RESULTS

Chemico-osmotic test results

The chemico-osmotic test was performed using the oven-dried squeezed material, rehydrated with DW and then

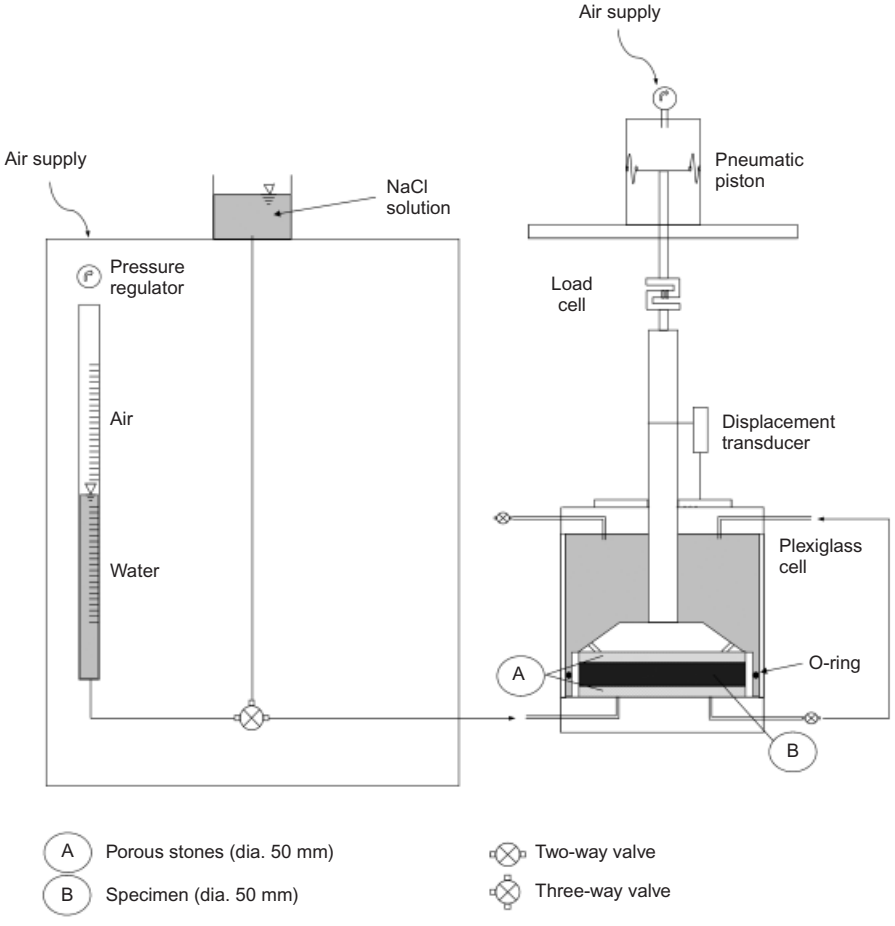

Fig. 4. Schematic view of the swelling pressure apparatus

statically compacted, in a drained compaction mould, at a porosity n equal to 0·81 ($e = 4{\cdot}26$). After the preparation phase, the 17 mm thick specimen was transferred to the cell for the osmotic test.

After assembling the cell, DW was circulated through the top piston and the bottom pedestal for 2 weeks in order to establish a steady baseline differential pressure, before a concentration gradient was applied to the specimen. A source concentration of sodium chloride was then injected into the top porous stone, while DW was continuously circulated in the bottom porous stone.

A multiple-stage chemico-osmotic test was performed by sequential circulation of chemical solutions containing 5·16, 10·27, 20·24, 51·94 and 109·31 mM sodium chloride concentrations at a constant flow rate of 0·05 ml/min.

The EC values of the salt mass fluxes withdrawn from the top and the bottom porous stones, measured during the testing stages, are shown in Fig. 5. The measured values depend on the sodium chloride concentrations imposed at the boundaries of the specimen: the EC values progressively increase during the test as the sodium chloride concentration of the injected solution in the top porous stone rises. The trends of the electrical conductivity of the flux withdrawn from the top porous stone, $EC_{t,exit}$, and of that withdrawn from the bottom porous stone, $EC_{b,exit}$, both show that a steady state has been reached for each stage.

Moreover, the difference between the EC values measured in the flux withdrawn from the top porous stone ($EC_{t,exit}$) and those of the solutions injected into the same stone ($EC_{t,ref}$) is due to the loss in sodium chloride mass induced by the diffusion through the bentonite from the top to the bottom boundary.

The global reflection coefficient values, ω_g, obtained during the multiple-stage chemico-osmotic test, are shown in Fig. 6 as a function of time. The ω_g values are determined using equation (74), on the basis of the differential pressure, Δu, measured during the test with a time step of 10 min, and the osmotic pressure, $\Delta\Pi$, calculated from the average of the top and bottom sodium chloride concentrations. The steady-state values of the variables are reported in Table 1 for each concentration stage. The sodium chloride concentrations were derived from the measured EC using the linear calibration reported in Fig. 3.

As far as the EC measurements are concerned, the trend of the global reflection coefficient shows that a steady state has been reached for each stage. The steady-state ω_g values tend to decrease as the salt concentration in the top porous stone increases. The recorded values range from 68%, for a

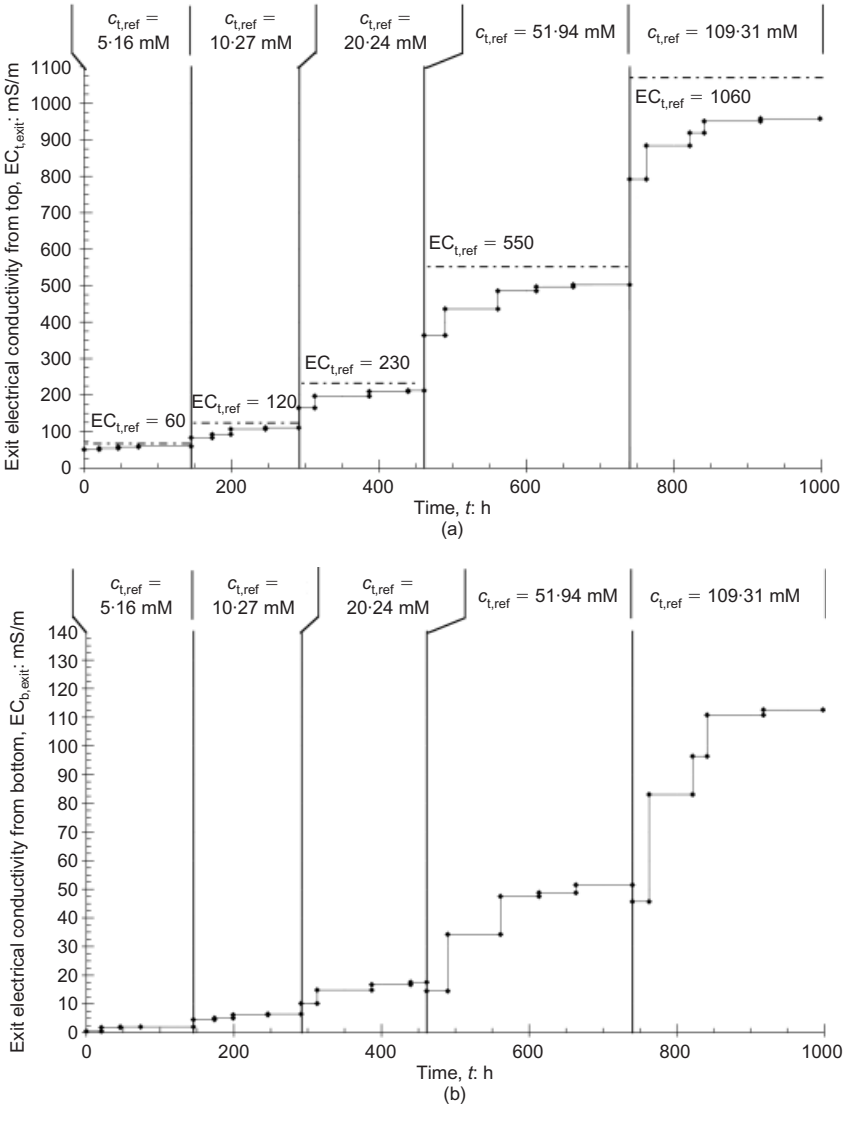

Fig. 5. Electrical conductivity of salt flux withdrawn from (a) top porous stone and (b) bottom porous stone as a function of time during multiple-stage chemico-osmotic test

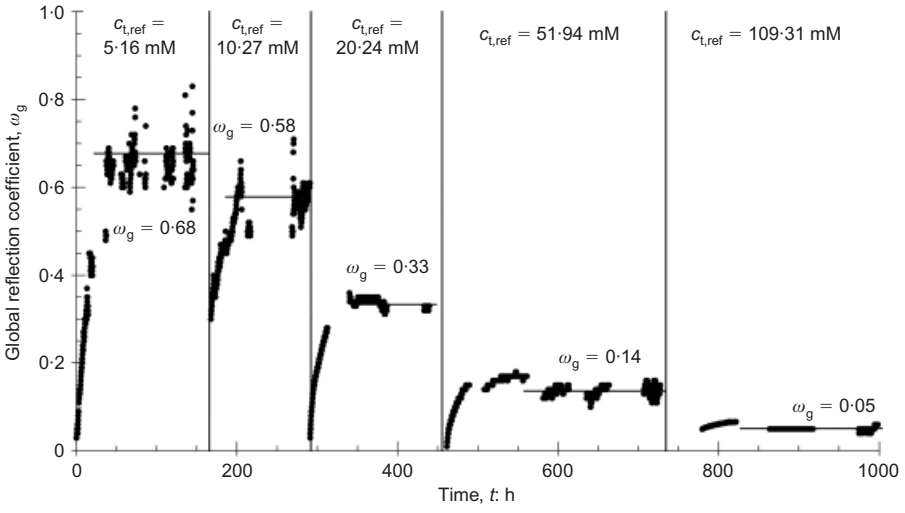

Fig. 6. Global reflection coefficient as a function of time during multiple-stage chemico-osmotic test

Table 1. Steady-state values of variables involved in multiple-stage chemico-osmotic test

$c_{t,ref}$: mM	$c_{t,exit}$: mM	$c_{b,exit}$: mM	$c_{t,avg}$: mM	$c_{b,avg}$: mM	Δu: kPa	$\Delta\Pi$: kPa	ω_g	$D^*_{\omega g}$: m^2/s
5·16	5·12	0·83	5·14	0·42	15·65	23·02	0·68	–
10·27	9·61	0·85	9·94	0·43	26·87	46·33	0·58	$2{\cdot}54 \times 10^{-10}$
20·24	18·93	1·45	19·58	0·72	30·32	91·89	0·33	$3{\cdot}52 \times 10^{-10}$
51·94	47·39	4·39	49·67	2·19	32·38	231·30	0·14	$4{\cdot}19 \times 10^{-10}$
109·31	97·18	9·78	103·24	4·89	23·96	479·21	0·05	$4{\cdot}60 \times 10^{-10}$

5·16 mM sodium chloride source concentration, to 5%, for a 109·31 mM sodium chloride source concentration. The global reflection coefficient can be assumed approximately null for higher molarities.

The cumulative molar mass per unit area, Q, of the sodium chloride that migrated through the specimen during the multiple-stage test is reported in Fig. 7. The values of the global osmotic effective diffusion coefficient, $D^*_{\omega g}$, which

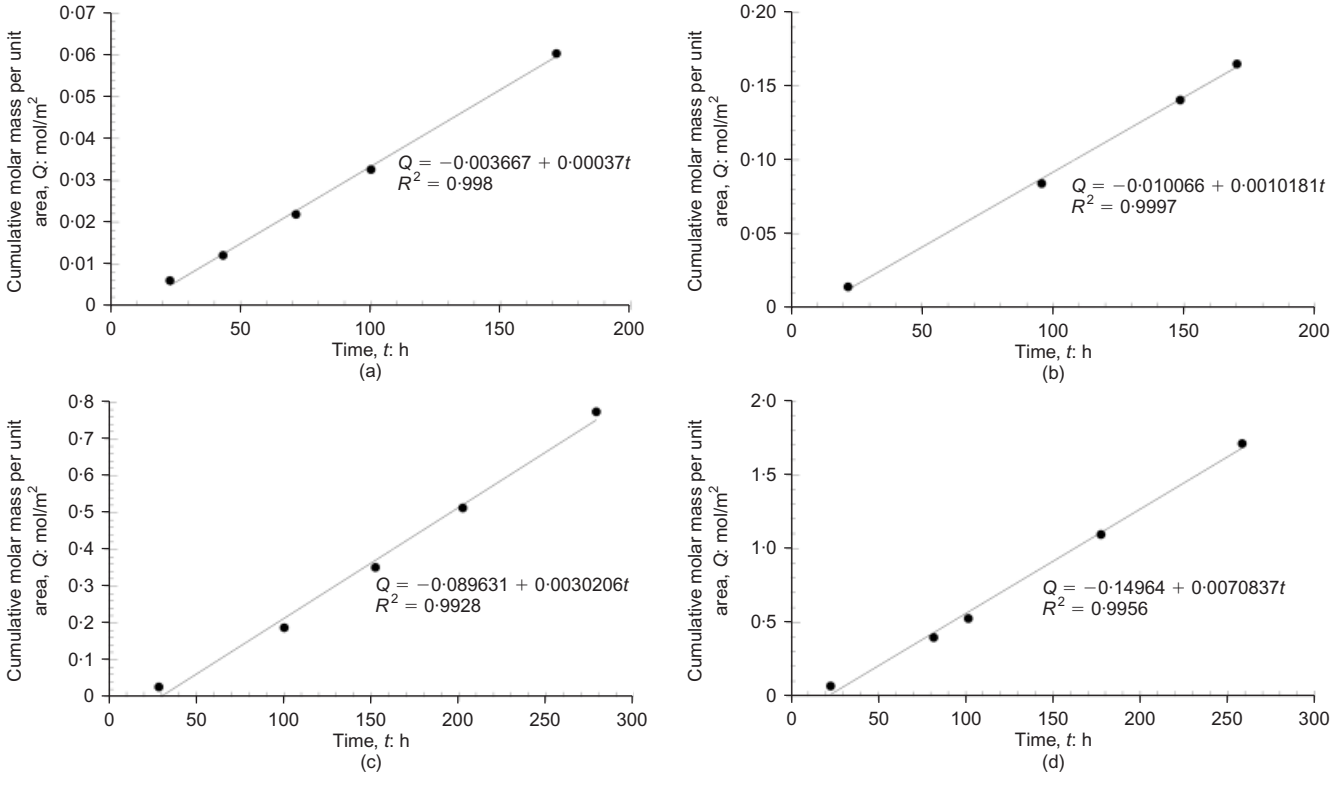

Fig. 7. Cumulative molar mass of sodium chloride per unit area as a function of time during multiple-stage chemico-osmotic test: (a) $c_{t,ref}$ = 10·27 mM; (b) $c_{t,ref}$ = 20·24 mM; (c) $c_{t,ref}$ = 51·94 mM; (d) $c_{t,ref}$ = 109·31 mM

have been obtained from the Q measurements shown in Fig. 7, are reported in Table 1.

Swelling pressure test results

The swelling pressure test was performed using dry specimens, prepared with the squeezed, oven-dried bentonite and characterised by an initial dry height of 5 mm, which were allowed to swell to 10 mm during hydration. The final hydrated volume of the specimens corresponded to $n = 0{\cdot}81$.

The test was performed by hydrating five specimens with five different sodium chloride solutions, characterised by increasing concentrations: 5, 10, 20, 50 and 100 mM. After hydration, the specimen volume change was inhibited, and the value of the swelling pressure was recorded after a short transitional phase.

The swelling pressure trend is reported in Fig. 8 for each test as a function of time. Since, during the tests, the load cell was unloaded until the specimen swelled to 10 mm, the initial swelling/hydration phase of the dry material (from 5 to 10 mm) was characterised by null swelling pressure values.

All the tests show that the swelling pressure increases for approximately 15–20 h, during the controlled hydration phase (i.e. when the volumetric strain is inhibited), and that the equilibrium swelling pressure is reached when the hydration phase is completed. Moreover, in the tests with lower sodium chloride concentrations (i.e. for 5 and 10 mM sodium chloride equilibrium solutions), the specimens were successively back-pressurised to 300 kPa. The obtained results show that the swelling pressure value does not change after back-pressurisation.

In the test performed using the 100 mM sodium chloride solution, the bentonite specimen did not rise to 10 mm, as it stopped at a height of 9·5 mm, and the load cell was never loaded during the test. For this reason, the swelling pressure for this test was taken equal to zero.

INTERPRETATION OF TEST RESULTS

The experimental results can be related to the physical and chemical properties of the tested bentonite under the assumption that the microscopic deviations of the state variables from their average values are negligible. In such a case, both the global reflection coefficient and the swelling pressure depend on the solid skeleton electric charge through equations (19) and (77). Therefore, from the best-fitting of the theoretical curves with the experimental data of both tests, a value of $\bar{c}_{sk,0}$ equal to 90 mM was found. The obtained theoretical curves are reported in Figs 9 and 10, together with the experimental data.

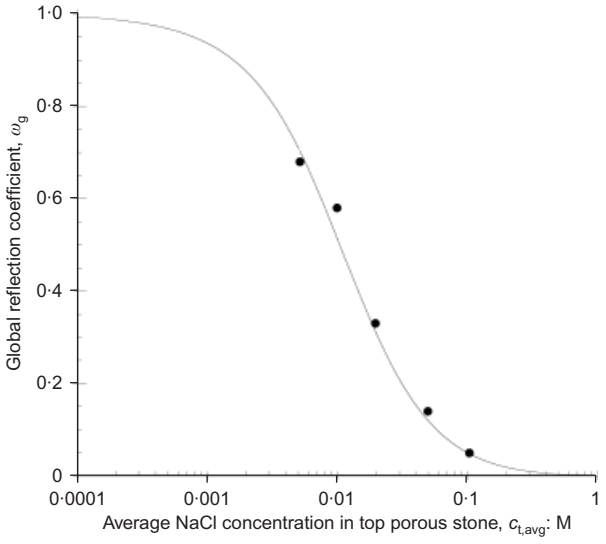

Fig. 9. Global reflection coefficient, ω_g, as a function of average sodium chloride (NaCl) concentration at top boundary of bentonite specimen, with best-fitting theoretical curve, obtained for $\bar{c}_{sk,0} = 90$ mM in equation (77) (continuous line)

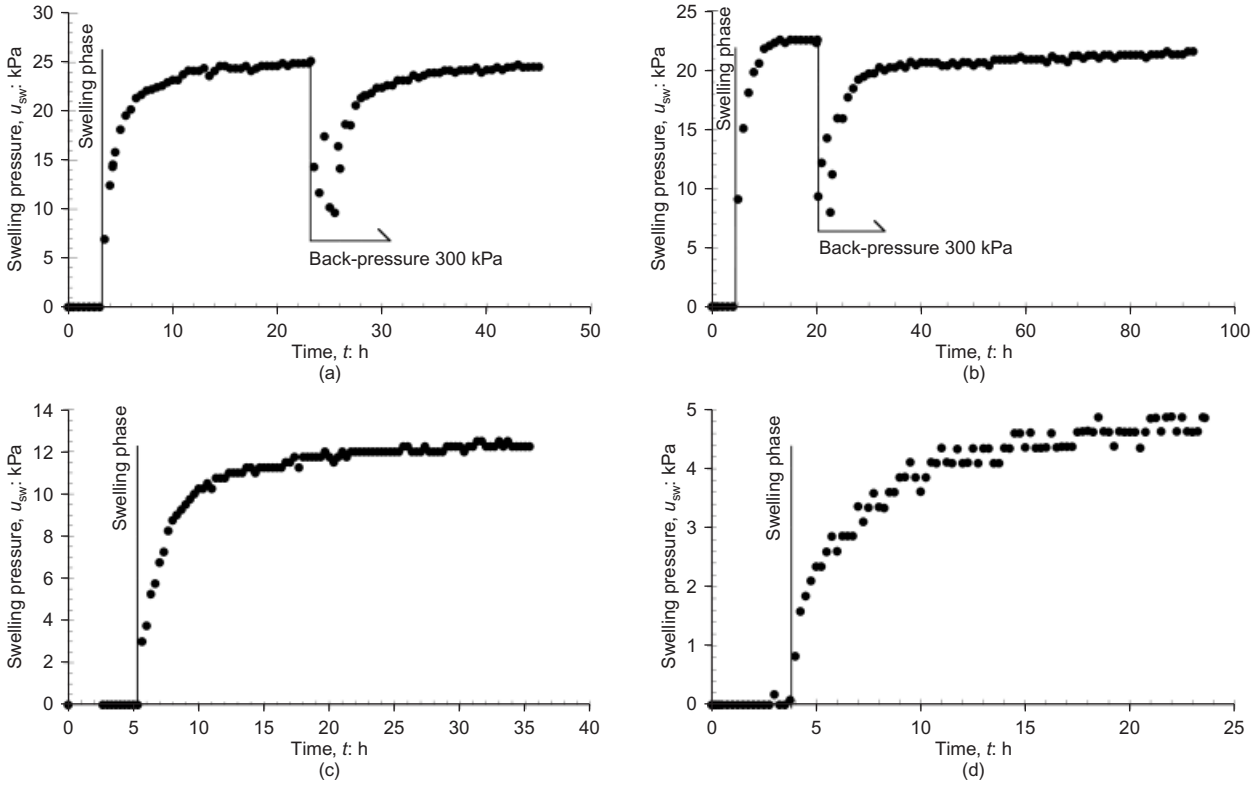

Fig. 8. Swelling pressure as a function of time. (a) $c_s = 5$ mM; (b) $c_s = 10$ mM; (c) $c_s = 20$ mM; (d) $c_s = 50$ mM

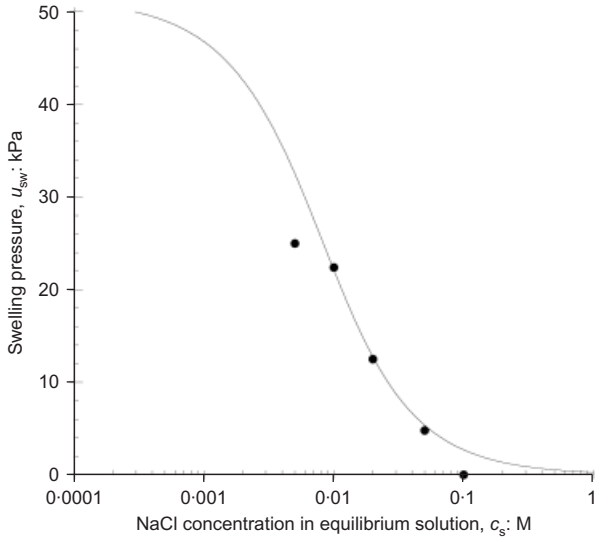

Fig. 10. Swelling pressure, u_{sw}, as a function of sodium chloride (NaCl) equilibrium concentration, with best-fitting theoretical curve, obtained for $\bar{c}_{sk,0} = 90$ mM in equation (19) (continuous line)

The salt concentration at the top boundary was taken equal to $c_{t,avg}$ to determine ω_g, and the salt concentration at the bottom boundary was considered equal to zero: that is, $c_b \cong c_{b,avg} \cong 0$. The sodium transport number was calculated from the sodium and chloride free-solution diffusion coefficient values (Shackelford & Daniel, 1991): $D_{Na,0} = 13{\cdot}3 \times 10^{-10}$ m^2/s, $D_{Cl,0} = 20{\cdot}3 \times 10^{-10}$ m^2/s.

In Fig. 11, the experimental reflection coefficient data were also fitted with the empirical semi-log linear curve proposed by Shackelford *et al.* (2003) and Malusis *et al.* (2003),

$$\omega_g = A + B \log (c_{t,avg}) \tag{83}$$

where A and B are the regression parameters. The value of the coefficient of determination R^2 close to 1 confirms the ability of this empirical curve to fit the ω_g experimental data, as was found by Malusis *et al.* (2003) for the Kemper & Rollins (1966) and Malusis & Shackelford (2002a) data. However, the regression parameters A and B should be intended as functions of the soil porosity (Malusis *et al.*, 2003) and of the bottom boundary condition (i.e. $c_{b,avg}$). The advantage of interpreting the experimental data with the proposed theoretical model is that, when the single unknown parameter, $\bar{c}_{sk,0}$, has been calibrated on a restricted experimental dataset, the global reflection coefficient values can be estimated for different soil porosities and boundary conditions through equation (77).

The tortuosity factor was determined by plotting the measured values of $D^*_{\omega g}$ as a function of the corresponding values of the complement to 1 of ω_g – that is, $(1 - \omega_g)$ – and finding the intercept of the linear regression with the ordinate axis at $(1 - \omega_g) = 1$ – that is, $\omega_g = 0$ (Fig. 12). The tortuosity factor in equation (76) is in fact given by

$$\tau_m = \left(\frac{D^*_{\omega g}}{D_{s,0}} \right)_{\omega_g = 0} \tag{84}$$

where $D_{s,0}$ is the sodium chloride free-solution diffusion coefficient, which is equal to 16×10^{-10} m^2/s (Shackelford & Daniel, 1991).

A value of τ_m equal to 0·31 was obtained from the data plotted in Fig. 12. The resulting theoretical curve of $D^*_{\omega g}$ is reported in Fig. 13 as a function of the top boundary salt concentration.

The obtained values of $\bar{c}_{sk,0}$ and τ_m are compared in Table 2 with those derived by Dominijanni & Manassero (2012b) from the interpretation of the experimental results of Malusis & Shackelford (2002a, 2002b), relative to a geosynthetic clay liner, with a bentonite porosity, n, of 0·79 for different concentrations of potassium chloride (KCl). The differences in the parameters obtained from the two studies can be attributed both to the different mineralogical compositions of the tested bentonites and to the different salts contained in the pore solutions.

The theoretical linear relationship between $D^*_{\omega g}$ and $(1 - \omega_g)$ in Fig. 12 is a consequence of assuming that the pore-scale variations in the hydraulic pressure, ion concentrations and water velocity within the soil are negligible; as a result, the agreement of the experimental data with the linear relationship is an indication of the acceptability of this assumption.

The goodness of the linear fitting shown in Fig. 12 ($R^2 = 0{\cdot}9810$) and the possibility of fitting both the global reflection coefficient and the swelling pressure data with a single value of $\bar{c}_{sk,0}$ are indications of the ability of the

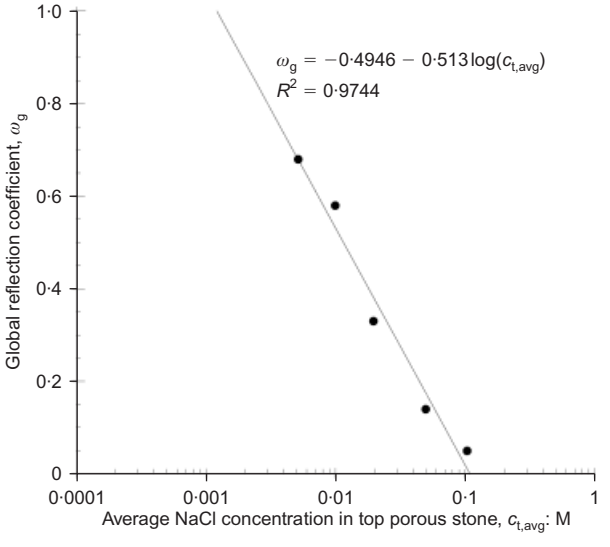

Fig. 11. Semi-log linear regression of measured global reflection coefficients against average sodium chloride (NaCl) concentration at top boundary of bentonite specimen

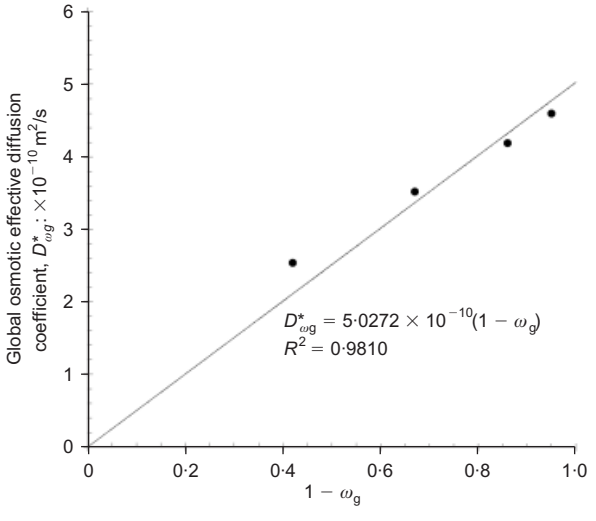

Fig. 12. Global osmotic effective diffusion coefficient, $D^*_{\omega g}$, as a function of the complement to 1 of the global reflection coefficient, ω_g, with theoretical linear relation given by equation (76) (continuous line)

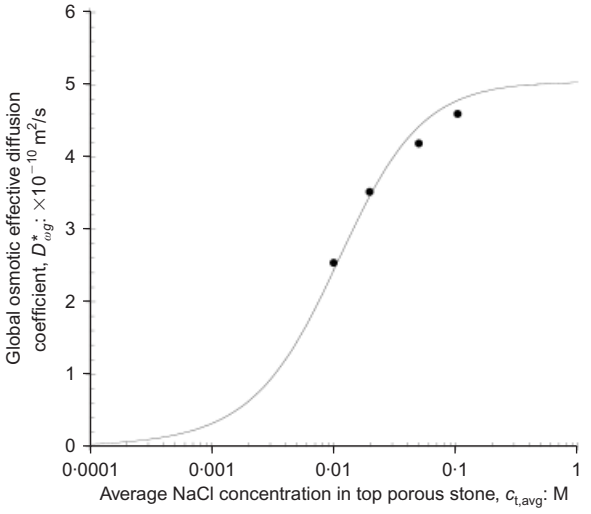

Fig. 13. Global osmotic effective diffusion coefficient, $D^*_{\omega g}$, as a function of average sodium chloride (NaCl) concentration at top boundary of bentonite specimen, with the best-fitting theoretical curve, obtained for $\bar{c}_{sk,0} = 90$ mM and $\tau_m = 0{\cdot}31$ in equations (76) and (77) (continuous line)

proposed theoretical approach to simulate the bentonite behaviour.

CONCLUSIONS

A theoretical approach that takes into account the interaction between the electric charge of the bentonite solid skeleton and the ions contained in the pore solution has been proposed. The phenomenological parameters introduced in this theoretical approach were measured for a bentonite specimen with porosity, n, of 0·81, over a range of sodium chloride concentrations in the pore solution varying from 5 mM to 100 mM. Both the global reflection coefficient, ω_g, and the swelling pressure, u_{sw}, were found to decrease with an increase in the salt concentration. This result is in agreement with the trends given by the proposed theoretical model, assuming that the microscopic deviations of the pore solution state variables from their average values are negligible. If this assumption is accepted, the experimental data can be used to derive the electric charge of the solid skeleton (per unit solid volume), $\bar{c}_{sk,0}$, and the tortuosity factor, τ_m. The mechanical behaviour and the transport properties of bentonite can be estimated from these physical properties to evaluate its performance as a hydraulic and contaminant barrier in field applications. However, in order to verify the applicability of the proposed model under different boundary conditions and for different salts contained in the pore solution, further experimental evaluations must be conducted. Moreover, the results obtained for a single salt contained in the bentonite pore solution need to be extended to the more general problem of a solution containing an unspecified number of salts, in order to evaluate the performance of bentonites that are used as contaminant barriers for real leachates.

NOTATION

A, B	regression parameters
A_S	cross-section of specimen
c_b	salt concentration at bottom boundary of specimen
$c_{b,avg}$	average salt concentration at bottom boundary of specimen
$c_{b,exit}$	salt concentration of flux withdrawn from bottom porous stone
c_i	molar concentration of ith ion in equilibrium bulk solution
$\bar{c}_i$	molar concentration of ith ion in pore solution
c_k	molar concentration of kth fluid component in equilibrium bulk solution
$\bar{c}_k$	molar concentration of kth fluid component in pore solution
c_s	salt molar concentration in equilibrium bulk solution
Δc_s	salt concentration difference
$\bar{c}_{sk,0}$	molar concentration per unit solid volume of solid skeleton electric charge
c_t	salt concentration at top boundary of specimen
$c_{t,avg}$	average salt concentration at top boundary of specimen
$c_{t,exit}$	salt concentration of flux withdrawn from top porous stone
$c_{t,ref}$	source salt concentration
c_w	water molar concentration in equilibrium bulk solution
$\bar{c}_w$	water molar concentration in pore solution
D_i	macroscopic diffusion coefficient of ith ion
$D_{i,0}$	free (aqueous) solution diffusion coefficient of ith ion
D^*_i	effective diffusion coefficient of ith ion
D_s	macroscopic salt diffusion coefficient
$D_{s,0}$	free (aqueous) solution salt diffusion coefficient
D^*_s	effective salt diffusion coefficient
D^*_ω	osmotic effective diffusion coefficient
$D^*_{\omega g}$	global osmotic effective diffusion coefficient
$EC_{b,exit}$	electrical conductivity of flux withdrawn from bottom porous stone
$EC_{t,exit}$	electrical conductivity of flux withdrawn from top porous stone
$EC_{t,ref}$	electrical conductivity of source solution
e	void ratio
e_0	initial void ratio
F	Faraday's constant (96 485 C/mol)
F_k	free energy per unit molar mass of kth component of fluid phase

Table 2. Comparison between physical parameters derived from interpretation of experimental results in this work and those obtained by Dominijanni & Manassero (2012b) from interpretation of tests carried out by Malusis & Shackelford (2002a, 2002b)

Experimental data	Material	Method for removing soluble salts	Tests	Salt in pore solution	Porosity, n	Solid skeleton charge concentration, $\bar{c}_{sk,0}$: mM	Tortuosity factor, τ_m
This study	Natural sodium bentonite	Squeezing	Chemico-osmotic test and swelling pressure test	NaCl	0·81	90	0·31
Malusis & Shackelford (2002a, 2002b)	Geosynthetic clay liner containing natural sodium bentonite	Flushing	Chemico-osmotic test	KCl	0·79–0·80	46	0·14

f_i external force per unit volume acting on ith ion
f_w external force per unit volume acting on water
G_V^{sk} Gibbs free energy of solid skeleton per unit (undeformed) volume of porous medium
$\boldsymbol{g}$ gravitational acceleration
I_e electric current density
$\Im_V$ free energy per unit (undeformed) volume of porous medium
$\Im_V^{sk}$ free energy of solid skeleton per unit (undeformed) volume of porous medium
J_i molar flux of ith ion relative to solid skeleton
J_s salt molar flux
k hydraulic conductivity
L length of specimen
M unidimensional elastic modulus of porous medium
m_i momentum supply of ith ion
m_i^E extra-momentum supply of ith ion
m_k momentum supply of kth fluid component
m_k^E extra-momentum supply of kth fluid component
$m_{l,m}^E$ extra-momentum supply exchanged between lth and mth components of porous medium (sk = solid skeleton, w = water, 1 = cation, 2 = anion)
m_w momentum supply of water
n porosity
Q cumulative salt molar mass per unit area
ΔQ increment in cumulative salt molar mass per unit area
q water volumetric flux relative to solid skeleton
R universal gas constant (= 8·314 J/(mol K))
T absolute temperature in equilibrium bulk solution
$\bar{T}$ absolute temperature in pore solution
t time
Δt time interval
t_1 cation transport number
u hydraulic pressure in equilibrium bulk solution
Δu hydraulic pressure difference
$\bar{u}$ hydraulic pressure in pore solution
u_b hydraulic pressure at bottom boundary of specimen
u_i partial pressure of ith ion component in equilibrium bulk solution
$\bar{u}_i$ partial pressure of ith ion component in pore solution
u_k partial pressure of kth fluid component in equilibrium bulk solution
$\bar{u}_k$ partial pressure of kth fluid component in pore solution
u_{sw} swelling pressure
u_t hydraulic pressure at top boundary of porous medium
u_w partial pressure of water in equilibrium bulk solution
$\bar{u}_w$ partial pressure of water in pore solution
ΔV^m volume of solution circulating in porous stones
v_i velocity of ith ion
v_{sk} velocity of solid skeleton
v_w water velocity
x spatial coordinate
z_i electrochemical valence of ith ion
z_{sk} electrochemical valence of solid skeleton electric charge
α, β_i friction coefficients
β_{ss}, β_{sv}, β_{vs}, β_{vv} phenomenological parameters in chemo-mechanical constitutive laws
Γ_i partial coefficient of ith ion
γ_w water unit weight ($=\rho_w \boldsymbol{g}$)
ε scalar strain in unidimensional geometry
$\boldsymbol{\varepsilon}$ strain tensor
μ_i chemical potential of ith ion in equilibrium bulk solution
$\bar{\mu}_i$ chemical potential of ith ion in pore solution
μ_i^0, $\bar{\mu}_i^0$, μ_w^0, $\bar{\mu}_w^0$ integration constants
μ_i^{ec} electrochemical potential of ith ion in equilibrium bulk solution
$\bar{\mu}_i^{ec}$ electrochemical potential of ith ion in pore solution
μ_k chemical potential of kth fluid component in equilibrium bulk solution
$\bar{\mu}_k$ chemical potential of kth fluid component in pore solution
μ_s salt chemical potential in equilibrium bulk solution
μ_w water chemical potential in equilibrium bulk solution
$\bar{\mu}_w$ water chemical potential in pore solution
ν_i stoichiometric coefficient of ith ion
Π osmotic pressure in equilibrium bulk solution
$\Delta\Pi$ osmotic pressure difference
$\bar{\Pi}$ osmotic pressure in pore solution
Π_b osmotic pressure at bottom boundary of specimen
Π_t osmotic pressure at top boundary of specimen
ρ_w water density
σ scalar total stress in unidimensional geometry
σ' scalar effective stress in unidimensional geometry
$\boldsymbol{\sigma}$ total stress tensor
τ_m matrix tortuosity factor
τ_r restrictive tortuosity factor
ϕ electric potential in equilibrium bulk solution
$\bar{\phi}$ electric potential in pore solution
$\bar{\psi}$ Donnan's electric potential
ω reflection coefficient
ω_g global reflection coefficient
$\bar{\varpi}$ swelling pressure coefficient

Indexes

i index for ions (1 = cation, 2 = anion)
j index for ions (1 = cation, 2 = anion)
k index for fluid components (w = water, 1 = cation, 2 = anion)

Subscripts

1 cation
2 anion
b bottom of specimen
g global value
sk solid skeleton
t top of specimen
w water

REFERENCES

Auclair, B., Nikonenko, V., Larchet, C., Métayer, M. & Dammak, L. (2002). Correlation between transport parameters of ion-exchange membranes. *J. Membrane Sci*. **195**, No. 1, 89–102.

Coussy, O. (2004). *Poromechanics*. Chichester, UK: Wiley.

Di Emidio, G. (2010). *Hydraulic and chemico-osmotic performance of polymer treated clays*. PhD thesis, Ghent University, Belguim.

Dominijanni, A. & Manassero, M. (2010). Chemico-osmosis and solute transport through geosynthetic clay liners. In *Geosynthetic clay liners for waste containment* (eds A. Bouazza and J. J. Bowders), pp. 105–125. Leiden, the Netherlands: CRC Press.

Dominijanni, A. & Manassero, M. (2012a). Modelling the swelling and osmotic properties of clay soils. Part I: The phenomenological approach. *Int. J. Engng Sci*. **51**, February, 32–50.

Dominijanni, A. & Manassero, M. (2012b). Modelling the swelling and osmotic properties of clay soils. Part II: The physical approach. *Int. J. Engng Sci*. **51**, February, 51–73.

Donnan, F. G. (1911). Theorie der Membrangleichgewichte und Membranpotentiale bei Vorhandensein von nicht dialysierenden Elektrolyten. Ein Beitrag zur physikalisch-chemischen Physiologie [Theory of membrane equilibria and membrane potentials in the presence of non-dialysing electrolytes. A contribution to

physical-chemical physiology]. *Z. Elektrochem. Angew. Phys. Chem*. **17**, No. 14, 572–581. English translation republished 1995 in *J. Membrane Sci*. **100**, No. 1, 45–55.

Dormieux, L., Barboux, P., Coussy, O. & Dangla, P. (1995). A macroscopic model of the swelling phenomenon of a saturated clay. *Eur. J. Mech. A Solids* **14**, No. 6, 981–1004.

Dormieux, L., Lemarchand, E. & Coussy, O. (2003). Macroscopic and micromechanical approaches to the modelling of the osmotic swelling in clays. *Transp. Porous Media* **50**, No. 1, 75–91.

Ehlers, W. (2002). Foundations of multiphasic and porous materials. In *Porous media: Theory, experiments and numerical applications* (eds W. Ehlers and J. Bluhm), pp. 3–86. Berlin, Germany: Springer-Verlag.

Kang, J.-B. & Shackelford, C. D. (2009). Clay membrane testing using a flexible-wall cell under closed-system boundary conditions. *Appl. Clay Sci*. **44**, No. 1–2, 43–58.

Katchalsky, A. & Curran, P. F. (1965). *Nonequilibrium thermodynamics in biophysics*. Cambridge, MA, USA: Harvard University Press.

Kemper, W. D. & Rollins, J. B. (1966). Osmotic efficiency coefficients across compacted clays. *Soil Sci. Soc. Am. J*. **30**, No. 5, 529–534.

Malusis, M. A., Shackelford, C. D. & Olsen, H. W. (2001). A laboratory apparatus to measure chemico-osmotic efficiency coefficients for clay soils. *Geotech. Test. J*. **24**, No. 3, 229–242.

Malusis, M. A. & Shackelford, C. D. (2002a). Chemico-osmotic efficiency of a geosynthetic clay liner. *J. Geotech. Geoenviron. Engng* **128**, No. 2, 97–106.

Malusis, M. A. & Shackelford, C. D. (2002b). Coupling effects during steady-state solute diffusion through a semipermeable clay membrane. *Environ. Sci. Technol*. **36**, No. 6, 1312–1319.

Malusis, M. A., Shackelford, C. D. & Olsen, H. W. (2003). Flow and transport through clay membrane barriers. *Engng Geol*. **70**, No. 3–4, 235–248.

Malusis, M. A., Shackelford, C. D. & Maneval, J. E. (2012). Critical review of coupled flux formulations for clay membranes based on nonequilibrium thermodynamics. *J. Contam. Hydrol*. **138–139**, 40–59.

Manassero, M. & Dominijanni, A. (2003). Modelling the osmosis effect on solute migration through porous media. *Géotechnique* **53**, No. 5, 481–492, http://dx.doi.org/10.1680/geot.2003.53.5.481.

Shackelford, C. D. & Daniel, D. E. (1991). Diffusion in saturated soil: I. Background. *J. Geotech. Engng* **117**, No. 3, 467–484.

Shackelford, C. D., Malusis, M. A. & Olsen, H. W. (2003). Clay membrane behavior for geoenvironmental containment. In *Soil and Rock America Conference 2003* (*Proc. Joint 12th Panamerican Conf. Soil Mech. Geotech. Engng and 39th US Rock Mech. Symp*.) (eds P. J. Culligan, H. H. Einstein and A. J. Whittle), Vol. 1, pp. 767–774. Essen, Germany: Verlag Glückauf GmbH.

Shackelford, C. D. & Lee, J.-M. (2003). The destructive role of diffusion on clay membrane behavior. *Clays Clay Miner*. **51**, No. 2, 186–196.

Yaroshchuk, A. E. (1995). Osmosis and reverse osmosis in fine-charged diaphragms and membranes. *Adv. Colloid Interface Sci*. **60**, No. 1–2, 1–93.

Yeo, S.-S., Shackelford, C. D. & Evans, J. C. (2005). Membrane behaviour of model soil-bentonite backfill mixtures. *J. Geotech. Geoenviron. Engng* **131**, No. 4, 418–429.

Hu, M. M. & Hueckel, T. (2013). *Géotechnique* **63**, No. 4, 313–321 [http://dx.doi.org/10.1680/geot.SIP13.P.020]

Environmentally enhanced crack propagation in a chemically degrading isotropic shale

M. M. HU* and T. HUECKEL*

Crack propagation is studied in a geomaterial subject to weakening by the presence of water, which dissolves a mineral component. Such weakening is common when tensile microcracks develop, constituting sites of enhanced mineral dissolution. A previous concept is adopted of reactive chemo-plasticity, with the yield limit depending on the mineral mass dissolved, causing chemical softening. The dissolution is described by a rate equation and is a function of variable internal specific surface area, which in turn is assumed to be a function of dilative plastic deformation. The crack vicinity in plane strain is subject to a constant subcritical all-round uniform radial tensile traction. The behaviour of the material is rigid-plastic with chemical softening. The extended Johnson approximation is adopted, meaning that all fields involved are axisymmetric around the crack tip, with a small, unstressed cavity around it. Initial dissolution proportional to the initial porosity activates the plastic yielding. The total dissolved mass diffuses out from the process zone and the exiting mineral mass flux can be correlated with the displacement of the crack tip. A simplified semi-analytical solution for this model is presented.

KEYWORDS: geology; numerical modelling; rocks/rock mechanics

INTRODUCTION

This paper focuses on understanding the mechanisms of crack propagation caused by chemically induced weakening of intact rock material, with a view to application to shale and industrial argillites. There are multiple geochemical changes that induce mechanical response in earthen materials; these include deformational or permeability reactions of clays to changes in ionic concentration, or dielectric constant of the invading pore fluid (Hueckel, 1992, 1997, 2002; Gajo *et al.*, 2002; Loret *et al.*, 2002; Wahid *et al.*, 2011); changes in mechanical properties of rocks and sands as a result of their inundation with water (Hueckel *et al.*, 2001, 2005; Hu & Hueckel, 2007a, 2007b); and slope instabilities in response to infiltration of acid rain water into cracks between clay mineral layers (Zhao *et al.*, 2011). The specific mechanisms of these chemo-mechanical interactions are various and include osmotic effects, diffuse double layer changes, ion replacement phenomena, dissolution and precipitation of minerals, and transformation of clay minerals (Hueckel & Pellegrini, 2002; Zhao *et al.*, 2011).

This study addresses a possible mechanism in which rocks or cohesive soils undergo a chemical reaction of dissolution resulting in the removal of the mineral mass and hence weakening of soil/rock mass at and around the chemical reaction site. The focus is on a particular situation at a crack tip, at which degradation is induced in the form of an advanced irreversible deformation aside and ahead of the crack, as a swarm of microfissures in mode I (Lin & Labuz, 2011). The chemically induced propagation of a stressed crack under a constant mechanical load is investigated. An extension of the Cam-Clay model into a chemical domain is used (Hueckel, 1992, 1997, 2002), in particular a concept of chemical softening, which is coupled with irreversible deformation (Hu & Hueckel, 2007a). A simplified semi-analytical solution of an extended cavity expansion concept is applied to model the crack vicinity; this can be easily coupled with an axisymmetric solution for the chemical fields around the crack tip process zone.

In the past few decades, there has been a growing understanding that a number of problems in relation to rock mechanics and rock engineering in general could be, or need to be, tackled by addressing fracture mechanics. Some of the examples stem from areas of energy engineering and slope stability. The technique of hydraulic fracturing has been increasingly used all over the world owing to its advantages in efficiently creating fractures in the rock formation, which dramatically enhances rock or sediment permeability and hence oil/gas production (Howard & Fast, 1970; Carter *et al.*, 2000; Dershowitz *et al.*, 2001; Rahman, 2008; Jackson *et al.*, 2011), as well as heat extraction from geothermal fields (Portier & Vuataz, 2010; Zimmermann *et al.*, 2011). More recently, attention has shifted towards fracture propagation enhancement by acidising the rock (i.e. injecting chemically active fluids), especially for low-permeability carbonate reservoirs (He *et al.*, 2010) or to enhance a geothermal system (Portier & Vuataz, 2010; Zimmermann *et al.*, 2011).

Meanwhile, a heated debate on acidising treatment in hydraulic fracturing performance arose, owing to the potential harm caused by disposal and transport of the toxic wastewater, which may include formaldehyde, boric acid, hydrochloric acid and isopropanol (Jackson *et al.*, 2011). Poorly controlled hydraulic fracturing, often due to inadequate understanding of fracture mechanisms involving acid–rock interactions, may not only pose threats to the environment, but also result in unnecessary costs and low productivity (Rahman, 2008).

This paper addresses possible chemo-mechanical mechanisms of rock/shale weakening resulting in fracture propagation enhancement, to arrive at an effective predictive tool to control the efficiency of hydraulic fracture and the fate of possible contaminants.

CONCEPT OF CHEMO-PLASTICITY

Solid–fluid interaction in geomaterials has been studied for many years, focusing on the effect of pore pressure on

Manuscript received 5 March 2012; revised manuscript accepted 17 October 2012.
Discussion on this paper closes on 1 August 2013, for further details see p. ii.
* Duke University, Durham, North Carolina, USA.

the rock and soil matrix. The concept of reactive chemo-plasticity is based on the notion that a mineral mass removed from or added to a solid can affect both the medium compliance and strength (Hueckel *et al.*, 1998; Hueckel, 2002; Hu & Hueckel, 2007a, 2007b). As one of the primary sources of mass removal, chemical dissolution has attracted much attention. A key mechanism that links the chemical process and mechanical degradation has been known for some time to be rock microcracking. Bathurst (1958) and Ostapenko (1968, 1975) noted that microcracking leads to the generation of a new solid–fluid interface, where enhanced mineral dissolution takes place. Tada *et al.* (1987) found that micro-fractures and plastic deformation play an important role in the process of pressure solution.

The concept of chemical dissolution coupled with plasticity was addressed by Hu & Hueckel (2007a, 2007b), linking the irreversible dilatancy and the related increase of free specific surface area to the amount of mineral dissolution per unit volume. This coupling mechanism, usually referred to as 'reactive chemo-plasticity', acts at a comparatively long time scale, as distinguished from 'non-reactive chemo-plasticity', which is when the mechanical properties of a solid skeleton can be affected instantaneously by an altered concentration (of selected species) in the pore fluid.

From a microscopic point of view, reactive chemo-plasticity starts when a mineral mass dissolves into water at available dissolution sites on the solid–fluid interface. It is commonly assumed that the dissolution reaction rate and hence mass removal rate is proportional to the specific surface area of the interface. It is hence postulated that the irreversible damage-induced dilatancy is associated with the generation of new microcrack walls. The increased wall surface area adds to the pre-existing specific surface area of the pores, hence advancing the overall mineral mass production of the medium. Because mass removal affects the strength of the medium, the central part of the description of the chemo-mechanical coupling is how to quantify the amount of weakening of the material owing to dissolution. Therefore, the coupling between the irreversible strain and the chemically induced mass removal is a two-way coupling (see also Hueckel & Hu (2009)).

To quantify the above coupling mechanisms, a representative elementary volume (REV) of the drained porous medium is considered, represented by a single geometrical point, to which both mechanical and chemical properties are attributed. The solid phase material is assumed as rigid-plastic. This assumption is a matter of convenience because it enables a semi-analytical solution to be obtained. On the other hand, the elastic stress component is much smaller than the irreversible one in the area of interest near the crack tip. The partial stress carried by the fluid phase is considered negligible. The theory of plasticity states that the yield locus of a material is affected by stress σ_{ij} and, when a sufficient load is applied, that induces initial yielding, also owing to variation of a set of internal variables. In reactive chemo-plasticity (Hueckel, 2002), the internal chemical variables denoted as ξ_n ($n = 1, 2, \ldots$) are the accumulated dissolved masses of the n th species of mineral per unit volume of the porous medium. The mechanical, strain-hardening variable is chosen as the irreversible deviatoric strain intensity ($\varepsilon_q^{\mathrm{irr}}$).

The rate of the deviatoric strain intensity is defined as an invariant of deviation strain rate $\dot{e}_{ij}^{\mathrm{irr}}$

$$\dot{\varepsilon}_q^{\mathrm{irr}} = \left(\frac{2}{3}\dot{e}_{ij}^{\mathrm{irr}}\dot{e}_{ij}^{\mathrm{irr}}\right)^{1/2} \tag{1}$$

where

$$\dot{e}_{ij}^{\mathrm{irr}} = \dot{\varepsilon}_{ij}^{\mathrm{irr}} - \frac{1}{3}\dot{\varepsilon}_{kk}^{\mathrm{irr}}\delta_{ij}$$

With the assumption of rigid-plasticity, there are no elastic strain rates and no strain at all for a stress state below the yield limit, that is when $f(\sigma_{ij}) < 0$. With the stress at the yield locus, the strain rate is non-zero and irreversible. Hence

$$f = f(\sigma_{ij}, p_{\mathrm{c}}), \text{ and } \dot{f} = \dot{f}(\dot{\sigma}_{ij}, \dot{p}_{\mathrm{c}}) \tag{2}$$

$$\dot{\varepsilon}_{ij} = 0 \text{ when } f < 0, \text{ or } f = 0, \dot{f} < 0 \tag{3}$$

$$\dot{\varepsilon}_{ij} = \dot{\varepsilon}_{ij}^{\mathrm{irr}} \neq 0 \text{ when } f = 0 \text{ and } \dot{f} = 0 \tag{4}$$

where the superimposed dot over a symbol denotes the time rate. Tensile stress and strain are considered as negative. p_{c} denotes a geometric size characteristic of the yield locus, and it plays the role of the hardening function of irreversible deviatoric strain ($\varepsilon_q^{\mathrm{irr}}$) and of the accumulated relative dissolved mass of each mineral species ($\xi_1, \ldots, \xi_n$), hence $p_{\mathrm{c}} = p_{\mathrm{c}}(\varepsilon_q^{\mathrm{irr}}, \xi_1, \ldots, \xi_n)$. During the process of dissolution, the material is chemically softened to the condition where there is dilatant microcracking; on the other hand, plastic deviatoric strain induces a hardening effect. This indicates that the two factors, plastic deviatoric strain and chemical softening, affect the yield locus of the material with opposite contributions. At an imposed constant stress at yielding, the plastic deviatoric strain hardening compensates for the dissolution-induced strength loss.

The chemical softening parameters ($\xi_1, \ldots, \xi_n$), representing the accumulated mass removal of each particular mineral species, can be calculated from the rates of reactions in which the given species is involved. In reality, multiple reactions may affect the strength of any geomaterial, the processes of which might be simultaneous or sequential, with varied rates of progression or within different time scales. However, there is currently no widely accepted approach to identify and quantify contributions of individual mineral components to the overall degradation of material strength or other mechanical properties. Meanwhile, it is common for one type of chemical reaction to be predominant, as, for instance, in the case of carbonate reservoirs subjected to an acid environment or calcite exposed to water (Ciantia & Hueckel, 2013). In what follows, a single reaction effect with a single rate will be considered only, and the chemical softening parameter becomes the reaction progress variable ξ, and hence, $p_{\mathrm{c}} = p_{\mathrm{c}}(\varepsilon_q^{\mathrm{irr}}, \xi)$. The mechanisms of chemically induced mass removal will be detailed in the following section.

The irreversible strain rate can be obtained through the associated flow rule

$$\dot{\varepsilon}_{ij}^{\mathrm{irr}} = \dot{\Lambda}\frac{\partial f}{\partial \sigma_{ij}} \tag{5}$$

where the multiplier $\dot{\Lambda}$ can be expressed as a function of the rate of stress and the chemical reaction process

$$\dot{\Lambda} = \frac{\left(\partial f/\partial \sigma_{ij}\right)\dot{\sigma}_{ij} + \left(\partial f/\partial \xi\right)\dot{\xi}}{-\dfrac{\partial f}{\partial \varepsilon_q^{\mathrm{irr}}}\left[\dfrac{2}{3}\dfrac{\partial f}{\partial s_{kl}}\dfrac{\partial f}{\partial s_{kl}}\right]^{1/2}}; \tag{6}$$

$$\dot{\Lambda} = 0 \text{ if } f < 0 \text{ or } f = 0 \text{ and } \dot{f} < 0$$

and is determined by way of the extended Prager consistency law, $\dot{f}(\sigma_{ij}, \varepsilon_q^{\mathrm{irr}}, \xi) = 0$. The yield locus gradient $\partial f/\partial \sigma_{ij}$ determines the mode of strain rate, whereas the magnitude of strain rate is controlled by the multiplier $\dot{\Lambda}$, which implies that a purely chemical process can promote the development of irreversible strain when stress is fixed (see Hu & Hueckel (2007a, 2007b) for details).

MECHANISMS OF MINERAL DISSOLUTION IN A CARBONATE GEOMATERIAL COUPLED WITH VOLUMETRIC STRAIN

As one of the two major reservoir lithotypes, carbonates (the other is sandstones) have been intensely studied in the petroleum industry (Dusseault, 2011). The most common chemical process in carbonate reservoirs is the dissolution of calcite and dolomite (André *et al.*, 2007). Because the dissolution of dolomite, described as

$$CaMg(CO_3)_2 + 2H^+ \leftrightarrow Ca^{2+} + Mg^{2+} + 2HCO_3^-$$

is found to be geochemically similar to calcite, calcite dissolution is discussed here as a representative for carbonate minerals in general. When subjected to low-concentration acid in an aqueous environment, calcite undergoes the predominant reaction described as

$$CaCO_3(s) + H^+(aq) \leftrightarrow Ca^{2+}(aq) + HCO_3^-(aq) \tag{7}$$

This is usually the first step of the calcite–water interaction; the product HCO_3^- formed in aqueous solution is unstable and inclined to convert to $CO_2(g)$ with the presence of excessive H^+. However, since it is the most significant reaction involved in solid mass removal, the present authors believe it is acceptable to omit the subsequent reactions and consider reaction (7) as the dominant and hence only reaction. Based on the mass conservation of calcium, the mole number of calcite removed from the solid phase ($CaCO_3$) is equal to the change in number of calcium ions in the solution, and the reaction rate is expressed as

$$\frac{da_{Ca^{2+}}}{dt} = \tilde{A}\gamma_{Ca^{2+}}(k_+ a_{CaCO_3} a_{H^+} - k_- a_{Ca^{2+}} a_{HCO_3^-}) \tag{8}$$

where $\tilde{A}$ is a non-dimensional quantity denoting the total fluid–solid interface surface area per unit volume; a_i are activities and γ_i are activity coefficients of the ith species; k_+ and k_- are rate constants of the forward and backward reactions, respectively.

The rate of calcite removal from the solid phase of carbonate material can be represented by the rate of change of activity of Ca^{2+} in pore water, written as

$$\dot{\xi} = s\frac{da_{Ca^{2+}}}{dt} \tag{9}$$

where s denotes a ratio between the number of moles of water and that of calcite in the initial state. To maintain the linearity of the proposed model, the precipitation term in equation (8) is omitted.

Scalar variable $\tilde{a}$ is introduced to represent a normalised amount of the increased surface area per unit volume of the medium, which is linked to the dimensionless total reactive surface area per unit volume of fluid (denoted by $\tilde{A}$) by way of

$$\tilde{a} = \tilde{A}\frac{n\rho_w}{\rho^0}$$

where $\rho^0 = 1\ \mathrm{kg/m^3}$, ρ_w is the density of water and n denotes the porosity taken at its initial value.

The newly generated specific surface area can be assumed as proportional to the irreversible dilatant volumetric strain, as suggested by a model of a two-dimensional hexagonal crystal assembly (Hu & Hueckel, 2007b). Then, $\tilde{a} = 8/(\sqrt{3}\delta)|\varepsilon_v^{irr}| \cdot 1m$ for $\varepsilon_v^{irr} < 0$, where δ denotes an average microcrack opening at the apex. Hence

$$\tilde{A} = f(\varepsilon_v^{irr}) = \phi|\varepsilon_v^{irr}| + \phi_c,\ \varepsilon_v^{irr} < 0 \tag{10}$$

$$\phi = 0,\ \varepsilon_v^{irr} > 0 \tag{11}$$

where ϕ is a proportionality constant and ϕ_c denotes the dimensionless specific surface area of the pre-existing voids per unit volume. When the volumetric strain is compressive, it is assumed that there is no microcracking and that the specific surface area remains constant.

NUMERICAL SIMULATION OF CRACK PROPAGATION IN THE PRESENCE OF COUPLED DAMAGE–DISSOLUTION PROCESSES

There are at least two circumstances of industrial interest involving the chemical enhancement of crack propagation. One typical scenario features a remote constant radial tensile stress, which goes to zero at the inner (artificial) boundary of the process zone, $r = a$. At the same time, yielding, which induces irreversible deviatoric strain, is localised near the crack tip, also producing a proportional amount of irreversible dilatancy (meaning microcracking). The latter induces the chemical mass removal enhanced by its rate dependence. Owing to the chemical action of the fluid, the material weakens in that zone. The circumferential stress is also tensile everywhere. Because of boundary constraints, the stress state does not evolve significantly, hence the whole process is dominated by compensation of the chemical softening by the strain hardening (Hueckel, 2009).

One other scenario describes a single crack being affected by the pressure of the fluid acting on the walls of the crack, and at the same time by a chemical infiltrating from the crack and weakening the crack surroundings. No other load is considered. The action of the pressure transmitted to the rock causes dilatant damage near the crack tip and hence engages the chemo-mechanical coupling in that location. The stress state near the crack tip is different from the previous one in that the stress near the crack tip is compressive orthogonally to the crack edges. This problem is dealt with elsewhere.

From the field point of view, in the former scenario the chemical effect plays a primary role, whereas the stress field plays a secondary role. In what follows this case becomes the focus. It corresponds to a situation of a pre-existing crack inundated with water or an aggressive liquid (e.g. acid rain), while a tensile stress source is remote. A possible field analogue could be a reactivation of a landslide with a pre-existing slip zone (see, for example, Zhao *et al.* (2011)). In the latter case, both factors, chemical and mechanical, are equally important. This case is likely to occur during a fluid pressure (static) pulse assisted by the chemically aggressive fluid component.

Classically, a mechanically stimulated crack extends when a sufficiently high level of stress intensity is attained in the material at the crack tip. The microcracking can be represented macroscopically through the inelastic strain near the crack tip and its yielding is affected by the strain softening. In contrast, in the considered case, the external tractions are kept constant, while the process is activated and driven by way of the chemical field.

To address the solution of the boundary-value problem for the system of equations describing the coupled chemo-mechanical processes around the crack tip, the extended Johnson approximation is adopted (Johnson, 1970), assuming that all the fields involved are axisymmetric around the crack tip point with a small, unstressed cavity around it, as shown in Fig. 1. This is analogous to the cylindrical cavity expansion problem often used for pile or piezocone modelling in geotechnical problems – see, for example, Collins & Stimpson (1994) or Bigoni & Laudiero (1989). For simplicity, the plane strain is considered. The boundary conditions impose the radial stress at the external boundary as constant and uniform, and zero at the inner boundary

$$\sigma_r|_{r=a} = 0;\ \sigma_r|_{r=b} = \text{const.} \tag{12}$$

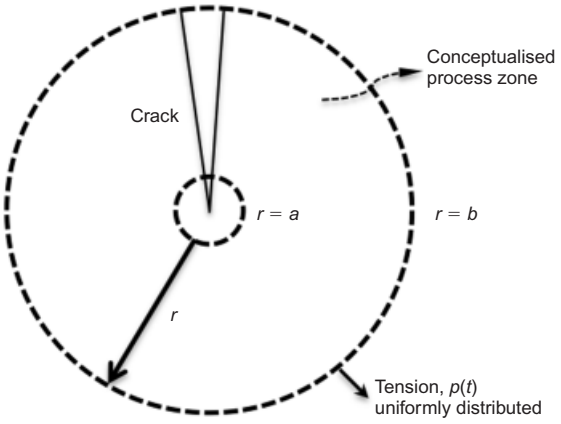

Fig. 1. Schematic diagram of the process zone around the crack tip

Note that the other boundary conditions that one normally would impose on a boundary-value problem, as shown in Fig. 1, such as zero circumferential stress at the crack faces, are ignored by virtue of adopting the Johnson approximation, which makes it possible to use axial symmetry fields. While notably the obtained solutions are not exact, the benefit from capturing principal interrelationships between the variables involved and their distribution and evolution is significant. Note also that assuming zero radial stress at the inner boundary excludes any realistic description of the stress concentration near the crack tip. However, the current focus is rather on the adjacent process zone of microcracking, which is away from the crack tip by a non-negligible distance, represented in this case by the radius a (Bazant & Kazemi, 1990; Lin & Labuz, 2011).

The equilibrium equation and kinematic relationships for the plane strain axisymmetric problem are given as

$$\frac{\mathrm{d}\sigma_r}{\mathrm{d}r} + \frac{\sigma_r - \sigma_\theta}{r} = 0 \tag{13}$$

$$\dot{\varepsilon}_r = -\frac{\mathrm{d}\dot{u}}{\mathrm{d}r},\ \dot{\varepsilon}_\theta = -\frac{\dot{u}}{r},\ \dot{\varepsilon}_z = 0 \tag{14}$$

where θ and r denote the circumferential and radial coordinates (respectively) and u, which denotes a radial displacement, is defined as positive when pointing outwards. The circumferential displacement is null owing to axisymmetry.

A linearised yield surface is chosen for simplicity after Mróz & Kwaszczyńska (1971) and Hueckel & Mróz (1973), as shown in Fig. 2(a). Tensile stress or strain is considered negative in the present system, hence, the process of yielding starts from the third quadrant in Figs 2(a) and 2(b). The locus segment ED determines the relationship between σ_r and σ_θ at the initial yielding

$$\sigma_{\theta 0} = \tan\left(\frac{\pi}{4} - \vartheta\right)\sigma_{r0} - \left[\tan\left(\frac{\pi}{4} - \vartheta\right) + \tan\phi\right]\sigma_{01}$$

where ϑ, ϕ and σ_{01} are parameters shown in Fig. (2a). The linearised yield locus undergoes an expansion with an increase of the shear strain intensity (equation (1)), while it shrinks with the square of the loss of the mineral mass, ξ. The assumed hardening rules are

$$\sigma_r = \sigma_{r0}(1 + \alpha\varepsilon_q^{irr} - \beta\xi^2); \tag{15}$$

$$\sigma_\theta = \tan\left(\frac{\pi}{4} - \vartheta\right)\sigma_r - \left[\tan\left(\frac{\pi}{4} - \vartheta\right) + \tan\phi\right] \times \sigma_{01}(1 + \alpha\varepsilon_q^{\mathrm{irr}} - \beta\xi^2) \tag{16}$$

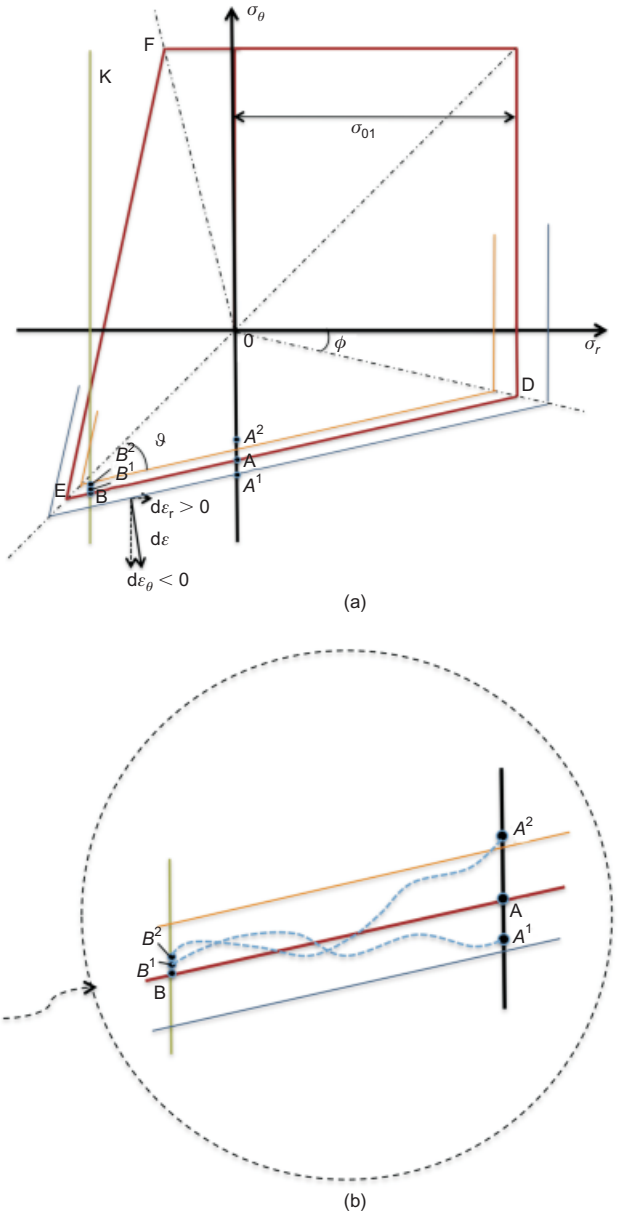

Fig. 2. (a) Linearised yield locus for the material. (b) Sketch of stress profiles within the process zone

It should be noticed that equation (15) and equation (16) apply exclusively for $\sigma_\theta < \sigma_r < 0$. α and β are constant coefficients for strain hardening and chemical weakening, respectively. Deviatoric strain intensity $\varepsilon_q^{\mathrm{irr}}$ can be calculated using equation (1) integrated with time. The axial stress component σ_z is assumed not to influence yielding in the plane strain rate conditions. It can be calculated through equation (5) from the condition $\mathrm{d}\varepsilon_z^{\mathrm{irr}} = 0$ as

$$\sigma_z = \frac{1}{2}(\sigma_r + \sigma_\theta) \pm 3BJ_2^{1/2}$$

where B is a constant and J_2 is the second invariant of deviatoric stress, and the sign $\pm$ refers to either the top or the bottom part of the yield locus in Fig. 2(a) (see also Mróz & Kwaszczyńska (1971)).

Recall that the precipitation effect has been neglected. Hence, the combination of equations (8) and (9) yields

$$\dot{\xi} = s\tilde{A}\gamma_{\mathrm{Ca}^{2+}}k_+ a_{\mathrm{CaCO_3}}a_{\mathrm{H}^+} \tag{17}$$

It is further assumed that the activities and activity coeffi-

cients are unities for the convenience of simulation, and hence $\dot{\xi}$ can be rewritten as

$$\dot{\xi} = sk_+(\phi|\varepsilon_v| + \phi_c),\ \varepsilon_v < 0 \tag{18}$$

Hence, if ε_v is negative

$$\beta\xi^2 = \beta\left(\int_0^t \dot{\xi}\mathrm{d}t\right)^2 = \beta s^2 k_+^2\left(\phi\int_0^t |\varepsilon_v|\mathrm{d}t + \phi_c t\right)^2 \tag{19}$$

which leads to

$$\beta\xi^2 = K^2\left(\int_0^t |\varepsilon_v|\mathrm{d}t\right)^2 + 2KK_c t\left(\int_0^t |\varepsilon_v|\mathrm{d}t\right) + K_c^2 t^2 \tag{20}$$

where $K = \sqrt{\beta}sk_+\phi$ and $K_c = \sqrt{\beta}sk_+\phi_c$ represent the overall chemical softening rate coefficients associated with newly generated microcracking and the initial void ratio, respectively.

An initial dissolution, proportional to a constant specific surface area associated with the initial porosity, even for a low stress prior to yielding, that is, for

$$\sigma_{ij} : f = f\left(\sigma_{ij} = \text{const.}, \xi = \frac{K_c}{\beta}t\right) < 0$$

through a slow mass removal $\dot{\xi} > 0$ and corresponding shrinkage of the yield locus can eventually activate the plastic yielding at ED (Fig. 2(a)), in other words, bring the condition $f = 0$ around the initially subcritical crack. At that point, with the continuing reaction, $\dot{\xi} > 0$, but now also enhanced by the microcracking as manifested by $\dot{\varepsilon}_v > 0$, the coupled process is significantly intensified.

Numerical solutions were obtained by solving (using Matlab©) the above-mentioned system of equations, given the initial and boundary conditions, as specified earlier. The input parameters are $\alpha = 1$, $\beta = 1$, $\vartheta = \pi/6$, $\tan\phi = 0{\cdot}2$, $b/a = 10$, $K_c = 2{\cdot}0 \times 10^{-8}\ \mathrm{s}^{-1}$, and K is set to be $5{\cdot}0 \times 10^{-6}\ \mathrm{s}^{-1}$, unless it is a subject of a parametric study. The displacement u_a at the internal circumference is used to represent propagation of the crack tip and its dimensionless form u_a/a, as shown in Fig. 3. If the value of the chemical softening coefficient, K, is increased by one order of magnitude, the displacement u_a within 1 month (30 days) starts growing exponentially, meaning an accelerated crack propagation, which is an expected result of the damage–dissolution coupling. Fig. 4 further

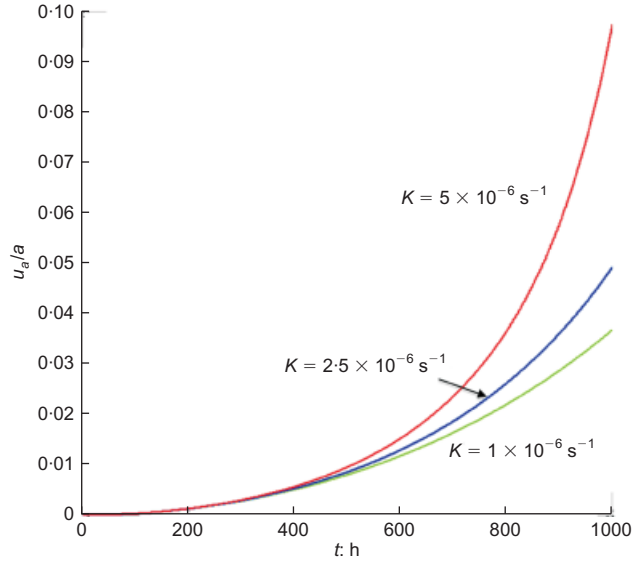

Fig. 3. Propagation of the crack tip

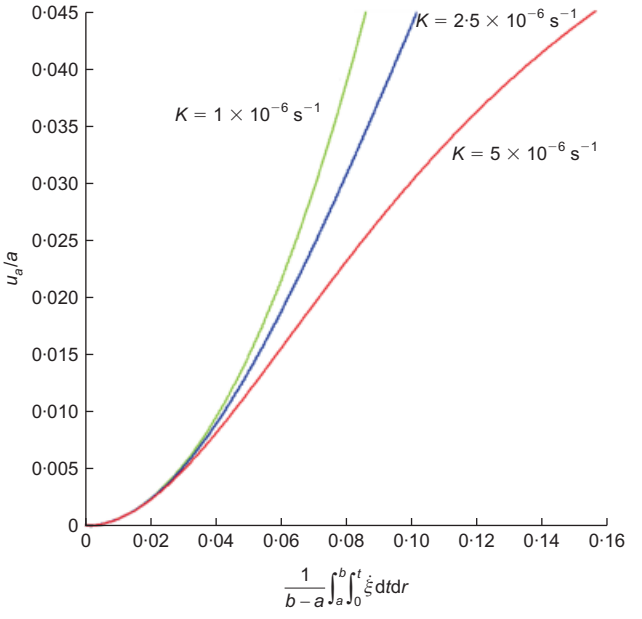

Fig. 4. Influence of total mass removal on crack propagation

demonstrates the relationship between the crack propagation as represented by u_a/a and a total integrated dissolved mass

$$\frac{1}{b-a}\int_a^b\int_0^t \dot{\xi}\mathrm{d}t\mathrm{d}r$$

Notably, within the range studied at an advanced mass removal, a decelerating crack propagation is observed for a sufficiently high valued K. As seen also, for the same accumulated mass of dissolution, a smaller chemical coefficient K leads to a deeper crack penetration, as $\dot{\xi}$ is proportional to K and $\varepsilon_v^{\mathrm{irr}}$, whereas the latter is linked to u_a. The evolution of the distribution of relative mass dissolution as well as the evolution of the dissolution rate is shown in Fig. 5 and Fig. 6, respectively. Fig. 5 indicates that the evolution of the accumulated dissolved mass distribution along the radius is confined to the near-crack-tip area. The maximum accumulated relative mass removal reaches 0·67, which is very high. Note that dissolution of carbonate rock can be very fast and advanced (see, for example, Ciantia & Hueckel

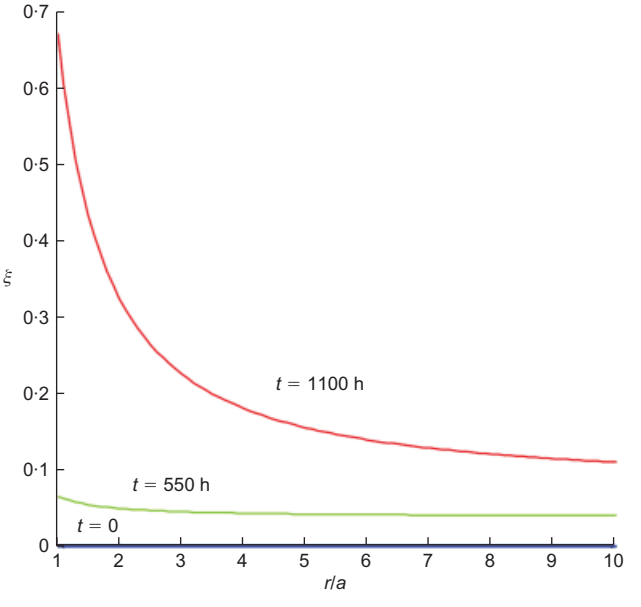

Fig. 5. Evolution of the distribution of relative mass dissolution

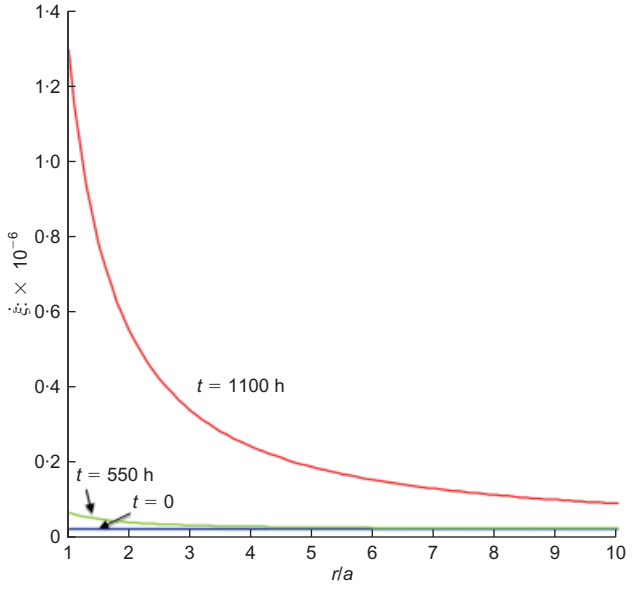

Fig. 6. Evolution of the distribution of dissolution rate

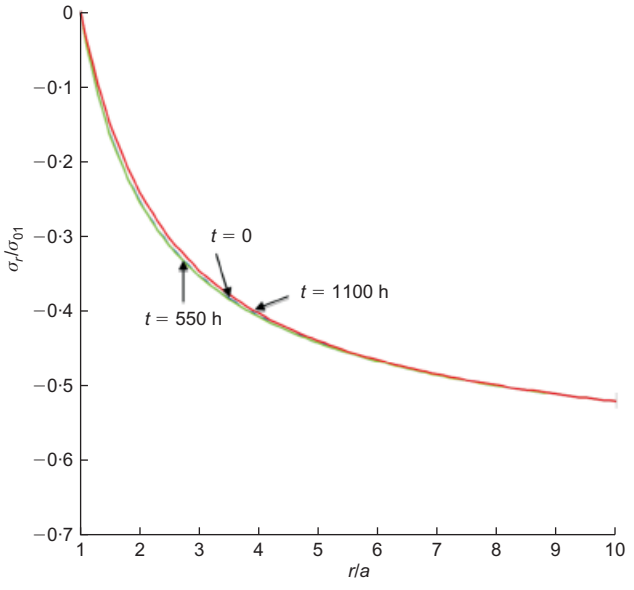

Fig. 8. Evolution of the radial stress distribution

(2013)). The confinement to the near-tip zone is even sharper in the dissolution rate distribution; as Fig. 6 demonstrates, the rate of chemical dissolution in the inner area of the process zone undergoes a huge change, while that outside the area is almost negligible because it comes mainly from the pre-existing surface area of the initial porosity. The rate distribution is clearly linked to that of dilatancy, along the radius, which (as shown in Fig. 7) develops in a similar fashion, indicating that the near-crack-tip area is subject to the most severe damage. Given the linear form of the yield locus and the normality rule, there is no compaction in the process zone. Fig. 8 and Fig. 9 show the evolution of the radial and circumferential stress component distribution, respectively. Because the radial stresses on both the interior and exterior boundaries are fixed, there is little freedom for any evolution. However, the distribution of σ_θ undergoes a noticeable change, specifically from $t = 550$ h to $t = 1100$ h, during which the crack penetrates almost ten times deeper (as observed in Fig. 3). It is interesting to notice that in the near-crack-tip area, the tensile (negative) stress experiences a

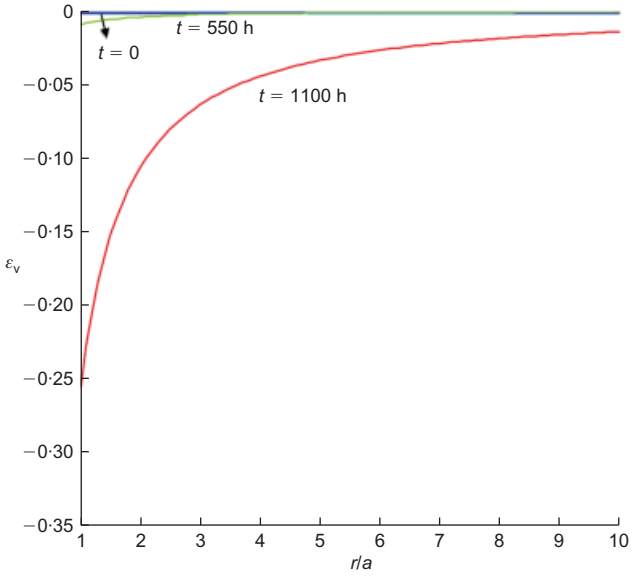

Fig. 7. Evolution of the distribution of irreversible volumetric strain

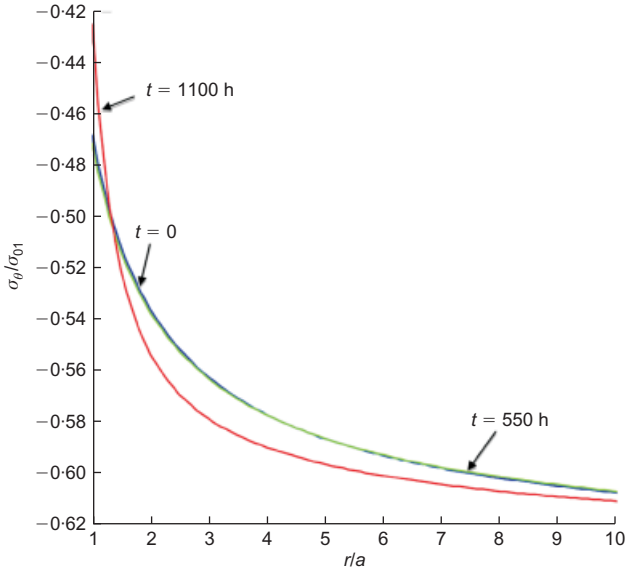

Fig. 9. Evolution of the circumferential stress distribution

small increase before it collapses back, which indicates an initially dominating strain-hardening followed by the progressive overtaking by chemical softening. This is visible at the stress profiles for two representative moments in the evolution delineated in Fig. 2(b), where A^1, A^2 stand for stress state at the interior, $r = a$, and B^1, B^2 represent the counterpart exterior, $r = b$, respectively. The exterior of the process zone is subjected to consistent but much more modest chemical weakening, mainly linked to the background dissolution, because the deformational effect is very small.

MODELLING OF DIFFUSION OF DISSOLVED CALCITE COUPLED WITH IRREVERSIBLE DAMAGE INSIDE THE PROCESS ZONE

Inside the process zone, the phenomenon of diffusion occurs once the solute, that is the calcite, is dissolved in water. The reference condition is set as a uniform dissolution at the surface of pre-existing voids within an REV. Interconnected voids within the process zone form microchannels, providing pathways for calcite transport (see Fig. 10).

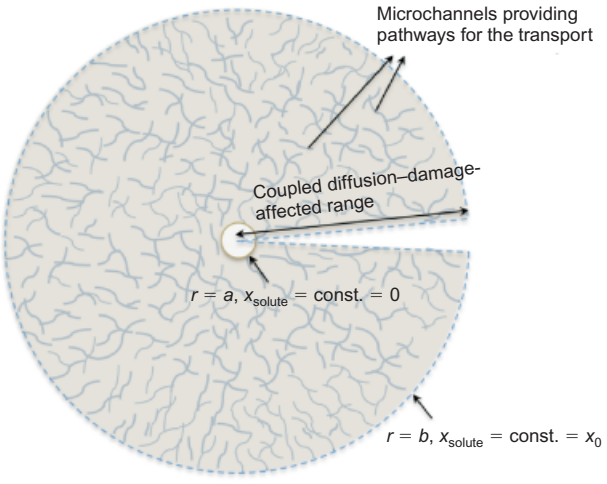

Fig. 10. Coupled diffusion–damage-affected zone around the crack tip

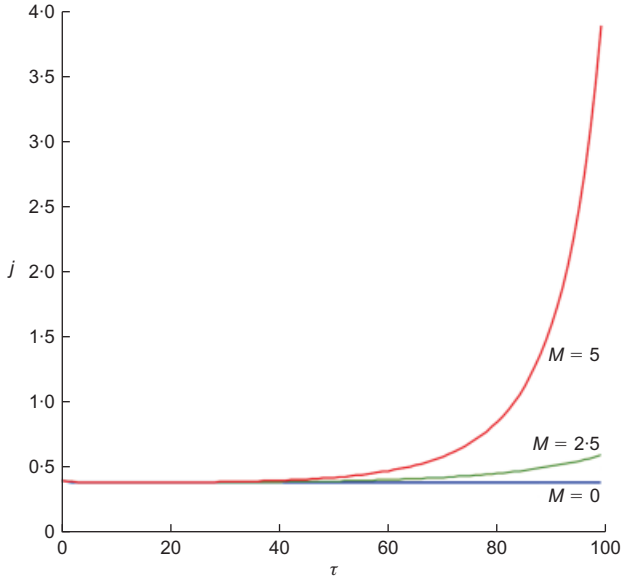

Fig. 11. Evolution of the dimensionless mass flux at the crack tip

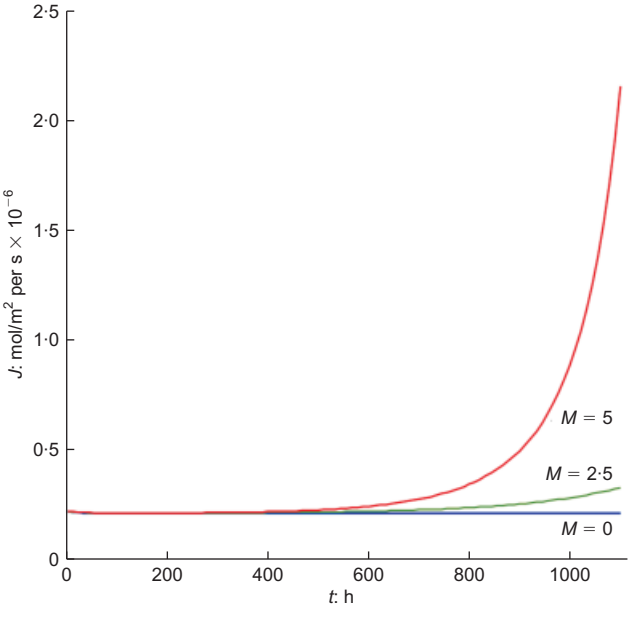

Fig. 12. Evolution of the mineral mass flux at the crack tip

At the crack tip, it is assumed that within the macro-pore, water washes away the excess mineral, and for simplicity zero concentration is assumed, hence $x_{Ca^{2+}} = 0$ at $r = a$. The exterior of the process zone is an artificial boundary and is assumed to stay as it was at the initial state of the material, when dissolution was limited to the pre-existing micropores, hence $x_{Ca^{2+}} = x_0$ at $r = b$. An initial background steady-state diffusion field is created with the imposed boundary conditions.

The reactive diffusion is approximated as an axisymmetric field of concentrations (molar fraction of calcite) with uniformly distributed sources (reaction sites) described by the following governing partial differential equation with given boundary conditions as well as the initial conditions.

$$\frac{\partial x_{Ca^{2+}}}{\partial t} = D\left(\frac{\partial^2 x_{Ca^{2+}}}{\partial r^2} + \frac{1}{r}\frac{\partial x_{Ca^{2+}}}{\partial r}\right) + k_+(\phi|\varepsilon_v(r, t)| + \phi_c) \tag{21}$$

where $x_{Ca^{2+}}$ is the molar fraction of calcium in the fluid phase within the process zone, and D represents the calcium diffusion coefficient, which is assumed a constant within the process zone. As seen in equation (21), the source term depends on the amount of volumetric deformation, hence its solution is coupled to the solution of independent equations (12)–(21).

The damage-affected zone of the material induces evolution of the concentration of solutes, coupled with the evolving deformation (microcracking). The distribution of mineral concentration and the flux of the solute mass are hence affected by the solid mechanics of the problem. The diffusive flux at the inner boundary, representing the influence of the mechanical damage on the net dissolved mass, is of particular interest, and it can be correlated with the displacement of the crack tip, or crack propagation. Figs 11 and 12 show the evolution of mass flux J at $r = a$ and its dimensionless counterpart. M is a coefficient representing the effect of deformation/damage associated with the dilatant volumetric strain on the mass transfer, $M = s\phi k_+ a^2/Dx_0$. $M = 0$ means a pure diffusion process without the presence of chemo-mechanical coupling. As indicated in both Fig. 11 and Fig. 12, the reactive dissolution coupled with the irreversible damage of the medium plays an important role in the diffusion processes. Finally, it is possible to set the crack propagation against the flux of the solute at the near-tip perimeter, Fig. 13. Because the total flux of mass removal is experimentally measurable, it is possible to verify the simulation results against an experiment and perform an in situ calibration.

CONCLUSIONS

A damage-enhanced reactive chemo-plasticity model was adopted to describe a simplified scenario of a chemically induced propagation, of an otherwise subcritical crack in a pre-stressed geomaterial. An open system was selected, meaning that the local precipitation is neglected, and chemical dissolution was considered as a form of mass removal. The chemo-plasticity coupling effect was investigated with an assumption of simple hardening rules, the linear form of the yield condition and rigid behaviour prior to yielding; yet a number of meaningful conclusions were reached. The results have demonstrated a significant role of the compensatory mechanism between strain hardening and chemical softening. It was possible to obtain the rate of crack propagation against time, against total accumulated relative mass removal and against the exiting mineral flux. Chemical softening

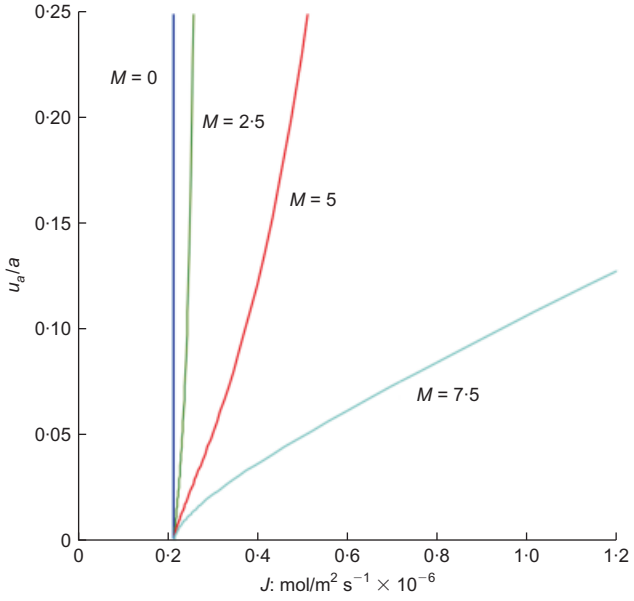

Fig. 13. Correlation between the exiting mass flux and penetration of the crack tip

intensity, dominating the rate of mineral dissolution, has been proved essential to the progress of crack propagation, as well as that of soil/rock degradation.

Most importantly, it is seen that with the mass removal, the rate of crack penetration initially substantially increases. However, at some point (around 700 h) the penetration rate starts decelerating (for $K = 5 \times 10^{-6}$ s^{-1}). This time corresponds to the moment when the quadratic nature of the chemical hardening formula in the hardening law starts to be felt. In other words, starting from that time, there needs to be much more of the mass loss to compensate for the linear strain hardening term (which is a linear function of the crack tip displacement). The findings of this paper may be applied to several energy source harvesting areas including petroleum/natural gas and geothermal engineering (to such processes as acid-enhanced hydraulic fracturing or reservoir engineering), as well as in the area of slope stability, and so on, where the soil/rock mass is subjected to chemically induced degradation.

ACKNOWLEDGEMENTS

The authors acknowledge the partial support given to Duke University by ENI Spa, Milan, Italy. The support of US National Science Foundation through grant no. 0700294 is also gratefully acknowledged.

NOTATION

A^1, A^2 stress states at the interior, $r = a$
$\tilde{A}$ non-dimensional quantity denoting total fluid–solid interface surface area per unit volume
a radius
$\tilde{a}$ scalar variable
a_i activities of ith species
B constant
B^1, B^2 stress states at the exterior, $r = b$
D calcium diffusion coefficient
$\dot{e}_{ij}^{\text{irr}}$ invariant of deviation strain rate
f function
$\partial f/\partial \sigma_{ij}$ yield locus gradient
J mineral mass removal
J_2 second invariant of deviatoric stress
K $= \sqrt{\beta} s k_+ \phi$, overall chemical softening rate coefficient associated with newly generated microcracking
K_c $= \sqrt{\beta} s k_+ \phi_c$, overall chemical softening rate coefficients associated with initial void ratio
k_+, k_- rate constants of forward and backward reactions respectively
M coefficient representing the effect of deformation/damage associated with dilatant volumetric strain on the mass transfer
n porosity taken at its initial value
p_c geometric size characteristics of the yield locus
r radial coordinate
s ratio between number of moles of water and that of calcite in the initial state
u radial displacement
$x_{Ca^{2+}}$ molar fraction of calcium in the fluid phase within the process zone
α constant coefficient for strain hardening
β constant coefficient for chemical weakening
γ_i activity coefficients of ith species
δ average microcrack opening at the apex
$(\varepsilon_q^{\text{irr}})$ irreversible deviatoric strain intensity
θ circumferential coordinate
ϑ angle, as denoted in Fig. 2(a)
$\dot{\Lambda}$ multiplier
ξ reaction progress variable
$(\xi_1, \ldots, \xi_n)$ accumulated relative dissolved mass of each mineral species
ξ_n, $(n = 1, 2, \ldots)$ accumulated dissolved masses of the nth species of mineral per unit volume of porous medium
ρ_w density of water n denotes porosity taken at its initial value
σ_{ij} stress
σ_r radial stress component
σ_z axial stress component
σ_θ circumferential stress component
σ_{01} initial yield criterion constant
ϕ proportionality constant
ϕ_c dimensionless specific surface area of pre-existing voids per unit volume

REFERENCES

André, L., Audigane, P., Azaroual, M. & Menjoz, A. (2007). Numerical modelling of fluid-rock chemical interactions at the supercritical CO_2–liquid interface during supercritical CO_2 injection into a carbonate reservoir, the Dogger aquifer (Paris Basin, France). *Energy Conversion Manag.* **48**, No. 6, 1782–1797.

Bathurst, G. C. (1958). Diagenetic fabrics in some British Dinantian limestones. *Liverpool Manchester Geol. J.* **2**, 11–36.

Bazant, Z. P. & Kazemi, M. T. (1990). Determination of fracture energy process zone length and brittleness number from size effect with application to rock and concrete. *Int. J. Fracture* **44**, No. 2, 111–131.

Bigoni, D. & Laudiero, F. (1989). The quasi-static finite cavity expansion in a non-standard elasto-plastic medium. *Int. J. Mech. Sci.* **31**, No. 11–12, 825–837.

Carter, B. J., Desroches, J., Ingraffea, A. R. & Wawrzynek, P. A. (2000). Simulating fully 3D hydraulic fracturing. In *Modeling in geomechanics* (eds M. Zaman, J. Booker and G. Gioda). New York, NY, USA: Wiley.

Ciantia, M. O. & Hueckel, T. (2013). Weathering of stressed submerged calcarenites: chemo-mechanical coupling mechanisms. *Géotechnique*, http://dx.doi.org/10.1680/geot.SIP13.P.024

Collins, I. F. & Stimpson, J. R. (1994). Similarity solutions for drained and undrained cavity expansions in soils. *Géotechnique* **44**, No. 1, 21–34.

Dershowitz, W., La Pointe, P., Parney, B. & Cladouhos, T. (2001). Multiphase discrete fracture modeling in support of improved oil recovery from the North Oregon Basin, Wyoming. *Proc. 38th US Rock Mech. Symp., Washington, DC*, 663–668. Lisse, the Netherlands: AA Balkema.

Dusseault, M. B. (2011). Geomechanical challenges in petroleum reservoir exploitation. *KSCE J. Civ. Engng* **15**, No. 4, 669–678.

Gajo, A., Loret, B. & Hueckel, T. (2002). Electro-chemo-mechanical couplings in saturated porous media: elastic–plastic behaviour of heteroionic expansive clays. *Int. J. Solids Structs* **39**, No. 16, 4327–4362.

He, C., Guo, J., Wang, W. & Liu, C. (2010). Study on acidizing wormhole of tight carbonate reservoir. *Duankuai Youqitian (Fault-Block Oil & Gas Field)* **17**, No. 2, 235–238.

Howard, G. C. & Fast, C. R. (1970). *Hydraulic fracturing*. New York, NY, USA: Society of Petroleum Engineering of AIME.

Hu, L. B. & Hueckel, T. (2007a). Creep of saturated materials as a chemically enhanced rate-dependent damage process. *Int. J. Numer. Anal. Methods Geomech*. **31**, No. 14, 1537–1565.

Hu, L. B. & Hueckel, T. (2007b). Coupled chemo-mechanics of intergranular contact: toward a three-scale model. *Comput. Geotech*. **34**, No. 4, 306–327.

Hueckel, T. (1992). Water–mineral interaction in hydro-mechanics of clays exposed to environmental loads: a mixture theory approach. *Can. Geotech. J.* **29**, No. 6, 1071–1086.

Hueckel, T. (1997). Chemo-plasticity of clays subjected to stress and flow of a single contaminant. *Int. J. Numer. Analyt. Methods Geomech*. **21**, No. 1, 43–72.

Hueckel, T. (2002). Reactive plasticity for clays during dehydration and rehydration. Part I: concepts and options. *Int. J. Plasticity* **18**, No. 3, 281–312.

Hueckel, T. (2009). Thermally and chemically induced failure in geomaterials. *Eur. J. Environ. Civ. Engng* **13**, No. 7–8, 831–867.

Hueckel, T. & Hu, L. B. (2009). Feedback mechanisms in chemo-mechanical multi-scale modeling of soil and sediment compaction. *Comput. Geotech*. **36**, No. 6, 934–943.

Hueckel, T. & Mróz, Z. (1973). Some boundary value problems for variable density materials. In *Problèmes de la rhéologie*, pp. 173–191. Warsaw, Poland: PWN.

Hueckel, T. & Pellegrini, R. (2002). Reactive plasticity for clays: application to a natural analog of long-term geomechanical effects of nuclear waste disposal. *Engng Geol*. **64**, No. 2–3, 195–215.

Hueckel, T., Pellegrini, R. & Del Olmo, C. (1998). A constitutive study of thermo-elastoplasticity of deep carbonatic clays. *Int. J. Numer. Analyt. Methods Geomech*. **22**, No. 7, 549–574.

Hueckel, T., Cassiani, G., Fan, T., Pellegrino, A. & Fioravante, V. (2001). Aging of oil/gas-bearing sediments, their compressibility, and subsidence. *J. Geotech. Geoenviron. Engng, ASCE* **127**, No. 11, 926–938.

Hueckel, T., Cassiani, G., Prevost, J. H. & Walters, D. A. (2005). Field derived compressibility of deep sediments of the Northern Adriatic. In *Land subsidence. Special volume: Multi-disciplinary assessment of subsidence in the Ravenna area*, pp. 35–51. Rotterdam, the Netherlands: Millpress.

Jackson, R. B., Pearson, B. R., Osborn, S. G., Warner, N. R. & Vengosh, A. (2011). *Research and policy recommendations for hydraulic fracturing and shale extraction*. Durham, NC, USA: Center on Global Change, Duke University.

Johnson, K. L. (1970). The correlation of indentation experiments. *J. Mech. Phys. Solids* **18**, No. 2, 115–126.

Lin, Q. & Labuz, J. (2011). Process-zone length from image analysis. *Proc. 45th US Rock Mech./Geomech. Symp. 2011, San Francisco, CA*, vol. 2, pp. 400–406. Red Hook, NY, USA: Curran Associates.

Loret, B., Hueckel, T. & Gajo, A. (2002). Chemo-mechanical coupling in saturated porous media: elastic–plastic behaviour of homoionic expansive clays. *Int. J. Solids Structs* **39**, No. 10, 2773–2806.

Mróz, Z. & Kwaszczyńska, K. (1971). Certain boundary value problems for pulverized media with density hardening. *Engng Trans*. **19**, No. 1, 15–42 (in Polish).

Ostapenko, G. T. (1968). Recrystallization of minerals under stress. *Geochem. Int*. **5**, 183–186.

Ostapenko, G. T. (1975). Theories of local and absolute chemical potential, their experimental testing and application of the phase rule to the systems with nonhydrostatically stressed solid phases. *Geochem Int*. **11**, 355–389.

Portier, S. & Vuataz, F. D. (2010). Developing the ability to model acid–rock interactions and mineral dissolution during the RMA stimulation test performed at the Soultz-sous-Forêts EGS site, France. *Comptes Rendus Geosci*. **342**, No. 7–8, 668–675.

Rahman, M. M. (2008). Constrained hydraulic fracture optimization improves recovery from low permeable oil reservoirs. *Energy Sources, Part A* **30**, No. 6, 536–551.

Tada, R., Maliva, R. & Siever, R. (1987). A new mechanism for pressure solution in porous quartzose sandstone. *Geochim. Cosmochim. Acta*. **51**, No. 9, 2295–2301.

Wahid, A. S., Gajo, A. & Di Maggio, R. (2011). Chemo-mechanical effects in kaolinite. Part 2: exposed samples and chemical and phase analyses. *Géotechnique* **61**, No. 6, 449–457, http://dx.doi.org/10.1680/geot.8.P.068.

Zhao, Y., Duan, X. K., Hu, L. B., Cui, P. & Hueckel, T. (2011). Multi-scale chemo-mechanical analysis of the slip surface of landslides in the Three Gorges, China. *Sci. China Ser. E: Technol. Sci*. **54**, No. 7, 1757–1765.

Zimmermann, G., Blöcher, G., Reinicke, A. & Brandt, W. (2011). Rock specific hydraulic fracturing and matrix acidizing to enhance a geothermal system – concepts and field results. *Tectonophysics* **503**, No. 1–2, 146–154.

Masoudian, M. S. *et al.* (2013). *Géotechnique* **63**, No. 3, 235–243 [http://dx.doi.org/10.1680/geot.SIP13.P.026]

A chemo-poro-mechanical model for sequestration of carbon dioxide in coalbeds

M. S. MASOUDIAN*, D. W. AIREY* and A. EL-ZEIN*

To reduce the emissions of carbon dioxide into the atmosphere, it is proposed to inject anthropogenic carbon dioxide into deep geological formations. Deep, unmineable coalbeds are considered to be a possible carbon dioxide repository because coal is able to adsorb a large amount of carbon dioxide inside its microporous structure. However, the response of coalbeds is complex because of coupling between the flow and mechanical responses. Injection of carbon dioxide causes coal to swell, which leads to reductions in permeability and hence makes injection more difficult, and at the same time leads to changes in the mechanical properties that can affect the stress state in the coal and overlying strata. Apart from the influence of swelling on permeability, the chemo-mechanical aspects of carbon dioxide sequestration in coalbeds have been little studied. In this paper, the results of a series of triaxial tests on a bituminous coal are presented that show a reduction in elastic modulus as a result of carbon dioxide adsorption. Using these experimental results, a linear relationship between the reduction in elastic modulus and the amount of adsorbed gas was found. This relationship, in conjunction with a dual-porosity model, has been employed to simulate the hydromechanical response of a coal bed to carbon dioxide injection. The results of the numerical simulation show that the softening of the coal can change the permeability and stresses in the coal, and suggest that considering the softening effect is crucial for accurate assessment of the performance and safety of carbon dioxide storage in coalbeds.

KEYWORDS: laboratory tests; numerical modelling; permeability; rock/rock mechanics

INTRODUCTION

To reduce the emissions of anthropogenic greenhouse gases into the atmosphere, it has been proposed that carbon dioxide be stored in deep geological formations such as coalbeds. Coalbeds are favourable because the methane they contain can be displaced by injecting carbon dioxide, and if captured, this can partly offset the sequestration expenses. This process is known as carbon-dioxide-enhanced coalbed methane recovery (ECBM). A number of studies have demonstrated the economic feasibility of carbon dioxide sequestration in coalbeds (Gentzis, 2000), and demonstration projects have been undertaken in the USA, Europe and Asia to investigate its technical feasibility (e.g. Reeves, 2001; Yamaguchi *et al.*, 2006; Wong *et al.*, 2007; Botnen *et al.*, 2009). However, large-scale projects have not commenced, partly because of insufficient understanding of the coalbed response to carbon dioxide injection, especially in the long term.

Coal is an organic sedimentary rock that has a polymeric structure composed of varying amounts of carbon, hydrogen and other elements, including mineral matter (Ward & Suárez-Ruiz, 2008). Coal is generally considered to be a dual-porosity medium (Fig. 1) that contains fractures, also known as cleats, and matrix blocks (Harris & Yust, 1976; Pashin, 2008). The cleats provide the large-scale porosity of coal, and the matrix contains smaller micropores.

In coalbed geosequestration, carbon dioxide is injected into deep coal seams. The gas flows through the cleats, a process that is usually described by Darcy's law (Pashin, 2008), and diffuses into the microporous matrix, where it is absorbed by the coal matrix, and this is where the major part of the stored gas resides (Parkash & Chakrabartty, 1986). The diffusion process is usually described by Fick's law and the adsorption by an isotherm such as Langmuir's.

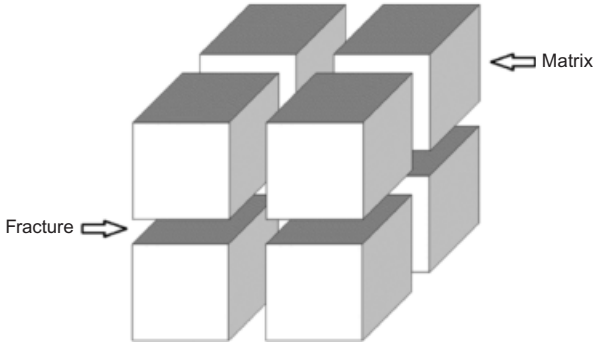

Fig. 1. Idealised representation of coal as a dual porous medium

The adsorption of carbon dioxide is accompanied by changes in volume of the coal matrix – that is, coal swelling. Some authors explain this process by the plasticising effect of the carbon dioxide causing a shortening of the polymer chains and a partial breakdown of the coal structure (Larsen, 2004). Other authors simply consider the substitution of carbon dioxide molecules in the nanoporous structure to be responsible (Vandamme *et al.*, 2010; Hol *et al.*, 2012), while again others consider changes in surface energy (Pan & Connell, 2007). As the coal matrix swells, it reduces the cleat aperture and hence the permeability of the coal. Swelling is also a concern because it can lead to stress changes in the sealing (low permeability) cap rock, possibly inducing fractures and flow paths for the gas to return to the surface. Many studies have investigated the swelling of the coal matrix (e.g. Walker *et al.*, 1988; Day *et al.*, 2008) and its

Manuscript received 5 May 2012; revised manuscript accepted 8 October 2012.
Discussion on this paper closes on 1 August 2013, for further details see p. ii.
* Centre for Geotechnical Research, University of Sydney, Darlington, Australia.

effect on the cleat permeability (Viete & Ranjith, 2006; Mazumder & Wolf, 2008), and various models have been proposed (e.g. Palmer & Mansoori, 1996; Shi & Durucan, 2004; Liu & Rutqvist, 2010). It is believed that coal swelling is responsible for the large decreases in measured carbon dioxide injection rates with time in trial ECBM projects in the USA (Reeves, 2001; Botnen *et al.*, 2009), Japan (Reeves, 2001) and Poland (Van Bergen *et al.*, 2006).

In addition to matrix swelling, the adsorption of carbon dioxide has also caused accompanying reductions in stiffness (Viete & Ranjith, 2006; Hol *et al.*, 2011) and strength (Viete & Ranjith, 2006; Masoudian *et al.*, 2011; Perera, 2011; Wang *et al.*, 2011). However, the results of Ates & Barron (1988) have been shown to be inconclusive on the topic of strength reductions. These reductions can be significant, with Perera (2011) reporting reductions of the elastic modulus of a black coal from 3·7 GPa to 1·1 GPa as the carbon dioxide saturation pressure was increased from 0 to 8 MPa. However, these large reductions were measured from unconfined compressive strength (UCS) tests, whereas in a test when a confining stress of 10 MPa was applied the reduction in stiffness was less (Viete & Ranjith, 2007). Although the reductions in stiffness and strength were observed in various studies, there are few data on the magnitude of this effect for different coals. or on the influence of confining stress, and the tests described in this paper have been conducted to address this deficiency. In addition, the effect of confining stress on the diffusivity and adsorption has received little study, with Hol *et al.* (2011) suggesting that adsorption decreases with increasing confining stress, as later explained and modelled by Hol *et al.* (2012).

From the preceding discussion, it is apparent that numerical models for reservoir simulation studies need a coupled hydro-mechanical code to capture the important features of the response of coalbeds to carbon dioxide injection. Various strategies have been employed to capture the coupling in previous numerical studies of coal seam reservoirs, as shown in Table 1. Although these studies have employed some coupling between the chemical, hydraulic and mechanical effects, they have all made simplifying assumptions about the transfer of gas between the fractures and the matrix, and in none of these analyses were the changes to the stiffness considered.

This paper presents the results of a series of triaxial compression tests showing the effect of carbon dioxide adsorption on the mechanical properties of coal, and introduces a chemo-hydro-elastic model in which the experimental results are implemented. The numerical model used in this paper employs a recent dual-porosity model (Connell & Lu, 2007; Lu & Connell, 2007, 2011) that employs a fully transient fracture–matrix transfer function to estimate the gas transport in both fractures and the coal matrix. The model includes the effects of strain on fluid flow, the effects of stress on permeability, and the softening effect of carbon dioxide on the elasticity of coal. The results of a numerical simulation of carbon dioxide injection into a coal layer are presented to demonstrate the effects of the modulus reduction on the flow and stress changes.

EXPERIMENTAL OBSERVATIONS

In this paper, the results of a series of triaxial tests on specimens of black coal are reported to show the influence of saturation with carbon dioxide on the mechanical response. These results are then used to develop a model that accounts for the effect of carbon dioxide adsorption on the elastic modulus of coal.

Experimental procedure

Specimens with a diameter of 25 mm and a height-to-diameter ratio of 2 were cored from blocks of bituminous black coal obtained from the stockpile of a mine in the Sydney Basin. The specimens had dry densities of 1·23–1·41 g/cm^3 (mean 1·29 g/cm^3) and porosities of 6·8–21·1% (mean 14·9%), determined by the water displacement method. Only specimens that appeared to be homogeneous and contained no cleats were used for the triaxial tests. The triaxial tests were performed using a standard soil mechanics cell mounted in a 70 kN load frame in a room with a controlled temperature (22°C). Water pressure inside the triaxial cell was provided from a GDS pressure controller, which could also measure volume changes during carbon dioxide saturation. Thirty-three triaxial tests were carried out with confining stresses up to 2·5 MPa. Water-saturated specimens were prepared by first permeating the air-dry coal specimen with water, followed by the use of an elevated back-pressure to ensure saturation before isotropic compression to the desired stress level. The carbon-dioxide-saturated specimens were prepared by isotropic compression of the air-dry coal to the desired stress level, and then by permeation with carbon dioxide. During permeation, the carbon dioxide injection pressure was chosen to be the same as the confining pressure, while the other end of the specimen was open to the atmosphere. The carbon-dioxide-saturated samples were exposed to carbon dioxide for at least 72 h, by which time volume changes had ceased. Shearing commenced after closing the gas injection tap, and specimens were loaded to failure with a strain rate of 0·01 mm/min, with the drain line open to the atmosphere. To ensure fully drained conditions during shearing, the loading was paused in two tests, and no significant change in the applied load was observed; then the tests were resumed. A schematic illustration of the experimental set-up is shown in Fig. 2.

Experimental results

Typical results from the shearing stage of the triaxial tests are shown in Fig. 3(a). The initially soft responses are related to end effects, but otherwise the responses are very linear until close to failure, and elastic moduli have been determined from the linear portion of the responses. When the results from all 33 triaxial specimens are considered together, as illustrated in Fig. 3(b), it is evident that the elastic moduli of the carbon-dioxide-saturated specimens are lower than those of the water-saturated samples. There is considerable scatter in the data for both the water- and

Table 1. Recent coupled hydromechanical models for gas transport in coalbeds

References	Effect of strain on fluid flow	Matrix–fracture transfer function	Swelling/permeability	Softening effect	Main feature/objective
Connell (2009) Connell & Detournay (2009)	No	Pseudo-steady state	Yes	No	Improving permeability predictions
Liu & Smirnov (2009)	Yes	Pseudo-steady state	Yes	No	Coupled response of coalbed
Wei & Zhang (2010)	Yes	Pseudo-steady state	Yes	No	Coupled response of coalbed
Wu *et al.* (2010)	Yes	Pseudo-steady state	Yes	No	Dual poro-elastic model for permeability

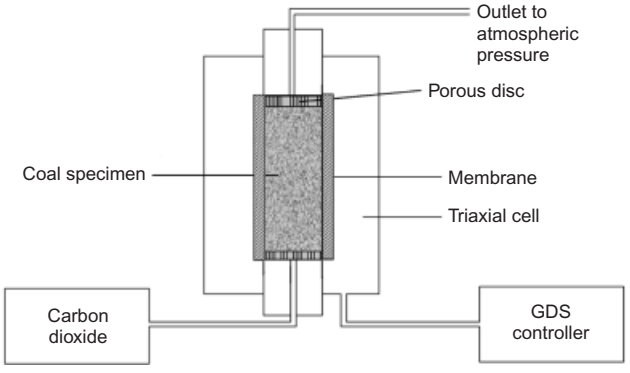

Fig. 2. Schematic illustration of the experimental set-up used

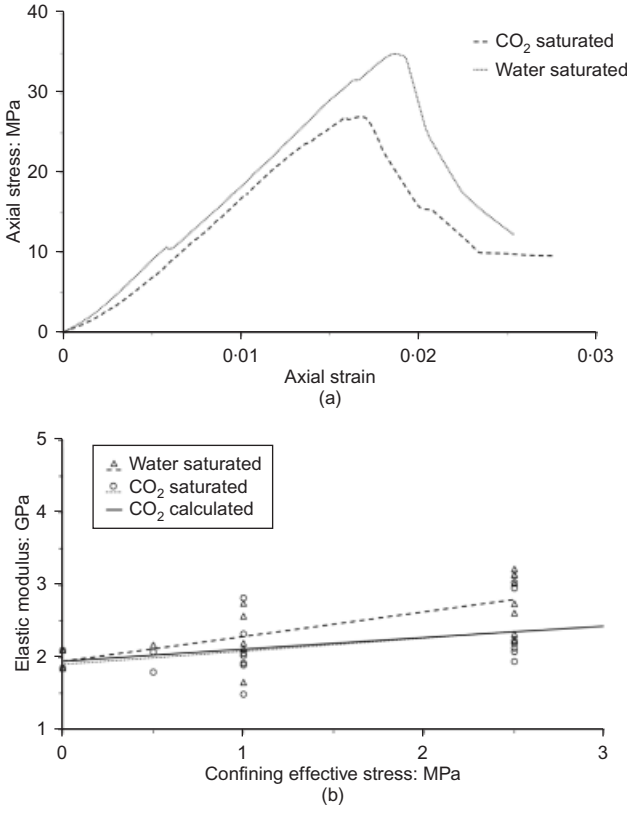

Fig. 3. (a) Typical deviator stress–axial strain curves for black coal ($\sigma'_c = 1$ MPa); (b) elastic modulus of water- and carbon-dioxide-saturated coal specimens

carbon-dioxide-saturated specimens, which is primarily a consequence of the natural variability of the coal. It is possible that very small cleats could have influenced the scatter, but care was used in selecting specimens that were visually cleat free, and this is not believed to have significantly affected the results. These results are consistent with previous studies in showing a reduction in modulus for carbon-dioxide-saturated specimens, and previous studies have also shown that there is little difference between the moduli measured for specimens that have been oven-dried, saturated with nitrogen, and saturated with water (Viete & Ranjith, 2007; Masoudian *et al.*, 2011). It may also be noted from Fig. 3(a) that there is a reduction in strength for the carbon-dioxide-saturated specimen, and this reduction increased with carbon dioxide saturation pressure in a similar manner to the modulus.

As discussed above, the cause of the swelling and change of the coal mechanical properties is believed to result from the damaging plasticising effect that carbon dioxide saturation has on the polymeric structure of coal (Larsen, 2004). Carbon dioxide is a known plasticiser, being used in the polymer industry to increase the fluidity of several polymers (Tomasko *et al.*, 2003). Fig. 4 shows typical scanning electron microscope pictures of the coal before and after saturation with carbon dioxide. It is clear from Fig. 4 that there has been a significant change in the appearance of the coal, and the well-defined structure of the water-saturated specimen is not as clearly evident in the carbon-dioxide-saturated specimen. Larsen (2004) has explained that coal has a chemical structure similar to that observed in short-chain polymers. Carbon dioxide acts as a plasticiser, shortening the polymer chain length and reducing the entanglement of the polymer chains, thus reducing the resistance to deformation so that the modulus reduces. This process also reduces the strength, which is a function of the degree of entanglement of the polymer chains. It has also been suggested that the process of adsorption of carbon dioxide molecules on the surface of the coal releases energy, which stimulates the partial breakdown of the macromolecular structure, allowing the coal to reach a state with higher entropy or lower internal energy, and this can be related to the swelling effect (Pan & Connell, 2007).

Elastic modulus reduction model

As shown earlier in Fig. 3(b), the elastic modulus of coal decreases when it is saturated with carbon dioxide. To simplify the modelling, we consider a linear relationship

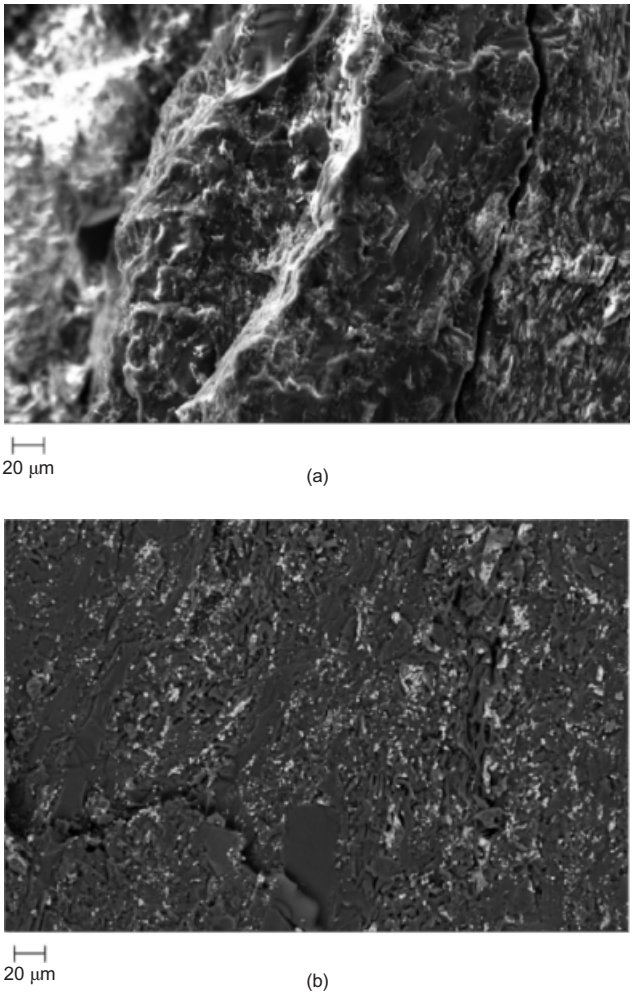

Fig. 4. Scanning electon microscope images of coal (a) before and (b) after carbon dioxide saturation

between the concentration of adsorbed carbon dioxide and the change in the properties. In order to determine this, a model to estimate the amount of adsorbed gas is required. The most widely used adsorption model is the Langmuir model for ideal gases, which is described by

$$\varsigma^{s} = \frac{\varsigma_M P}{P_L + P} \tag{1}$$

where ς^{s} is the adsorbed volume of gas per unit mass of coal; ς_M is a constant that represents the maximum monolayer adsorption volume; P is the gas pressure; and P_L is the Langmuir pressure, the pressure at which the adsorbed volume of gas is half of the maximum monolayer adsorption. Previous studies of the adsorption of carbon dioxide on black coals from the Sydney Basin (Saghafi *et al.*, 2007) have shown that the Langmuir model provides a reasonable fit to the experimental data from adsorption tests. Saghafi *et al.* (2007) have reported a range of values for P_L, and we choose a value of 3·0 MPa, which is within their reported range. Using this value, the amount of adsorbed gas can be estimated from equation (1). If this is then combined with an assumed linear relationship between carbon dioxide concentration and the elastic modulus of the coal, the effect of carbon dioxide on the modulus can then be evaluated according to

$$\frac{E_{CO_2}}{E_{water}} = 1 - \lambda \frac{\varsigma^{s}}{\varsigma_M} \tag{2}$$

where λ is a dimensionless coefficient that could be expected to vary with coal type or rank. Substituting equation (1) into equation (2) gives the final equation for the elastic modulus reduction due to carbon dioxide adsorption as

$$\frac{E_{CO_2}}{E_{water}} = 1 - \lambda \frac{P}{P_L + P} \tag{3}$$

As explained earlier, the gas injection pressure, P_i, was the same as the confining stress in the experiments. However, the discharge valve was open to atmospheric pressure during the saturation time, and therefore, if we assume that the gas pressure throughout the height of the coal sample is linear, the average pressure in the specimen can be assumed to be half of the injection pressure. Knowing this, the gas pressure can be replaced by half of the injection pressure, P_i, which leads to

$$\frac{E_{CO_2}}{E_{water}} = 1 - \lambda \frac{0{\cdot}5P_i}{P_L + 0{\cdot}5P_i} \tag{4}$$

The difference between the best-fit lines to the data presented in Fig. 3(b) can be described by equation (3) using a value of 0·54 for λ. In fact, λ is a parameter that represents the maximum possible reduction in elastic modulus due to carbon dioxide adsorption. In other words, when ς^{s} is equal to ς_M, the value of the elastic modulus decreases by 54%.

It should be noted that Fig. 3(b) shows that the reduction in modulus increases with confining pressure up to the maximum gas pressure used in these experiments of 3·0 MPa. However, the in situ stresses and gas pressures at underground formations suitable for sequestration purposes are likely to be significantly greater than 3 MPa. Nevertheless, it has been shown by Perera (2011) that the stiffness continues to decrease, approximately linearly, for carbon dioxide saturation pressures up to 10 MPa, and thus it is reasonable to expect that equation (3) can apply for higher gas pressures. Further tests covering a wider range of carbon dioxide saturation pressures, as well as a wider range of confining stresses, are required to confirm its reliability and applicability.

MODELLING APPROACH

To formulate the coupled chemo-hydro-elastic model, several assumptions are invoked, as listed below.

(*a*) The fluid contains only one phase and component, which is carbon dioxide.
(*b*) The flow of gas inside the fractures is a bulk flow, which is described by Darcy's law.
(*c*) The gas is assumed to be slightly compressible, and its viscosity is constant.
(*d*) The movement of gas inside the matrix blocks is assumed to be driven by the gradient of concentration, and is described by Fick's law.
(*e*) The temperature remains constant during carbon dioxide injection.
(*f*) Coal is a homogeneous, isotropic elastic continuum.
(*g*) The elastic modulus of the coal is a linear function of the amount of adsorbed gas according to equation (2), where the value of λ is assumed to be 0·54.

Gas flow in coal

With the assumptions described earlier, and following the basic flow equation in poroelasticity (Detournay & Cheng, 1993), the flow of gas in the dual porous structure of coal can be written as

$$\frac{\partial P(t, X_f)}{\partial t} - \frac{k_f}{\phi_f \mu_f c_f} \nabla^2 P(t, X_f) = \frac{Q(t, X_f)}{\phi_f c_f \rho_{f0} \{1 + [c_f P(t, X_f) - P_0]\}} - \frac{\alpha}{\phi_f c_f} \frac{\partial \varepsilon_v(t, X_f)}{\partial t} \tag{5}$$

where ϕ_f is the fracture porosity of coal; k_f is the absolute permeability of the fracture continuum; c_f is the total compressibility of fractures and the fluid within them; α is the Biot coefficient; μ_f is the dynamic viscosity of the fluid; ρ_f is the density of the fluid within fractures; ρ_{f0} is the density of the fluid at the reference pressure, P_0; t represents the time; X_f represents the position in the fracture continuum; and ∇^2 is the Laplacian operator. Note that X_f can be in any arbitrary system of coordinates, and in this paper a cylindrical system is used. In addition, there are three parameters that are defined as functions of time and position: P represents the pressure of gas in the fractures; Q is the matrix–fracture transfer function, which defines the amount of gas transferred into the matrix blocks; and ε_v is the volumetric strain. Note that the second term on the right-hand side of this equation is the expression that couples the fluid flow to mechanical deformation of the coal seam.

The matrix–fracture function, Q, represents the dual-porosity effect. In order to evaluate this function, Fick's law needs to be solved alongside the boundary and initial conditions.

$$\begin{aligned} \frac{\partial \varsigma(t, X_m, X_f)}{\partial t} &= D_m \nabla^2 \varsigma(t, X_m, X_f) \\ \left.\frac{\partial \varsigma(t, X_m, X_f)}{\partial X_m}\right|_{centroid} &= 0 \\ \varsigma(t, X_m, X_f)|_{outer\ boundary} &= \varsigma^{s}[P(t, X_f)] \\ \varsigma(t, X_m, X_f)|_{t=0} &= 0 \end{aligned} \tag{6}$$

where D_m is the effective diffusion coefficient of gas in a coal matrix block; ς is the concentration of gas at any point

inside the matrix block; ς^s is the equilibrium amount of gas at $P(t, X_f)$, which is determined by the Langmuir adsorption isotherm (equation (1)); and X_m is the position inside the matrix blocks, which can be in any arbitrary system of coordinates, regardless of the chosen system of coordinates in the fractures. Assuming that the adsorption on the external surface of the matrix blocks is instantaneous, the adsorption isotherm can provide a boundary condition for this equation. Lu & Connell (2007) applied an analytical solution for the concentration, ς, inside the matrix block. The concentration inside the matrix block can be related to Q, and then the matrix–fracture transfer function for a rectangular isotropic matrix block can be obtained (Lu & Connell, 2011) as

$$\begin{aligned} Q(t, X_f) = & -\frac{8}{\pi^2}\sum_{m=1}^{\infty}\sum_{n=1}^{\infty}\sum_{p=1}^{\infty}\frac{H_s^2(m, n, p)\times D_m}{(mnp)^2} \\ & \times\left(\frac{m^2}{l_x^2}+\frac{n^2}{l_y^2}+\frac{p^2}{l_z^2}\right) \\ & \times\int_0^t e^{-D_m\left(m^2/l_x^2+n^2/l_y^2+p^2/l_z^2\right)}\frac{\partial\varsigma^s(t, X_f)}{\partial\iota}d\iota \end{aligned} \tag{7}$$

where l_x, l_y, l_z are the side lengths of the rectangular blocks in the x, y and z directions respectively, and

$$\begin{aligned} H_s(m, n, p) = & [1-\cos(m\pi)]\times[1-\cos(n\pi)] \\ & \times\left[1-\cos(p\pi)\right] \end{aligned} \tag{8}$$

Also, ς^s is the equilibrium amount of gas at the pressure $P(t, X_f)$, and is determined by an adsorption isotherm, which is Langmuir's isotherm (equation (1)) in this paper. Substituting equation (5) into equation (7) gives

$$\begin{aligned} & \frac{\partial P(t, X_f)}{\partial t}-\frac{k_f}{\phi_f\mu_f c_f}\nabla^2 P(t, X_f) = -\frac{\alpha}{\phi_f c_f} \\ & \times\frac{\partial\varepsilon_v(t, X_f)}{\partial t}-\frac{1}{\phi_f c_f\rho_{f0}\left\{1+[c_f P(t, X_f)-P_0]\right\}} \\ & \times\frac{8}{\pi^2}\sum_{m=1}^{\infty}\sum_{n=1}^{\infty}\sum_{p=1}^{\infty}\frac{H_s^2(m, n, p)\times D_m}{(mnp)^2}\times\left(\frac{m^2}{l_x^2}+\frac{n^2}{l_y^2}+\frac{p^2}{l_z^2}\right) \\ & \times\int_0^t e^{-D_m\left(m^2/l_x^2+n^2/l_y^2+p^2/l_z^2\right)}\frac{\partial\varsigma^s(t, X_f)}{\partial\iota}d\iota \end{aligned} \tag{9}$$

Equation (9) is the equation that needs to be solved numerically to simulate the flow of gas in the coal seam.

Chemoelasticity of coal

The elastic constitutive equations used in this paper are expressed in rate form, and relate the strain to stress and the concentration of adsorbed carbon dioxide. The strain rate can be decomposed into a mechanical part, $\dot{\varepsilon}^m$, and a chemical (sorption) part, $\dot{\varepsilon}^s$.

$$\dot{\varepsilon} = \dot{\varepsilon}^m + \dot{\varepsilon}^s \tag{10}$$

Assuming that the stiffness of the coal is constant during small time steps, the relationship between effective stress, $\dot{\sigma}$, and mechanical elastic strain is given by

$$[\dot{\sigma}] = [D^e]\times[\dot{\varepsilon}] \tag{11}$$

where $[D^e]$ is the stiffness tensor. The assumption of constant elastic modulus is unrealistic, but it has been adopted for simplicity, and because the experimental observations suggest it is not unreasonable if the increments of analysis are small enough. However, the value of elastic modulus is updated anyway, using equation (2), during the analysis. Now the stress–strain equation can be written in an incremental form, following the approach used by Shi & Durucan (2004), where the chemical strains can be also included in the stress–strain formulation. This leads to the following expanded form in cylindrical coordinates.

$$\begin{aligned} \bar{\sigma}_{rr}-\alpha\bar{P} &= \frac{E}{(1+\nu)(1-2\nu)}\left[(1-\nu)\bar{\varepsilon}_{rr}^m+\nu\left(\bar{\varepsilon}_{\theta\theta}^m+\bar{\varepsilon}_{zz}^m\right)\right] \\ &\quad +\frac{E}{1-2\nu}\bar{\varepsilon}_{rr}^s \\ \bar{\sigma}_{\theta\theta}-\alpha\bar{P} &= \frac{E}{(1+\nu)(1-2\nu)}\left[(1-\nu)\bar{\varepsilon}_{\theta\theta}^m+\nu\left(\bar{\varepsilon}_{rr}^m+\bar{\varepsilon}_{zz}^m\right)\right] \\ &\quad +\frac{E}{1-2\nu}\bar{\varepsilon}_{\theta\theta}^s \\ \bar{\sigma}_{zz}-\alpha\bar{P} &= \frac{E}{(1+\nu)(1-2\nu)}\left[(1-\nu)\bar{\varepsilon}_{zz}^m+\nu\left(\bar{\varepsilon}_{\theta\theta}^m+\bar{\varepsilon}_{rr}^m\right)\right] \\ &\quad +\frac{E}{1-2\nu}\bar{\varepsilon}_{zz}^s \end{aligned} \tag{12}$$

where E is the elastic modulus and ν is Poisson's ratio. By assuming an isotropic sorption strain ($\bar{\varepsilon}_{rr}^s=\bar{\varepsilon}_{\theta\theta}^s=\bar{\varepsilon}_{zz}^s=\bar{\varepsilon}_v^s/3$) and uniaxial strain conditions ($\bar{\varepsilon}_{rr}^m=\bar{\varepsilon}_{\theta\theta}^m=0$), the equation below is obtained.

$$\begin{aligned} \bar{\sigma}_{rr}-\alpha\bar{P} &= \bar{\sigma}_{\theta\theta}-\alpha\bar{P} \\ &= \frac{\nu}{1-\nu}(\bar{\sigma}_{zz}-\alpha\bar{P})+\frac{E}{3(1-\nu)}\bar{\varepsilon}_v^s \end{aligned} \tag{13}$$

If we assume that total vertical stress is constant during carbon dioxide sequestration ($\bar{\sigma}_{zz}=\bar{\sigma}_{zz}^e+\alpha\bar{P}=0$), this reduces to the Shi & Durucan (2004) expression

$$\bar{\sigma}_{rr}=\bar{\sigma}_{\theta\theta}=\frac{1-2\nu}{1-\nu}\alpha\bar{P}+\frac{E}{3(1-\nu)}\bar{\varepsilon}_v^s \tag{14}$$

Thus, the change in effective stress is

$$\bar{\sigma}_{rr}^e=\bar{\sigma}_{\theta\theta}^e=-\frac{\nu}{1-\nu}\alpha\bar{P}+\frac{E}{3(1-\nu)}\bar{\varepsilon}_v^s \tag{15}$$

Note that sorption strain has a maximum of ε_{max}^s, and is assumed to be a linear function of the average concentration of adsorbed gas, ς^{avg}, as

$$\varepsilon_v^s=\varepsilon_{max}^s\frac{\varsigma^{avg}}{\varsigma_m} \tag{16}$$

Now the incremental change in vertical strain can be expressed by

$$\begin{aligned} \bar{\varepsilon}_v &= \bar{\varepsilon}_{zz}=\bar{\varepsilon}_{zz}^m+\bar{\varepsilon}_{zz}^s \\ &= \frac{1}{E}\left[-\nu(\bar{\sigma}_{rr}+\bar{\sigma}_{\theta\theta})-(1-2\nu)\alpha\bar{P}\right] \end{aligned} \tag{17}$$

Permeability of coal

Owing to adsorption-induced swelling, the fracture porosity decreases, and as a result the permeability of the fracture decreases. In this paper, the permeability model is similar to the one developed by Shi & Durucan (2004,) and therefore the change in porosity and permeability in each increment

of analysis can be evaluated using the incremental change in horizontal effective stress.

$$k_2 = k_1 \exp\left(-3c_f \bar{\sigma}^e_{rr}\right) \quad (18)$$

$$\phi_2 = \phi_1 \exp\left(-c_f \bar{\sigma}^e_{rr}\right) \quad (19)$$

where subscripts 1 and 2 denote the previous and current increments of analysis.

Solution procedure

To model the chemo-hydro-mechanical processes successfully, we need to implement all the necessary equations in the numerical engine. Thus the integro-partial differential term in equation (9) is solved in each time step; then, using equations (15) and (16), the incremental change in effective stress is calculated; and then the values of porosity (equation (19)), permeability (equation (18)) and elastic modulus (equation (2)) are updated for the next time step. Note that the rate of volumetric strain at each time step is estimated using the value of incremental change in strain calculated by equations (14) and (17) divided by the value of the time step. The numerical scheme used in this paper is an implicit finite-difference method. However, solving equation (9) is not straightforward, and its solution is numerically expensive, as described by Connell & Lu (2007). On the right-hand side of the equation there is an integral term inside a triple infinite series, and at each time step it needs to be solved from time zero to the current time of the analysis. Therefore, to decrease the analysis run time, the value of the integral can be saved from time zero to the current time at each time step, and then it can be restored in the next time step; hence the integral needs to be solved only for the last time step (Lu & Connell, 2010). However, this algorithm needs a lot of memory, as three values should be saved for each spatial node, to be called for the next time step calculations.

NUMERICAL SIMULATIONS

Example description

A series of numerical simulations were conducted to model the storage of carbon dioxide in a hypothetical isolated coal seam with a thickness of 1 m. We have assumed that carbon dioxide is continuously injected into a horizontal homogeneous isotropic coal seam at a constant pressure, surrounded by impermeable rocks, through a central wellbore drilled at its centre (Fig. 5). The parameters used in this simulation are given in Table 2. Although the parameters given here do not represent a particular site, they have been chosen to be typical of deep coal seams and are in the range of values used by Shi & Durucan (2004), Connell & Detournay (2009) and Wu *et al.* (2010). To simplify, we have assumed that deformation occurs only in the vertical direction, and that the horizontal stress is initially isotropic.

Table 2. Input parameters for the numerical simulation

Parameter	Value
Coal density: kg/m^3	1400
Cleat porosity, ϕ_f	0·01
Initial intrinsic permeability, k_f: m^2	5×10^{-15}
Fracture compressibility, c_f: Pa^{-1}	$0{\cdot}5 \times 10^{-7}$
Matrix block size, $l_x = l_y = l_z$: m	0·1
Effective diffusion coefficient, D_m: m^2/s	1×10^{-10}
Maximum monolayer adsorption, ς_{max}: kg/m^3	80
Langmuir pressure, P_L: Pa	3×10^6
Maximum swelling, ε^s_{max}	0·01
Linear elastic modulus, E: Pa	3×10^9
Elastic modulus reduction factor (case 2), λ	0·54
Poisson's ratio, ν	0·35
Gas viscosity, μ_f: Pas	1×10^{-4}
Reference gas density, ρ_{f0}: kg/m^3	955·3
Reference gas pressure, P_0: Pa	7×10^6
Initial reservoir pressure: Pa	0
Gas injection rate: kg/s	5×10^{-5}
Radius of coal seam: m	100
Injection time: days	150
Numerical time step, Δt: h	0·36

Numerical results and discussion

The described model has been used to simulate carbon dioxide injection for two cases. For the first case the modulus is assumed to be constant ($\lambda = 0$), whereas in the second case the modulus is assumed to decrease with carbon dioxide adsorption, as described by equation (3) with parameter $\lambda = 0{\cdot}54$. Fig. 6 illustrates the profiles of the pressure in the coal seam during the injection period. It can be seen that the pressure in the coal seam increases as the injection continues. However, the rate with which the pressure increases is slightly different for the two studied cases. At the beginning of the injection there is not much difference between them, but after 75 days the pressure in the coal seam in the case of a constant elastic modulus is significantly higher than that for a varying elastic modulus. In both cases carbon dioxide is injected at a constant mass flow rate, but the higher injection pressure when the elastic modulus is constant occurs because the permeability is lower, as shown in Fig. 7. This is a consequence of the swelling, which leads

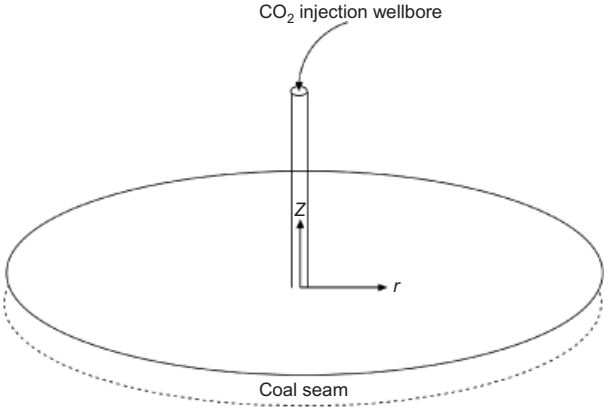

Fig. 5. Hypothetical coal seam where carbon dioxide was injected from the vertical wellbore at the centre

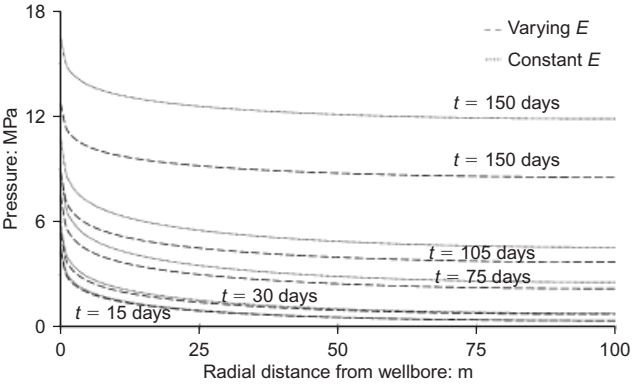

Fig. 6. Profiles of pressure in the coal seam for both cases of a constant and a varying elastic modulus

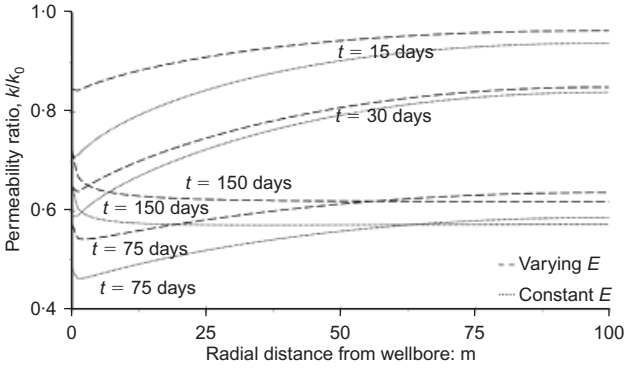

Fig. 7. Profiles of permeability in the coal seam for both cases of a constant and a varying elastic modulus

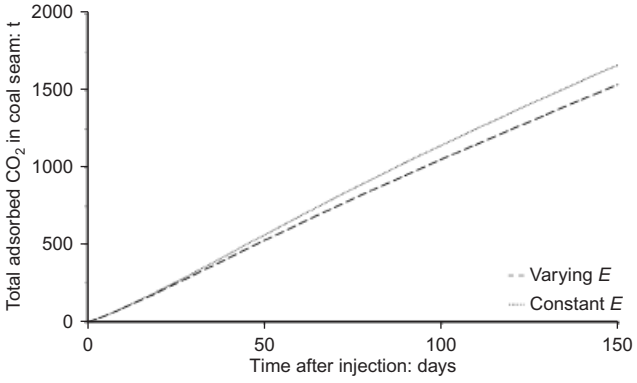

Fig. 9. Estimated amount of carbon dioxide stored in the micropores of the coal seam

to increases in effective stress and hence reductions in permeability in the cleats. When the modulus reduces, the changes in effective stress due to swelling are reduced, and therefore the reduction in permeability is reduced. Because the permeability is a function of concentration, and it takes time for the gas to reach the far boundary, the difference in the permeabilities reduces with radius for small times. It should be noted that at later times the permeability starts to increase slightly, which is due to the reducing effect of swelling.

The profiles of carbon dioxide concentration inside the matrix blocks of the coal seam are shown in Fig. 8. As explained earlier, the total amount of adsorbed carbon dioxide in the coal is proportional to the pressure in the fractures according to Langmuir's equation. Thus, the concentration of gas in the vicinity of the wellbore is higher than that in the far field. However, the evolution of concentration in the coal is much slower than that of pressure, and because of this difference, and the interrelationship between diffusion and permeation, it takes a longer time to reach the steady state when compared with a regular, single-porosity reservoir. As illustrated before, the pressure is higher when the elastic modulus is constant, and thus one can expect a higher concentration, as is shown in Fig. 8. The amount of stored carbon dioxide in the whole layer of coal is shown in Fig. 9. Note that these estimations do not take the free gas (unadsorbed carbon dioxide residing in the cleats) into account. Fig. 9 illustrates that assuming the modulus is constant is likely to result in a slight overestimation of the storage capacity of the coalbed, and this overestimation increases as injection continues.

Figure 10 shows the profiles of elastic modulus inside the coal seam for the case where the modulus changes with carbon dioxide adsorption. As the carbon dioxide is injected, the gas pressure inside the fractures increases, and hence the concentration in the coal increases. As a linear relationship

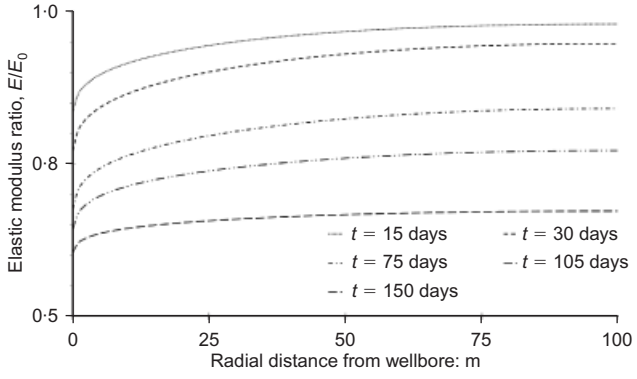

Fig. 10. Change in the elastic modulus of the coal seam due to carbon dioxide adsorption

between the change in elastic modulus and gas concentration is assumed, Fig. 10 shows, as expected, that the elastic modulus is reduced, with a maximum reduction in the vicinity of the wellbore and a minimum reduction at the outer boundary of the model, and the modulus reduction increases as the gas injection continues.

Carbon dioxide injection also alters the stress state of the coal bed. The incremental changes, between time steps, in the horizontal effective stress are shown in Fig. 11. From equation (15) it can be seen that the incremental swelling has a positive sign, while the pore pressure effect has a negative sign. As a result, swelling initially has a larger effect on the stress changes, but these reduce with time. Therefore, the incremental stress changes are initially positive, and gradually become negative as the injection proceeds. When the elastic modulus is constant, the gas pressures in the cleats are larger, and this leads to a larger

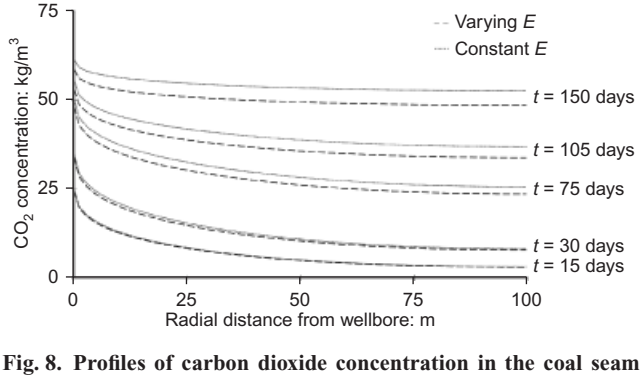

Fig. 8. Profiles of carbon dioxide concentration in the coal seam for both cases of a constant and a varying elastic modulus

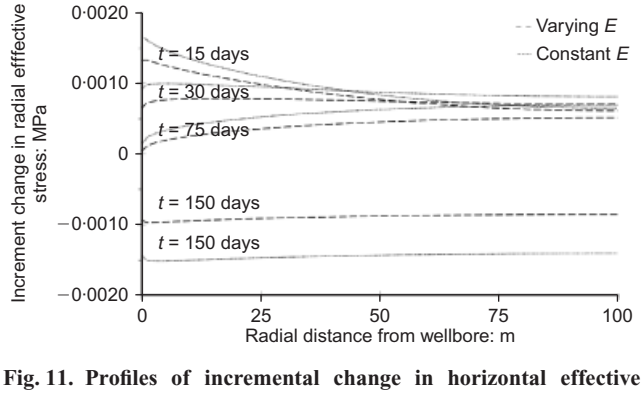

Fig. 11. Profiles of incremental change in horizontal effective stress due to carbon dioxide injection

effect of swelling. Thus, the incremental stresses are always larger for a constant modulus than for a varying modulus. At later stages, when the swelling effect is smaller, the higher pore pressure results in a more negative incremental stress in the first case, whereas in the second case the lower elastic modulus further reduces the swelling effect.

As shown in Fig. 12, the cumulative change in horizontal effective stress is increasing at the beginning, and then at some point it starts to decrease; it is shown that, after 150 days, the change in horizontal effective stress is lower than that at 75 days. Fig. 12 also shows that the horizontal effective stress is higher when the elastic modulus reduction is not considered. The profiles of change in total stress are depicted in Fig. 13, showing that they are higher if the elastic modulus is assumed to be constant. However, the total stress becomes larger as the injection continues. The vertical strain is shown in Fig. 14. The strain is lower when the elastic modulus reduction is taken into account. This is due mainly to the significantly higher pore pressure in the case of a constant elastic modulus.

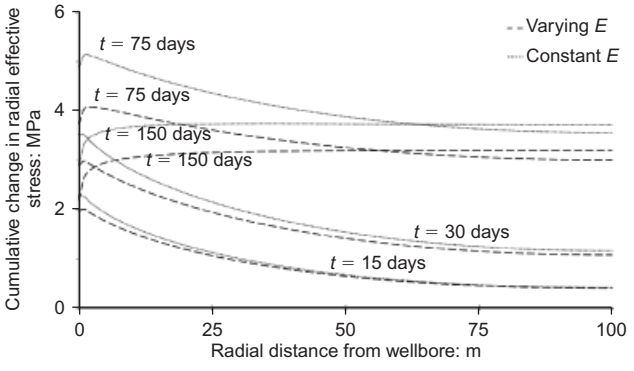

Fig. 12. Profiles of cumulative change in horizontal effective stress due to carbon dioxide injection

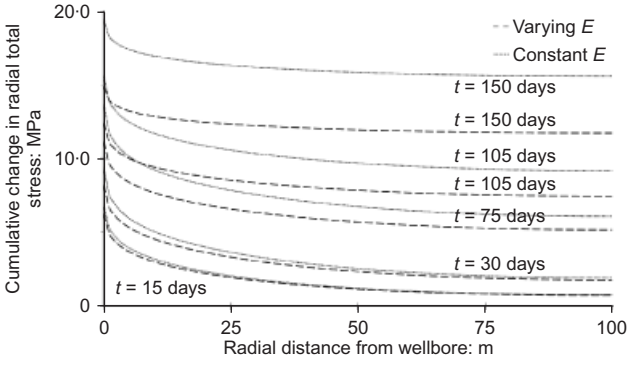

Fig. 13. Profiles of cumulative change in total horizontal stress due to carbon dioxide injection in coal seam

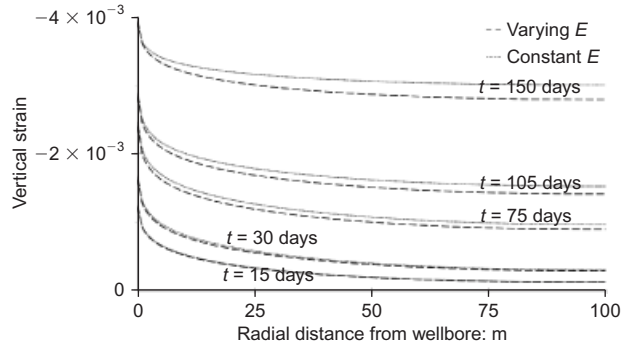

Fig. 14. Profiles of vertical strain after carbon dioxide injection in coal seam

CONCLUSION

This study has presented the results of a series of experiments on black coal that show a significant reduction in the elastic modulus of coal when carbon dioxide is adsorbed. It is shown that carbon dioxide adsorption damages the coal structure, allowing it to swell, soften and weaken. A chemo-hydro-mechanical model has been developed that considers the damaging effect of carbon dioxide on the mechanical properties of coal, and employs a dual-porosity model that can predict the fully transient flow of gas inside the coal seam with an accurate matrix–fracture function to consider the effect of gas diffusion and adsorption on the pressure distribution in the cleat system of the coalbed. A simple elastic constitutive model has been used to study the mechanical response of the coalbed. A numerical example was solved for a single coalbed to demonstrate the effects that the reduction in elastic modulus can have on the fluid flow and geomechanical behaviour of the coalbed when carbon dioxide is injected. It has been shown that the pore pressure, permeability predictions and estimated storage can be significantly different when the damaging effect of carbon dioxide on the mechanical properties is considered.

This study has demonstrated the complex interactions between coal and carbon dioxide, and has shown that coupling between the chemical, flow and mechanical properties is required to understand the process of carbon dioxide geosequestration in coal. Further studies of the effects of carbon dioxide on the mechanical properties at the stresses relevant to deep sequestration are required to improve the reliability and relevance of this study.

NOTATION

c_f	compressibility of fractures and containing fluid
$[D^e]$	tensor of elastic stiffness
D_m	effective diffusion coefficient of carbon dioxide into coal matrix
E	elastic modulus of coal
E_{CO_2}	elastic modulus of carbon dioxide-saturated coal
E_{water}	elastic modulus of water-saturated coal
H_s	cosine function of the Fourier series
k_f	fracture permeability of coal
l_x, l_y, l_z	dimensions of coal matrix blocks in x, y and z directions respectively
m, n, p	counter identifiers of triple series
P	pressure of carbon dioxide in fractures
P_i	gas injection pressure
P_L	Langmuir pressure; pressure at which absorbed carbon dioxide on coal is 50% of ς_M
P_0	reference pressure
Q	flux of gas transferred into coal matrix
t	time
X_f	position in fracture
X_m	position in coal matrix
α	Biot coefficient
$\dot{\varepsilon}$	rate of total strain
$\dot{\varepsilon}^m$	rate of mechanical strain
$\dot{\varepsilon}^s$	rate of chemical (sorption) strain
ε^s_{max}	maximum volumetric sorption strain
ε_v	volumetric strain
ι	variable of integration (time, from zero to current)
λ	elastic modulus reduction factor
μ_f	viscosity of fracture fluid
ν	Poisson's ratio
ρ_f	density of fracture fluid
ρ_{f0}	density of fracture fluid at reference pressure
$\dot{\sigma}$	rate of total stress
σ_{conf}	confining stress in triaxial tests
ς	concentration of gas at any point inside matrix block
ς^{avg}	average concentration of carbon dioxide inside coal matrix blocks

ς_M maximum monolayer adsorption of carbon dioxide on coal
ς^s concentration of absorbed carbon dioxide on surface of coal matrix
ϕ_f fracture porosity of coal
∇^2 Laplacian operator

REFERENCES

Ates, Y. & Barron, K. (1988). The effect of gas sorption on the strength of coal. *Mining Sci. Technol*. **6**, No. 3, 291–300.

Botnen, L. S., Fisher, D. W., Dobroskok, A. A., Bratton, T. R., Greaves, K. H., Mclendone, T. R., Steinerf, G., Sorensena, J. A., Steadmana, E. N. & Harjua, J. A. (2009). Field test of CO_2 injection and storage in lignite coal seam in North Dakota. *Energy Procedia* **1**, No. 1, 2013–2019.

Connell, L. D. (2009). Coupled flow and geomechanical processes during gas production from coal seams. *Int. J. Coal Geol.* **79**, No. 1–2, 18–28.

Connell, L. D. & Detournay, C. (2009). Coupled flow and geomechanical processes during enhanced coal seam methane recovery through CO_2 sequestration. *Int. J. Coal Geol*. **77**, No. 1–2, 222–233.

Connell, L. D. & Lu, M. (2007). A dual-porosity model for gas reservoir flow incorporating adsorption behaviour. Part II: Numerical algorithm and example applications. *Transp. Porous Media* **69**, No. 2, 139–158.

Day, S., Fry, R. & Sakurovs, R. (2008). Swelling of Australian coals in supercritical CO_2. *Int. J. Coal Geol*. **74**, No. 1, 41–52.

Detournay, E. & Cheng, A. H.-D. (1993). Fundamental of poroelasticity. In *Comprehensive rock engineering: Principles, practice, and projects. Vol. II, Analysis and design method* (ed. C. Fairhurst), pp. 113–171. Oxford, UK: Pergamon Press.

Gentzis, T. (2000). Subsurface sequestration of carbon dioxide: an overview from an Alberta (Canada) perspective. *Int. J. Coal Geol*. **43**, No. 1–4, 287–305.

Harris, L. A. & Yust, C. S. (1976). Transmission electron microscope observations of porosity in coal. *Fuel* **55**, No. 3, 233–236.

Hol, S., Peach, C. J. & Spiers, C. J. (2011). Applied stress reduces the CO_2 sorption capacity of coal. *Int. J. Coal Geol*. **85**, No. 1, 128–142.

Hol, S., Peach, C. J. & Spiers, C. J. (2012). Effect of 3-D stress state on adsorption of CO_2 by coal. *Int. J. Coal Geol*. **93**, No. 1, 1–15.

Larsen, J. W. (2004). The effects of dissolved CO_2 on coal structure and properties. *Int. J. Coal Geol*. **57**, No. 1, 63–70.

Liu, H. & Rutqvist, J. (2010). A new coal-permeability model: internal swelling stress and fracture–matrix interaction. *Transp. Porous Media* **82**, No. 1, 157–171.

Liu, G. & Smirnov, A. V. (2009). Carbon sequestration in coal-beds with structural deformation effects. *Energy Conv. Management* **50**, No. 6, 1586–1594.

Lu, M. & Connell, L. D. (2007). A dual-porosity model for gas reservoir flow incorporating adsorption behaviour. Part I: Theoretical development and asymptotic analyses. *Transp. Porous Media* **68**, No. 2, 153–173.

Lu, M. & Connell, L. D. (2010). Dual porosity processes in coal seam reservoirs: the effect of heterogeneity of coal matrices. *Proceedings of the SPE Asia Pacific Oil and Gas Conference and Exhibition, Brisbane*, 782–803.

Lu, M. & Connell, L. D. (2011). A statistical representation of the matrix–fracture transfer function for porous media. *Transp. Porous Media* **86**, No. 3, 777–803.

Masoudian, M. S., Airey, D. W., Gainey, A., Morris, T. & Berger, J. (2011). The mechanical properties of CO_2-saturated coal specimens. *Proc. 12th Congress of International Society for Rock Mechanics, Beijing*, 727–730.

Mazumder, S. & Wolf, K. H. (2008). Differential swelling and permeability change of coal in response to CO_2 injection for ECBM. *Int. J. Coal Geol*. **74**, No. 2, 123–138.

Palmer, I. & Mansoori, J. (1996). How permeability depends on stress and pore pressure in coalbeds: a new model. *Proc. SPE Annual Technical Conference and Exhibition, Denver, CO*, 539–544.

Pan, Z. & Connell, L. D. (2007). A theoretical model for gas adsorption-induced coal swelling. *Int. J. Coal Geol*. **69**, No. 4, 243–252.

Parkash, S. & Chakrabartty, S. K. (1986). Microporosity in Alberta Plains coals. *Int. J. Coal Geol*. **6**, No. 1, 55–70.

Pashin, J. C. (2008). Coal as a petroleum source rock and reservoir rock. In *Applied coal petrology: The role of petrology in coal utilization* (eds I. Suárez-Ruiz and J. C. Crelling), pp. 227–262. Amsterdam, the Netherlands: Elsevier/Academic Press.

Perera, M. S. A. (2011). *Investigation of the effect of carbon dioxide sequestration on the hydro-mechanical properties of coal*. PhD thesis, Monash University, Melbourne, Australia.

Reeves, S. R. (2001). Geological sequestration of CO_2 in deep, unmineable coalbeds: an integrated research and commercial-scale field demonstration project. *Proc. SPE Annual Technical Conference and Exhibition, New Orleans, LA*.

Saghafi, A., Faiz, M. & Roberts, D. (2007). CO2 storage and gas diffusivity properties of coals from Sydney Basin, Australia. *Int. J. Coal Geol*. **70**, No. 1–3, 240–254.

Shi, J. Q. & Durucan, S. (2004). Drawdown induced changes in permeability of coalbeds: a new interpretation of the reservoir response to primary recovery. *Transp. Porous Media* **56**, No. 1, 1–16.

Tomasko, D. L., Li, H., Liu, D., Han, X., Wingert, M. J., Lee, L. J. & Koelling, K. W. (2003). A review of CO_2 applications in the processing of polymers. *Ind. Engng Chem. Res*. **42**, No. 25, 6431–6456.

Van Bergen, F., Pagnier, H. & Krzystolik, P. (2006). Field experiment of enhanced coalbed methane-CO_2 in the upper Silesian basin of Poland. *Environ. Geosci*. **13**, No. 3, 201–224.

Vandamme, M., Brochard, L., Lecampion, B. & Coussy, O. (2010). Adsorption and strain: the CO_2-induced swelling of coal. *J. Mech. Phys. Solids* **58**, No. 10, 1489–1505.

Viete, D. R. & Ranjith, P. G. (2006). The effect of CO_2 on the geomechanical and permeability behaviour of brown coal: implications for coal seam CO_2 sequestration. *Int. J. Coal Geol*. **66**, No. 3, 204–216.

Viete, D. R. & Ranjith, P. G. (2007). The mechanical behaviour of coal with respect to CO_2 sequestration in deep coal seams. *Int. J. Coal Geol*. **86**, No. 17–18, 2667–2671.

Walker, P. L., Verma, S. K., Rivera-Utrilla, J. & Khan, M. R. (1988). A direct measurement of expansion in coals and macerals induced by carbon dioxide and methanol. *Fuel* **67**, No. 5, 719–726.

Wang, S., Elsworth, D. & Liu, J. (2011). Permeability evolution in fractured coal: the roles of fracture geometry and water-content. *Int. J. Coal Geol*. **87**, No. 1, 13–25.

Ward, C. R. & Suárez-Ruiz, I. (2008). Introduction to applied coal petrology. In *Applied coal petrology: The role of petrology in coal utilization* (eds I. Suárez-Ruiz and J. C. Crelling), pp. 1–18. Amsterdam, the Netherlands: Elsevier/Acadmic Press.

Wei, Z. & Zhang, D. (2010). Coupled fluid-flow and geomechanics for triple-porosity/dual-permeability modeling of coalbed methane recovery. *Int. J. Rock Mech. Mining Sci.* **47**, No. 8, 1242–1253.

Wong, S., Law, F., Deng, X., Robinson, J., Kadatz, B., Gunter, W. D., Jianping, Y., Sanil, F. & Zhiqiang, F. (2007). Enhanced coalbed methane and CO_2 storage in anthracitic coals: micro-pilot test at South Qinshui, Shanxi, China. *Int. J. Greenhouse Gas Control* **1**, No. 2, 215–222.

Wu, Y., Liu, J., Elsworth, D., Chen, Z., Connell, L. & Pan, Z. (2010). Dual poroelastic response of a coal seam to CO_2 injection. *Int. J. Greenhouse Gas Control* **4**, No. 4, 668–678.

Yamaguchi, S., Ohga, K., Fujioka, M. & Masao, N. (2006). Field test and history matching of the CO_2 sequestration project in coal seams in Japan. *Int. J. Soc. Mater. Engng Resources* **13**, No. 2, 64–69.

Guo, R. & Hueckel, T. (2013). *Géotechnique* **63**, No. 4, 322–330 [http://dx.doi.org/10.1680/geot.SIP13.P.021]

Growth of polymer microstructures between stressed silica grains: a chemo-mechanical coupling

R. GUO* and T. HUECKEL*

Laboratory tests on the micro scale are reported in which two amorphous silica cubes were compressed in a liquid environment, in solutions with different silica ion concentrations, for up to 3 weeks. Such an arrangement represents an idealised representation of two sand grains. The grain surfaces and asperities were examined in the scanning electron microscope and atomic force microscope (AFM) for fractures, silica gel growth and polymer strength. In 500 ppm solution, silica gel structures a few hundred micrometres long appeared between stressed silica cubes. In 200 ppm solution, silica deposits were found around damaged grain surfaces, while at 90 ppm (below silica solubility in neutral pH), fibres a few micrometres in length were found growing in cube cracks. AFM pulling tests found polymers with strength of the order of 100 nN. It was concluded that prolonged compression produced damage in grains, raising local silicon ion concentration and accelerating precipitation, polymerisation and gelation of silica on grain surfaces, enhancing soil strength at the micro scale, and hence most likely contributing to the ageing phenomenon observed at the macro scale.

KEYWORDS: chemical properties; particle-scale behaviour; sands; stiffness; time dependence

INTRODUCTION

Soils exhibit significant stiffening when subjected to prolonged compression at a constant load – what is known under the name of soil ageing (Mitchell & Solymar, 1984; Hueckel *et al.*, 2005).

Soil ageing occurring in silts, sands and sand–clay mixtures at the engineering timescale (hours, weeks or months; Joshi *et al.*, 1995; Hueckel *et al.*, 2001, 2005; Bowman & Soga, 2003) bears many common features with pressure solution phenomenon during diagenesis. Diagenesis is of interest in geochemistry, structural geology and petroleum engineering, and is believed traditionally to occur over geological times (Sorby, 1862; Rutter, 1976). Notably, the focus in pressure solution studies is on mineral mass transfer and on porosity and permeability evolution, rather than stiffening of the medium. In both phenomena, creep is seen as a main component of the process.

While the phenomenon has been extensively measured in the field and in the laboratory experiments, the mechanisms behind soil ageing and variables controlling it remain a subject of intense research (Baxter & Mitchell, 2004). Ageing in dry clean sand is attributed to creep or secondary consolidation of sand. It is suggested that particles continuously rearrange until stable equilibrium positions are reached under applied load and kinematic constraints (Mesri *et al.*, 1990; Schmertmann, 1991; Bowman & Soga, 2003; Wang *et al.*, 2008). The presence of fines in dry sand soils also increases creep strain and ageing rate (Wang & Tsui, 2009). The mechanical properties of granular assemblies at the macroscopic level are known to be affected by contact networks, on the one hand, and the local response of grain contact neighbourhoods on the other (Parry, 2004). In the latter case, the response is determined not only by the material itself, but also by how the grains of the material interact with each other under stress. The physical (or chemical) driving processes behind particle system rearrangement under constant load and their rates are not well known, and are hypothesised to be mostly local, interparticle processes: time-dependent interparticle friction, plastic yielding of grain asperities following a chemical reaction rate law (Eyring, 1936; Kuhn & Mitchell, 1993), capillary condensation of atmospheric moisture (Paterson & Kekulawala, 1979; Israelachvili, 2011), and plastic or visco-plastic microcracking due to indentation in the contact area (Scholz & Engelder, 1976; Tada *et al.*, 1987; Hickman & Evans, 1995; Hu & Hueckel, 2007a). However, the links between such microscopic and localised processes and possibly ensuing reconfiguration of particle chains, and then the strengthening of soil at a macro scale, while very likely, are far from being proven, as stressed by Kuhn & Mitchell (1993).

Still efforts using numerical tools to show that such hypothetical micro-scale mechanisms are consistent with the upscaled macroscopic behaviour of soils (e.g. Kuhn & Mitchell, 1993; Hu & Hueckel, 2007a).

In saturated conditions, sand exhibited a 200% (with seawater) to 220% (with distilled water) larger penetration resistance after 1 year of ageing compared with 30% larger penetration in dry conditions (Joshi *et al.*, 1995). Cohesion was also significantly larger in sand when submerged in water under constant load, compared with the same sand in dried conditions. Joshi *et al.* indicated the presence of cement bonding between grains due to dissolution and precipitation of salts, and possibly silica, as the source of the difference. Hence the mechanisms of ageing in the wet condition are not purely mechanical, but are coupled with much more significant chemical processes, such as dissolution, precipitation and possibly polymerisation and gelation of materials around the contact region (Hu & Hueckel, 2007a, 2007b). Therefore there is sufficient evidence to claim that strain and stress alone cannot alter the mechanical properties of granular materials over time to the level that they do in the presence of pore fluid. It is not known at present what the specific mechanisms of coupling are

Manuscript received 4 March 2012; revised manuscript accepted 23 October 2012.
Discussion on this paper closes on 1 August 2013, for further details see p. ii.
* Department of Civil and Environmental Engineering, Duke University, Durham, NC, USA.

between the chemical process and grain structure rearrangement, to produce such a significant overall change in the mechanical properties of soil.

In nature, the processes of dissolution and redistribution of mass in tight rocks takes time on the geological scale, such as during the formation of sandstone by the amorphous silica mass that binds the sand grains together (Worden & Morad, 2000). However, experiments at both the macro scale and the micro scale have shown that such processes can also occur on a timescale of days, weeks or months (Denisov & Reltov, 1961; Hueckel *et al.*, 2001, 2005; Meyer *et al.*, 2006; Hu & Hueckel, 2007b). Interestingly, in terms of compressibility decline monitored over 3 months, up to 85% of the change occurs in the first 2 weeks of the process (Hueckel *et al.*, 2001). A similar conclusion in terms of mass transfer was reached by Oelkers *et al.* (2008).

One of the earliest hypotheses explaining the changes in the strength of sand was put forward by Denisov & Reltov (1961), who conducted experiments indicating that the strength of the compacted submerged granular medium increases gradually, owing to the formation of silicic acid gel at the quartz surfaces in contact. On the other hand, in studies of pressure solution it was noticed that the presence of clay in the vicinity of contact substantially enhances the dissolution of quartz (Becker, 1995; Bjorkum, 1996; Kristiansen *et al.*, 2011). Much more recently, atomic force microscopy (AFM) and scanning electron microscopy (SEM) studies of the stressed silica–muscovite contact have indeed shown a silica dissolution rate almost an order of magnitude higher at room temperature and low pressure to maintain contact. This has previously been observed in sandstones in the presence of mica (Heald, 1955; Renard *et al.*, 1997). It is believed that the enhanced silica dissolution has a much higher rate, and is due to the difference in surface electrochemical potentials (Meyer *et al.*, 2006). Meyer *et al.* (2006) also revealed the development of silica gel structures in the vicinity of the stressed contact.

The present work aims at clarifying the role and conditions of formation of polymeric silica structures between synthetic silica grains, as suggested originally by Denisov & Reltov (1961), and endorsed by numerous subsequent studies. In previous work (Hu & Hueckel, 2007a) the authors have theorised a mechanism through which a granular material stiffens in submerged stressed conditions. It is the generation of microcracking near the stressed intergranular contact that constitutes a source of an increasing specific surface area of interphase interface at which dissolution of quartz occurs. This dissolution removes the mineral from the solid phase, making the material in that zone weaker and further enhancing the process of microcracking (Hueckel *et al.*, 2001). The dissolved mineral may either migrate away in the presence of advective gradients or, in their absence, when local concentrations grow sufficiently, precipitate, polymerise or gelate. Driven by these hypotheses, the grains will be brought in contact to stress conditions that are slightly below the onset of microcracks, and the system will be kept closed to any dissolved silica transport.

Specifically, this study presents preliminary findings from a set of experiments on the effect of the polymerisation of silica in the intergranular space on the bonding of one quartz grain asperity and another quartz grain during environmentally mediated indentation. The experiments included: precipitation and quantifications of silica polymerising on unstressed quartz grains; the AFM tensile strength of individual silica polymer chains; the enhancement of silica polymerisation due to stressing and damage of indenting grains; the tensile strength of intergranular silica gel bonds; the effect of the presence of muscovite mica sheet, and a lowered pH of the fluid, on gelation, polymerisation and structure formation.

The study focuses on short-timescale phenomena (2–3 weeks), seen to produce sufficient dissolution and precipitation, as well as compressibility change (Hueckel *et al.*, 2001, 2005; Meyer *et al.*, 2006; Kristiansen *et al.*, 2011). Laboratory experiments are presented where amorphous silica grains were compressed in a liquid environment rich in silicon ions for up to 3 weeks. Silica deposits and polymers observed in the stressed contact region using SEM and AFM are measured and tested mechanically.

MATERIALS AND METHODS

Silica cubes and silicic acid

The quartz grains in stressed contact were simulated using amorphous silica cubes (Figs 1(a) and 1(b)). Silica is found in both crystalline and amorphous forms in nature. Crystalline silica has long-range orders, involving a tetrahedral coordination of four oxygen atoms around a silica atom. Quartz is by far the most common crystalline form of silica, found in natural sand (Iler, 1955). Amorphous silica, on the other hand, does not have any long-range order, but a tetrahedral arrangement between oxygen and silica atoms still exists locally. The choice of amorphous silica for the test was motivated by two substantial considerations. First, the rate of dissolution of amorphous silica is about one order of magnitude greater than that of its crystalline counterpart (Iler, 1955). It appears that this would not only reduce the time of the tests, but also would lower the risk of biological contamination. Second, most quartz grains in nature, which are predominantly crystalline, are enveloped by a layer of amorphous quartz (Oelkers *et al.*, 1992). It is believed that such an envelope is generated by silica dissolved from the rock in the presence of mica (muscovite). Hence, for two grains in contact, the indentation of an asperity would penetrate first through the amorphous coating.

The silica cubes used are made of unpolished amorphous quartz (Prism Research Glass Inc.). Quartz sheets are either laser-cut into 1·5 mm × 1·5 mm × 1 mm parallelepipeds, or blade-cut in to 30 mm × 30 mm × 30 mm cubes to simulate common natural sand grain size. The laser processing of cubes has the disadvantage of producing edges that are relatively round, and of irregular length and inclination. This reduced the effectiveness of such edges as indenters.

The indenting amorphous quartz cubes are placed in a liquid environment containing an already high concentration

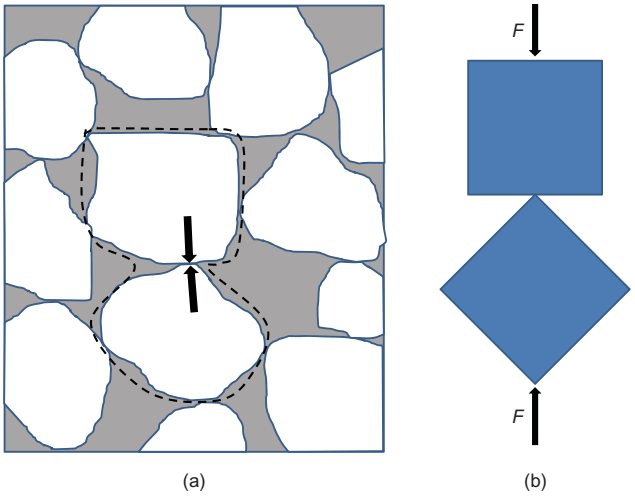

Fig. 1. Configurations of compressed cubes in nature and in laboratory setting to simulate intergranular stress: (a) 2D representation of granular material; (b) laboratory simulation of two grains in stressed contact in dotted line in (a)

of silica to accelerate precipitation. To prepare the solution to be used in the liquid chamber, silicic acid powder (H_2SiO_3; Fisher Scientific) was added to 5 M sodium hydroxide solution for complete ionisation. Solutions with different silicon ion concentrations can then be made by diluting this solution with nano-pure water. The pH value of the solution remained above 10·0 to prevent the silicon ions from precipitating and polymerising. Immediately before each experiment, 1 M nitric acid was used to lower the pH value of the solution to between 5·0 and 5·5, to simulate natural water. No glass containers were used during the experiment, to prevent extra silicon ions from glass dissolving in the solutions.

Quartz cube indenter

To simulate soil grains in compression, a quartz cube environmental indenter as constructed at Duke University by C. J. Rubin (Rubin, 2009) was used (Fig. 2). The central part of the apparatus is the sample holder, where one silica cube is placed on a platform in the liquid chamber at a 45° angle in such a way that its corner edge faces the side of the other cube held in a pincer. The liquid chamber is made of stainless steel, and is connected to a pneumatic actuator (Bimba TB-1625) by a rod, also made of stainless steel. The rod passes through an O-ring, which prevents leakage around the rod. A small pincer is screwed onto the rod in the liquid chamber, allowing the mobile silica cube to be indented with a monitored displacement into the other cube. The indentation force is recorded.

After placing two silica cubes in their respective positions, the actuator is activated, which pushes the rod forwards and presses one silica cube at the end of the rod against the other cube on the platform in the liquid chamber. The pressure in the pneumatic actuator is then gradually increased to 170 kPa to prevent sudden movement of the rod crushing the cubes. A solution containing silicon ions is immediately added to the liquid chamber, and the chamber is sealed off by Parafilm and left to mature under constant force for up to 3 weeks using a pressure controller (Norgren Excelon Pro). Details of the indenter design and characteristics can be found in Rubin (2009). Images of the contact region between cubes before and after the experiment were taken using SEM (FEI XL30 ESEM) for comparison.

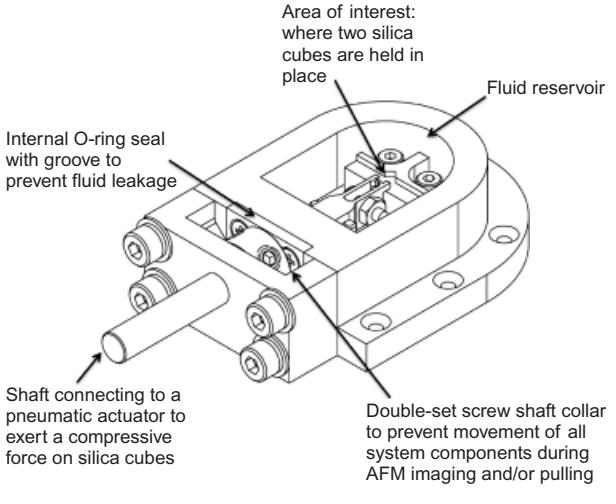

Fig. 2. Central part of pneumatic cube indentation device. Left cube sits on platform with edge pointing to the right. Right cube secured by a pincer and pushed to the left by shaft connected to pneumatic actuator (not shown). Double-set screw collar on the right prevents shaft movement during AFM imaging and/or pulling

Silica polymer strength

In another experiment, designed to measure the mechanical strength of silica micropolymer chains, an amorphous silica cube was placed in solution with a predetermined silicon ion concentration for 3 weeks. A liquid pulling experiment was conducted on the cube surface using AFM (Digital Instruments Dimension 3100) and Veeco TESP k cantilevers. The cantilever tip was repeatedly lowered onto the cube surface with silica polymers on it and then raised. If the tip has picked up a silica-polymer-linked backbone on the cube surface, raising it would straighten the polymer and cause the cantilever to bend until the polymer chain broke. The force required to break the silica polymer chain can be calculated using the recorded cantilever tip deflection and tip spring constant.

Silica gel growth in solution

Since solutions prepared for most of the cube compression experiments were supersaturated in silica, it is necessary to find the undisturbed precipitation and polymerisation rate of silica and determine the extent to which the supersaturation of silica contributes to the growth of polymers and deposits found around stressed contact regions. Part of the same solution with 300 ppm silicon ion concentration that was used to fill the liquid chamber for cube compression experiments was stored in Petri dishes and allowed to mature for silica gel growth in an undisturbed environment. Samples from the solutions were examined by AFM fluid imaging in tapping mode at various stages over 3 weeks to determine the size and growth rate of the silica gels.

Silica cube indenter-puller

An indenter-puller device was built in order to measure the tensile strength of the intergranular silica polymer (Fig. 3). The two cubes are pushed together with a layer of 10 μm mica sheet between. The force applied can be calculated by multiplying the springs' compression length with their spring constants. The spring compression can be changed by turning the four wing-nuts on the top plate. The cubes are submerged in a liquid bath with a predetermined silicon ion concentration. The whole device is then sealed in a Styrofoam box together with a wetted sponge to minimise water evaporation. A ring is inserted on the bottom plate around the cubes to create a semi-enclosed environment to help

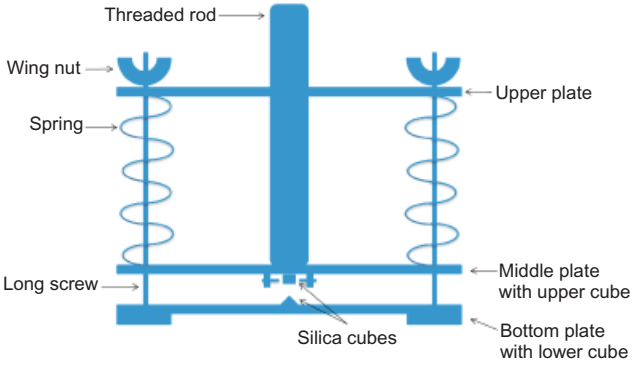

Fig. 3. Schematic of cube indenter-puller. One cube sits on bottom plate with one edge pointing upwards. Other cube clamped on middle plate by screws with flat face facing downwards. Four long screws through all three plates keep them together. Springs compressed by turning wing nuts on top plate. Long threaded rod connects middle plate to load frame during extension experiment

retain dissolved silica ions in the vicinity of the contact region. The plates and the ring are made of aluminium, and all other screws are made of stainless steel.

After 10–20 days, the device is taken out of the Styrofoam box and connected to a load frame (Tinius Olsen H50K-S) by a long threaded rod and lowered onto an analytic scale (Mettler Toledo AL204) until the reading on the scale slightly exceeds the total weight of the bottom plate and the lower cube, measured before the experiment. The upper plate, springs and screws are then removed from the device, while the cubes on the lower and middle plates are still sitting on the scale and pressed together. The load frame is then raised at a speed of 0·050 mm/min until the two cubes are completely detached from each other. The reading on the scale is captured by a video camera. Immediately before the two cubes separate, any intergranular silica polymers grown between the two cubes are stretched, and an uplifting force is created on the lower cube. Such an uplifting force lowers the reading on the analytical scale momentarily until all polymer contacts are broken and the weight on the scale returns to a constant. The intergranular mechanical force is calculated by taking the difference in mass reading recorded by the analytical scale.

Two experiments were conducted, one using a solution with 500 ppm silicon ion concentration and aged for 10 days; and the other a solution with 300 ppm silicon ion concentration and aged for 20 days. In both experiments the compression force applied to the cubes was 180 N.

Experiments in the presence of muscovite

To investigate the effect that muscovite has on the dissolution, precipitation and polymerisation of silica around the contact region, the cube indentation experiment mentioned in the 'Quartz cube indenter' section is repeated with a 10 μm highest-grade muscovite mica sheet (S&J Trading, New York) inserted between the two quartz cubes. The cubes were under 140 kPa pressure for 2 weeks in a solution with 300 ppm silicon ion concentration. SEM images of the contact region are taken at the end of the experiment.

RESULTS

Silica cubes compressed in solutions containing silicon ions

A series of tests to assess the rate of production of silica polymer were conducted at different elevated concentrations of silica ions in the environmental solution. The rationale for using an initial elevated concentration (Rubin, 2009), after finding a concentration high enough to induce polymerisation or gelation, is to bring the concentration somewhat below that level, and allow some time for sufficient dissolution from the damaged material to bring the solution to the level at which silica will polymerise. (The concentration of silica in the pore solution may be much higher locally and instantaneously near the asperities and stressed and dissolving contacts than the average pore water concentration.)

In 500 ppm silicon ion concentration solution. After two silica cubes were pressed against each other for 3 weeks in solution with 500 ppm silicon ion concentration, polymers were observed on the surfaces of both cubes in the SEM (Fig. 4). Some of the polymers connected to both cubes near the contact regions were up to several hundred micrometres long. A composition analysis of such polymers using an energy dispersive X-ray spectrometer (EDS) on the SEM showed that the structures were mostly silica, with minor traces of chlorine, chromium, iron, sodium, carbon and oxygen elements (Fig. 5). The minimal amount of carbon in the sample may come from dust in the environment, and shows that the structure is not of biological origin, otherwise carbon would be a dominant element in the polymer structure.

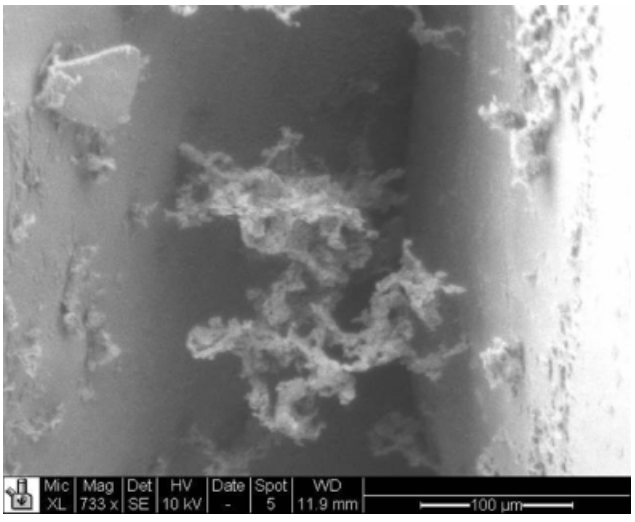

Fig. 4. SEM image of silica polymers growing around stressed contact region between two silica cubes after 3 weeks in solution with 500 ppm silicon ion concentration and neutral pH

In 300 ppm silicon ion concentration solution. A similar experiment with the same set-up, but using 300 ppm silicon ion concentration solution for 2 weeks, showed extensive silica deposits with size of the order of 10 μm developed near the asperities as a result of compression (Fig. 6(a)). The experiment was repeated with a lower pressure (120 kPa) applied to the cubes from the pneumatic actuator. It was found that no microcracks had developed on either cube, and no silica polymer deposits were found anywhere in the liquid chamber (Fig. 6(b)).

In 90 ppm silicon ion concentration solution. Polymers a few micrometres in length were found between a cube's main body and a piece of silica debris that was chipped off by compression (Fig. 7). No extensive silica deposits were found otherwise.

Comparing the size of these silica deposits with that of silica polymers found growing in solution with the same silicon ion concentration, but without compressed silica cubes in the solution, the rate of silica gel growth around the stressed contact was found to be greater than in the undisturbed solution.

AFM pulling experiments on silica cube surfaces

Undisturbed (not loaded) silica cubes left in solutions with silicon ion concentrations ranging between 130 ppm and 210 ppm for 2 weeks were put in the AFM, and pulling experiments in water were conducted on the cube surfaces. On the surfaces of the cube that was in the 210 ppm solution, distinctive kinks were consistently captured on the force curves (Figs 8(a) and 8(b)). The darker curve represents the force curve as the cantilever tip approaches the surface. The lighter curve below the dark curve represents the force curve as the cantilever pulls away from the surface. The vertical distance between the two curves can be converted to the additional force required for the cantilever to overcome surface tension, short-range forces, and any potential polymers connecting the tip to the surface, by multi-

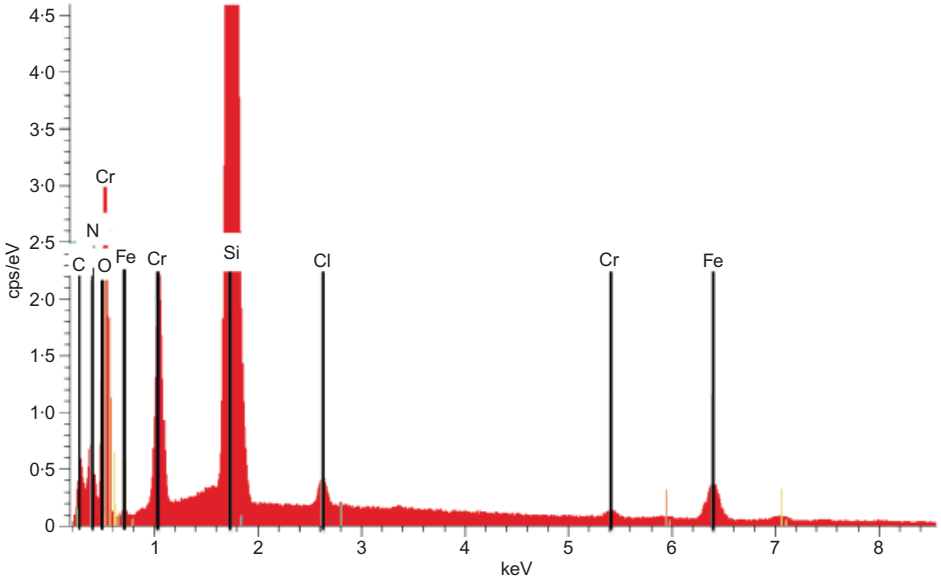

Fig. 5. EDS spectrometer analysis of polymer chemical compositions. Silica the dominant element; other elements include chromium, iron, chloride, sodium, oxygen and carbon

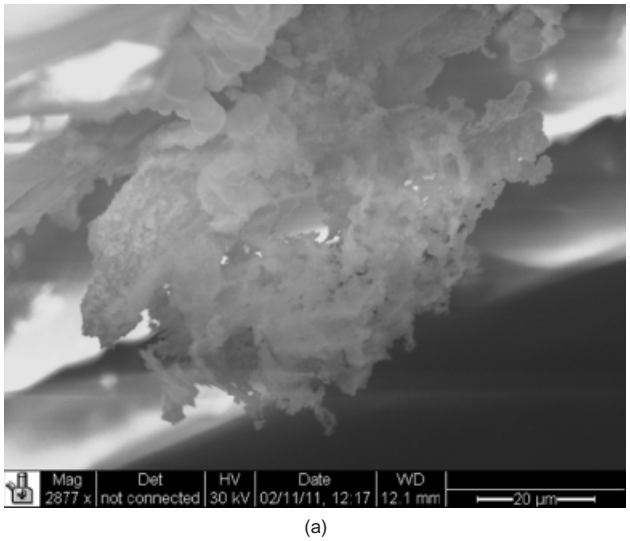

(a)

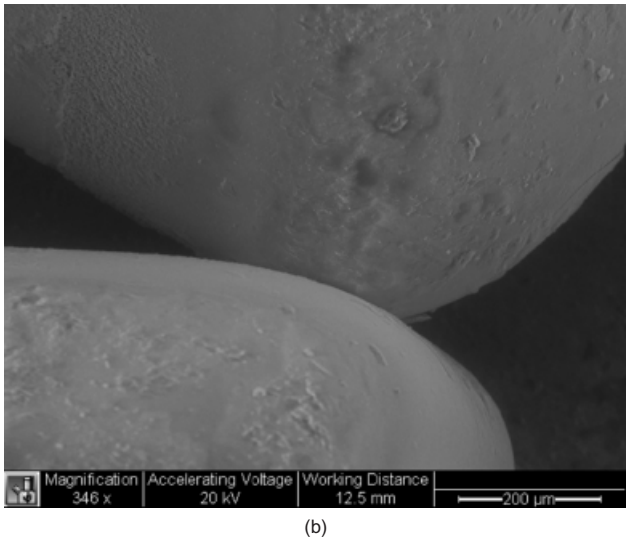

(b)

Fig. 6. SEM images of contact regions between silica cubes in 300 ppm silicon ion concentration solution for 3 weeks: (a) silica deposits growing in cube cracks when cubes under 170 kPa pressure; (b) clean cube surfaces with no microcracks and no silica deposits when cubes under 120 kPa pressure

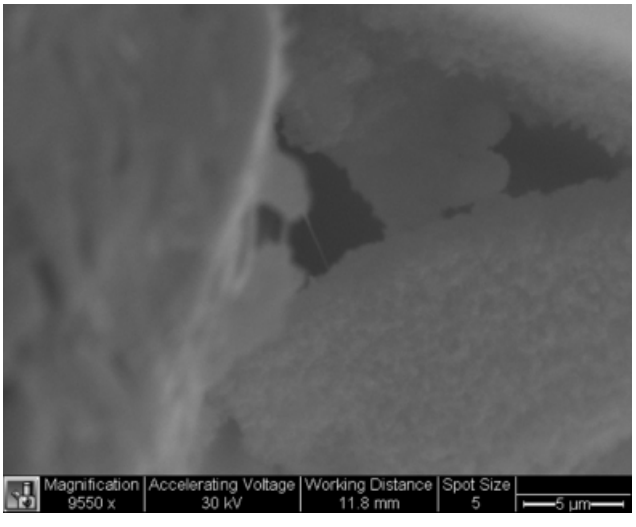

Fig. 7. SEM image of two silica polymers less than 5 µm long growing between silica cube main body and piece of silica debris at centre of image

plying the cantilever deflection sensitivity (30 nm/mV) and the spring constant (0·74 nN/nm). The peaks shown in Figs 8(a) and 8(b) may represent instances when polymer segments were broken as the cantilever was pulling away, and therefore the vertical distances between the peaks of the two curves can be converted to force magnitude for an estimation of polymer strength. In Fig. 8(a) the average vertical distance from a peak is about 15 mV, which converts to about 330 nN, whereas in Fig. 8(b) the average peak distance is 21 mV, equivalent to about 450 nN force. Such force patterns were not obtained on cube surfaces in solutions with 130 ppm and 170 ppm silicon ion concentrations. Small jumps were recorded when the tip was about to leave the cube surfaces, but they most probably occurred as a result of surface tension.

Growth of silica gels in undisturbed supersaturated solution

Samples of 300 ppm silica ion concentration solution were taken from a sealed plastic test tube 1 week and 2 weeks

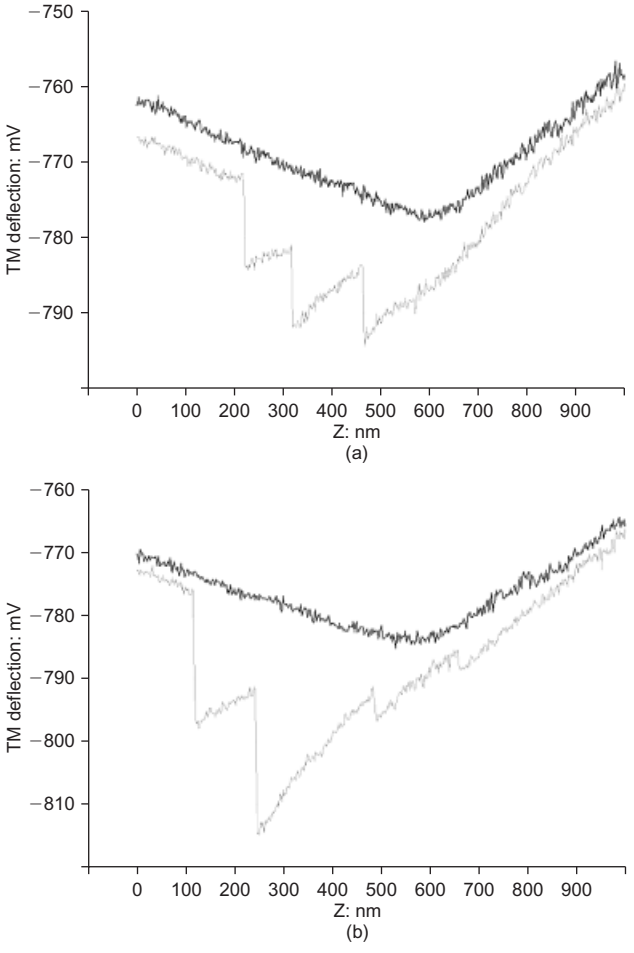

Fig. 8. AFM force curves of silica polymers growing on cube surface in solution with 210 ppm silicon ion concentration and neutral pH

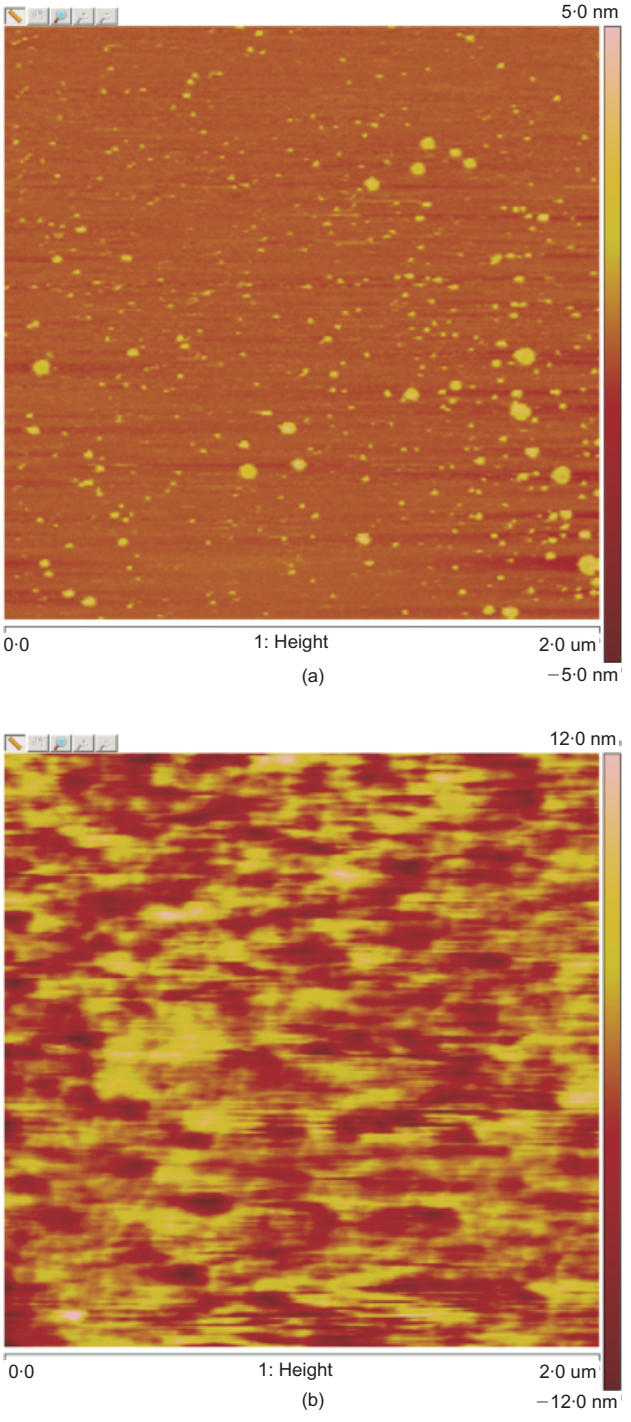

Fig. 9. AFM images of solution with 300 ppm silicon ion concentration on mica substrate: (a) silica gel seeds (bright spots) as large as 10 nm in diameter appeared after 8 days; (b) network of silica gel developed after 15 days

after the experiment started at day 0, and imaged in AFM fluid imaging mode. To maintain the concentration of silica ions in the solution, the test tube was filled fully to minimise the air space between the liquid surface and lid in order to minimise evaporation. Figs 9(a) and 9(b) show the growth of silica structures at day 8 and day 15 respectively. At day 8 (Fig. 9(a)), many silica seeds with diameter of the order of tens of nanometres appear in the solution, represented as bright spots on the mica substrate; at day 15 (Fig. 9(b)), an interconnected network of gel appears in the solution, but the height of the structure was only around 30 nm, and each polymer width was at least one magnitude less than 1 μm. Nevertheless, the density of such structures and their interconnectivity is quite impressive.

Silica cube environmental compression with damage followed by an extension test

The test made it possible to calculate the resultant force at rupture of the entire gel, as follows. The scale measures the mass of the bottom plate and cube, minus an uplifting intergranular force between the top and bottom cube. The minimum reading of the scale during cube separation represents the value at the onset of the decrease of the intergranular force. Hence the difference between that reading and the final reading after two cubes are well separated represents the maximum intergranular force. To isolate the capillary force between the cubes from this result, a control experiment was performed in which clean silica cubes and mica sheet were compressed and immediately separated. The force value from the control experiment is taken off from the actual experiment. For the experiment in solution with 500 ppm silicon ion concentration after 10 days of ageing, that value was 0·235***g***, or equivalent to 2305 μN. Thus 2305 μN is an estimate of the intergranular forces from the silica polymer chains between the two cubes.

SEM images taken of the cubes in solution with 500 ppm silicon ion concentration after 10 days of compression in the indenter-puller device showed substantial silica deposits growing around damaged sites, concentrated at one corner of the cube. Not only was the silica gel structure growing on the cube surface around the contact region, it was seen to bridge over microcracks at multiple sites (Fig. 10). In the

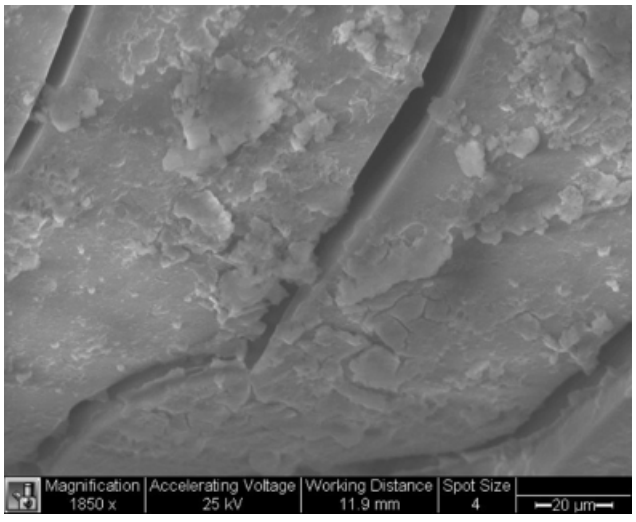

Fig. 10. SEM image of cube in cube indenter-puller for 10 days, submerged in 500 ppm silicon ion concentration and under 180 N force, after pulling experiment conducted. Three microcracks visible, with extensive silica gel growth on cube surface

figure, three microcracks with width less than 10 µm are visible. Dehydrated hydrogel structures are indicated covering the cube surface, and other gel structures joining the three microcracks are also marked. No significant amounts of such a deposit were observed on other parts of the cube, where no cracks were present.

For the experiment in solution with 300 ppm silicon ion concentration, after 20 days of ageing, extensive silica gel was found between the silica cube debris and the mica sheet (Fig. 11). The massive gel had covered the mica surface near the stressed contact region. It can be clearly seen that the silica cube debris was attached to the mica sheet by the growth of silica gel.

Growth of silica gel in stressed contact region between silica cubes and muscovite mica sheet

Two silica cubes, 1·5 mm × 1·5 mm × 1 mm, were compressed in the pneumatic quartz cube indenter in 300 ppm silicon ion concentration solution for 2 weeks with a layer of 10 µm muscovite mica sheet between them. SEM images have shown plenty of polymers growing in the vicinity of the contact region on the mica sheet, as well as between the mica sheet and the silica cubes, even though there was no damage on either silica cube (Fig. 12). It can be seen clearly from the image that silica polymers as long as 100 µm were growing only near the contact region between the silica cube and the muscovite mica sheet, with several polymers having roots on both the cube and the mica. Further away from the contact region, however, no polymers were seen growing on the mica sheet.

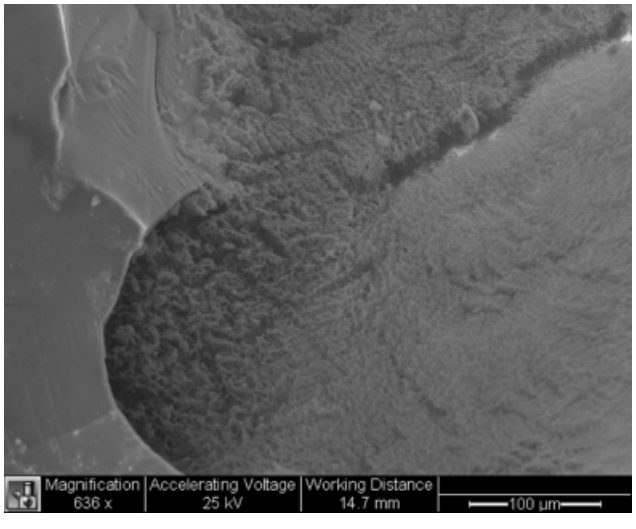

Fig. 11. SEM image of silica gel growth on mica sheet near silica cube contact region after 20 days of ageing in 300 ppm Si ion concentration solution. Piece of silica cube debris from contact region adhered to mica sheet by presence of silica gel

DISCUSSION AND CONCLUSION

EDS analysis of the polymers found growing between compressed silica cubes in 500 ppm silicon ion concentration solution has confirmed that they were indeed made of silica. Traces of chromium and iron may come from the stainless steel chamber in the background. Sodium, nitrogen and chlorine elements may come from the sodium hydroxide and nitric acid used for pH control. If the polymers were of biological origin, carbon would be a major element, but only minor traces of carbon were found.

In the cube-in-compression experiment in 500 ppm silicon ion concentration solution, polymers a few hundred micrometres in length were found near the contact region. It can be seen in Fig. 4 that the silica polymers in the contact region adhere to both the left and right silica cubes. Such a configuration would create adhesion between the silica cubes at the microscopic level that would enhance the macroscopic strength of sand. In the experiment using the same set-up, but in 300 ppm silicon ion concentration solution, deposits of silica gel were found in the cracks. Such deposits were roughly one magnitude smaller than those found at 500 ppm silicon ion concentration.

To determine how much effect the stressed contact region has on the precipitation and polymerisation of silica, two types of approach were taken. In the first approach, the experiment was repeated but with a force exerted that was high enough to bring the two cubes in contact, but low enough to prevent any damage to the cubes. No cracks were found on either cube after 3 weeks, and no silica gel deposits were observable anywhere on the cube surfaces. In

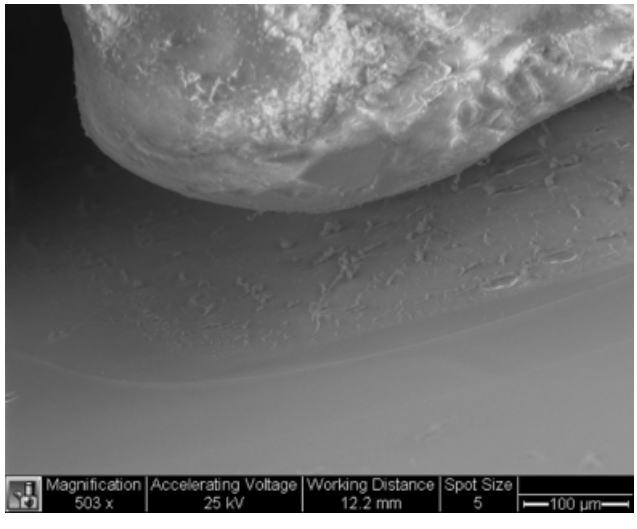

Fig. 12. SEM image of stressed contact region between muscovite mica sheet (bottom) and silica cube (top) in 300 ppm silicon ion concentration solution under 120 kPa pressure after 2 weeks. Silica polymers growth observed between mica sheet and silica cube in form of filaments between solids in clearly defined region around contact area

the second approach, some 300 ppm silicon ion concentration solution was stored separately, undisturbed, and imaged 1 week and 2 weeks later. AFM tapping-mode imaging of the solutions confirmed that, while silica was precipitated and gel structures formed in the solution, their sizes were much smaller than those found in the contact region between stressed silica cubes. Therefore a higher rate of silica precipitation and polymerisation in the liquid chamber around the stressed contact region is detected to have occurred than in the undisturbed solution.

AFM pulling experiments conducted on silica cube surfaces submerged in 210 ppm silicon ion concentration for 15 days have shown distinctive, step-like patterns, attributed to silica polymers growing on the cube surfaces. The vertical displacement at each peak, multiplied by the spring constant of the AFM cantilever, yields the average force required to break a single silica polymer chain at 0·39 μN.

The data collected from the indenter-puller showed that the gel structures found between the two silica cubes and the mica sheet contributed an equivalent of 2000 μN force before they were broken when the upper cube was slowly pulled away from the lower cube. These data are the first in the literature to record the magnitude of the force present between silica grains due to intergranular polymers. Even though this force is larger, by four orders of magnitude, than the tensile failure force of a single silica polymer measured in the AFM pulling experiment described above, such a difference is expected, because it represents the force required to break large silica gels composed of a large number of interwoven silica chains.

The solubility of silica at 25°C and neutral pH is 116 ppm (Rimstidt, 1997), but it is thought that the water layer on the surface of silica grain asperities may contain supersaturated silica ions dissolved due to stress. Some of the silicon ions may be transported to regions with a lower silica ion concentration, but some of the ions may precipitate near the contact regions and allow the polymerisation process to occur. Although it is still clear how or what quantity of silica is dissolved in saturated solution, the laboratory findings have indicated that silica cubes brought together under compression can accelerate silica precipitation and polymerisation processes, and produce gels that are attached to silica cubes.

Other recent studies have shown that the rate of silica dissolution and precipitation is accelerated in the presence of muscovite mica (e.g. Meyer *et al.*, 2006). The laboratory results confirm such a phenomenon. When two silica cubes were compressed in 300 ppm silicon ion concentration solution for 2 weeks without a sheet of mica between them, no polymers were seen anywhere in the liquid chamber when no cracks were initiated in the cubes. When the same experiment was conducted with a muscovite mica layer inserted between the cubes, numerous polymer structures were observed in the contact region on the mica sheet, on the silica cubes, and within the cracks.

Another interesting observation made during the 300 ppm indentation experiment with mica was that all the polymers seen under SEM were in the vicinity of the stressed contact region. Further away from the contact region, no polymers were seen. Such a phenomenon may be due to accelerated dissolution of silica from unobserved microcracks in nearby contact regions and subsequent precipitation from higher silica concentration potential. It indicates the important role of the stressed contact in the dissolution, precipitation and polymerisation of silica.

The results presented are only preliminary. However, they are very important, because for the first time we have a chain of observations that confirms a long-existing hypothesis that a stressed contact with microcracks generates dissolved silica in the contact (asperity) vicinity, which eventually polymerises, forming a structure between the grain that is sufficiently strong to represent a significant increase of strength, either tensile or eventually, through a rotational deformational mode, also compressive, within a period of time that is of the order of weeks. One of the most important findings is that the failure pulling force of a single chain of the polymer is 330–450 nN. At the grain scale, the failure force of the intergranular bond was found to be 2 mN. Multiple interwoven polymer chains are contained in a single intergranular polymer bond. Notably, such a force is 2·5–10 times higher than the typical capillary force between two spherical grains (8 mm in diameter) at contact failure, being of the order of 0·2–0·8 mN (Hueckel *et al.*, 2013). An experimental parametric study is under way to determine the range of validity of the presented findings over different durations of the contact.

ACKNOWLEDGEMENTS

The authors acknowledge the support of US NSF grant no. 0700294 of the Civil, Mechanical and Manufacturing Innovation Division, Geomechanics and Geomaterials Program, and, in part, of a grant from ENI Spa, Milan, Italy.

REFERENCES

Baxter, C. D. P. & Mitchell, J. K. (2004). Experimental study on the aging of sands. *J. Geotech. Geoenviron. Engng* **130**, No. 10, 1051–1062.

Becker, A. (1995). Quartz pressure solution: influence of crystallographic orientation. *J. Struct. Geol*. **17**, No. 10, 1395—1405.

Bjorkum, P. (1996). How important is pressure in causing dissolution of quartz in sandstones? *J. Sediment. Res*. **66**, No. 1, 147–154.

Bowman, E. T. & Soga, K. (2003). Creep, ageing and microstructural change in dense granular materials. *Soils Found*. **43**, No. 4, 107–117.

Denisov, N. Y. & Reltov, B. F. (1961). The influence of certain processes on the strength of soils. *Proc. 5th Int. Conf. Soil Mech. Found. Engng, Paris* **1**, 75–78.

Eyring, H. (1936). Viscosity, plasticity, and diffusion as examples of absolute reaction rates. *J. Chem. Phys*. **4**, No. 4, 283–291.

Heald, M. T. (1955). Stylolites in sandstones. *J. Geol*. **63**, No. 2, 101–114.

Hickman, S. & Evans, B. (1995). Kinetics of pressure solution at halite-silica interfaces and intergranular clay films. *J. Geophys. Res*. **100**, No. B7, 13113–13132.

Hu, L. B. & Hueckel, T. (2007a). Coupled chemo-mechanics of intergranular contact: toward a three-scale model. *Comput. Geotech*. **34**, No. 4, 306–327.

Hu, L. B. & Hueckel, T. (2007b). Creep of saturated materials as a chemically enhanced rate-dependent damage process. *Int. J. Numer. Anal. Methods Geomech*. **31**, No. 14, 1537–1565.

Hueckel, T., Cassiani, G., Tao, F. & Pellegrino, A. (2001). Aging of oil/gas-bearing sediments, their compressibility, and subsidence. *J. Geotech. Geoenviron. Engng* **127**, No. 11, 926–938.

Hueckel, T., Cassiani, G., Prévost, J. H. & Walters, D. A. (2005). Field derived compressibility of deep sediments of the Northern Adriatic. *Proc. 7th Int. Symp. on Land Subsidence, Shanghai*, 35–49.

Hueckel, T., Mielniczuck, B. & El Youssoufi, M. S. (2013). Micro-scale study of rupture in desiccating granular media. *Proc. Geo-Frontiers 2013: Stability and Performance of Slopes and Embankments, San Diego, CA*, paper no. 307 (accepted for publication).

Iler, R. K. (1955). The colloid chemistry of silica and silicates. *Soil Sci*. **80**, No. 1, 86.

Israelachvili, J. N. (2011). *Intermolecular and surface forces*, 3rd edn. Burlington, MA, USA: Academic Press.

Joshi, R. C., Achari, G., Kaniraj, S. R. & Wijeweera, H. (1995). Effect of aging on the penetration resistance of sands. *Can. Geotech. J*. **32**, No. 5, 767–782.

Kristiansen, K., Valtiner, M., Greene, G. W., Boles, J. R. & Israelachvili, J. N. (2011). Pressure solution: the importance of

the electrochemical surface potentials. *Geochim. Cosmochim. Acta* **75**, No. 22, 6882–6892.

Kuhn, M. R. & Mitchell, J. K. (1993). New perspectives on soil-creep. *J. Geotech. Engng ASCE* **119**, No. 3, 507–524.

Mesri, G., Feng, T. & Benak, J. (1990). Postdensification penetration resistance of clean sands. *J. Geotech. Engng ASCE* **116**, No. 7, 1095–1115.

Meyer, E. E., Greene, G. W., Alcantar, N. A., Israelachvili, J. N. & Boles, J. R. (2006). Experimental investigation of the dissolution of quartz by a muscovite mica surface: implications for pressure solution. *J. Geophys. Res. Solid Earth* **111**, No. B08202, http://dx.doi.org/10.1029/2005JB004010.

Mitchell, J. K. & Solymar, Z. V. (1984). Time-dependent strength gain in freshly deposited or densified sand. *J. Geotech. Engng ASCE* **110**, No. 11, 1559–1576.

Oelkers, E. H., Bjorkum, P. A. & Murphy, W. M. (1992). The mechanism of porosity reduction, styolite development and quartz cementation in North Sea sandstones. *Proc. 7th Int. Symp. on Water-rock Interaction, Park City, UT*, 1183–1186.

Oelkers, E. H., Schott, J., Gauthier, J.-M. & Herrero-Roncal, T. (2008). An experimental study of the dissolution mechanism and rates of muscovite. *Geochim. Cosmochim. Acta* **72**, No. 20, 4948–4961.

Parry, R. H. G. (2004). *Mohr circles, stress paths and geotechnics*, 2nd edn. London, UK: Spon Press.

Paterson, M. S. & Kekulawala, K. (1979). Role of water in quartz deformation. *Bull. Mineralog*. **102**, No. 2–3, 92–98.

Renard, F., Ortoleva, P. & Gratier, J. P. (1997). Pressure solution in sandstones: influence of clays and dependence on temperature and stress. *Tectonophysics* **280**, No. 3–4, 257–266.

Rimstidt, J. D. (1997). Quartz solubility at low temperatures. *Geochim. Cosmochim. Acta* **61**, No. 13, 2553–2558.

Rubin, C. J. (2009). *A novel apparatus for the study of intergranular silica microstructures*. Durham, NC, USA: Duke University.

Rutter, E. H. (1976). Kinetics of rock deformation by pressure solution. *Phil. Trans. R. Soc. London Ser. A* **283**, No. 1312, 203–219.

Schmertmann, J. H. (1991). The mechanical aging of soils. *J. Geotech. Engng ASCE* **117**, No. 9, 1288–1330.

Scholz, C. H. & Engelder, J. T. (1976). Role of asperity indentation and plowing in rock friction.1. Asperity creep and stick–slip. *Int. J. Rock Mech. Mining Sci*. **13**, No. 5, 149–154.

Sorby, H. C. (1862). The Bakerian Lecture: On the direct correlation of mechanical and chemical forces. *Proc. R. Soc. London* **12**, 538–550.

Tada, R., Maliva, R. & Siever, R. (1987). A new mechanism for pressure solution in porous quartzose sandstone. *Geochim. Cosmochim. Acta* **51**, No. 9, 2295–2301.

Wang, Y. H. & Tsui, K. Y. (2009). Experimental characterization of dynamic property changes in aged sands. *J. Geotech. Geoenviron. Engng ASCE* **135**, No. 2, 259–270.

Wang, Y. H., Xu, D. & Tsui, K. (2008). Discrete element modeling of contact creep and aging in sand. *J. Geotech. Geoenviron. Engng ASCE* **134**, No. 9, 1407–1411.

Worden, R. H. & Morad, S. (2000). Quartz cementation in oil field sandstones: a review of the key controversies. In *Quartz cementation in sandstones* (eds R. H. Worden and S. Morad), Special Publication 29, International Association of Sedimentologists, pp. 1–20. Malden, MA, USA: Blackwell Science.

Jefferis, S.A. (2013). *Géotechnique* **63**, No. 3, 256–261 [http://dx.doi.org/10.1680/geot.SIP13.P.029]

Some unexpected effects of natural and anthropogenic chemicals on construction

S.A. JEFFERIS*

From time to time chemicals present in the ground induce reactions that are sufficiently severe to cause structural damage, or risks to the health and safety of construction workers or end users of construction work. Such chemicals include those from contaminated land, which can complicate the design of underground works and may add significantly to costs. However, investigation techniques and remedial procedures are now well established for many contaminated land chemicals, and their effects should no longer come as a surprise to the construction team. In contrast, chemicals naturally present in the ground or deliberately introduced into it can lead to unexpected problems – especially if their effect is greatly out of proportion to their concentration in the ground. This paper gives brief case histories of some unanticipated effects of changes in redox potential associated with carbon, iron, nitrogen and sulfur species.

KEYWORDS: case history; chemical properties; grouting; soil stabilisation; tunnels

INTRODUCTION

Occasionally, and often unexpectedly, chemicals present in the ground produce reactions that are sufficiently severe to cause structural damage, or risks to the health and safety of construction workers or end users of construction work. When considering chemicals that might be in the ground, it is convenient to consider three classes of materials.

(*a*) Chemicals present in the ground as a result of spills or deliberate deposit of wastes and so on. These chemicals can be classed as contaminated land chemicals.
(*b*) Chemicals naturally present in the ground.
(*c*) Chemicals injected into the ground to modify its properties: for example, grouts to strengthen or watertighten the ground. The use of grouts can result in the introduction of organic carbon (e.g. components of chemical grouts) and change of pH of the soil (cementitious grouts are likely to have a pH in excess of 13).

Chemicals from contaminated land can complicate the design of underground works, and add significantly to costs. However, investigation techniques and remedial procedures are now well established, and contaminated land chemicals and their effects should no longer come as a surprise to those involved in construction works.

In contrast, chemicals naturally present in the ground or deliberately introduced into it can lead to unexpected problems, because they may not have been included in the original testing associated with site investigations, or may not have been recognised as significant.

When investigating chemicals naturally present in the ground, site investigation analyses tend to be focused on pH and sulfate. Again, as for contaminated land chemicals, pH and sulfate are unlikely to cause problems to a project, as there are well-established design rules (e.g. BRE, 2005). A subtler problem that can come as a surprise is the change of speciation of some chemicals associated with change of the redox conditions in the ground: for example, the oxidation of sulfide to sulfate.

Construction work can significantly alter the redox conditions: by mechanical processes such as excavation and exposure of soils to atmospheric air; by dewatering, which may allow air entry; or by flooding, which prevents air entry, and so promotes anaerobic conditions. Redox conditions may also be changed by chemical additions or injections that promote biological activity.

A well-recognised effect of the change in redox from reducing to oxidising conditions is the conversion of soluble Fe^{2+} iron species to the insoluble Fe^{3+} state, which often precipitates as part of a voluminous biological slime. Such slimes can lead to the biofouling of water supply and dewatering wells. In a more complex redox process, organic carbon naturally present in a soil or introduced as part of a chemical grout can be disproportionated, by which process one part of the organic molecule is oxidised, with the production of carbon dioxide, and the other is reduced, with the production of methane.

REDOX REACTIONS

Atoms can exist in different oxidation states. For example, as noted above, iron salts can exist in the Fe^{2+} (ferrous) or Fe^{3+} (ferric) states. Any change of oxidation state must involve a redox reaction, and these reactions must occur as a matched pair in which one species is oxidised and another reduced. A redox reaction can thus be seen as the sum of two half reactions: one an oxidation and the other a reduction. Redox reactions can be very important in the formation and mobilisation of minerals in the ground.

In biology, redox reactions are crucial, as both photosynthesis and cellular respiration are redox processes. Indeed, all utilisation of chemical energy in living systems involves redox reactions. The energy source (the primary electron donor) is oxidised, and the terminal electron acceptor is reduced. The process occurs via carrier enzymes (Konhauser, 2007), and it is important to recognise that the overall reactions must be thermodynamically possible (in terms of free energy). Living organisms thus act as redox

Manuscript received 5 March 2012; revised manuscript accepted 8 October 2012.
Discussion on this paper closes on 1 August 2013, for further details see p. ii.
* Environmental Geotechnics Ltd and Department of Engineering Science, University of Oxford, UK.

catalysts facilitating electron transfer (Stumm & Morgan, 1996).

A redox parameter pε, a measure of soil redox intensity, may be defined on the same basis as pH, recalling that pH is defined as

$$\mathrm{pH} = -\log_{10}[\mathrm{H}^+] \quad (1)$$

and thus pH is a measure of the hydrogen ion (proton activity) in a solution. pε is defined as

$$\mathrm{p}\varepsilon = -\log_{10}[\varepsilon^-] \quad (2)$$

where ε is the relative electron activity measured against a standard hydrogen electrode. pε is a measure of the relative tendency of a solution to accept or transfer electrons, just as pH is a measure of the relative tendency of a solution to accept or transfer protons. A high pε represents a relatively high tendency for oxidation, and a low pε a tendency for reduction. It should be noted that some authors prefer to use the redox potential E_h rather than pε. The relationship between pε and E_h is a function of temperature, and at 25°C

$$E_h = 0{\cdot}059\mathrm{p}\varepsilon \text{ (volts)} \quad (3)$$

Stumm & Morgan (1996) state that in a closed aqueous system containing organic matter, the oxidation of organic material occurs first by the reduction of oxygen, followed by the reduction of nitrate and nitrite and manganese dioxide if present. At strongly reducing levels of pε, sulfate and carbon dioxide may be reduced. Redox reactions tend to occur in a stepwise progression of reducing or increasing pε, probably because of competition between biological species, which may mediate the oxidation or reduction processes.

In typical geotechnical environments, the elements most often affected by redox changes are carbon, iron, nitrogen and sulfur. The following sets out some brief case histories of the effects of redox and speciation, and their impacts on construction works. Each case history could be the subject of a separate paper, but the intention here is to raise awareness of the effects of redox reactions. The author has been involved with all the case histories discussed below. They span several decades, and it is only with hindsight that he has been able to appreciate that the many diverse impacts were all the result of a single class of reaction – redox. The case histories will be discussed in terms of the principal element involved, but first it is necessary to add a caution in relation to the availability of data.

AVAILABILITY OF DATA

In the following pages some brief case histories are presented on unexpected chemical impacts on construction. However, identification of a problem at a site does not mean that it will be investigated with the rigour of a funded research project. Rather, very often, investigation will be limited to that essential for the management of the issues arising. Reports of case histories are therefore often regarded as insufficiently complete to merit journal publication. Sadly, this means that many lessons that could and should be learned, and matters that could and should be debated, remain hidden in consultancy reports that are never published. The author fully acknowledges that this paper, in places, verges on the anecdotal, especially as limits on publication length have severely limited the amount of detail that could be provided. He would therefore welcome discussion of the analyses as presented, or fuller explanations of the phenomena observed.

NITROGEN

In order of decreasing redox activity pε, inorganic nitrogen in soils may be present as nitrate, nitrite, nitrogen gas and ammonium species. Nitrogen may also be present in organic matter. Nitrate, nitrite and ammonium salts are mostly very soluble in water, and so are easily lost from permeable soils. Elemental nitrogen can be lost as a gas. In low-permeability soils such as clays some nitrogen species may persist, the nitrogen possibly derived from organic species in the soils. In fine or waterlogged (saturated) soils, strongly reducing conditions may develop if oxidisable material (e.g. oxidisable organics) is present, and nitrogen species may be reduced to the ammonium form. At the near-neutral pHs and modest temperatures typical of temperate zone soils, the ammonium ion will pass unnoticed, and indeed may not be determined in soil chemical analyses for construction or contaminated land purposes. However, if the temperature or pH or both are raised, the ammonium ion can be converted to ammonia gas.

Bracegirdle & Jefferis (2001) give an example of the unexpected effects of reduced nitrogen species in marine clay through which a tunnel was being excavated in 1984–1985. The ground had previously been subjected to treatment by jet-grouting around the periphery of the planned tunnel bore. However, in addition to strengthening the weak marine clay, the jet-grouting had also raised the pH (as a result of the alkaline components of the cement) and the temperature (from the heat of reaction of the cement) of the soil, resulting in the release of ammonia into the tunnel drive, which was being excavated under compressed air. The combination of compressed air, ammonia at concentrations up to 35 ppm and temperatures up 45°C (15°C above ambient) made for a very challenging working environment.

Permissible levels of exposure to gases may be defined by a time-weighted average (TWA), a short-term exposure limit (STEL) and a concentration at which gases are immediately dangerous to life or health (IDLH). The TWA is defined as the concentration for an 8 h workday of a 40 h workweek to which nearly all workers can be exposed without adverse effects. Anhydrous ammonia has a TWA of 25 ppm, and it is instructive to assess the groundwater concentration of ammonium ion at which the air concentration of ammonia would be 25 ppm.

Scoping calculations with the chemical speciation programme PHREEQC (Parkhurst & Appelo, 1999) show that for an air concentration of 25 ppm and a soil pH of 10·5–12, the groundwater concentration would need to be about 47–41 mg/l for a soil at 15°C. The higher pH shifts the equilibrium between ammonium ion and ammonia in the pore solution towards ammonia. At 45°C the required concentration is reduced to about 11 for both pHs, and above pH 12 there is little further reduction in the required concentration. If all the ammonium ion were in solution in the soil pore water, a concentration range of 11–47 mg/l would correspond to about 4–19 mg/kg of soil (assuming a saturated fine soil of moisture content 40%) – a level at which it might well pass unremarked. It should be noted that a concentration of 11–47 mg/l would be very high for a typical groundwater, and it seems that ammonium ion must have been desorbed from the soil, possibly as a result of ion exchange from the clay fraction (for example, exchange of ammonium ion for calcium, potassium or sodium from the cement). Therefore, when testing for the potential for ammonia release, soil rather than groundwater samples should be tested, and the soil extract should be prepared at high pH.

The above case history is an example of the importance of understanding the speciation of elements in the ground, especially when works may change other very important properties of the soil or groundwater – the pH and/or the

temperature. It also illustrates the fact that very small concentrations of ammonium ion – a few milligrams per kilogram of soil – can have substantial effects. Since the 1984–1985 ammonia problem, the author has been involved in another incident, and it is clear that potential ammonia levels should be carefully evaluated if jet-grouting is to be undertaken in areas that will subsequently require man-entry – for example, tunnels and shafts where ventilation may be limited.

IRON

At typical environmental pH values, iron salts in the reduced Fe^{2+} (ferrous) state are readily soluble in water, but are almost insoluble if oxidised to the Fe^{3+} (ferric) state. If a water containing Fe^{2+} species is subject to atmospheric oxygen or other oxidising conditions, Fe^{3+} species will precipitate. For example, in Perth, Australia, Fe^{3+} precipitates can be observed as a brown staining where groundwater is used for spray irrigation if the water lands on concrete or other light-coloured materials.

Surface staining, although it can be visually undesirable, is not of engineering consequence. However, in boreholes, clogging by iron deposits can occur and greatly reduce borehole yield. Such clogging can occur even at low iron concentrations ($<0{\cdot}1$ mg/l), and is often associated with *Gallionella ferruginea* bacteria (Howsam, 1990a; Konhauser, 2007), which can play an important role in the oxidation of Fe^{2+} to Fe^{3+}. Iron bioslimes are initially soft, and if well elements can be disassembled, the slime may be wiped off by hand. However, the slime can harden with time. Bioslime growth does not appear to be reduced in regions of high flow velocity. Indeed, it should be recognised that high flow velocity implies a high rate of delivery of species providing food (organic or inorganic carbon etc.) and energy (reduced iron), and thus an ideal environment for biological growth in an adjacent bioslime. Turbulence in high-flow regions may also enhance growth, as it will increase mass transfer rates. As evidence of this, Howsam (1990b) reports the growth of iron fouling on pump impellers, fouling that was increased by a change from low-speed to high-speed pumps.

A largely unreported issue with iron bioslimes is that the deposited iron hydroxides can act as a sorbent, removing heavy metals and other species such as arsenic and phosphate that can form low-solubility precipitates with iron hydroxides. For example, a concentration of arsenic of 0·9 g/kg dry weight was found in the iron bioslime that had developed in the track ballast of a rail tunnel where there had been long-term seepage of groundwater. Modelling by the author predicted that arsenic concentrations could reach 6 g/kg near the source of the water where sorbed concentrations would be highest. Unfortunately, concentrations were not measured in this area, as the full chemistry of the deposit was not apparent until after sampling was complete. It should be noted that iron bioslimes can be very loose, with high water contents. In the tunnel, the bioslime had a solids content in the range 25–40 g/l.

Iron bioslimes can be found in many natural and man-made water seeps and flows. When working near such seeps it is important to recognise that, as discussed above, the deposits may contain heavy metals, arsenic and so on, which may be liberated if chemical conditions change – for example, if acids are used to dissolve iron deposits. The intriguing conclusion is that bioslimes can act as natural permeable reactive barriers, removing contaminants from the water flowing through or over them (Jefferis, 2002). Bioslimes are of course the essence of trickling filters used for the reduction of the biochemical oxygen demand of wastewaters (Viessman *et al.*, 2009).

SULFUR

Sulfur can exist in soils in several oxidation states, but the mostly commonly encountered states in civil engineering are probably sulfate (oxidation state +6), elemental sulfur (oxidation state 0) and sulfide (oxidation state −2). Other states include sulfite (+4), dithionite (+3), thiosulfate (+2), polysulfides (−2/3, −1/2, −2/5) and bisulfide (−1) (Lindsay, 1979). A considerable range of archea and bacteria are involved in sulfur/sulfide oxidation and sulfate reduction (Paul, 2007). Changes of the local redox environment can thus have profound effects on the behaviour of sulfur species in soils.

In UK soils, gypsum is the most common sulfate mineral, although it may be associated with significant amounts of magnesium and sodium sulfates. Gypsum is only slightly soluble in water, whereas sodium and magnesium sulfates are very soluble. Barytes (barium sulfate), a rarer form of sulfate in the UK, is almost insoluble. Soluble sulfates and gypsum can be leached from permeable soils. In clay soils subject to normal seasonal wetting and drying, gypsum may tend to build up at a little depth below the ground surface. As a result it is usual for the top metre or so of undisturbed clay soils in the UK to be very low in sulfates (BRE, 2005). At greater depths in oxygen-deficient environments sulfur may be present in the reduced sulfide form – often as pyrite (iron disulfide, FeS_2).

The variation in the speciation of sulfur from sulfate to sulfide with depth has been a source of problems for lime stabilisation. Sulfate is well known to cause expansion of lime- and cement-stabilised soils. Sulfide does not cause expansion, but soils containing sulfide can be oxidised to sulfate, leading to the potential for heave. In the UK, stabilisation is often carried out during the summer months to avoid wetting of the soils by rainwater during the stabilisation process. Sulfide, if present, can be oxidised in the damp soils (the soils must be slightly moist for stabilisation), but expansion does not occur, as the expansive reaction requires water (Jefferis, 2011). Once water is available, the expansive reaction can be very rapid, and the first autumn/winter rains on a sulfate-containing stabilised soil can lead to expansion of up to 200% of the thickness of the stabilised soil.

It should be noted that the heave is not, to any significant extent, due to increase in volume of the chemical species involved. Rather, the reaction produces ettringite and thaumasite, which form needle-like crystals that jack the soil apart, drawing water into the system (it seems that the soil must be in a saturated or near-saturated state for this to occur; Jefferis, 2011). Sulfate-induced heave is now well recognised but, sadly, problems still occur, particularly on sites where soil is removed prior to stabilisation and the depth of cut varies. Testing of surface or shallow soils may give confidence that sulfates are absent or at acceptable levels but fail to identify the oxidisable sulfides in the deeper soils, which may be exposed to stabilisation after cutting.

The mechanism of pyrite oxidation in stabilised soils needs further research. Pyrite oxidation occurs via a series of sub-reactions, and in the absence of bacteria it can be slow (Fell *et al.*, 1993). The binders used for soil stabilisation typically include lime (pH of saturated solution 12·6) and Portland cement ($pH > 13$), so that the pH of a stabilised soil is likely to be high enough to make it inimical to microbiological activity, and indeed to make it effectively sterile for a considerable time after addition of the stabilising agent (lime, cement, ground granulated blastfurnace slag plus lime etc.). In the longer term the pH may drop, owing to continuing pozzolanic reaction with the soil and carbonation by atmospheric carbon dioxide. Despite the high initial pH, the author has observed sulfate-induced heave occurring

within a few months of stabilisation of sulfide-rich soils that had a low original sulfate content. A better understanding of the processes underlying the apparently abiotic oxidation of pyrite in stabilised soils may provide insights into processes by which sulfide-related heave may be reduced.

Sulfide in soils adjacent to tunnels

The oxidation of sulfide in pyritic soils and the potential to cause expansion of lime-stabilised soils is a well-recognised problem. A less well-publicised situation in which sulfide oxidation can be problematic is that of soils adjacent to tunnel linings.

If a tunnel passes through pyritic soils (or soils containing other oxidisable sulfur species) there is potential for both sulfate and acid production as a result of air introduced by the tunnel. In permeable soils below the groundwater table the tunnel lining will have to be effectively watertight so as to avoid excess water inflow. As a result oxygen egress, if any, will be limited to diffusive transport at seeps against a tendency for water inflow to the tunnel under the hydrostatic pressure differential. However, above the water table, air may move into (and out of) the soil as a result of atmospheric pressure changes and those induced by train movements. In low-permeability soils below the groundwater table there may be potential for some air inflow if drying occurs in the soil immediately around the tunnel and there is partial desaturation.

The overall equation for the oxidation of pyrite can be represented as (Fell *et al.*, 1993)

$$FeS_2 + \tfrac{15}{4}O_2 + \tfrac{7}{2}H_2O \rightarrow Fe(OH)_3 + 2SO_4^{2-} + 4H^+ \qquad (4)$$

Thus 1 gram mole (gram molecular weight) of pyrite (120 g) can produce 4 gram moles (4 g) of acid – hydrogen ion. Numerically this may seem a modest production, but 1 gram mole of hydrogen ion can, for example, dissolve 29 g of calcium hydroxide – a significant component of hydrated Portland cement compounds. One cubic metre of soil containing 1% pyrite by weight could therefore produce sufficient acid to dissolve about 17 kg of calcium hydroxide, and thereby damage a substantial volume of concrete or grout.

In 1962, groundwater ingress at Old Street Station on the London Underground railway was found to be strongly acidic. The ingress had been identified much earlier, in 1945, and it is possible that water was acidic at that time as well. The tunnel was constructed in the 1890s. The external groundwater level was at about tunnel axis level. In a ground investigation in 1989 (reported in Robins *et al.*, 1997) the pH of the water was found to be typically <3 with a sulfate concentration > 100 g/l. The minimum recorded pH was 0·73 and the maximum sulfate content was 300 g/l (Edmunds & Cook, 1987). The source of the acid and sulfate-rich water had been attributed to both natural and anthropogenic sources (Follenfant, 1975).

Pyrite was identified as present in the soil (Robins *et al.*, 1997), and thus the acidity and sulfate content of the water ingress were not unexpected, although the maximum sulfate content was much higher and the minimum pH much lower than typical for waters from pyrite oxidation. The acid water was expected to corrode the tunnel lining, and indeed there were signs of acid corrosion at seepages. The contact grout around the tunnel was also expected to be dissolved by the acid. However, unexpectedly, the tunnel was found not to be squatting, as might be expected if the grout was lost, but rather it was found to be squeezing inwards at axis level and expanding upwards at the crown.

The author hypothesised that the squeezing of the lining was the result of sulfate attack on Portland cement in the contact grout, despite the fact that the sulfate was being supplied by a strongly acidic groundwater, and the minerals most commonly associated with sulfate-induced expansion – ettringite and thaumasite – are not stable below a pH of about 10–11 (Skalny *et al.*, 2002). On exposure of the grout to the groundwater, both acid and sulfate will diffuse into it. However, a typical cement-based grout can be expected to contain significantly more acid-reactive material than sulfate-reactive material (much more acid is required to dissolve a Portland cement than to cause sulfate expansion). Furthermore, the relative content of sulfate in the groundwater was much greater than that of acid. For example, a pH of 0·73 corresponds to a hydrogen ion concentration of about 186 milliequivalent/litre (meq/l) of acid, and 300 g/l sulfate ion corresponds to 6250 meq/l sulfate – a ratio of reacting concentrations of sulfate to acid of about 33 times. At higher pHs the reacting ratio was found to be much higher – up to 3000 times. Thus, as regards the combined acid and sulfate attack on the grout, the sulfate attack will advance into the grout much more rapidly than the acid attack; the diffusion of both ions will be retarded by reaction, but the acid front will be the more strongly retarded. The sulfate front, as it moves through the grout, will cause the formation of ettringite and thaumasite and expansion. The acid front, when it arrives, will dissolve much of the grout and destroy the ettringite and thaumasite. Thus, if the groundwater moves uniformly through the grout, there should be an initial expansion phase followed by a slower contraction phase. This mechanism was confirmed from study of cores taken from grout in contact, at the outer surface, with the acid water. Sulfate expansion had propagated through much of the thickness of the grout, but acid attack was limited to near the contact zone. As the acid and sulfate are known to have been present for many decades, it is apparent just how slow the propagation of sulfate and acid attack can be.

The Old Street case history shows that the progress of reactions can be very slow, and that it is important to consider intermediate as well as final states of reaction.

Sulfate reduction and carbon reduction

During the final stages of construction of a deep basement founded in Gault clay, substantial quantities of groundwater were found to be entering the void beneath a suspended basement floor slab. To allow for long-term heave of the clay, the slab had been cast on a collapsible degradable void former, and the water was percolating through this (Nash *et al.*, 1997). Unfortunately, the water was found to be contaminated with hydrogen sulfide, an unpleasant and highly toxic gas. The source of the water was an unrecorded and ungrouted borehole. The water contained sulfate ion at about 300 mg/l but no sulfide. However, after percolation through the void former towards a catch-pit, the sulfate ion concentration was found to be reduced, and sulfide concentration was 20 mg/l.

A number of small-diameter inspection holes were drilled through the basement slab, and water samples were collected. These were checked for hydrogen sulfide by the author by shaking in a sealed, wide-mouthed jar and gently opening the jar and cautiously sniffing for the characteristic rotten eggs smell. However, the procedure had to be abandoned, as it was not repeatable – the nose fatigued too rapidly, and repeat tests could show a blank result. Thus not only is the procedure unreliable, but also those minded to repeat such a test should be warned that no smell does not mean no hydrogen sulfide. The author is now aware that at high concentrations there may be no warning smell, and that a non-detect may result from nasal fatigue.

It may be noted that a sulfide concentration in water of

30 mg/l, if all present as hydrogen sulfide (rather than as a soluble metal sulfide), would give an equilibrium concentration in air of over 1000 ppm. The US Centers for Disease Control and Prevention sets an IDLH value of 100 ppm for hydrogen sulfide (CDC, 1994), and it was recognised that there would be risks, especially in confined spaces such as drainage sumps. Once the cause of the problem was identified, remedial action was taken, grouting the borehole to remove the source of the water and the sulfate.

Under conditions sufficiently reducing for hydrogen sulfide formation, methane could also be formed. No specific evidence of methane generation was identified, but it was recognised that it could be generated from the carbon content of the void former in the effectively anaerobic environment beneath the basement slab. Methane was found at another site (Johnson, 1997). Furthermore, on a separate project where large quantities of a chemical grout were injected into the ground and the hardener appeared to have separated from the gelling phase, both methane and hydrogen sulfide were identified. On this latter project the groundwater also developed a sickening smell, and indeed it was this smell that caused the matter to be investigated. With hindsight the smell was possibly from the formation of reduced organo-sulfur compounds such as thiols (compounds containing a carbon–sulfur–hydrogen group), but at the time no analyses were undertaken. Hydrogen sulfide was confirmed as present in the samples, using lead acetate papers applied to the headspace of water samples. A specimen of the water was then treated with ferrous sulfate to remove the hydrogen sulfide. It was sealed in a glass bottle, and after a few days a black mirror of iron-sulfide-like precipitate developed on the walls of the bottle. On opening the bottle and applying a lighted taper a brief flash of flame was seen, suggesting methane release (hydrogen sulfide is also a flammable gas, but was suppressed by the ferrous sulfate treatment). The test was repeated at intervals over a period of two years, and on each occasion there was a brief flame. Once a plausible explanation for the smell had been developed, and despite the confirmed presence of hydrogen sulfide and probably methane, no further chemical investigations were undertaken to confirm the putative explanation. Scoping calculations based on the amount of grout used suggested that very large quantities of methane could have been produced (hundreds of kilograms). Lessons to be drawn from this case history are that on site, as opposed to in a research laboratory, investigations may not be continued to confirm provisional findings. However, it is felt that sufficient evidence was gathered to enable others confronted with a similar situation to formulate investigative procedures. These findings also confirmed that reactions can be slow and continuing. It should not be assumed that a reaction is complete once it has been identified. Long-term as well as short-term behaviour must be considered.

CARBON

Carbon can be oxidised to carbon dioxide and reduced to methane, and there is an enormous literature associated with both these gases. For example, it is well known that organic carbon in municipal waste landfills can be disproportionated – part reduced and part oxidised – to produce methane and carbon dioxide respectively, and measures to protect developments from landfill gases are well documented. However, it is perhaps less well appreciated that methane can be microbiologically oxidised. The author has observed the microbiological oxidation of methane escaping from fissures in chalk adjacent to an old unlined landfill. In dry weather the bacterial mass gave the walls of the fissures a red-brown coloration. In cold weather steam could be seen emanating from the fissures apparently, as a result of microbial methane oxidation. Whereas methane emissions adjacent to an unlined landfill are predictable, high temperatures might not be expected, and it has been suggested to the author that thermal imaging might provide a useful way of detecting methane escape.

CONCLUSIONS

This paper is intended to collect together examples of chemical and microbiological processes that have affected, or have had the potential to have effects on, construction workers and/or the works. Within the confines of a summary paper it has not been possible to provide detailed analyses of the chemical and microbiological processes. However, it is hoped that the paper will alert readers to the fact that redox-sensitive elements such as carbon, iron, nitrogen and sulfur can change speciation, causing or in response to redox changes in the ground. Other elements that may change speciation within the redox environment of soils include arsenic, manganese, phosphorus and uranium. Of these, the author has yet to identify or investigate a situation where change of phosphorus speciation has adversely affected construction works.

ACKNOWLEDGEMENTS

The author is indebted to the many owners, consultants and contractors who have given him the opportunity to study chemical and biochemical problems that have occurred on their sites.

REFERENCES

Bracegirdle, A. & Jefferis, S. A. (2001). Heat and ammonia associated with jet grouting in clay. In *Geoenvironmental engineering: Geoenvironmental environmental impact management* (eds R. N. Yong and H. R. Thomas), pp. 501–506. London, UK: Thomas Telford.

BRE (2005). *Concrete in aggressive ground*, BRE Special Digest 1, 3rd edn. Bracknell, UK: BRE Press.

CDC (1994). *Documentation for immediately dangerous to life or health concentrations (IDLHs): Hydrogen sulfide*. Atlanta, GA, USA: Centers for Disease Control and Prevention. http://www.cdc.gov/niosh/idlh/7783064.HTML (accessed 5 March 2012).

Edmunds, W. M. & Cook, J. M. (1987). *Old Street station: Groundwater investigations*, Hydrogeology Research Group Report 87/3. Keyworth, UK: British Geological Survey.

Fell, R., Phillips, A. & Gerrard, C. (eds) (1993). *Geotechnical management of waste and contamination*. Rotterdam, the Netherlands: A. A. Balkema.

Follenfant, H. G. (1975). *Reconstructing London's underground*, 2nd edn. London, UK: London Transport Executive.

Howsam, P. (ed.) (1990a). *Water wells, monitoring, maintenance and rehabilitation*. London, UK: E. & F. N. Spon.

Howsam, P. (ed.) (1990b). *Microbiology in civil engineering*, FEMS Symposium No. 59. London, UK: E. & F. N. Spon.

Jefferis, S. A. (2002). Engineering design of reactive treatment zones and potential monitoring problems. In *Advanced groundwater remediation: Active and passive technologies* (eds F. G. Simon, T. Meggyes and C. McDonald), pp. 75–86. London, UK: Thomas Telford.

Jefferis, S. A. (2011). Discussion of 'Addressing sulfate-induced heave in lime treated soils'. *J. Geotech. Geoenviron. Engng ASCE* **137**, No. 8, 812–813.

Johnson, R. W. (1997). Methane generation from void formers used in foundations on clay sites. In *Ground chemistry: Implications for construction* (ed. A. B. Hawkins), pp. 161–166. Rotterdam, the Netherlands: A. A. Balkema.

Konhauser, K. (2007). *Introduction to geomicrobiology*. Malden, MA, USA: Blackwell Science.

Lindsay, W. L. (1979). *Chemical equilibria in soils*. Chichester: Wiley.

Nash, D. F. T., Lings, M. & Jefferis, S. A. (1997). Hydrogen sulphide generation beneath a deep basement in Gault clay. In *Ground chemistry: Implications for construction* (ed. A. B. Hawkins), pp. 187–196. Rotterdam, the Netherlands: A. A. Balkema.

Parkhurst, D. & Appelo, C. A. J. (1999). *Users guide to Phreeqc (Version 2): A computer program for speciation, batch-reaction, one-dimensional transport, and inverse geochemical calculations*, Water-Resources Investigations Report 99-4259. Denver, CO, USA: US Geological Survey, US Department of the Interior.

Paul, E. (2007). *Soil microbiology, ecology and biogeochemistry*. Amsterdam, the Netherlands: Academic Press.

Robins, N. S., Kinniburgh, D. G. & Bird, M. J. (1997). Generation of acid groundwater beneath City Road, London. In *Ground chemistry: Implications for construction* (ed. A. B. Hawkins), pp. 139–158. Rotterdam, the Netherlands: A. A. Balkema.

Skalny, J., Marchand, J. & Odler, I. (2002). *Sulfate attack on concrete*. London, UK: Spon Press.

Stumm, W. & Morgan, J. J. (1996). *Aquatic chemistry: Chemical equilibria and rates in natural waters*, 3rd edn. New York, NY, USA: Wiley.

Viessman, W., Hammer, M. J., Perez, E. M. & Chadik, P. A. (2009). *Water supply and pollution control*, 8th edn. Upper Saddle River, NJ, USA: Pearson/Prentice Hall.

ice
Institution of Civil Engineers
publishing

Session 2. Bio-chemo-mechanical aspects in geomechanics

Al Qabany, A. & Soga, K. (2013). *Géotechnique* **63**, No. 4, 331–339 [http://dx.doi.org/10.1680/geot.SIP13.P.022]

Effect of chemical treatment used in MICP on engineering properties of cemented soils

A. AL QABANY* and K. SOGA†

Despite the large number of studies concerned with microbially induced carbonate precipitation (MICP) on soils, little attention has been paid to the effect of the chemical concentration used in the treatment on the precipitation pattern of calcium carbonate and their influence on engineering properties of MICP cemented soils. In this study, unconfined compressive strength tests were conducted on sand samples treated using 0·1, 0·25, 0·5 and 1 M urea–calcium chloride solutions. It was found that, although the strength of tested samples all increased after MICP treatment, the magnitude of this increase depended on the concentration used in the treatment and that the use of a low-chemical-concentration (i.e. urea and calcium chloride) solution resulted in stronger samples. Permeability test results showed that the use of a high-urea–calcium chloride-concentration solution resulted in a rapid drop in permeability at the early stage of calcite precipitation, whereas the use of a low-chemical-concentration solution was found to result in a more gradual and uniform decrease in permeability. This observed effect of chemical concentration on the strength and permeability of MICP cemented soils can have implications for the design of MICP for field applications.

KEYWORDS: ground improvement; laboratory tests; microscopy; permeability; soil stabilisation; stiffness

INTRODUCTION

Turning sand into a cement-like material using bacteria (biocementation) is considered to be one of the emerging biogeotechnologies. The most successful process for bio-cementation to date is microbially induced carbonate precipitation (MICP) using *Sporosarcina pasteurii*. In this process the bacteria hydrolyse urea to raise the pH of the system and carbonate is produced, which in turn results in the precipitation of calcium carbonate ($CaCO_3$) in the presence of a calcium source. The precipitated calcium carbonate holds sand particles together and turns unconsolidated sand into a cement-like material.

$$CO(NH_2)_2 + 2H_2O \rightarrow 2NH_4^+ + CO_3^{2-} \text{ pH} \uparrow$$

$$Ca + CO_3^{2-} \rightarrow CaCO_3 \text{ pH} \downarrow$$

MICP is quite flexible and could be tailored for different applications using different injection methods. Its use in geotechnical applications has been studied by several researchers over the past few years to examine its potential for strength enhancement and permeability reduction (e.g. DeJong *et al.*, 2006; Whiffin *et al.*, 2007; Ivanov & Chu, 2008; Al Qabany, 2011).

The use of MICP for reducing permeability is often discussed in literature as a mineral plugging mechanism associated with filling of voids (restricting water flow) by calcium carbonate crystals (Kantzas *et al.*, 1992; Stocks-Fischer *et al.*, 1999; Rebata-Landa, 2007; DeJong *et al.*, 2010). However, there are other bio-induced mechanisms for permeability reduction such as pore plugging and bio-binding of soil particles with polysaccharides and biomass (Ivanov & Chu, 2008; Stewart & Fogler, 2001). In Ivanov *et al.* (2010), a ferrous/ferric-containing solution produced by iron-reducing bacteria from iron ore and organic waste was used with an addition of urea- and urease-producing bacteria to increase the pH and cement sandy soils. They discussed the suitability of iron-based precipitation and calcium-based MICP for permeability reduction, where iron-based precipitation was found to be cheaper but less effective in reducing permeability compared with calcium-based precipitation.

Calcium carbonate precipitation at particle contacts results in an increase in soil stiffness and strength while causing minimal disturbance to the soil (Whiffin, 2004; DeJong *et al.*, 2006). van Paassen (2009) reported results of unconfined compressive strength (UCS) tests on MICP cemented samples to obtain a correlation between strength increase and calcium carbonate content. He also conducted triaxial compression tests on MICP cemented sands to show that the strengths obtained were generally higher than those obtained from UCS tests owing to the confinement and that the peak strengths were found to increase with confinement.

Because of this increased strength, the use of MICP for soil improvement is the most widely investigated function in literature. Applications often discussed are foundations strengthening (Ivanov & Chu, 2008), settlement reduction (Martinez & DeJong, 2009), soil improvement for construction of retaining walls, embankments and dams (van Paassen, 2011), increased soil resistance to seismically induced liquefaction (Inagaki *et al.*, 2011; Mortensen & DeJong, 2011) and improved oil and gas extraction by reducing sand production potential and increasing well stability (Latil *et al.*, 2008).

In a previous work by the present authors (Al Qabany *et al.*, 2012), laboratory tests were conducted to investigate the effect of changing MICP treatment conditions such as chemical concentration, retention time and effective input rates (mole/l per h) on chemical efficiency. Chemical efficiency was defined based on the amount of calcium carbonate precipitation compared to the amount of chemical

Manuscript received 5 March 2012; revised manuscript accepted 15 October 2012.
Discussion on this paper closes on 1 August 2013, for further details see p. ii.
* Young Professionals Program, Islamic Development Bank, Jeddah, Saudi Arabia.
† Engineering Department, University of Cambridge, Cambridge, UK.

reactants (urea and calcium chloride ($CaCl_2$)) injected to samples. Results showed that, below a urea and calcium chloride input rate of 0·042 mole/l per h and for a bacterial optical density (OD_{600}) between 0·8 and 1·2, the chemical efficiency remained high and the amount of precipitation was not affected by the treatment chemical concentration. However, it was found that, although the external appearance of cemented samples using MICP was similar, the calcium carbonate precipitation pattern at the pore scale was found to be affected by the chemical concentration adopted in the treatment. Cemented samples treated using urea–calcium chloride concentrations varying from 0·1 M to 1 M were examined microscopically; some scanning electron microscopy (SEM) images taken in the study are shown in Fig. 1. In that study, it was found that the use of a solution of lower chemical concentration in MICP treatment resulted in better distribution of calcite precipitation, with a typical crystal size of 3–5 μm for the 0·25 M samples. For these samples, calcite crystals had a similar size, were very well distributed spatially and covered the sand grains' contact areas uniformly. As the chemical concentration increased, it was found that both the uniformity of distribution and crystal size decreased. For example, the calcite crystal size was found to be as high as 35 μm in the 1 M samples. The precipitation of calcium carbonate in MICP is a complex process, because many variables such as chemical concentrations, bacterial activity and the presence of organic macromolecules such as enzymes could all affect the formation of the calcium carbonate crystals, as discussed in Al Qabany *et al.* (2012).

Following this previous work, the main objective of the work presented in the current paper is to examine the effect of using different chemical (namely urea and calcium chloride) concentration solutions on the increase in strength and reduction in permeability of MICP cemented sand samples. It is hypothesised that different calcite precipitation patterns observed at the micro-scale would have an effect on the overall mechanical and hydraulic properties of the cemented samples.

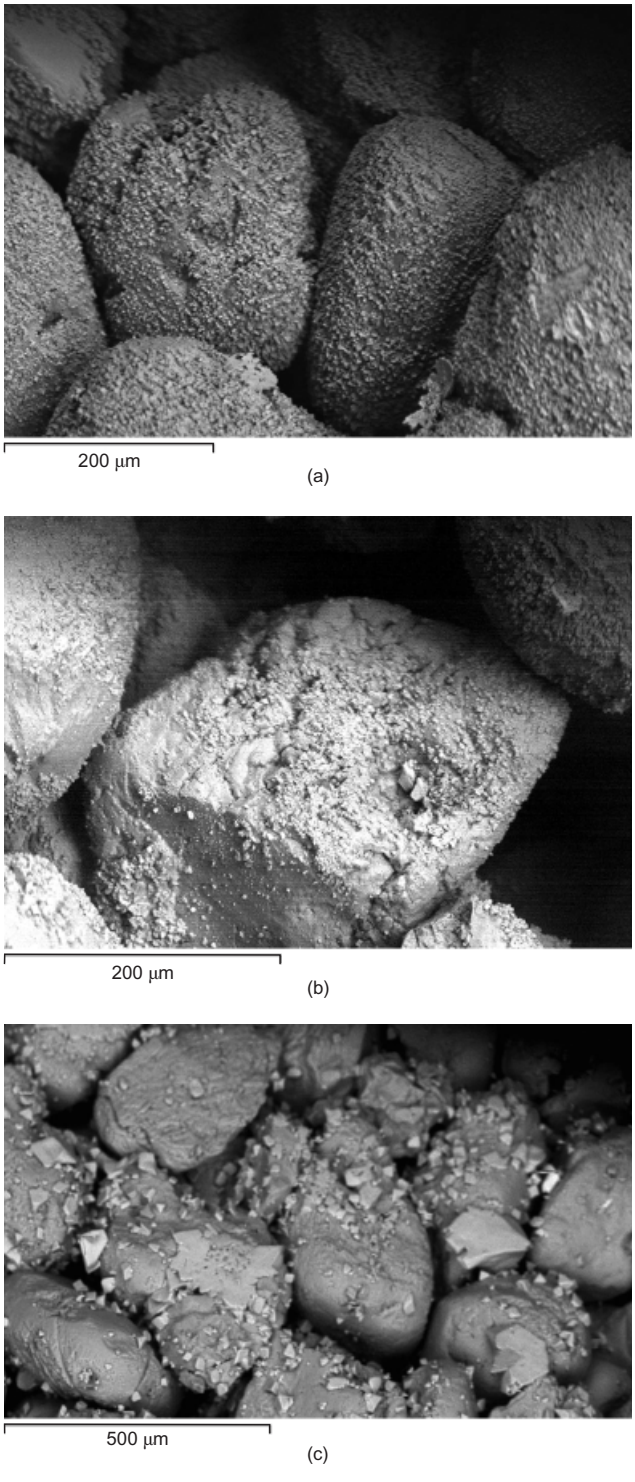

Fig. 1. Scanning electron microscopy images of samples going through different chemical treatments: (a) 0·25 M at 100 kg/m^3; (b) 0·5 M at 73·5 kg/m^3; (c) 1 M at 70 kg/m^3

EXPERIMENTAL WORK

Bacterial media and chemical concentrations

Sporosarcina pasteurii (American Type Culture Collection (ATCC) 11859) was used in all tests conducted in this study. Cells from the frozen stock were grown on ATCC 1376 ammonium–yeast extract (NH_4–YE) medium plates (20 g yeast extract, 10 g of ammonium sulphate ($(NH_4)_2SO_4$) and 20 g of agar in 0·13 M Tris buffer in pH 9·0). Bacteria were then harvested and grown in an ammonium–yeast extract liquid medium (usually for 24–36 h) to an optical density of 0·8–1·2 (OD_{600}) (10^7 cells/ml) before they were injected directly into the samples. Abiotic (without bacteria) bottles of media were prepared and incubated under the same conditions as control samples to check for contamination and to ensure that the growth obtained in the remaining inoculated liquid media was indeed only *S. pasteurii*.

Bacteria were only introduced to the samples either during packing (where sand was poured in bacterial solution directly into rigid cells to facilitate sand compaction for small samples) or in an initial injection (where sand was packed dry into the cells followed by injection of two pore volumes of deionised water to ensure saturation of the samples, then injection of one pore volume of bacterial solution). This was followed by chemicals only in all subsequent injections. The test liquid media used for chemical injections contained an equimolar amount of urea and calcium chloride, in addition to 3 g nutrient broth as a nutrient source for bacteria, 10 g ammonium chloride (NH_4Cl), and 2·12 g sodium bicarbonate ($NaHCO_3$) per litre of deionised water for stabilisation of the pH of the solution before injections. 0·25, 0·5 and 1 M urea–calcium chloride concentrations were used in order to assess the effect of using different chemical concentrations on the change in permeability with cementation, and 0·1 M urea–calcium chloride concentration was added to this range for the strength tests. Chemical retention time in the samples (time between injections) was determined based on the conclusion of a previous study to ensure full chemical reaction (Al Qabany *et al.*, 2012) and the retention times adopted were 6, 12 and 24 h for the 0·25, 0·5 and 1 M urea–calcium

chloride solutions, respectively. Different chemical treatments used in the study are summarised in Table 1. The total amount of chemicals introduced to any specimen in different experiments was based on chemical stoichiometric calculations, and the amount of precipitation targeted in each sample varied from 40 to 160 kg calcium carbonate per cubic metre of sand. This was assuming that all injected urea and calcium chloride precipitated as calcium carbonate, which was verified by measuring the amount of precipitation. This was done by adding hydrochloric acid (HCl) and calculating the weight difference of the sample before and after dissolving the precipitated calcium carbonate.

Permeability tests

A rigid wall permeability test set-up was used for measuring permeability during the bio-cementation process. In total, 30 samples were tested and samples had different amounts of calcite precipitation produced by different urea–calcium chloride concentrations (0·25 M, 0·5, 1 M). British standard grade D silica sand was used in all tests conducted in this study ($d_{50} = 165$ μm, $d_{90} = 250$ μm, maximum void ratio = 0·9875 and minimum void ratio = 0·585). The sand was placed inside rigid cells ($D = 100$ mm, $L = 250$ mm) by dry pluviation. The dry relative density was varied between 0·2 and 1 to examine the density effect and a confining pressure of 20 kPa was applied to the samples. Permeability measurements were carried out during various stages of chemical injections, such that change in permeability was measured at different amounts of precipitation. Permeability value was obtained by measuring the pressure difference across the sample at constant flow conditions. Injections were made from the bottom of the sample using a peristaltic pump and the effluent solution was allowed to overflow at the top of the cell during injections, such that the effluent level was constant at all times. Porous stone was placed at both ends of the sample in order to ensure uniform flow through the samples. When the permeability of soil becomes small, rigid cells may not be suitable, because the flow along the wall can be bigger than the flow through the soil sample. However, as shown in the results, this was not found to occur because the chemical efficiency of the samples was consistently high at all levels of cementation and hence there was no chemical loss as a result of non-uniform flow. Visual observation of cemented samples also showed no difference along the cross-section of the samples. After completion of the tests, the amount of calcite cementation was measured.

Unconfined compressive strength tests

Unconfined compressive strength tests were conducted on oven-dried samples with different amounts of calcite precipitation produced by solutions of different urea–calcium chloride concentrations (0·1, 0·25, 0·5 and 1 M). Tests were performed on samples of two different sizes: (a) $D = 100$ mm and $L = 250$ mm and (b) $D = 35{\cdot}4$ mm and $L = 100$ mm, where the smaller size had a simpler set-up and enabled a large number of samples to be treated at the same time. UCS tests are commonly used to characterise the strength property of cemented soils; a total of 60 samples were tested in this study. Much of the experimental work with cemented soils reported in literature has been carried out using this type of test (Consoli *et al.*, 2009), which allowed comparison of data.

A Wykeham Farrance constant-displacement mode UCS machine was used for testing. After MICP-induced cemented samples were created in the same manner as for the permeability tests, they were taken out of the moulds and any irregularities at the two ends of the samples were removed to ensure that they could be uniformly loaded. Samples were loaded at a rate of 1·14 mm/min (BS EN 12390–3:2002 (British Standards Institution, 2002)). During testing, they were placed in plastic bags to preserve all the pieces of the samples after they were broken. After the completion of the tests, the amount of calcite cementation was measured.

Table 1. Chemical treatments used in the study

Chemical concentration	Frequency (retention time): h	Normalised input rate: mole/l per h
0·1 M urea and calcium chloride	3	0·033
0·25 M urea and calcium chloride	6	0·042
0·5 M urea and calcium chloride	12	0·042
1 M urea and calcium chloride	24	0·042

RESULTS

Samples extracted from the rigid cells (shown in Fig. 2) were found to be fully cemented and also had very high efficiency, a similar finding to previous studies (Al Qabany, 2011). The chemical efficiency, which is defined by the percentage of injected urea and calcium chloride that precipitate as calcium carbonate, was found to vary from 70% to 100% for all samples treated by 0·25 and 0·5 M urea–calcium chloride solutions. In contrast, the samples treated by 1 M urea–calcium chloride solution had significantly lower efficiencies of around 20%. This may be attributed to the crystal morphology of the precipitated calcium carbonate, as discussed in a previous study (Al Qabany *et al.*, 2012). The use of chemical concentrations of 1 M and larger in MICP treatment was found to result in the precipitation of a less stable form of calcium carbonate (namely vaterite), which may be flushed out during injections after precipitation. This form of calcium carbonate (as confirmed by energy dispersive X-ray (EDX) analysis) was reported to be vaterite based on its spherical shape observed microscopically. Also, van Paassen (2009) reported the spherical-shaped calcium carbonate resulting from MICP to be vaterite based on X-ray diffraction (XRD) analysis.

Figure 3 shows the reductions in permeability with increase in the amount of calcium carbonate precipitation for three different concentrations. Although the degree of reduction was variable, even for samples treated with the same chemical concentration, large reduction occurred at the beginning of the precipitation. This indicated that larger pores where the chemical solution was accessible were reducing their pore sizes by the development of calcite precipitation (see 'Discussion' section).

As shown in Fig. 3, permeability tests were performed on samples with different relative densities (RDs). Both loose and dense samples showed reduction in permeability with increase in the amount of calcium carbonate precipitation. However, for most samples with RD greater than 0·7, the decrease in permeability was not as significant as the more loosely packed samples (i.e. over 90% reduction for many samples of RD = 60%). Furthermore the rates of permeability reduction on samples with higher RDs were greater than those with low RDs. This implies that MICP as a permeability reduction method is more effective for loose samples than for dense samples. Nevertheless, there was large scatter and uncertainty in the results obtained, so further study is required to improve the consistency of the treatment.

In Fig. 4, the measured permeability values at different levels of calcium carbonate precipitation are normalised with the initial permeability value before the MICP treatment, and the normalised permeability values are plotted against

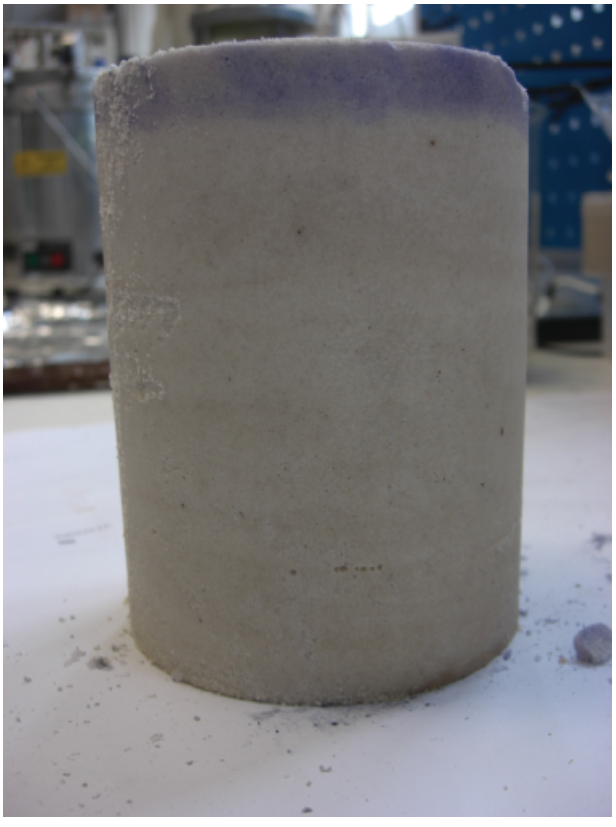

(a)

(b)

Fig. 2. Cemented sample after extraction from rigid cells for (a) 0·25 M chemical treatment and (b) 1 M treatment

the amount of calcium carbonate precipitation for samples with initial relative density between 0·75 and 0·85. For most samples, permeability was reduced to between 10% (for 0·25 M samples) and 30% (for 1 M samples) of its initial

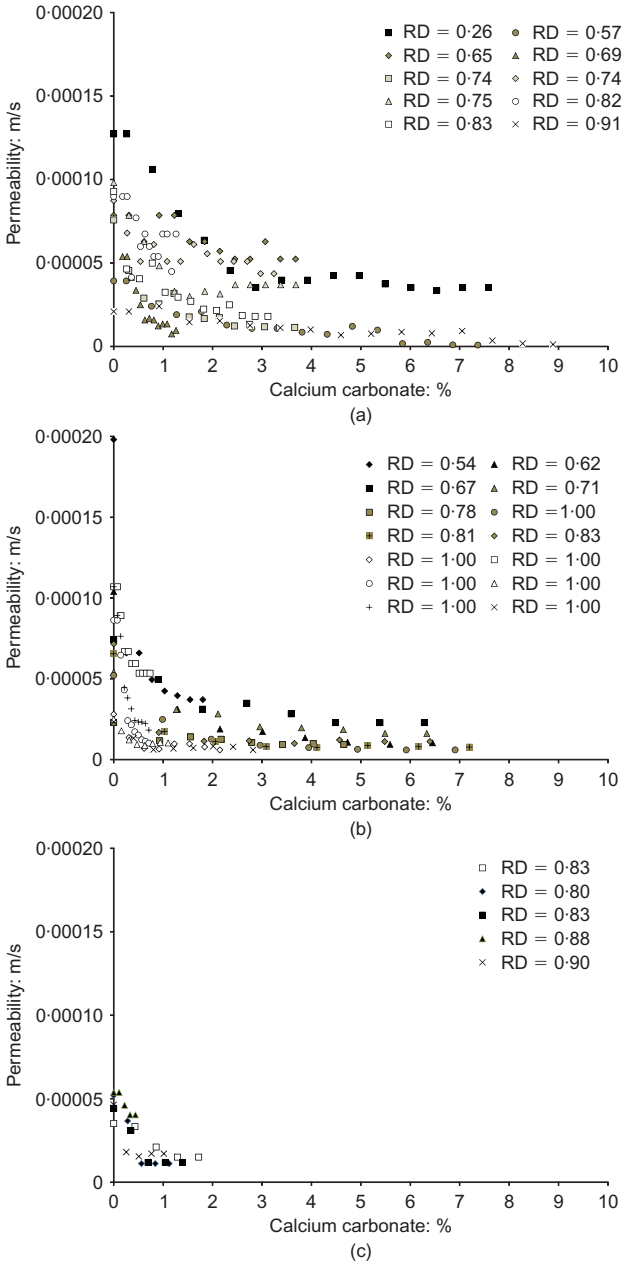

Fig. 3. Decrease in permeability with calcium carbonate precipitation for different relative densities and chemical concentrations: (a) 0·25 M; (b) 0·5 M; (c) 1 M

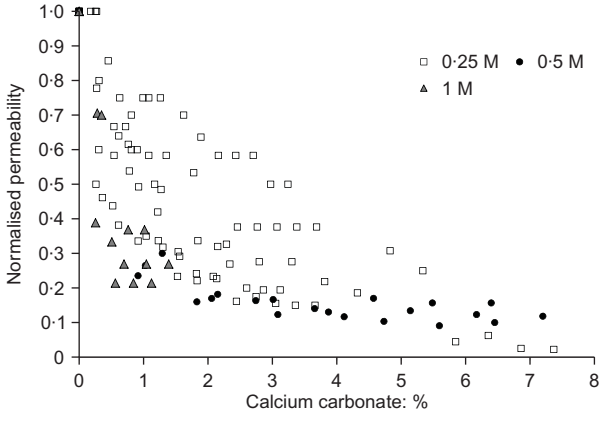

Fig. 4. Decrease in normalised permeability with calcium carbonate precipitation for three chemical concentrations

value. It was also found that the higher the concentration of the chemical solution was, the faster the reduction in permeability happened before it became constant. On average, the permeability value stopped decreasing significantly at approximately 3%, 1% and 0·5% cementation for 0·25 M, 0·5 M and 1 M samples, respectively. When a high-concentration solution was used, larger precipitation crystals were produced, which in turn clogged the pores (see Fig. 1(c)). Hence the rate of permeability reduction (with precipitation) was greater in samples treated with 0·5 M and 1 M solutions compared with those treated with 0·25 M solution. In other words, to achieve the same degree of permeability reduction, a smaller amount of precipitation was needed when a solution of a higher concentration was used in the MICP treatment. However, localised clogging resulted in inhomogeneity in cementation. Further discussion on the results is given later in this paper.

Unconfined compressive strength tests

On UCS testing, the failure pattern was found to be tensile for almost all samples, as shown in Fig. 5. Some of the weakly cemented samples with non-uniform cementation collapsed as soon as loading started and such samples were treated as having null strength.

The measured UCS values were plotted against the calcium carbonate precipitation values, as shown in Fig. 6. In general, UCS increased with the amount of calcium carbonate precipitation. Large variation in UCS data was mainly attributable to the tensile mode of failure. Such failure inherently caused the measurements to be variable, as UCS would be governed by the propagating pattern of tensile fractures within the test specimens.

Most of the null strength samples were 1 M samples, which related to the inhomogeneity in cementation resulting from the use of such large concentration in the treatment, as

Fig. 5. Typical failure pattern for all UCS samples

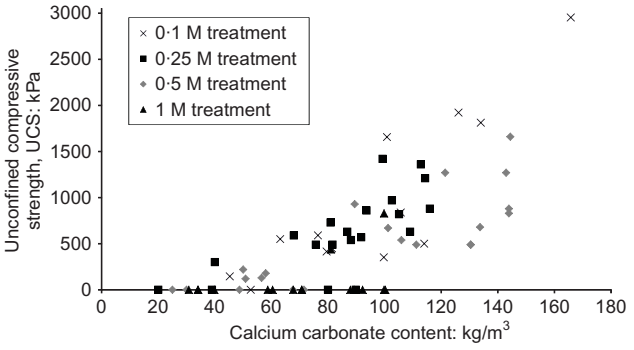

Fig. 6. Unconfined compressive strength plotted against calcite precipitation for different treatments

demonstrated by Al Qabany *et al.* (2012). This inhomogeneity caused the samples to deform locally, giving very small shear resistance for the sample as a whole, especially at lower calcium carbonate precipitation levels.

For the same amount of calcite precipitation, larger UCS values were obtained when the solution concentration was low. The 0·1 M samples were clearly the most homogeneous and the strongest by visual inspection before testing. As shown in Fig. 6, they gave larger UCS values in comparison with the samples treated with 0·25 M solutions, which were in turn stronger than the samples treated with 0·5 M and 1 M solutions. These results were obtained for all tested samples across a range of different initial relative densities; the effect of relative density on the measured UCS is discussed in a later section.

DISCUSSION

Permeability reduction

The degree of reduction in permeability measured in this study was similar to or slightly higher than that obtained in previous studies for the same levels of precipitation (2–8% cementation). For example, van Paassen (2009) reports 60% reduction of the initial permeability value using 1 M solutions at approximately 100 kg/m^3 calcium carbonate precipitation, whereas Ivanov *et al.* (2010) report from 50 to over 99% reduction. Results in Fig. 3 show that permeability decreases with increasing calcium carbonate precipitation and that the level of chemical concentration used in the treatment has an effect. The use of a higher chemical concentration solution resulted in a less homogeneous precipitation at both micro scale (Fig. 1) and macro scale (Fig. 2). The early reduction in permeability observed in 1 M samples is associated with localised clogging inside the samples (see Fig. 7) rather than an overall reduction in permeability, despite the fact that the samples are not really fully cemented.

The observed clogging was not necessarily at (or even near) the injection point as there were no indications that this was the case when the samples were dissected. Nevertheless, it was clear that the mechanism of reduction in permeability in these samples was different from that of samples treated with a low concentration solution and was actually more like biomass plugging described by Stewart & Fogler (2001). In their study, a reduction in pore volume in the vicinity of the plug was reported to take place at regions where biomass accumulated, resulting in clogging of the sample, with some flow channels developing and remaining unclogged within the samples. This mechanism resulted in non-uniform flow of chemical solution through the samples and subsequently an uneven distribution of precipitation and

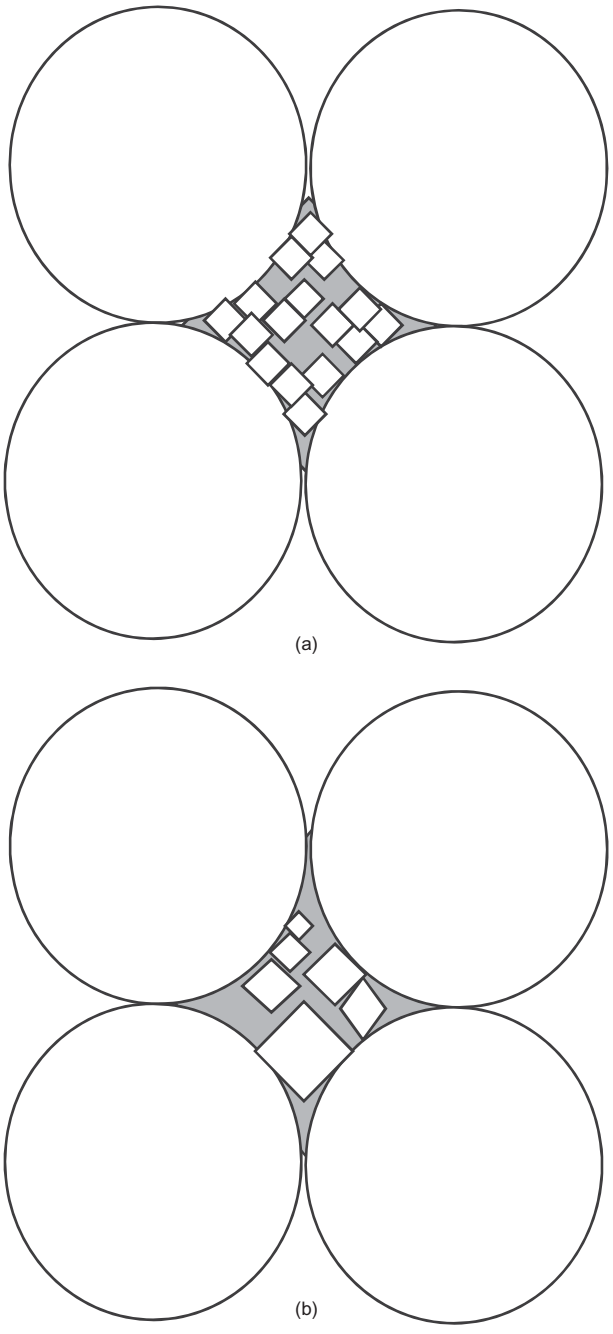

Fig. 7. Schematic diagram of pore clogging as a result of MICP using (a) a low chemical concentration and (b) a high chemical concentration

low overall chemical efficiency were obtained for these samples, as reported in Al Qabany *et al.* (2012).

When a low-concentration solution was used for the MICP treatment, precipitation took place at pore throats (contact points) where there was an abundance of bacteria and nutrients, as reported by DeJong *et al.* (2010). This is supported by the fact that, for most of these samples, precipitation was more distributed throughout the entire sample and no sudden clogging occurred.

Effect of density on UCS increase with calcium carbonate

Unconfined compressive strength test results demonstrated that the magnitude and the rate of UCS increase with calcium carbonate precipitation would be influenced by treatment concentrations, highlighting the significance of calcium carbonate precipitation pattern on the properties of MICP cemented soil. The more uniform distribution obtained when using a low-concentration solution was found to yield a higher sample strength, which could be attributed to a better distribution (or larger amount) of precipitation at particle contacts.

Several studies, such as Consoli *et al.* (2007, 2009) and Huang & Chen (2007), have investigated the key parameters (such as cement content, samples porosity and compaction effort) that affected the strength of artificially cemented soils using Portland cement, gypsum and calcite. Ismail *et al.* (2002a) examined factors such as intrinsic strength of soil grains, particle size and distribution as well as particle shape of the host grains. In particular, they highlighted that the number of effective point-to-point contacts, which was higher for dense soils than for loose ones, was a critical factor in the strength of the cemented soils (Ismail *et al.*, 2002a). Martinez & DeJong (2009) reported that the degradation of cemented sand particles at the micro scale was governed by the calcite bonds when silica sand was used. Hence, it is expected that denser soils, which have more particle contact numbers, will exhibit greater increase in UCS compared with loose ones.

The effect of relative density on strength is examined by plotting the data for samples treated with 0·5 and 0·1 M solutions, as shown in Fig. 8. With the exception of three points in Fig. 8(a) and two points in Fig. 8(b), which are circled in the figures, it can be seen that the rate of strength increase is larger for denser samples than looser samples. Similar to the observation made in the permeability tests, some inconsistencies were noticed in sample packing and homogeneity, which might explain why some points did not fit the trends.

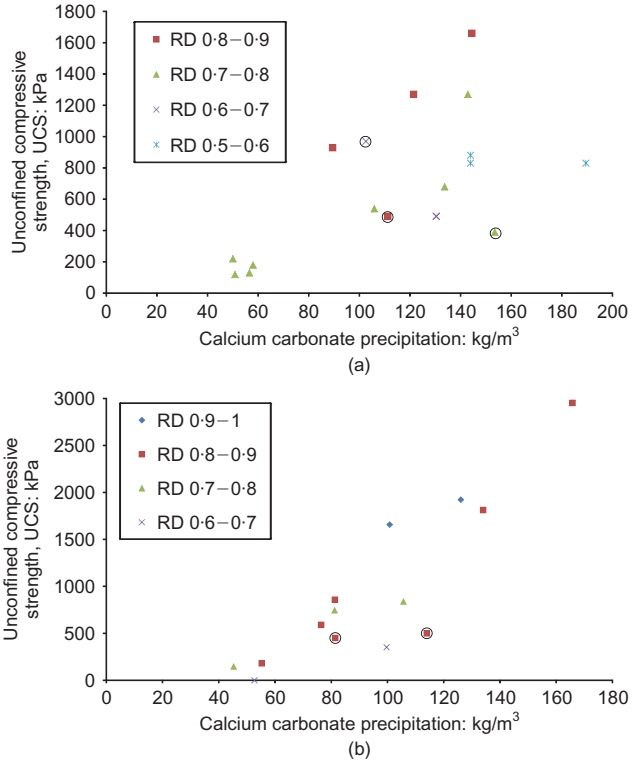

Fig. 8. Unconfined compressive strength plotted against calcite precipitation based on relative density for a single chemical treatment: (a) 0·5 M; (b) 0·1 M

Comparing strength from ureolytic MICP to other soil improvement techniques

When the UCS test results produced in this study were compared with those reported in previous studies, it was found that similar patterns of increasing strength were obtained. Fig. 9 shows that the 0·5 M sample data are similar to those produced by van Paassen (2009) who used the same concentration solution but different experimental set-up. Whiffin *et al.* (2007) created cemented samples using 1 M solution and their data are plotted with the 1 M and 0·25 M data obtained from this study, as shown in Fig. 10. The strength values of the 1 M samples from both studies are smaller than those of the 0·25 M samples. It is worth noting that Whiffin *et al.* (2007) only reported the strength of core samples that were fully cemented, unlike this study where null strength was reported for the samples that were not fully cemented.

The UCS values obtained from the MICP samples in this study are compared to UCS values of cemented samples using other soil cementation techniques, as shown in Fig. 11. The non-MICP data presented are Portland cement mixed samples by Ismail *et al.* (2002b) and Muhunthan & Sariosseiri (2008), and iron-based bio-grouted samples by Ivanov *et al.* (2010). Muhunthan & Sariosseiri (2008) tested two soils (Aberdeen soil ($D_{50} = 600$ μm) and Everett soil ($D_{50} = 20$ μm)), Ismail *et al.* (2002b) used an offshore calcareous sand ($D_{50} = 300$ μm) and Ivanov *et al.* (2010) used sand without providing further details. In the figure, UCS values are plotted against cement content (as percentage of dry weight of soil) for Portland cement mixed samples and percentage ferric chloride for iron-based bio-grouted samples.

The comparison shows that the MICP samples using ureolytic bacteria (calcium-based grouting) have higher UCS values than the samples treated by iron-based bio-grouting regardless of the chemical concentration used in the treatment, which is similar to what is reported by Ivanov *et al.* (2010).

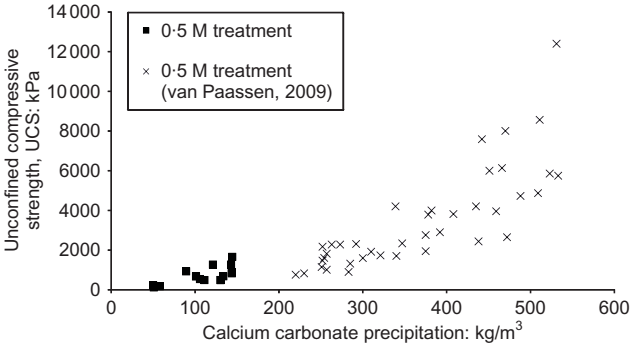

Fig. 9. Unconfined compressive strength plotted against calcium carbonate precipitation for MICP in the present study compared to van Paassen (2009) (0·5 M)

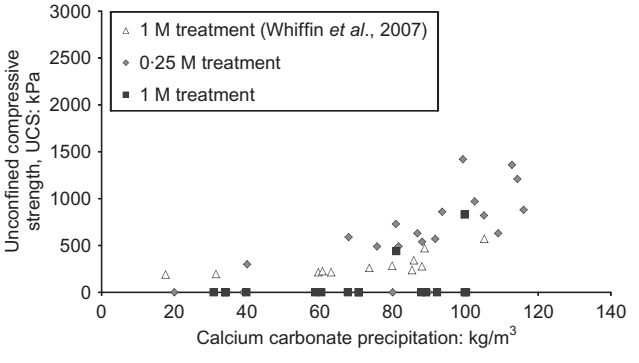

Fig. 10. Unconfined compressive strength plotted against calcium carbonate precipitation for MICP in the present study (0·25 M) compared to Whiffin *et al.* (2007) (1 M)

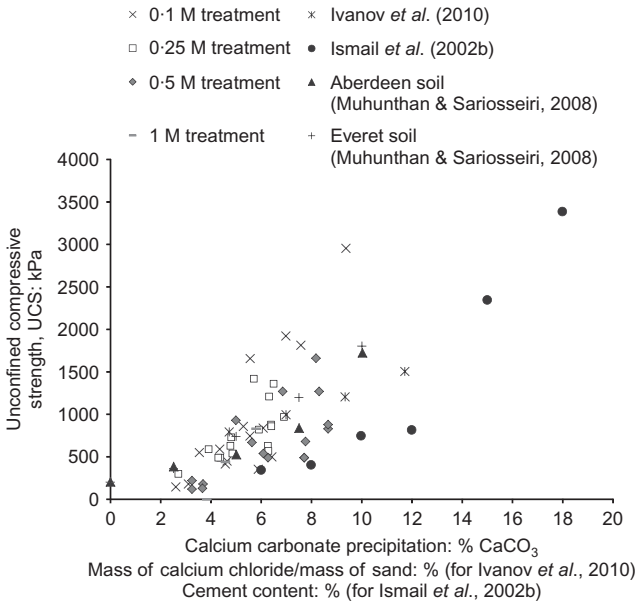

Fig. 11. Unconfined compressive strength plotted against calcium carbonate precipitation for different bio-cementation treatments, cement mixing (Ismail *et al.*, 2002b) and iron-based bio-grouting (Ivanov *et al.*, 2010)

The UCS strengths of the Portland cement mixed samples are similar to or smaller than those of the MICP samples. It is worth noting that the UCS results from cement mixed samples can be highly variable depending on mixing conditions such as water–cement ratio and soil relative density (e.g. Huang & Chen, 2007; Muhunthan & Sariosseiri, 2008) and the ones plotted are taken as representative strength values of Portland cement mixed soil samples. The values are obtained at an optimal set of water content and density of soil, and high variation is expected when these factors are changed, in particular at low cement content conditions.

In addition to Portland cement, Ismail *et al.* (2002b) tested soil samples cemented by mixing gypsum or treated by chemically induced calcite precipitation (as opposed to microbially induced). They found that, in order to achieve the same UCS value obtained from mixing Portland cement, a larger amount of gypsum and a smaller amount of calcite were needed. For example, 3·5% calcite, 8% Portland cement and 10% gypsum were required for UCS value of 500 kPa, whereas 7% calcite, 15% Portland cement and 20% gypsum were required for UCS value of 2500 kPa. It is expected that calcite precipitation using MICP would be similar to the chemically induced case because in both cases calcite precipitation takes place out of an aqueous solution that permeates into the soil matrix, and no hydration takes place inside the samples, unlike gypsum and Portland cement mixed samples.

Implication for engineering applications

The findings from this study show that different micro-scale precipitation distributions from different chemical treatments result in different macro-scale permeability and strength values, which potentially has implications for how MICP could be applied in engineering practice. Larger concentrations resulted in the precipitation of relatively larger calcium carbonate crystals along with inhomogeneous precipitation patterns, which led to a faster decrease of permeability with precipitation, and overall weaker UCS

values compared with samples treated using lower urea–calcium chloride concentrations.

Different permeability reduction patterns that can be obtained by varying the concentration of the chemical solution can be useful when determining whether the reduction in permeability needs to be distributed over a large area or possibly only at specific localised locations. With the use of a low-concentration solution, more consistency in permeability reduction is ensured and the possibility of flow channel development is potentially smaller. Furthermore, it would result in a uniform precipitation distribution, whereas a high-concentration solution may be used when a relatively rapid reduction in permeability is needed and a complete and robust plugging of soil is not required.

For field applications that require an increase in strength, a higher-concentration solution may be used in applications where soil homogeneity after cementation is not a necessity and only an overall increase in soil strength is needed and in situations where multiple injections are not possible. However, a low-concentration solution would be used if homogeneity of cemented soil is required.

To achieve the same amount of calcium carbonate precipitation, a greater number of injections would be required when a low-chemical-concentration solution is used. However, for practical reasons, the number of injections should preferably be minimised. One possible approach that could be examined is to start with a low-chemical-concentration solution for an initial homogeneous distribution of precipitation and a large number of nucleation sites, then increase the chemical concentration of the solution in order to reduce the subsequent number of injections. Such an approach could be applicable, yet further research is needed to prove its effectiveness.

CONCLUSIONS

Previous study by Al Qabany *et al.* (2012) showed that calcium carbonate precipitation pattern at the pore scale was affected by the chemical concentration adopted in the treatment. In this study, permeability and UCS tests were conducted on MICP samples treated by solutions of different chemical concentrations (i.e. urea–calcium chloride concentrations) ranging from 0·1 to 1 M in order to investigate the effect of precipitation pattern on engineering properties.

Results show that permeability values were reduced to approximately 20% of their original values when the amount of calcium carbonate precipitation became 2% of the sample weight. Large reduction occurred at the beginning of the precipitation, indicating that larger pores where the chemical solution was accessible were reducing their pore sizes by the development of calcite precipitation. When a high-concentration solution was used, larger precipitation crystals were produced, which in turn clogged the pores. Hence the rate of permeability reduction was greater on samples treated with a high-concentration solution compared with those treated with a low-concentration solution. However, localised clogging resulted in inhomogeneity in cementation. If a more uniform reduction in permeability is required for MICP treatment, the use of a low-concentration solution should be the way to proceed as it would ensure more consistency in results.

Chemical concentration used in the MICP treatment was found to have an effect on the strength of cemented samples. It was found that the use of a low-concentration solution and a higher number of injections resulted in stronger samples for a given amount of calcium carbonate precipitation. The UCS values obtained by MICP were either similar to or greater than those obtained by Portland cement mixing, chemically induced calcite precipitation or iron-based bio-grouting.

Results suggest that chemical concentration used in the treatment should be considered carefully when designing the MICP treatment. A solution with low chemical concentration may produce a more uniform precipitation pattern and stronger samples for a given amount of calcite precipitation. However, this means that more volume of fluid injection is required compared to the case of using a solution with higher chemical concentration, which in turn may increase operation costs. Further work is needed to find an optimal condition that not only gives targeted engineering properties for soil improvement but also requires less operational complexity in the field.

REFERENCES

Al Qabany, A. (2011). *Microbial carbonate precipitation in soils*. PhD thesis, University of Cambridge, Cambridge, UK.

Al Qabany, A., Soga, K. & Santamarina, J. C. (2012). Factors affecting efficiency of microbially induced calcite precipitation. *J. Geotech. Geoenviron. Engng* **138**, No. 8, 992–1001.

British Standards Institution (BSI) (2002). BS EN 12390–3:2002: Testing hardened concrete. Compressive strength of test specimens. London, UK: BSI.

Consoli, N. C., Foppa, D., Festugato, L. & Heineck, K. S. (2007). Key parameters for strength control of artificially cemented soils. *J. Geotech. Geoenviron. Engng* **133**, No. 2, 197.

Consoli, N. C., Viana da Fonseca, A., Cruz, R. C. & Heineck, K. S. (2009). Fundamental parameters for the stiffness and strength control of artificially cemented sand. *J. Geotech. Geoenviron. Engng* **135**, No. 9, 1347.

DeJong, J. T., Fritzges, M. B. & Nusslein, K. (2006). Microbially induced cementation to control sand response to undrained shear. *J. Geotech. Geoenviron. Engng* **132**, No. 11, 1381–1392.

DeJong, J. T., Mortensen, B. M., Martinez, B. C. & Nelson, D. C. (2010). Bio-mediated soil improvement. *Ecol. Engng* **36**, No. 2, 197–210.

Huang, D.-Z. & Chen, L.-Z. (2007). Studies on parallel seismic testing for integrity of cemented soil columns. *J. Zhejiang Univ. Sci. A* **8**, No. 11, 1746–1753.

Ismail, M. A., Joer, H. A., Randolph, M. F. & Meritt, A. (2002a). Cementation of porous materials using calcite. *Géotechnique* **52**, No. 5, 313–324, http://dx.doi.org/10.1680/geot.2002.52.5.313.

Ismail, M. A., Joer, H. A., Sim, W. H. & Randolph, M. F. (2002b). Effect of cement type on shear behavior of cemented calcareous soil. *J. Geotech. Geoenviron. Engng* **128**, No. 6, 520–529.

Inagaki, Y., Tsukamoto, M., Mori, H., Nakajima, S., Sasaki, T. & Kawasaki, S. (2011). A centrifugal model test of microbial carbonate precipitation as liquefaction countermeasure. *Japan. Geotech. J.* **6**, No. 2, 157–167 (in Japanese).

Ivanov, V. & Chu, J. (2008). Applications of microorganisms to geotechnical engineering for bioclogging and biocementation of soil in situ. *Rev. Environ. Sci. Biotechnol*. **7**, No. 2, 139–153.

Ivanov, V., Chu, J., Stabnikov, V., He, J. & Naeimi, M. (2010). Iron-based bio-grout for soil improvement and land reclamation. *Proc. 2nd Int. Conf. Sustainable Construction Mater. Technol, Ancona* **Special**, 415–420.

Kantzas, A., Stehmeier, L., Marentette, D., Ferris, F., Jha, K. & Maurits, F. (1992). A novel method of sand consolidation through bacteriogenic mineral plugging. *Proceedings of annual technical meeting*, pp. 92–46. Calgary, Alberta, Canada: Petroleum Society of Canada.

Latil, M.-N., van der Zon, W., Lehnen, C., Ineke, E., Marcelis, F., van Eijden, J., Baaijens, T., Baaijens, T. & Bol, G. (2008). Environmental friendly technology for biological sand-consolidation of oiland gas wellbore. *Proc. 1st Bio-Geo Engng Conf., Deltares*, 82–89.

Martinez, B. C. & DeJong, J. T. (2009). Bio-mediated soil improvement: load transfer mechanisms at the micro-and macro-scales. *Proceedings of conference on advances in ground improvement: research to practice in the United States and China*, ASCE Geotechnical Special Publication No. 188, pp. 242–251.

Mortensen, B. M. & DeJong, J. T. (2011). Strength and stiffness of MICP treated sand subjected to various stress paths. *Proceedings of conference on geo-frontiers 2011: advances in geotechnical engineering*, ASCE Geotechnical Special Publication No. 211, pp. 4012–4020.

Muhunthan, B. & Sariosseiri, F. (2008). *Interpretation of geotechnical properties of cement treated soils*, report WA-RD 715.1. Olympia, WA, USA: Washington State Department of Transportation.

Rebata-Landa, V. (2007). *Microbial activity in sediments: effects on soil behaviour*. PhD thesis, Georgia Institute of Technology, Atlanta, GA, USA.

Stewart, T. L. & Fogler, H. S. (2001). Biomass plug development and propagation in porous media. *Biotechnol. Bioengng* **72**, No. 3, 353–363.

Stocks-Fischer, S., Galinat, J. K. & Bang, S. S. (1999). Microbiological precipitation of $CaCO_3$. *Soil Biol. Biochem*. **31**, No. 11, 1563–1571.

van Paassen, L. A. (2009). *Biogrout (ground improvement by microbially induced carbonate precipitation*). PhD thesis, Delft University of Technology, the Netherlands.

van Paassen, L. A. (2011). Bio-mediated ground improvement: from laboratory experiment to pilot applications. *Proceedings of conference on geo-frontiers 2011: advances in geotechnical engineering*, ASCE Geotechnical Special Publication No. 211, pp. 4099–4108.

Whiffin, V. (2004). *$CaCO_3$ precipitation for the production of biocement*. PhD thesis, Murdoch University, Perth, Australia.

Whiffin, V. S., van Paassen, L. A. & Harkes, M. P. (2007). Microbial carbonate precipitation as a soil improvement technique. *Geomicrobiology J.* **24**, No. 5, 417–423.

He, J. *et al.* (2013). *Géotechnique* **63**, No. 4, 267–275 [http://dx.doi.org/10.1680/geot.SIP13.P.004]

Mitigation of liquefaction of saturated sand using biogas

J. HE*, J. CHU*† and V. IVANOV*

Some recent studies have indicated that the liquefaction potential of saturated sand can be greatly reduced if the sand can be made slightly unsaturated. One way to reduce the degree of saturation of sand is to inject gas into sand. This approach offers a cost-effective solution for mitigating liquefaction hazard over a large area. However, it is not easy to inject gas into sand in a uniform manner. A biogas method was developed in this study to overcome this difficulty. In this method, denitrifying bacteria are used to generate tiny, inert nitrogen gas bubbles in sand. Shaking table tests using a fully instrumented laminar box are conducted on both saturated sand and sand containing microbially generated nitrogen gas bubbles. Comparisons of the results of these tests indicate that the pore water pressure generated in the partially saturated sand was much smaller than that in saturated sand. Thus the proposed method is effective in reducing the liquefaction potential of sand.

KEYWORDS: ground improvement; liquefaction; sands

INTRODUCTION

In recent years, attempts have been made to apply microbiology to geotechnical engineering. Most of these studies have been focused on either enhancement of shear strength (DeJong *et al.*, 2006; Whiffin *et al.*, 2007; Ivanov & Chu, 2008; Harkes *et al.*, 2010) or reduction of permeability of soil (Stabnikov *et al.*, 2011; Chu *et al.*, 2012) by induction of calcite crystallisation using microbial hydrolysis of urea. Another potential application of biotechnologies in geotechnical engineering is to mitigate liquefaction hazard of saturated sand deposits by formation of tiny gas bubbles in situ using a microbial denitrification (i.e. nitrate reduction) process.

Some recent studies have shown that inclusion of gas bubbles in soil leads to a reduction in the degree of saturation and an increase in the liquefaction resistance of sand (Copp, 2003; Pietruszczak *et al.*, 2003; Okamura & Soga, 2006; Okamura & Teraoka, 2006; Okamura *et al.*, 2006, 2011; Yegian *et al.*, 2006, 2007; Pande & Pietruszczak, 2008). Several methods have been proposed to introduce gas bubbles into sand. These include

(*a*) air injection (Okamura *et al.*, 2011)
(*b*) water electrolysis (Yegian *et al.*, 2006)
(*c*) sand compaction pile (Okamura *et al.*, 2006)
(*d*) use of sodium perborate (Eseller-Bayat, 2009).

Biogas will offer another method for mitigation of liquefaction after it has been established.

An important question regarding the desaturation method is whether or not gas bubbles in sands can remain for a long time. According to Yegian *et al.* (2007), within a duration of 442 days, there was little change in the degree of saturation (from 82·1% to 83·9%) under hydrostatic conditions. Similar tests were also carried out by He (2012) using biogas. The result was similar to that in Yegian *et al.* (2007). Thus, the tiny gas bubbles generated by bacteria will be stable at least under hydrostatic conditions.

For the biogas method adopted, nitrogen gas was generated through a dissimilatory reduction of nitrate, or in common terms, denitrification. Denitrification is a biological process in which nitrate (NO_3^-) is reduced stepwise to nitrogen gas (N_2). Electron donors are almost all organic compounds. For example, biogas production in reactions of denitrification using methanol, ethanol, or sodium acetate as electron donors is shown by the following equations

$$5CH_3OH + 6NO_3^- \rightarrow 3N_2 + 5CO_2 + 7H_2O + 6OH^- \quad (1)$$

$$5C_2H_5OH + 12NO_3^- \rightarrow 6N_2 + 10CO_2 + 9H_2O + 12OH^- \quad (2)$$

$$5CH_3COO^- + 8NO_3^- \rightarrow 4N_2 + 10CO_2 + H_2O + 13OH^- \quad (3)$$

Nitrogen (N_2) produced by the denitrification process is the most suitable biogas for sand desaturation because it is chemically inert and its solubility in water is very low −0·017 g/l, (i.e. 0·014 l of gas per litre of water, at 25°C at atmospheric pressure). Another biogas, carbon dioxide (CO_2), has much higher solubility −1·5 g/l (i.e. 0·76 l of gas per litre of water at 25°C at atmospheric pressure). For the objective of using gas to lower the degree of saturation of initially saturated sand and maintain it for as long as possible, the contribution should come mainly from the nitrogen gas, not the carbon dioxide.

There are different approaches to study the effect of sand saturation on its liquefaction potential. Shaking table tests in a rigid box have been carried out by Okamura & Teraoka (2006). A strain-controlled model box with flexible walls was used by Yegian *et al.* (2006, 2007). Laminar box tests have been widely used in both 1***g*** shaking table and centrifuge tests to study liquefaction of sand owing to earthquake (Ling *et al.*, 2003; Kagawa *et al.*, 2004; Elgamal *et al.*, 2005; Ueng *et al.*, 2006; Thevanayagam *et al.*, 2009; Sharp *et al.*, 2010; Ueng, 2010; Zhou *et al.*, 2010; Dobry *et al.*, 2011). In this study, the effects of biogas on sand liquefaction were studied by conducting 1***g*** shaking table tests using a fully instrumented laminar box model.

Manuscript received 27 February 2012; revised manuscript accepted 15 October 2012.
Discussion on this paper closes on 1 August 2013, for further details see p. ii.
* School of Civil and Environmental Engineering, Nanyang Technological University, Singapore.
† Department of Civil, Construction and Environmental Engineering, Iowa State University, USA.

MATERIALS AND METHODS

Isolation and cultivation of denitrifying bacteria for biogas production

The denitrifying bacteria used for this study were isolated from anaerobic sludge of municipal wastewater treatment plant. Denitrifying enrichment culture was obtained by non-aseptic anaerobic cultivation on the liquid medium of the following content, in mg/l of tap water: ethanol, 500 mg/l; potassium nitrate (KNO_3), 1010 mg/l, ammonium chloride (NH_4Cl), 12 mg/l; monopotassium phosphate (KH_2PO_4), 75 mg/l; dipotassium phosphate (K_2HPO_4), 250 mg/l; magnesium sulfate heptahydrate ($MgSO_4{\cdot}7H_2O$), 10 mg/l; ferrous sulfate heptahydrate ($FeSO_4{\cdot}7H_2O$), 1 mg/l; calcium chloride dihydrate ($CaCl_2{\cdot}2H_2O$), 1·5 mg/l. Isolation of pure culture was made aseptically from the colony on the same but sterile and solidified medium with addition of Bactoagar Difco, 12 000 mg/l. Pure culture was isolated from cells of the dominant type colony and labelled as strain DN1.

The 16S rRNA gene sequence analysis of this pure culture was carried out as described in detail in Chu *et al.* (2012). The dominant species in the enrichment culture was *Acidovorax sp.*, which is known as a common species of denitrifying bacteria in wastewater treatment facilities.

Cells from the colonies of *Acidovorax sp*. strain DN1 were used to inoculate 0·5 l of sterile liquid medium in a 1 l bottle. The medium was purged with nitrogen gas before sterilisation. Cultivation was at 30°C for 5 days. The concentration of biomass in the suspension after cultivation was measured by filtrating 50 ml bacterial suspension through a filter paper with 0·2 μm pores and drying the filter paper at 60°C for 12 h. The volume of introduced bacterial suspension for denitrification in sand was about 1% of pore volume of sand. The content of bacterial biomass introduced into the sand for denitrification was about 0·02 mg dry biomass/kg of sand. The composition of liquid medium used for the soil treatment was similar to that used for the cultivation of bacteria. The concentrations of the nitrate and the electron donor should be adjusted according to the stoichiometric proportions in equations (1)–(3) to obtain the required volume of gas. The concentrations of other chemicals were one-tenth of those used in the cultivation medium to minimise the ground water contamination.

The test set-up

A picture of the test set-up is shown in Fig. 1. It consists of two parts. The upper part is a laminar box and the lower part is a manual shaking table. A metal frame is also installed to surround the laminar box for safety and installation of measuring devices. The details of the design and the test preparation are given below.

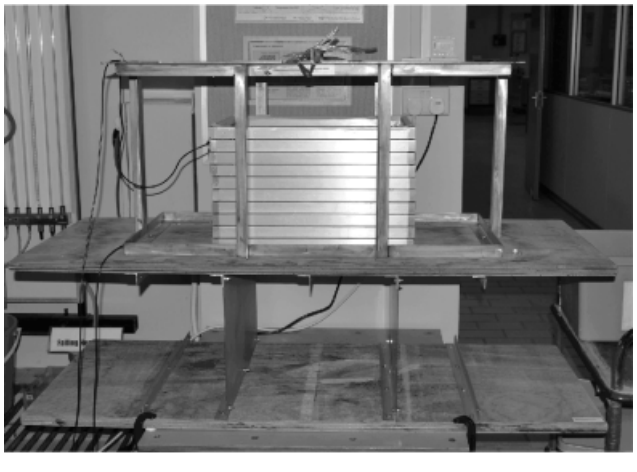

Figure 1. Model test set-up

Laminar box

A laminar box was made of ten layers of aluminium laminates stacked together as shown in Fig. 2. Ball bearings were used at the interface of each layer so that the interface friction was very small. This also allowed each layer to move freely in the lateral direction during shaking. The laminar box had an inner size of 45 cm × 30 cm × 29·7 cm (length × width × height) when all the laminates were used. An impervious plastic sheet was used to line the inner boundary before the sand sample was placed. The plastic sheet was cut and sewn to a size that was a little bigger than the inner size of the laminar box, so that the laminar box could deform freely.

Shaking table

The design of the manual shaking table follows the concept proposed by Prasad *et al.* (2004) to allow it to provide a horizontal translational seismic loading. A picture of the shaking table is shown in Fig. 1 and a sketch is given in Fig. 3. Two pieces of mild steel plate were installed

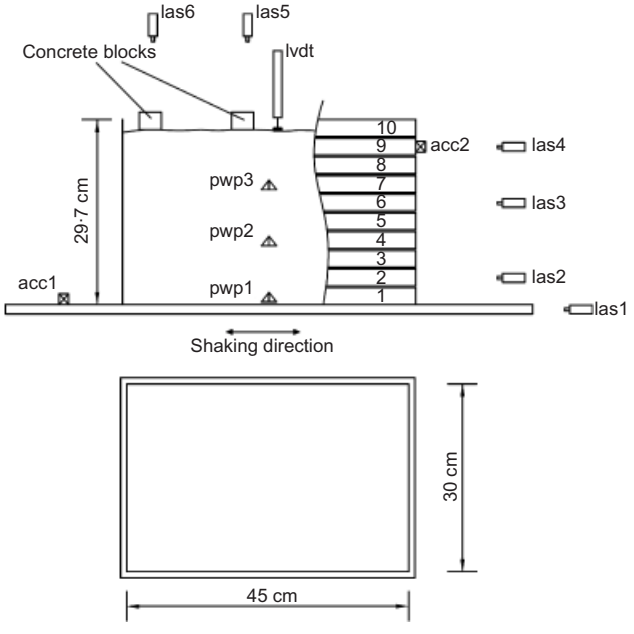

Figure 2. Design of the laminar box and instrumentations (acc: accelerometer; pwp: pore water pressure transducer; las: laser displacement transducer)

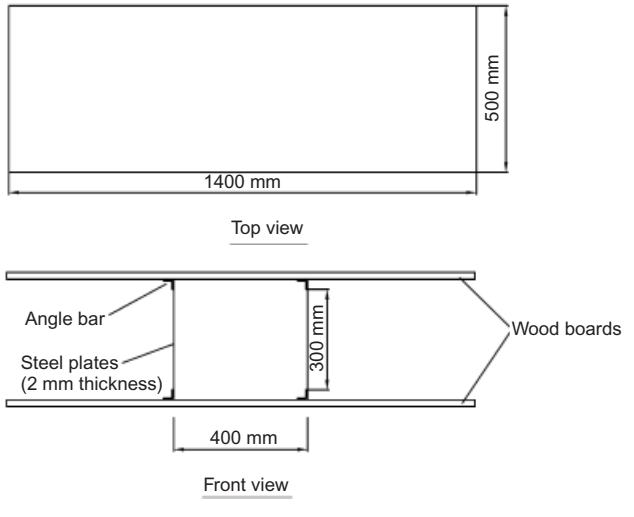

Figure 3. Design of the manual shaking table

between two wooden boards, fixed by angle bars along the transverse direction. The wooden board dimensions were 1·4 m × 0·5 m × 2 cm (length × width × thickness). The mild steel plates were 0·3 m high (distance between tips of angle bars) and 2 mm thick. Such a shaking table can be treated as a system with one degree of freedom. The frequency of the shaking wave was controlled to around 2 Hz. The acceleration in the test was monitored by an accelerometer adhered to the surface of the shaking table. The real-time monitoring data of acceleration were displayed as a graph on a computer monitor. A typical input acceleration chart is shown in Fig. 4. This test was intended to control the peak acceleration at 1·5 m/s^2. As can be seen from Fig. 4, the peak values achieved were in the range around 1·5 ± 0·1 m/s^2, which was sufficiently accurate for the intended purpose.

Sample preparation

ASTM graded sand was used in the test; the basic engineering properties are given in Table 1. The sample was prepared using the following steps.

(*a*) The laminar box was assembled. After checking the water-tightness of the liner, 2 l of either liquid medium with addition of 0·02 l of grown bacterial suspension or distilled water (for the fully saturated sample) were poured into the laminar box.
(*b*) Dry sand was placed into the liquid through a funnel until the sand level almost reached the water level. During deposition, the funnel moved back and forth to allow the sand to be spread uniformly. The above step was repeated until the sample reached the desired height. The samples prepared in this way gave a relative density of around 20%.
(*c*) For tests with biogas, the sample was left for several days to allow sufficient time for the generation of nitrogen gas.

In the shaking table tests, the degree of saturation of sand could not be evaluated by the pore water pressure coefficient B as in triaxial tests. Two other methods were used instead. The first was to measure the concentrations of nitrate before and after the bioreaction and then calculate the gas generation using equations (1)–(3). The second was to measure the water level rise attributable to the gas bubbles generation and replacement in sand. The degrees of saturation measured by these two methods were similar.

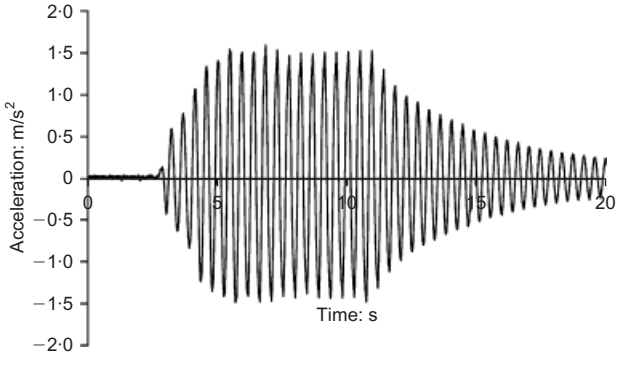

Figure 4. Typical input acceleration (test 5c)

Instrumentation

The layout of the transducers is shown in Fig. 2. The following five types of transducers were used

- two accelerometers (acc1 and acc2) to measure the input acceleration of the shaking table and the acceleration of the second top laminate (no. 9), respectively
- three miniature pore water pressure transducers (pwp1 to pwp3) of PDCR81 type to measure the pore water pressures at the bottom, two-thirds depth, and one-third depth of the sample along the centreline, respectively
- four laser displacement transducers (las1 to las4) to measure the lateral movements of the laminar box at three different elevations and the input lateral movement
- two laser displacement transducers (las5 and las6) to monitor the vertical movement of two concrete blocks placed on the sand surface; the blocks will sink when liquefaction occurs
- one linear variable differential transducer (LVDT) to measure the subsidence of the sand surface.

TEST RESULTS

Test conditions

Test conditions and some results are listed in Table 2. Test 8 was fully saturated sand, whereas tests 5, 6 and 7 were biogas-treated sand with degree of saturation of 80%, 90% and 95%, respectively. The volumes of gas produced could be determined by measuring the water level rises in the model box (2·2, 0·9 and 0·5 cm for tests 5, 6 and 7, respectively) owing to the gas bubble replacement in the pore space of sand. The degrees of saturation could then be calculated using the phase relations of sand samples. For each sample prepared, several tests were carried out using different accelerations ranging from 0·05***g*** to 0·2***g***. The first test was carried out under 0·05***g***. If liquefaction did not occur and the amount of ground settlement was small (i.e. the change in density of the sand was small), another test using higher acceleration would be carried out. A time interval of 10 min was used between tests for pore water pressure to dissipate fully. If there was no liquefaction and the settlement was small in the second test, a third test at an even higher acceleration would be conducted. This process was repeated until liquefaction or relatively large deformation occurred. For each test, 18 oscillations at the required acceleration were applied for around 10 s, as shown in Fig. 4 as an example. The new relative density was calculated for each test based on the settlement monitored.

The efficiency in the conversion of nitrate to nitrogen gas bubbles that were retained in the sand samples was also measured using a set-up under conditions similar to those used for the model tests. The set-up is shown in Fig. 5. A sand sample was prepared in a syringe by following the same procedure as was used for the sample preparation in the model tests. Bacteria and substrates were supplied to generate gas bubbles. The syringe was linked to a burette. When gas bubbles were generated, the bubbles squeezed some liquid from the syringe into the burette. Because no gas bubbles were observed to come out of the water into the burette, the change in water level in the burette was a good indication of the volume of gas generated. An automatic photography system was used to take pictures of the water

Table 1. Typical engineering properties of ASTM graded sand

Description	Grain shape	Mean size: mm	Chemical content	Specific gravity	Maximum void ratio	Minimum void ratio
ASTM graded sand	Round	0·40	99·5 + % SiO_2	2·65	0·8	0·5

Table 2. Test conditions and test results

		Acceleration: m/s^2			Relative density	Volumetric strain	Settlement of structure: mm		Pore pressure ratio			Cyclic stress ratio		
		Input	Soil surface response	Amplification coefficient			At centre	At edge	Bottom	2/3 depth	1/3 depth	Bottom	2/3 depth	1/3 depth
Test 5	Test 5a	0·50	0·57	1·13	20%	0·23%	—	—	0·14	0·14	0·13	0·064	0·081	0·147
($S_r = 80\%$)	Test 5b	1·00	1·18	1·18	21%	0·97%	—	—	0·29	0·34	0·23	0·099	0·118	0·186
	Test 5c	1·50	1·80	1·20	27%	1·08%	—	—	0·25	0·30	0·34	0·230	0·310	0·626
	Test 5d	1·50	1·68	1·12	33%	0·35%	—	—	0·12	0·13	0·19	0·192	0·245	0·459
	Test 5e	2·00	3·00	1·50	35%	1·37%	—	—	0·40	0·41	0·59	0·197	0·262	0·462
	Test 5f	1·50	1·64	1·09	43%	0·38%	—	—	0·11	0·15	0·28	0·230	0·303	0·628
Test 6	Test 6a	0·50	0·54	1·07	17%	0·15%	0·39	0·13	0·08	0·11	—	0·049	0·057	0·085
($S_r = 90\%$)	Test 6b	1·00	1·27	1·27	18%	2·70%	0·00	2·14	0·42	0·60	—	0·153	0·209	0·413
	Test 6c	1·50	1·80	1·20	33%	1·21%	0·77	0·86	0·29	0·42	0·36	0·192	0·250	0·475
	Test 6d	1·50	1·67	1·11	40%	0·31%	0·55	0·94	0·08	0·16	0·17	0·148	0·174	0·280
	Test 6e	1·50	1·62	1·08	42%	0·13%	0·66	0·58	0·03	0·09	0·07	0·229	0·300	0·610
	Test 6f	2·00	2·72	1·36	43%	1·03%	4·27	4·02	0·36	0·56	0·59	0·256	0·352	0·719
Test 7	Test 7a	0·50	0·54	1·08	20%	0·21%	0·08	0·00	0·10	0·11	0·06	0·077	0·099	0·191
($S_r = 95\%$)	Test 7b	1·00	1·44	1·44	22%	5·02%	15·56	6·08	0·55	0·63	—	0·128	0·179	0·354
	Test 7c	1·50	1·80	1·20	51%	0·66%	2·60	2·22	0·39	0·40	0·47	0·148	0·181	0·313
	Test 7d	1·50	1·64	1·09	54%	0·11%	1·61	0·84	0·14	0·11	0·48	0·231	0·306	0·673
	Test 8e	1·50	1·58	1·05	55%	0·05%	0·83	0·73	0·10	0·06	0·06	0·193	0·243	0·489
	Test 8f	2·00	3·56	1·78	55%	0·44%	5·75	6·54	0·54	0·63	0·27	0·198	0·286	0·571
Test 8	Test 8a	0·50	0·54	1·07	21%	5·37%	17·42	15·85	0·55	0·81	0·95	0·064	0·080	0·144
($S_r = 100\%$)	Test 8b	1·50	2·43	1·62	52%	3·83%	>20	>20	0·86	1·02	1·03	0·148	0·205	0·396
	Test 8c	1·50	2·76	1·84	73%	3·11%	22·77	17·19	0·47	0·70	0·85	0·231	0·388	1·123
	Test 8d	1·50	2·06	1·37	89%	0·29%	2·70	0·38	0·06	0·09	0·12	0·194	0·276	0·746
	Test 8e	2·00	2·86	1·43	91%	0·35%	0·71	1·38	0·09	0·13	0·17	0·198	0·264	0·590

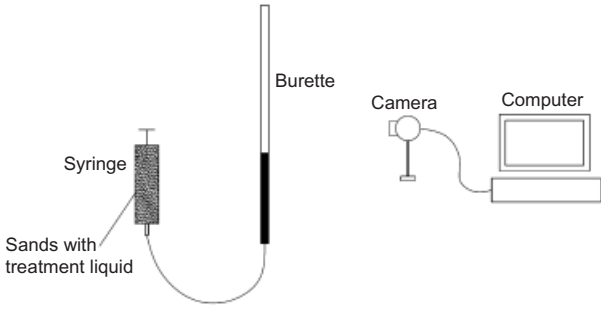

Figure 5. Set-up for the measurement of gas volume

level in the burette at a given time interval, so that not only the yield of the gas, but also the rate of gas production could be measured.

Three samples were tested. The initial concentrations of nitrate-N used were 125, 250 and 374 mg/l, respectively. The initial concentrations of ethanol used were 446, 893 and 1336 mg/l, respectively. The volumes of gas produced were 8·1%, 17·3% and 23·5% per volume of pore space, respectively. The average efficiency measured was around 80% for a nitrate concentration in the tested range. According to the test results, the relationship between the gas production and the initial nitrate concentration manifests a linear correlation as shown in Fig. 6. This relationship indicates that the amount of gas produced can be controlled by adjusting the initial nitrate concentration. The reasons that some nitrate could not be transformed into gas bubbles might be that

(*a*) some gas bubbles close to the sand surface might escape (although this was not observed in the syringe test)
(*b*) some gas could dissolve in water, although the solubility of nitrogen gas in water is very low
(*c*) the reaction was not fully completed, so some nitrate or intermediates might be retained in the system.

Previous studies have shown that some strains of denitrifying bacteria can denitrify from nitrate to nitrogen completely, provided that some factors, such as pH (Saleh-Lakha *et al.*, 2009), level of nitrate concentration (Glass & Silverstein, 1998), composition of medium (Blaszczyk, 1993), temperature (Stanford *et al.*, 1975) and so on, are suitable. The rate of gas production was around 0·5% of pore volume of sand per hour.

Pore water pressure generation

A comparison of the pore water pressure generations in tests on samples with various degrees of saturation is presented in Fig. 7. The pore water pressures were measured by the pore water pressure transducers in kPa, but were converted to water heads for convenience of comparison. The three samples had similar relative densities and experienced the same input acceleration of $a_{max} = 1{\cdot}5\ m/s^2$. A drastic increase in pore water pressure was observed in Fig. 7(a) for test 8b with $S_r = 100\%$. The pore water pressure increased to a peak in less than 3 s and then was maintained at almost the peak value for 5–10 s. The pore water pressure generations for test 7c were substantially smaller than those in test 8b, as shown in Fig. 7(b), even though S_r was reduced to merely 95%. The smallest pore water pressures were observed in test 5f for a sample with $S_r = 80\%$, as shown in Fig. 7(c), even though the relative density of the sample used for this test was a little smaller.

The pore water pressure ratio against relative density of sand curves are plotted in Fig. 8 using pore water pressure data measured at different elevations. The pore water pres-

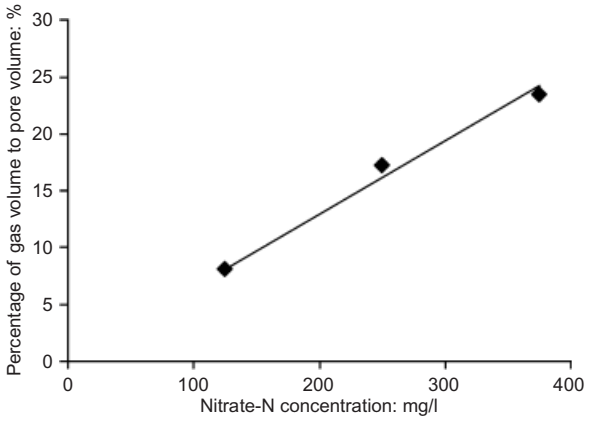

Figure 6. Relationship between the volume of gas produced and the initial nitrate concentration

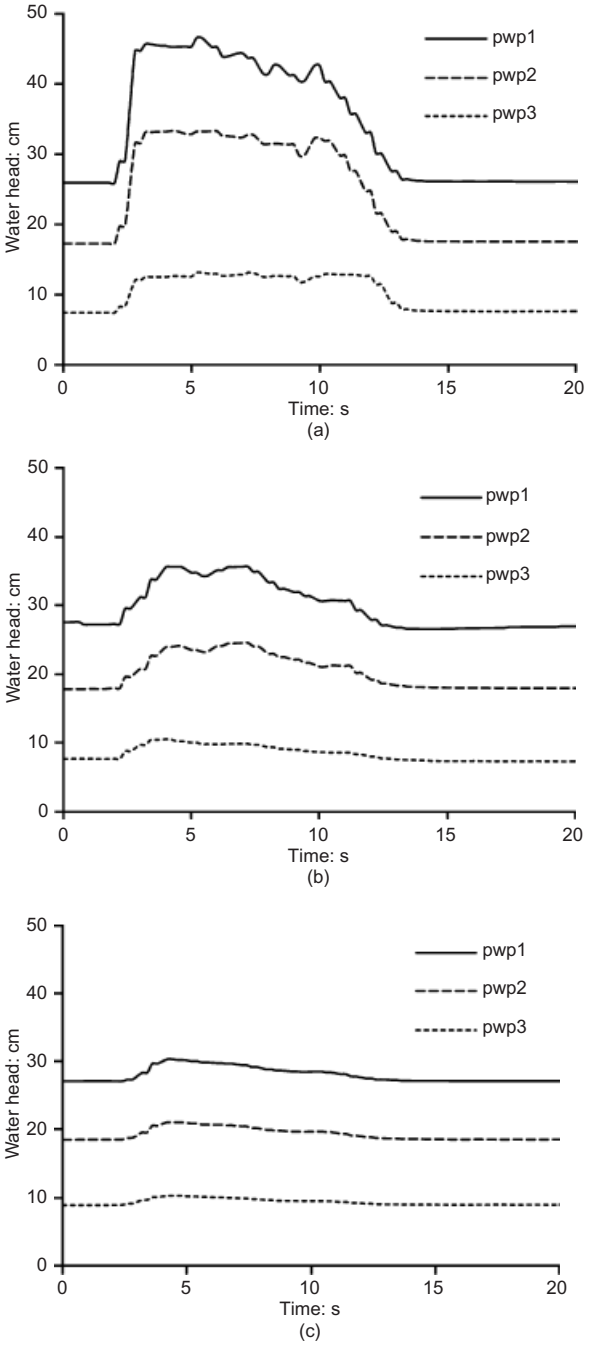

Figure 7. Pore water pressure: (a) test 8b ($D_r = 52\%$, $S_r = 100\%$); (b) test 7c ($D_r = 51\%$, $S_r = 95\%$); (c) test 5f ($D_r = 43\%$, $S_r = 80\%$)

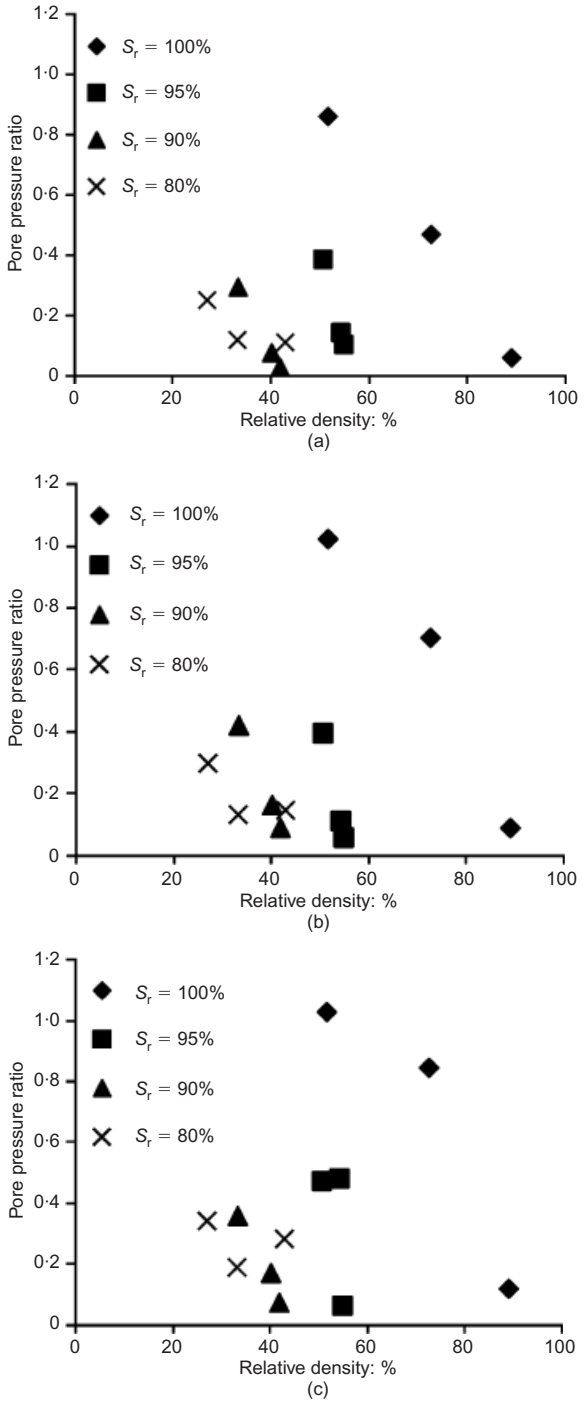

Figure 8. Plots of pore water pressure ratios against relative densities under $a_{max} = 1{\cdot}5$ m/s^2 when pore water pressure was measured by pore water pressure transducers at (a) bottom, (b) two-thirds depth and (c) one-third depth

sure ratio is defined as the ratio of maximum excess pore water pressure to initial effective overburden stress. It can be seen that at a relative density of 52%, the saturated sample liquefied with a pore water pressure ratio of 1. When the degree of saturation was lowered to 95% for soil with the same relative density, the pore water pressure ratio reduced to be less than 0·5, as shown in Fig. 8. Similar observations can be made in Fig. 8 for samples with $S_r = 90$ and 80% at lower relative density ranging from 27 to 43%. Thus the use of biogas generated in situ to reduce the degree of saturation of sand is an effective way to increase the liquefaction resistance of sand. Fig. 8 also indicates that for the fully saturated sample to attain the same pore water pressure ratio as for partially saturated sand, the relative density of the sample has to be around 90%.

Table 2 also shows that the pore water pressure ratio became smaller with increasing depth, although this was not always the case. This trend can be explained from two aspects: the shear strength of soil (termed cyclic resistance ratio, CRR) and the mobilised shear stress (termed cyclic stress ratio, CSR). Because the sample was uniform, the total and effective overburden stress increased with depth. The increase in the effective confining stress gave a higher cyclic resistance ratio (CRR). Another reason could be the magnitudes of cyclic stress ratio (CSR), which can be calculated as (Seed & Idriss, 1971)

$$\mathrm{CSR} = \frac{\tau_{av}}{\sigma'_{vo}} = 0{\cdot}65\frac{a_{max}}{g}\frac{\sigma_{vo}}{\sigma'_{vo}}r_d \tag{4}$$

where r_d is a stress reduction coefficient and in this test a value of 1 was used because the soil model was relatively shallow. It is shown in Table 2 that the cyclic stress ratios calculated by equation (4) were larger at shallower locations for all tests.

Volumetric change

Compared with the fully saturated sand, partially saturated sand manifested a much smaller volumetric change, as shown in Fig. 9. The volumetric strain was calculated using the surface settlement by assuming the soil deformed one-dimensionally. Tokimatsu & Seed (1987) pointed out that pore water pressure generation and volumetric strain also occurred in a non-liquefiable soil; however, the magnitude was often much smaller and the volumetric strains observed in non-liquefiable cases were usually less than 1%. The levels of volumetric strains for partially saturated soil were mostly within 1% strain, indicating that the partially saturated soil had strong resistance to liquefaction and volumetric change. Fig. 9 also shows that the higher the relative density, the lower the volumetric strain, given that other conditions are the same. It is also interesting to note that the data shown in Fig. 9 follow the same pattern as seen in Fig. 8. This implies that when the pore water pressure ratio was higher, the volumetric change would be higher too.

Sinking of structures in sand

It is well known that when soil liquefies, a structure which is heavier than the unit weight of the underlying liquefied soil will sink into the soil. Two circular concrete blocks 40 mm high and 73 mm in diameter were used to simulate the structure resting on the sand surface in the model. One

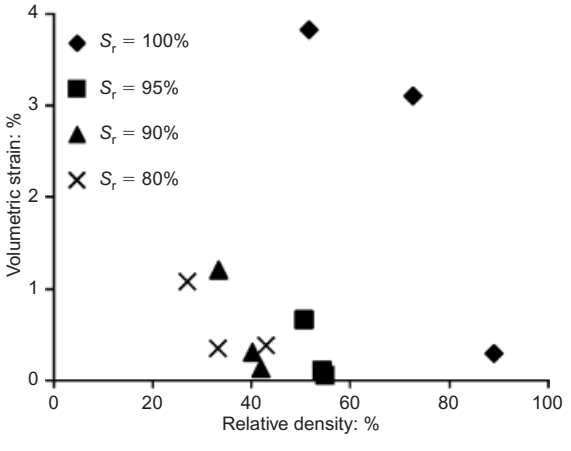

Figure 9. Plots of volumetric strains against relative densities ($a_{max} = 1{\cdot}5$ m/s^2)

block was placed along the centreline and the other near the edge of the laminar box, as shown in Fig. 2. The base pressure acting on the soil was 4·8 kPa.

A comparison of the amount of sinking of the concrete block into the ground measured in two tests for sand with degrees of saturation of 100% and 90% is shown in Fig. 10. The relative density of the soil in the two tests was similar, 17% for test 6a and 21% for test 8a. It can be seen that the structure sank 18 mm in test 8a for saturated soil when liquefaction occurred, whereas little sinking occurred for test 6a for partially saturated soil. A significant amount of sinking was also observed in test 8c in saturated sand, even when the relative density of the sand was 73%, as shown in Table 2.

Response of the laminar box

During the model tests, the accelerations at the sand surface were amplified to some extent, as measured by the accelerometer installed on the second top (or ninth) layer of the laminar box. The acceleration amplification coefficients, defined as the ratio of acceleration measured at the soil surface to that at the base, are plotted against relative density in Fig. 11. It can be seen that the acceleration amplification coefficients decreased with the increase in void ratio and the decrease in the degree of saturation, which is similar to the trends shown in Figs 8 and 9.

The lateral displacements of the laminar box at different elevations were monitored during tests. As an example, the lateral displacements, measured at the second top (or ninth) layer of the laminar box in a non-liquefied test (test 5c) and in a liquefied test (test 8c), are shown in Fig. 12. In both cases, the lateral displacements were too small to be discussed. This might be because the laminar box was placed in the horizontal position and thus there was a lack of a triggering factor to cause a large lateral movement.

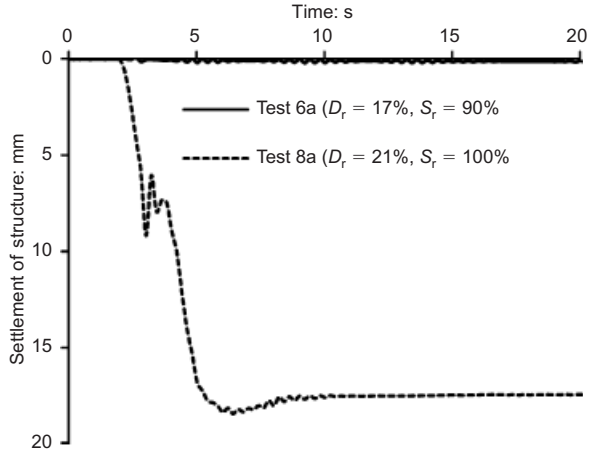

Figure 10. Sinking of structures

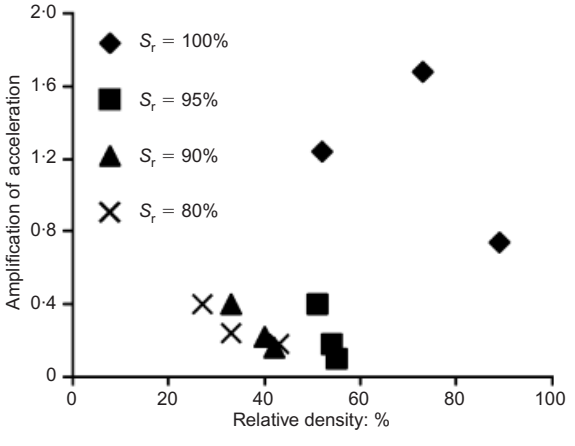

Figure 11. Acceleration amplification coefficients plotted against relative densities (a_{max} = 1·5 m/s^2)

DISCUSSION

Based on the model tests, a relationship between volumetric strain and pore water pressure ratio is established in Fig. 13. It can be seen that the volumetric strain starts to increase at an accelerating rate when the pore water pressure ratio is higher than 0·4. This observation is consistent with those made in other studies (Lee & Albaisa, 1974; Tokimatsu & Seed, 1987). As a single relationship is formed, the trend line appears to be applicable to soil with different densities and degrees of saturation. Hence, the pore water pressure

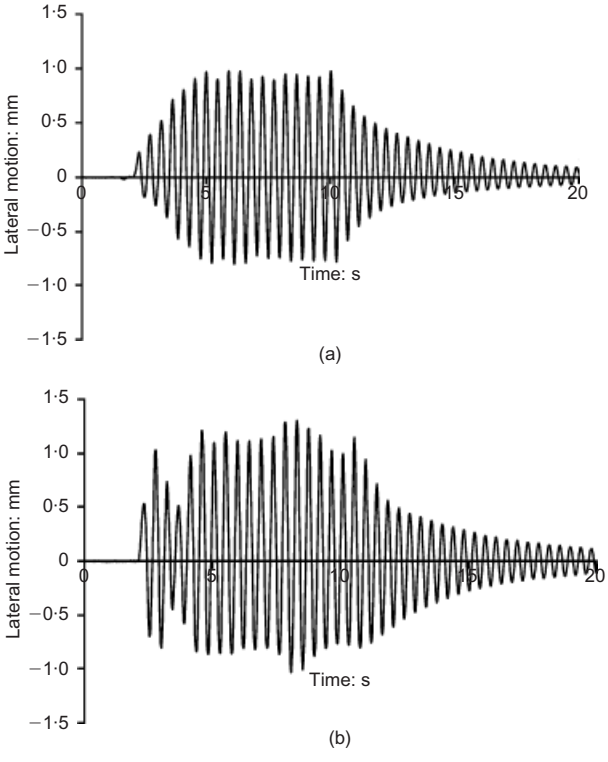

Figure 12. Lateral displacement of the ninth laminate in (a) test 5c and (b) test 8c

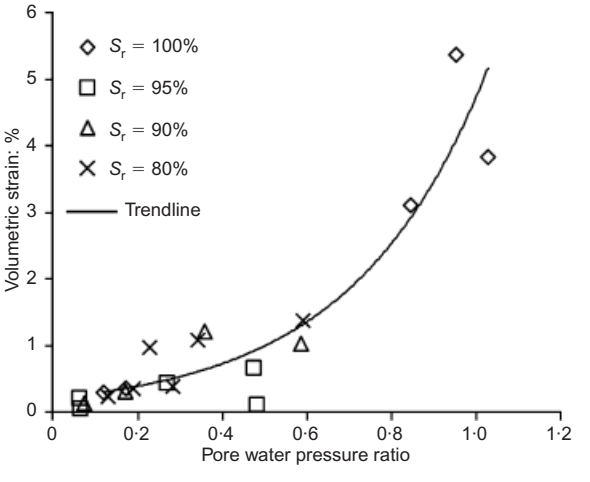

Figure 13. Plot of volumetric strains against pore water pressure ratios

ratio may be a good parameter to use in the design for deformation control.

Figure 13 also shows that reducing the degree of saturation of saturated sand using biogas is an effective method in the mitigation of liquefaction. Most of the pore water pressure ratios for partially saturated samples were smaller than 0·5.

In this study, the effect of the increase of biomass and mineralisation did not have any apparent effect on the mechanical behaviour of sands. The initial amount of mineral substrates and biomass introduced into sands was around 1 g/l of pore volume. The specific amounts of each chemical and biomass have been introduced previously. So the increment of solid materials (both biomass and mineral precipitation) was supposed to be less than this value, which was also by far smaller than the mass of sands. Hence, the effects of liquefaction resistance improvement should be attributable to the gas bubbles, not to other factors such as biomass or mineral precipitation.

It is worth pointing out that denitrification can also potentially be used as a biocementation technique and this has been explored by van Paassen *et al.* (2010). One major difficulty for biocementation using the denitrification process is that nitrate reduction can be limited at a nitrate concentration higher than around 100 mmol (van Paassen *et al.*, 2010). According to Whiffin *et al.* (2007), at least 60 kg of calcium carbonate per cubic metre of soil is needed to obtain a sufficient cementation effect. This requires around 2400 mmol potassium nitrate (KNO_3) for the reaction to complete when ethanol is used as the electron donor. (It does not make much difference when other types of electron donors are used according to equations (1)–(3).) This amount of calcite cannot be achieved at one time. The amount of nitrate required in the biogas method, on the other hand, is much less than 100 mmol; 26·7 mmol/l of nitrate (or 374 mg/l of nitrate-N) is enough to reduce the degree of saturation to 77% according to Fig. 6. This comparison indicates that, for the purpose of mitigation of liquefaction, the biogas method is more cost effective and the process for nitrogen gas production is also simpler than that for mineral precipitation as required for biocementation. However, biocementation may also serve other purposes, such as increasing the shear strength of soil.

CONCLUSIONS

The feasibility of using microbially generated gas bubbles in sand as a liquefaction remedial method has been explored in this paper. Denitrifying bacteria were used to generate tiny, inert nitrogen gas bubbles in situ to reduce the degree of saturation of sand from 100% to the range of 80∼95%. The suspension of bacterial cells and substrates of nutrients have low viscosity and can be easily distributed in sand. The gas generated in this way tends to be more uniform than gas injected into soil.

Shaking table tests with a fully instrumented laminar box were conducted on samples with various degrees of saturation. Test results showed that liquefaction occurred for saturated samples at loose states under $a_{max} = 0{\cdot}5$ m/s^2 and at medium dense states under $a_{max} = 1{\cdot}5$ m/s^2. However, liquefaction did not occur for biogas desaturated samples at the same range of relative density under the same input accelerations. The pore water pressure ratios observed in those tests were also lower than 0·5 in most cases, and ground settlements and volumetric strains were small as well. The shaking table test data also show that the pore water pressure ratio is a good parameter to be used to describe the potential of liquefaction. Under the test conditions, a single relationship between volumetric strain and pore water pressure ratio was established for tests with different degrees of saturation, relative densities and input accelerations. The model tests have demonstrated that the biogas method is effective in lowering the degree of saturation and reducing significantly the liquefaction potential of saturated sand deposit.

NOTATION

a_{max}	maximum acceleration
D_r	relative density
$\boldsymbol{g}$	gravitational acceleration
r_d	stress reduction coefficient
S_r	degree of saturation
σ_{vo}	total overburden stress
σ'_{vo}	effective overburden stress
τ_{av}	average shear stress

REFERENCES

Blaszczyk, M. (1993). Effect of medium composition on the denitrification of nitrate by *Paracoccus denitrificans. Appl. Environ. Microbiol*. **59**, No. 11, 3951–3953.

Chu, J., Stabnikov, V. & Ivanov, V. (2012). Microbially induced calcium carbonate precipitation on surface or in the bulk of soil. *Geomicrobiol. J.* **29**, No. 6, 544–549.

Copp, D. (2003). *Partial saturation as a means of liquefaction mitigation in granular materials*. PhD thesis, Swansea University, UK.

DeJong, J. T., Fritzges, M. B. & Nusslein, K. (2006). Microbially induced cementation to control sand response to undrained shear. *J. Geotech. Geoenviron. Engng, ASCE* **132**, No. 11, 1381–1392.

Dobry, R., Thevanayagam, S., Medina, C., Bethapudi, R., Elgamal, A., Bennett, V., Abdoun, T., Zeghal, M., El Shamy, U. & Mercado, V. M. (2011). Mechanics of lateral spreading observed in a full-scale shake test. *J. Geotech. Geoenviron. Engng, ASCE* **137**, No. 2, 115–129.

Elgamal, A., Yang, Z. H., Lai, T., Kutter, B. L., & Wilson, D. W. (2005). Dynamic response of saturated dense sand in laminated centrifuge container. *J. Geotech. Geoenviron. Engng, ASCE* **131**, No. 5, 598–609.

Eseller-Bayat, E. E. (2009). *Seismic response and prevention of liquefaction failure of sands partially saturated through introduction of gas bubbles*. PhD thesis, Northeastern University, Boston, MA, USA.

Glass, C. & Silverstein, J. (1998). Denitrification kinetics of high nitrate concentration water: pH effect on inhibition and nitrite accumulation. *Water Res*. **32**, No. 3, 831–839.

Harkes, M. P., van Paassen, L. A., Booster, J. L., Whiffin, V. S. & van Loosdrecht, M. C. M. (2010). Fixation and distribution of bacterial activity in sand to induce carbonate precipitation for ground reinforcement. *Ecol. Engng* **36**, No. 2, 112–117.

He, J. (2012). *Mitigation of liquefaction of sands using microbial methods*. PhD thesis, Nanyang Technological University, Singapore.

Ivanov, V. & Chu, J. (2008). Applications of microorganisms to geotechnical engineering for bioclogging and biocementation of soil in situ. *Rev. Environ. Sci. Biotechnol*. **7**, No. 2, 139–153.

Kagawa, T., Sato, M., Minowa, C., Abe, A. & Tazoh, T. (2004). Centrifuge simulations of large-scale shaking table tests. Case studies. *J. Geotech. Geoenviron. Engng, ASCE* **130**, No. 7, 663–672.

Lee, K. L. & Albaisa, A. (1974). Earthquake induced settlements in saturated sands. *J. Geotech. Engng Div., ASCE* **100**, No. 4, 387–406.

Ling, H. I., Mohri, Y., Kawabata, T., Liu, H., Burke, C. & Sun, L. (2003). Centrifugal modeling of seismic behavior of large-diameter pipe in liquefiable soil. *J. Geotech. Geoenviron. Engng, ASCE* **129**, No. 12, 1092–1101.

Okamura, M. & Soga, Y. (2006). Effects of pore fluid compressibility on liquefaction resistance of partially saturated sand. *Soils Found*. **46**, No. 5, 695–700.

Okamura, M. & Teraoka, T. (2006). Shaking table tests to investigate soil desaturation as a liquefaction countermeasure. *Proceedings of seismic performance and simulation of pile foundations*

in liquefied and laterally spreading ground (GSP 145), pp. 282–293. University of California, Davis, CA, USA.

Okamura, M., Ishihara, M. & Tamura, K. (2006). Degree of saturation and liquefaction resistances of sand improved with sand compaction pile. *J. Geotech. Geoenviron. Engng, ASCE* **132**, No. 2, 258–264.

Okamura, M., Takebayashi, M., Nishida, K., Fujii, N., Jinguji, M., Imasato, T., Yasuhara, H. & Nakagawa, E. (2011). In-situ desaturation test by air injection and its evaluation through field monitoring and multiphase flow simulation. *J. Geotech. Geoenviron. Engng, ASCE* **137**, No. 7, 643–652.

Pande, G. N. & Pietruszczak, S. (2008). Assessment of risk of liquefaction in granular materials and its mitigation. *Proc. 12th Int. Conf. Int. Assoc. Comput. Methods Adv. Geomech. (IACMAG), Goa, India*, 2619–2627.

Pietruszczak, S., Pande, G. N. & Oulapour, M. (2003). A hypothesis for mitigation of risk of liquefaction. *Géotechnique* **53**, No. 9, 833–838, http://dx.doi.org/10.1680/geot.2003.53.9.833.

Prasad, S. K., Towhata, I., Chandradhara, G. P. & Nanjundaswamy, P. (2004). Shaking table tests in earthquake geotechnical engineering. *Curr. Sci*. **87**, No. 10, 1398–1404.

Saleh-Lakha, S., Shannon, K. E., Henderson, S. L., Goyer, C., Trevors, J. T., Zebarth, B. J. & Burton, D. L. (2009). Effect of pH and temperature on denitrification gene expression and activity in *Pseudomonas mandelii. Appl. Environ. Microbiol*. **75**, No. 12, 3903–3911.

Seed, H. B. & Idriss, I. M. (1971). Simplified procedure for evaluating soil liquefaction potential. *J. Soil Mech. Found. Engng Div., ASCE* **97**, No. 9, 1249–1273.

Sharp, M. K., Dobry, R. & Phillips, R. (2010). CPT-based evaluation of liquefaction and lateral spreading in centrifuge. *J. Geotech. Geoenviron. Engng, ASCE* **136**, No. 10, 1334–1346.

Stabnikov, V., Naemi, M., Ivanov, V. & Chu, J. (2011). Formation of water-impermeable crust on sand surface using biocement. *Cement Concrete Res*. **41**, No. 11, 1143–1149.

Stanford, G., Dzienia, S. & Vanderpol, R. A. (1975). Effect of temperature on denitrification rate in soils. *Soil Sci. Soc. Am. J.* **39**, No. 5, 867–870.

Thevanayagam, S., Kanagalingam, T., Reinhorn, A., Tharmendhira, R., Dobry, R., Pitman, M., Abdoun, T., Elgamal, A., Zeghal, M., Ecemis, N. & El Shamy, U. (2009). Laminar box system for 1-g physical modeling of liquefaction and lateral spreading. *Geotech. Test. J.* **32**, No. 5, 438–449.

Tokimatsu, K. & Seed, H. B. (1987). Evaluation of settlements in sands due to earthquake shaking. *J. Geotech. Engng Div.*, *ASCE* **113**, No. 8, 861–878.

Ueng, T. S. (2010). Shaking table test for studies of soil liquefaction and soil–pile interation. *Geotech. Engng J. SEAGS & AGSSEA* **41**, No. 1, 1–10.

Ueng, T. S., Wang, M. H., Chen, M. H., Chen, C. H. & Peng, L. H. (2006). A large biaxial shear box for shaking table test on saturated sand. *Geotech. Test. J.* **29**, No. 1, 1–8.

van Paassen, L. A., Daza, C. M., Staal, M., Sorokin, D. Y., van der Zon, W. & van Loosdrecht, M. C. M. (2010). Potential soil reinforcement by biological denitrification. *Ecol. Engng* **36**, No. 2, 168–175.

Whiffin, V. S., van Paassen, L. A. & Harkes, M. P. (2007). Microbial carbonate precipitation as a soil improvement technique. *Geomicrobiol. J.* **24**, No. 5, 417–423.

Yegian, M. K., Eseller, E. & Alshawabkeh, A. (2006). Preparation and cyclic testing of partially saturated sands. *Proc. 4th Int. Conf. on Unsaturated Soils (GSP 147), Carefree, AZ*, 508–518.

Yegian, M. K., Eseller-Bayat, E., Alshawabkeh, A. & Ali, S. (2007). Induced-partial saturation for liquefaction mitigation: experimental investigation. *J. Geotech. Geoenviron. Engng, ASCE* **133**, No. 4, 372–380.

Zhou, Y.-G., Chen, Y.-M. & Shamoto, Y. (2010). Verification of the soil-type specific correlation between liquefaction resistance and shear-wave velocity of sand by dynamic centrifuge test. *J. Geotech. Geoenviron. Engng, ASCE* **136**, No. 1, 165–177.

Montoya, B. M. *et al.* (2013). *Géotechnique* **63**, No. 4, 302–312 [http://dx.doi.org/10.1680/geot.SIP13.P.019]

Dynamic response of liquefiable sand improved by microbial-induced calcite precipitation

B. M. MONTOYA*, J. T. DEJONG† and R. W. BOULANGER†

Microbial-induced calcite precipitation (MICP), a novel bio-mediated ground improvement method, was explored to mitigate liquefaction-prone soils. Geotechnical centrifuge tests were used to evaluate cementation integrity and the response of MICP cemented sands to dynamic loading. The cementation integrity testing reveals a change in behaviour from 'soil like' to 'rock like', with an increase in treatment level. Results from dynamic testing demonstrate a clear increase in resistance to liquefaction of MICP-treated sands compared to untreated loose sand. The MICP sands were treated to varying levels of cementation (light, moderate and heavy cementation levels) and assessed using non-destructive shear wave velocity measurements. The centrifuge models were all subjected to ground motions consisting of sine waves with increasing amplitudes. Accelerations, pore pressures and settlements were measured in the soil during shaking, and the changes in soil behaviour and post-shaking shear wave velocity for soils prepared to different cementation levels are discussed. Increased resistance to liquefaction was demonstrated with a decrease in excess pore pressure ratios in the MICP-treated models, as well as in reduced post-shaking settlements; however, surface accelerations were amplified at heavy levels of cementation. A tradeoff between improving liquefaction resistance and minimising undesirable higher surface accelerations needs to be considered when designing the soil improvement level.

KEYWORDS: centrifuge modelling; dynamics; ground improvement; liquefaction; sands

INTRODUCTION

Liquefiable soils are often a major concern for new or rehabilitated infrastructure. These soils generally consist of loose, saturated cohesionless soils with insufficient cyclic shear strength for the expected cyclic load. Liquefiable soils are conventionally improved using a variety of ground improvement methods, including densifying the soil with mechanical energy or injecting a binding agent such as cement, epoxy or silicates (Karol, 2003). However, alternative techniques have emerged that may provide a more natural and sustainable solution. These techniques utilise biological metabolic processes to mediate improvement of soil properties (e.g. strength and stiffness) (DeJong *et al.*, 2010, 2011). Microbial-induced calcite precipitation (MICP) is a natural biologically mediated method to create cementation in situ and improve the mechanical soil properties (DeJong *et al.*, 2006; Whiffin *et al.*, 2007). MICP utilises urea hydrolysis as the chemical reaction to increase the alkalinity of the pore fluid and induce calcite precipitation (Fujita *et al.*, 2008). *Sporosarcina pasteurii*, a common alkalophilic soil bacterium, has a high urease activity and is used to facilitate the chemical reaction that induces cementation (Mortensen *et al.*, 2011).

Geotechnical centrifuge tests were used to evaluate and establish the potential of MICP treatment to increase soil resistance to liquefaction triggering and to reduce the consequences if liquefaction does occur. The response of the soil at varying levels of treatment, from light to heavy cementation levels (determined using shear wave velocity measurements), was assessed. The cementation integrity, the pore pressure generation and the soil settlement were among the metrics used to evaluate the response of the treated soil. The MICP-treated soil response was compared to untreated loose and dense soil responses as baselines of poor and adequate behaviour, respectively. Each centrifuge model was constructed identically, except for variation of cementation level or sand density. In addition to evaluating the seismic response of the MICP-treated soil, the cementation integrity of the MICP treatment at varying levels of confinement and cementation was also assessed.

The materials and methods implemented, including the MICP treatment process, are presented first. This is followed by a results and discussion section where the centrifuge results are evaluated. Finally, conclusions regarding the effectiveness of MICP to mitigate the potential for liquefaction-induced damage are presented.

MATERIALS AND METHODS

Centrifuge model preparation

The dynamic centrifuge model tests were conducted on the 1 m radius Schaevitz centrifuge at the NEES Center for Geotechnical Modeling at the University of California (UC), Davis. The small, flexible shear beam (SFSB) container was used for the centrifuge tests (container design described in Narayanan (1999)). The interior model dimensions were 494 mm long, 235 mm wide and 120 mm deep (model units). Tests were conducted at a centrifugal acceleration of 50***g***. Unless otherwise stated, all test results are presented in equivalent prototype units, and the scaling laws used to convert model units to equivalent prototype units are summarised in Kutter (1995). All dynamic centrifuge tests presented herein are listed in Table 1; all of the test information and data are archived at the NEEShub project warehouse (https://nees.org/). Additional information regard-

Manuscript received 1 March 2012; revised manuscript accepted 18 October 2012.
Discussion on this paper closes on 1 August 2013, for further details see p. ii.
* Department of Civil, Construction, and Environmental Engineering, North Carolina State University, Raleigh, NC, USA.
† Department of Civil and Environmental Engineering, University of California, Davis, CA, USA.

Table 1. Centrifuge model test information

Test number	D_R of Ottawa 50–70* sand: %	Treatment level	Mass of calcite:† %	Initial V_s:‡ m/s at 50***g***
MICP-09	40	Untreated	0·0	155
MICP-11	85	Untreated	0·0	180
MICP-10	40	Light cement	3·0	350
MICP-12	40	Moderate cement	2·6	660
MICP-08	40	Heavy cement	8·0	1200

* The Ottawa 50–70 sand used has the following properties: mean particle size, $D_{50} = 0{\cdot}22$ mm; coefficient of uniformity, $C_u = 1{\cdot}4$; coefficient of curvature, $C_c = 0{\cdot}9$; specific gravity, $G_s = 2{\cdot}65$; minimum void ratio, $e_{min} = 0{\cdot}55$; maximum void ratio, $e_{max} = 0{\cdot}87$; quartz mineralogy; round shape.
† The mass of calcite for the lightly cemented model (MICP-10) is inflated owing to plugging of the drains at the base of the model container. The plugging allowed for precipitation to occur outside the particle contacts, which increased the mass of calcite without increasing the shear wave velocity, V_s, of the soil.
‡ Average values of V_s.

ing the equipment and instrumentation used at the UC Davis centrifuge facility is available at their website (http://nees.ucdavis.edu/).

The centrifuge model consisted of a flat soil surface with a simple structure in the centre of the model; however, the results presented herein are from the behaviour of the free field sensors only. The primary soil deposit consists of a 5·5 m thick, liquefiable, loose, poorly graded sand layer (Ottawa 50–70; properties presented in Table 1) overlying a thin 0·5 m thick layer of dense Monterey sand. The thin layer of coarse Monterey sand at the centrifuge container base provided drainage during treatment and enabled uniform saturation. The accelerometers (ACCs) and pore pressure transducers (PPTs) were placed as pairs in a vertical array in the free field (a profile view of the sensors is included later, in Fig. 3). Bender elements were installed in pairs at two depths and three horizontal locations at each depth to track shear wave velocity during treatment, spin-up and before/after shaking. Linear displacements were measured at the soil surface above the free field vertical array of ACCs and PPTs.

Model saturation following treatment consisted of application of 25 in mercury (inHg) vacuum followed by slow saturation with de-aired deionised water. Water was used as the pore fluid to eliminate the potential for negative effects on the MICP process if a different material was used as pore fluid. However, the use of water as the pore fluid instead of a more viscous material (e.g. a solution of hydroxypropyl methylcellulose and water) results in an inconsistency between the scaling laws for the dynamic time and diffusion time. This inconsistency in the time scaling laws results in the generated pore pressures dissipating quicker than they would in the true prototype environment. The model was not flushed with carbon dioxide, as commonly done, because the carbon dioxide is slightly acidic and can degrade the calcite cementation. The response of the soil after the saturation process was consistent with fully saturated soil, including the PPTs measuring the appropriate hydrostatic pore pressures and exhibiting a rapid response during shaking.

Each centrifuge test was subjected to a series of ground motions, as indicated in Table 2. The five ground motions presented consist of sine waves at a prototype frequency of 2 Hz and increasing amplitudes of maximum base accelerations ranging from about 0·1***g*** to 0·7***g***.

Biological treatment

The centrifuge models were biologically treated to varying levels of cementation (as in Table 1). Conceptually, the 'light' cementation (target shear wave velocity, $V_s = 300$ m/s) represents an aged sand, the 'moderate' cementation level ($V_s = 650$ m/s) represents a cemented sand and the 'heavy' cementation level ($V_s = 1200$ m/s) represents rock-like (i.e. sandstone) material. These target levels of cementation were chosen to cover a spectrum of possible treatment levels; they were also chosen to transition from behaviours that can be described using critical state soil mechanics (e.g. 'soil like') to behaviour that can be better described using fracture mechanics (e.g. 'rock like'). Because of the large model size (and therefore large treatment volume) in comparison to laboratory specimens, the biological treatment process was simplified from previous studies (see Mortensen *et al.*, 2011). The bacteria, *S. pasteurii*, were grown for 40 h following American type culture collection (ATCC) recommendations before harvesting. One litre of turbid bacterial suspension ($OD_{600} = 0{\cdot}8–1{\cdot}0$) was diluted with 7 l of 0·5 M urea solution. The sand was inoculated with the bacteria–urea medium by flooding the sand at the surface and allowing it to drain freely out of the container bottom (i.e. percolation). Percolation was used as a treatment method

Table 2. Ground motion sequence for centrifuge model tests

Shake no.	Motion	Description			Range of a_{max} at container base for MICP-8–13	Average a_{max} at container base
		Displacement:* in	Frequency:* Hz	No. of cycles		
1	Sinusoidal	0·008	100	15	0·11–0·15***g***	0·12***g***
2	Sinusoidal	0·015	100	15	0·21–0·27***g***	0·24***g***
3	Sinusoidal	0·03	100	15	0·43–0·52***g***	0·47***g***
4	Sinusoidal	0·04	100	15	0·59–0·68***g***	0·65***g***
5	Sinusoidal	0·05	100	15	0·62–0·85***g***	0·74***g***

* The displacement and frequency commands sent to the shaker are in model scale. Therefore, the equivalent prototype frequency of the sine waves is 2 Hz.

because preliminary laboratory tests found that percolating the treatment fluid through free-draining soil resulted in similar or improved uniformity of cementation distribution compared to specimens that underwent treatment by a more traditional injection method. The mass of calcite was measured in each centrifuge model, and cementation was found to be uniform both laterally and vertically within the model, with a standard deviation in mass of calcite of about 20%. In addition, percolation provided a more controlled treatment environment for the centrifuge container than an injection scheme, such as arrays of injection and extraction wells. Although percolation was the chosen treatment method for the model preparation, injection methods may be more realistic for field treatments. Based on microscale investigations by the research team, the calcite precipitation is similar for percolation and injection methods; therefore, the behaviour of the cemented sands from the MICP treatments is similar whether percolation or injection methods were used. The behaviour presented herein from the models prepared using a percolation treatment method can be expected to be representative of MICP-treated sands from injection methods, if the injection procedures are successful in obtaining similar degrees of treatment uniformity. For surficial stability during treatment, a neoprene mesh and $\frac{1}{2}$ in crushed rock were placed on the surface of the sand. The crushed rock also provided a light overburden that increased the amplitude of the received bender element signal at 1***g***.

The cementation process was initiated after the inoculated bacteria were retained in the model for at least 6 h to allow bacterial attachment to sand grains. Urea–calcium cementation medium (1 M urea: 0·5 M calcium chloride) was used to induce ureolytic-driven calcite precipitation. Cementation treatments were repeated every 4–6 h until the target shear wave velocity (see Table 1) was attained.

The cementation increase was monitored in real time using shear wave velocity. Bender elements (Piezo Systems, Inc.) required special preparation for the highly conductive environmental conditions (Montoya *et al.*, 2012). Shear waves were applied using a 9 V, 100 Hz square wave and the received bender element response was recorded in a *LabView* (National Instruments, Austin, TX) program (Brandenberg *et al.*, 2008). The shear wave velocity was determined from visually interpreted travel times and measured bender element spacing in the model (including corrections for bender element movement from soil deformations).

Cyclic direct simple shear test

Cyclic direct simple shear (DSSc) tests were performed to compare to the centrifuge tests. The DSSc tests were performed with a Geotac DigiShear apparatus configured for constant-volume shear tests with full drainage to the specimen. This configuration, the equivalent undrained methodology developed by the Norwegian Geotechnical Institute, allows for a constant volume, or 'undrained', test to be performed, even though drained conditions are maintained (e.g. sample drain lines are open) and no pore pressures are developed. The change in normal stress measured during the constant-volume test is assumed to be the equivalent to the excess pore pressure generation under true undrained loading. The specimens were 63·5 mm in diameter, and approximately 16·5 mm tall. The loose sand specimens were consolidated to a vertical effective stress of 100 kPa, and then underwent the MICP treatment procedure outlined above for the centrifuge tests. The specimens were then subjected to strain-controlled loading at a strain rate of 50% shear strain per hour. If, after a significant number of cycles, shear wave velocities and test data indicated the specimen had neither yielded nor changed structurally, the cyclic stress limits were increased to accelerate the test.

BIOCEMENTATION INTEGRITY DURING STRESS CYCLING

The integrity of the cementation is dependent on the confinement stress and the stress at which the cementation was precipitated (i.e. curing stress). For centrifuge testing, the cementation treatments occurred at 1***g***, whereas dynamic shaking occurred at 50***g***. The influence of the increased ***g***-field on cementation integrity was quantified to ensure the target V_s at 50***g*** was consistently achieved.

The effect of the change of confinement on the cementation integrity was monitored using shear wave velocity measurements on specimens prepared to different degrees of cementation and then subjected to slow cycles of vertical stress by increasing and decreasing the centrifugal acceleration. As the centrifuge model spun up from 1***g*** to 50***g***, bender elements were used to measure the shear wave velocity at discrete centrifugal accelerations. Results are presented in Fig. 1 as shear stiffness plotted against effective vertical stress. When the confinement increases, the stress at the contacts between the sand particles increases, which results in an increase in shear wave velocity. However, the cementation has a preference to precipitate at the particle contacts and, as the stresses at the contacts increase, cementation may be damaged (DeJong *et al.*, 2010). The extent of cementation degradation depends on the cementation level and loading path. Therefore, as the confinement stress changes, corresponding changes in the measured shear wave

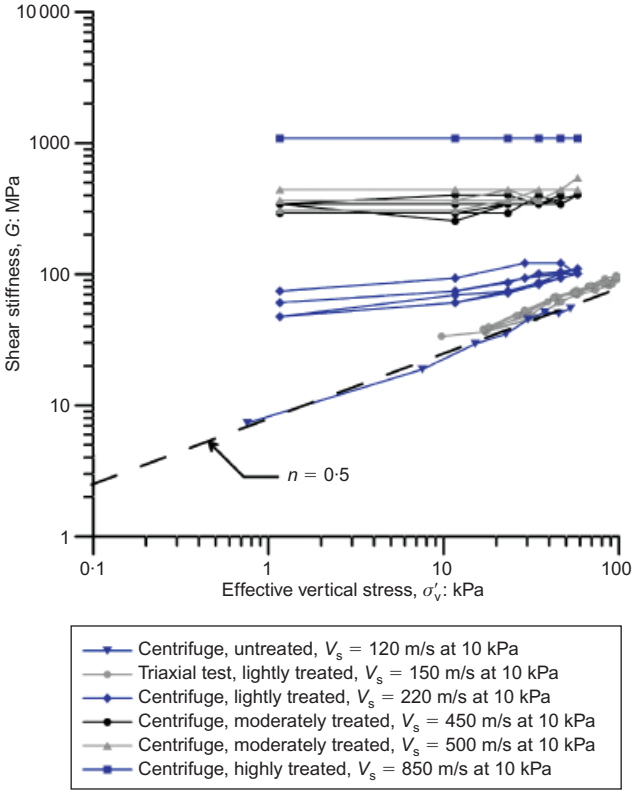

Fig. 1. Variation of small-strain shear modulus of untreated to highly treated sands during repeated cycles of increasing and decreasing effective confining stress. The black dashed line has a slope of $n = 0{\cdot}5$, following the general relationships for untreated soils outlined by Stokoe *et al.* (1985) and Hardin & Black (1968). This black line is used as a reference to compare the results of both untreated and cemented soils

velocity are due to the increase (or decrease) in confinement and the degradation of the cementation.

Effects of confinement on shear stiffness, G, are well established for uncemented soils (e.g. Hardin & Black, 1968; Stokoe *et al.*, 1985). In general, the relationship of log G against log σ'_v for uncemented sands has a slope of 0·5 (slope indicated by dashed line in Fig. 1). This slope is similar to the value obtained in the tests with untreated sand specimens.

The slope of log G against log σ'_v for cemented sands varies as a function of cementation level (Fig. 1). As cementation increases, the slope decreases until the stiffness is no longer dependent on the confinement stress (e.g. slope equal to zero). In general, as the cementation degrades, the slope of the log G against log σ'_v relationship begins to increase, becoming more similar to that of the uncemented sand (as illustrated in Fig. 2 and discussed below).

The influence of confinement and cementation degradation on the shear stiffness of one specimen of MICP-treated sand is presented in Fig. 2. A lightly cemented sand ($V_s = 220$ m/s at 10 kPa) was subjected to cycles of vertical stress loading and unloading utilising the centrifuge. As the centrifuge spins up from 1***g*** to 25***g*** (cycle 0, Fig. 2), the shear stiffness continually increases (non-linearly). Above 25***g***, the cementation begins to degrade and the shear stiffness remains constant, even with an increase in confinement (higher ***g*** level). The cementation (shear stiffness) degrades further with an increase to 50***g***. During unloading (spin down to 1***g***), the cumulative cementation degradation is represented by the permanent reduction of the shear stiffness (cycle 1, Fig. 2). Cementation continues to degrade with another cycle, producing a further decrease in shear stiffness (cycle 2, Fig. 2). After two full loading–unloading cycles, the behaviour of the cemented sand stabilises, with the shear stiffness no longer degrading (cycle 3, Fig. 2). This final slope is still lower than the slope of the uncemented sands ($n < 0{\cdot}5$). This behaviour indicates that the light cementation, although slightly degraded, still improves the small-strain stiffness compared to the untreated sand. The improvement in stiffness after degradation of the cementation is also influenced by the decreased void ratio from the precipitated calcite in the voids (whether intact to sand grains or degraded into fines). As an example, an approximate decrease in void ratio of 0·03 can be expected for about 1·5% mass of calcite (Weil *et al.*, 2011). Similar cementation degradation behaviour with stress cycling is also evident in the moderately cemented sands (Fig. 1, $V_s = 450$–500 m/s). However, once the cementation becomes sufficient such that the soil stiffness is no longer dependent on the confinement stress, the cementation does not degrade with cyclic loading–unloading (Fig. 1, $V_s = 850$ m/s).

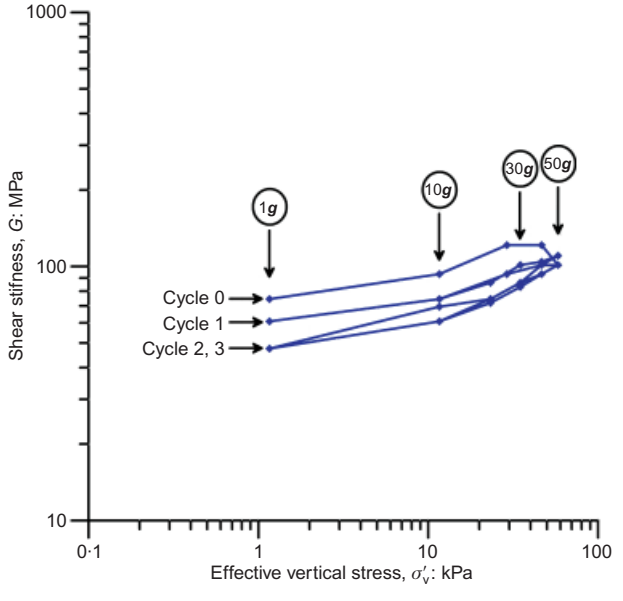

Fig. 2. Cementation integrity of lightly cemented sand ($V_s = 220$ m/s at 10 kPa)

By understanding the relationship between shear stiffness and confining stress at the various levels of cementation, the bio-treatment levels could be designed for the centrifuge experiment. The centrifuge models were treated at 1***g*** to a certain value of shear wave velocity so that the desired shear wave velocity was achieved at a confinement of 50***g***. The results from the cementation integrity testing (Fig. 1) were used to design the 1***g*** treatment levels.

FREE-FIELD DYNAMIC PERFORMANCE

Results

The response of the free-field MICP-treated soil to dynamic loading is examined using time histories from the following two events: sine waves with a 'low' a_{max} value (about 0·2***g***) and a 'high' a_{max} value (about 0·7***g***) at the container base. Results from five models are presented: loose untreated sand, dense untreated sand, loose lightly cemented sand, loose moderately cemented sand, and loose heavily cemented sand (Table 1). The response of each soil is compared to the untreated loose sand (considered the baseline). The dynamic response from each sine wave amplitude motion (Table 2) is summarised at the end of the discussion.

Baseline untreated loose and dense sand response. The untreated loose soil response at the low shaking level (Fig. 3, dashed line) reached excess pore pressure ratios (r_u = excess pore pressure/vertical effective stress) ranging from 0·4 at depth to 1·0 near the surface of the profile. The untreated loose sand developed similar levels of surface acceleration across all the cycles of the ground motion, even though liquefaction occurs (e.g. $r_u \sim 100\%$) near the surface (Fig. 3, dashed line). At low shaking levels, the acceleration amplification is expected to be equal to or greater than 1·0 and largely in phase with the base motion because the base motion frequency ($f_{in} = 2$ Hz) is smaller than the natural soil frequency ($f_n = 6{\cdot}5$ Hz). When the soil softens due to seismic loading, the natural frequency reduces (Table 3), yet it remains larger than the base motion frequency ($f_{in} = 2$ Hz) such that the amplitude and phasing of the surface motion did not change dramatically (Fig. 3, dashed line).

The untreated loose sand response at the high shaking level (Fig. 4, dashed line) has a notable difference in behaviour relative to that of the lower shaking level. The accelerations, especially the near-surface recording (AH 7), exhibit a spiky shape, indicating strain-stiffening non-linearity in the stress–strain behaviour of the soil (Chou & Kutter, 2008). When the soil is undergoing strain-stiffening behaviour during cyclic loads, a shock wave may form that corresponds to discontinuities in shear stress and large spikes in the acceleration record (Chou & Kutter, 2008). This strain-stiffening non-linearity behaviour has also been observed in laboratory tests (Ishihara, 1985) and field seismic recordings (Youd & Holzer, 1994). The non-linearity in the centrifuge time history is more pronounced at the high shaking level than at the lower shaking amplitudes, as expected. In addition, the excess pore pressures generated are greater than at the lower shaking levels. At the high shaking level, the untreated loose soil generated significant excess pore pressures at all depths, with r_u values of 0·7 at depth to 1·0 near the surface. High pore pressure continues until the end of shaking, after which

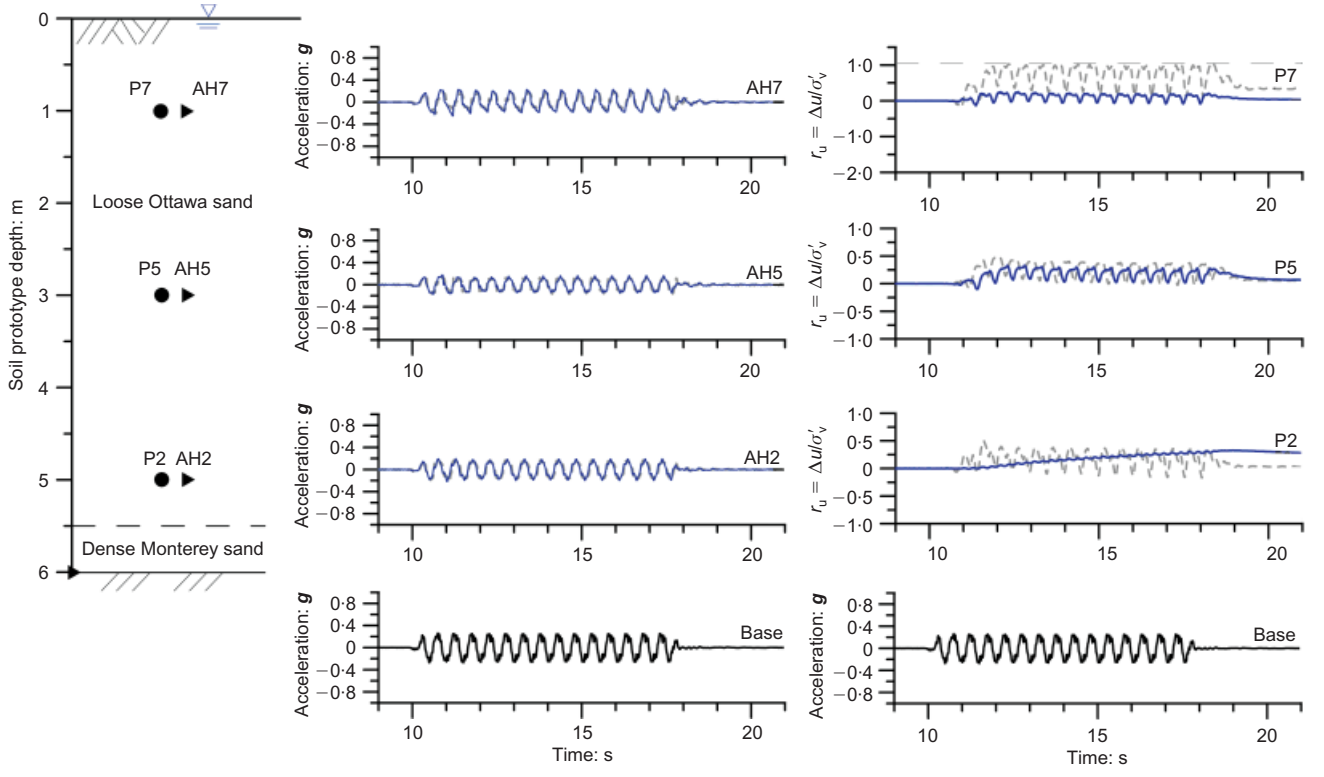

Fig. 3. Free-field untreated dense sand behaviour under dynamic loading (base $a_{max} = 0{\cdot}2g$) (solid line) compared to untreated, loose sand behaviour under the same dynamic load (dashed line)

Table 3. Natural frequencies of the soil column for each centrifuge model test

Test number	Initial V_s: m/s at 50g	Initial f_n:* Hz	Wavelength: m	Initial G_{max}: MPa	Degraded f_n:† Hz	Wavelength: m	Ratio of degraded to initial G_{max}†
MICP-09	155	6·5	77·5	36·0	5·8	70·0	0·82
MICP-11	180	7·5	90·0	48·6	8·7	104	1·34
MICP-10	350	15	175	184	12	140	0·64
MICP-12	660	28	330	653	20	235	0·51
MICP-08	1000	42	500	1500	22	265	0·28

* The natural frequency of the soil prior to dynamic loading (e.g. stiffness degradation). The natural frequency of the soil column is: $f_n = V_s/4H$.
† Determined using the V_s after shaking, which is representative of the degraded cemented material.

pore pressure begins to dissipate. Offsets between the initial and final pore pressure values are attributable to transducer settlements that have taken place during and after shaking.

The response of the dense untreated sand to dynamic loading is significantly improved compared to the untreated loose soil. Under the 0·2g sine wave motion, the acceleration–time histories are equivalent to the recordings from the loose sand model (Fig. 3, solid line). The acceleration time histories during the 0·7g sine wave event have similar phasing when compared to the loose untreated sand; however, the acceleration amplitude is increased (Fig. 4, solid line). The acceleration amplitude at the deeper soil layer is equivalent, and the wave amplifies as it approaches the soil surface (1·5×) compared to the loose sand with similar nonlinearity evident in the recordings. The dense sand response also experienced lower generation of pore pressures at both levels of shaking, with the r_u value about 0·3 at depth and at about 0·8 near the surface.

Biotreated sand response. The behaviour of the lightly cemented loose sand ($V_s = 350$ m/s) presented in Figs 5–8 shows improved soil behaviour similar to the dense sand. The acceleration–time histories at 0·2g exhibit similar phasing and similar amplitudes compared to the loose sand. At the higher shaking level, acceleration–time histories exhibit similar phasing with slightly larger amplitudes than the loose sand at the deeper depths (1·2 times) and increasing amplitudes near the surface (1·1–1·5 times the loose sand amplitude). The lightly cemented sand response also experienced significantly lower pore pressure generation at both shaking levels, with the r_u value reaching 0·5 at depth and only ~0·3 near the surface.

The moderately cemented sand (Figs 5–8) also shows improved soil behaviour, similar to that of the lightly cemented and dense untreated sands. At 0·2g dynamic loading, the acceleration–time histories indicate similar phasing and amplitudes compared to those of the loose sand. The acceleration records from the 0·7g dynamic loading show similar phasing to the loose untreated sand, with amplitudes that are equivalent at the lower depth, lower at the mid-depth (0·5 times) and about 1·6 times higher near the surface. The generated excess pore pressures are significantly lower at both shaking levels (e.g. maximum $r_u = 0{\cdot}2$ at 0·2g shaking and maximum $r_u = 0{\cdot}6$ at 0·7g shaking).

The dynamic response of the heavily cemented sand (Figs 5–8) is largely similar to that of the moderately and lightly cemented sands. At 0·2g dynamic loading, the acceleration–

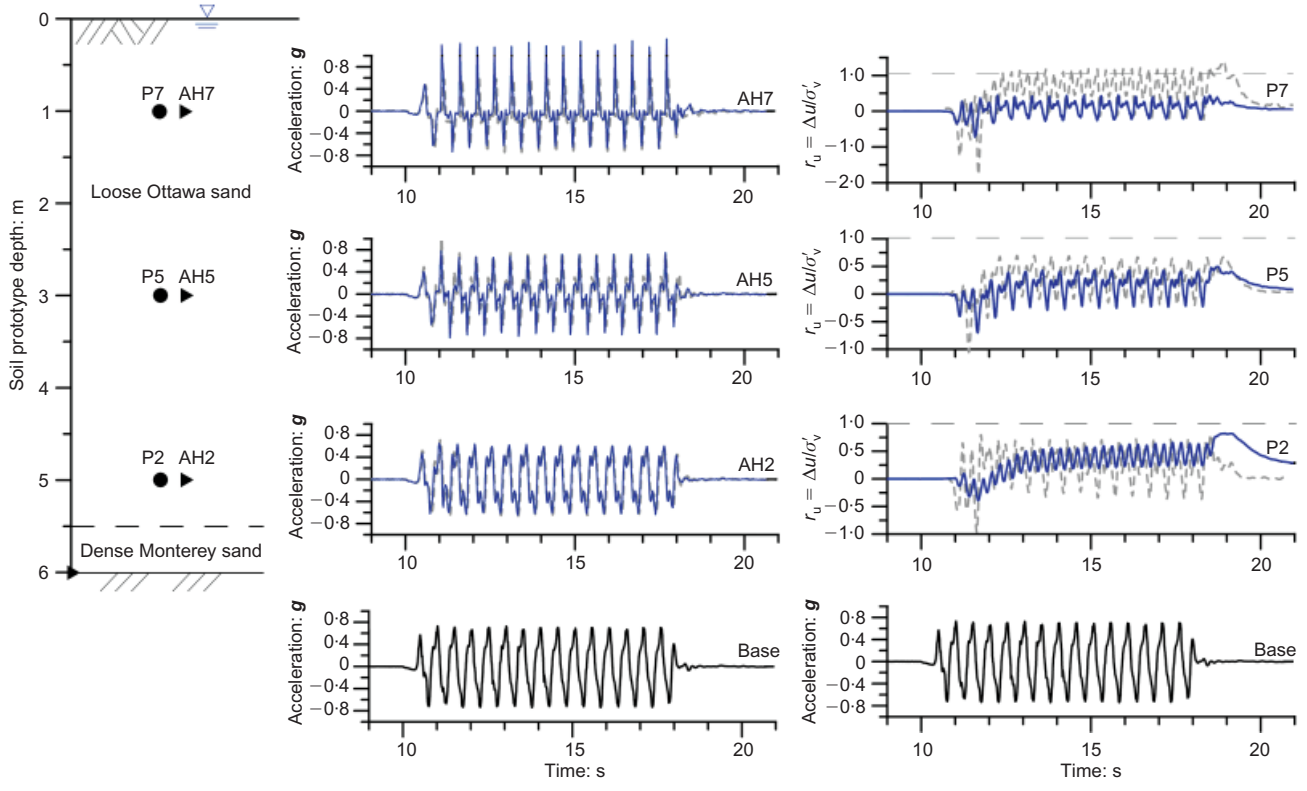

Fig. 4. Free-field untreated dense sand behaviour under dynamic loading (base $a_{max} = 0{\cdot}7g$) (solid line) compared to untreated, loose sand behaviour under the same dynamic load (dashed line)

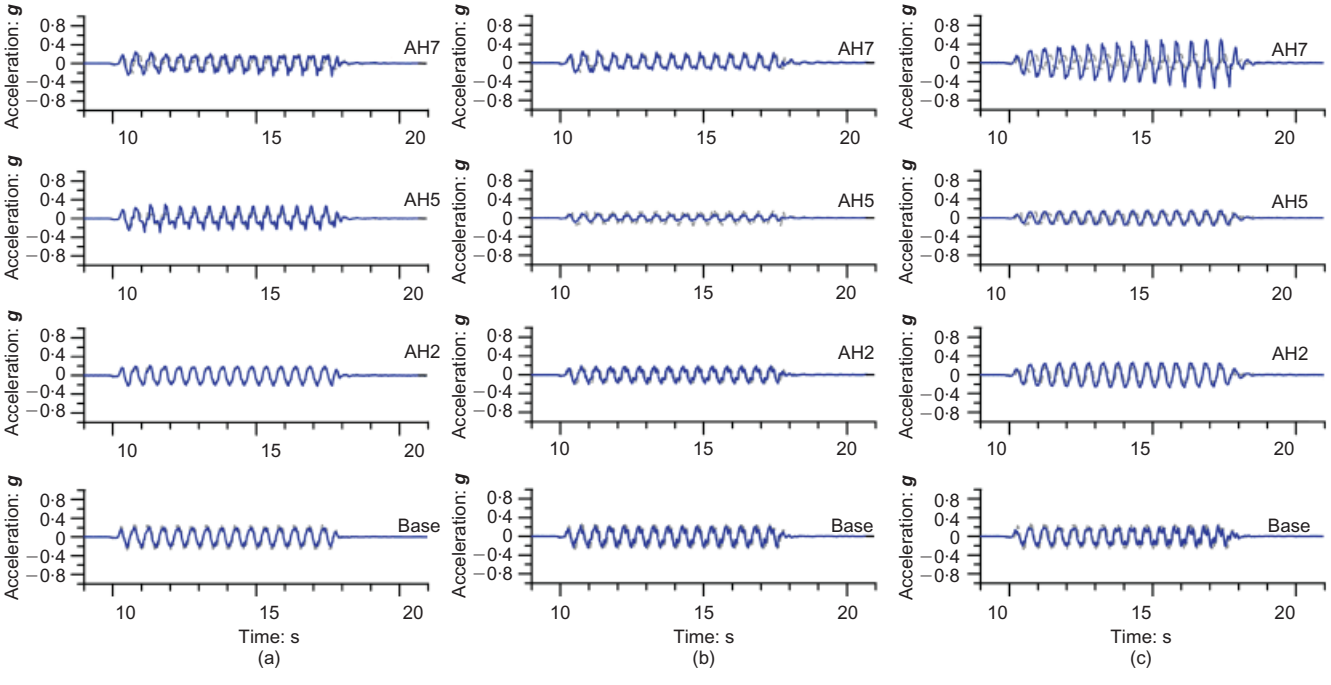

Fig. 5. Free-field cemented sand acceleration–time histories under dynamic loading (base $a_{max} = 0{\cdot}2g$) (solid line) compared to untreated, loose sand behaviour under the same dynamic load (dashed line): (a) lightly cemented sand; (b) moderately cemented sand; (c) heavily cemented sand

time histories at the lower and mid-depths contain similar phasing and amplitudes compared to those of the moderately and lightly cemented sands. However, the near-surface acceleration starts at a similar amplitude and then begins to increase incrementally in amplitude during the shaking event up to about twice that of the moderately and lightly cemented sand. This increase in acceleration with each cycle of $0{\cdot}2g$ shaking was accompanied by a transition to a spikey response. At $0{\cdot}7g$ dynamic loading, the acceleration recordings at mid-depth and near the surface exhibit one-sided spikes for all three cementation levels, similar to those shown in Chou & Kutter (2008), which indicate strain-stiffening non-linearity. The heavily, moderately and lightly cemented sands also experienced similar mean levels of excess pore pressures at both levels of shaking, although the transient spikes in r_u varied in magnitude at the various

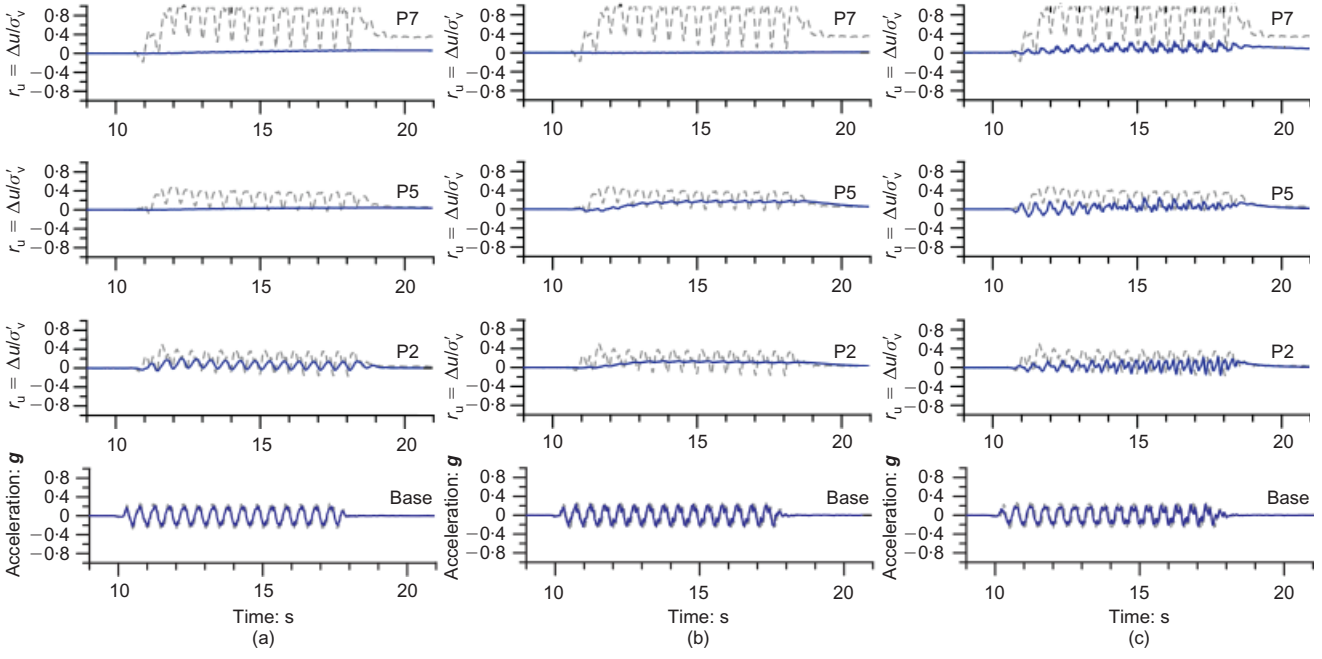

Fig. 6. Free-field cemented sand normalised excess pore pressure–time histories under dynamic loading (base $a_{max} = 0{\cdot}2g$) (solid line) compared to untreated, loose sand behaviour under the same dynamic load (dashed line): (a) lightly cemented sand; (b) moderately cemented sand; (c) heavily cemented sand

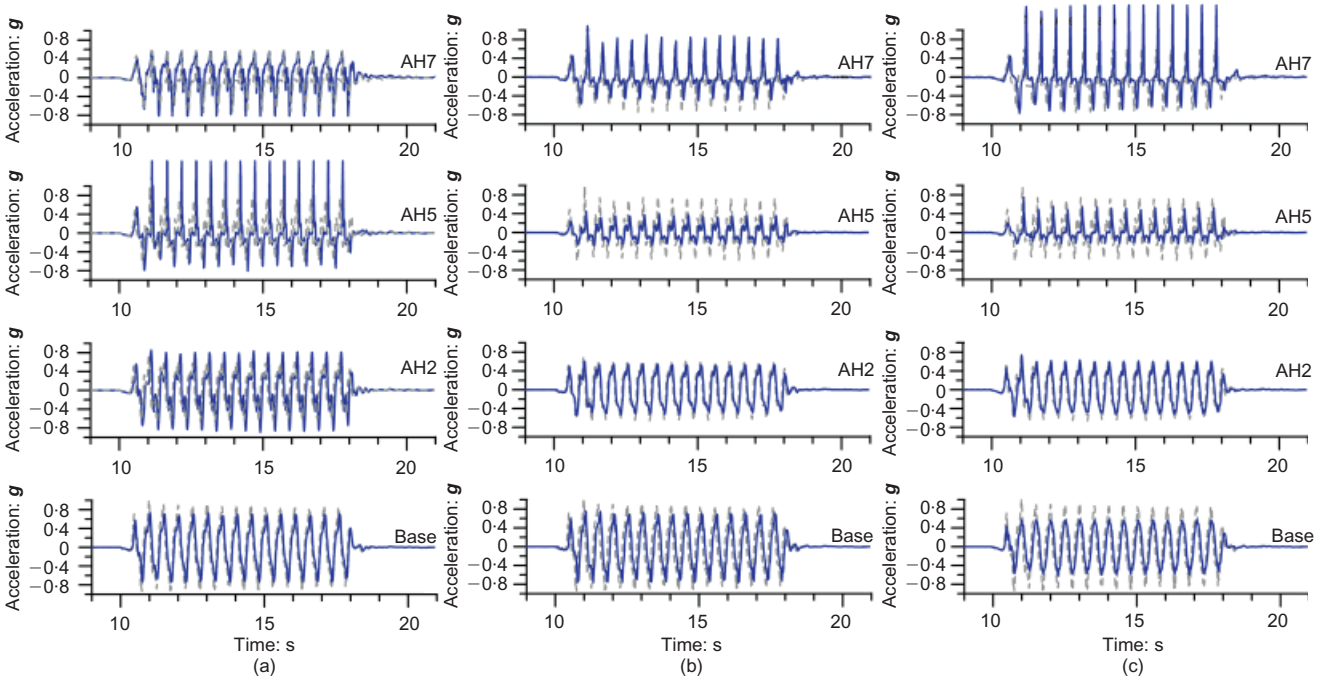

Fig. 7. Free-field cemented sand acceleration–time histories under dynamic loading (base $a_{max} = 0{\cdot}7g$) (solid line) compared to untreated loose sand behaviour under the same dynamic load (dashed line): (a) lightly cemented sand; (b) moderately cemented sand; (c) heavily cemented sand

depths in these three models. The heavily cemented sand had peak r_u values up to 0·25 at depth and about 0·65 near the surface in the stronger shaking event. The positive spikes in the pore pressure are in phase with the spikes of the acceleration–time history at the same elevation, which indicates that this feature may be due to a temporary pulse in mean stress (e.g. from compression waves reflecting off the side walls). The fact that the spikes in pore pressure are slightly one-sided may indicate an asymmetric gapping or contact against the end walls. Even with this behaviour, the amplitudes of the generated excess pore pressures are still less than an r_u value of 1·0.

Discussion

The MICP-treated soils developed lower levels of excess pore pressure and higher peak ground surface accelerations for similar base input accelerations compared to the loose untreated sand baseline. The acceleration–time histories at 0·2***g*** are, in general, quite similar to that of the loose sand

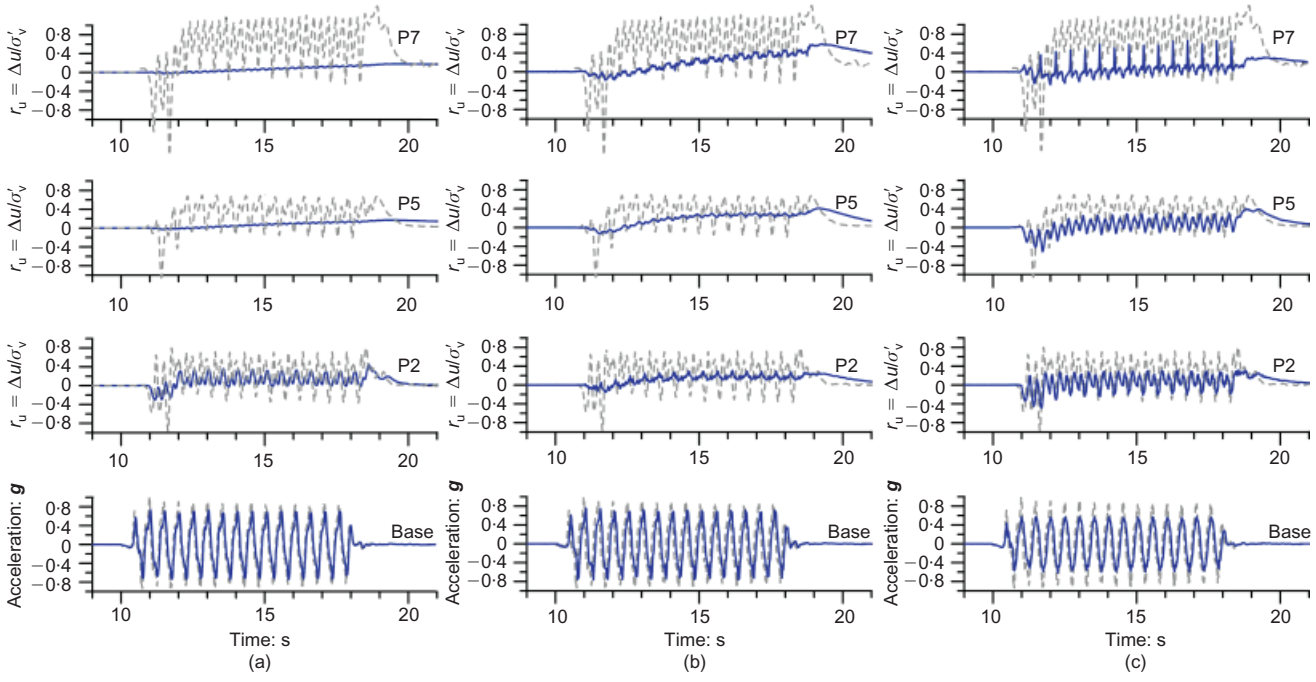

Fig. 8. Free-field cemented sand normalised excess pore pressure–time histories under dynamic loading (base $a_{max} = 0{\cdot}7g$) (solid line) compared to untreated loose sand behaviour under the same dynamic load (dashed line): (a) lightly cemented sand; (b) moderately cemented sand; (c) heavily cemented sand

(equivalent or less in amplitude, and in phase with the ground motion) (Fig. 5). The pore pressures generated from the 0·2***g*** dynamic event are significantly reduced in the MICP-treated soils compared to the loose untreated sand (Fig. 6). Under 0·7***g*** dynamic loading, the acceleration–time histories are similar, with an increase in amplitude near the surface (about 1·1 up to 2·0 times that of loose sand) (Fig. 7). The MICP-treated sand shows similar spikiness as the loose untreated sand, and it is relatively in phase with the ground motion. The pore pressures generated under 0·7***g*** dynamic loading are also significantly reduced compared to those in the loose untreated sand and are well below $r_u = 1{\cdot}0$ (Fig. 8).

The shaking-induced settlements in the free field indicate a reduction in settlements of MICP-treated soils compared to loose untreated sand. The cumulative settlements contain similar settlement trends to that of the dense sand until the cementation begins to break down, as indicated by the V_s measurements (Fig. 9). Once a significant amount of cementation degrades, the settlements of the MICP-treated soil increase in magnitude and approach that of the loose untreated sand. The point at which this occurs is indicated within the V_s plots in Fig. 9; A indicates significant cementation degradation and settlement accumulation for the lightly cemented sand, B indicates significant cementation degradation and settlement accumulation for the moderately cemented sand, C indicates initial cementation degradation in the heavily cemented sand (limited settlement accumulation), and C′ indicates additional cementation degradation and settlement accumulation in the heavily cemented sand. The amount of settlement of the MICP-treated sand remains below that of the loose sand; the improvement from the cementation is still realised, even after the cementation is degraded. The loose untreated sand experiences comparatively large settlements, especially above a maximum near-surface acceleration, a_{max}, of 0·4***g***. As indicated in Fig. 9, the cumulative settlement pattern of the lightly cemented sand begins to deviate from the dense, untreated sand and trends towards that of the loose untreated sand around an a_{max} value of 0·8***g***. The cumulative settlement pattern of the moderately cemented sand begins to deviate from the dense sand above an a_{max} value of about 1·0***g***; the moderately cemented sand does not experience the accumulation of settlements within a narrow surface a_{max} range that the loose and lightly cemented sands do. The cumulative settlements of the heavily cemented sands are less than the dense, untreated sands at an equivalent a_{max}. However, the settlements appear to be approaching the dense sand settlements at an a_{max} value of about 1·5***g***, at which point the settlements appear to be accumulating at a narrow surface a_{max} range, as seen in the loose and lightly cemented sand. This behaviour may indicate that the cementation is degrading; however, the shear wave velocity of the heavily cemented sand appears to begin degrading at lower a_{max} values (above about 0·5***g***).

In theory, the cemented sand would resist shaking-induced settlements until a threshold acceleration is reached (approximately indicated by the letters A, B and C′ in Fig. 9), at which point the cementation would break down and additional settlements are experienced. In general, this is the behaviour observed in the free-field data, as described above. The early cementation degradation of the heavily cemented sand may be due to the nature of the cementation bonds within the soil (e.g. at particle contacts as opposed to spanning across particle faces); some cementation is strong enough to stay intact up to larger shear stresses, whereas some cementation is strong enough to increase the shear wave velocity but degrade quickly at even low levels of shaking. The incremental settlement (Fig. 9) also indicates that the MICP-treated sands experience less settlement than the loose untreated sand at all levels of shaking, and in general have similar magnitude settlements to the dense sand until the cementation is degraded. In addition, the incremental settlement also indicates that the soil tested experiences a peak magnitude of settlement from a single shaking event, after which less settlement is experienced (likely due to sand densification from previous shaking events). The peak magnitude of incremental settlement occurs at about 0·5***g*** for the loose untreated sand, 0·7***g*** for lightly cemented sand and about 1·0***g*** for the heavily cemented sand (the moderately

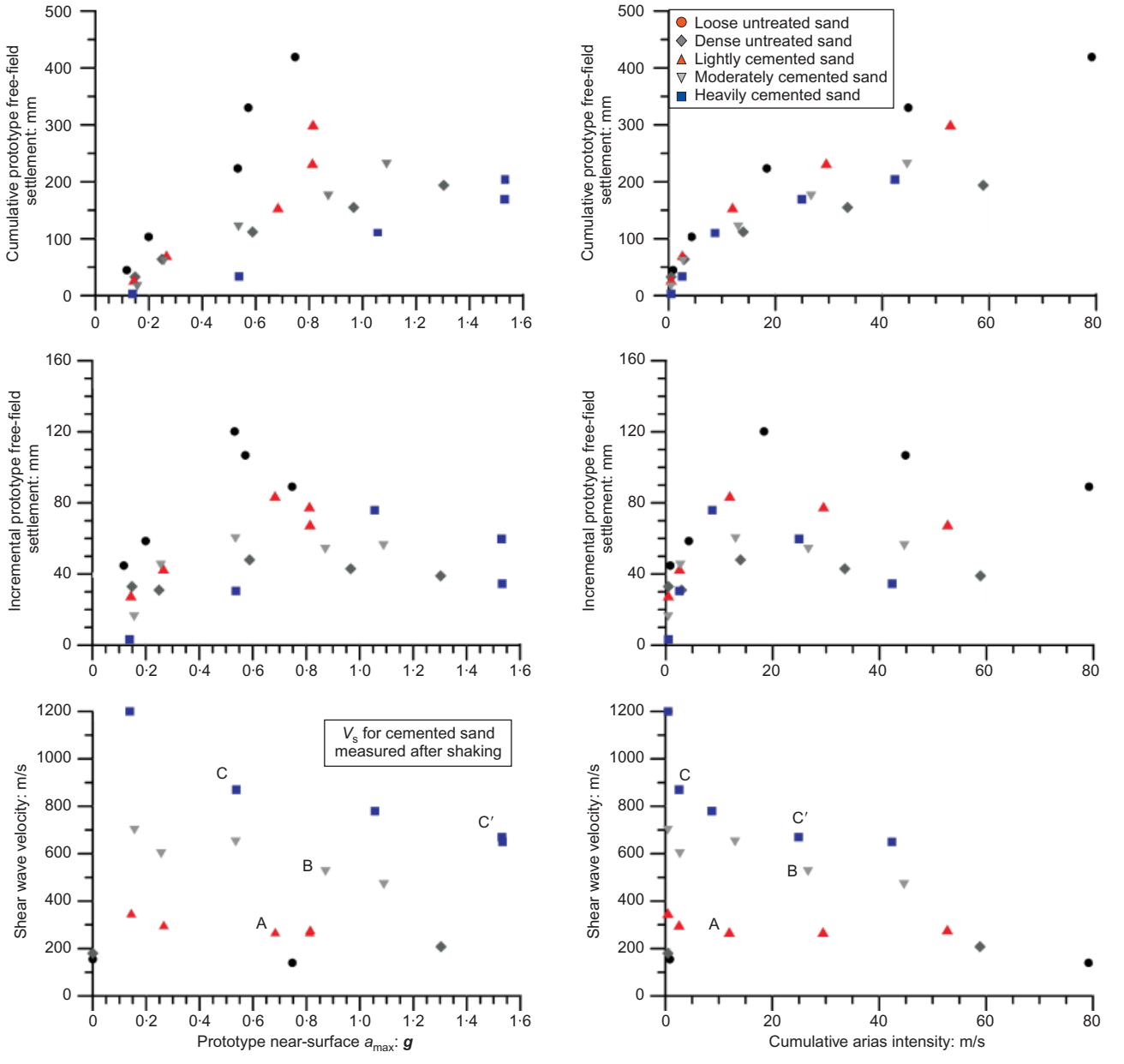

Fig. 9. Summary of free-field settlement and shear wave velocity related to the increasing prototype near-surface a_{max} and the cumulative arias intensity. The V_s measurements for the cemented sands are taken after the shaking events; the V_s measurements for the untreated sands are taken before the first shake and after the last shaking event. The shaking sequence used is outlined in Table 2

cemented sand does not show a peak value). The behaviour of both the cumulative and incremental settlement compared to a_{max} is highly dependent on the sequence of the shaking events. The data presented in Fig. 9 are applicable to the specific shaking sequence imposed, with increasing intensity packets of sine wave motions for each successive event. If a different order of shaking events was used (e.g. from high magnitude to low, or several events at the same magnitude) a different pattern of settlement would be expected.

The shaking-induced settlement data were also compared to the cumulative arias intensity of the surface motions during the shaking sequence (Fig. 9). The cumulative arias intensity represents the cumulative shaking sequence, and therefore the settlement trends are more independent from the specific shaking sequence used for the tests. The overall trends of the arias intensity plots agree with the settlement against near-surface a_{max} trends previously discussed: the MICP-treated sands have similar cumulative settlement values as the dense sand until significant cementation degrades (letters A, B and C′ in Fig. 9), at which point settlements begin to increase. The incremental settlement–arias intensity trends show a peak incremental settlement was reached for each soil (at an arias intensity of 20 m/s or lower), which is similar to the near-surface a_{max} trends.

Cyclic soil behaviour

Cyclic direct simple shear (DSSc) tests were performed on MICP-treated soil to complement the centrifuge testing; the results of the MICP-treated soil were compared to that of the loose untreated sand. The loose sand specimen was cemented to a moderate level ($V_s = 650$ m/s; equivalent to the moderate level attained in the centrifuge test) and then subjected to cyclic loading. A detailed presentation of all of the DSSc data is provided in the Pacific Earthquake Engineering Research Center report (Faison & Mahin, 2012).

A summary of the cyclic data is presented as the cyclic

stress ratio (CSR) plotted against number of cycles to cause liquefaction (N) curve (Fig. 10) (e.g. liquefaction is defined as 3% strain, which is comparable to the dynamic strains experienced during centrifuge testing). The MICP treatment provides a substantial increase in liquefaction resistance, with the CSR increasing by about 0·3 across the cycle number range examined. This increase in liquefaction resistance is consistent with the behaviour observed in the centrifuge test performed at the same moderate level of cementation. The CSR against N relationship for the MICP-treated soils was developed based on a series of monotonic and multi-stage cyclic tests. The data point labelled A in Fig. 10 is an estimate made from the stress at which the treated specimen tested in monotonic direct simple shear had strained approximately 3%. The test represented by data point B experienced unmeasured disturbance during the previous 2114 cycles of loading at a smaller stress level; therefore, the test would likely have required a larger number of cycles to fail without the prior disturbance. Points C and D on Fig. 10 are lower bound estimates, as additional cycles are needed to achieve 3% strain.

CONCLUSIONS

MICP treatment increased the cyclic strength and stiffness of the sand and provided sufficient improvement to resist liquefaction. Under dynamic loading, the MICP-treated soils showed reduced excess pore pressure generation at all levels of shaking, reduced settlements and generally greater peak surface accelerations compared to the untreated, loose saturated sand. Shaking-induced settlements were also lower than those observed in the untreated, loose sand model; the settlements of the MICP-treated soils were similar to or smaller than those of the dense, untreated sand until the cementation began to degrade, at which point the settlements were larger than the dense sand but still lower than the loose sand. The results of the centrifuge testing illustrate that the MICP treatment improves the soil behaviour under dynamic loading by reducing the generated pore pressures and shaking-induced settlements, but also increases the maximum accelerations at the ground surface. These results indicate the importance of evaluating the site response when considering MICP treatment. The changes to the soil behaviour and shear stiffness will affect the site response, as shown in the centrifuge tests; therefore, a tradeoff between improved liquefaction resistance and minimising undesirable amplified ground surface motions needs to be considered when designing the treatment level.

The centrifuge testing of the MICP-treated soils revealed a transition in soil behaviour from 'soil-like' to 'rock-like' behaviour. The cementation integrity testing indicated that as the cementation increased from an untreated soil (V_s = 120 m/s) to a heavily cemented soil (V_s = 800 m/s), the shear stiffness dependency on confinement stress decreased until the stiffness was no longer dependent on confinement (e.g. 'rock like').

The MICP treatment process offers an alternative novel ground improvement method to reduce the liquefaction susceptibility and the damage associated with dynamic loading. This treatment process provides a way to target a cementation level (or stiffness level) that will provide the desired level of performance under dynamic loading, provided that the effects on dynamic site response are accounted for.

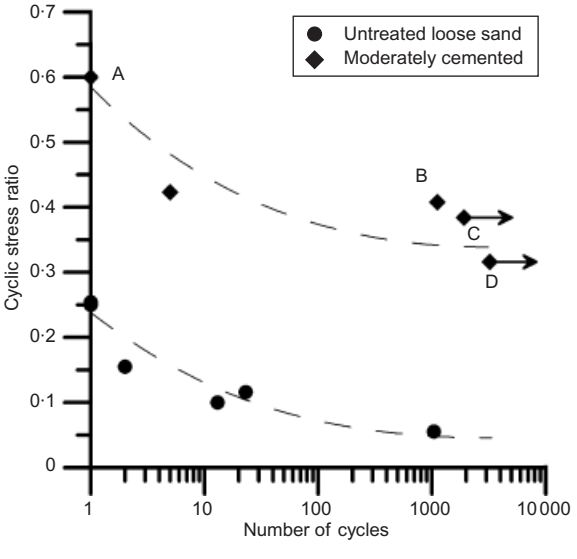

Fig. 10. Cyclic stress ratio plotted against number of cycles to reach liquefaction (defined as 3% strain for the cyclic direct simple shear (DSSc) tests (Idriss & Boulanger (2008)). These results are from DSSc tests performed on untreated loose and moderately cemented sand

ACKNOWLEDGEMENTS

Funding from the National Science Foundation (CMMI-0727463 and -0830182) is appreciated. The use of the Center for Geotechnical Modeling Facilities was made possible by support through NEEScomm at Purdue University through NSF award CMMI-0927178. Any opinions, findings and conclusions or recommendations expressed in this material are those of the authors and do not necessarily reflect the views of the National Science Foundation. The DSSc testing was performed as part of the PEER REU programme. The authors would also like to thank Doug Spitzer, Gail da Silva, Dr Daniel Wilson and the UC Davis NEES ES staff for their assistance.

REFERENCES

Brandenberg, S. J., Kutter, B. L. & Wilson, D. W. (2008). Fast stacking and phase corrections of shear wave signals in a noisy environment. *J. Geotech. Geoenviron. Engng* **134**, No. 8, 1154–1165.

Chou, J. C. & Kutter, B. (2008). Nonlinear shear wave propagation in strain stiffening and strain softening soil. *Proc. Geotech. Earthquake Engng and Soil Dynamics IV, Sacramento, CA*, ASCE Geotechnical Special Publication 181 (CD-ROM).

DeJong, J. T., Fritzges, M. B. & Nüsslein, K. (2006). Microbial induced cementation to control sand response to undrained shear. *J. Geotech. Geoenviron. Engng* **132**, No. 11, 1381–1392.

DeJong, J. T., Mortensen, B. M., Martinez, B. C. & Nelson, D. C. (2010). Bio-mediated soil improvement. *Ecol. Engng* **36**, No. 2, 197–210.

DeJong, J. T., Soga, K., Banwart, S. A., Whalley, W. R., Ginn, T., Nelson, D. C., Mortensen, B. M., Martinez, B. C. & Barkouki, T. (2011). Soil engineering in vivo: harnessing natural biogeochemical systems for sustainable, multi-functional engineering solutions. *J. R. Soc. Interface* **8**, No. 54, 1–15.

Faison, H. & Mahin, S. A. (2012). The effect of microbially induced calcite precipitation on the liquefaction resistance of sand. In *PEER 2011/10 – Earthquake engineering for resilient communities: 2011 PEER internship program research report collection*. Berkeley, CA, USA: Pacific Earthquake Engineering Research Center.

Fujita, Y., Taylor, J. L., Gresham, T. T., Delwiche, M., Colwell, F., McLing, T. L., Petzke, L. M. & Smith, R. W. (2008). Stimulation of microbial urea hydrolysis in groundwater to enhance calcite precipitation. *Environ. Sci. Technol*. **42**, No. 8, 3025–3032.

Hardin, B. O. & Black, W. L. (1968). Vibration modulus of

normally consolidated clay. *J. Soil Mech. Found. Div., ASCE* **94**, No. 2, 353–369.

Idriss, I. M. & Boulanger, R. W. (2008). *Soil liquefaction during earthquakes*, MNO-12. Oakland, CA, USA: Earthquake Engineering Institute.

Ishihara, K. (1985). Stability of natural deposits during earthquakes. *Proc. 11th Int. Conf. Soil Mech. Found. Engng, San Francisco* **2**, 321–376.

Karol, R. H. (2003). *Chemical grouting and soil stabilization*, p. 558. New York, NY, USA: Marcel Dekker.

Kutter, B. L. (1995). Recent advances in centrifuge modeling of seismic shaking. *Proc. 3rd Int. Conf. Recent Adv. Geotech. Earthquake Engng Soil Dynamics, University of Missouri-Rolla, Rolla, MO* **2**, 927–942.

Montoya, B. M., Gerhard, R., DeJong, J. T., Wilson, D., Weil, M., Martinez, B. C. & Pederson, L. (2012). Fabrication, operation, and health monitoring of bender elements for aggressive environments. *Geotech. Testing J. ASTM* **35**, No. 5, GTJ103300.

Mortensen, B. M., Haber, M. J., DeJong, J. T., Caslake, L. F. & Nelson, D. C. (2011). Effects of environmental factors on microbial induced calcium carbonate precipitation. *J. Appl. Microbiol*. **111**, No. 2, 338–349.

Narayanan, K. R. (1999). *Modeling the seismic response of stratified soil*. MSc thesis, University of California, Davis, CA, USA.

Stokoe, K. H., Lee, S. H. H. & Knox, D. P. (1985). Shear moduli measurements under true triaxial stresses. In *Advances in the art of testing soils under cyclic conditions* (ed. V. Khosla), pp. 166–185. New York, NY, USA: ASCE.

Weil, M. H., DeJong, J. T., Martinez, B. C. & Mortensen, B. M. (2011). Seismic and resistivity measurements for real-time monitoring of microbially induced calcite precipitation in sand. *Geotech. Testing J., ASTM* **35**, No. 2, GTJ103365.

Whiffin, V. S., van Paassen, L. A. & Harkes, M. P. (2007). Microbial carbonate precipitation as a soil improvement technique. *Geomicrobiol. J.* **25**, No. 5, 417–423.

Youd, T. L. & Holzer, T. L. (1994). Piezometer performance at the wildlife liquefaction site, California. *J. Geotech. Engng* **120**, No. 6, 975–995.

McDougall, J. R. *et al.* (2013). *Géotechnique* **63**, No. 3, 262–266 [http://dx.doi.org/10.1680/geot.SIP13.T.002]

TECHNICAL NOTE

Volumetric consequences of particle loss by grading entropy

J. R. McDOUGALL*, E. IMRE†, D. BARRETO* and D. KELLY*

Chemical and biological processes, such as dissolution in gypsiferous sands and biodegradation in waste refuse, result in mass or particle loss, which in turn lead to changes in solid and void phase volumes and grading. Data on phase volume and grading changes have been obtained from oedometric dissolution tests on sand–salt mixtures. Phase volume changes are defined by a (dissolution-induced) void volume change parameter (Λ). Grading changes are interpreted using grading entropy coordinates, which allow a grading curve to be depicted as a single data point and changes in grading as a vector quantity rather than a family of distribution curves. By combining Λ contours with pre- to post-dissolution grading entropy coordinate paths, an innovative interpretation of the volumetric consequences of particle loss is obtained. Paths associated with small soluble particles, the loss of which triggers relatively little settlement but large increase in void ratio, track parallel to the Λ contours. Paths associated with the loss of larger particles, which can destabilise the sand skeleton, tend to track across the Λ contours.

KEYWORDS: constitutive relations; fabric/structure of soils; laboratory tests; particle-scale behaviour; settlement; soil classification

BACKGROUND

Particle loss leads to changes in (a) grading and (b) volumetric state, for both solid and void phase volumes. Investigations into settlement and void ratio changes due to dissolution in soluble sand–salt mixtures have been undertaken by Fam *et al.* (2002), Shin & Santamarina (2009) and Truong *et al.* (2010). These studies have focused on the influence of different amounts of particle loss on the post-dissolution volumetric states. More recently an experimental study of the effect of different particle amounts and sizes on volume changes has been presented (McDougall *et al.*, 2013).

Knowledge of particle or mass loss effects is relevant to a range of natural processes and soils, for example biodegradation in landfilled waste, erosion of fines from embankment dams and dissolution in gypsiferous or calcareous soils. However, the incorporation of this phenomenon into geomechanical models is at an early stage of development.

Examples do exist; landfilled waste settlement models such as those developed by White *et al.* (2004), Lobo *et al.* (2008), McDougall (2007) and Machado *et al.* (2008) couple a mass loss control model with hydraulic and/or geomechanical models. In an alternative approach, grading change, principally fines loss, rather than mass loss has been used as a means of controlling the mechanical properties in embankment soils (Muir Wood & Maeda, 2008).

This note introduces a method of coupling changes in void volume with changes in both mass loss and grading, accounting for a range of particle amounts and sizes. Changes in sample volume, specifically void volume change, are quantified by a mass loss void volume change parameter, Λ. The value of Λ is related to grading changes when those changes are defined in terms of the grading (statistical) entropy coordinates. The method is demonstrated using a suite of oedometric dissolution tests on salt–sand mixtures. The mixtures comprised Leighton Buzzard sand with specific amounts and sizes of salt particles. The salt particles were dissolved by inundation and circulation of initially distilled water in the oedometer.

Manuscript received 28 February 2012; revised manuscript accepted 15 October 2012.
Discussion on this paper closes on 1 August 2013, for further details see p. ii.
* School of Engineering and Built Environment, Edinburgh Napier University, UK.
† Geotechnical Department, Budapest University of Technology and Economics, Hungary.

Λ: MASS-(PARTICLE)-LOSS-INDUCED VOID VOLUME CHANGE PARAMETER

A quantitative interpretation of the volumetric consequences of dissolution is provided by Λ, a dissolution-induced void volume change parameter, defined as

$$\Lambda = \frac{\mathrm{d}V_\mathrm{V}}{\mathrm{d}V_\mathrm{S}} \tag{1}$$

where V_V is the volume of voids and V_S is the solid volume. An advantage of Λ is that by normalising the change in void volume by the amount of mass dissolved, particle size effects are clearly drawn. An expression relating total volume (V_T) changes due to dissolution can be derived, for example

$$\mathrm{d}V_\mathrm{T} = (1 + \Lambda)\,\mathrm{d}V_\mathrm{S} \tag{2}$$

and a change in void ratio due to dissolution by

$$\mathrm{d}e = (\Lambda - e)\,\frac{\mathrm{d}V_\mathrm{S}}{V_\mathrm{S}} \tag{3}$$

Key values of Λ are summarised in Table 1. For example, when $\Lambda = -1$, loss of solids results in a direct and equal increase in void volume, that is, there is no change in overall volume and the increase in void ratio is at a maximum. An increase in void ratio occurs at all values of $\Lambda < e$, with the magnitude decreasing until $\Lambda = e$, whereupon there is no change in void ratio. At higher Λ values, loss of solid matter leads to a more compact particle arrangement. In this case

Table 1. Reference values of Λ and associated volumetric responses

Reference values of Λ	Void ratio	Volumetric response
$\Lambda = -1$	Maximum increase	No change in overall volume
$\Lambda = 0$	Increasing	No change in void volume
$\Lambda = e$	Constant	
$\Lambda > e$	Decreasing	Maximum change in overall volume

significant settlement would occur since there is a reduction in both solid and void phase volumes. A fuller derivation and explanation of Λ can be found in McDougall & Pyrah (2004).

GRADING ENTROPY – COORDINATES

In classical thermodynamics, entropy is an expression of the amount of energy that is unavailable for doing work. As a concept it is difficult to define summarily, being strictly a phenomenon of the second law. The term is commonly associated with the macroscopic disorder of a system. In the context of grading, the meaning of the term 'entropy' can be traced back to statistical thermodynamics, where it refers to a 'multiplicity of the microstates of a system' (Warn, 1969). This is more a probabilistic concept in which entropy is a measure of the number of ways the microstate can be arranged. The entropy coordinates define the particular microstate. In the present case, this is the particle size distribution.

The concept of entropy in statistical thermodynamics extends the description of the system beyond that of its classical thermodynamic state variables such as pressure and volume. Statistical entropy allows the microscopic configuration of a system to be described, in this case the representation of a particle size distribution, as a coordinate pair. A vectorial depiction of a change in grading, rather than a family of distribution curves, is then available. The method was introduced by Lőrincz (1986), who coined the term grading entropy. Further details can be found in Lőrincz *et al.* (2005).

The grading entropy coordinates are the relative base entropy A, and the normalised entropy increment B. Lőrincz *et al.* (2005) show that

$$A = \frac{S_0 - S_{0\ \min}}{S_{0\ \max} - S_{0\ \min}} \tag{4}$$

where S_0 is the so-called base entropy and $S_{0\max}$ and $S_{0\ \min}$ denote the eigen-entropies (defined below) of the largest and smallest fractions in the mixture respectively. The base entropy is calculated using

$$S_0 = \sum_{i=1}^{N} x_i \frac{\ln C_i}{\ln 2} \tag{5}$$

where N is the number of fractions (or sieves), x_i is the relative frequency of the fraction i (where relative frequency of the fraction is the mass of the fraction as a proportion of total mass, i.e. $\sum_{i=1}^{N} x_i = 1$) and C_i is the number of elementary cells in the fraction i. With fraction intervals comprising multiples of elementary cells doubling in number from a minimum particle size (note that Imre (1995) proposes a minimum particle size of 2^{-22} mm, i.e. the height of a SiO_4 tetrahedron), $d_{\min}$ (in other words a sieve stack in which the sizes increase by a factor of two), C_i is equal to 2^i

$$C_i = \frac{2^{i+1} d_{\min} - 2^i d_{\min}}{d_{\min}} = 2^i \tag{6}$$

From equations (5) and (6) is obtained the expression for the eigen-entropy (where the prefix eigen- is used to convey a sense of own or self (identification); the eigen-entropy is the value of the entropy of a single sieve fraction, which, under the sieve fraction notation scheme used, is equivalent to the notation scheme index) of a single fraction S_{0i}

$$S_{0i} = \frac{\ln C_i}{\ln 2} = i \tag{7}$$

from which $S_{0\ \max}$ and $S_{0\ \min}$ are obtained.

The normalised entropy increment

$$B = \frac{\Delta S}{\ln (N)} \tag{8}$$

where ΔS is the entropy increment and

$$\Delta S = -\frac{1}{\ln 2} \sum_{i=1}^{N} x_i \ln x_i \tag{9}$$

GRADING ENTROPY – DIAGRAM

The normalised coordinates define a grading entropy diagram in which particle size distributions can be plotted as coordinates (Fig. 1). The grading entropy diagram has a number of notable features, as described below.

Relative base entropy, A. Base entropy is a measure of the skewness or symmetry of a particle size frequency distribution. Relative base entropy defines the base entropy in terms of the number and range of fractions. Point R in Fig. 1, where $A = 1$ and $B = 0$, corresponds to a single uniform particle size – the most skewed distribution and the starting point for a laboratory crushing test. If the distribution is symmetrical then the products of the relative fraction frequencies, x_i, and the corresponding fraction eigen-entropies, S_{0i}, are balanced moments about the central fraction. The S_0 term in equation (5) is then equivalent to the eigen-entropy of the central fraction (or average of the central pair) and from equation (4), it is found that $A = 0{\cdot}5$.

Normalised entropy increment, B. Entropy 'increment' is a measure of the kurtosis or peakiness of a particle size frequency distribution. It reflects the uniformity of the spread of a distribution over its fraction range. The normalised entropy increment normalises the entropy increment by the logarithm of the number of fractions. Values range between 0 and $1/\ln(2)$. Point S in Fig. 1 where $A = 0{\cdot}5$ and $B = 1{\cdot}442$ corresponds to a distribution in which the relative frequencies are equal. Movement down the diagram, to lower B values, denotes increasing peakiness in the distribution, for example with a symmetrical bimodal distribution (point V; $A = 0{\cdot}5$) or a skewed monomodal distribution (point W, $A < 0{\cdot}5$).

Bounding lines. For a given relative base entropy and number of fractions (N), there exists a maximum entropy increment. Lőrincz *et al.* (2005) show that the locus of maximum entropy increment coordinates marks out a bounding line on the right-hand side of the diagram. This line is followed closely by entropy coordinates obtained during the

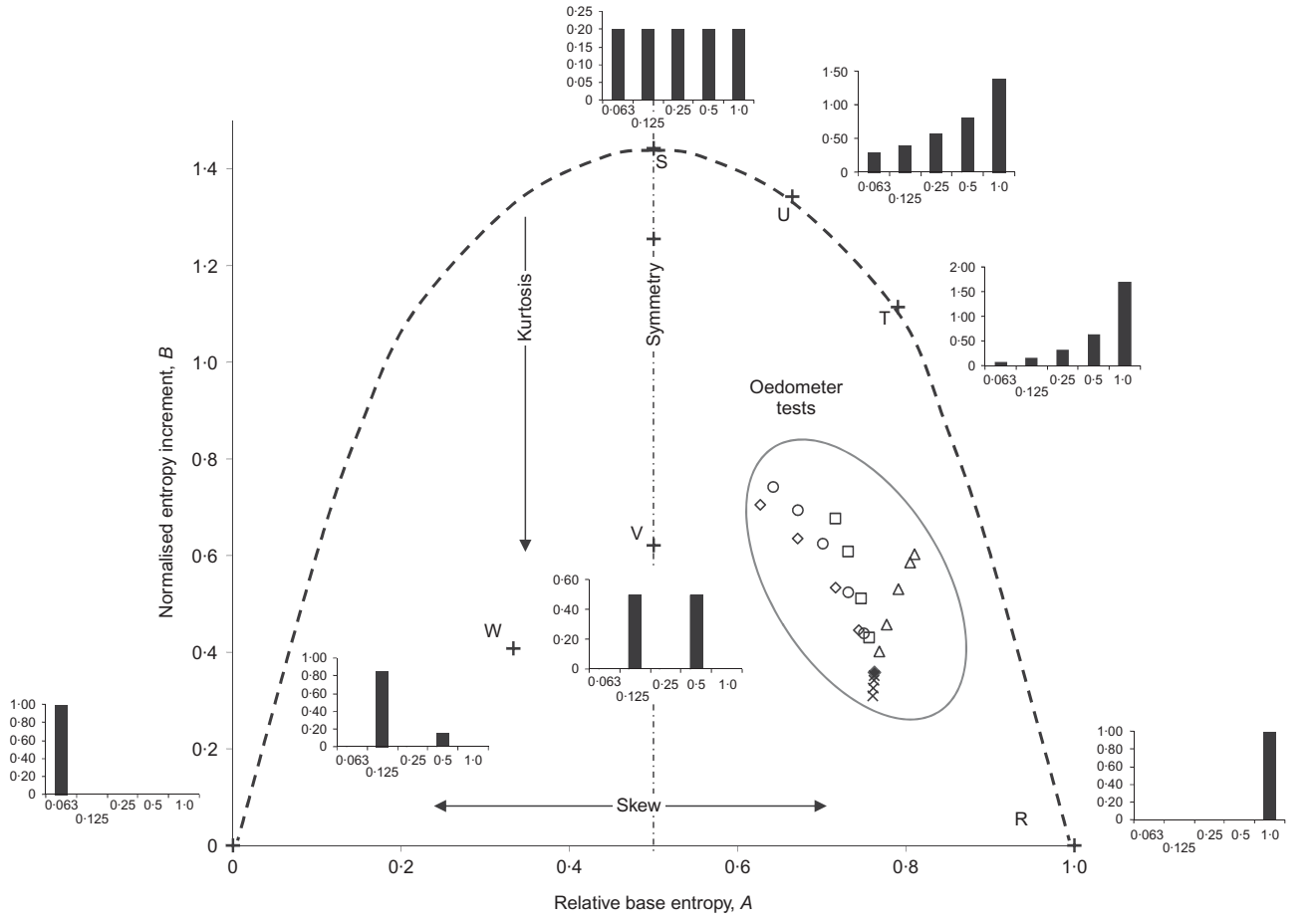

Fig. 1. Normalised grading entropy diagram showing various coordinate locations and corresponding particle size frequency distributions (relative mass retained for a five fraction sample). Location of oedometer test particle size frequency distributions also shown

repeated crushing of an initially single-particle-size sand (commencing at point R in Fig. 1). Entropy coordinates of fractal distributions also lie close to this line; distributions with fractal dimension of $D = 2{\cdot}0$ (point T), 2·5 (point U) and 3·0 (point S, the uniform frequency distribution) are plotted on Fig. 1.

OEDOMETER TESTS

Laboratory tests were performed on sand–salt mixtures, loaded in a modified permeation oedometer, and subsequently dissolved. The oedometer is 100 mm in diameter and has an extended confining ring to accommodate a sample height of up to 30 mm. The test programme tackled the influence of both the size and the amount of particle loss on the volumetric state of the remaining sand skeleton.

In total, 40 dissolution tests were performed, in two groups of 20. In each group, five different single salt particle size fractions (0·063, 0·125, 0·25, 0·50 and 1·00 mm) were added to the sand in four different proportions (2%, 5%, 10% and 15% of total mass). The sand is Leighton Buzzard B ($D_{50} = 0{\cdot}85$ mm). All samples were prepared dry, a vertical stress applied, after which they were inundated with distilled water at room temperature. The two test groups differ by the vertical stress at which dissolution occurred; $\sigma'_v = 62$ kPa in one group, 250 kPa in the other. A full description of the test procedures and results is given in McDougall *et al.* (2013).

Two significant observations about the volumetric consequences of particle loss were made. First, overall volume changes are directly related to the amount of dissolved particles and to a lesser extent, the size of particle lost. Second, particle loss leads to an increase in void ratio, the magnitude of which is related to the amount of dissolved particles but appears to be insensitive to particle size. However, this insensitivity masks the combined and compensatory effects of the initial void ratio and associated Λ value. Equation (3) reveals the compensatory effects. Where a mixture comprises large amounts (10–15%) of small 'nestling' salt particles, the initial void ratio is low ($e \approx 0{\cdot}4$) and Λ tends to a minimum ($\Lambda \approx -0{\cdot}8$). In contrast, where salt particles are large, both initial void ratio and Λ tend to be greater ($e \approx 0{\cdot}6$ and $\Lambda \approx -0{\cdot}55$). Hence, because of the combination of (Λ–e), the change in void ratio as defined by equation (3) is relatively insensitive to particle size.

The cluster of coordinate points on right-hand side of Fig. 1 denoted as oedometer tests are the grading entropy coordinates for the initial salt–sand mixes and the post-dissolution Leighton Buzzard sand (the common end point of the oedometer tests).

GRADING ENTROPY COORDINATES AND Λ

Figure 2 shows, in closer view, the grading entropy coordinates for salt particle additions as noted. The Leighton Buzzard endpoint is clearly visible. Note also the apparently anomalous location of the 0·5 mm added salt particle path. This plots below the endpoint because, in the sieve stack used (0·063, 0·125, 0·250, 0·5, 1·0 mm), the addition of 0·5 mm salt particles adds to the dominant fraction and

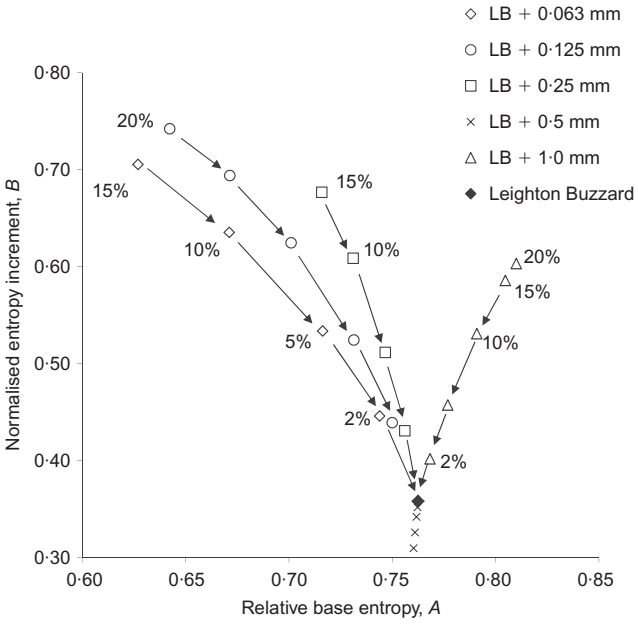

Fig. 2. Grading entropy coordinates of salt–sand mixtures with given salt particle amounts (2% to 20%) and sizes (0·063 mm to 1·0 mm) and post-dissolution Leighton Buzzard sand only coordinates

hence the peakiness of the distribution. As already stated, such a characteristic is represented by a move down the normalised grading entropy diagram. This should not be an obstacle as a locus for the 0·5 mm salt particles could be fitted within the family of other paths, to allow meaningful interpretation of all grading changes.

In Fig. 3 the grading entropy coordinate paths are overlain by contours drawn from the Λ values for all 40 permeation oedometer tests (also shown). The combination of contours and paths provides a useful means of interpreting the coupling between particle loss and void volume changes.

Consider the 0·063 mm added salt particle path. From 15% to 2% of added salt, this path tracks parallel to the Λ contour field. Λ values are at their lowest, approximately $-0{\cdot}8$ to $-0{\cdot}9$; the removal of 0·063 mm particles is accompanied by a near-equivalent increase in void volume and little change in overall volume. With increasing salt particle size, the entropy coordinate path increasingly tracks across the Λ contours.

In the case of 1·0 mm salt particles, entropy path and contours are almost orthogonal. This orientation implies a changing response to dissolution as dissolution proceeds. When the amount of salt particles is of the order of 15%, $\Lambda \approx -0{\cdot}4$ to $-0{\cdot}5$, there is significant change in volume. One possible explanation for this might be the presence of large particles participating in strong force columns and disrupting the load-carrying skeleton on dissolution. As the amount of salt particles decreases, fewer (large) salt particles reside in strong force columns and their removal occurs with much less disruption. At this stage, the response to particle loss tends to a near equivalent increase in void volume and Λ tends towards $-0{\cdot}8$.

SUMMARY

This note has shown that the volumetric consequences of dissolution can be related in a meaningful way to particle loss where the loss accounts for both amount and particle size. Void volume changes are defined in terms of Λ, an

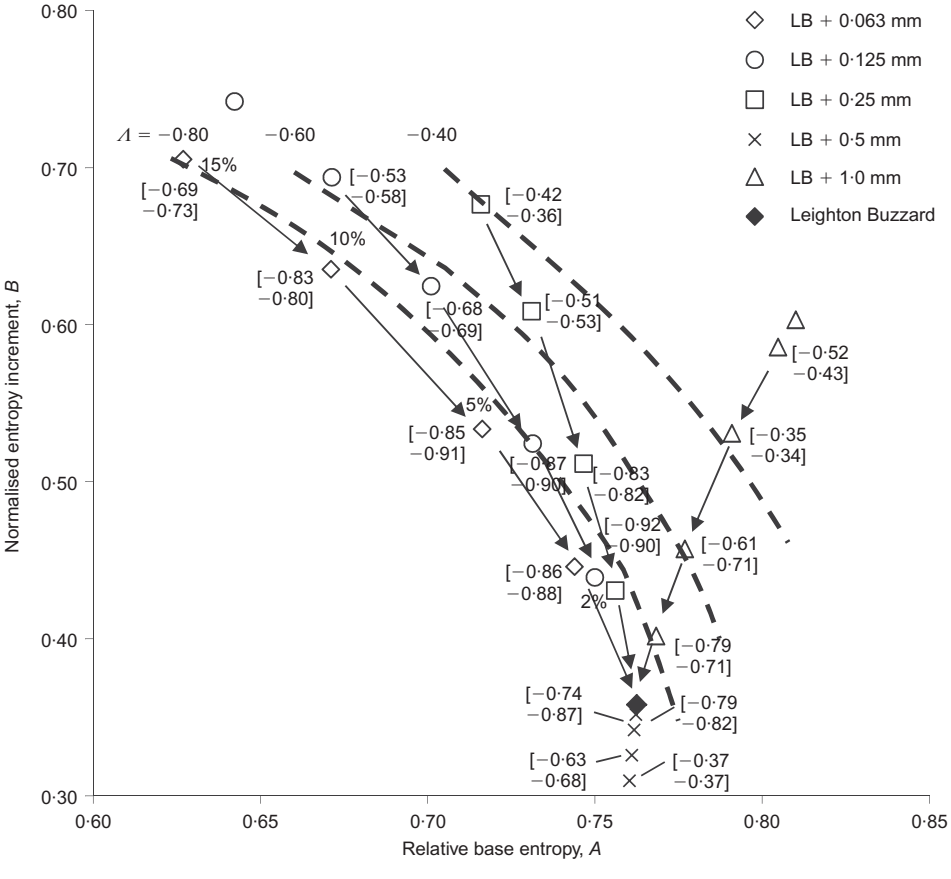

Fig. 3. Grading entropy coordinate paths combined with contours of Λ values (broken lines) obtained from the corresponding oedometer tests. Λ values shown in square brackets alongside grading entropy coordinates with 62 kPa value overlying 250 kPa value

induced void volume change parameter. Here volume change is induced by dissolution of soluble salts, but it could be biodegradation of organic matter. From the experimental results presented, when Λ values are plotted according to their normalised entropy coordinates, a consistent set of Λ contours is obtained. It is then possible to describe the volumetric consequences of mass loss using Λ values determined according to the amount and size of particles lost.

NOTATION

A	relative base entropy
B	normalised entropy increment
C_i	number of elementary cells in fraction i
e	void ratio
N	number of fractions (or sieves)
S_0	base entropy
$S_{0\,i}$	eigen-entropy
$S_{0\,\min}$, $S_{0\,\max}$	eigen-entropies of smallest and largest fractions
ΔS	entropy increment
V_S	solid volume
V_T	total volume
V_V	volume of voids
x_i	relative frequency of fraction i (relative frequency of the fraction is the mass of the fraction as a proportion of total mass, i.e. $\sum_{i=1}^{N} x_i = 1$)
Λ	dissolution-induced void volume change parameter
σ'_v	vertical stress

REFERENCES

Fam, M. A., Cascante, G. & Dusseault, M. B. (2002). Large and small strain properties of sands subjected to local void increase. *J. Geotech. Geoenviron. Engng* **128**, No. 12, 1018–1025.

Imre, E. (1995). Characterization of dispersive and piping soils. *Proc. 11th ECSMFE, Copenhagen, Denmark* **2**, 49–55.

Lobo, A., Lopez, A., Cobo, N. & Tejero, I. (2008). Simulation of municipal solid waste reactors using Moduelo. *Proc. Instn Civ Engrs – Waste Resource Managmt* **161**, No. 3, 99–104.

Lőrincz, J. (1986). *Grading entropy of soils*. PhD thesis, Technical Sciences, Technical University of Budapest, Budapest, Hungary.

Lőrincz, J., Imre, E., Gálos, M., Trang, Q. P., Rajkai, K., Fityus, S. & Telekes, G. (2005). Grading entropy variation due to soil crushing. *Int. J. Geomech*. **5**, No. 4, 311–320, http://dx.doi.org/10.1061/(ASCE)1532–3641(2005)5:4(311).

Machado, S. L., Vilar, O. M. & Carvalho, M. F. (2008). Constitutive model for long term municipal solid waste mechanical behavior. *Comput. Geotech.* **35**, No. 5, 775–790.

McDougall, J. R. (2007). A hydro-bio-mechanical model for settlement and other behaviour in landfilled waste. *Comput. Geotech.* **34**, No. 4, 229–246.

McDougall, J. R., Kelly, D. & Barreto, D. (2013). Particle loss and volume change on dissolution: Experimental results and analysis of particle size and amount effects. *Acta Geotech.* in press.

McDougall, J. R. & Pyrah, I. C. (2004). Phase relations for decomposable soils. *Géotechnique* **54**, No. 7, 487–494, http://dx.doi.org/10.1680/geot.2004.54.7.487.

Muir Wood, D. & Maeda, K. (2008). Changing grading of soil: effect on critical states. *Acta Geotech.* **3**, No. 1, 3–14, http://dx.doi.org/10.1007/s11440–007–0041–0.

Shin, H. & Santamarina, J. C. (2009). Mineral dissolution and the evolution of k_0. *J. Geotech. Geoenviron. Engng* **135**, No. 9, 1141–1147.

Truong, Q. H., Eom, Y. H. & Lee, J. S. (2010). Stiffness characteristics of soluble mixtures. *Géotechnique* **60**, No. 4, 293–298, http://dx.doi.org/10.1680/geot.8.T.032.

Warn, J. R. W. (1969). *Concise chemical thermodynamics*. London, UK: Van Nostrand Reinhold.

White, J., Robinson, J. & Ren, Q. (2004). Modelling the biochemical degradation of solid waste in landfills. *Waste Managmt* **24**, No. 3, 227–240.

ice
Institution of Civil Engineers
publishing

Session 3. Overview and future challenges

DeJong, J. T. *et al.* (2013). *Géotechnique* **63**, No. 4, 287–301 [http://dx.doi.org/10.1680/geot.SIP13.P.017]

Biogeochemical processes and geotechnical applications: progress, opportunities and challenges

J. T. DEJONG[1], K. SOGA[2], E. KAVAZANJIAN[3], S. BURNS[4], L. A. VAN PAASSEN[5], A. AL QABANY[2], A. AYDILEK[6], S. S. BANG[7], M. BURBANK[8], L. F. CASLAKE[9], C. Y. CHEN[10], X. CHENG[11], J. CHU[12], S. CIURLI[13], A. ESNAULT-FILET[14], S. FAURIEL[15], N. HAMDAN[16], T. HATA[17], Y. INAGAKI[18], S. JEFFERIS[19], M. KUO[2], L. LALOUI[14], J. LARRAHONDO[20], D. A. C. MANNING[21], B. MARTINEZ[22], B. M. MONTOYA[23], D. C. NELSON[24], A. PALOMINO[25], P. RENFORTH[26], J. C. SANTAMARINA[4], E. A. SEAGREN[27], B. TANYU[28], M. TSESARSKY[29] and T. WEAVER[30]

Consideration of soil as a living ecosystem offers the potential for innovative and sustainable solutions to geotechnical problems. This is a new paradigm for many in geotechnical engineering. Realising the potential of this paradigm requires a multidisciplinary approach that embraces biology and geochemistry to develop techniques for beneficial ground modification. This paper assesses the progress, opportunities, and challenges in this emerging field. Biomediated geochemical processes, which consist of a geochemical reaction regulated by subsurface microbiology, currently being explored include mineral precipitation, gas generation, biofilm formation and biopolymer generation. For each of these processes, subsurface microbial processes are employed to create an environment conducive to the desired geochemical reactions among the minerals, organic matter, pore fluids, and gases that constitute soil. Geotechnical applications currently being explored include cementation of sands to enhance bearing capacity and liquefaction resistance, sequestration of carbon, soil erosion control, groundwater flow control, and remediation of soil and groundwater impacted by metals and radionuclides. Challenges in biomediated ground modification include upscaling processes from the laboratory to the field, in situ monitoring of reactions, reaction products and properties, developing integrated biogeochemical and geotechnical models, management of treatment by-products, establishing the durability and longevity/reversibility of the process, and education of engineers and researchers.

KEYWORDS: chemical properties; environmental engineering; ground improvement; remediation; soil stabilisation

Manuscript received 2 March 2012; revised manuscript accepted 23 October 2012.
Discussion on this paper closes on 1 August 2013, for further details see p. ii.

[1] Department of Civil and Environmental Engineering, University of California, Davis, CA, USA.
[2] Department of Engineering, University of Cambridge, Cambridge, UK.
[3] School of Sustainable Engineering and the Built Environment, Arizona State University, Phoenix, AZ, USA.
[4] School of Civil and Environmental Engineering, Georgia Institute of Technology, Atlanta, GA, USA.
[5] Department of Geoscience and Engineering, Delft University of Technology, The Netherlands.
[6] Department ofCivil and Environmental Engineering, University of Maryland, College Park, MD, USA.
[7] Department of Chemical and Biological Engineering, South Dakota School of Mines and Technology, Rapid City, SD, USA.
[8] Environmental Biotechnology Institute, University of Idaho, Moscow, ID, USA.
[9] Department of Biology, Lafayette College, Easton, PA, USA.
[10] Department of Earth and Environmental Sciences, National Chung Cheng University, Taiwan.
[11] Department of Civil Engineering, Tsinghua University, Beijing, China.
[12] Department of Civil, Construction and Environmental Engineering, Iowa State University, Ames, IA, USA.
[13] Department of Agro-Environmental Science and Technology, University of Bologna, Bologna, Italy.
[14] Research & Development Department, Soletanche Bachy, Rueil Malmaison, France.
[15] Laboratory for Soil Mechanics, Ecole Polytechnique Fédérale de Lausanne (EPFL), Lausanne, Switzerland.
[16] Department of Civil, Environmental and Sustainable Engineering, Arizona State University, Tempe, AZ, USA.
[17] Department of Civil Engineering, Nagano National College of Technology, Nagano, Japan.
[18] Geology and Geotechnical Engineering Research Group, Public Works Institute, Japan.
[19] Environmental Geotechnics Ltd and Department of Engineering Science, University of Oxford, Banbury, UK.
[20] INGETEC S. A., Bogota, Columbia.
[21] School of Civil Engineering & Geosciences, Newcastle University, Newcastle upon Tyne, UK.
[22] Geosyntec Consultants, Oakland, CA, USA.
[23] Department of Civil, Construction, and Environmental Engineering, North Carolina State University, Raleigh, NC, USA.
[24] Department of Microbiology, University of California, Davis, CA, USA.
[25] Department of Civil and Environmental Engineering, University of Tennessee, Knoxville, TN, USA.
[26] Department of Earth Sciences, University of Oxford, Oxford, UK.
[27] Department of Civil and Environmental Engineering, Michigan Technological University, Houghton, MI, USA.
[28] Department of Civil, Environmental, and Infrastructure Engineering, George Mason University, Fairfax, VA, USA.
[29] Department of Structural Engineering and Department of Geological and Environmental Sciences, Ben Gurion University of the Negev, Beer-Sheva, Israel.
[30] Office of Research, Nuclear Regulatory Commission, USA.

INTRODUCTION

Biology in the evolution of geotechnical engineering

The field of geotechnical engineering has advanced steadily throughout history; the durability of several ancient geotechnical systems (e.g. Egyptian dams and canals, Greek strip and raft foundations, and Roman bridges along the Appian Way) testifies to a working knowledge of geotechnics by their creators. However, formal initiation of the discipline may be attributed to Coulomb's definitive work on earth pressures in the 1770s. Numerous advances in mechanics and water flow followed Coulomb's work, including Darcy's law (Darcy, 1857), Boussinesq stress distribution (1871), Rankine earth pressure theory (1875), Mohr's circle of strain (1885), Reynolds volumetric behaviour (1885), and more. Karl Terzaghi's work, from the 1920s onwards (e.g. Terzaghi, 1924), revolutionised the discipline by developing the principle of effective stress and analyses for the bearing capacity of foundations and consolidation of soils. Later work by Gibson on analytical techniques (see the first issue of *Géotechnique*), by Taylor (1948) on dilation and interlocking, by Roscoe *et al.* (1958) and Schofield & Wroth (1968) on plasticity and critical state, and by many others since then and through to the present day, have continued the development of mechanics concepts and analysis methods for geotechnical systems.

The natural origins of soils, and hence their variability and changes in properties over time, result in engineering mechanics alone being insufficient to address many practical problems. The geologic origin of a soil, its depositional mode and environment, thixotropic processes, and other post-depositional phenomena must often be considered. Early on (e.g. Terzaghi, 1955), the importance of considering these formational and time-dependent processes was recognised and addressed through the field of geology. Work by Mitchell (e.g. Mitchell, 1975) and others in the second half of the 20th century recognised the critically important role of chemistry in the behaviour of fine-grained soils, and how macro-scale performance depends directly on micro- (or nano-) scale conditions. For example, some ground improvement methods specifically target chemical changes in the clay fabric to stabilise soils for construction (e.g. pozzolanic changes).

Harnessing of biological processes in soils promises to be the next transformative practice in geotechnical engineering. For many years, the influence of plant roots on slope stability has been recognised and exploited (e.g. Gray & Sotir, 1996). There is now the opportunity to exploit many chemical processes that are mediated by biology. Although ignored for centuries with respect to geotechnical behaviour, microbes are ubiquitous in soils at surprisingly high concentrations, almost regardless of saturation, mineralogy, pH, and other environmental factors. Near the ground surface, more than 10^{12} microbes exist per kilogram of soil (Mitchell & Santamarina, 2005). At depths typical in geotechnical systems (e.g. 2 to 30 m), the microbial population decreases to about 10^{11} to 10^{6} microorganisms per kilogram respectively (Whitman *et al.*, 1998) (for context, about 10^{14} bacteria exist in the typical human body; Berg, 1996). Living organisms at other length scales are also present. For example, worms at larger length (cm) scales recompact soil, create preferential drainage conditions, and otherwise impact on soil characteristics, and spores at smaller length scales (< 1 μm) can be transported into smaller pore spaces.

A permanent biological presence (microbes have been active geotechnical engineers for 3+ billion years, much longer than the 0·0002 billion years for humans; Kohnhauser, 2007) in soil provides opportunities for geotechnical engineering to consider soil as a living ecosystem rather than as an inert construction material. Biological activity in soil can potentially explain observations in some case histories that have troubled experts (Mitchell & Santamarina, 2005) and provides the opportunity to manipulate soil using natural or stimulated processes (as expanded upon herein).

Emergence of bio-soils as a subdiscipline

One of the first explicit discussions of the application of biological processes in geotechnical engineering was presented by Mitchell & Santamarina (2005), and in parallel it was identified as an important research topic by the US National Research Council (NRC, 2006) for the 21st century. The first international workshop on biogeotechnical engineering in 2007 facilitated interdisciplinary discussions and prioritisation of research topics in this emerging field (DeJong *et al.*, 2007). Research advanced quickly, with a bio-geo-civil-engineering conference in 2008, and several dedicated sessions at national and international conferences, additional papers assessing the potential of the field (Ivanov & Chu, 2008; Kavazanjian & Karatas, 2008; Ivanov, 2010; Seagren & Aydilek, 2010; DeJong *et al.*, 2011; Hata *et al.*, 2011), and more than 100 technical conference and journal papers dedicated to this topic since. Research programmes on biogeotechnical engineering are currently active in more than 15 countries around the world.

The Second International Workshop on Bio-Soils Engineering and Interactions, funded by the US National Science Foundation, was held in September 2011 at the University of Cambridge. This workshop assembled 35 of the leading researchers in the field, and provided an opportunity to assess progress to date, identify the primary challenges and opportunities that lie ahead, and develop strategies for advancing this rapidly developing field. This paper presents the outcomes of the workshop, along with a perspective on the possible role of biological processes in geotechnical engineering, including examples of their application and a discussion of salient issues.

POTENTIAL OF BIOLOGY TO MODIFY ENGINEERING PROPERTIES OF SOILS

Length scales of biological processes

The processes by which biology can modify the engineering properties of soil depend on the length scale of organisms, both in absolute dimension and relative to the particle size. Multicellular organisms, ranging from plant roots down to insects and invertebrates (e.g. ants, worms), alter soils through both mechanical and biological processes. For example, ants are effective at soil grading, densification, and creating preferential flow paths (macropores); they also adapt and optimise their efforts considering capillarity forces at particle contacts (Espinoza & Santamarina, 2010). Similarly, mucous excretion from worms can strengthen soil along tunnelling paths, and help bind (geotechnically strong) faecal pellets to such an extent that the cone penetration test (CPT) measures the strength increase (Kuo, 2011).

Unicellular microbial organisms in soil consist primarily of bacteria and archaea (see Woese *et al.*, 1990, for definitions of terms), which typically range in diameter from 0·5 to 3 μm, and have morphologies that are typically spherical (coccus) or cylindrical; the latter may be straight (rods), curved (vibrio), or corkscrew shaped (spirilla). These are present in soil either through entrapment during deposition (the typical mode in fine-grained sediments offshore; Rebata-Landa & Santamarina, 2006) or through migration through pore space via hydraulic flow transport or self-motility. Geometric compatibility between bacteria and archaea and the pore space (pore throats to be specific)

dictates mobility (Mitchell & Santamarina, 2005; DeJong *et al.*, 2010; Phadnis & Santamarina, 2012) and survivability (Rebata-Landa & Santamarina, 2006).

Unicellular activity, in general, does not affect soil properties directly. Rather, it is how biological activity locally exploits geochemical processes, which in turn affect soil properties. Microbe activity creates 'microniche' conditions surrounding individual cells that critically alter when, where, and at what rate geochemical processes occur. A given geochemical process can often occur in the absence of biological activity, and indeed, for it to occur as a microbial process, it must be viable in the absence of biological activity, although the rate may be exceedingly slow (i.e. bioprocesses are often regarded as biocatalysis). However, doing so may result in widely distributed reactions, resulting, for example, in precipitation in the pore fluid that is subsequently transported outside the targeted treatment zone.

The ability of microbes to regulate processes (depending on the specific process utilised) often stems from the unicells containing the enzyme(s) critical to the geochemical reaction. The location of the enzyme, usually within the cell membrane or within the membrane-bound cytoplasm, regulates (through diffusion or active transport) the rate at which the reaction can occur. Increased enzymatic activity within a given cell or an increased number of cells both increase the bulk reaction rate. Although not widely explored to date, it may also be possible to use free enzymes (a non-biological approach) to improve soil properties in applications where the treatment time is relatively brief (e.g. dust suppression; Bang *et al.*, 2011).

Methods of application: processes and products

Development of a biomediated soil improvement technique requires an application strategy. The two primary strategies – bioaugmentation (where the required microbes are injected into the soil) and biostimulation (where natural microbes are stimulated) – build on bioremediation techniques developed over the last 30+ years. While the former has been the primary strategy used to date in exploring geotechnical applications, the geoenvironmental field is increasingly using biostimulation. Bioaugmentation is generally considered less favourable than biostimulation, owing to the introduction of exogenous (non-native) microbes, in some cases the permissions required, the increased costs, the practical difficulty of uniform application in the subsurface due to filtration of microbes (akin to filter design intended to protect clay cores of dams), and the potential for die-off or dormancy if the environment is not favourable for their proliferation. Biostimulation is generally preferable, owing to the stimulation and growth of native microbes, which are adapted to the subsurface environment, and to the reduction in permission difficulties. However, many challenges exist in applying biostimulation, including obtaining uniform treatment across a site, and accommodating the increased time associated with stimulation and growth. A compromise between these two approaches may be bioaugmentation at a low concentration followed by stimulation in situ, or 'microdosing' (Martinez, 2012).

Geochemical processes regulated through biostimulation or bioaugmentation often result in multiple products. The primary product is typically the one that is designed to be the desired outcome (e.g. calcite precipitation to bind soil particles together). In addition, there are often additional 'by-products' generated by the geochemical process (e.g. ammonium ions). The generation, transport and fate of these by-products must be addressed, often as a waste, although in some cases they may be repurposed for other applications (e.g. ammonium for fertilisation of plants).

Potential improvements to engineering properties with biogeochemical processes

Biomediated geochemical processes have the potential to modify physical properties (density, gradation, porosity, saturation), conduction properties (hydraulic, electrical, thermal), mechanical properties (stiffness, dilation, compressibility, swell/shrink, cohesion, cementation, friction angle, erodibility, and soil-water characteristic curve), and chemical composition (buffering, reactivity, cation exchange capacity) of soils. This may be conceptualised by considering how different biogeochemical processes may influence an assemblage of sand grains and/or an aggregation of clay platelets.

Biomineralisation processes that precipitate inorganic solids (including microbially induced calcite precipitation, or MICP) can clearly have a mechanical effect: for example, reduction in pore space, brittle cementation at particle contacts, increased fines in the pore space, and increased stiffness. These effects will predictably result in reduced hydraulic conductivity, increased small-strain stiffness, increased large-strain strength, and increased dilative behaviour.

Biofilm formation, and the production of other extracellular polymeric substances (EPS), are additional biogeochemical processes that can impact on soil behaviour. These processes generate organic solids that occupy a portion of the pore space with a soft, ductile, elastomeric-like material that reduces pore size, reduces rearrangement of particles during soil deformation, and increases ductility. These changes can reduce hydraulic conductivity, and perhaps reduce rapid strain-softening during undrained shearing. However, property changes due to biofilm and EPS production may be lost, and thus be applicable only for short-term ground modification, as these living systems must be continuously nourished or their engineering performance may become unreliable.

Biogas generation from denitrification or other biogeochemical processes may enable long-term reduction in the degree of saturation of a soil. Reduction in the degree of saturation increases pore space compressibility, and may thereby reduce excess pore pressure build-up during cyclic loading, mitigating earthquake-induced liquefaction potential in some soils.

Other processes that have been identified, but are currently less developed, include algal and fungal growth for near-surface soil stabilisation, bacteria and worms for methane oxidation, biopolymers for drilling applications, organic slurries for hydraulic control, and silicate precipitation.

RESEARCH ACTIVITY AND APPLICATIONS

Research activity in biogeotechnical engineering to date has investigated many of the above potential processes, with a significant portion of activity focused on biomediated cementation via calcite precipitation. The following examples highlight the extent to which soil properties can be modified or improved by biogeochemical processes. These examples are not comprehensive, with additional references provided.

Microbially induced calcite precipitation

Microbially induced calcite precipitation, or MICP, has been the primary focus of research in biogeotechnical engineering to date. In MICP, the creation of calcium carbonate (calcite) occurs as a consequence of microbial metabolic activity (Stocks-Fischer *et al.*, 1999; Ramakrishnan *et al.*, 2001). Calcite precipitation may be achieved by many different processes (DeJong *et al.*, 2010), including urea hydrolysis (Benini *et al.*, 1999; Ciurli *et al.*, 1999);

denitrification (Karatas *et al.*, 2008; Van Paassen *et al.*, 2010a; Hamdan *et al.*, 2011b); sulphate reduction, inducing dolomite precipitation (Warthmann *et al.*, 2000); and iron reduction, inducing ankerite and other mixed mineral precipitation (Roden *et al.*, 2002; Weaver *et al.*, 2011). Enzymatic hydrolysis of urea by microbes is the most energy efficient of these processes (DeJong *et al.*, 2010), and urease activity is found in a wide range of microorganisms and plants (Bachmeier *et al.*, 2002). *Bacillus pasteurii* (American Type Culture Collection 6453), which was recently reclassified as *Sporosarcina pasteurii* (ATCC 11859), an alkalophilic bacterium with a highly active urease enzyme (Ferris *et al.*, 1996), has been used in laboratory studies where bioaugmentation has been performed to produce calcite precipitation (Mortensen *et al.*, 2011). More recently, biostimulation of native microbes has reportedly been successful (Burbank *et al.*, 2011, 2012a), and the influence of competing microbe species/processes has been explored (Gat *et al.*, 2011). Limited studies have also explored precipitation of other minerals (e.g. Chu *et al.*, 2011; Weaver *et al.*, 2011).

Research has provided insights into MICP from micrometre- to metre-length scales (Fig. 1). Microscopy techniques show that the calcite structure varies with treatment formulation (Al Qabany *et al.*, 2012), cementation occurs preferentially at particle contacts (Chou *et al.*, 2008; Martinez & DeJong, 2009), calcite precipitation occurs directly on or around individual microbes and their aggregates, and cementation breakage during shearing occurs within the calcite crystals (DeJong *et al.*, 2011). Laboratory-scale element tests have shown substantial ($> 10^3\times$) increases in strength (DeJong *et al.*, 2006; Whiffin *et al.*, 2007; Van Paassen *et al.*, 2009; Chu *et al.*, 2011, 2013; Al Qabany & Soga, 2013), decreases in hydraulic conductivity greater than two orders of magnitude (Al Qabany, 2011; Rusu *et al.*, 2011; Martinez *et al.*, 2013), increases in small-strain stiffness by three orders of magnitude (DeJong *et al.*, 2006; Van Paassen *et al.*, 2010b; Van Paassen, 2011; Esnault-Filet *et al.*, 2012), and an increase in dilative tendencies (Chou *et al.*, 2011; Mortensen & DeJong, 2011; Tagliaferri *et al.*, 2011). Even after cementation degrades owing to shearing, the reduction in pore space (or increase in solids density) due to the precipitated calcite alters the behaviour of the material. Re-establishment of properties following MICP degradation from shearing can be rapid and efficient (Montoya, 2012). Geophysical methods (shear wave velocity in particular) are effective for real-time monitoring of the cementation process, as the precipitated calcite stiffens particle–particle contacts (Al Qabany *et al.*, 2011; Montoya *et al.*, 2012; Weil *et al.*, 2012).

One-dimensional column, two-dimensional flow and three-dimensional model tests have enabled enquiry into treatment uniformity, formulation optimisation, and self-equilibrating ability, as well as demonstration of conceptual ideas about property improvement due to MICP (DeJong *et al.*, 2009; Martinez & DeJong, 2009; Van Paassen, 2009; Van Paassen *et al.*, 2009; Inagaki *et al.*, 2011a; Tobler *et al.*, 2012; Martinez *et al.*, 2013) (Fig. 1). One-dimensional column experiments have shown pulsed flow injection and flow reversal to increase uniformity, lowering the molar ratio of urea to calcium to reduce by-product formation, and geophysical seismic measurement to spatially monitor improvement (Martinez, 2012). Two-dimensional models of field treatment patterns have explored the efficacy of bioaugmentation compared with biostimulation, and linkages between microbial distribution, ureolysis activity, shear wave velocity and total precipitated calcite (Al Qabany, 2011; Martinez, 2012). Scale model tests have demonstrated the effectiveness of MICP in reducing wind- and water-induced erosion (Bang *et al.*, 2011), improving resistance to liquefaction (Inagaki *et al.*, 2011b; Montoya *et al.*, 2013), creating impermeable crusts

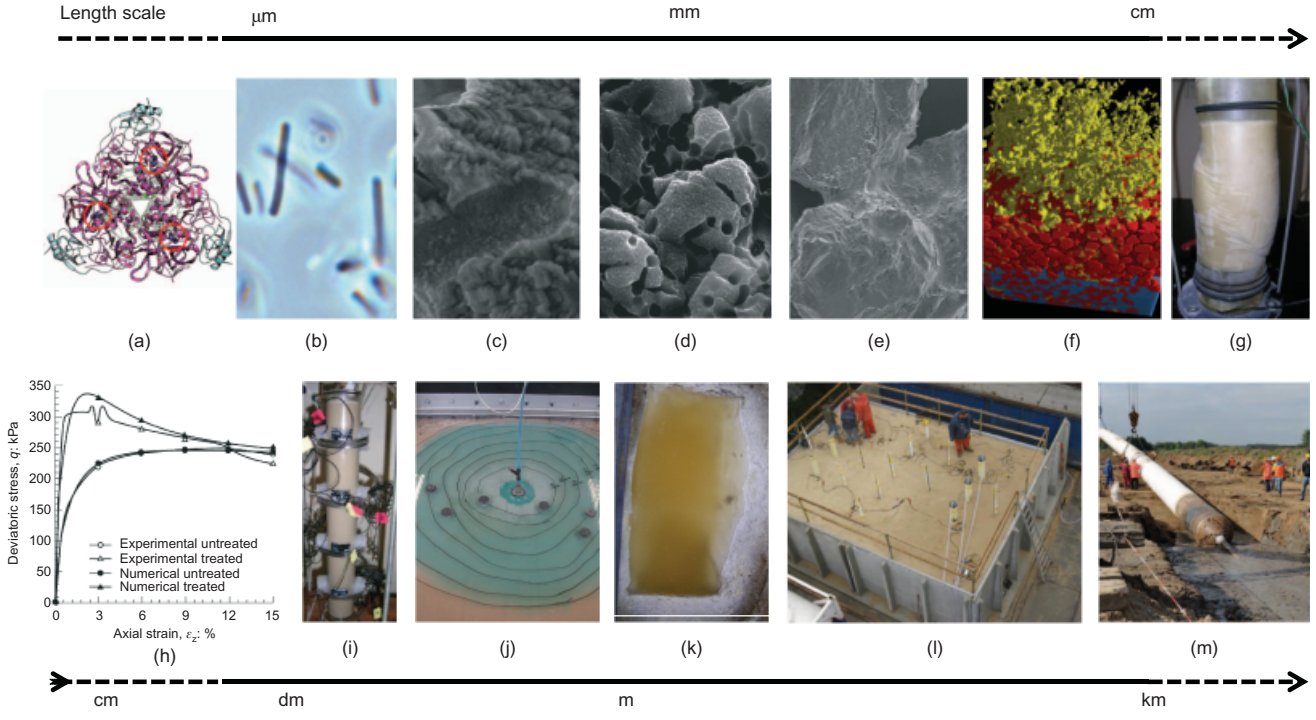

Fig. 1. Overview of upscaling of MICP: (a) urease enzyme structure housed within microbes (Benini *et al.*, 1999); (b) *Sporosarcina pasteuri* microbe (image supplied by DeJong); (c) bacterial impression within precipitated calcite (Martinez & DeJong, 2009); (d) structure of precipitated calcite (Day *et al.*, 2003); (e) MICP-cemented sand grains (Chou *et al.*, 2008); (f) CT scan of MICP-cemented sand (image supplied by DeJong); (g) MICP-cemented triaxial specimen (Mortensen *et al.*, 2011); (h) modelling of MICP triaxial compression test (Fauriel, 2012); (i) 1D column tests (Martinez, 2012); (j) radial flow treatments (Al Qabany, 2011); (k) MICP impermeable skin for retention basin (Stabnikov *et al.*, 2011); (l) MICP treatment of 100 m^3 sand (Van Paassen *et al.*, 2010b; Esnault-Filet *et al.*, 2012); (m) field trial

for catchment facilities (Stabnikov *et al.*, 2011; Chu *et al.*, 2012), healing/stabilising cracks in concrete and masonry (Ramachandran *et al.*, 2001; Bang *et al.*, 2010; Yang *et al.*, 2011), treating waste (Chu *et al.*, 2009), immobilising heavy metals (Fujita *et al.*, 2004, 2008, 2010; Hamdan *et al.*, 2011a; Li *et al.*, 2011), and performing shallow carbon sequestration (Manning, 2008; Renforth *et al.*, 2009, 2011; Washbourne *et al.*, 2012). MICP has also been shown to increase cone tip resistance (Burbank *et al.*, 2012b).

Modelling of MICP requires coupling of biological, chemical, hydrological, and mechanical processes. Modelling efforts have generally focused either on prediction of biogeochemical processes (Barkouki *et al.*, 2011; Fauriel & Laloui, 2011b, 2012; Laloui & Fauriel, 2011; Martinez *et al.*, 2011; Van Wijngaarden *et al.*, 2011, 2012; Martinez, 2012) and calcite distribution, or on prediction of the mechanical behaviour of biocemented soils (Fauriel & Laloui, 2011a; Fauriel, 2012). Models to date have captured and predicted biogeochemical processes, provided first-order predictions of precipitated calcite distributions, and captured the mechanical behaviour of MICP-treated sand (Fig. 1(h)).

As discussed later in the section on field applications, two field trials using MICP have been performed to date.

Biofilm formation

Biofilms form when microorganisms adhere to a surface and excrete EPS as part of their metabolism. This 'slimy' EPS enhances further attachment of more microorganisms and other particles, thereby forming a biofilm that can affect the physical properties of soils (Fig. 2(a); Banagan *et al.*, 2010). Close to the surface in riverine and marine environments, biofilms play an important role in trapping and stabilising sediments, and increasing the resistance to erosion (Stal, 2010). In the subsurface, it has been shown already that the growth of biofilms can reduce hydraulic conductivity (Slichter, 1905), a process referred to as bioclogging. Much of the research on bioclogging is focused on preventing and/or removing the clogging material (Howsam, 1990), for example by flushing with formaldehyde, in order to restore or maintain the functionality of wells or drains (Baveye *et al.*, 1998). However, some researchers have found that biofilm formation in soil could also be advantageous (e.g. Mitchell *et al.*, 2009). For example, Talsma & van der Lelij (1976) observed that water losses from rice fields were limited, owing to bacterial clogging. Attempts have been made to use bioclogging to decrease hydraulic conductivity in situ beneath and within dams and levees, to reduce infiltration from ponds, to reduce leakage at landfills, to plug high hydraulic conductivity layers surrounding oil bearing layers, and to control groundwater migration with subsurface barriers (Fig. 2(b); Seki *et al.*, 1998; James *et al.*, 2000; Lambert *et al.*, 2010).

Biogas generation

Biological activity in the subsurface is frequently accompanied by the development of discrete gas bubbles in otherwise saturated environments. A variety of gases can be produced by microbial processes (e.g. carbon dioxide, hydrogen, methane and nitrogen), with both the organism and the oxidative/reductive environment of the pore fluid influencing the ultimate products of the reaction. For example, aerobic microbes (obligate or facultative) use oxygen as the terminal electron acceptor during the process of microbial respiration. Typically, an organic molecule is used as the carbon and energy source, and the products resulting from the reaction include water and carbon dioxide. By contrast, anaerobic respiration by methanogenic archaea occurs in the absence of oxygen, and results in the production of methane and

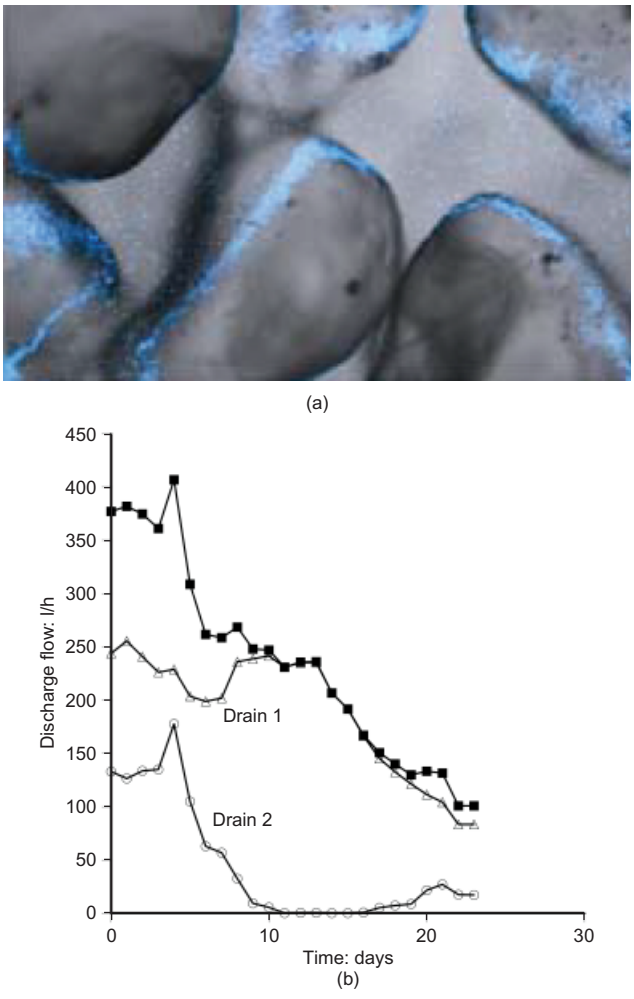

Fig. 2. Example results of biofilm treatment for permeability reduction; (a) laser confocal fluorescence microscopy image of biofilm-coated sand grains; (b) field data showing reduction in seepage flow in a dam following biofilm hydraulic conductivity reduction treatment (Blauw *et al.*, 2009; used by permission)

often carbon dioxide (i.e. part of the carbon is oxidised to carbon dioxide and part is reduced to methane). The process uses part of the carbon, as opposed to oxygen, as the terminal electron acceptor. Respiratory denitrification occurs through the reduction of nitrate, producing nitrogen and carbon dioxide gas as the end products of the reaction in environments that have high ratios of nitrate to carbon. Numerous laboratory studies have demonstrated the feasibility of producing microbially generated discrete gas bubbles at the bench scale, with a review of the processes given in Rebata-Landa & Santamarina (2012), and shaking-table tests provided by He *et al.* (2013). In practical terms, the presence of gas bubbles within an otherwise saturated soil results in a decrease in the measured P-wave velocity; this decrease is transient in coarse-grained soils, but not in fine-grained soils that can trap the generated gas bubbles (Fig. 3(a); Rebata-Landa & Santamarina, 2012). Even small reductions in the level of saturation of a soil are known to significantly reduce a soil's susceptibility to liquefaction (Fig. 3(b); e.g. Sherif *et al.*, 1977; Chaney, 1978; Yoshimi *et al.*, 1989; Ishihara *et al.*, 2001; Pietruszczk *et al.*, 2003).

Biopolymers and EPS

Both in situ and ex situ applications of biopolymers for soil improvement have been explored. Biopolymers mixed with soils have been shown to reduce hydraulic conductivity

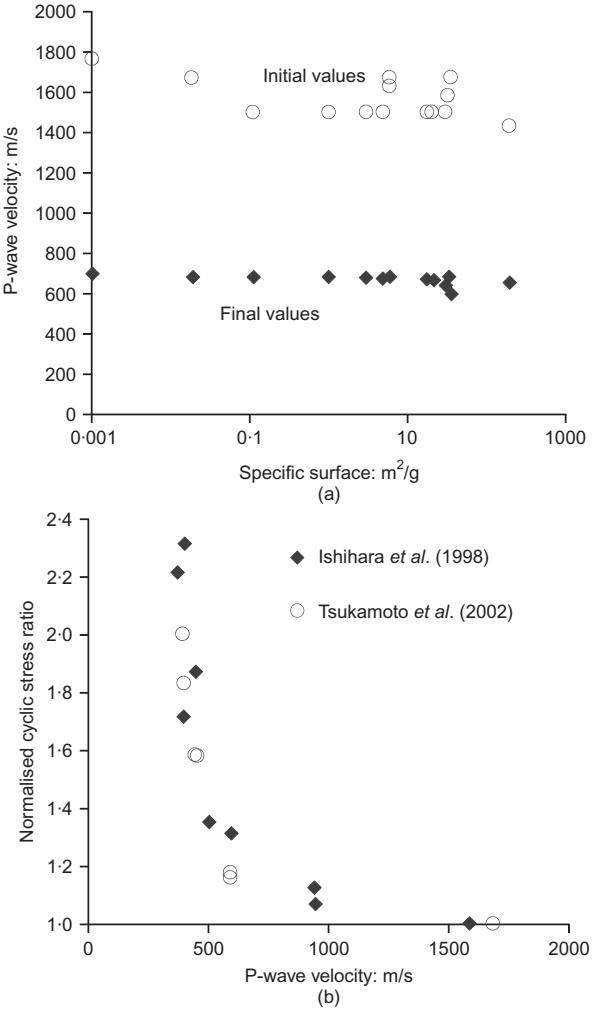

Fig. 3. Reduction in saturation monitored by P-wave velocity in initially saturated sand due to nitrogen gas generation via biogeochemical treatment process of denitrification: (a) P-wave velocities pre- and post-treatment, with consistent performance across a broad range of specific surfaces (grain sizes); (b) published relationship between P-wave velocity (corollary to saturation) and cyclic strength, indicating that reduction in saturation (via denitrification) could increase liquefaction resistance (Rebata-Landa & Santamarina, 2012; used by permission)

and increase shear strength (Kavazanjian *et al.*, 2009; Nugent *et al.*, 2010). Martinez *et al.* (2011) showed that mixing silt with 0·3% (by weight) xanthan gum, a commercially available biopolymer, can reduce saturated hydraulic conductivity by two orders of magnitude (down to $\sim 10^{-6}$ cm/s) and increase the drained shear strength by up to 30%. The observed reduction in hydraulic conductivity is a function of soil grading and the applied hydraulic gradient (Jefferis, personal communication, 2012). Biopolymers are used in biodegradable drilling muds owing to their propensity for bioplugging (Hamed & Belhadri, 2009). They have also been used as temporary excavation support fluids to create permeable reactive barriers for groundwater remediation, with biopolymer degradation accelerated by the introduction of a high-pH 'enzyme breaker' after placement of the permeable reactive material in an open trench (Sivavec *et al.*, 2003). Khachatoorian *et al.* (2003) observed permeability decreases in less than 2 weeks in sand treated with a biopolymer slurry. Some investigators have explored increasing soil shear strength in situ by biopolymer generation (e.g. Cabalar & Canakci, 2005). However, most investigations of applications of in situ biopolymer growth and EPS generation have focused on reduction in hydraulic conductivity to form hydraulic barriers (e.g. Wu *et al.*, 1997; Bonala & Reddi, 1998; Seki *et al.*, 1998). Furthermore, there are many case histories of clogging of filters in dams, landfills and water treatment plants caused by the growth of biofilms (Cullimore, 1990; Ivanov & Chu, 2008). For example, in October 1985 an investigation of subsurface drain clogging at the Ergo Tailings Dam (ETD) in South Africa, after only 6 months' service, revealed that the geotextile drain filter was clogged by the growth of arsenic-resistant microorganisms (Legge *et al.*, 1985).

Mechanical processing by marine worms

Many deep ocean clays are subject to thousands of cycles of biological activity that transform virgin material into processed material. Burrowing invertebrates (worms), through the process of bioturbation, digest sediment that has fallen through the water column to the seabed. They are one example of a biological agent that has been active for millennia. During feeding, the ingested sediment, containing clay, organic matter, foraminifera, diatoms, shell fragments and other detritus, is processed in the gut, removing material of nutritional value. The remaining material is expelled by the worm's hind gut (Barnes *et al.*, 1988) in the form of faecal pellets that are compacted and bound by mucus (see Fig. 4(a)). These resulting pellets are significantly stronger than the material initially ingested, and have undrained shear strengths of between 1 kPa and 12 kPa (Kuo & Bolton, 2012). If sufficiently numerous, these pellets can produce measurable increases in bulk sediment strength within the top few metres of deep ocean clay sediments. The sedimentation rate in many of these locations may only be of the order of 0·1 mm per year (Kuo, 2011). Worms, however, may digest material at a rate of 0·75 mm each year if hypothetically located at a plan spacing of 1 m (Gingras *et al.*, 2008). It is therefore plausible that, over the sediment's lifetime, worms are biologically engineering all material settling on the seabed into robust pellets. These pellets' collective presence (in some cases 20–60% of total sediment by dry mass; Kuo, 2011) can be measured as a crust-like feature during in situ strength testing with conventional tools, including ball and T-bar full-flow penetrometers (see Fig. 4(b), following Kuo & Bolton, 2011). Because of their proximity to the seabed, faecal pellets are of significant engineering interest in the design of offshore pipelines and shallow foundations.

Shallow carbon fixation through plant roots

It may be possible to design a carbon sequestration function in soils through exploiting and extending natural processes of pedogenic carbonate function. Widely observed in natural soils, pedogenic carbonate minerals form as a consequence of reaction between plant root exudates and calcium derived from silicate mineral weathering. It has recently been shown that this process also occurs in urban soils, as a consequence of reaction between root exudates and calcium derived from the dissolution or weathering of cement-based construction materials (Manning, 2008; Renforth *et al.*, 2009, 2011; Washbourne *et al.*, 2012). Plants exude 10–30% of carbon captured from the atmosphere by photosynthesis through their roots and associated mycorrhizal fungal associations (Kuzyakov & Domanski, 2000; Taylor *et al.*, 2009). Root tissue compounds are released into the soil as exudates (Jones *et al.*, 2009), which are complex materials composed of polysaccharides, proteins, phospholipids, cells that detach from roots, and other compounds. Respired carbon dioxide and organic acid anions that naturally decompose and can react with calcium-rich silicates

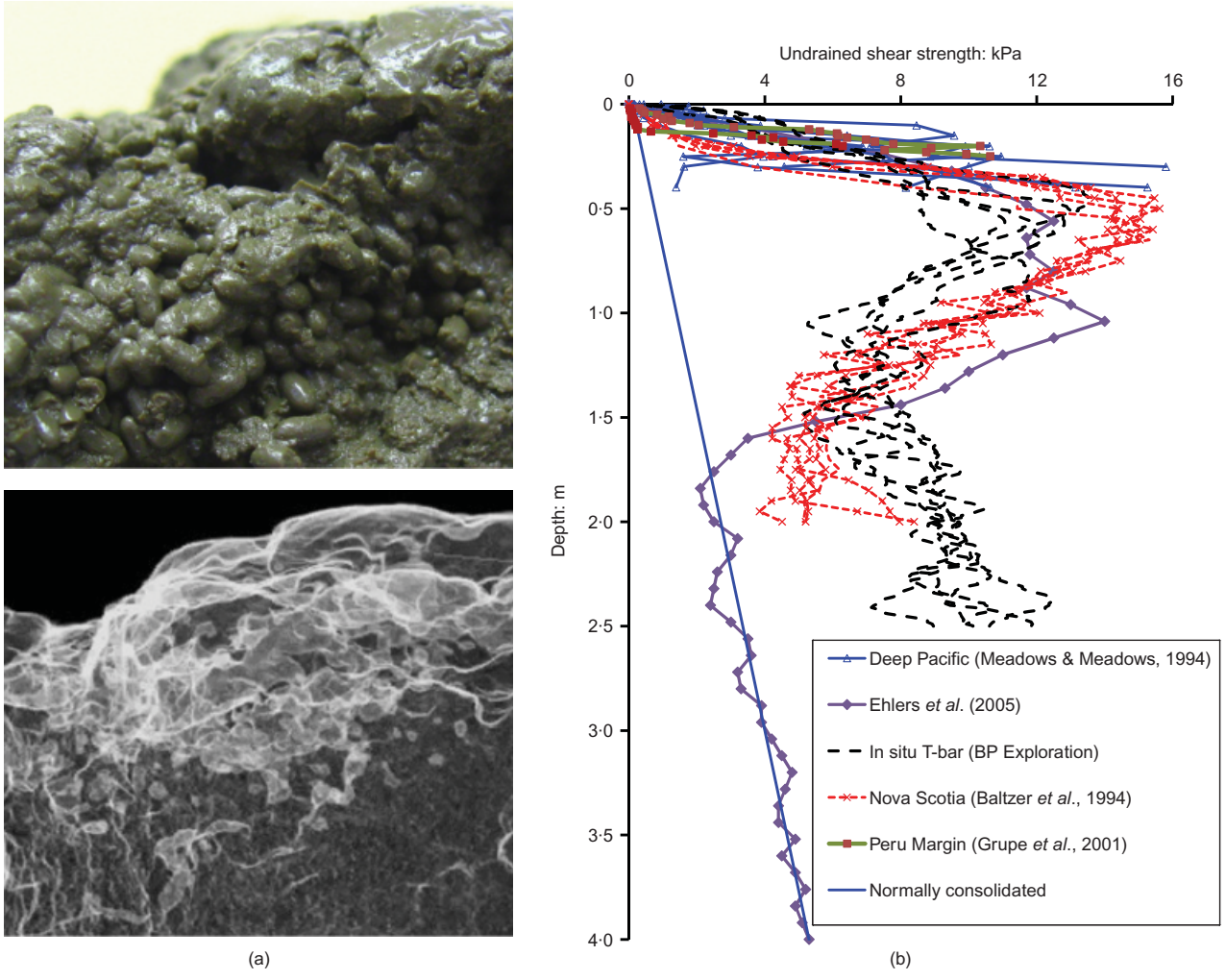

Fig. 4. Natural example of bioturbation by multicellular organisms such as worms, etc.: (a) image and SEM of faecal pellets from near-surface offshore fine-grained sediments (note micro- and macropores evident in SEM) (Kuo *et al.*, 2010; used by permission); (b) clearly detectable crystal layer, formation is attributed largely to bioturbation (Baltzer *et al.*, 1994; Meadows & Meadows, 1994; Grupe *et al.*, 2001; Ehlers *et al.*, 2005)

within soils are of particular interest. Manning (2008), Renforth *et al.* (2009, 2011) and others (Sanderson, 2008) have recorded that this process occurs naturally in soils at brownfield sites and can be very rapid (Washbourne *et al.*, 2012). As summarised in Fig. 5, the resequestration of carbon emitted during cement/lime production into the sub-surface may be possible through the admixing of recycled concrete and furnace slag into soils used for non-food crops and urban revegetation (Manning, 2008).

FIELD APPLICATIONS

Completed/ongoing field trials

To date, only a few field trials have been performed in which microbes have actively been used to either increase the strength and stiffness of soils by microbially induced carbonate precipitation or reduce the hydraulic conductivity through biofilm formation, although such processes will have been occurring naturally for millennia.

Two field trials using MICP are reported in the literature, the first using a bioaugmentation strategy and the second stimulating the indigenous species to induce precipitation. Contractor Visser & Smit Hanab applied a MICP treatment for gravel stabilisation to enable horizontal directional drilling (HDD) for a gas pipeline in the Netherlands in 2010 (Fig. 6; from Van Paassen, 2011). The treatment was applied to a 1000 m^3 volume at depths varying between 3 and 20 m below the surface. The treatment involved injection of a 200 m^3 bacterial suspension that was cultivated in the laboratory, two injections of 300–600 m^3 of reagent solution containing urea and calcium chloride, and extraction of groundwater until electrical conductivity and ammonium concentrations returned to background values. MICP was monitored using electrical resistivity, groundwater sampling and physical sampling for calcite content measurements, with varying degrees of success. Overall, the MICP treatment was a success, as HDD was possible without instability in the loose gravel deposit.

A second set of MICP field trials using biostimulation to evaluate the capability of co-precipitation of heavy metals (strontium-90) with calcium carbonate (to immobilise the heavy metals) was initiated at the Vadose Zone Research Park (VZRP) at the Idaho National Laboratory (INL), and is ongoing at the US Department of Energy site in Rifle, Colorado, USA (Fujita *et al.*, 2010). These trials have employed injection of dissolved molasses and urea in the target treatment zone (calcium available in groundwater), with contemporaneous withdrawal of groundwater from a well several metres away from the injection point. At the Rifle site the well-to-well cycle is closed by reinjection of withdrawn water. To date, native microbes have been successfully stimulated at both sites, and calcite precipitation appears to be in progress. The rate of precipitation is slower than in the bioaugmentation application in the Netherlands

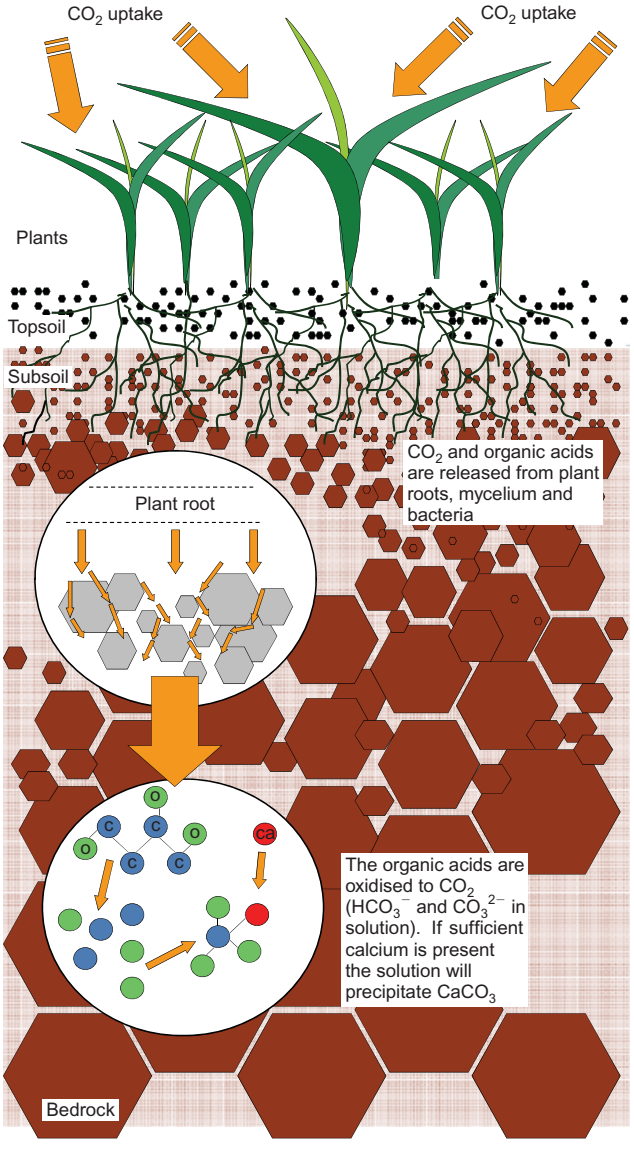

Fig. 5. Overview of biomediated (plants) near-surface carbon sequestration observed and documented by Manning & Renforth (described in Manning, 2008)

described above, but is nonetheless advancing at a sufficient rate for the project requirements.

Successful field trials of bioclogging have also been reported in the Netherlands and Austria, with the objective of reducing leakage through water-retaining constructions (Van Meurs *et al.*, 2006; Blauw *et al.*, 2009). In Austria, nutrient solutions were injected through a screen of injection wells in the crest of a 'leaking' dike along the Danube river in Greifenstein (Blauw *et al.*, 2009; Lambert *et al.*, 2010). Injection was performed in two stages. During and following the first injection phase (November–December), no significant flow reduction was observed in downstream drains. However, during the second treatment phase (July–August), a significant reduction in discharge rate was observed (Fig. 2(b)). The measurement of a significant reduction in redox potential indicated biochemical activity in the treated area. The actual mechanism behind the reduction in permeability is not yet fully understood (Blauw *et al.*, 2009). Whether it is the biofilm itself that clogs the pores, or some trapped particles in the biofilm, or perhaps the biogeochemical conversions that stimulate attachment, detachment or precipitation of particles that can reduce the hydraulic conductivity still needs to be resolved.

In southern Ontario, Canada, researchers (Lambert *et al.*, 2010) have also been successful in reducing hydraulic conductivity in a fractured dolostone formation in order to block the flow of contaminated groundwater. Nutrient solutions (molasses) were injected several times into the ground to stimulate bioclogging. Geochemical measurements indicated that microbial growth and a significant increase in microbial diversity were observed. The longevity of the biofilm appeared to be limited, as the hydraulic conductivity returned to its initial condition 230 days after the nutrient injections had stopped.

Challenges for field implementation

The process of upscaling to the field, following experimental and modelling research at the element and bench scales, raises the following challenges that must be considered and addressed.

Characterisation of subsurface heterogeneity. The treatment of 100+ m^3 of naturally deposited soil requires characterisation of both soil and microbial spatial distributions at different scales. Similar to chemical injection methods, preferential flow – and therefore initial treatment – will occur within zones of larger pore space (hydraulic conductivity). Recent work indicates that MICP may be 'self-equilibrating' to some extent, as the precipitated calcite does reduce conductivity; when the level of reduction is sufficient in fine-grained soils, treatment may redirect towards untreated (and relatively higher conductivity) zones (Martinez, 2012). The spatial microbial distribution does not necessarily map with soil particle variations, and hence targeted delivery of microbes to the improvement area may be required. From a practical standpoint, the primary interest is the bulk reactivity level in the soil (i.e. the rate at which a chemical reaction can occur in a soil volume) required for a given biogeochemical process; the exact microbial species, their absolute population, and other environmental factors are not critically important. Instead it is the bulk activity level that the biota (all microbes) provide for a specific process that is the key factor. For ureolysis-based MICP, the critical bulk activity is the rate at which urea is hydrolysed. The bulk ureolysis rate can be tested by injecting and monitoring the spatial degradation of aqueous urea temporally (Martinez *et al.*, 2013).

Treatment schemes for uniform improvement. The first task in developing a treatment scheme is to identify the level of improvement required. Laboratory test results enable identification of an ideal improvement threshold (akin to grouting methods), but the actual application level of treatment is often higher in the field because of allowances for spatial variability. To minimise the additional application level that must be achieved in the field, the treatment scheme must be optimised for treatment uniformity. The treatment scheme selected depends largely on whether the nutrients and/or microbes can be delivered relatively uniformly across the treatment zone through injection; this uniformity is directly a function of solution viscosity and density as well as microbe size relative to soil pore throat size and of course, critically, the soil uniformity. In situ treatment is typically possible in gravels, sands and silty sands. Uniform treatment using biogeochemical processes can utilise technologies from the ground improvement, geoenvironmental remediation and oil production industries. For example, grouting methods, including injection/extraction well patterns, point injection sources and treatment solution mixing equipment, were successfully used in the MICP field trial in the Netherlands (Van Paassen, 2011).

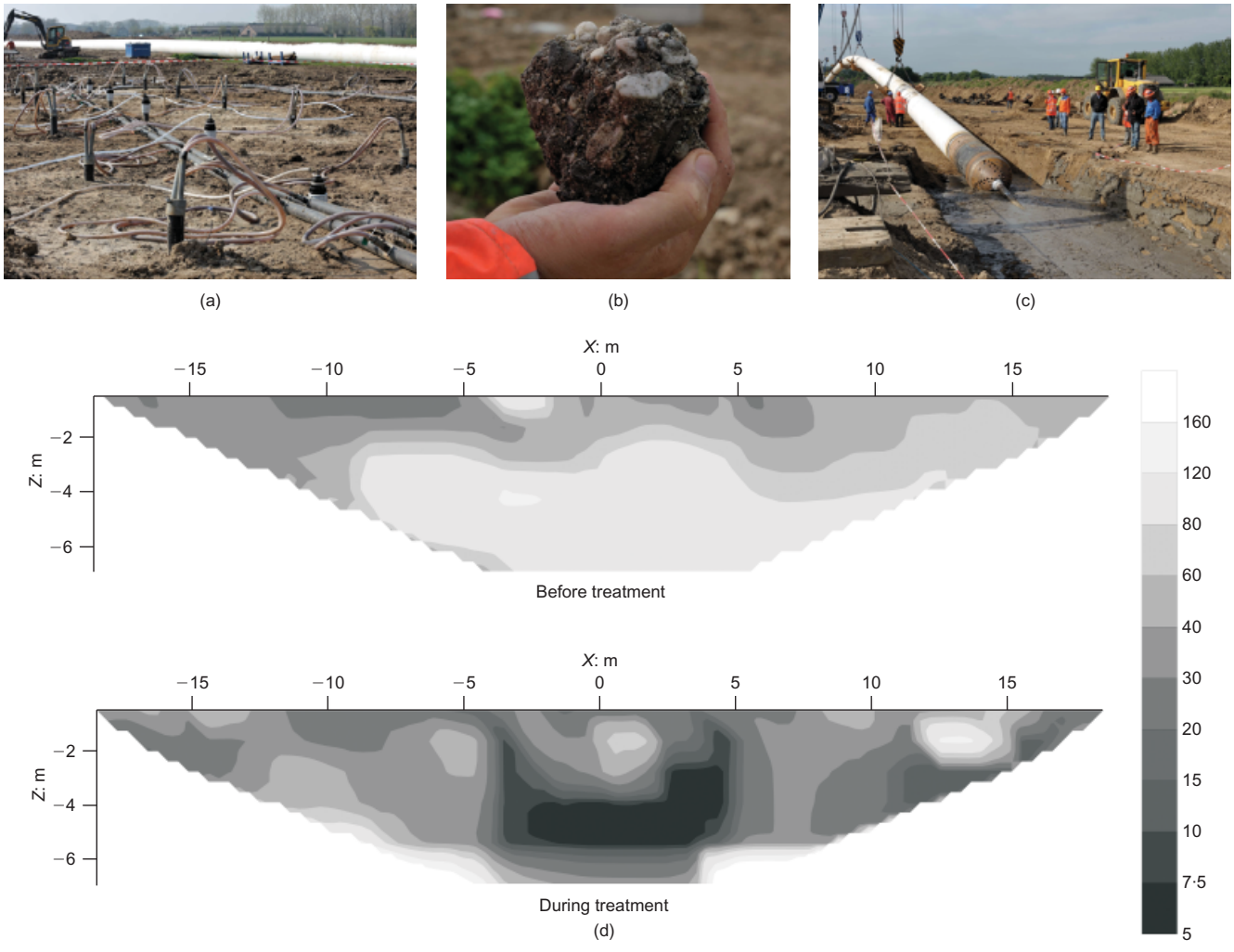

Fig. 6. Overview of MICP field trial for stabilisation of loose gravel for horizontal directional drilling (project described by Van Paassen (2011)): (a) repeating well pattern; (b) sample of MICP-stabilised gravel; (c) pipeline installation after horizontal directional drilling (provided by Visser & Smit Hanab); (d) resistivity mapping before and during treatment (provided by Deltares)

A more localised approach using a five-spot injection/extraction well pattern with pulsed injections following geoenvironmental and oil production techniques has also been successful at both field and model scales (Fujita *et al.*, 2010; Martinez, 2012). If treatment of fine-grained soils such as clay is desired, mechanical mixing, either in situ or ex situ, may be necessary. These methods have been marginally successful in the laboratory, and implementation using conventional ground improvement equipment such as deep soil mixing tools may be problematic, as rapid pressure drops and high shearing stresses may cause lysing (bursting) of cells. Other variables that must also be considered but are not yet fully understood include single versus multiple phase injections schemes, continuous versus pulsed injection, surficial flooding versus deep injection, and short, high-concentration treatments versus slow, low-concentration treatments.

Construction, operation and maintenance. Nearly all research performed to date has focused on implementation of the biogeochemical processes for improvement/modification of the soil properties. However, realising the treatment in situ is only the first stage of development of an application. As discussed above, biogeochemical processes may have by-products (such as ammonia) that must be managed. By-product management requires consideration of the fate and transport of the by-products, as well as verification that the treatment does not degrade with time owing to geotechnical mechanical loading (e.g. an earthquake), or chemical (e.g. dissolution by carbon-dioxide-rich waters) or biochemical processes that may change the rate of chemical processes. Use of the observational method may be appropriate for this technology. If degradation over time is of concern, then retreatment, or 'healing', of the biogeochemical treatment might be a possible solution, although inducing additional costs and implementation constraints (Montoya, 2012).

Service life. Selection of an appropriate biogeochemical treatment for a specific application requires compatibility of its permanence and durability with service life requirements. MICP-treated sand is expected to be stable for more than 50 years, provided alkaline conditions persist (DeJong *et al.*, 2009), as its longevity is expected to be consistent with that of natural calcite-rich geomaterials. A 50+ year time frame is compatible with the expected service life of many structures, and occasional retreatment can be applied to extend this service life. On the other hand, biofilms require a continuous nutrient source, and therefore may be more suitable for short-term hydraulic control applications (Cunningham *et al.*, 1997). In either case, a risk assessment with respect to treatment longevity, including assessment of the groundwater–precipitate interaction and a performance-monitoring programme, may be appropriate.

Performance monitoring. Central to any improvement method – biogeochemical or conventional – is monitoring during treatment to verify that the required distribution and magnitude of improvement are realised, and, after treatment, to verify that the improvement level remains adequate throughout the service life. This typically requires a rigorous quality assurance/quality control (QA/QC) process during construction by the contractor to verify the 'certainty of execution' (an issue for conventional ground improvement techniques). The QA/QC programme would be likely to include a verification testing programme that specifies the number of samples obtained, tests to be performed on samples, field tracer tests, monitoring of reactants and products during treatment, and/or geophysical measurements. In addition, a reduced, but continuous, level of monitoring by the owner/operator throughout the service life (perhaps bi-monthly to yearly) is likely to be required. Post-improvement monitoring may also become a regulatory compliance issue similar to that for geoenvironmental remediation projects.

Modelling of biogeochemical treatment processes. The inter-disciplinary nature of biomediated geochemical processes requires integration of the biological and chemical components within the hydraulic and mechanical modelling techniques already established in geotechnical finite-element and finite-difference modelling codes, as well as the development of new constitutive models for the behaviour of bio-treated soil. Current models can predict final spatial MICP calcite distribution, and model the mechanical element behaviour of MICP-treated sand. Issues that remain include the integration of relevant biogeochemical reaction networks, small-scale biochemical processes (i.e. microbial growth, enzymatic rates, gas generation, etc.), local changes in porosity (and hydraulic conductivity) and saturation, modelling of degradative processes in treated soils, and more. Modelling of spatial variability (microbes versus soil particles) and identifying the appropriate transition from discrete to continuum scales (i.e. microbes and soil particle versus bulk reaction rate and porosity) will be particularly challenging, as the biogeochemical processes occur at the micrometre length scale.

Sustainability: life cycle analysis and embodied energy. One of the attractive attributes of biogeotechnology is the utilisation of natural, biogeochemical processes to improve soil. These processes have the potential for significant reduction in embodied energy and carbon emissions, relative to conventional ground improvement methods such as soil stabilisation using Portland cement. Sustainability analyses to date are limited, and challenges regarding the definition of system boundaries and the service life period must still be resolved. However, with respect to MICP, soil improvement with calcite production requires less carbon than cement stabilisation, but additional analysis is required to study the energy required for manufacturing of the urea and calcium chloride, for injection of the improvement media into the ground, and for treatment of by-products.

Cost. The cost of biogeochemical treatment schemes will be dependent on the process used, and on details of the specific field project. With very limited field applications, the actual costs of the various improvement processes are largely unknown. Studies and cost estimates to date vary widely, owing to suboptimised treatment schemes being implemented to date. Ivanov & Chu (2008) estimated material costs for MICP (e.g. urea, calcium) of about US\$5/m^3 (range from 0·5 to 9), and total costs of MICP treatment (materials, equipment, and installation) in saturated soils range from US\$25–75/m^3 (DeJong, personal communication, 2011) to about US\$500/m^3 (Esnault-Filet, personal communication, 2011). Recent work by Cheng & Cord-Ruwisch (2012) found that materials and costs may be reduced through more efficient cementation. While their estimate encompasses a wide range, the lower half of this range is competitive with many conventional ground improvement techniques, such as deep soil mixing, jet grouting and chemical grouting. It also shows that, in common with many other ground treatment processes, the major cost is in delivery. If processes can be developed that enable biotreatment to be delivered more economically, then strong potential exists.

Feasibility for different applications

Realistically, biogeochemical-based soil improvement technologies will never replace all conventional ground improvement techniques. However, the following general attributes make these technologies potentially favourable in many instances: they are based on natural processes; they often require less energy; they are deployable beneath and around existing structures, and are non-disruptive to those structures; and they may enable improvement over larger distances, owing to their low viscosity and injection pressure requirements. Thanks to these attributes, biogeochemical soil improvement technologies may provide opportunities to address broad societal priorities, such as climate change, energy, food, shelter, infrastructure, urbanisation, sustainability, waste management, safety, water availability and economic stability.

Considering the general attributes of biogeochemical processes, the challenges for implementation in the field, and society's needs, the applications with the highest likelihood of success will, in general, require simple implementation, provide a unique answer to a problem, have competitive costs, and have a potential for rapid take-up by industry and society. Within this context, 24 different biogeochemical applications were identified and evaluated in a qualitative manner against the criteria of cost, implementation, probability of success, and social acceptance as part of the 2012 Workshop activities. The applications and their approximate 'ranking' against these criteria are presented in Table 1.

The applications that seem most feasible in the near term include erosion control, environmental remediation, dust control, improvement of rural roads, surface carbon dioxide sequestration, repair of sandstone structures, and solidification of fly ash. All of these applications still require further development, but they all represent problems for which current solutions are insufficient. Longer-term 'blue sky' applications include the creation of underground space (for storage or transport), deep carbon dioxide sequestration, stabilisation of sink holes, and control of underground hydraulic flow. In all these cases, the current capital-cost-driven construction industry essentially forces consideration of a new biogeochemical technique, because current best practices are insufficient. However, if capital costs are merely competitive with current industry methods, the tried-and-true established methods in industry that have decades of experience will often be preferred.

CLOSURE: RESEARCH AND DEVELOPMENT NEEDS

The rapid development of biomediated soil improvement methods over the last decade has generated exciting advances in geotechnology, from the micro scale up through successful field-scale application. Experimental, analytical and numerical techniques from the fields of geotechnical

Table 1. Evaluation of application alternatives and their potential, considering implementation feasibility, probability of success, cost/viability, and social acceptance

Application	Implementation Easy: 5 Difficult: 1	Probability of success High: 5 Low: 1	Cost/viability Economic: 5 Expensive: 1	Societal acceptance High: 5 Low: 1	Total score out of 20
Structural repair	5	5	3	5	18
Erosion control	4	5	4	5	18
Co-precipitation/immobilisation of contaminants	5	4	4	5	18
Dust mitigation	4	5	4	5	18
Ground improvement for rural roads	5	5	3	4	17
Shallow carbon sequestration	5	3	4	5	17
Leak management	4	3	4	5	16
Rehabilitation of ancient monuments	3	3	5	5	16
Ground improvement for urban road subgrading	5	3	3	4	15
Soil liquefaction mitigation (MICP)	3	5	3	3	14
Ground improvement for ash ponds	1	4	4	5	14
Recycling/reuse of dredging materials	3	2	3	5	13
Soil liquefaction mitigation (biogas)	3	3	3	3	12
Enhanced water/oil/gas recovery	1	3	3	5	12
De-desertification	1	5	1	5	12
Sediment weakening by fluidisation	3	2	3	3	11
Underground creation (pipeline)	3	4	1	3	11
Stabilisation of sinkholes	1	3	2	5	11
Landfills as new energy resource	3	4	1	2	10
Construction products (bricks) using soil-biocementation	2	4	1	3	10
Water storage	3	2	2	2	9
De-swelling of clays	1	1	1	4	7
Deep carbon sequestration	1	1	1	3	6
Underground creation (tunnel)	1	1	2	1	5

engineering, geoenvironmental engineering, microbiology and geochemistry have been integrated, making this a truly interdisciplinary field. MICP has evidently been the primary focus of efforts to employ biogeotechnical ground improvement technology to date. The focus on MICP is simultaneously encouraging, as this focus has resulted in a successful field-scale trial within a decade of its initial development in the laboratory, and unsatisfying, as there are probably so many other biogeochemical processes that have yet to be identified and/or be subject to intensive research. Advances within MICP include the development of biostimulation and bioaugmentation techniques, quantified improvements in stiffness, strength, conductivity, etc., developed geophysical methods for real-time monitoring, optimised treatment in one-dimensional and two-dimensional models, demonstrated improvement to liquefaction resistance through centrifuge modelling, the development and verification of bio-geochemical-mechanical numerical models, field-scale implementation, and much more. This has clearly validated and demonstrated the potential influence of biological processes on engineering soil properties, and on opportunities for geotechnical field applications.

Many alternative biogeochemical processes have received little attention compared with MICP, and there are undoubtedly many such processes that have yet to be discovered. Promising results of biogas via denitrification, biofilm formation, biocementation through alternative geochemical pathways, and the generation of biopolymers and biofilms for strength enhancement and permeability reduction all show potential, but require further development.

Monitoring techniques to verify treatment success, and to monitor durability and performance over the project's service life, have been identified as an important consideration. However, implementation and interpretation of various monitoring techniques in field trials are required to develop reliable monitoring methods. While appropriate monitoring techniques will vary, depending on the biogeochemical process selected, geophysical methods have a high potential for indirectly mapping the effect that a treatment process may have on engineering soil properties. The permanence, or longevity, of a treatment method must match or exceed the required service life; this is a challenging criterion to satisfy, as physical experiments to date extend at most 2 years (although modelling results indicate a potential service live of 50 years or more).

While not addressed explicitly herein, a new workforce is required to embrace and help realise the development of biogeochemical treatment methods in the geotechnical community. To develop this workforce, education and training must include the fundamentals of biology and chemistry, producing engineers who can intelligibly converse and engage with experts in these areas on interdisciplinary teams. Indeed, many emerging fields lie at the intersection of disciplines, and participation in these discoveries and advances requires engineers equipped to engage in cross-disciplinary discovery.

The adoption of biogeotechnical methods in industry will take time. Often, the primary conventional ground improvement methods that compete with biogeochemical techniques are likely to be cement-based techniques, which the general public view largely as harmless/clean, in spite of the energy-intensive, carbon-producing, manufacturing process for cementitious materials, which involves the quarrying of large volumes of raw materials and associated land impairment, coupled with their high pH. Furthermore, there has often been public resistance to biotechnologies using exogenous organisms. Activities designed to raise awareness may be needed, as well as industry training, as field-scale applications of biogeotechnology become increasingly common.

ACKNOWLEDGEMENTS

The Second International Workshop on Bio-Soil Engineering and Interactions was funded in part by the United States

National Science Foundation under Grant No. CMMI-1110409. Any opinions, findings and conclusions or recommendations expressed in this material are those of the author(s), and do not necessarily reflect the views of the National Science Foundation.

REFERENCES

Al Qabany, A. (2011). *Microbial carbonate precipitation in soils*. Doctoral dissertation, University of Cambridge, UK.

Al Qabany, A. & Soga, K. (2013). Effect of chemical treatment used in MICP on engineering properties of cemented soils. *Géotechnique* **63**, No. 4, 331–339, http://dx.doi.org/10.1680/geot.SIP13.P.022.

Al Qabany, A., Mortensen, B., Martinez, B., Soga, K. & DeJong, J. (2011). Microbial carbonate precipitation: correlation of S-wave velocity with calcite precipitation. *Proc. Geofrontiers 2011: Advances in Geotechnical Engineering, Dallas, TX*, ASCE Geotechnical Special Publication 211, 3993–4001.

Al Qabany, A., Soga, K. & Santamarina, J. C. (2012). Factors affecting efficiency of microbially induced calcite precipitation. *ASCE J. Geotech. Geoenviron. Engng* **138**, No. 8, 992–1001.

Bachmeier, K. L., Williams, A.E., Warmington, J. R. & Bang, S. S. (2002). Urease activity in microbiologically-induced calcite precipitation. *J. Biotechnol*. **93**, No. 2, 171–181.

Baltzer, A., Cochonat, P. & Piper, D. J. W. (1994). In situ geotechnical characterisation of sediments on the Nova Scotian Slope, eastern Canadian continental margin. *Marine Geol*. **120**, No. 7, 291–308.

Banagan, B. L., Wertheim, B. M., Roth, M. J. S. & Caslake, L. F. (2010). Microbial strengthening of loose sand. *Lett. Appl. Microbiol*. **51**, No. 2, 138–142.

Bang, S. S., Lippert, J. J., Yerra, U., Mulukutla, S. & Ramakrishnan, V. (2010). Microbial calcite, a bio-based smart nanomaterial in concrete remediation. *Int. J. Smart Nano Mater.* **1**, No. 1, 28–39.

Bang, S., Min, S. H. & Bang, S. S. (2011). Application of microbiologically induced soil stabilization technique for dust suppression. *Int. J. Geo-Engng* **3**, No. 2, 27–37.

Barkouki, T., Martinez, B. C., Mortensen, B. M., Weathers, T. S., DeJong, J. T., Ginn, T. R., Spycher, N. F., Smith, R. W. & Fujita, Y. (2011). Forward and inverse bio-geochemical modeling of microbially induced calcite precipitation in half-meter column experiments. *Transp. Porous Media* **90**, No. 1, 23–39.

Barnes, R. S. K., Calow, P. & Olive, P. J. W. (1988). *The invertebrates: A new synthesis*, 1st edn. Oxford, UK: Blackwell Scientific.

Baveye, P., Vandevivere, P., Hoyle, B. L., DeLeo, P. C. & Sanchez de Lozada, D. (1998). Environmental impact and mechanisms of the biological clogging of saturated soils and aquifer materials. *Crit. Rev. Environ. Sci. Technol*. **28**, No. 2, 123–191.

Benini, S., Rypniewski, W. R., Wilson, K. S., Miletti, S., Ciurli, S. & Mangani, S. (1999). A new proposal for urease mechanism based on the crystal structures of the native and inhibited enzyme from *Bacillus pasteurii*: why urea hydrolysis costs two nickels. *Structure* **7**, No. 2, 205–216.

Berg, R. D. (1996). The indigenous gastrointestinal microflora. *Trends Microbiol*. **4**, No. 11, 430–435.

Blauw, M., Lambert, J. W. M. & Latil, M. N. (2009). Biosealing: a method for in situ sealing of leakages. *Proceedings of the International Symposium on Ground Improvement Technologies and Case Histories, ISGI'09, Singapore*, 125–130.

Bonala, M. V. S. & Reddi, L. N. (1998). Physicochemical and biological mechanisms of soil clogging: an overview. In *Filtration and drainage in geotechnical/geoenvironmental engineering* (eds L. N. Reddi and M. V. S. Bonalo), ASCE Geotechnical Special Publication 78, pp. 43–68. Reston, VA, USA: ASCE.

Burbank, M., Weaver, T., Green, T., Williams, B. & Crawford, R. (2011). Precipitation of calcite by indigenous microorganisms to strengthen liquefiable soil. *Geomicrobiol. J.* **28**, No. 4, 301–312.

Burbank, M., Weaver, T., Williams, B. & Crawford, R. (2012a). Urease activity of ureolytic bacteria isolated from six soils in which calcite was precipitated by indigenous bacteria. *Geomicrobiol. J.* **29**, No. 4, 389–395.

Burbank, M., Weaver, T., Lewis, R., Crawford, R. & Williams, B. (2012b). Geotechnical tests of sands following bio-induced calcite precipitation catalyzed by indigenous bacteria. *ASCE J. Geotech. Geoenviron. Engng*, http://dx.doi.org/10.1061/(ASCE)GT.1943-5606.0000781.

Cabalar, A. F. & Canakci, H. (2005). Ground improvement by bacteria. *Proc. 3rd Biot Conference on Poromechanics, Norman, OK*, 707–712.

Chaney, R. (1978). Saturation effects on the cyclic strength of sand. *Proceedings of the ASCE Specialty Conference on Earthquake Engineering and Soil Dynamics, Pasadena, CA*, pp. 342–359.

Cheng, L. & Cord-Ruwisch, R. (2012). In situ soil cementation with ureolytic bacteria by surface percolation. *Ecol. Engng* **42**, 64–72.

Chou, C.-W., Seagren, E. A., Aydilek, A. H. & Maugel, T. K. (2008). *Bacterially-induced calcite precipitation via ureolysis*. Washington, DC, USA: ASM Microbe Library, Visual Media Briefs, http://www.microbelibrary.org/library/laboratory-test/3174-bacterially-induced-calcite-precipitation-via-ureolysis.

Chou, C.-W., Seagren, E. A., Aydilek, A. H. & Lai, M. (2011). Biocalcification of sand through ureolysis. *ASCE J. Geotech. Geoenviron. Engng* **137**, No. 12, 1179–1189.

Chu, J., Ivanov, V., Lee, M. F., Oh, X. M. & He, J. (2009). Soil and waste treatment using biocement, *Proceedings of the International Symposium on Ground Improvement Technologies and Case Histories, ISGI'09, Singapore*, 165–170.

Chu, J., Ivanov, V., Naeimi, M., Li, B. & Stabnikov, V. (2011). Development of microbial geotechnology in Singapore. *Proc. Geofrontiers 2011: Advances in Geotechnical Engineering, Dallas, TX*, ASCE Geotechnical Special Publication 211, 4070–4078.

Chu, J., Stabnikov, V. & Ivanov, V. (2012). Microbially induced calcium carbonate precipitation on surface or in the bulk of soil. *Geomicrobiol. J.* **29**, No. 6, 544–549.

Chu, J., Ivanov, V., Stabnikov, V. & Li, B. (2013). Microbial method for construction of aquaculture pond in sand. *Géotechnique*, http://dx.doi.org/10.1680/geot.SIP13.P.007.

Ciurli, S., Benini, S., Rypniewski, W. R., Wilson, K. S., Miletti, S. & Mangani, S. (1999). Structural properties of the nickel ions in urease: novel insights into the catalytic and inhibition mechanisms. *Coordination Chem. Rev.* **190–192**, 331–355.

Cullimore, D. R. (1990). Microbes in civil engineering environments: biofilms and biofouling. In *Microbiology in civil engineering* (ed. P. Howsam), pp. 15–23. London, UK: E & FN Spon.

Cunningham, A., Warwood, B., Sturman, P. *et al.* (1997). Biofilm processes in porous media. In *The microbiology of the terrestrial deep subsurface* (eds P. Amy and D. Haldeman), pp. 325–346. New York, NY, USA: Lewis Publishers.

Darcy, H. (1857). *Recherches expérimentales relatives au mouvement de l'eau dans les tuyaux*. Paris, France: Imprimerie Impériale (in French).

Day, J. L., Ramakrishnan, V. & Bang, S. S. (2003). Microbiologically induced sealant for concrete crack remediation. *Proc. 16th Engng Mech. Conf., Seattle, WA*.

DeJong, J. T., Fritzges, M. B. & Nüsslein, K. (2006). Microbial induced cementation to control sand response to undrained shear. *ASCE J. Geotech. Geoenviron. Engng* **132**, No. 11, 1381–1392.

DeJong, J. T., Mortensen, B. & Martinez, B. (2007). *Bio-soils interdisciplinary science and engineering initiative*, Final Report on Workshop, 84 pp. Arlingon, VA, USA: National Science Foundation.

DeJong, J. T., Martinez, B. C., Mortensen, B. M., Nelson, D. C., Waller, J. T., Weil, M. H., Ginn, T. R., Weathers, T., Barkouki, T., Fujita, Y., Redden, G., Hunt, C., Major, D. & Tanyu, B. (2009). Upscaling of bio-mediated soil improvement. *Proc. 17th Int. Conf. Soil Mech. Geotech. Engng, Alexandria*, 2300–2303.

DeJong, J. T., Mortensen, M. B., Martinez, B. C. & Nelson, D. C. (2010). Biomediated soil improvement. *Ecol. Engng* **36**, No. 2, 197–210.

DeJong, J. T., Soga, K., Banwart, S. A., Whalley, W. R., Ginn, T., Nelson, D. C., Mortensen, B. M., Martinez, B. C. & Barkouki, T. (2011). Soil engineering in vivo: harnessing natural biogeochemical systems for sustainable, multi-functional engineering solutions. *J. R. Soc. Interface* **8**, No. 54, 1–15.

Ehlers, C. J., Chen, J., Roberts, H. H. & Lee, Y. C. (2005). The origin of near-seafloor crust zones in deepwater. *Proc. Int. Symp.*

on Frontiers in Offshore Geotechnics: ISFOG 2005, Perth, 927–934.

Esnault-Filet, A., Gadret, J. P., Loygue, M. & Borel, S. (2012). Biocalcis and its application for the consolidation of sands. In *Grouting and deep mixing 2012* (eds L. F. Johnsen, D. A. Bruce and M. J. Byle), Geotechnical Special Publication 288, vol. 2, pp. 1767–1780. Reston, VA, USA: ASCE.

Espinoza, D. & Santamarina, J. C. (2010). Ant tunneling: a granular media perspective. *Granular Matter* **12**, No. 6, 607–616.

Fauriel, S. (2012). *Bio-chemo-hydro-mechanical modeling of soils in the framework of microbial induced calcite precipitation*. PhD thesis, Ecole Polytechnique Fédérale de Lausanne, Switzerland.

Fauriel, S. & Laloui, L. (2011a). A bio-hydro-mechanical model for propagation of biogrout in soils. *Proc. Geo-Frontiers 2011: Advances in Geotechnical Engineering, Dallas, TX*, ASCE Geotechnical Special Publication 211, 4041–4048.

Fauriel, S. & Laloui, L. (2011b). Modelling of biogrout propagation in soils. *Proc. 2nd Int. Symp. Computat. Geomech., Rhodes*, 578–586.

Fauriel, S. & Laloui, L. (2012). A bio-chemo-hydro-mechanical model for microbially induced calcite precipitation in soils. *Comput. Geotech*. **46**, 104–120.

Ferris, F. G., Stehmeier, L. G., Kantzas, A. & Mourits, F. M. (1996). Bacteriogenic mineral plugging. *J. Can. Petrol. Technol*. **35**, No. 8, 56–61.

Fujita, Y., Redden, G. D., Ingram, J. S., Cortez, M. M. & Smith, R. W. (2004). Strontium incorporation into calcite generated by bacterial ureolysis. *Geochim. Cosmochim. Acta* **68**, No. 15, 3261–3270.

Fujita, Y., Taylor, J. L., Gresham, T. L. T., Delwiche, M. E., Colwell, F. S., McLing, T. L., Petzke, L. M. & Smith, R. W. (2008). Stimulation of microbial urea hydrolysis in groundwater to enhance calcite precipitation. *Environ. Sci. Technol*. **42**, No. 8, 3025–3032.

Fujita, Y., Taylor, J. L., Wendt, L. M., Reed, D. W. & Smith, R. W. (2010). Evaluating the potential of native ureolytic microbes to remediate a ^{90}Sr contaminated environment. *Environ. Sci. Technol*. **44**, No. 19, 7652–7658.

Gat, D., Tsesarsky, M. & Shamir, D. (2011). Ureolytic $CaCO_3$ precipitation in the presence of non-ureolytic competing bacteria. *Proc. Geo-Frontiers 2011: Advances in Geotechnical Engineering, Dallas, TX*, ASCE Geotechnical Special Publication 211, 3966–3974.

Gingras, M. K., Pemberton, S. G., Dashtgard, S. & Dafoe, L. (2008). How fast do marine invertebrates burrow? *Palaeogeog. Palaeoclimatol. Palaeoecol*. **270**, No. 3–4, 280–286.

Gray, D. H. & Sotir, R. B. (1996). *Biotechnical and soil bioengineering stabilization*. New York, NY, USA: John Wiley & Sons.

Grupe, B., Becker, H. J. & Oebius, H. U. (2001). Geotechnical and sedimentological investigations of deep-sea sediments from a manganese nodule field of the Peru Basin. *Deep-Sea Res. Part II* **48**, No. 17–18, 3593–3608.

Hamdan, N., Kavazanjian, E. Jr & Rittmann, B. E. (2011a). Sequestration of radionuclides and metal contaminants through microbially-induced carbonate precipitation. *Proc. 14th Pan American Conf. Soil Mech. Geotech. Engng, Toronto*, 5 pp.

Hamdan, N., Kavazanjian, E. Jr, Rittmann, B. E. & Karatas, I. (2011b). Carbonate mineral precipitation for soil improvement through microbial denitrification. *Proc. GeoFrontiers 2011: Advances in Geotechnical Engineering, Dallas, TX*, ASCE Geotechnical Special Publication 211, 3925–3934.

Hamed, B. S. & Belhadri, M. (2009). Rheological properties of biopolymer drilling fluids. *J. Petrol. Sci. Engng* **67**, No. 3–4, 84–90.

Hata, T., Tsukamoto, M., Mori, H., Kuwano, R. & Gourc, J. P. (2011). Evaluation of multiple soil improvement techniques based on microbial functions. *Proc. GeoFrontiers 2011: Advances in Geotechnical Engineering, Dallas, TX*, ASCE Geotechnical Special Publication 211, 3945–3955.

He, J., Chu, J. & Ivanov, V. (2013). Mitigation of liquefaction of saturated sand using biogas. *Géotechnique*, **63**, No. 4, 267–275, http://dx.doi.org/10.1680/geot.SIP13.P.004.

Howsam, P. (ed.) (1990). *Water wells, monitoring, maintenance and rehabilitation*. London, UK: E & FN Spon.

Inagaki, Y., Tsukamoto, M., Mori, H., Sasaki, T., Soga, K., Al Qabany, A. & Hata, T. (2011a). The influence of injection conditions and soil types on soil improvement by microbial functions. *Proc. GeoFrontiers 2011: Advances in Geotechnical Engineering, Dallas, TX*, ASCE Geotechnical Special Publication 211, 4021–4030.

Inagaki, Y., Tsukamoto, M., Mori, H., Nakajiman, S., Sasaki, T. & Kawasaki, S. (2011b). A centrifugal model test of microbial carbonate precipitation as liquefaction countermeasure. *Jiban Kogaku Janaru* **6**, No. 2, 157–167.

Ishihara, K., Tsuchiya, H., Huang, Y. & Kamada, K. (2001). Recent studies on liquefaction resistance of sand: effect of saturation. *Proc. 4th Int. Conf. Recent Adv. Geotech. Earthquake Engng Soil Dynamics, San Diego, CA*.

Ivanov, V. (2010). Microbial geotechniques. In *Environmental microbiology for engineers*, pp. 279–286. Boca Raton, FL, USA: CRC Press.

Ivanov, V. & Chu, J. (2008). Applications of microorganisms to geotechnical engineering for bioclogging and biocementation of soil in situ. *Rev. Environ. Sci. Biotechnol*. **7**, No. 2, 139–153.

James, G. A., Warwood, B. K., Hiebert, R. & Cunningham, A. B. (2000). Microbial barriers to the spread of pollution. In *Bioremediation* (ed. J. J. Valdes), pp. 1–14. Amsterdam, the Netherlands: Kluwer Academic.

Jones, D. L., Nguyen, C. & Finlay, R. D. (2009). Carbon flow in the rhizosphere: carbon trading at the soil–root interface. *Plant and Soil* **321**, No. 1, 5–33.

Karatas, I., Kavazanjian, E. Jr & Rittmann, B. E. (2008). Microbially induced precipitation of calcite using *Pseudomonas denitrificans. Proc. 1st Int. Conf. Biogeotech. Engng, Delft* (CD-ROM).

Kavazanjian, E. Jr & Karatas, I. (2008). Microbiological improvement of the physical properties of soil. *Proc. 6th Int. Conf. on Case Histories in Geotech. Engng, Rolla, MO* (CD-ROM).

Kavazanjian, E. Jr, Iglesias, E. & Karatas, I. (2009). Biopolymer soil stabilization for wind erosion control. *Proc. 17th Int. Conf. Soil Mech. Geotech. Engng, Alexandria* **2**, 881–884.

Khachatoorian, R., Petrisor, I. G., Kwan, C.-C. & Yen, T. F. (2003). Biopolymer plugging effect: laboratory-pressurized pumping flow studies. *J. Petrol. Sci. Engng* **38**, No. 1–2, 13–21.

Kohnhauser, K. (2007). *Introduction to geomicrobiology.* Malden, MA, USA: Blackwell Publishing.

Kuo, M. Y. H. (2011). *Deep ocean clay crusts: Behaviour and biological origin*. Doctoral dissertation, University of Cambridge, UK.

Kuo, M. Y. H. & Bolton, M. D. (2011). Faecal pellets in deep marine soft clay crusts: implications for hot-oil pipeline design. *Proc. 30th Int. Conf. on Ocean, Offshore and Artic Engineering, Rotterdam*, 883–892.

Kuo, M. Y. H. & Bolton, M. D. (2012). The nature and origin of deep ocean clay crust from the Gulf of Guinea. *Géotechnique*, http://dx.doi.org/10.1680/geot.10.P.012.

Kuo, M.Y.-H., Hill, A., Rattley, M. & Bolton, M. D. (2010). New evidence for the origin and behaviour of deep ocean crusts. *Proc. 2nd Int. Symp. on Frontiers in Offshore Geotechnics, Perth*, 365–370.

Kuzyakov, Y. & Domanski, G. (2000). Carbon input by plants into the soil: review. *J. Plant Nutrition Soil Sci*. **163**, No. 4, 421–431.

Laloui, L. & Fauriel, S. (2011). Biogrout propagation in soils. *Proceedings of the international workshop on multiscale and multiphysics processes in geomechanics*, Stanford, CT, pp. 77–80.

Lambert, J. W. M., Novakowski, K., Blauw, M., Latil, M. N., Knight, L. & Bayona, L. (2010). Pamper bacteria, they will help us: application of biochemical mechanisms in geo-environmental engineering. In *GeoFlorida 2010: Advances in Analysis, Modeling & Design* (eds D. O. Fratta, A. J. Puppala and B. Muhunthan), ASCE Geotechnical Special Publication 199, pp. 618–627. Reston, VA, USA: ASCE.

Legge, K. R., Scheurenburg, R., Clever, C., James, G. & Claus, R. (1985). *Investigation into apparent clogging of a geotextile recovered from Ergo Tailings Dam wall drain*, Preliminary Report. Pretoria, Republic of South Africa: Department of Water Affairs and Forestry.

Li, M., Yang, Z., Guo, H. & Cheng, X. (2011). Heavy metals removal by biomineralization of urea hydrolyzed bacteria isolated from soil. *Proc. 1st Int. Conf. on Geomicrobial Ecotoxicology, Wuhan*, 312–315.

Manning, D. A. C. (2008). Biological enhancement of soil carbonate precipitation: passive removal of atmospheric CO_2. *Mineral. Mag*. **72**, No. 2, 639–649.

Martinez, B. C. (2012). *Experimental and numerical upscaling of MICP for soil improvement*. Doctoral dissertation, University of California, Davis, CA, USA.

Martinez, B. C. & DeJong, J. T. (2009). Bio-mediated soil improvement: load transfer mechanisms at micro- and macro-scales. *Proc. 2009 ASCE US-China Workshop on Ground Improvement Technologies, Orlando, FL*, 242–251.

Martinez, B. C., Barkouki, T. H., DeJong, J. T. & Ginn, T. R. (2011). Upscaling of microbial induced calcite precipitation in 0·5m columns: experimental and modeling results. *Proc. GeoFrontiers 2011: Advances in Geotechnical Engineering, Dallas, TX*, ASCE Geotechnical Special Publication 211, 4049–4059.

Martinez, B. C., DeJong, J. T., Ginn, T. R., Mortensen, B. M., Barkouki, T. H., Hunt, C., Tanyu, B. & Major, D. (2013). Experimental optimization of microbial induced carbonate precipitation for soil improvement. *ASCE J. Geotech. Geoenviron. Engng* (in press).

Meadows, A. & Meadows, P. S. (1994). Bioturbation in deep-sea pacific sediments. *J. Geol. Soc*. **151**, No. 2, 361–375.

Mitchell, A. C., Phillips, A. J., Hiebert, R., Gerlach, R., Spangler, L. H. & Cunningham, A. B. (2009). Biofilm enhanced geological sequestration of supercritical CO_2. *Int. J. Greenhouse Gas Control* **3**, No. 1, pp. 90–99.

Mitchell, J. K. (1975). *Fundamentals of soil behavior*. New York, NY, USA: Wiley.

Mitchell, J. K. & Santamarina, J. C. (2005). Biological considerations in geotechnical engineering. *ASCE J. Geotech. Geoenviron. Engng* **131**, No. 10, 1222–1233.

Montoya, B. M. (2012). *Bio-mediated soil improvement and the effect of cementation on the behavior, improvement, and performance of sand*. Doctoral dissertation, University of California, Davis, CA, USA.

Montoya, B. M., Gerhard, R., DeJong, J., Weil, M., Martinez, B., Pederson, L. & Wilson, D. (2012). Fabrication, operation, and health monitoring of bender elements for aggressive environments. *Geotech. Test. J*. **35**, No. 5, 15 pp.

Montoya, B. M., DeJong, J. T. & Boulanger, R. W. (2013). Dynamic response of liquefiable sand improved by microbial induced calcite precipitation. *Géotechnique*, **63**, No. 4, 302–312, http://dx.doi.org/10.1680/geot.SIP13.P.019.

Mortensen, B. M. & DeJong, J. T. (2011). Strength and stiffness of MICP treated sand subjected to various stress paths. *Proc. GeoFrontiers 2011: Advances in Geotechnical Engineering, Dallas, TX*, ASCE Geotechnical Special Publication 211, 4012–4020.

Mortensen, B. M., Haber, M., DeJong, J. T., Caslake, L. F. & Nelson, D. C. (2011). Effects of environmental factors on microbial induced calcite precipitation. *J. Appl. Microbiol*. **111**, No. 2, 338–349.

NRC (2006). *Geological and geotechnical engineering in the new millennium: Opportunities for research and technological innovation*. Washington, DC, USA: National Research Council.

Nugent, R. A., Zhang, G. & Gambrell, R. P. (2010). The effect of exopolymers on the erosional resistance of cohesive sediments. *Proc. 5th Int. Conf. on Scour and Erosion, San Francisco, CA*, 162–171.

Phadnis, H. & Santamarina, J. C. (2012). Bacteria in sediments: pore size effects. *Géotechnique Lett*. **1**, 91–93.

Pietruszczk, S., Pande, G. N. & Oulapour, M. (2003). A hypothesis for mitigation of risk of liquefaction. *Géotechnique* **53**, No. 9, 833–838, http://dx.doi.org/10.1680/geot.2003.53.9.833.

Ramachandran, S. K., Ramakrishnan, V. & Bang, S. S. (2001). Remediation of concrete using micro-organisms. *ACI Mater. J*. **98**, No. 1, 3–9.

Ramakrishnan, V., Ramesh, K. P. & Bang, S. S. (2001). Bacterial concrete. *Proc. SPIE* **4234**, 168–176.

Rebata-Landa, V. & Santamarina, J. C. (2006). Mechanical limits to microbial activity in deep sediments. *Geochem. Geophys. Geosyst*. **7**, No. 11, 1–12.

Rebata-Landa, V. & Santamarina, J. C. (2012). Mechanical effects of biogenic nitrogen gas bubbles in soils. *ASCE J. Geotech. Geoenviron. Engng* **138**, No. 2, 128–137.

Renforth, P., Manning, D. A. C. & Lopez-Capel, E. (2009). Carbonate precipitation in artificial soils as a sink for atmospheric carbon dioxide. *Appl. Geochem*. **24**, No. 9, 1757–1764.

Renforth, P., Edmondson, J., Leake, J. R., Gaston, K. J. & Manning, D. A. C. (2011). Designing a carbon capture function into urban soils. *Proc. ICE – Urban Design and Planning* **164**, No. 2, 121–128.

Roden, E. E., Leonardo, M. R. & Ferris, F. G. (2002). Immobilization of strontium during iron biomineralization coupled to dissimilatory hydrous ferric oxide reduction. *Geochim. Cosmochim. Acta* **66**, No. 16, 2823–2839.

Roscoe, K. H., Schofield, A. N. & Wroth, C. P. (1958). On the yielding of soils. *Géotechnique* **8**, No. 1, 22–53, http://dx.doi.org/10.1680/geot.1958.8.1.22.

Rusu, C., Cheng, X. & Li, M. (2011). Biological clogging in Tangshan sand columns under salt water intrusion by *Sporosarcina pasteurii*. *Adv. Mater. Res*. **250–253**, 2040–2046.

Sanderson, K. (2008). Waste concrete could help to lock up carbon. *Nature*, http://dx.doi.org/10.1038/news.2008.732.

Schofield, A. N. & Wroth, C. P. (1968). *Critical state soil mechanics*. London, UK: McGraw-Hill.

Seagren, E. A. & Aydilek, A. H. (2010). Biomediated geomechanical processes. In *Environmental microbiology*, 2nd edn (eds R. Mitchell and J.-D. Gu), pp. 319–348. Hoboken, NJ, USA: John Wiley & Sons.

Seki, K., Miyazaki, T. & Nakano, M. (1998). Effects of microorganisms on hydraulic conductivity decrease in infiltration. *Eur. J. Soil Sci*. **49**, No. 2, 231–236.

Sherif, M. A., Ishibashi, I. & Tsuchiya, C. (1977). Saturation effect on initial soil liquefaction. *ASCE J. Geotech. Engng* **103**, No. 8, 914–917.

Sivavec, T., Krug, T., Berry-Spark, K. & Focht, R. (2003). Performance monitoring of a permeable reactive barrier at the Somersworth, New Hampshire Landfill Superfund site. In *Chlorinated solvent and DNAPL remediation* (eds S. M. Henry and S. D. Warner), American Chemical Society, Symposium Series, Vol. 837, pp. 259–277. Washington, DC, USA: ACS Publications.

Slichter, C. S. (1905). *Field measurements of the rate of movement of underground waters*, USGS Water Supply and Irrigation Paper 140. Washington, DC, USA: Government Printing Office.

Stabnikov, V., Naeimi, M., Ivanov, V. & Chu, J. (2011). Formation of water-impermeable crust on sand surface using biocement. *Cement Concrete Res*. **41**, No. 11, 1143–1149.

Stal, L. J. (2010). Microphytobenthos as a biogeomorphological force in intertidal sediment stabilization. *Ecol. Engng* **36**, No. 2, 236–245.

Stocks-Fischer, S., Galinat, J. K. & Bang, S. S. (1999). Microbiological precipitation of $CaCO_3$. *Soil Biol. Biochem*. **31**, No. 11, 1563–1571.

Tagliaferri, F., Waller, J., Ando, E., Hall, S. A., Viggiani, G., Besuelle, P. & DeJong, J. T. (2011). Observing strain localisation processes in bio-cemented sand using X-ray imaging. *Granular Matter* **13**, No. 3, 247–250.

Talsma, T. & van der Lelij, A. (1976). Infiltration and water movement in an in situ swelling soil during prolonged ponding. *Aust. J. Soil Res*. **14**, No. 3, 337–349.

Taylor, D. (1948). *Fundamentals of soil mechanics*. New York, NY, USA: Wiley.

Taylor, L. L., Leake, J. R., Quirk, J., Hardy, K., Banwart, S. A. & Beerling, D. J. (2009). Biological weathering and the long-term carbon cycle: integrating mycorrhizal evolution and function into the current paradigm. *Geobiology* **7**, No. 2, 171–191.

Terzaghi, K. (1924). *Erdbaumechanik*. Vienna, Austria: Franz Deuticke (in German).

Terzaghi, K. (1955). Influence of geological factors on the engineering properties of sediments. *Econ. Geol*. **50**, 557–618.

Tobler, D. J., Maclachlan, E. & Phoenix, V. R. (2012). Microbially mediated plugging of porous media and the impact of different injection strategies. *Ecol. Engng* **42**, 270–278.

Van Meurs, G., Van Der Zon, W., Lambert, J., Van Ree, D., Whiffin, V. & Molendijk, W. (2006). The challenge to adapt soil properties. *Proc. 5th ICEG: Environ. Geotechnics: Opportunities, Challenges and Responsibilities for Environ. Geotechnics*, **2**, 1192–1199.

Van Paassen, L. A. (2009). *Biogrout, ground improvement by microbially induced carbonate precipitation*. Doctoral dissertation, Department of Biotechnology, Delft University of Technology, the Netherlands.

Van Paassen, L. A. (2011). Bio-mediated ground improvement: from laboratory experiment to pilot applications. *Proc. GeoFrontiers 2011: Advances in Geotechnical Engineering, Dallas, TX*, ASCE Geotechnical Special Publication 211, 4099–4108.

Van Paassen, L. A., Harkes, M. P., Van Zwieten, G. A., Van der Zon, W. H., Van der Star, W. R. L. & Van Loosdrecht, M. C. M. (2009). Scale up of BioGrout: a biological ground reinforcement method. *Proc. 17th Int. Conf. Soil Mech. Geotechn. Engng, Alexandria*, 2328–2333.

Van Paassen, L. A., Daza, C. M., Staal, M., Sorokin, D. Y., van der Zon, W. & van Loosdrecht, M. C. M. (2010a). Potential soil reinforcement by biological denitrification. *Ecol. Engng* **36**, No. 2, 168–175.

Van Paassen, L. A., Ghose, R., van der Linden, T. J. M., van der Star, W. R. L. & van Loosdrecht, M. C. M. (2010b). Quantifying biomediated ground improvement by ureolysis: large-scale biogrout experiment. *ASCE J. Geotech. Geoenviron. Engng* **136**, No. 12, 1721–1728.

Van Wijngaarden, W. K., Vermolen, F. J., van Meurs, G. A. M. & Vuik, C. (2011). Modelling biogrout: a new ground improvement method based on microbial-induced carbonate precipitation. *Transp. Porous Media* **87**, No. 2, 397–420.

Van Wijngaarden, W. K., Vermolen, F. J., van Meurs, G. A. M. & Vuik, C. A. (2012). Mathematical model and analytical solution for the fixation of bacteria in biogrout. *Transp. Porous Media* **92**, No. 3, 847–866.

Warthmann, R., van Lith, Y., Vasconcelos, C., McKenzie, J. A. & Karpoff, A. M. (2000). Bacterially induced dolomite precipitation in anoxic culture experiments. *Geology* **28**, No. 12, 1091–1094.

Washbourne, C.-L., Renforth, P. & Manning, D. A. C. (2012). Investigating carbonate formation in urban soils as a method for capture and storage of atmospheric carbon. *Sci. Total Env.* **431**, 166–175.

Weaver, T., Burbank, M., Lewis, R., Lewis, A., Crawford, R. & Williams, B. (2011). Bio-induced calcite, iron, and manganese precipitation for geotechnical engineering applications. *Proc. GeoFrontiers 2011: Advances in Geotechnical Engineering, Dallas, TX*, ASCE Geotechnical Special Publication 211, 3975–3983.

Weil, M. H., DeJong, J. T., Martinez, B. C. & Mortensen, B. M. (2012). Seismic and resistivity measurements for real-time monitoring of microbially induced calcite precipitation in sand. *ASTM Geotech. Test. J.* **35**, No. 2, GTJ103365.

Whiffin, V. S., Van Paassen, L. A. & Harkes, M. P. (2007). Microbial carbonate precipitation as a soil improvement technique. *Geomicrobiol. J.* **24**, No. 5, 417–423.

Whitman, W. B., Coleman, D. C. & Wiebe, W. J. (1998). Prokaryotes: the unseen majority. *Proc. Nat. Acad. Sci*. **95**, No. 12, 6578–6583.

Woese, C. R., Kandler, O. & Wheelis, M. L. (1990). Towards a natural system of organisms: proposal for the domains of Archaea, Bacteria, and Eucarya. *Proc. Nat. Acad. Sci*. **87**, No. 12, 4576–4579.

Wu, J. G., Stahl, P. & Zhang, R. (1997). Experimental study on the reduction of soil hydraulic conductivity by enhanced biomass growth. *Soil Sci*. **162**, No. 10, 741–748.

Yang, Z., Cheng, X. & Li, M. (2011). Engineering properties of MICP-bonded sandstones used for historical masonry building restoration. *Proc. GeoFrontiers 2011: Advances in Geotechnical Engineering, Dallas, TX*, ASCE Geotechnical Special Publication 211, 4031–4040.

Yoshimi, Y., Tanaka, K. & Tokimatsu, K. (1989). Liquefaction resistance of a partially saturated sand. *Soils Found*. **29**, No. 3, 157–162.

Related content

Hu, L. & Wu, H. (2014). *Géotechnique* **64**, No. 2, 155–164 [http://dx.doi.org/10.1680/geot.13.P.096]

Mathematical model of electro-osmotic consolidation for soft ground improvement

L. HU* and H. WU*

Electro-osmotic consolidation is an attractive, soft ground improvement technique. In this paper a theoretical model is proposed for electro-osmotic consolidation by coupling the seepage field, electric field, and the stress and strain field. The soil mass deformation, pore-water pressure and the electrical voltage are the basic variables in the governing equations. A three-dimensional numerical model based on the finite-element method was developed to simulate the electro-osmotic consolidation process, predicting the tempo-spatial variation of soil mass displacement. The numerical model is compared with previous analytical solutions. Three common electrode installation patterns are illustrated and analysed with the numerical model, and the results indicate that the triangular pattern can achieve the largest average surface settlement and the smallest differential settlement. The effect of the penetrating depth of the electrodes on the ground settlement is also investigated. An engineering field application is simulated to validate the developed numerical formulation.

KEYWORDS: consolidation; ground improvement; numerical modelling; pore pressures; settlement

INTRODUCTION

The rapid development of infrastructure calls for time-efficient ground improvement technology. Buildings on soft soils require effective and fast consolidation methods such as surcharge preloading, vertical drains and vacuum preloading. Field applications of such ground improvement methods have been reported extensively in the literature, for example, Barron (1948), Hansbo (1981), Xie & Zeng (1989) and Indraratna *et al.* (2005). Electro-osmotic consolidation is an alternative attractive technique for soft soil improvement. If an electrical potential is applied to a soil mass, pore water flows from the anode toward the cathode causing pore-water pressure change and consolidation of soils. This phenomenon is a result of the exchangeable nature of the adsorbed cations in clay particles and the dipolar nature of the water molecules. The electro-osmosis conductivity may be assumed constant in spite of soil grain diameters, which indicates that soils with fine particles and low permeability can be treated effectively with this technology (Mitchell & Soga, 2005). Reuss (1809) was the first to observe this phenomenon, and Cassagrande made use of this electrical treatment to improve the shear strength and stability of fine-grained soils (Casagrande, 1948). Up to now, numerous laboratory studies have been conducted to investigate the development of pore-water pressure and the settlement of the soil mass during electro-osmotic consolidation, and this technology has been employed in various geotechnical engineering field applications, including stabilisation of slopes, excavations and embankments, controlling of groundwater flow, increasing of pile capacity, strengthening of clays, and dewatering of tailings and sludge (Casagrande, 1983; Lo & Ho, 1991; Glendinning *et al.*, 2005; Zhuang & Wang, 2007; Jones *et al.*, 2008; Lamont-Black & Weltman, 2010; Jeyakanthan *et al.*, 2011). Various techniques have been developed to improve the efficiency of electro-osmotic consolidation, including electrode reversal, intermittent electrical current, chemical treatment of soil–electrode contact and electro-kinetic geosynthetics (EKG) (Wan & Mitchell, 1976; Micic *et al.*, 2001; Lefebvre & Burnotte, 2002; Glendinning *et al.*, 2005, 2008; Fourie *et al.*, 2007; Jones *et al.*, 2008, 2011).

Several analytical models have been developed to describe the process of electro-osmotic consolidation. Esrig (1968) first proposed a one-dimensional (1D) analytical model to calculate the excess pore-water pressure due to a uniform electric field. Wan & Mitchell (1976) proposed an analytical solution for electro-osmotic treatment coupled with surcharge preloading, and showed that uniform improvement can be achieved by reversing the polarity of the electrodes. Su & Wang (2003) proposed an analytical solution of excess pore-water pressure in soils during electro-osmosis in a hypothetical two-dimensional (2D) electric field.

Based on the principles of conservation of water and electric charge in a soil mass, Lewis & Humpheson (1973) established governing equations for electro-osmotic flow and electrical current, and developed a finite-element model to analyse the electro-osmotic flow in a 2D electric field. Rittirong & Shang (2008) proposed a 2D finite-difference model to indirectly analyse the subsurface ground settlement during electro-osmotic consolidation. Hu *et al.* (2012) developed an analytical model and numerically implemented it to predict the ground settlement during electro-osmotic consolidation. Recently, numerical models incorporating the modified Cam Clay model and large deformation analysis were developed respectively to study the process of electro-osmotic consolidation (Yuan & Hicks, 2013; Yuan *et al.*, 2013).

The applied voltage and the layout of the electrodes and drains govern the distribution of the electric field intensity, and the development of excess pore-water pressure and ground settlement are also affected during electro-osmosis field application with vertical drains. Hence, it is a three-dimensional (3D) problem with complicated boundary conditions and variable soil properties, and the numerical model is needed to adequately describe the electro-osmotic consolidation process. In addition, the ground settlement is the major concern during ground improvement; however, most of the previous models cannot directly predict the ground

Manuscript received 20 June 2013; revised manuscript accepted 16 October 2013. Published online ahead of print 28 November 2013. Discussion on this paper closes on 1 July 2014, for further details see p. ii.

* State Key Laboratory of Hydro-Science and Engineering, Department of Hydraulic Engineering, Tsinghua University, Beijing, People's Republic of China.

settlement. Therefore, it is necessary to couple the deformation of the soil mass into the governing equations for the electro-osmotic consolidation process.

The purpose of this study is to develop a theoretical model to adequately describe the behaviour of soil mass subjected to a multi-physics system, coupling the mechanical, electrical and hydraulic fields. The soil deformation was incorporated into the analysis to accurately predict the soil behaviour during electro-osmosis. A time-dependent 3D finite-element method (FEM) model was developed based on the proposed theory to simulate the mechanical and hydraulic behaviour of soft soils under electro-osmotic treatment. Subsequently, the numerical results were compared to the previously published analytical solutions to verify the numerical model. Three different electrode installation patterns were described and analysed numerically to compare the average surface settlement and differential surface settlement. The partially penetrating electrode situation was also analysed. The rationality and accuracy of the proposed electro-osmotic consolidation model is verified by using data from a field case study.

THEORETICAL MODEL FOR ELECTRO-OSMOTIC CONSOLIDATION

To develop the theory for the electro-osmotic consolidation of saturated soils, the following assumptions are made in this study.

- The soil is fully saturated and the pore water is incompressible.
- The soil skeleton is assumed to be linear elastic.
- The velocity of water flow due to electro-osmosis is directly proportional to the voltage gradient, and $\boldsymbol{k}_e$ is a tensor of electro-osmosis conductivity for soils.
- The velocity of water flow by hydraulic gradient and electro-osmosis complies with Darcy's law, and $\boldsymbol{k}_h$ is a tensor of hydraulic conductivity for soils.
- Both the hydraulic conductivity and electro-osmosis conductivity remain constant during the consolidation process.
- The water movement in soil is linear superposition of water flows due to electro-osmosis and hydraulic gradient.
- Only electro-osmosis occurs under the applied electric field, and no soil particle movement occurs due to electrophoresis. There are no electrochemical reactions and streaming potential development during the electro-osmotic consolidation.

Flow of pore water

The following equation can be used for the saturated soil based on the continuity equation

$$\frac{\partial \varepsilon_v}{\partial t} = \nabla \cdot \boldsymbol{v} = \frac{\partial v_x}{\partial x} + \frac{\partial v_y}{\partial y} + \frac{\partial v_z}{\partial z} \tag{1}$$

where ε_v is the volumetric strain of soil mass and $\boldsymbol{v}$ is the velocity vector of the pore water, where v_x, v_y and v_z are the pore-water flow velocities in the x, y and z directions, respectively.

The pore-water flow consists of hydraulic and electro-osmotic flows. The hydraulic flow is described by Darcy's law

$$\boldsymbol{v}_h = -\boldsymbol{k}_h \nabla H \tag{2}$$

where $\boldsymbol{v}_h$ is the hydraulic flow velocity vector; $\boldsymbol{k}_h$ is the hydraulic conductivity tensor; H is the total head equal to the sum of the elevation and pressure heads.

Casagrande (1948) showed that electro-osmotic flow through porous media induced by a voltage gradient had the same form as Darcy's law, that is

$$\boldsymbol{v}_e = -\boldsymbol{k}_e \nabla V \tag{3}$$

where $\boldsymbol{v}_e$ is the electro-osmotic flow velocity vector; $\boldsymbol{k}_e$ is the electro-osmosis conductivity tensor; and V is the electrical potential.

The electro-osmotic and hydraulic water flows follow the principle of superposition producing the coupled pore-water flow equation

$$\boldsymbol{v} = \boldsymbol{v}_h + \boldsymbol{v}_e = -\boldsymbol{k}_h \nabla H - \boldsymbol{k}_e \nabla V \tag{4}$$

Combining equations (1) and (4), it is possible to obtain the equation for the conservation of mass or the equation for water flow during electro-osmosis

$$\nabla \cdot (\boldsymbol{k}_h \nabla H + \boldsymbol{k}_e \nabla V) = -\frac{\partial \varepsilon_v}{\partial t} = \frac{\partial}{\partial t}(\nabla \cdot \boldsymbol{u}) \tag{5}$$

where $\boldsymbol{u}$ is the vector of soil mass displacement.

Static equilibrium

According to Biot's theory (Biot, 1941), the governing constitutive equation between stress and strain can be written in tensor form (Wang, 2000)

$$\nabla^2 \boldsymbol{u} + \frac{1}{1-2\nu} \nabla(\nabla \cdot \boldsymbol{u}) - \gamma_w \frac{2(1+\nu)}{E} \nabla(H - z) = 0 \tag{6}$$

where υ is the Poisson ratio; E is the Young's modulus; z is the elevation head; and γ_w is the unit weight of water.

Conservation of electrical charge

The electrical current in the soil mass is due to both the voltage and the hydraulic gradients (Lewis & Humpheson, 1973). As mentioned before, the streaming potential development during the electro-osmotic consolidation is ignored, and the electrical current density can be expressed as follows according to Ohm's law

$$\boldsymbol{j} = \boldsymbol{\sigma}_e \nabla V \tag{7}$$

where $\boldsymbol{j}$ is the electrical current density vector; $\boldsymbol{\sigma}_e$ is the electrical conductivity tensor.

According to the law of conservation of electrical charge, the governing equation for the electric field can be represented by the following equation

$$\boldsymbol{\sigma}_e \nabla^2 V = C_p \frac{\partial V}{\partial t} \tag{8}$$

where C_p is the capacitance per unit volume.

Based on the above, the governing equations for electro-osmotic consolidation can be described using the following equations.

$$\begin{aligned} &\nabla^2 \boldsymbol{u} + \frac{1}{1-2\nu} \nabla(\nabla \cdot \boldsymbol{u}) - \gamma_w \frac{2(1+\nu)}{E} \nabla(H - z) = 0 \\ &\nabla \cdot (\boldsymbol{k}_h \nabla H + \boldsymbol{k}_e \nabla V) = \frac{\partial}{\partial t}(\nabla \cdot \boldsymbol{u}) \\ &\boldsymbol{\sigma}_e \nabla^2 V = C_p \frac{\partial V}{\partial t} \end{aligned} \tag{9}$$

The basic variables of the above equations are the displacement vector $\boldsymbol{u}$, the total head H and the electrical potential V. With equation (9), the practical problems for electro-osmotic consolidation can be solved according to the

actual boundary and initial conditions by numerical simulation. The non-linear variation of the mechanical and electrical parameters, such as the hydraulic and electro-osmosis conductivities, the electrical conductivity and the coefficient of compressibility can be incorporated to obtain accurate predictions (Wu, 2009; Hu *et al.*, 2010, 2012; Wu & Hu, 2013b).

NUMERICAL MODEL FOR ELECTRO-OSMOTIC CONSOLIDATION

Based on the above theory described in equation (9), a 3D numerical model was developed to simulate the electro-osmotic consolidation of soft clay. The spatial discretisation is based on the FEM, and the time discretisation uses the FEM. The basic variables for this numerical model are the displacement of soil mass, total head and voltage. The model can directly predict the soil displacement, that is, the ground settlement. At the same time, the tempo-spatial distributions of the total head and electrical voltage as well as the stresses and strains of the soils can be predicted.

Finite-element method formulation

Tetrahedron elements were used in the FEM analysis. There are five main unknowns at each node, including three displacements in three directions, denoted by u^s, v^s and w^s, the total head H and the voltage V. For a tetrahedral element, if the four nodes are marked as 1, 2, 3 and 4, the variables can be expressed as

$$\{\boldsymbol{\delta}\}^e = \left\{ u_1^s \quad v_1^s \quad w_1^s \quad u_2^s \quad v_2^s \quad w_2^s \quad u_3^s \quad v_3^s \quad w_3^s \quad u_4^s \quad v_4^s \quad w_4^s \right\}^{\mathrm{T}} \tag{10}$$

$$\{\boldsymbol{\Psi}\}^e = \left\{ H_1 \quad H_2 \quad H_3 \quad H_4 \quad V_1 \quad V_2 \quad V_3 \quad V_4 \right\}^{\mathrm{T}} \tag{11}$$

Based on Galerkin's approach, the governing equation for the stress and strain and the equation for the seepage can be written in the finite-difference form as (Lewis & Humpheson, 1973; Hu *et al.*, 2012)

$$[\mathbf{K}]^e\{\boldsymbol{\delta}\}^e + [\mathbf{K}_c]^e\{\boldsymbol{\Psi}\}^e = \{\boldsymbol{R}_f\}_h^e \tag{12}$$

$$[\mathbf{K}_s]^e\{\boldsymbol{\Psi}\}^e + [\mathbf{K}_b]^e\{\dot{\boldsymbol{\Psi}}\}^e - [\mathbf{K}_a]^e\{\dot{\boldsymbol{\delta}}\}^e = \{\boldsymbol{R}_q\}_h^e \tag{13}$$

where $\boldsymbol{\delta}$ is the nodal displacement vector and $\boldsymbol{\Psi}$ is the nodal hydraulic and electrical potential vector. $\mathbf{K}$ and $\mathbf{K}_a$ are coefficient matrices for $\boldsymbol{\delta}$, and $\mathbf{K}_c$, $\mathbf{K}_s$ and $\mathbf{K}_b$ are coefficient matrices for $\boldsymbol{\Psi}$. $\boldsymbol{R}_{fh}$ is the element load vector; $\boldsymbol{R}_{qh}$ is the hydraulic and voltage vector. The incremental form of the two equations can be derived as

$$\begin{bmatrix} \mathbf{K} & \mathbf{K}_c \\ \mathbf{K}_a & -(\theta\Delta t[\mathbf{K}_s]^e + [\mathbf{K}_b]^e) \end{bmatrix} \begin{Bmatrix} \Delta\boldsymbol{\delta} \\ \Delta\boldsymbol{\Psi} \end{Bmatrix} = \begin{Bmatrix} \Delta\boldsymbol{R}_{fh} \\ \Delta t(\mathbf{K}_s\boldsymbol{\Psi}_{n-1} - \boldsymbol{R}_{qh}) \end{Bmatrix} \tag{14}$$

where $\boldsymbol{\Psi}_{n-1}$ is calculated at the $n-1$ time step and θ is the coefficient of the time step.

Boundary/initial conditions

The boundary conditions for displacement, seepage and the electric fields are listed as follows.

The Dirichlet conditions specify the values or function for the basic variants at the boundary

$$\begin{aligned} \boldsymbol{u} &= \boldsymbol{u}(t) \\ H &= H(t) \\ V &= V(t) \end{aligned} \tag{15}$$

The Neumann conditions give the constraint force and flux conditions at the boundary

$$\begin{aligned} \boldsymbol{n}\cdot\boldsymbol{\sigma} &= \boldsymbol{F}(t) \\ \boldsymbol{n}\cdot\boldsymbol{v} &= v_n(t) \\ \boldsymbol{n}\cdot\boldsymbol{j} &= j_n(t) \end{aligned} \tag{16}$$

where $\boldsymbol{\sigma}$ is the stress tensor; $\boldsymbol{F}$ is the external force acting on the boundary; and $\boldsymbol{n}$ is the normal vector at boundary.

To obtain a unique solution, the initial values of the basic variants should be provided

$$\begin{aligned} \boldsymbol{u}(0) &= \boldsymbol{u}_1 \\ H(0) &= H_1 \\ V(0) &= V_1 \end{aligned} \tag{17}$$

where $\boldsymbol{u}_1$, H_1 and V_1 are the initial displacements, total head and electrical voltage, respectively. In general, $\boldsymbol{u}_1$ is 0 before the electro-osmotic consolidation.

By incorporating the above, the 3D electro-osmotic consolidation process can be simulated by the developed FEM software. Furthermore, the 3D numerical model can be simplified to simulate the 2D and 1D cases. The numerical model can also simulate different electrode installation patterns during electro-osmotic consolidation, as well as the partially penetrating electrode situation.

Comparison with a previous analytical solution

Su & Wang (2003) proposed a 2D electro-osmotic consolidation model in a horizontal plane as shown in Fig. 1(a). The electrodes were installed in rows with spacing L in the x direction and p in the y direction. The electric field is in the horizontal plane while the displacement occurs in the vertical direction, and the water flows in the x and y directions. Because of the symmetrical arrangement of the electrodes, a representative element with one anode and one cathode is used for the analysis as shown in Fig. 1(b). The electrodes are treated as point on the representative element. The four boundaries are all impermeable, except that the cathode point is a sink.

The analytical solution for the total head is derived by the separation of variables (Su & Wang, 2003)

$$\begin{aligned} H(x, y, t) = &-\frac{k_e}{k_h}V(x, y) + \sum_{m=1}^{\infty}\sum_{i=0}^{\infty} B_{m,i} \\ &\times \sin\frac{(2m-1)\pi}{L}x\ \cos\frac{2i\pi}{p}y \\ &\times \mathrm{e}^{-\left[(2m-1/2L)^2+(2iL/p)^2\right]\pi^2 T_v} \end{aligned} \tag{18}$$

$$B_{m,i} = \frac{8}{Lp}\int_0^L\int_0^{p/2}\frac{k_e}{k_h}V(x, y, 0)\ \sin\frac{(2m-1)\pi}{L}x\ \cos\frac{2i\pi}{p}y\,\mathrm{d}x\mathrm{d}y \tag{19}$$

where T_v is the time factor and $B_{m,i}$ is a calculating factor.

The average degree of consolidation was derived as

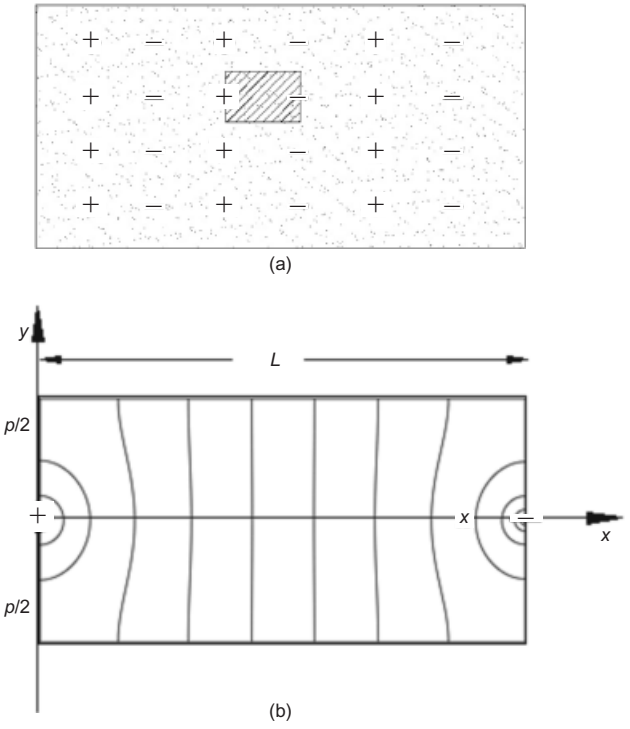

Fig. 1. Schematic illustration of 2D model in the horizontal plane and corresponding voltage distribution: (a) schematic illustration of 2D model in horizontal plane; (b) voltage distribution in orthogonal coordinate system

$$\bar{U} = 1 - \frac{4}{\pi^3}\sum_{m=1}^{\infty}\frac{(-1)^{m-1}}{(m-1/2)^3}\mathrm{e}^{-[m-(1/2)]^2\pi^2 T_v} \tag{20}$$

Figure 2 shows the comparison of the analytical result obtained from Su & Wang (2003) and the numerical result based on the analytical model proposed in this paper. The degree of consolidation based on Su & Wang (2003) is larger than that obtained from the numerical analysis by about 50% at $T_v = 1$, which is due to the inaccurate assumption of the voltage distribution by Su & Wang (2003). The distribution of the voltage in the representative element is obtained by the proposed numerical model and is shown in Fig. 1(b). Since the electrodes are symmetrically arranged,

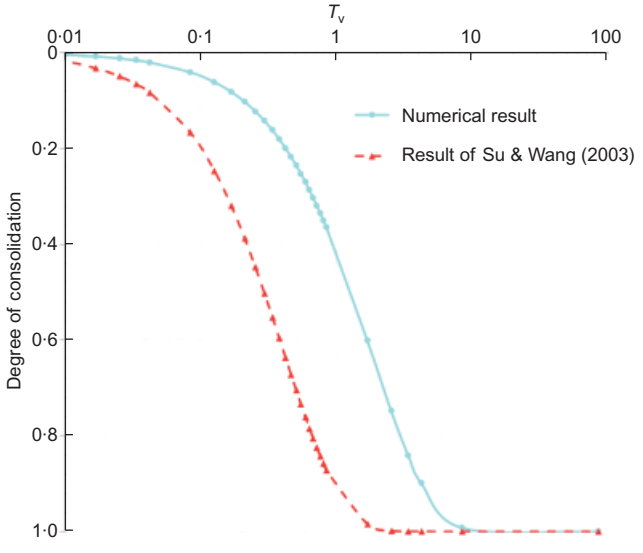

Fig. 2. Comparison of numerical result and previous analytical solution for 2D model in horizontal plane

the boundary conditions for the voltage can be expressed as follows

$$\begin{cases} \dfrac{\partial V}{\partial x} = 0 \quad (x = 0 \text{ and } y \neq 0;\ x = L \text{ and } y \neq 0) \\ \dfrac{\partial V}{\partial y} = 0 \quad (y = \pm p/2) \\ V = V_0 \quad (x = 0 \text{ and } y = 0) \\ V = 0 \quad (x = L \text{ and } y = 0) \end{cases} \tag{21}$$

However, Su & Wang (2003) assumed the voltage distribution as

$$V(x, y) = [(L - x)/L](1 - 2|y|/p)V_0 \tag{22}$$

where V_0 is the applied voltage. Based on this assumption, the voltage is 0 when $x = L$ or $y = \pm(p/2)$, which is not consistent with that shown in Fig. 1(b). Because of the inaccurate assumption about the voltage distribution, the voltage gradient was overestimated, and the corresponding degree of consolidation was larger than that obtained from the proposed numerical analysis.

Comparison of different electrode installation patterns

Similar to the installation patterns of sand drains, three different electrode installation patterns are usually adopted in practice, as shown in Fig. 3 (Bjerrum *et al.*, 1967; Lo & Ho, 1991; Burnotte *et al.*, 2004; Glendinning *et al.*, 2008). In general, the diameter of the central electrical vertical drain (EVD) employed as cathode is larger than that of the steel bar used as anode. In patterns A and B, the electrodes are installed in a square pattern, and the anodes and cathodes are placed row by row in pattern A and interlaced in pattern B. In pattern C, the electrodes are installed in a triangular pattern. The representative elements for the three installation patterns, which will be used in the numerical simulation process, are also illustrated in Fig. 3. In pattern A, every electrode is shared by two representative elements and one anode and one cathode are used in one representative element. In pattern B, every anode is shared by four representative elements and one anode and one cathode are used in one representative element. In pattern C, two anodes and one cathode are used in one representative element since every anode is shared by three representative elements.

The treatment area of the three representative elements is 8 m^2. The soil parameters adopted in the numerical analysis are listed in Table 1.

The ratio of the average ground settlement to the depth of the model, S_a/h, is shown in Fig. 4. The average ground settlements of patterns A and B are almost the same, whereas pattern C achieves the largest average ground settlement, which is about 1·5 times that of patterns A and B. Fig. 5 shows the ratio of the differential settlement to the depth of the model, $\Delta S/h$, and indicates that although patterns A and B obtain approximately the same average ground settlement, the differential settlement of pattern B is smaller than that of pattern A. In addition, pattern C not only achieves the largest average surface settlement but also obtains the smallest differential settlement. The average surface settlement of pattern C is about 1·5 times that of patterns A and B, and the differential settlement is about 0·5 times. With an added anode, pattern C gives a larger and more uniform electrical current intensity in the soil mass. In practice, the steel bar was commonly used as anode, which is much cheaper than the central EVD, so pattern C may be the best way to install the electrodes among the three patterns.

The proposed 3D theoretical and numerical model was

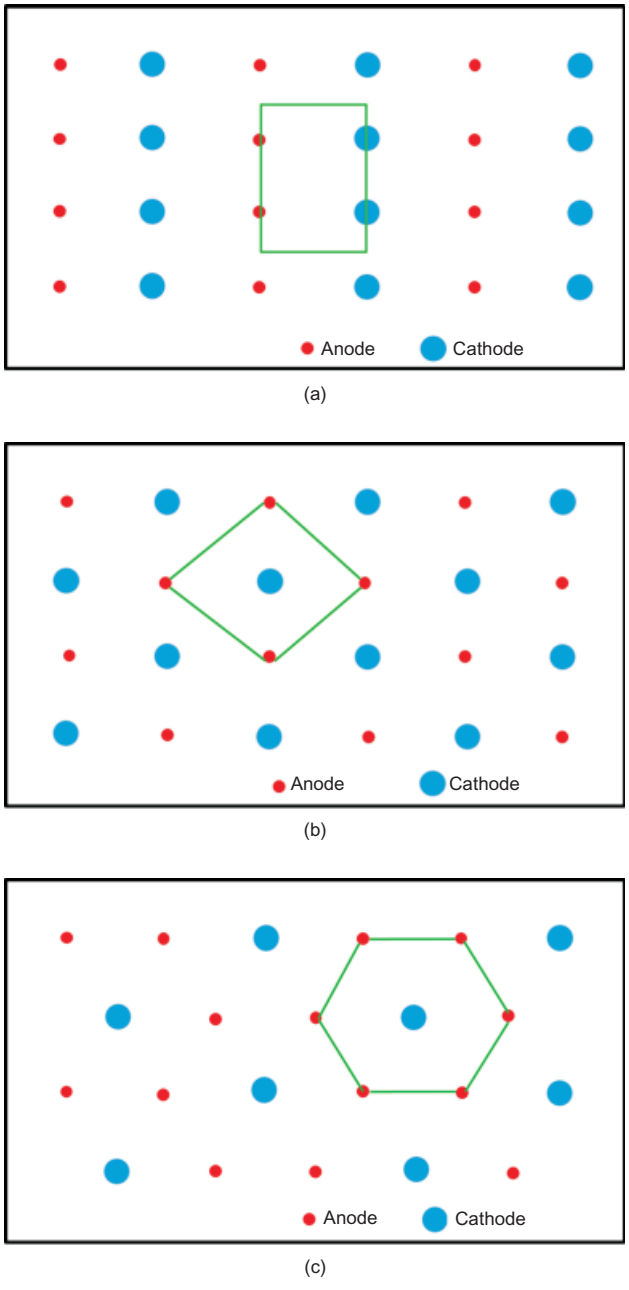

Fig. 3. Three installation patterns of electrodes during electro-osmotic consolidation: (a) pattern A: anodes and cathodes placed row by row in a square pattern; (b) pattern B: anodes and cathodes interlaced with each other in a square pattern; (c) pattern C: electrodes installed in a triangular pattern

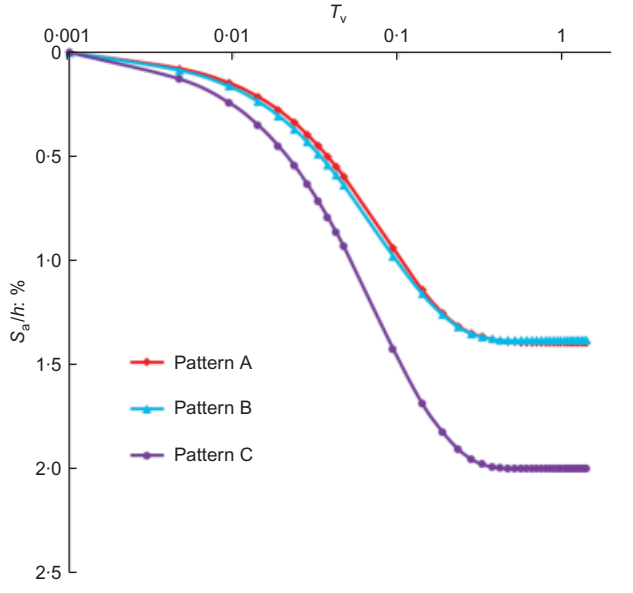

Fig. 4. Ratio of average surface settlement to depth of model of the three installation patterns

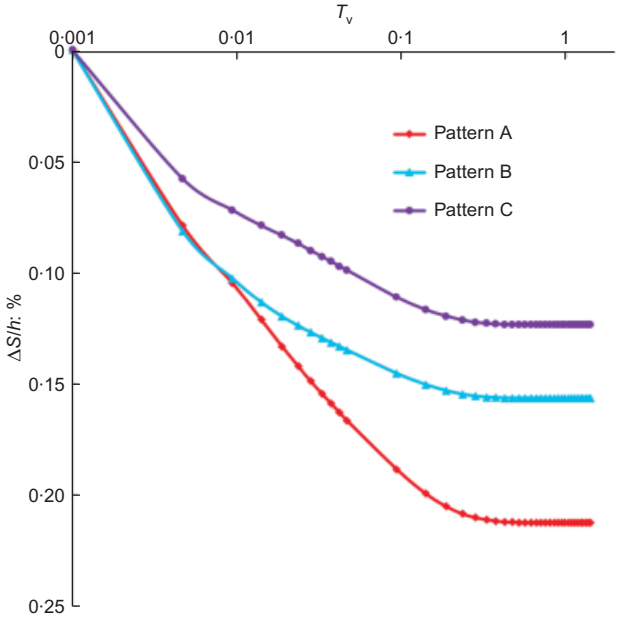

Fig. 5. Ratio of differential settlement to depth of model of the three installation patterns

Table 1. Soil parameters and model dimensions used in the theoretical analysis

Parameter	Value
Unit weight of water, γ_w: kN/m^3	9·81
Hydraulic conductivity in radial direction, k_r: m/s	5×10^{-9}
Hydraulic conductivity in vertical direction, k_z: m/s	5×10^{-9}
Electro-osmotic permeability, k_e: m^2/s per V	3×10^{-9}
Coefficient of volume compressibility, m_v: MPa^{-1}	0·37
Applied voltage, V_0: V	20
Radius of central EVD, r_w: m	0·1
Radius of steel bar used as anode, r_s: m	0·02
Height of model, h: m	5

used to analyse the effect of three different installation patterns of EVD in the application of electro-osmotic consolidation. However, the practical situation is far more complicated. The influence of the heterogeneity of soil layer, the anisotropy of soil parameters and the smear zone formed during the installation on the electro-osmotic consolidation process need further investigation based on the proposed model.

Simplification of the 3D model to the axisymmetric model

In the analysis of a drain well consolidation problem, the 3D model is often simplified to a 2D axisymmetric model and a series of analytical solutions is obtained (Barron, 1948; Hansbo, 1981; Xie & Zeng, 1989; Indraratna *et al.*, 2005). In a similar way, the 3D model for electro-osmotic consolidation can also be simplified to become a 2D

axisymmetric model when electrodes are installed in patterns B and C (Nicholls & Herbst, 1967; Li *et al.*, 2010; Wu & Hu, 2013a). In this section, the proposed 3D numerical model is used to analyse the distribution of electric current intensity and average ground settlement in patterns B and C, as well as the equivalent cylinder model developed based on the equal area assumption.

Figure 6 illustrates the electric field distribution in sections of pattern B, pattern C and the equivalent cylinder model. The numerical result shows that the electrical current in the sections of patterns B and C are 0·44 times and 0·58 times respectively the electrical current of the equivalent cylinder model. Therefore, the average surface settlements of patterns B and C can be obtained from an equivalent cylinder model by changing the applied voltage from V_0 to $0{\cdot}44V_0$ and $0{\cdot}58V_0$ respectively. Nicholls & Herbst (1967) also analysed the electrical current in the section of pattern C and the equivalent cylinder model. They concluded that the electrical current flowing through the section of pattern C was 0·6 times the electrical current intensity obtained from the section of the cylinder model, which agrees well with the present authors' numerical result.

Most of the previous numerical models cannot directly predict the ground settlement, and the soil deformation is usually indirectly obtained by analysing the electrical current or the pore-water pressure (Nicholls & Herbst, 1967; Rittirong & Shang, 2008). Since the proposed numerical model couples the seepage field, the electric field, and the stress and strain field, the ground settlement can be directly obtained. Fig. 7 shows the ratio of the average surface settlement to the depth of the model during the electro-osmotic consolidation process, and the comparison of the three models shows that the cylinder model achieves the largest average surface settlement. However, the ratio of the average ground settlement of pattern B and pattern C to that of the equivalent cylinder model is different from that obtained by the electrical current prediction by Nicholls & Herbst (1967). Fig. 7 shows the curves obtained by multiplying the average ground settlement curve of the equivalent cylinder model by 0·44 and 0·58. It is shown that the electrical current prediction underestimates the settlement in patterns B and C. The average ground settlement of patterns B and C are about 0·5 and 0·7 times that of the equivalent cylinder model.

Wu & Hu (2013a) proposed an analytical solution for the 2D axisymmetric problem of electro-osmotic consolidation. Fig. 7 shows that the result from the analytical solution is larger than that of the 3D numerical model of a cylinder. Owing to the axisymmetric characteristics, the electric field distribution in the cylinder model is actually the same as that in the 2D axisymmetric model. However, the axisymmetric analytical model (Wu & Hu, 2013a) only considered the electric field and the seepage field, while the stress and strain field was not taken into account. The comparison of the analytical result and the numerical result indicates that neglect of the stress and strain field will cause a larger average ground settlement than the actual situation.

The electro-osmotic consolidation is a multi-physics problem, which is related to the mechanical, electrical and hydraulic characteristics of the soil–water system. The prediction for ground settlement may be underestimated from the electrical current prediction because the influence of the seepage field and the stress and strain field is not considered (Nicholls & Herbst, 1967). The ground settlement may be overestimated if the electrical and hydraulic field is considered while the stress and strain field is uncoupled (Wu & Hu, 2013a). The proposed 3D numerical model can predict the actual situation reasonably by coupling the seepage, electrical and stress/strain field together.

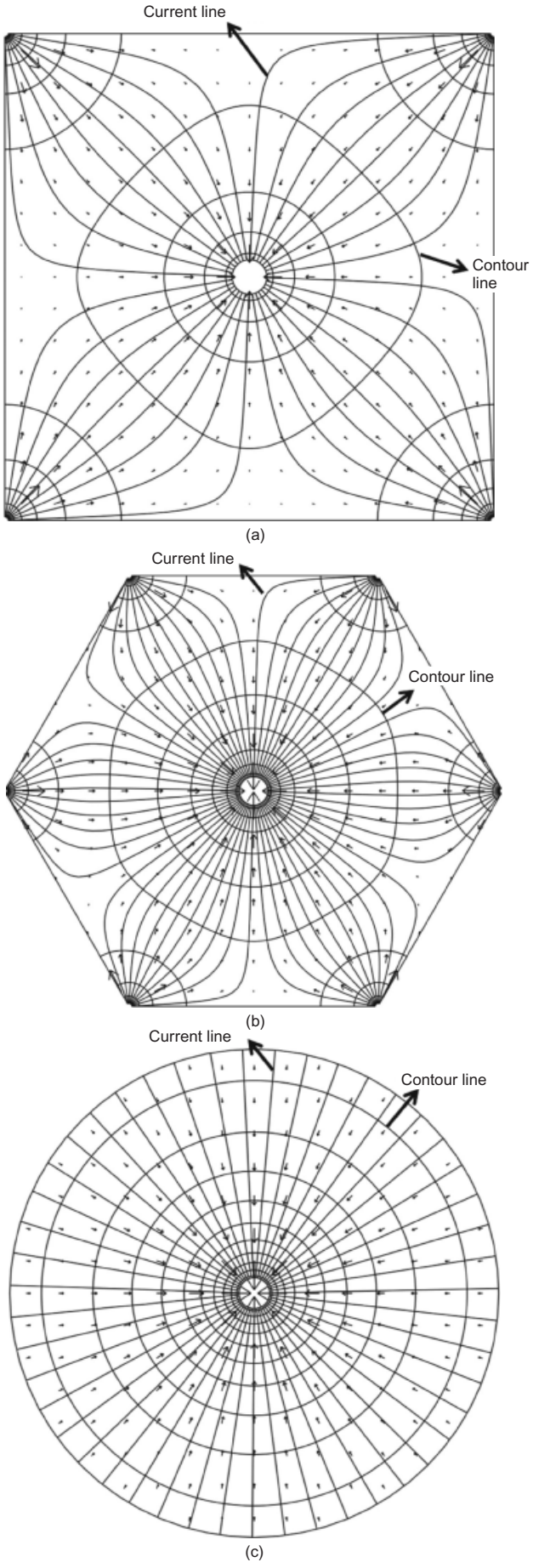

Fig. 6. Electrical flow in: (a) pattern B; (b) pattern C; and (c) the equivalent cylinder model

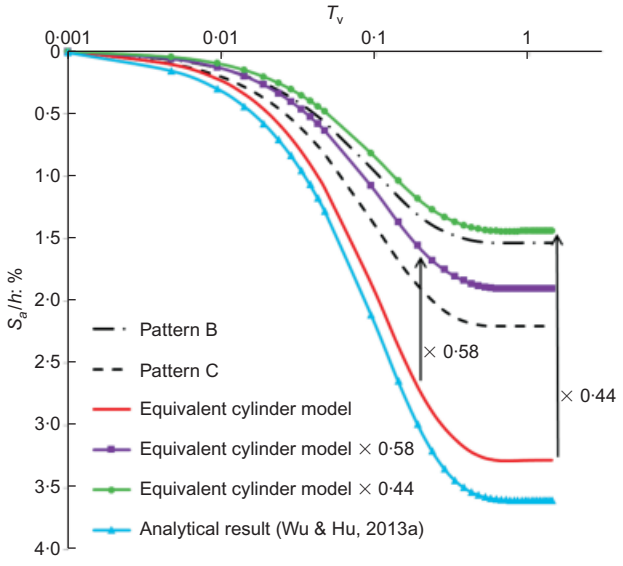

Fig. 7. Comparison of the average surface settlement of patterns B, C and the equivalent cylinder model, and the analytical solution

Finite-element method results for partially penetrating electrode and totally penetrating electrode

When the ground is treated by electro-osmotic consolidation, a partially penetrating EVD can also be used to consolidate the soil, which is similar to partially penetrating prefabricated vertical drains commonly used in vacuum preloading ground treatment to reduce cost. The ratio between the depth of the EVD and the depth of the ground to be treated is denoted by l'. When $l' = 1$, the EVD penetrates through the whole drainage layer.

The 3D numerical model was performed for the above situation and the soil parameters are shown in Table 1. Fig. 8 shows the numerical result in combination with partially penetrating EVD at different depths. The y-coordinate denotes the ratio of the average surface settlement, S_a, to the depth of the model. Based on Fig. 8, the decrease in EVD depth slows down the ground consolidation. When the ratio l' is larger than 0·9, the development of the average surface settlement is almost identical to that when $l' = 1$. However, when l' decreases to 0·8 or less, the development of the average surface settlement is much slower. Therefore, the EVD does not need to penetrate to the bottom of the drainage layer in electro-osmotic consolidation; a partially penetrating EVD with $l' = 0{\cdot}9$ will acquire almost the same settlement as the totally penetrating one.

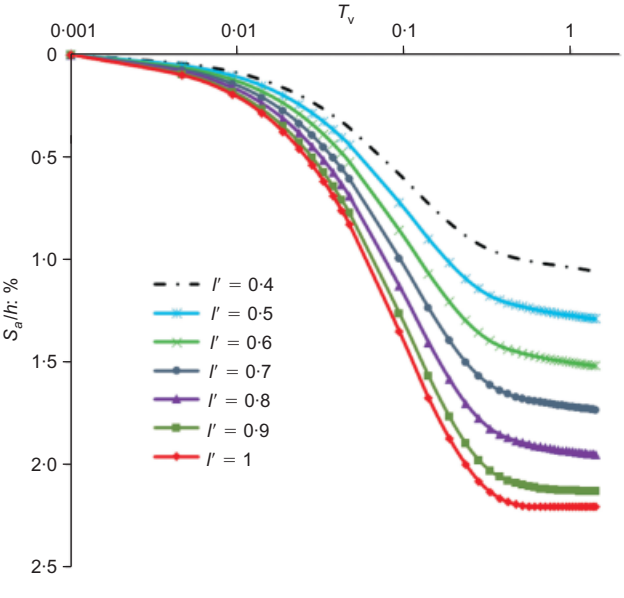

Fig. 8. Average surface settlement of soil treated by electro-osmotic consolidation with partially penetrated EVD

The developed 3D numerical model can analyse the variation of current, the pore pressure and the energy consumption during the electro-osmotic consolidation process in practical engineering. Based on these results, engineers can optimise the electro-osmotic consolidation process and save cost by choosing the optimal treatment time and electrode distance, as well as the optimal depth of EVD. The combination of electro-osmotic consolidation with other ground treatment techniques such as surcharge preloading and vacuum preloading can also be simulated by the proposed model.

A CASE STUDY OF ELECTRO-OSMOTIC CONSOLIDATION

To validate the proposed analytical and numerical model, the present authors performed a numerical simulation of the field case by Bjerrum *et al.* (1967), improving soft soils in Oslofjord, Norway, 30 km south of Oslo. Several 9·6 m long steel bars were embedded into the soil as the electrodes. The electrodes were arranged at 0·6 m intervals in rows with a space of 2 m between the anode and the cathode, as shown in Fig. 9(a). The consolidation of the 2 m deep weathered crust was ignored because its consolidation settlement was much smaller compared with that of the 7·6 m deep soft soil beneath.

The soil was treated as a single layer in the numerical simulation. Owing to the symmetry of the electrode arrangement in the ground, a 3D numerical simulation was performed for a representative element of 2·0 m (length) × 0·6 m (width) × 7·6 m (depth) with one impervious anode and one fully drained cathode, as shown in Fig. 9(b). Fig. 9(c) shows the FEM mesh of the representative element, which has 2624 nodes and 10 714 tetrahedral finite elements.

Meanwhile, a 2D numerical model was also developed, 2 m long and 7·6 m deep, to compare with the 3D model. The reported parameters of the soft clay in the field are shown in Table 2. According to Bjerrum *et al.* (1967), the soil was treated under intermittent electrical current as shown in Fig. 10, which was adopted in the numerical simulation. The average settlement between the anode and the cathode was calculated in the numerical simulation and compared with the field data obtained from a settlement gauge installed near to the middle of the anode and the cathode.

The results of the numerical simulations and the field data are shown in Fig. 11. It is demonstrated that in the early stage, the predicted settlement from the 3D numerical simulation is larger than the field measurements, and coincides well with the field measurements at the later part of the test. The reason for the deviation in the early stage is that the elastic modulus is assumed to be constant in the calculating process of the numerical experiment for this case study. In the real situation, the elastic modulus increases with the drainage of pore water and the corresponding surface settlement will decrease in this process. The 2D numerical model gives a larger ground settlement than the 3D model because the 2D model produced a stronger electrical current intensity. Rittirong & Shang (2008) performed a 2D numerical simulation for this case study, by considering the seepage and the electric field in the model, and the settlement was indirectly calculated from the pore-water pressure and empirical formula. The

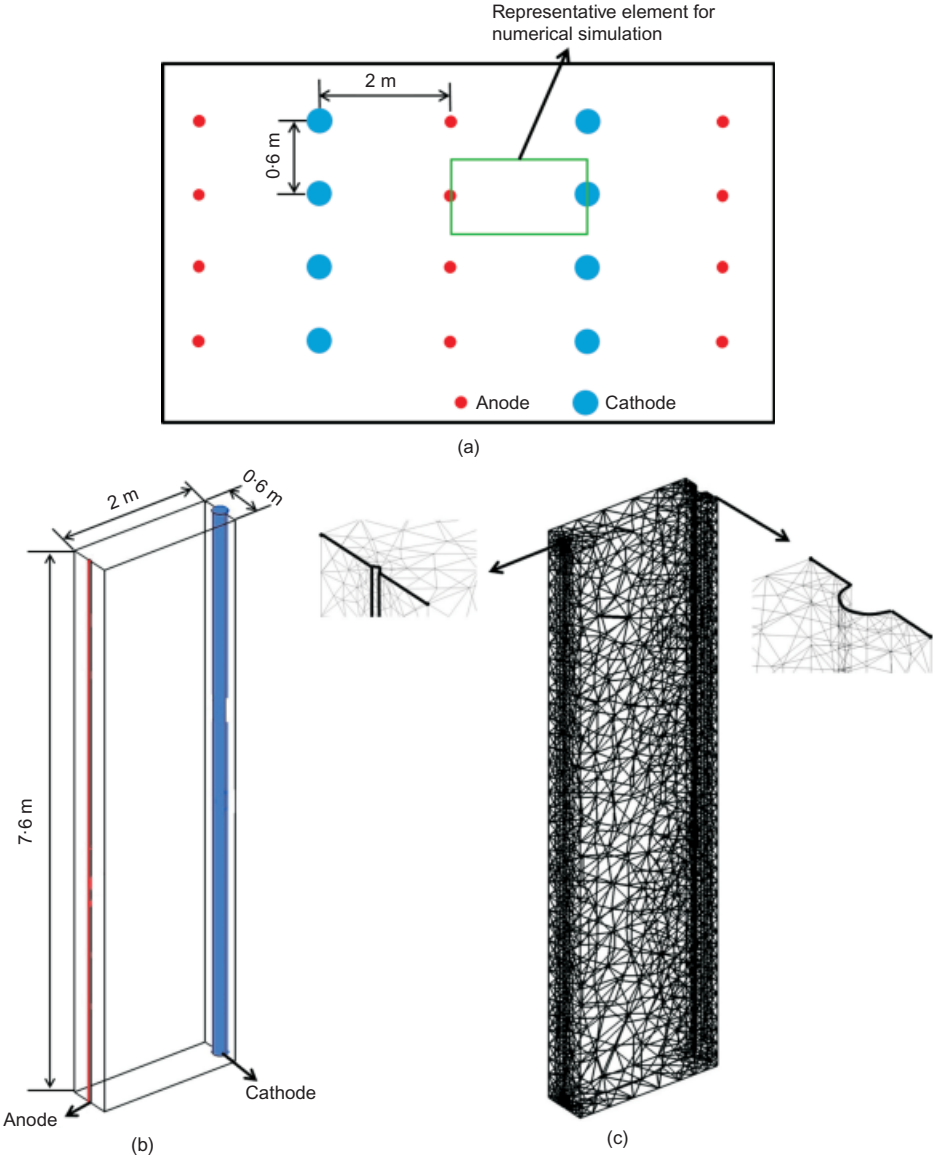

Fig. 9. (a) Electrodes arrangement and representative element for the numerical simulation; (b) diagram of the 3D numerical model; (c) mesh of the 3D numerical model

Table 2. Parameters of soft clay in field test (Bjerrum *et al.*, 1967)

Parameter	Value
Natural water content, w: %	31
Plastic limit, w_p: %	14
Liquid limit, w_L: %	19
Specific gravity, G_s	2·75
Bulk density, γ: kN/m^3	1·94
Sensitivity, S_t	100
Coefficient of consolidation, C_v: m^2/s	5×10^{-8}
Hydraulic conductivity, k_h: m/s	2×10^{-10}
Electro-osmotic permeability, k_e: m^2/s per V	2×10^{-9}

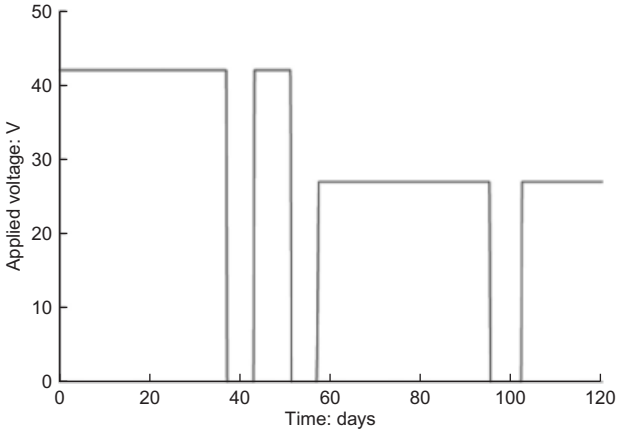

Fig. 10. Variation of applied electrical voltage with time (Bjerrum *et al.*, 1967)

numerical model proposed in this paper coupled the seepage field, the electric field, and the stress and strain field to provide a more realistic simulation, and the ground settlement could be directly obtained. Fig. 11 also illustrates that the settlement stopped or even rebounded after interrupting the electrical currents, which was also captured in the numerical simulation.

SUMMARY AND CONCLUSION

A theoretical model is proposed to describe the displacement, pore-water pressure and electrical voltage during electro-osmotic consolidation, by means of coupling of the

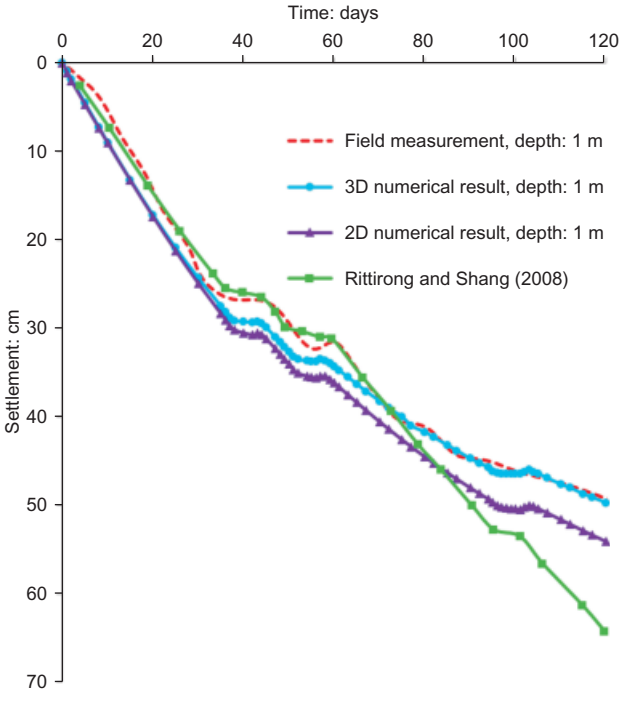

Fig. 11. Comparison of ground settlement at the depth of 1 m in the numerical model and field test

seepage field, the electric field, and the stress and strain field. Based on the proposed theory, a 3D FEM numerical model is developed for electro-osmotic consolidation, which can directly predict the ground settlement. Several different numerical simulations are conducted to analyse the effect of different installation patterns of EVD, the simplification of the 3D model and the partially penetrating electrode. A case study is also performed to verify the capability of the proposed 3D theory.

With the 3D numerical model, three patterns commonly used for electrode installation are analysed. The result indicates that the triangular installation pattern can obtain more ground settlement than the other two patterns.

The equivalent cylinder model is developed to investigate the impact of the simplification from a hexahedron model and a hexagonal prisms model to a cylinder model based on the equal area assumption. The simplification is often used in the theoretical analysis, and the numerical results illustrate that the equivalent model will achieve a much larger settlement. A reduction factor for the applied voltage is then suggested in order to apply the cylinder model for electro-osmotic consolidation.

The effect of the penetrating depth of the electrodes on the ground settlement is also investigated. The numerical result shows that a partially penetrating EVD with $l' = 0{\cdot}9$ will acquire almost the same settlement as the totally penetrating one.

An engineering case of electro-osmotic consolidation was simulated to demonstrate the capability of the developed theoretical and numerical models, and the calculated ground settlement agrees well with the field data. The developed numerical model has potential use in the engineering design of a ground improvement system.

ACKNOWLEDGEMENTS

Financial support from the National Natural Science Foundation of China (NSFC50978139), National Key Basic Research Program (2012CB719804), the State Key Laboratory of Hydro-Science and Engineering (SKLHSE-2012-KY-01, 2013-D-01) and Tsinghua University (2010THZ02-1) is gratefully acknowledged.

NOTATION

$B_{m,i}$	calculating factor for 2D model in horizontal plane
C_p	soil capacitance per unit volume
E	Young's modulus
$\boldsymbol{F}$	external force acting on boundary in numerical model
H	total head due to pore-water pressure and elevation
H_1	initial total head in numerical model
h	depth of model
$\boldsymbol{j}$	electrical current density vector in x, y and z directions
$\boldsymbol{K}$, $\boldsymbol{K}_a$	coefficient tensors for $\boldsymbol{\delta}$ in the numerical model
$\boldsymbol{K}_c$, $\boldsymbol{K}_s$, $\boldsymbol{K}_b$	coefficient tensors for $\boldsymbol{\Psi}$ in the numerical model
k_e	electro-osmosis conductivity
k_h	hydraulic conductivity
$\boldsymbol{k}_e$	electro-osmosis conductivity tensor for anisotropic soils
$\boldsymbol{k}_h$	hydraulic conductivity tensor for anisotropic soils
L	length of 2D model in horizontal plane
l'	ratio between depth of EVD and depth of ground to be treated
$\boldsymbol{n}$	normal vector at boundary in numerical model
p	height of 2D model in horizontal plane
$\boldsymbol{R}_{fh}$	element load vector in numerical model
$\boldsymbol{R}_{qh}$	vector of hydraulic and voltage condition in numerical model
r_e, r_w	radii of central EVD and steel bar used as anode
S_a	average surface settlement
ΔS	differential settlement
T_v	time factor
t	time
$\boldsymbol{u}$	soil displacements vector
$\boldsymbol{u}_0$	initial displacements in numerical model
$\boldsymbol{v}$	pore-water flow velocity in x, y and z directions
$\boldsymbol{v}_h$, $\boldsymbol{v}_e$	pore-water flow velocity vectors due to hydraulic gradient and electrical gradient
v_x, v_y, v_z	pore-water flow velocity in the x, y and z directions
V	electrical potential
V_0	applied voltage
V_1	initial electrical voltage in the numerical model
w	water content
w_L	liquid limit
w_p	plastic limit
z	elevation head
γ	bulk weight of soil
γ_w	unit weight of water
$\boldsymbol{\delta}$	vector of nodal displacements in numerical model
ε_v	volume strain of soil mass
θ	coefficient of time step in numerical model
υ	Poisson ratio
$\boldsymbol{\sigma}$	stress tensor in the numerical model
σ_e	electrical conductivity
$\boldsymbol{\sigma}_e$	electrical conductivity tensor
$\boldsymbol{\Psi}$	vector of nodal hydraulic and electrical potentials in numerical model

REFERENCES

Barron, R. A. (1948). Consolidation of fine-grained soils by drain wells. *ASCE Trans.* **113**, 718–754.

Bjerrum, L., Moum, J. & Eide, O. (1967). Application of electro-osmosis to a foundation problem in Norwegian quick clay. *Géotechnique* **17**, No. 3, 214–235, http://dx.doi.org/10.1680/geot.1967.17.3.214.

Biot, M. A. (1941). General theory of three-dimensional consolidation. *J. Appl. Phys.* **12**, No. 2, 155–164.

Burnotte, F., Lefebvre, G. & Grondin, G. (2004). A case record of electro-osmotic consolidation of soft clay with improved soil-electrode contact. *Can. Geotech. J.* **41**, No. 6, 1038–1053.

Casagrande, L. (1948). Electroosmosis in soils. *Géotechnique* **1**, No. 3, 159–177, http://dx.doi.org/10.1680/geot.1948.1.3.159.

Casagrande, L. (1983). Stabilization of soils by means of electro-

osmotic state-of-art. *J. Boston Soc. Civ. Engng, ASCE* **69**, No. 3, 255–302.

Esrig, M. I. (1968). Pore pressures, consolidation and electrokinetics. *J. Soil Mech. Found. Engng Div., ASCE* **94**, No. SM4, 899–921.

Fourie, A. B., Johns, D. G. & Jones, C. J. F. P. (2007). Dewatering of mine tailings using electrokinetic geosynthetics. *Can. Geotech. J.* **44**, No. 2, 160–171.

Glendinning, S., Jones, C. J. F. P. & Pugh, R. C. (2005). Reinforced soil using cohesive fill and electrokinetic geosynthetics. *Int. J. Geomech., ASCE* **5**, No. 2, 138–146.

Glendinning, S., Lamont-Black, J., Jones, C. J. F. P. & Hall, J. (2008). Treatment of lagooned sewage sludge in situ using electrokinetic geosynthetics. *Geosynthetics Int*. **15**, No. 3, 192–204.

Hansbo, S. (1981). Consolidation of fine-grained soils by prefabricated drains. *Proceedings of the 10th international conference on soil mechanics and foundation engineering*, Stockholm, vol. 3, 677–682.

Hu, L. M., Wu, W. L. & Wu, H. (2010). Theoretical analysis and numerical simulation of electro-osmosis consolidation for soft clay. *Rock Soil Mech*. **31**, No. 12, 3977–3983.

Hu, L. M., Wu, W. L. & Wu, H. (2012). Numerical model of electro-osmotic consolidation in clay. *Géotechnique* **62**, No. 6, 537–541, http://dx.doi.org/10.1680/geot.11.T.008.

Indraratna, B., Rujikiatkamjorn, C. & Sathananthan, L. (2005). Analytical and numerical solutions for a single vertical drain including the effects of vacuum preloading. *Can. Geotech. J.* **42**, No. 4, 994–1014.

Jeyakanthan, V., Gnanendran, C. T. & Lo, S. C. R. (2011). Laboratory assessment of electro-osmotic stabilization of soft clay. *Can. Geotech. J.* **48**, No. 12, 1788–1802.

Jones, C. J. F. P., Lamont-Black, J., Glendinning, S., Bergado, D., Eng, T., Fourie, A., Hu, L., Pugh, C., Romantshuk, M., Simpanen, S. & Zhuang, Y. (2008). Recent research and applications in the use of electro-kinetic geo-synthetics. Keynote paper. *Proceedings of the 4th European geosynthetics conference*, Edinburgh, paper no. 329 (CD-ROM).

Jones, C. J. F. P., Lamont-Black, J. & Glendinning, S. (2011). Electrokinetic geosynthetics in hydraulic applications. *Geotextiles and Geomembranes* **29**, No. 4, 381–390.

Lamont-Black, J. & Weltman, A. (2010). Electrokinetic strengthening and repair of slopes. *Ground Engng* **43**, No. 4, 28–31.

Lefebvre, G. & Burnotte, F. (2002). Improvement of electro-osmotic consolidation of soft clays by minimizing power loss at electrodes. *Can. Geotech. J.* **39**, No. 2, 399–408.

Lewis, R. W. & Humpheson, C. (1973). Numerical analysis of electro-osmotic flow in soils. *J. Soil Mech. Found. Div., ASCE* **99**, No. SM8, 603–616.

Li, Y., Gong, X. N., Lu, M. M. & Guo, B. (2010). Coupling consolidation theory under combined action of load and electro-osmosis. *Chin. J. Geotech. Engng* **32**, No. 1, 77–81 (in Chinese).

Lo, K. Y. & Ho, K. S. (1991). Electroosmotic strength of soft sensitive clays. *Can. Geotech. J.* **28**, No. 1, 62–73.

Micic, S., Shang, J. Q., Lo, K. Y., Lee, Y. N. & Lee, S. W. (2001). Electro-kinetic strengthening of a marine sediment using intermittent current. *Can. Geotech. J.* **38**, No. 22, 287–302.

Mitchell, J. K. & Soga, K. (2005). *Fundamentals of soil behavior*, 3rd edn. Hoboken, NJ, USA: Wiley.

Nicholls, R. L. & Herbst, R. L. (1967). Consolidation under electrical -pressure gradients. *J. Mech. Found. Div.* **93**, No. SM5, 139–151.

Reuss, F. F. (1809). Sur un nouvel effet de l'électricité galvanique. *Memoires de la Societé Imperiale des Naturalistes de Moscou*, vol. 2, pp. 327–337. Moscow, Russia: Societé Imperiale de Naturalistes (in French).

Rittirong, A. & Shang, J. Q. (2008). Numerical analysis for electro-osmotic consolidation in two-dimensional electric field. *Proceedings of the 18th international offshore and polar engineering conference*, Vancouver, Canada, pp. 566–572.

Su, J. Q. & Wang, Z. (2003). Theory of two-dimensional electro-osmotic consolidation of soils. *Géotechnique* **53**, No. 8, 759–763, http://dx.doi.org/10.1680/geot.2003.53.8.759.

Wan, T. Y. & Mitchell, J. K. (1976). Electro-osmotic consolidation of soils. *J. Geotech. Eng. Div., ASCE* **102**, No. 5, 473–491.

Wang, H. F. (2000). *Theory of linear poroelasticity: with application to geomechanics and hydrogeology.* Princeton, NJ, USA: Princeton University Press.

Wu, H. & Hu, L. M. (2013a). Analytical solution for axisymmetric electro-osmotic consolidation. *Géotechnique* **63**, No. 12, 1074–1079, http://dx.doi.org/10.1680/geot.12.P.133.

Wu, H. & Hu, L. M. (2013b). Numerical simulation of electro-osmosis consolidation considering variation of electrical conductivity. *Chin. J. Geotech. Engng* **35**, No. 4, 734–738 (in Chinese).

Wu, W. L. (2009). *Theoretical model and numerical simulation of electro-osmotic consolidation on soft clay.* MS thesis, Tsinghua University, Beijing, China.

Xie, K. H. & Zeng, G. X. (1989). Consolidation theories for drain wells under equal strain condition. *Chin. J. Geotech. Engng* **11**, No. 2, 3–17 (in Chinese).

Yuan, J., Hicks, M. A. & Dijkstra, J. (2013). Numerical model of elasto-plastic electro-osmosis consolidation of clays. In *Poromechanics V: Proceedings of the 5th biot conference on poromechanics, Vienna, Austria* (eds C. Hellmich, B. Pichler and D. Adam), pp. 2076–2085. Reston, VA, USA: ASCE.

Yuan, J. & Hicks, M. A. (2013). Large deformation elastic electro-osmosis consolidation of clays. *Comput. Geotech.* **54**, 60–68.

Zhuang, Y. F. & Wang, Z. (2007). Interface electric resistance of electro-osmotic consolidation. *J. Geotech. Geoenviron. Engng, ASCE* **133**, No. 12, 1617–1621.

Wu, H. & Hu, L. (2013). *Géotechnique* **63**, No. 12, 1074–1079 [http://dx.doi.org/10.1680/geot.12.P.133]

TECHNICAL NOTE

Analytical solution for axisymmetric electro-osmotic consolidation

H. WU* and L. HU†

Electro-osmotic consolidation is a potential method for soil improvement. An axisymmetric electro-osmotic consolidation model with coupled horizontal and vertical seepage is proposed and the analytical solution is derived without the equal strain hypothesis, which was used in previous models. The proposed analytical model can predict the distribution of pore-water pressure in the radial direction, and comparison with previous analytical models indicates that the degree of consolidation is overestimated if the model is simplified from an axisymmetric model to a planar model. A design chart is developed to facilitate the evaluation of applying electro-osmotic consolidation for soil improvement.

KEYWORDS: consolidation; dewatering; electrokinetics; ground improvement; seepage; theoretical analysis

INTRODUCTION

Electro-osmosis, in which an electrical field is applied to a saturated soil to cause water flow from the anode to the cathode, has been proved to be an effective method to consolidate soil and enhance the bearing capacity of ground (Bjerrum *et al.*, 1967; Casagrande, 1983; Casagrande *et al.*, 1986; Chew *et al.*, 2004; Hu *et al.*, 2010). Esrig (1968) first proposed a one-dimensional analytical model to calculate the excess pore-water pressure. Wan & Mitchell (1976) considered the surcharge preloading, and coupled the two methods. Thereafter several analytical models were proposed for electro-osmotic consolidation, including the two-dimensional model in a vertical plane (Shang, 1998; Xu *et al.*, 2011) and the two-dimensional model in a horizontal plane (Su & Wang, 2003). Prefabricated vertical drain (PVD) and electric vertical drain (EVD) are often installed in an equilateral triangular pattern in the ground so that an axisymmetric model is more appropriate to describe the behaviour of soil than the planar models (Glendinning *et al.*, 2008).

The unit cell theory proposed by Barron (1948) was the most popular method to analyse axisymmetric seepage problems, such as ground treatment with PVD (Carrillo, 1942; Barron, 1948; Hansbo, 1981; Onoue, 1988; Xie & Zeng, 1989; Indraratna *et al.*, 2005; Wu & Hu, 2012a), as well as electro-osmotic consolidation (Li *et al.*, 2010; Wu & Hu, 2012b). Li *et al.* (2010) developed an axisymmetric model to analyse the soil behaviour of electro-osmotic consolidation with surcharge preloading. Wu & Hu (2012b) proposed an axisymmetric analytical model for electro-osmotic consolidation coupled with vacuum preloading. However, both of the above analytical models ignored the vertical flow of pore water and used the equal strain hypothesis, which assumes equal vertical soil displacement along the radial direction at an identical depth. The equal strain hypothesis is not applicable for all situations, and only average excess pore-water pressure can be obtained.

In this paper, an axisymmetric model considering both the radial and vertical flows for electro-osmotic consolidation is proposed, and the analytical solution is derived to describe the behaviour of the soil mass. Results from the analytical model are compared with previous model predictions and design charts are obtained to evaluate the suitability of electro-osmotic consolidation to given site conditions.

THEORETICAL ANALYSIS

Two-dimensional axisymmetric model

A schematic diagram of the two-dimensional axisymmetric model for electro-osmotic consolidation with a central EVD is shown in Fig. 1. The top of the model and the central EVD are permeable boundaries, while the peripheral and bottom boundaries are impermeable. The radii of the model and the drain are r_e and r_w, respectively. The voltage is distributed along the radial direction and is independent of time and the vertical position z. The electrical capacitance per unit volume and the electrochemical reactions are neglected. The electro-osmosis conductivity and the electrical conductivity in r and z directions are supposed to be the same and remain constant.

Governing equations, boundary conditions and initial condition

The combined pore-water flow under the hydraulic gradient and electrical gradient can be described as (Esrig, 1968; Hu *et al.*, 2012)

$$\begin{aligned} v_r &= -k_r \frac{\partial H}{\partial r} - k_e \frac{\partial V}{\partial r} \\ v_z &= -k_z \frac{\partial H}{\partial z} \end{aligned} \tag{1}$$

where H is the total water head and V is the electrical potential; v_r and v_z are the pore-water flow velocity in the radial and vertical directions; k_r and k_z are radial and vertical hydraulic conductivities, and k_e is the electro-osmosis conductivity.

Based on the principle of conservation of pore water in a

Manuscript received 9 September 2012; revised manuscript accepted 25 March 2013. Published online ahead of print 8 May 2013.
Discussion on this paper closes on 1 February 2014, for further details see p. ii.
* Department of Hydraulic Engineering, Tsinghua University, Beijing, People's Republic of China.
† Key State Laboratory of Hydro-Science and Engineering, Tsinghua University, Beijing, People's Republic of China (corresponding author).

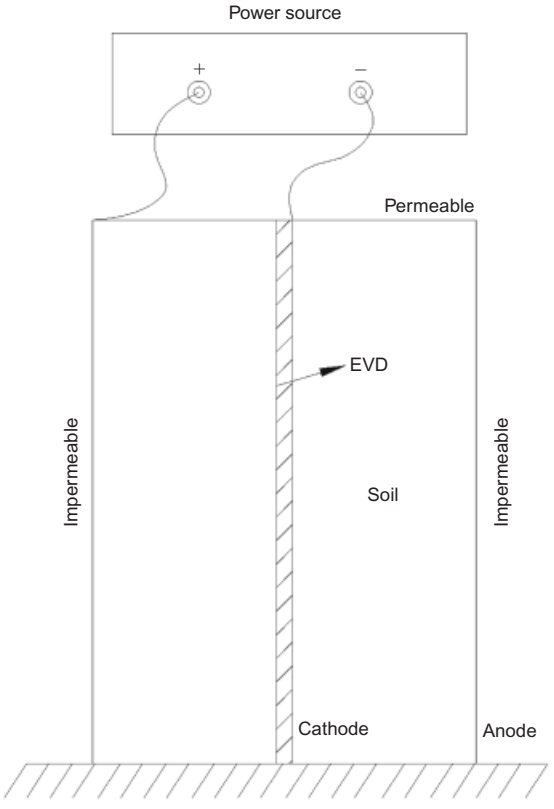

Fig. 1. Diagram of the two-dimensional axisymmetric model of electro-osmotic consolidation

saturated soil system, the following equation can be derived under axisymmetric conditions

$$\frac{v_r}{r}+\frac{\partial v_r}{\partial r}+\frac{\partial v_z}{\partial z}=-m_{\mathrm{v}}\,\gamma_{\mathrm{w}}\,\frac{\partial H}{\partial t} \tag{2}$$

where m_{v} is the coefficient of volume compressibility and γ_{w} is the unit weight of water.

The governing equation for electro-osmotic consolidation under axisymmetric condition can be obtained by substituting equation (1) into equation (2)

$$k_r\left(\frac{1}{r}\frac{\partial H}{\partial r}+\frac{\partial^2 H}{\partial r^2}\right)+k_z\frac{\partial^2 H}{\partial z^2}+\frac{k_{\mathrm{e}}}{r}\frac{\partial V}{\partial r}+k_{\mathrm{e}}\frac{\partial^2 V}{\partial r^2} = m_{\mathrm{v}}\gamma_{\mathrm{w}}\frac{\partial H}{\partial t} \tag{3}$$

The equation for the electric field can be obtained based on the law of conservation of electrical charge

$$\frac{\partial V^2}{\partial r^2}+\frac{1}{r}\frac{\partial V}{\partial r}=0 \tag{4}$$

The boundary conditions for V can be expressed as

$$V(r_{\mathrm{e}},\,z,\,t)=V_{\mathrm{a}} \tag{5}$$

$$V(r_{\mathrm{w}},\,z,\,t)=0 \tag{6}$$

where V_{a} is the applied voltage.

Then the solution for equation (4) can be derived as

$$V(r)=\frac{V_{\mathrm{a}}}{\ln n}\ln\frac{r}{r_{\mathrm{w}}} \tag{7}$$

where n denotes the ratio of the diameter of the model to the diameter of the EVD. Considering equation (7), equation (3) can be simplified as

$$k_r\left(\frac{1}{r}\frac{\partial H}{\partial r}+\frac{\partial^2 H}{\partial r^2}\right)+k_z\frac{\partial^2 H}{\partial z^2}=m_{\mathrm{v}}\gamma_{\mathrm{w}}\frac{\partial H}{\partial t} \tag{8}$$

The peripheral boundary is impermeable so that the boundary condition can be expressed as

$$v_r(r_{\mathrm{e}},\,z,\,t)=-k_r\frac{\partial H}{\partial r}-k_{\mathrm{e}}\frac{\partial V}{\partial r}=0 \tag{9}$$

Substituting equation (7) into equation (9), the following boundary equation can be obtained as

$$\frac{\partial H(r_{\mathrm{e}},\,z,\,t)}{\partial r}=\frac{k_{\mathrm{e}}}{k_r}\frac{V_{\mathrm{a}}}{\ln n}\frac{1}{r_{\mathrm{e}}} \tag{10}$$

The bottom boundary is impermeable and since the voltage is distributed only in the radial direction, the mathematical expression for the bottom boundary can be described as

$$\left.\frac{\partial H(r,\,z,\,t)}{\partial z}\right|_{z=L}=0 \tag{11}$$

where L is the depth of the model.

The boundary of the EVD and the top boundary can be expressed as

$$H(r_{\mathrm{w}},\,z,\,t)=H_0 \tag{12}$$

$$H(r,\,0,\,t)=H_0 \tag{13}$$

where H_0 is the total hydraulic head. When the other methods such as vacuum preloading are used together with electro-osmosis, H_0 can be a certain value according to the actual conditions. When the electro-osmotic consolidation is used alone for the soil improvement and there is no water at the top of the model that can enter the model, the top boundary is actually a 0 flux boundary, which can be described by a one-dimensional axisymmetric model.

The initial condition can be described as

$$H(r,\,z,\,0)=0 \tag{14}$$

Analytical solutions

According to equations (8) to (14), the analytical solutions for H can be obtained by the separation of variables (details are given in the supplementary data available on-line)

$$\begin{aligned}H(r,\,z,\,t)=&\\ &\sum_{i=1}^{\infty}\sum_{m=1}^{\infty}\frac{k_{\mathrm{e}}}{k_r}\frac{-V_{\mathrm{a}}}{\ln n\,r_{\mathrm{w}}^2}\,F_{im}\,D_0(\sqrt{\lambda_i}r)\\ &\times\sin\left(\frac{2m-1}{2L}\pi z\right)\exp\left\{-C_{\mathrm{v}}\left[\lambda_i+\frac{(2m-1)^2\pi^2}{4L^2}\frac{k_z}{k_r}\right]t\right\}\\ &+\sum_{i=1}^{\infty}\frac{k_{\mathrm{e}}}{k_r}\frac{-V_{\mathrm{a}}}{\ln n\,r_{\mathrm{w}}^2}\,E_i\,D_0(\sqrt{\lambda_i}r)\\ &\times\left\{\exp\left(\sqrt{\frac{k_r}{k_z}}\lambda_i z\right)+\exp\left[\sqrt{\frac{k_r}{k_z}}\lambda_i(2L-z)\right]\right\}\\ &-\frac{k_{\mathrm{e}}}{k_r}\frac{V_{\mathrm{a}}}{\ln n}\ln\frac{r}{r_{\mathrm{w}}}+H_0\end{aligned} \tag{15}$$

$$F_{im} = \frac{\frac{2}{\lambda_i}\, D_0(\sqrt{\lambda_i} r_e)\, \frac{4}{(2m-1)\pi}}{D_1^2(\sqrt{\lambda_i} r_w) - n^2\, D_0^2(\sqrt{\lambda_i} r_e)} \frac{\frac{k_r}{k_z}\lambda_i \frac{4L^2}{(2m-1)^2\pi^2}}{1+\frac{k_r}{k_z}\lambda_i \frac{4L^2}{(2m-1)^2\pi^2}} - \frac{\frac{8}{\sqrt{\lambda_i}}\, r_w\, D_1(\sqrt{\lambda_i} r_w)\, \frac{H_0}{(2m-1)\pi}}{D_1^2(\sqrt{\lambda_i} r_w) - n^2\, D_0^2(\sqrt{\lambda_i} r_e)} \tag{16}$$

$$E_i = \frac{\frac{2}{\lambda_i}\, D_0(\sqrt{\lambda_i} r_e)}{[D_1^2(\sqrt{\lambda_i} r_w) - n^2\, D_0^2(\sqrt{\lambda_i} r_e)] \left[1 + \exp\left(2\sqrt{\frac{k_r}{k_z}\lambda_i} L\right)\right]} \tag{17}$$

$$D_j(\sqrt{\lambda_i} r) = \frac{J_0(\sqrt{\lambda_i} r_w)}{Y_0(\sqrt{\lambda_i} r_w)}\, Y_j(\sqrt{\lambda_i} r) - J_j(\sqrt{\lambda_i} r) \tag{18}$$

where J_j and Y_j are the first and the second Bessel functions respectively with an order of j, and λ_i is the solution for $D_0(\lambda^{1/2} \times r_e) = 0$ where i equals 1,2,3...; $C_v = k_r/(m_v \gamma_w)$ is the coefficient of consolidation in the radial direction. Then the degree of consolidation can be calculated as

$$U = 1 - \frac{\sum_{i=1}^{\infty}\sum_{m=1}^{\infty} F_{im}\left(1/\sqrt{\lambda_i}\right) D_1\left(\sqrt{\lambda_i} r_w\right)\left\{2L/[(2m-1)\pi]\right\} \exp\left\{-C_v\left[\lambda_i + \frac{(2m-1)^2\pi^2}{4L^2}\frac{k_z}{k_r}\right]t\right\}}{L\left\{\left(r_w^3/4\right)[n^2(2\ln n - 1)+1] + \left(H_0 r_w^2/2\right)(n^2-1)\right\} + \sum_{i=1}^{\infty} E_i\left\{\left[D_1(\sqrt{\lambda_i} r_w)\right]/\sqrt{\lambda_i}\right\}\sqrt{(k_z/k_r)(1/\lambda_i)}\left\{\exp\left[2\sqrt{\frac{k_r}{k_z}\lambda_i} L\right] - 1\right\}} \tag{19}$$

Equation (19) indicates that the degree of consolidation is independent of the electro-osmosis conductivity. The applied voltage will contribute to the excess pore-water pressure and settlement, but not the degree of consolidation if the electrochemical reactions are neglected.

When electro-osmotic consolidation is used alone, the one-dimensional axisymmetric model can be employed, in which the governing equation, the boundary conditions and the initial condition are shown as follows

$$\begin{cases} k_r\left(\frac{1}{r}\frac{\partial H}{\partial r} + \frac{\partial^2 H}{\partial r^2}\right) = m_v\, \gamma_w\, \frac{\partial H}{\partial t} \\ \frac{\partial H(r_e, t)}{\partial r} = \frac{k_e}{k_r}\frac{V_a}{\ln n}\frac{1}{r_e} \\ H(r_w, t) = 0 \\ H(r, 0) = 0 \end{cases} \tag{20}$$

The analytical solution can be derived as (details are given in the supplementary data available on-line)

$$H(r, t) = \sum_{i=1}^{\infty} \frac{k_e}{k_r}\frac{-V_a}{\ln n\, r_w^2}\, C_i\, D_0(\sqrt{\lambda_i} r)\, e^{-C_v \lambda_i t} - \frac{k_e}{k_r}\frac{V_a}{\ln n}\, \ln\frac{r}{r_w} \tag{21}$$

$$C_i = \frac{(2/\lambda_i) D_0\left(\sqrt{\lambda_i} r_e\right)}{D_1^2\left(\sqrt{\lambda_i} r_w\right) - n^2\, D_0^2\left(\sqrt{\lambda_i} r_e\right)} \tag{22}$$

DISCUSSION

The basic parameters adopted in the analytical model are listed in Table 1.

Table 1. Basic parameters for electro-osmotic consolidation in the numerical and analytical model

Parameter	Value
Radius of model, r_e: m	0·5
Depth of model, L: m	1
Unit weight of water, γ_{sat}: kN/m^3	10
Hydraulic conductivity in radial direction, k_r: m/s	5×10^{-9}
Hydraulic conductivity in vertical direction, k_z: m/s	$2{\cdot}5 \times 10^{-9}$
Coefficient of volume compressibility, m_v: MPa^{-1}	0·3
Electro-osmosis conductivity, k_e: m^2/s per V	2×10^{-9}
Applied voltage, V_a: V	10

Impact of vertical seepage on electro-osmotic consolidation

In order to focus on the effect of vertical seepage on the electro-osmotic consolidation process when vacuum preloading is also used, H_0 is set at 0 to remove the effect of vacuum preloading in the following analysis. The values for the ratio of vertical to radial hydraulic conductivity, k_z/k_r, were varied from 0·01 to 1 with a fixed k_r; the comparison is shown by the real lines in Fig. 2. The horizontal ordinate T_v denotes the time factor, which can be expressed as $T_v = C_v\, t/L^2$. The vertical ordinate denotes the ratio of the settlement at the anode to the depth of the model. The solid curves represent the results of $k_z/k_r = 1$, $k_z/k_r = 0{\cdot}5$, $k_z/k_r = 0{\cdot}1$ and $k_z/k_r = 0{\cdot}01$ respectively.

Figure 2 illustrates that with the increase of k_z, the settlement at the anode decreases. When $k_z/k_r = 0{\cdot}01$, the seepage in the vertical direction can be neglected and the ratio of the settlement to the depth of the model reaches 12%.

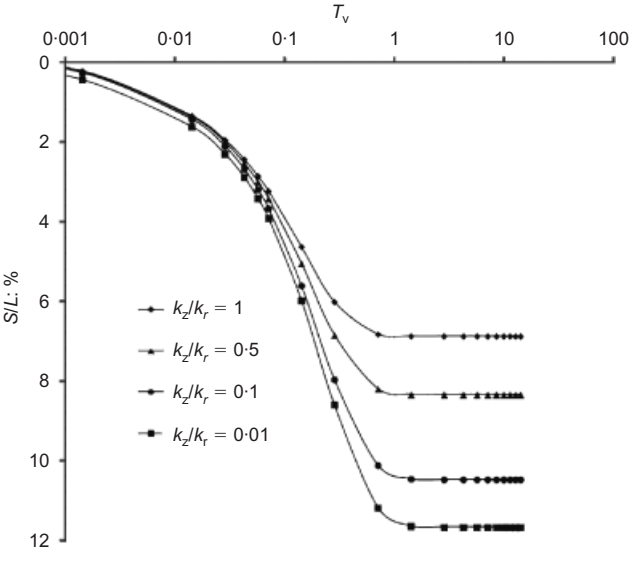

Fig. 2. Relationship between the ratio of settlement at the anode to the depth of the model and time under different k_z/k_r

Impact of the equal strain hypothesis

Wu & Hu (2012b) neglected the vertical seepage and derived an analytical solution for the one-dimensional axisymmetric model with the boundary conditions shown in equations (10) and (11) under the equal strain hypothesis

$$\bar{u}(t) = -MV_{\mathrm{a}}\,(1 - \mathrm{e}^{-t/B_{\mathrm{r}}}),\quad \bar{U} = 1 - \mathrm{e}^{-t/B_{\mathrm{r}}} \tag{23}$$

where $\bar{u}$ and $\bar{U}$ are the average excess pore-water pressure and the average degree of consolidation. $B_{\mathrm{r}} = \gamma_{\mathrm{w}} r_{\mathrm{e}}^2 m_{\mathrm{v}} F_i$, $M = k_{\mathrm{e}}\gamma_{\mathrm{w}}(F_j/k_r)$, $F_i = n^2/(n^2-1)\,(\ln n - 3/4) + (1 - 1/4/n^2)/(n^2 - 1)$, $F_j = n^2/(n^2 - 1) - 1/(2\ln n)$.

Figure 3 illustrates the excess pore-water pressure of the two analytical solutions shown in equations (21) and (23), representing the analytical solution with and without the equal strain hypothesis respectively. Because of the equal strain hypothesis, the excess pore-water pressure obtained from equation (23) is the same along the radial direction. Nevertheless, the proposed analytical solution can reflect the variation of the excess pore-water pressure from 0 at the cathode to a relative high negative excess pore-water pressure at the anode.

Comparison with previous analytical solutions

Shang (1998) and Xu *et al.* (2011) simplified the problem to a two-dimensional model in the vertical plane as shown in Fig. 4. Shang (1998) assumed the voltage to be 0 at the top boundary, which does not account for the actual situation. Xu *et al.* (2011) accounted for this boundary condition and derived the analytical solution

$$u(x, y, t) = \sum_{i=1}^{\infty} \frac{(2i-1)\pi y}{2L} \times \left\{ \sum_{m=1}^{\infty} [(\alpha_{mi} - \beta_{mi})\mathrm{e}^{-C_{mi}t} + \beta_{mi}] \times \sin\frac{(2m-1)\pi x}{2B} - \frac{4k_{\mathrm{e}}\gamma_{\mathrm{w}}V_{\mathrm{a}}x}{k_{\mathrm{h}}B(2i-1)\pi} \right\} \tag{24}$$

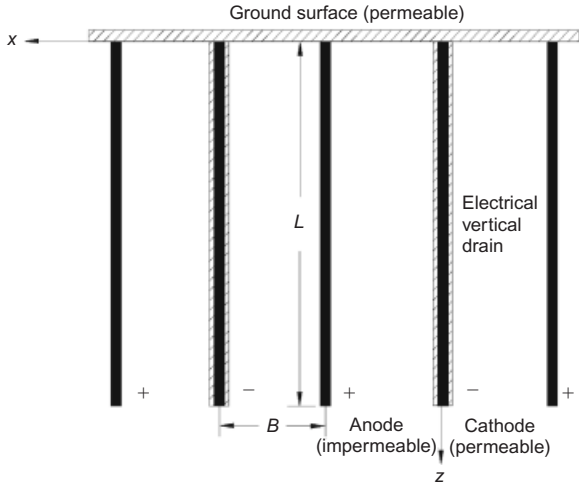

Fig. 4. Diagram of the two-dimensional model in vertical plane for electro-osmotic consolidation

$$C_{mi} = C_x\frac{(2m-1)^2\pi^2}{4B^2} + C_y\frac{(2i-1)^2\pi^2}{4L^2}$$

$$\alpha_{mi} = \frac{32k_{\mathrm{e}}\gamma_{\mathrm{w}}V_{\mathrm{a}}B(-1)^{m+1}}{k_{\mathrm{h}}(2m-1)^2(2i-1)\pi^3} \tag{25}$$

$$\beta_{mi} = \frac{8k_{\mathrm{e}}\gamma_{\mathrm{w}}V_{\mathrm{a}}BC_y(2i-1)(-1)^{m+1}}{C_{mi}k_{\mathrm{h}}(2m-1)^2\pi}$$

where C_x and C_y are the coefficients of consolidation in the horizontal and vertical directions; k_{h} is the hydraulic conductivity in the horizontal direction; B is the distance between the anode and the cathode.

Figure 5 shows the comparison of the proposed two-dimensional axisymmetric model with models proposed by Shang (1998) and Xu *et al.* (2011). The x-coordinate, T_x, is the time factor in the horizontal direction. The model proposed by Shang (1998) overestimates the degree of consolidation for the two-dimensional model in the vertical plane by about 8% at $T_x = 0{\cdot}01$, as there is a voltage gradient in the vertical direction attributable to the assumption of zero volts at the top boundary. The model proposed by Xu *et al.* (2011) overestimates the degree of consolida-

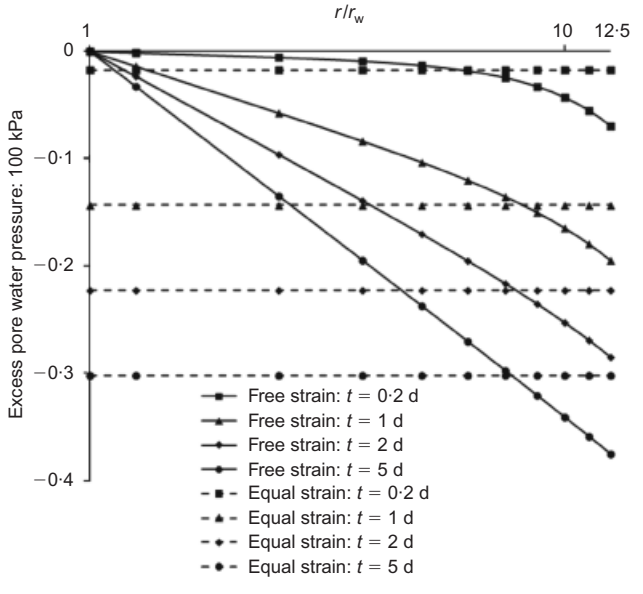

Fig. 3. Comparison of previous analytical result and proposed analytical result regarding excess pore-water pressure

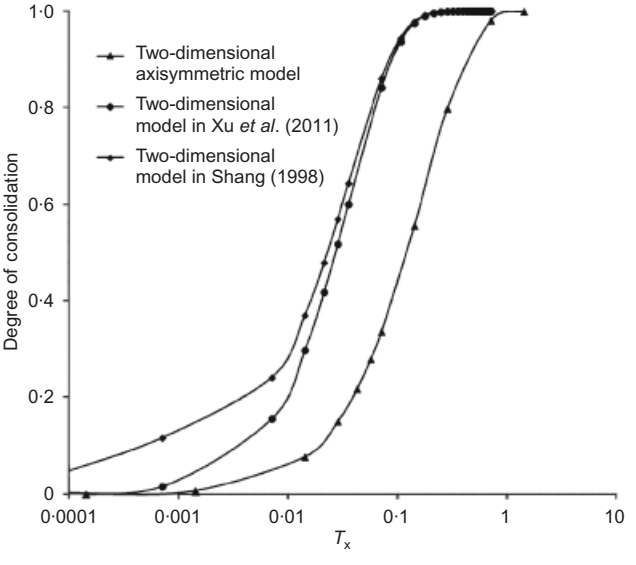

Fig. 5. Comparison of proposed analytical model and previous two-dimensional model in vertical plane about the degree of consolidation

tion by about 15% at $T_x = 0{\cdot}01$ and 50% at $T_x = 0{\cdot}1$ owing to the simplification from axisymmetric model to planar model.

Field application of the proposed analytical solution

Figure 2 gives the relationship between the degree of consolidation and the time factor. However, these curves are generated for a specific problem, given size of the EVD, basic properties of the soil and the electrical gradient. In order to develop useful information for practitioners, Fig. 6 was developed using three dimensionless variables, namely, r_e/L, S/L and G. The r_e/L value describes size of the treated zone, S/L is the ratio of final settlement at the anode to the thickness of the clay layer and G describes the electro-osmosis properties

$$G = \frac{k_e\, V_a}{k_r\, [(r_e + r_w)/2]\, \ln n} \tag{26}$$

With a designed EVD and treatment process, if the basic soil properties are measured, then Fig. 6 can be used to capture the relation between the final settlement and the electrical gradient. In the design of electro-osmotic consolidation, specifically for a given site with soil properties, it is possible either to select the treatment zone r or the treatment voltage to obtain desired settlement based on Fig. 6.

An example is analysed and the properties of the ground are supposed to be as follows: $k_e = 2{\cdot}5 \times 10^{-8}$ m^2/(s V), $k_r = 5 \times 10^{-10}$ m/s, $k_z = 2{\cdot}5 \times 10^{-10}$ m/s, $m_v = 0{\cdot}312$ MPa^{-1}, $L = 10$ m. The radius of the EVD is assumed to be 0·04 m and the applied voltage is set to be 12 V. If a settlement of 0·9 m is expected, then according to Fig. 6, r_e should be 0·75 m. When r_e is 0·75 m, G equals 520 and r_e/L equals 0·075. Then from the curve with G equals 520, S/H is 0·09, which means the settlement is 0·9 m. Therefore, during the installation of EVDs, the space between the anode and the cathode should be 0·75 m in order to obtain a settlement of 0·9 m, and this is also the optimal choice for r_e in this situation.

SUMMARY AND CONCLUSIONS

A two-dimensional axisymmetric model for electro-osmotic consolidation is proposed to describe the coupling of radial and vertical pore-water movement, and the analytical solution is derived to show the distribution of the excess pore water along the radial and vertical directions. Based on the developed analytical solutions, the following conclusions can be drawn.

(*a*) The proposed analytical model couples the pore-water movement in horizontal and vertical directions with electro-osmotic consolidation; the result indicates that with the decrease of vertical hydraulic conductivity, the settlement at the anode caused by electro-osmotic consolidation increases.

(*b*) The proposed analytical model is more general and can exactly describe the distribution of excess pore-water pressure along the radial direction, whereas previous models can only give the uniform excess pore-water pressure, owing to the equal strain hypothesis.

(*c*) Since EVDs are often installed in an equilateral triangular pattern, the axisymmetric model is more appropriate to describe the behaviour of soil than the planar model. The degree of consolidation is overestimated if the model is simplified from an axisymmetric model to a planar model.

(*d*) Design curves are developed for the electro-osmotic consolidation, which describes the relation between the final settlement, the electrode spacing, the soil properties and the applied voltage. Hence, the final settlement can be predicted using these charts for a given site configuration.

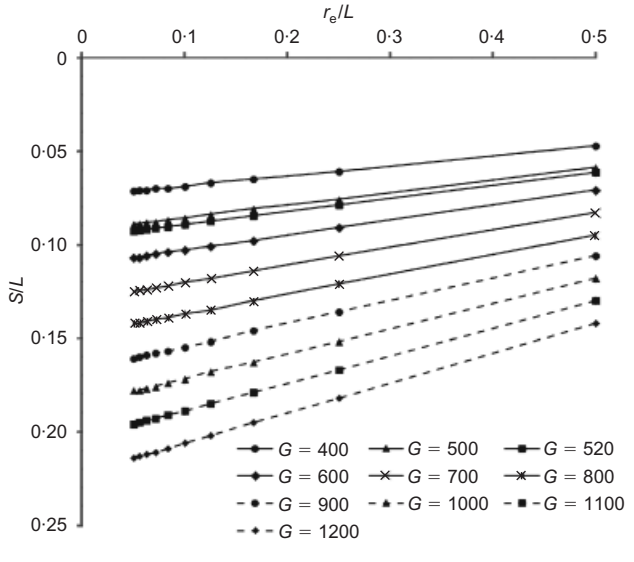

Fig. 6. Relation between S/L and r_e/L under different G

ACKNOWLEDGEMENTS

Financial support from the National Natural Science Foundation of China (NSFC50978139), National Key Basic Research Program (2012CB719804) of the Ministry of Science and Technology, and Tsinghua University (2010THZ02–1) is gratefully acknowledged.

NOTATION

B	length of the model
B_r	calculating factor for 1D axisymmetric model under equal strain condition, $B_r = \gamma_w r_e^2 m_v F_i$
C_i	calculating factor for 1D axisymmetric model without equal strain condition
C_v	coefficient of consolidation in the radial direction
C_x, C_y	coefficients of consolidation in horizontal and vertical directions for the planar model
D_0	function related to the first and second Bessel functions with an order of 0
D_1	function related to the first and second Bessel functions with an order of 1
E_0	Young's module
F_{im}	calculating factor for 2D axisymmetric model without equal strain condition
G	electro-osmosis properties of soil
H	total water head
H_0	total hydraulic head applied on the model
J_j, Y_j	the first and second Bessel functions with an order of j
k_e	electro-osmosis conductivity
k_r, k_z	hydraulic conductivities in the radial and vertical directions
L	depth of the model
M	calculating factor for 1D axisymmetric model under equal strain condition, $M = k_e \gamma_w (F_j/k_r)$
m_v	coefficient of volume compressibility
n	ratio of diameters of the model to the EVD
r_w, r_e	radii of the central EVD and the model
S/L	ratio of diameters of the final settlement at anode to thickness of clay layer
T_x	time factor in horizontal direction for the planar model
U	degree of consolidation for the 2D axisymmetric model
$\bar{U}$	average degree of consolidation for the 1D axisymmetric model

u pore-water pressure for the 2D model in the vertical plane
$\bar{u}$ average excess pore-water pressure in the radial direction for the 1D axisymmetric model
V voltage in the model
V_a applied voltage on the whole model
v_r, v_z pore-water flow velocities in the radial and vertical directions
γ_w unit weights of water and saturated soil
ε_v volumetric strain of soil mass
λ_i the solution for $D_0(\lambda^{1/2} \times r_e) = 0$ where i equals 1, 2, 3...
μ Poisson's ratio

REFERENCES

Barron, R. A. (1948). Consolidation of fine-grained soils by drain wells. *ASCE Trans*. **113**, 718–754.

Bjerrum, L., Moum, J. & Eide, O. (1967). Application of electro-osmosis to a foundation problem in Norwegian quick clay. *Géotechnique* **17**, No. 3, 214–235, http://dx.doi.org/10.1680/geot.1967.17.3.214.

Carrillo, N. (1942). Simple two and three dimensional cases in the theory of consolidation of soils. *J. Mathl Physics* **21**, No. 1, 1–5.

Casagrande, L. (1983). Stabilization of soils by means of electro-osmotic state-of-art. *J. Boston Civ. Eng. ASCE* **69**, No. 3, 255–302.

Casagrande, D. R., Casagrande, L. & Castro, G. (1986). Improvement of sensitive silty clay by electro-osmosis: Discussion. *Can. Geotech. J.* **23**, No. 1, 95–96.

Chew, S. H., Karunatatne, G. P., Kuma, V. M. (2004). A field trial for soft clay consolidation using electric vertical drains. *Geotextiles and Geomembranes* **22**, No. 1, 17–35.

Esrig, M. I. (1968). Pore pressures, consolidation and electrokinetics. *J. Soil Mech. Found. Engng Div., ASCE* **94**, SM4, No. 7, 899–921.

Glendinning, S., Lamont-Black, J., Jones, C. J. F. P. & Hall, J. (2008). Treatment of lagooned sewage sludge in situ using electrokinetic geosynthetics. *Geosynthetics Int*. **15**, No. 3, 192–204.

Hansbo, S. (1981). Consolidation of fine-grained soils by prefabricated drains. *Proc. 10th Int. Conf. Soil Mech. Found. Engng, Stockholm* **3**, 677–682.

Hu, L. M., Wu, W. L. & Wu, H. (2010). Theoretical analysis and numerical simulation of electro-osmosis consolidation for soft clay. *Rock Soil Mech.* **31**, No. 12, 3977–3983 (in Chinese).

Hu, L. M., Wu, W. L. & Wu, H. (2012). Numerical model of electro-osmotic consolidation in clay. *Géotechnique* **62**, No. 6, 537–541, http://dx.doi.org/10.1680/geot.11.T.008.

Indraratna, B., Rujikiatkamjorn, C. & Sathananthan, L. (2005). Analytical and numerical solutions for a single vertical drain including the effects of vacuum preloading. *Can. Geotech. J.* **42**, No. 4, 994–1014.

Li, Y., Gong, X. N., Lu, M. M. & Guo, B. (2010). Coupling consolidation theory under combined action of load and electro-osmosis. *Chin. J. Geotech. Engng* **32**, No. 1, 77–81 (in Chinese).

Onoue, A. (1988). Consolidation by vertical drains taking well resistance and smear into consideration. *Soils Found*. **28**, No. 4, 165–174.

Shang, J. Q. (1998). Electro-osmotic enhanced preloading consolidation via vertical drains. *Can. Geotech. J.* **35**, No. 3, 491–499.

Su, J. & Wang, Z. (2003). The two-dimensional consolidation theory of electro-osmosis. *Géotechnique* **53**, No. 8, 759–763, http://dx.doi.org/10.1680/geot.2003.53.8.759.

Wan, T. Y. & Mitchell, J. K. (1976). Electro-osmotic consolidation of soils. *J. Geotech. Engng Div., ASCE* **102**, No. 5, 473–491.

Wu, H. & Hu, L. (2012a). Analytical and numerical solutions for vacuum preloading considering a radius related strain distribution. *Mech. Res. Comm.* **44**, No. 1, 9–14.

Wu, H. & Hu, L. M. (2012b). Analytical models of the coupling of vacuum preloading and electro-osmosis consolidation for ground stabilization. *J. Tsinghua Univ. (Sci. & Tech.)* **52**, No. 2, 182–185 (in Chinese).

Xie, K. H. & Zeng, G. X. (1989). Consolidation theories for drain wells under equal strain condition. *Chin. J. Geotech. Engng* **11**, No. 2, 3–17 (in Chinese).

Xu, W., Liu, S. H., Wang, L. J. & Wang, J. B. (2011). Analytical theory of soft ground consolidation under vacuum preloading combined with electro-osmosis. *J. Hohai Univ. (Nat. Sci.)* **30**, No. 2, 169–175 (in Chinese).

Gajo, A. *et al.* (2013). *Géotechnique* **63**, No. 11, 977–982 [http://dx.doi.org/10.1680/geot.SIP13.P.013]

TECHNICAL NOTE

Improving the mechanical response of kaolinite and bentonite through exposure to organic and metallorganic compounds

A. GAJO*, A. MADASCHI*, F. GIRARDI* and R. DI MAGGIO*

The mechanical response of soft clays can be modified through change of the adsorbed ions or by adding lime or cement using deep mixing tools. This work focuses on analysing the effects induced by a new class of chemical agents, which can be driven through soft clays and lead to cementing bonds, without being associated with any deformation. The resulting technique could be of benefit for improving in situ soil properties, for instance beneath existing foundations. Both kaolinite and sodium- and potassium-bentonites are subjected to different chemical compounds, considering the effects on the liquid limit, residual friction angle and apparent preconsolidation pressure.

KEYWORDS: clays; chemical properties; compressibility; consolidation; laboratory tests; shear strength

INTRODUCTION

Few methods are proposed in the literature and put into practice to improve the in situ mechanical properties of clays; these include reducing their water content (by preloading embankments or electrosmosis); chemical changes induced by cation exchange (Ingles & Metcalf, 1972); and adding lime and/or cement with deep mixing tools (Broms & Boman, 1979). All traditional methods are associated with settlement, however, and are not applicable underneath building foundations.

The present work focuses on analysing the effects induced by a new class of chemical agents that can be driven through soft clays (e.g. by electro-grouting), leading to the formation of cementing bonds at interparticle contacts and reducing compressibility, owing to their good affinity with the surface groups on the faces and edges of clay particles. Laboratory tests have been conducted to assess the effects of polyvinyl alcohol (PVA), sodium polyvinyl alcoholate (sodium-PVA), silicon and/or aluminium alkoxides on the liquid limit, the residual friction angle and the apparent preconsolidation effects of both kaolinite and sodium (Na)- and potassium (K)-bentonites.

MECHANISMS OF INTERACTION BETWEEN ORGANIC AND METALLORGANIC COMPOUNDS AND CLAY PARTICLES

Organic–clay nanocomposites have recently been developed for numerous industrial applications (as a catalytic support, to adsorb organic or inorganic substances and in packaging), modifying clay mainly by means of cation exchange reactions with alkyl ammonium salts that increase the interlayer spacing where other molecules can be inserted, changing the clay's chemical nature (Stackhouse *et al.*, 2001; Adebajo *et al.*, 2003; Ray & Okamoto, 2003; Nakatsuji *et al.*, 2004; Viville *et al.*, 2004; Unuabonah *et al.*, 2008).

The sol–gel route (Brinker & Scherer, 1989) has also been explored with this aim: alkoxy silanes, such as tetraethylorthosilicate (TEOS) or 3-methacryloxypropyl trimethoxysilane (MPTMS), can adhere in thin, glassy layers to clay particles through hydrolysis and condensation with the silanols and aluminols (Si–OH and Al–OH) on their edges, and with the silanols on the defects in the clay basal planes. The residual hydroxyl groups on these thin layers can form bridging bonds between the clay particles, with cementing effects. Such effects can also be produced by aluminium hydroxide, prepared by way of sol–gel (sol–aluminium hydroxide ($Al(OH)_3$)) containing short oligomers, usually nuclei for the growth of aluminium oxide.

Polymers such as PVA can modify clays in other ways. Polymer bridging reportedly induced a remarkable increase in the viscosity of concentrated kaolin suspensions (Jarnstrom *et al.*, 1993). The adsorption of PVA onto kaolinite is also reported to occur weakly on basal planes and mainly on hydroxyl groups originating from octahedral sheets on clay edges (Sjoberg *et al.*, 1999). Some authors have suggested that the main mechanism behind PVA adsorption on montmorillonite (Isci *et al.*, 2004) is intercalation between the platelets, leading to cation displacement. Backfolk *et al.* (2006) stated that this latter mechanism is applicable to impurities of montmorillonite as well and accounts for PVA adsorption in kaolinite.

In the present study, sodium- and potassium-bentonite and kaolinite were modified using TEOS, MPTMS, sol–aluminium hydroxide, PVA and sodium-PVA in different concentrations.

MATERIALS AND METHODS

Tests were performed on commercial Speswhite kaolin and natural, active sodium-bentonite. The liquid limit and plastic index are $w_L = 63$ and $I_p = 22$ for kaolinite and $w_L = 436$ and $I_p = 384$ for sodium-bentonite. The specific surface is 14 m^2/g for kaolinite (supplier's data) and 260 m^2/g for sodium-bentonite (Di Maio, personal communication, 2005). Sodium-bentonite consists of almost pure smectite (Calvello *et al.*, 2005). Potassium-bentonite was prepared by mixing dry sodium-bentonite with a concentrated potassium chloride solution, leaving the resulting suspension to age for 2 days before washing it with distilled water. The liquid limit of the resulting potassium-bentonite was $w_L = 100$ (Di Maio & Fenelli, 1994; Di Maio, 1996, 1998).

For details of the experimental programme, see Gajo & Maines (2007) and Wahid *et al.* (2011a, 2011b).

Manuscript received 1 March 2012; revised manuscript accepted 15 January 2013. Published online ahead of print 25 March 2013. Discussion on this paper closes on 1 February 2014, for further details see p. ii.

*Dipartimento di Ingegneria Civile, Ambientale e Meccanica, Università di Trento, Trento, Italy.

The term 'prepared' refers here to a sample obtained by mixing dry clay (about 400 g) with 1 l of the selected sol, leaving the resulting clay suspension to age for 3–4 days, then repeatedly siphoning off the supernatant and adding distilled water to wash the clay. The term 'exposed' describes a sample initially prepared with water, then the pore fluid's chemical composition was changed under a given stress state in an oedometer apparatus.

RESULTS OF MECHANICAL TESTS

Liquid limit of clays prepared with different sols

The liquid limit, zeta-potential and pH of the kaolinite samples prepared with the different sols are given in Table 1. The effects induced by the different sols are much larger than those induced by acid and base solutions (Wahid *et al.*, 2011a): PVA and TEOS lower the liquid limit, whereas sol–aluminium hydroxide raises it. The effects on the liquid limit are completely unrelated to the effects on the zeta-potential, and correlate weakly with the variations in pH.

The effects on the sodium- and potassium-bentonite samples are given in Table 2. As in kaolinite, TEOS and sodium-PVA lower the liquid limit in sodium-bentonite, and sol–aluminium hydroxide raises it. In contrast, all the sols considered increase the liquid limit of potassium-bentonite. As in kaolinite, the zeta-potential and pH of both sodium- and potassium-bentonites are scarcely related to the liquid limit. Preparation with the different sols changes the sign of the potassium-bentonite's zeta-potential from positive to negative, however, denoting the change of electrical charge on the particle's surface.

Residual shear strength of clays prepared with different sols

The residual shear strength was assessed in the ring shear apparatus (Bromhead, 1979) applying a vertical stress of 100, 200 and 400 kPa. The results are plotted in Fig. 1 (for kaolinite) and Fig. 2 (for bentonite) in terms of the residual friction ratio ($\tan \phi'_r = \tau/\sigma'_v$) as proposed by Chattopadhyay (1972) to linearise the plots in the low-pressure range.

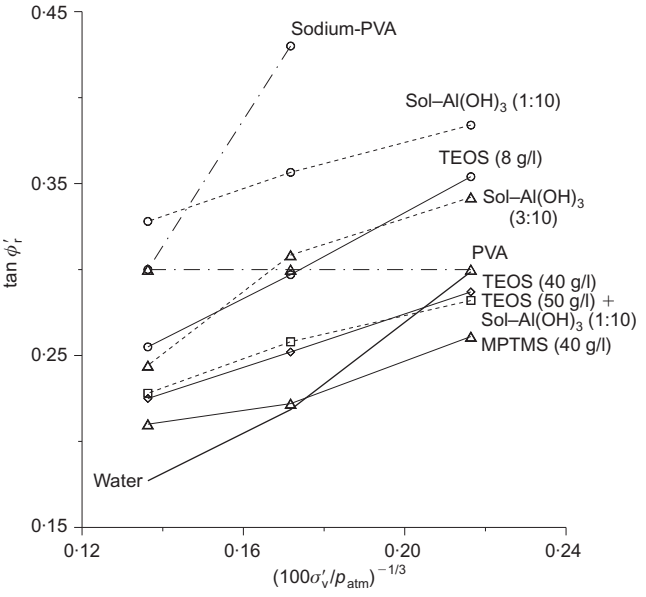

Fig. 1. Residual strength of kaolinite samples prepared with different sols of organic and metallorganic compounds

Figure 1 shows that TEOS (8 g/l), sol–aluminium hydroxide (dilution 1:10) and sodium-PVA greatly increase the residual strength of kaolinite. The changes in residual strength are not, however, related to changes in the liquid limit (from Table 1), probably attributable to rolling shearing.

Figure 2 shows that, unlike kaolinite, the changes induced in the residual strength of both sodium- and potassium-bentonites are fairly consistent with the variations of the liquid limit; that is, the compounds generally increase the liquid limit (and reduce the residual shear strength) of

Table 1. Influence of the sol's composition on the liquid limit, zeta-potential and pH of kaolinite, after a curing time of about 3–4 days

Materials	Liquid limit	Zeta-potential: mV	pH
Kaolinite + sodium-PVA	46	−34·89	10·12
Kaolinite + PVA	49	−23·07	6·41
Kaolinite + TEOS (40 g/l)	50	−23·26	5·21
Kaolinite + TEOS (50 g/l) + sol–aluminium hydroxide (1:10)	54	−5·40	4·72
Kaolinite + MPTMS (40 g/l)	61	−7·10	4·28
Kaolinite + distilled water	63	−55·82	5·27
Kaolinite + sol–aluminium hydroxide (1:10)	74	−15·00	4·75
Kaolinite + sol–aluminium hydroxide (3:10)	76	−32·62	4·80

Table 2. Influence of the sol's composition on the liquid limit, zeta-potential and pH of sodium- and potassium-bentonite, after a curing time of about 3–4 days

Materials	Liquid limit	Zeta-potential: mV	pH
Sodium-bentonite + TEOS (8 g/l)	343	—	—
Sodium-bentonite + sodium-PVA	356	−45·05	10·41
Sodium-bentonite + distilled water	436	−39·09	7·50
Sodium-bentonite + PVA(10 g/l)	450	−43·72	9·23
Sodium-bentonite + sol–aluminium hydroxide (1:10)	472	−60·55	9·01
Potassium-bentonite + distilled water	100	20·21	7·56
Potassium-bentonite + sodium-PVA	104	−43·51	10·47
Potassium-bentonite + TEOS (50 g/l)	130	−38·37	7·00
Potassium-bentonite + PVA	158	−43·36	9·71
Potassium-bentonite + TEOS (50 g/l) + sol–aluminium hydroxide (1:10)	176	−49·37	8·10
Potassium-bentonite + sol–aluminium hydroxide (1:10)	295	−49·18	8·17

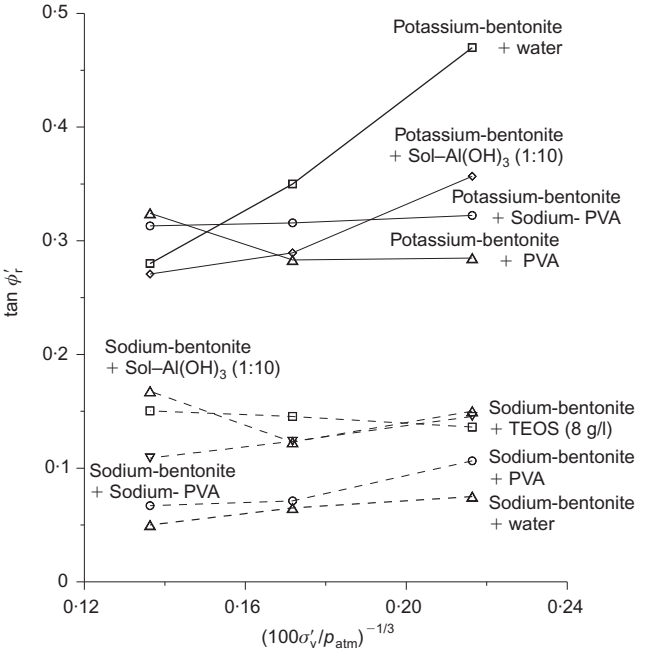

Fig. 2. Residual strength of sodium- and potassium-bentonite samples prepared with different sols of organic and metallorganic compounds

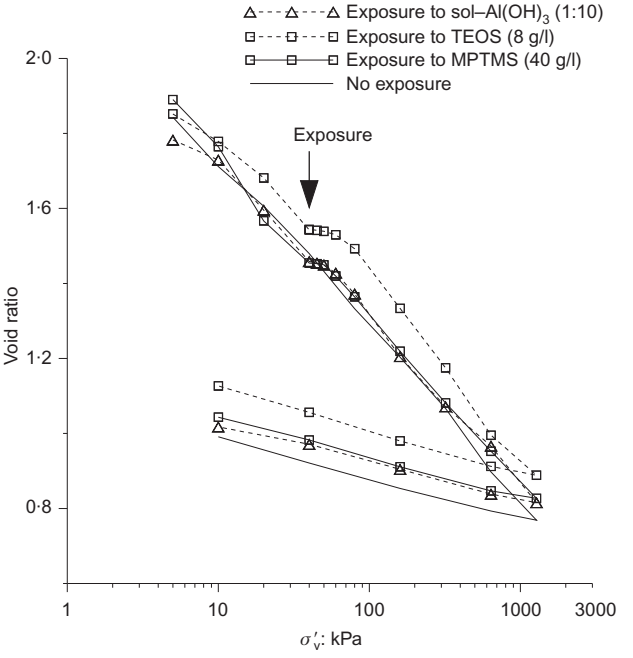

Fig. 3. Comparison of one-dimensional compression and swelling tests performed on three kaolinite samples prepared with deionised water and later exposed to TEOS (8 g/l), MPTMS (40 g/l) and sol-aluminium hydroxide (1:10) at the vertical effective stress of 40 kPa

potassium-bentonite, and decrease the liquid limit (and increase the residual shear strength) of sodium-bentonite.

Mechanical effects induced by exposing clay samples to different sols

Some water-prepared samples were submitted to a given effective stress (from 10 to 320 kPa) under oedometric conditions and then exposed to advection of the different sols by applying a small difference in hydraulic head ($h = 1{\cdot}00$ m) between the upper and lower porous stone. Then the percolating sol was replaced with distilled water to verify the stability of any cementation effects, even under a change of pore fluid. Flushing for about 1 week for kaolinite and 1 month for bentonite ensured the flow of a sufficiently large volume of fluid (2–3 times the pore volume of the sample). Then mechanical loading was resumed.

Figure 3 shows the results obtained in kaolinite samples exposed to TEOS (8 g/l), MPTMS (8 g/l) and sol–aluminium hydroxide (dilution 1:10), under a vertical effective stress of 40 kPa. Exposure to metallorganic compounds leads to a very small apparent preconsolidation pressure for MPTMS and sol–aluminium hydroxide, and a much larger one for TEOS. The apparent preconsolidation is presumably due to the formation of cementing bonds between kaolinite particles. These results can be compared with the null effects induced by the exposure of kaolinite to sodium chloride (Wahid *et al.*, 2011b).

Some kaolinite samples were also exposed to TEOS (8 g/l) under vertical effective stresses ranging between 10 and 320 kPa. As shown in Fig. 4, the greater the vertical effective stress on the sample, the smaller the apparent preconsolidation effects, in a logarithmic scale.

One kaolinite sample was prepared with TEOS (8 g/l) and submitted to conventional loading up to 40 kPa; loading was then interrupted for 1 week, and then resumed. No figure is shown here for the sake of brevity, but the results showed that apparent preconsolidation in the prepared sample after ageing for a week is somewhat smaller than in the sample exposed for 1 week.

The apparent preconsolidation induced by exposure to

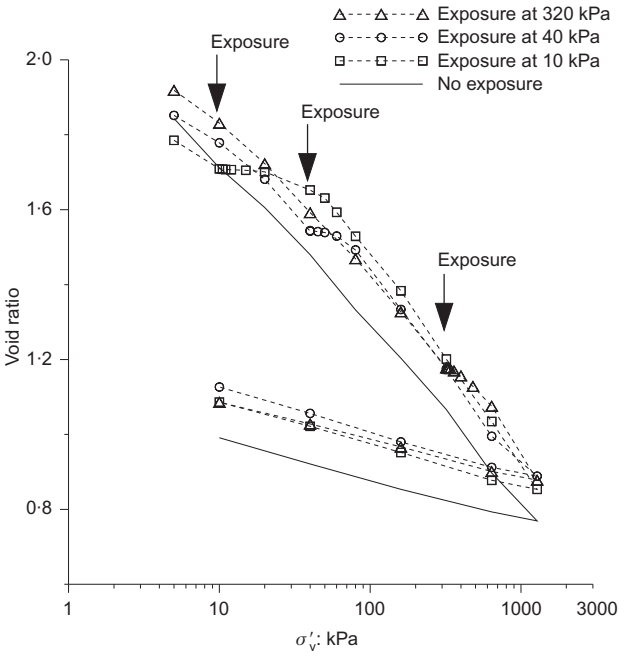

Fig. 4. Comparison of one-dimensional compression and swelling tests performed on three kaolinite samples prepared with deionised water and later exposed to TEOS at different vertical stresses (ranging between 10 kPa and 320 kPa).

TEOS (8 g/l) is consistent with some qualitative effects seen in kaolinite prepared with TEOS. After being washed with distilled water and left in a container for several days, the kaolinite samples prepared with TEOS displayed a sensitive behaviour (Fig. 5): their initial consistency was completely lost after remoulding, and the samples became fluid. The chemical bonds resulting from the clays' surfaces interacting with TEOS therefore remain active even after washing, prompting an apparent preconsolidation and a sensitive behaviour.

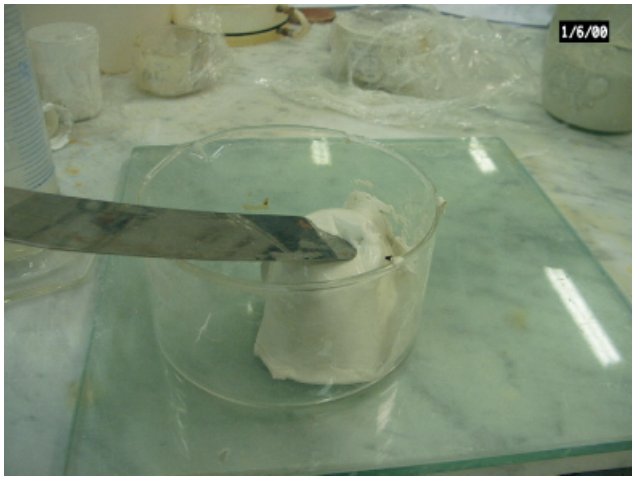

(a)

(b)

Fig. 5. Sensitive behaviour of a kaolinite sample which was first prepared with TEOS solution, then washed with distilled water and subsequently left for a few days at rest in a container: (a) initial consistency and (b) consistency after remoulding

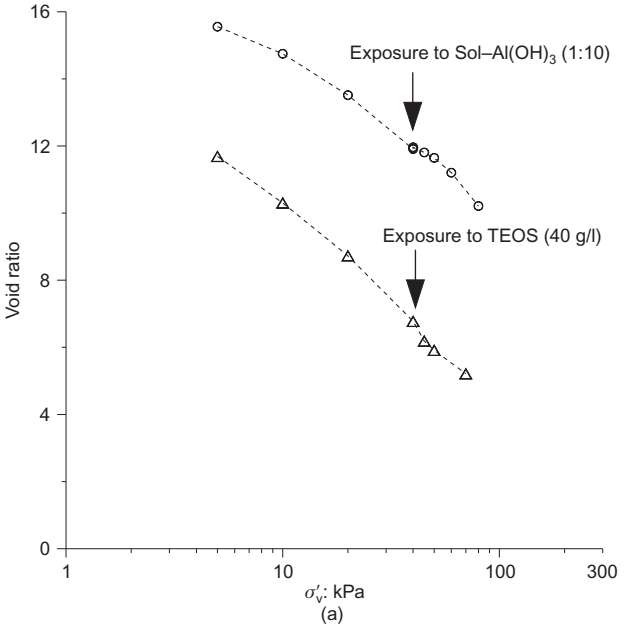

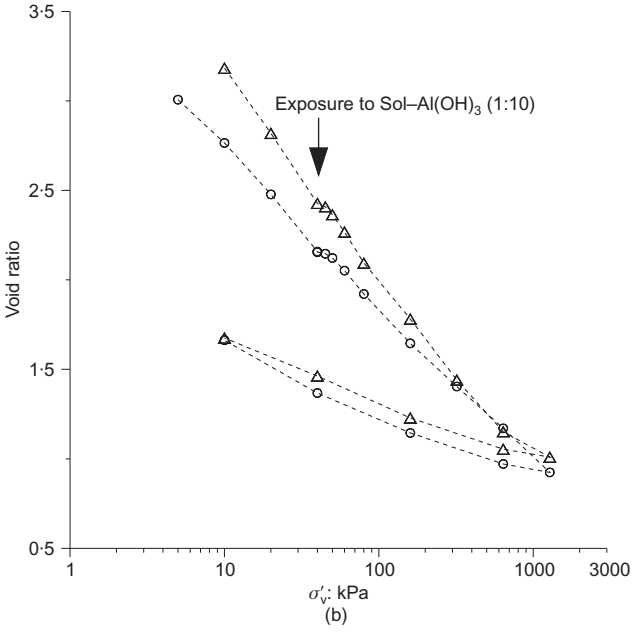

Fig. 6. Comparison of one-dimensional compression and swelling tests performed on (a) sodium-bentonite and (b) potassium-bentonite samples prepared with deionised water and later exposed to TEOS and sol–aluminium hydroxide at the vertical effective stress of 40 kPa

The tests performed on sodium- (Fig. 6(a)) and potassium-bentonite (Fig. 6(b)) were stopped because the exposure and washing times took too long (more than a month each), but the experimental data collected sufficed to identify the effects of the chemical exposure. In sodium-bentonite, mineral contacts were expected to be negligible owing to the strong surface interaction between particles, preventing the creation of cementation bonds. This prediction was confirmed in that sol–aluminium hydroxide induces a negligible apparent preconsolidation and TEOS has even smaller effects (Fig. 6(a)). In potassium-bentonite, on the other hand, because mineral contacts between the particles are relatively more common, cementation effects were expected to be stronger, and the experimental results confirmed as much (Fig. 6(b)). Given the negligible effects seen in sodium-bentonite (Fig. 6(a)), exposure to TEOS was not considered for potassium-bentonite (Fig. 6(b)). The fact that sol–aluminium hydroxide has a greater apparent preconsolidation effect than TEOS is consistent with the former having a greater affinity for the surface of bentonite particles than the latter. The apparent preconsolidation induced by sol–aluminium hydroxide in potassium-bentonite is smaller than in the case of kaolinite.

RESULTS OF SEM, HT-DSC AND XRD ANALYSES

Scanning electronic microscopy (SEM), high-temperature differential scanning calorimetry (HT-DSC) and X-ray diffraction (XRD) analyses on treated and untreated clays can provide some interesting insight. Untreated sodium-bentonite (Fig. 7(a)) has a powdery appearance and the clay's morph-

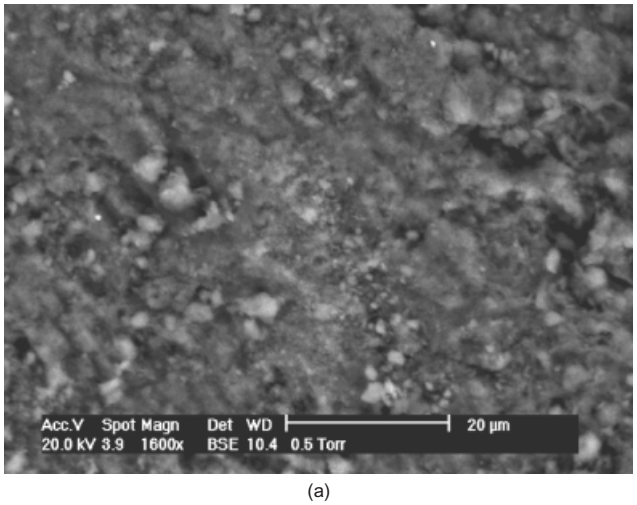

(a)

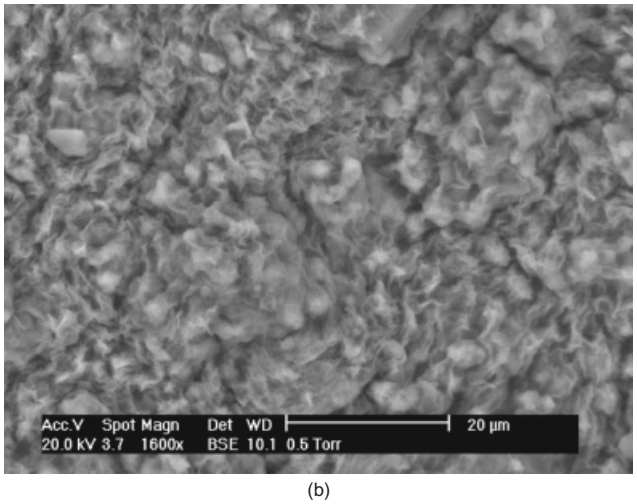

(b)

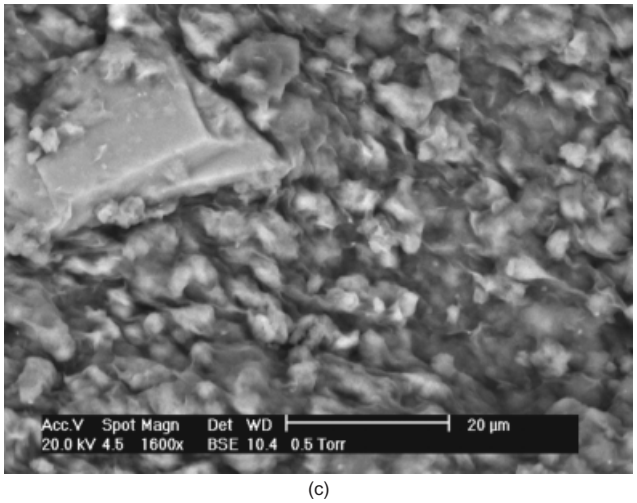

(c)

Fig. 7. Scanning electron microscopy photographs of (a) sodium-bentonite, sodium-bentonite prepared with (b) sodium-PVA and (c) sol–aluminium hydroxide (dilution 1:10), respectively

ology was profoundly modified by exposure to sodium-PVA and sol–aluminium hydroxide (Figs 7(b) and 7(c)), with the powder forming clumps in both cases.

Any change in the HT-DSC curves vis-à-vis the untreated clay suggests structural modifications induced by the chemical treatment. Based on results of the present study, sodium-PVA is more effective because the peak in Fig. 8, attributable to dehydroxylation, has almost disappeared owing to structural changes. This was confirmed by XRD analyses (Fig. 9).

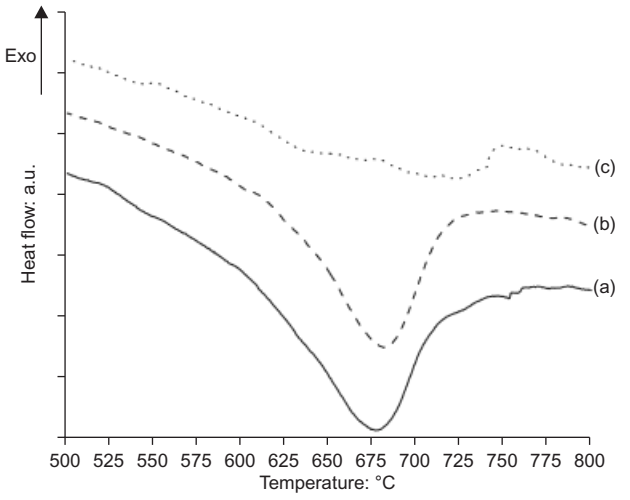

Fig. 8. High-temperature differential scanning calorimetry curves of: (a) sodium-bentonite; (b) sodium-bentonite + sol–aluminium hydroxide; (c) sodium-bentonite + sodium-PVA

Similar to the results of Nakao & Nogami (2005), the peak shift to a lower angle (from 8·7° to 7·3°) is observed in sodium-bentonite treated with sodium-PVA, corresponding to expansion of the interlayer spacing between the clay layers.

CONCLUSIONS

This paper focuses on the mechanical effects induced by a new class of metallorganic compounds with a good affinity for the surface groups on the faces and edges of clay particles, which have already been seen to modify the rheological properties of clay suspensions. The new compounds offer the chance to improve the mechanical response of clays under a given stress state, without inducing any deformation. Consequently, the possible use of these compounds beneath existing foundations is worthy of exploration.

A complete characterisation of their effects on kaolinite and sodium- and potassium-bentonites was conducted by evaluating the liquid limit, zeta-potential, pH and residual friction angle of clay samples prepared with different sols.

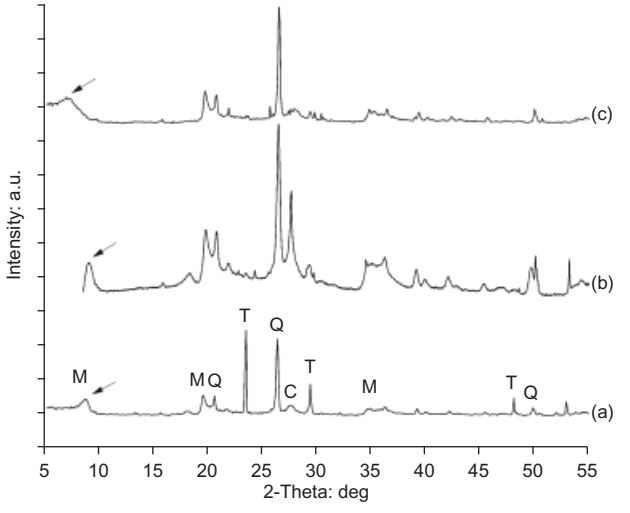

Fig. 9. X-ray diffraction spectra of: (a) sodium-bentonite; (b) sodium-bentonite + sol–aluminium hydroxide; (c) sodium-bentonite + sodium-PVA (M refers to montmorillonite, Q to quartz, T to trydimite and C to calcite)

Other samples were exposed to the different sols under a given vertical effective stress in an oedometer cell. Exposing kaolinite to TEOS was found to induce an apparent preconsolidation and a sensitive response. A similar (but slightly smaller) effect was seen in potassium-bentonite exposed to sol–aluminium hydroxide.

ACKNOWLEDGEMENTS

The financial support of University of Trento is gratefully acknowledged. The authors would like to thank Laviosa Chimica Mineraria for supplying natural sodium-bentonite and T. Leone, A. Casazza, L. Mazzi, E. Fietta and E. Gocevska for their invaluable help in performing some of the experimental tests; special thanks are also due to Mrs W. Vaona for the HT-DSC, zeta-potential and pH measurements.

NOTATION

h	hydraulic head
I_p	plastic index
p_{atm}	atmospheric pressure
$\tan \phi'_r$	tangent of residual friction angle
w_L	liquid limit
σ'_v	vertical effective stress
τ	shear stress

REFERENCES

Adebajo, M. O., Frost, R. L., Kloprogge, J. T. & Carmody, O. (2003). Porous materials for oil spill cleanup: A review of synthesis and absorbing properties. *J. Porous Mater.* **10**, No. 3, 159–170.

Backfolk, K., Rosenholm, J. B., Husband, J. & Eklund, D. (2006). The influence of surface chemical properties of kaolin surfaces on the adsorption of poly(vinyl alcohol). *Colloids and Surfaces A: Physicochem. Engng Aspects* **275**, No. 1–3, 133–141.

Brinker, C. J. & Scherer, G. W. (1989). *Sol–gel science: the physics and chemistry of sol–gel processes*. London, UK: Academic Press.

Broms, B. B. & Boman, P. (1979). Lime columns – a new foundation method. *J. Geotech. Engng Div. ASCE* **105**, No. 4, 539–556.

Bromhead, E. N. (1979). A simple ring shear apparatus. *Ground Engng* **12**, No. 5, 40–44.

Calvello, M., Lasco, M., Vassallo, R. & Di Maio, C. (2005). Compressibility and residual strength of smectite clays: influence of pore acqueous solutions and organic solvents. *Ital. Geotech. J.* **39**, No. 1, 34–46.

Chattopadhyay, P. K. (1972). *Residual shear strength of some pure clay minerals*. PhD thesis, University of Alberta, Edmonton, Canada.

Di Maio, C. & Fenelli, G. B. (1994). Residual strength of kaolin and bentonite: the influence of their constituent pore fluid. *Géotechnique* **44**, No. 2, 217–226, http://dx.doi.org/10.1680/geot.1994.44.2.217.

Di Maio, C. (1996). Exposure of bentonite to salt solution: osmotic and mechanical effects. *Géotechnique* **46**, No. 4, 695–707, http://dx.doi.org/10.1680/geot.1996.46.4.695.

Di Maio, C. (1998). Discussion on exposure of bentonite to salt solution: osmotic and mechanical effects. *Géotechnique* **48**, No. 3, 433–436, http://dx.doi.org/10.1680/geot.1998.48.3.433.

Ingles, O. G. & Metcalf, J. B. (1972). *Soil stabilization, principles and practice*. London, UK: Butterworths.

Isci, S., Gunister, E., Ece, O. I. & Gungor, N. (2004). The modification of rheologic properties of clays with PVA effect. *Mater. Lett.* **58**, No. 12–13, 1975–1978.

Gajo, A. & Maines, M. (2007). Mechanical effects of aqueous solutions of inorganic acids and bases on a natural active clay. *Géotechnique* **57**, No. 8, 687–699, http://dx.doi.org/10.1680/geot.2007.57.8.687.

Jarnstrom, L., Nickel, J. & Rigdahl, M. (1993). Aggregation in coating colours based on kaolin and poly(vinyl alcohol) and its effect on the properties of the coating. *Nord. Pulp Paper Res. J.* **2**, No. 1, 250–257.

Nakatsuji, M., Ishii, R., Wang, Z. & Ooi, K. (2004). Preparation of porous clay minerals with organic-inorganic hybrid pillars using solvent-extraction route. *J. Colloid Interface Sci.* **272**, No. 1, 158–166.

Nakao, T. & Nogami, M. (2005). Preparation of silica-pillared clays with micro- and meso-pores using aminopropyltriethoxysilane and tetraethoxysilane. *Mater. Lett.* **59**, No. 26, 3221–3225.

Ray, S. S. & Okamoto, M. (2003). Polymer/layered silicate nanocomposites: a review from preparation to processing. *Prog. Polym. Sci.* **28**, No. 11, 1539–1641.

Sjoberg, M., Bergstrom, L., Larsson, A. & Sjostrom, E. (1999). The effect of polymer and surfactant adsorption on the colloidal stability and rheology of kaolin dispersions. *Colloids Surf. A: Physicochem. Engng Aspects* **159**, No. 1, 197–208.

Stackhouse, S., Coveney, P. V. & Sandre, E. (2001). Plane-wave density functional theoretic study of formation of clay-polymer nanocomposite materials by self-catalyzed in situ intercalative polymerization. *J. Am. Chem. Soc.* **123**, No. 47, 11764–11774.

Unuabonah, E. I., Adebowale, K. O., Olu-Owolabi, B. I. & Yang, L. Z. (2008). Comparison of sorption of Pb^{2+} and Cd^{2+} on kaolinite clay and polyvinyl alcohol-modified kaolinite clay. *Adsorption* **14**, No. 6, 791–803.

Viville, P., Lazzaroni, R., Pollet, E., Alexandre, M. & Dubois, P. (2004). Controlled polymer grafting on single clay nanoplatelets. *J. Am. Chem. Soc.* **126**, No. 29, 9007–9012.

Wahid, A. S., Gajo, A. & Di Maggio, R. (2011a). Chemo-mechanical effects in kaolinite. Part 1: prepared samples. *Géotechnique* **61**, No. 6, 439–447, http://dx.doi.org/10.1680/geot.8.P.067.

Wahid, A. S., Gajo, A. & Di Maggio, R. (2011b). Chemo-mechanical effects in kaolinite. Part 2: exposed samples and chemical and phase analyses. *Géotechnique* **61**, No. 6, 449–457, http://dx.doi.org/10.1680/geot.8.P.068.

Ciantia, M. O. & Hueckel, T. (2013). *Géotechnique* **63**, No. 9, 768–785 [http://dx.doi.org/10.1680/geot.SIP13.P.024]

Weathering of submerged stressed calcarenites: chemo-mechanical coupling mechanisms

M. O. CIANTIA* and T. HUECKEL†

Long portions of the Apulian coast are steep cliffs in carbonate soft rocks. These, especially the calcarenite, are affected by weathering processes that markedly alter their mechanical properties with time, potentially leading to instability of coastal geomorphological structures. Such alterations are mainly due to chemical reactions between the solid and fluid phases, and are driven by chemical variables, which are internal variables and hence uncontrollable. In a search for the variables that drive the process of rock weakening, recourse is made to the micro scale, at which most of the chemical processes are observed and quantified. Observations using scanning electron microsope, thin sections and X-ray computed tomography analyses appear to be crucial for the understanding, interpretation and definition of the degradation mechanisms of the material. A chemo-mechanical coupled model at the meso scale of the chemically reactive stressed porous system is presented and framed in the context of a multi-scale scenario of an array of coupled phenomena. An analogous model at the macro scale is developed in parallel together with upscaling and identification procedures for meso-scale and macro-scale material constants. The main outcome of the study is a tool for predicting the progress of time-dependent weathering phenomena, potentially allowing the stability of geological structures to be assessed as it evolves with a progressing chemical degradation in a specific configuration and under a specific set of loads.

KEYWORDS: chemical properties; plasticity; rocks/rock mechanics; soft rocks

INTRODUCTION

The Apulian coast (south-east Italy) is affected by weathering processes that are typical of calcarenite cliffs (Fig. 1). The factors that control the degradation processes are multiple, but the main ones are the force of waves and rock strength decay (Andriani & Walsh, 2007a). A pressing question that arises is whether any portion of the shore may become mechanically unstable and, if so, how quickly. For parts of the coast that are relatively protected from wave energy, such as large caverns or inland abandoned mines, chemical weathering is the principal degradation mechanism. It is convenient to separate the interaction of rock with water over the short term from that over the long term. Calcarenite may instantly lose up to 60% of its dry strength at the point when water fills its pores (the short-term effect; Castellanza *et al.*, 2009; Eslami *et al.*, 2010; Ciantia *et al.*, 2013), while when it is continuously saturated, it weakens owing to dissolution of the grains and bonds over the long term (Castellanza & Nova, 2004; Ghabezloo & Pouya, 2006; Ciantia *et al.*, 2013). It is known that the strength of carbonate rocks depends on their volume fraction that is filled with calcite (Hueckel *et al.*, 1998). The short-term loss and regain of strength is seen as a result of suspension and re-sedimentation of solid mineral into and from the fluid (Ciantia *et al.*, 2013). It is a reversible process for a small number of wetting–drying cycles in a closed system (Castellanza *et al.*, 2009). However, for a larger number of cycles, the dry strength may not be fully recovered, whereas the strength in wet conditions remains about the same over the short term (Andriani & Walsh, 2007b). The long-term changes are seen as irreversible. In Fig. 2 the two types of behaviour are represented schematically. It is clear that the wet strength constitutes a lower bound for all the other above conditions, making the long-term mechanism of dissolution the most critical for the material stability.

Here, the authors concentrate on the long-term interaction of calcarenite with water. This process appears to be a fully coupled chemo-mechanical phenomenon, as the dissolution rate is proportional to the effective surface area (Sjöberg, 1976), which increases as a result of the formation of microcracks (Scholz, 1968; Krajcinovic, 1989). There are several situations where physico-chemical processes are the cause of instability inception and collapse, such as chemical decomposition of intact granite caused by water transforming feldspar and mica into clay (Lumb, 1962), and mudslides in clay slopes affected by a change in the salinity and/or acidity of pore water (Moore & Brunsden, 1996; Shuzui, 2001, 2002; Zhao *et al.*, 2011).

SUMMARY OF FINDINGS AT THE MICRO SCALE

The questions at hand are as follows. What phenomena occur upon long-term soaking of calcarenite in water? What are the controlling variables for the dissolution of stressed calcarenites? The answers are sought at the scale at which the considered phenomena could be quantified. The complexity of the mechanisms, and their dependence on different time and space scales, require the adoption of a multi-scale approach.

The material studied is a highly porous calcarenite of Gravina di Puglia; its features, as listed in Table 1, are taken from Ciantia *et al.* (2013). The structure of the calcarenite is seen in thin sections with both the polarised light microscope and the scanning electron microscope (SEM). The

Manuscript received 5 March 2012; revised manuscript accepted 6 November 2012. Published online ahead of print 1 February 2013. Discussion on this paper closes on 1 December 2013, for further details see p. ii.

* Politecnico di Milano, Milano, Italy.
† Duke University, Civil and Environmental Engineering, Durham, NC, USA.

This paper is dedicated to Professor Zenon Mróz on the occasion of his 80th birthday, and in recognition of the tremendous impact that his creativity, originality and scientific rigour have had on the area of geomechanics.

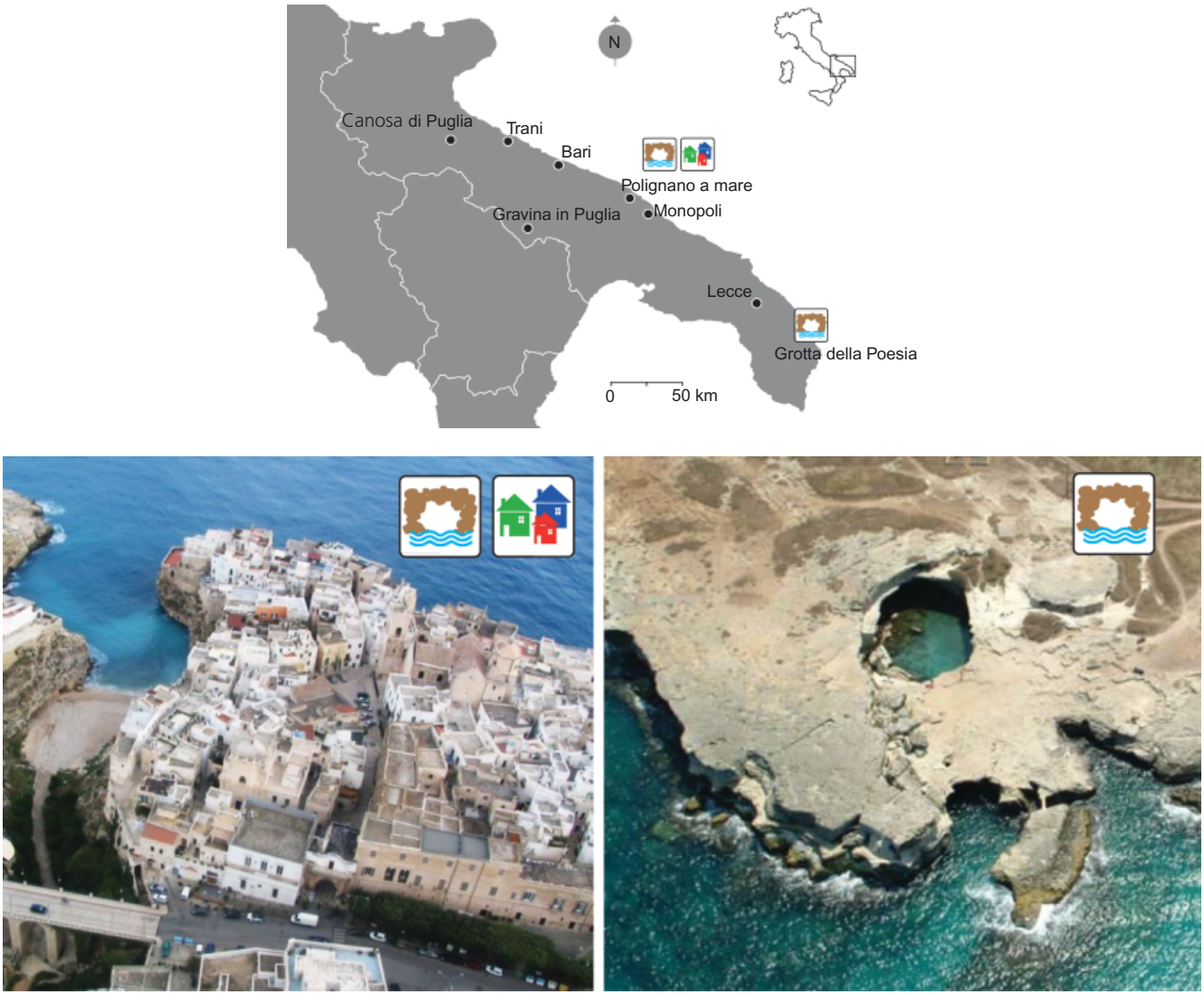

Fig. 1. Map of Apulian coast and two air views of coast morphology. A risk analysis study is necessary to predict the time evolution of cavern expansion in densely populated areas to avoid the scenario on the right occuring in the area shown on the left

chemical and pore space, and free surface area characterisation, are obtained via energy-dispersive X-ray spectroscopy (EDS), mercury intrusion porosimetry (MIP) and X-ray micro-computed tomography (MCT) respectively. The findings are as follows.

(*a*) Grains and bonds in the solid structure are formed of calcite microcrystals that have a characteristic length of 5 μm (Fig. 3(c)).
(*b*) About 50% of the pore volume is due to macropores that have an average radius ranging between 25 and 250 μm, while the rest is due to micropores ($25\ \mu m > r > 0{\cdot}01\ \mu m$) (Fig. 4).
(*c*) Two distinct types of bond – strong (type A) and weak (type B) – are visible in the microstructure. What distinguishes them is the history of formation of the bond. The strong bonds are bridges of calcite formed through a diagenetic process, whereas the weak bonds are formed by a mixture of the calcite 'powder' and seawater salts that precipitates as sediment into a meniscus-shaped bond when water evaporates; it is re-suspended when water refills the pores (Delenne *et al.*, 2011). These two types of bond are observed in SEM and in thin sections (Fig. 5) (Ciantia *et al.*, 2013).
(*d*) The chemical composition of the calcarenite of concern (determined by EDS) is 98% calcium carbonate and some traces of aluminium and magnesium.
(*e*) 99% of the porosity of calcarenite is connected (see X-ray MCT, yielding a three-dimensional structure; Fig. 6).
(*f*) The specific surface area results as $2{\cdot}7\ m^2/g$, as determined by X-ray MCT and MIP.

A SCENARIO OF THE LONG-TERM DEGRADATION PROCESS

In what follows, the material is considered as continuously saturated and perfectly drained. The main component of calcarenite, calcite ($CaCO_3$), dissolves easily in water (Plummer & Wigley, 1976; Kier, 1980; Morse *et al.*, 2007). We postulate that some calcite is dissolved in the pore fluid, diminishing the dimensions of bonds and grains (and increasing the porosity), and hence reducing the material strength at the macro scale (Castellanza, 2002) (Fig. 7).

To quantify such a process, the following meso-scale scenario is proposed. A meso-pore surrounded by deformable rock matrix is referred to as being filled with water, as shown in the micrograph in Fig. 3(b). Water penetrating radially from the fluid/rock interface is postulated to effect

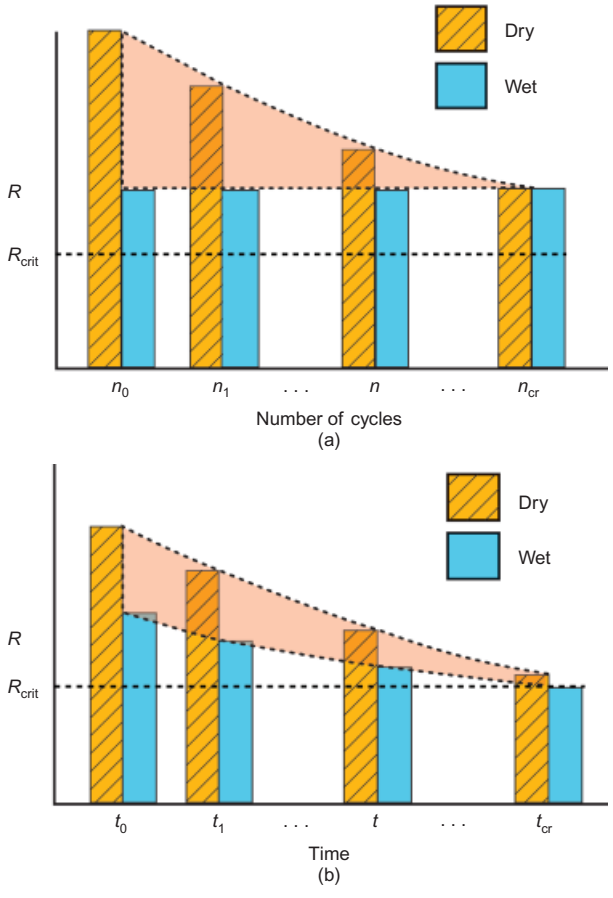

Fig. 2. (a) Short-term cyclic effect affects only the dry strength; (b) to reduce wet peak strength, long-term dissolution is required

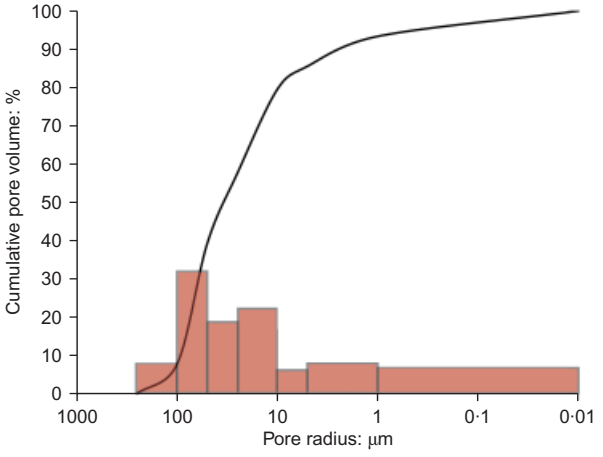

Fig. 4. Pore size distribution obtained as mean value of distributions obtained from mercury intrusion porosimetry, two-dimensional image analysis of thin sections and three-dimensional image analysis of micro-CT tests

Table 1. Geotechnical properties of the analysed calcarenite

γ_d: kN/m^3	γ_{sat}: kN/m^3	G_s	n	e
13	18	2·73	0·52	1·08

dissolution of the mineral. If the material is stressed and at yielding, the developing irreversible microcracks induce an increase in the specific surface area. As the reaction rate per volume of fluid is proportional to the surface area at the fluid/solid interface, it follows that the rate is coupled to the mechanical damage.

In order to develop a numerical model for such a mechanism, it is necessary to refer to representative elementary volumes (REV) and variables at the scale at which it is taking place. To arrive at predictions at a macro scale (Fig. 8(a)), or even a regional scale, a multi-scale model is necessary. The formulation for dissolution and specific surface area increase is developed at the micro scale (Fig. 8(c)), whereas the phenomena of damage described above are formulated at a meso-scale level of a pore (Fig. 8(b)). Finally, quantities from these two scales are transferred to the macro scale, at which continuum mechanics constitutive models are formulated.

CHEMICAL DISSOLUTION OF CALCARENITE IN STRESSED CONDITIONS

Whereas the kinetics of dissolution of calcite has been studied for some time (e.g. Krauskopf & Bird, 1995), the effect of stress and deformation on the material's dissolution has largely been ignored. The present authors present a possible approach to account for the influence of the material mechanical damage on the rate of mass loss from calcarenite. The rate at which calcium carbonate dissociates into water solution is directly proportional to the area of the interface between the two phases (Sjöberg, 1976). In acidic conditions it depends on the pH of the fluid (Sjöberg & Rickard, 1984). The rate constant k and the reacting surface

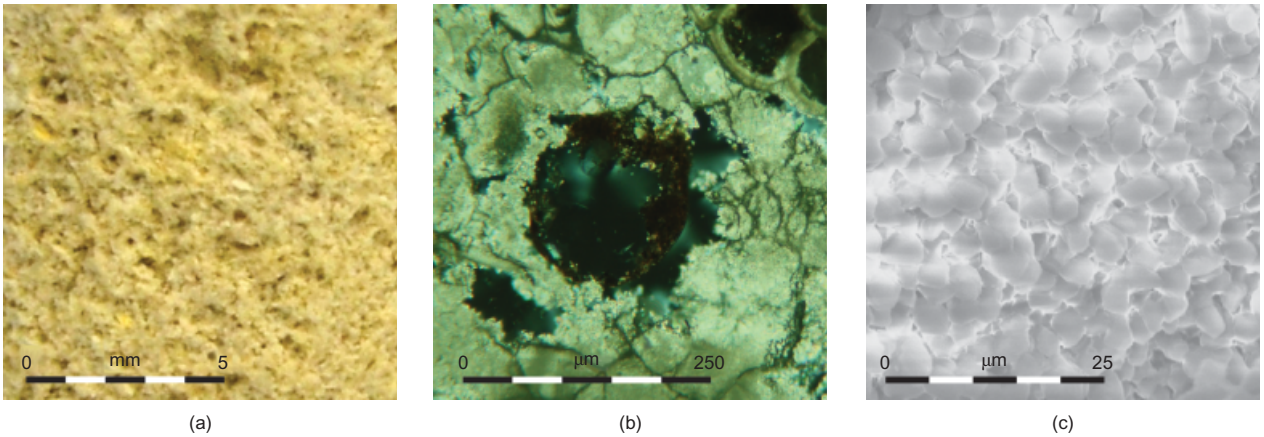

Fig. 3. (a) Macroscopic view of calcarenite; soft rock is porous, yellow-whitish stone. (b) A macro pore observed through polarised light microscope. (c) Calcite microcrystals with characteristic length 5 μm. The whole solid mass comprises these microcrystals

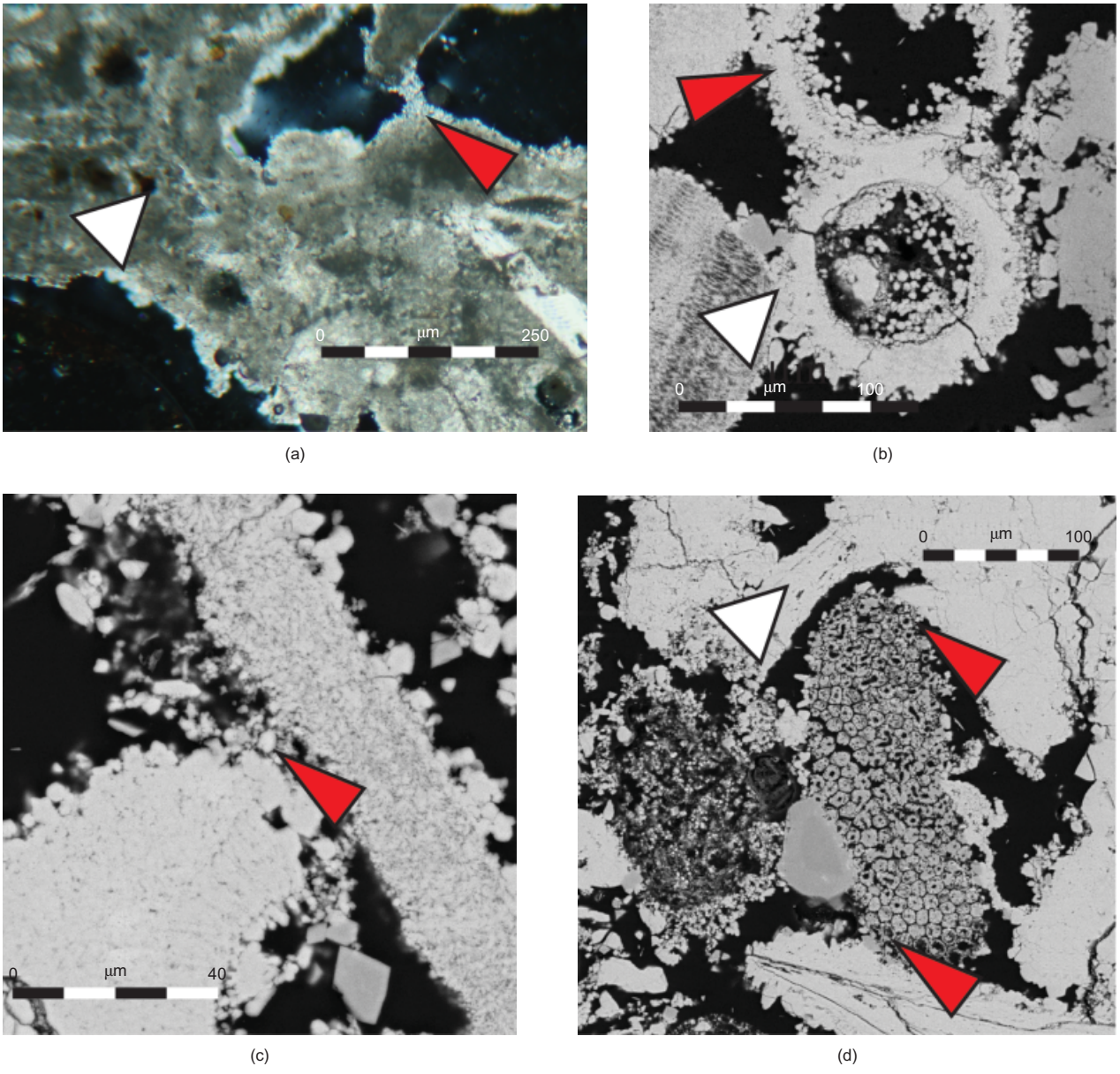

Fig. 5. Thin sections of calcarenite observed with (a) polarised light microscope and (b)–(d) scanning electron microscope. Thick white arrows indicate bonds classified as type A; darker thin arrows indicate type B bond

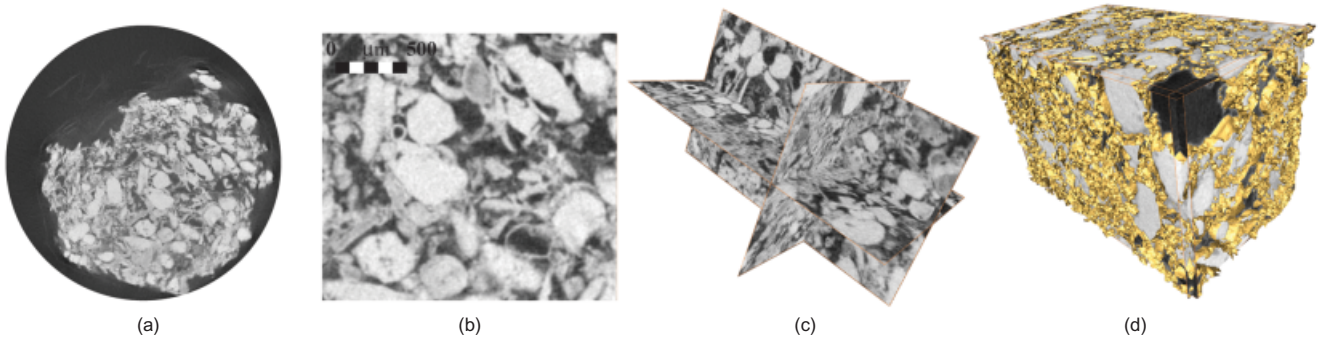

Fig. 6. Elaboration of X-ray micro computed tomography results. The structure is reconstructed in three dimensions, starting from (a) by scanning sample into slices and recomposing the whole solid slice by slice. Porosity, pore-size distribution and effective surface area can be estimated through detailed analyses. (a) Slice; (b) slice section; (c)–(d) three-dimensional reconstruction of part of the sample

area A in Sjöberg's equation are in $1/cm^2$s and cm^2 respectively. Generalising this rate equation, the present authors refer to the reactive surface area per the actual reacting fluid volume. Hence Sjöberg's rate constant needs to be recalculated to account for the actual reacting fluid volume. In the absence of the effective actual reacting fluid volume for Sjöberg's tests, a volume is estimated as follows. Buhmann & Dreybrodt (1985a, 1985b) observed that, beyond the layer thickness of the adjacent water of about 0·002–0·005 cm, the dissolution rate of calcite becomes independent of the

Fig. 7. Schematic representation of mass loss due to dissolution of calcium carbonate. (a) Initial state: structure is held together by type A and type B bonds. (b) As water fills the pores, type B bonds fall into suspension, and dissolution of structure begins. (c)–(f) With time, mass is lost, and material is weakened

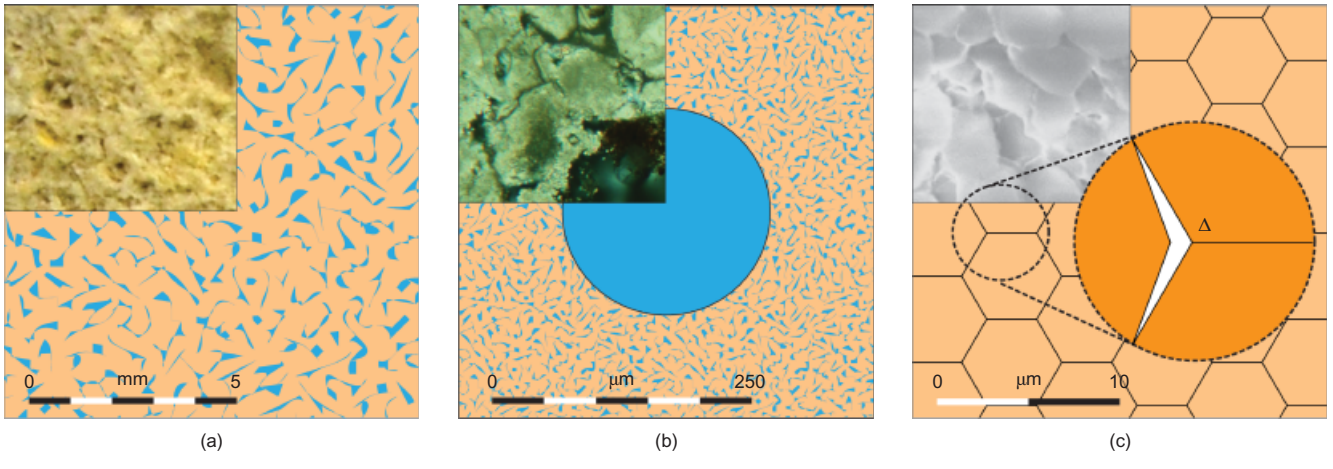

Fig. 8. (a) Macro-REV; (b) meso-REV; (c) micro-REV

reacting fluid volume. Calculating the actual reacting fluid volume by multiplying a unit area (1 cm^2) by the limit thicknesses just mentioned, an adjusted apparent rate constant k_b^* in cm/s is obtained for Sjöberg's tests. Hence, replacing Sjöberg's coefficient k with k_b^* or k_a^*, and the surface A with A^*, in cm^2/cm^3 the kinetic equation reads

$$\frac{d[M]}{dt} = -k_b^* A^* M^m \{C - [Ca^{2+}]^{1/2}[CO_3^{2-}]^{1/2}\} \quad \text{for } 7.5 < pH < 14$$
$$\frac{d[M]}{dt} = -k_a^* A^* M^m [H^+] \quad \text{for } 4 < pH < 7.5 \qquad (1)$$

where k_b^* and k_a^* are apparent rate constants (1 cm/s) for neutral and acidic pH conditions respectively; A^* is the calcite specific surface area per unit reacting fluid volume in cm^2/cm^3, M^m is the molecular mass of calcium carbonate in g/mol; $[H^+]$ is the concentration of hydrogen ions in the fluid; and C is a constant that is a function of the root of k_{sp}, equal to $2{\cdot}47e^{-7}$ mol/cm^3 (Sjöberg, 1976).

The accumulated relative mass removal of calcite from the solid (or reaction progress) reads

$$\xi = \frac{\Delta[M]}{[M_0]} = \frac{[M_0] - [M]}{[M_0]} \qquad (2)$$

where $[M_0]$ is the initial calcite mass per unit reacting fluid

volume. Therefore the rate of relative dissolved mass results as

$$\xi = k_b^* A^* \frac{M^m}{[M_0]}\{C - [Ca^{2+}]^{1/2}[CO_3^{2-}]^{1/2}\} \quad \text{for } 7.5 < \text{pH} < 14$$
$$\xi = k_a^* A^* \frac{M^m}{[M_0]}[H^+] \quad \text{for } 4 < \text{pH} < 7.5 \tag{3}$$

ξ is constrained by the inequality $0 \leqslant \xi \leqslant 1$ (De Groot, 1966). When $\xi = 1$, the reaction is completed: that is, all the calcite is removed.

The present authors adopt a recently developed concept (Hu & Hueckel, 2007a, 2007b) of dissolution, enhanced by the creation of a new internal surface area of solid/fluid interface generated by the local damage. The damage consists in the opening of microcracks, the walls of which become sites of additional dissolution. A scalar internal variable $\tilde{a}$ represents the amount of the added surface area. The surface area of the microcracks can be measured via acoustic emission, as proportional to the acoustic energy released during cracking. Variable $\tilde{a}$ is linked to the reaction area A^* in equation (3) according to

$$\tilde{a} = \frac{A^* - A_0^*}{A_0^*} \tag{4}$$

The internal interface surface area generated by the microcracking can be assessed using a model of a two-dimensional hexagonal crystal assembly (Hu & Hueckel, 2007b). The surface area is proportional to the volumetric irreversible strain, ε_v^{irr}, and inversely proportional to an average crack opening at the apex, Δ, considered as a rock characteristic (see e.g. Fig. 8(c)).

$$\tilde{a} = \frac{8}{\sqrt{3}\Delta}\left|\varepsilon_v^{irr}\right| \cdot 1 \text{ m} \quad \text{if } \varepsilon_v^{irr} < 0 \tag{5}$$

Hence

$$A^* = f\left(\varepsilon_v^{irr}\right) = \begin{cases} A_0^*\left(1 + \phi\left|\varepsilon_v^{irr}\right|\right) & \text{if } \varepsilon_v^{irr} < 0 \\ A_0^* & \text{if } \varepsilon_v^{irr} \geqslant 0 \end{cases} \tag{6}$$

where $\phi = (8/\sqrt{3}\Delta) \cdot 1$ m is a proportionality constant, and A_0^* represents the effective surface area of pre-existing voids. The former inequality restricts the range of validity of the expression to the dilatancy strain only. The latter inequality excludes possible compressive volumetric strains not associated with microcracking. Substituting equation (6) in equation (3) and using Macaulay brackets ($\langle x \rangle := (x + |x|/2)/2$),

$$\xi = k_b^* A_0^*(1 + \phi\langle -\varepsilon_v^{irr}\rangle)\{C - [Ca^{2+}]^{1/2}[CO_3^{2-}]^{1/2}\} \quad \text{with } 0 \leqslant \xi \leqslant 1 \text{ for a basic pH}$$
$$\xi = k_a^* A_0^*(1 + \phi\langle -\varepsilon_v^{irr}\rangle)\frac{M^m}{[M_0]}[H^+] \quad \text{with } 0 \leqslant \xi \leqslant 1 \text{ in acid} \tag{7}$$

Denoting

$$K_c^b = k_b^* A_0^* \frac{M^m}{[M_0]}\{C - [Ca^{2+}]^{1/2}[CO_3^{2-}]^{1/2}\}$$
$$K_c^a = k_a^* A_0^* \frac{M^m}{[M_0]}[H^+] \tag{8}$$
$$K^{b,a} = \phi K_c^{b,a}$$

equation (3) can be written as

$$\xi = K^j\langle -\varepsilon_v^{irr}\rangle + K_c^j \text{ with } 0 \leqslant \xi \leqslant 1 \text{ and } j = \text{a or b if in acid or base} \tag{9}$$

where K_c^j is a function related to the ionic concentrations in the fluid and the surface area of the pre-existent pore space per unit volume of water in the rock. Integrating equation (9) with respect to time, one may calculate the mass removal accumulated from the onset of the process. The time variable is the reaction time, which may depend on the history of the environmental conditions, such as water saturation, or on the general chemical conditions of the water, such as pH level.

$$\xi = \int_0^t K^j\langle -\varepsilon_v^{irr}\rangle dt + K_c^j t \tag{10}$$

In this work the system considered is an open system (Fig. 9), which means that fresh water constantly washes the pores at a rate greater than the reaction rate, keeping ionic concentration low. Notably, for pH values less than 8, $[CO_3^{2-}]$ becomes negligible, and dissolution is at its fastest rate (Sjöberg, 1976): hence equation (8) becomes

$$K_c^b = k_b^* A_0^* \frac{M^m}{[M_0]}C$$
$$K_c^a = k_a^* A_0^* \frac{M^m}{[M_0]}[H^+] \tag{11}$$
$$K^{b,a} = \phi K_c^{b,a}$$

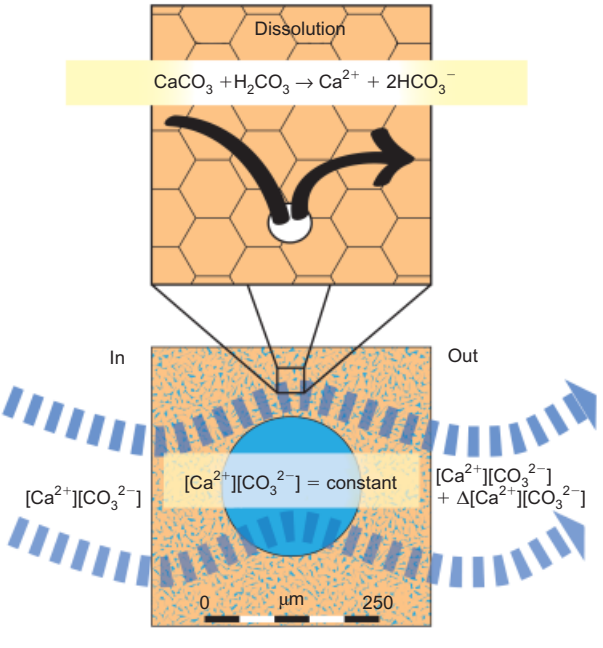

Fig. 9. Open-system scenario; ionic concentration in meso-REV is constant, as Ca^{2+} production due to dissolution is small compared with water entry/exit rate

The above assumptions make the accumulated mass removal (equation (10)) dependent only on deformation, the reaction time, and k_{sp} or $[H^+]$, depending on the pH regime. The strain rate, as formulated within rigid hardening plasticity theory, is a homogeneous function of order one of the stress rate and the rate of reaction (Hu & Hueckel, 2007a) (see also e.g. Mróz (1973)): hence the integrated mass removal ξ is a linear function of the reaction time. Experimental tests are performed in both acid and basic pH regimes in order to determine the two constants k_a^* and k_b^*. Calcarenite is dissolved, measuring pH and the mass variation with time. Tests 1–3, shown in Fig. 10, represent calcarenite dissolved in the acidic regime for a closed system. The pH grows from A to B as the $[H^+]$ ions are consumed during the reaction. By contrast, test 4 is performed in the basic regime for an open system scenario. The K_c^a/A_0^* line is obtained by interpolating the experimental points in the acid regime, whereas the K_c^b/A_0^* line is the horizontal line passing from experimental point 4. The $K^{a,b}/A_0^*$ lines are obtained by translating the $K_c^{a,b}/A_0^*$ lines vertically by an amount proportional to ϕ. In the same graph, Sjöberg's recalculated constants are also reported. In the basic regime, if the system is closed, the reaction continues until equilibrium is reached: hence $[Ca^{2+}]^{1/2}[CO_3^{2-}]^{1/2} = C$, at which point the reaction stops (see equation (8)). A larger set of experiments is obtained in the acidic regime because of the high reaction rate. By contrast, at neutral pH the reaction is so slow that very long periods are necessary to obtain measurable mass changes.

CHEMO-MECHANICAL COUPLING AT A SINGLE PORE SCALE

The objective is now to establish a relationship between the deformation due to compressive stress and ensuing damage, and dissolution of calcite at the interphase interfaces. The present authors consider a meso-scale representative elementary volume (meso-REV) of a single pore between four bonded grains and subjected to a constant isotropic compression (Fig. 11(a); after Hu & Hueckel (2007a)). The scenario of the chemo-mechanical loading process comprises the following circumstances and phenomena.

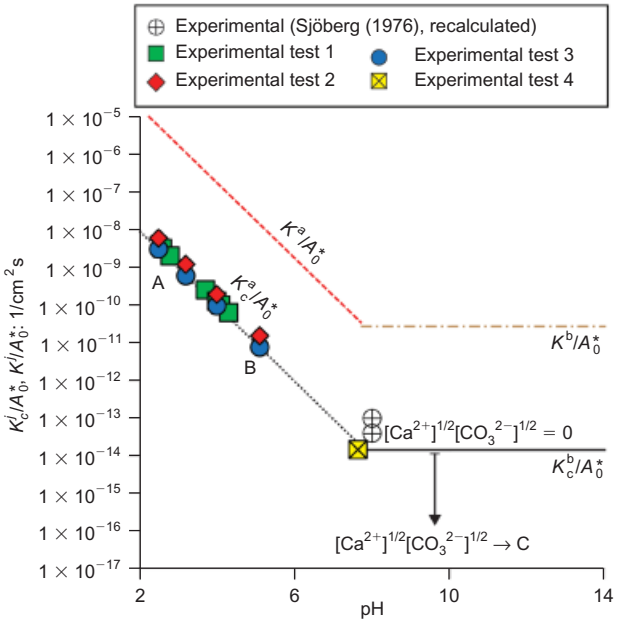

Fig. 10. Reaction rate per unit initial specific area as function of pH

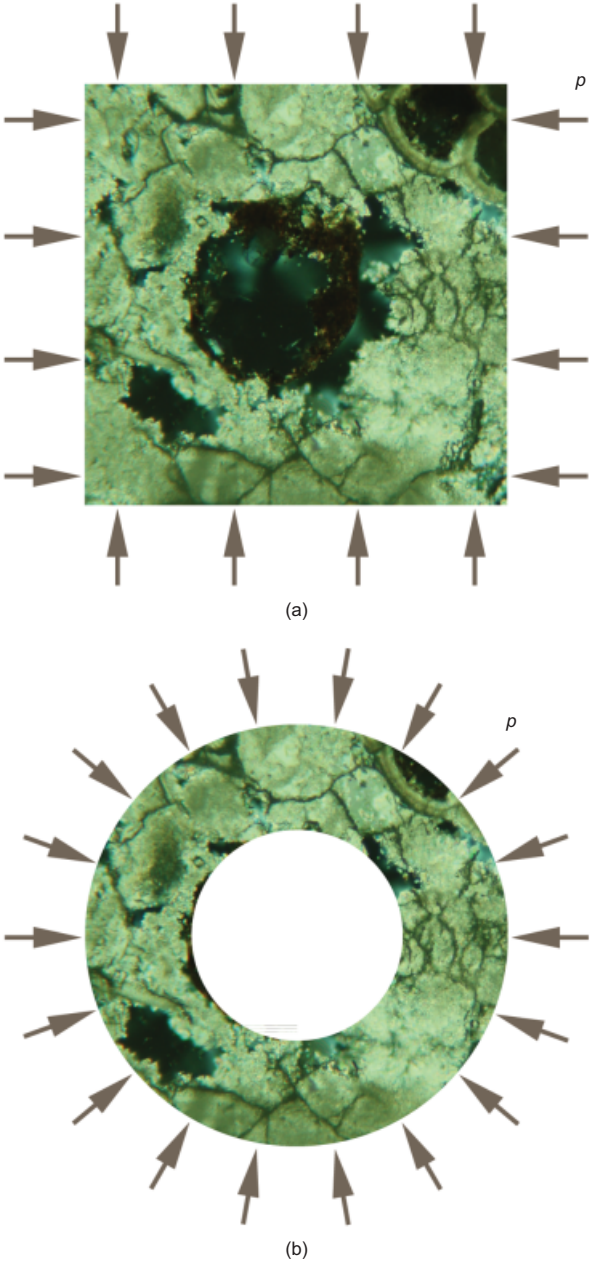

Fig. 11. Isotropic compression: (a) meso-REV, (b) corresponding thick cylinder

(*a*) The material is isotropic and rigid-plastic.
(*b*) Strains are small.
(*c*) The REV (Fig. 8) is saturated with water, the pore system is interconnected, and the material is drained.
(*d*) Initially, the material is in the rigid regime; yielding and deformation are induced by the dissolution.
(*e*) Yielding produces strain and dilatancy damage, linked to microcracking.
(*f*) Microcracking generates new solid/fluid interfaces diffused over the considered boundary value problem (BVP).
(*g*) Dissolution occurs as a kinetic process.
(*h*) The dissolution rate is proportional to specific surface area, and increases with the newly generated interfaces.
(*i*) Two coupled mechanisms contribute to the plastic hardening: volumetric strain-hardening and mass removal softening.
(*j*) The dissolved species in the micropores diffuse instantaneously across the solid.
(*k*) The chemo-mechanical behaviour of the meso-pore is

represented by that of a plain-strain cylinder surrounding the pore, which in turn is represented by its cavity (Fig. 11(b)).

(*l*) Both the mechanical and chemical processes are axially symmetric with respect to the centre of the cylinder cavity.

The above assumptions translate into solving the following problem: radial compression of a rigid-plastic cylinder affected by the chemical damage (Fig. 12). The problem is similar to the grain indentation addressed by Hu & Hueckel (2007a) to model soil ageing. The mathematical formulation of the BVP is an extension of an analogous problem formulated by Hill (1950), and investigated for granular media by Mróz & Kwaszczynska (1971) and Hueckel & Mróz (1973) to include the chemo-mechanical coupling.

Stress boundary conditions are applied at $r = a$ and $r = b$, while the lateral constraints are ignored. At the inner boundary $r = a$, $\sigma_r = 0$, while at the outer boundary $r = b$ $\sigma_r = p =$ constant. The equilibrium equation and the kinematic relationships of the plane-strain, axially symmetric problem are as follows.

$$\begin{aligned}
&\frac{\mathrm{d}\sigma_r}{\mathrm{d}r} + \frac{\sigma_r - \sigma_\vartheta}{r} = 0\\
&\dot{\varepsilon}_r^{\mathrm{irr}} = -\frac{\mathrm{d}\dot{u}}{\mathrm{d}r}\\
&\dot{\varepsilon}_\theta^{\mathrm{irr}} = -\frac{\dot{u}}{r}\\
&\dot{\varepsilon}_{\mathrm{v}}^{\mathrm{irr}} = -\frac{1}{r}\frac{\mathrm{d}(\dot{u}r)}{\mathrm{d}r} = \dot{\varepsilon}_\theta^{\mathrm{irr}} + \dot{\varepsilon}_r^{\mathrm{irr}}
\end{aligned} \tag{12}$$

where r and θ are outward radial and circumferential coordinates respectively, and u is a radial displacement. As the material is rigid-plastic, the total strain is identical to the plastic strain. The yield locus is defined solely via a combination of the radial and circumferential stress components, σ_r and $\sigma\theta$ respectively, as

$$f = \begin{cases}
\dfrac{1}{2}(\sigma_\theta - \sigma_r) - \dfrac{\alpha}{2}(\sigma_r + \sigma_\theta) - [1 + \gamma\varepsilon_{\mathrm{v}}^{\mathrm{irr}} - \delta\xi]\dfrac{\tan\phi_1 - \tan\theta_1}{\tan\theta_1 + 1}\sigma_{01}^* = 0; \quad \sigma_\theta \geqslant \sigma_r \tan\phi_1\\
\dfrac{1}{2}(\sigma_r - \sigma_\theta) - \dfrac{\alpha}{2}(\sigma_r + \sigma_\theta) - [1 + \gamma\varepsilon_{\mathrm{v}}^{\mathrm{irr}} - \delta\xi]\dfrac{\tan\theta_2 - \tan\phi_2}{\tan\theta_2 + 1}\sigma_{02}^* = 0; \quad \sigma_\theta \leqslant \sigma_r \tan\phi_2\\
\sigma_r - \sigma_{02}^*[1 + \gamma\varepsilon_{\mathrm{v}}^{\mathrm{irr}} - \delta\xi] = 0; \quad \sigma_r \tan\phi_2 \leqslant \sigma_\theta \leqslant \sigma_r\\
\sigma_\theta - \sigma_{02}^*[1 + \gamma\varepsilon_{\mathrm{v}}^{\mathrm{irr}} - \delta\xi] = 0; \quad \dfrac{\sigma_r}{\tan\phi_1} \leqslant \sigma_r \leqslant \sigma_\theta
\end{cases} \tag{13}$$

with the restriction that overall hardening function h

$$h = 1 + \gamma\varepsilon_{\mathrm{v}}^{\mathrm{irr}} - \delta\xi > 0 \tag{14}$$

is always positive.

The constants describing the yield locus are

$$\begin{aligned}
\tan\theta_1 &= \frac{1}{\tan\theta_2} = \frac{1+\alpha}{1-\alpha}\\
\tan\phi_1 &= \frac{1}{\tan\phi_2} = \frac{\sigma_{02}^*}{\sigma_{01}^*}
\end{aligned} \tag{15}$$

and γ and δ are respectively strain-hardening and chemical softening constants, taken here for simplicity to be the same for σ_r and σ_θ. The axial stress σ_z is assumed not to influence yielding in plane-strain rate conditions, and is calculated from equation (13) as $\sigma_z = \frac{1}{2}(\sigma_r + \sigma_\theta) \pm 3BJ_2^{1/2}$, where B is a constant and J_2 is the second invariant of deviatoric stress: the sign $\pm$ refers to either the top or the bottom part of the yield locus (Fig. 13; see also Mróz & Kwaszczynska (1971)).

The rate of relative mass removal ξ, defined by equation (9), is different in two distinct phases. An initial phase simulates the long-term dissolution of calcite from the pre-existing pores. The initial (constant) stress state is well within the initial yield locus in the entire domain. The initial yield locus shrinks homothetically once the chemical softening starts, until yielding is initiated at the stress state at the points of the external cylinder perimeter (Fig. 14). Until this point there is no deformation. Once the radial stress σ_r at the outer boundary is 'reached' by the shrinking yield locus – namely its segment AC_0 only, or two segments AC_0, D_0B, depending on the thickness of the cylinder – the whole cylinder yields at once (Hueckel & Mróz, 1973).

The irreversible strain rate is defined via the normality flow rule as

$$\dot{\varepsilon}_{ij}^{\mathrm{irr}} = \dot{\Lambda}\frac{\partial f}{\partial \sigma_{ij}} \tag{16}$$

The multiplier $\dot{\Lambda}$ is determined from the extended Prager's consistency condition, $\dot{f}(\sigma_{ij}, \varepsilon_{\mathrm{v}}^{\mathrm{irr}}, \xi) = 0$ (see e.g. Hueckel & Borsetto (1990), Hueckel (2002)), as a function of rates of stress and reaction progress, ξ

$$\dot{\Lambda} = \frac{(\partial f/\partial \sigma_{ij})\,\dot{\sigma}_{ij} + (\partial f/\partial \xi)\dot{\xi}}{-(\partial f/\partial \varepsilon_{\mathrm{v}}^{\mathrm{irr}})(\partial f/\partial \sigma_{kk})} \tag{17}$$

$$\dot{\Lambda} = 0 \text{ if } f < 0 \text{ or } f = 0 \text{ and } \dot{f} < 0$$

Three states can arise in the material during yielding (Fig. 15): the dilatant state for AC_0 ($\dot{\varepsilon}_{\mathrm{v}} < 0$); the compactant state for D_0B ($\dot{\varepsilon}_{\mathrm{v}} > 0$); and the critical state for the yield locus corner, C_0/D_0 (where the normality rule implies an infinity of the strain rate directions, and hence it may occur that $\dot{\varepsilon}_{\mathrm{v}} = 0$). When yielding proceeds, three corresponding zones develop, fulfilling the continuity conditions at the boundaries of the zones. A set of five transcendental equations is solved in order to determine stress, displacement and reaction progress fields. Prior to yielding, $\dot{\varepsilon}_{ij} = 0$, the yield locus changes only as a result of dissolution from the pre-existing pores. At the moment when yielding is initiated, the critical

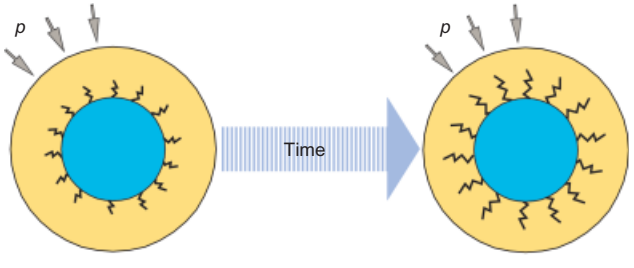

Fig. 12. Long-term dissolution of a stressed macropore

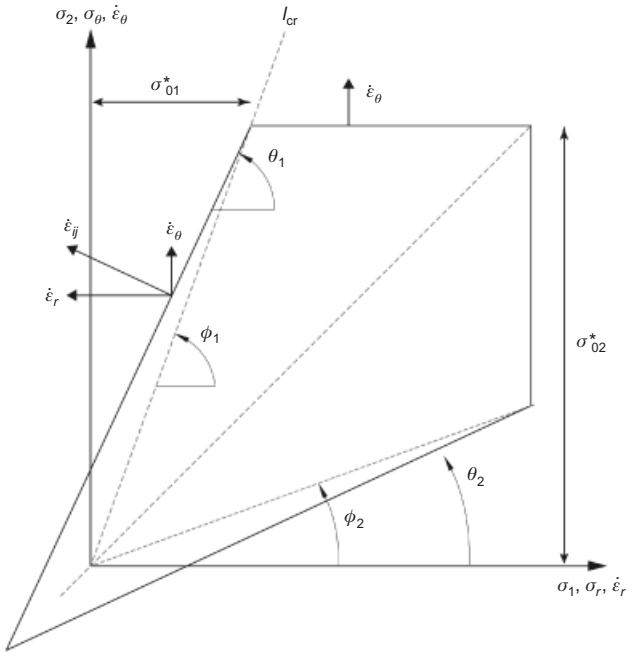

Fig. 13. Yield condition

zone has no thickness. This is used as an initial condition, from which it is possible to obtain the value of circumferential stress at the instant of yielding onset (Fig. 14(a)), which reads

$$\sigma_\theta^{\text{yield}} = p \Big/ \left(1 - \frac{a}{b}\frac{\tan\phi_1 - 1}{\tan\phi_1}\right)\left(\frac{\tan\phi_1 - 1}{\tan\phi_1 - \tan\theta_1}\right)^{1/\tan\theta_1 - 1} \tag{18}$$

Hence the time necessary to activate yielding of the calcarenite during continuous dissolution depends only on the reaction rate (K_c^j) and on the 'distance' between the circumferential stress at the onset of yielding ($\sigma_\theta^{\text{yield}}$) and the initial strength of the material (Fig. 14(b)), and reads

$$t^* = \frac{\sigma^*_{02} - \sigma_\theta^{\text{yield}}}{\delta K_c^j \sigma^*_{02}} \tag{19}$$

The onset of yielding of the outer perimeter is chosen as a starting moment ($t = 0$) for the subsequent phase, simulating a long-term process at a constant load driven by the mass removal, that is, after the initiation of yielding. With progression over time, the stress at the boundary $r = c$ grows along C_0C, and a critical zone, CD, develops between the dilatant and compactant zones: see Fig. 15. The dilatant and critical zones expand ($\dot{c} > 0$ and $\dot{d} > 0$), reducing the thickness of the compactant zone, until either $\xi = 1$ or $h = 0$. The linear yield function implies the following constraints: for the inner zone $a \leqslant r \leqslant c$, dilatant kinematics and a fixed ratio of the radial and circumferential strains ($\dot{\varepsilon}_r/\dot{\varepsilon}_\theta = -\tan\theta_1$), result. At the corner points the flow rule is non-unique, but the ratio of σ_r to σ_θ ratio is constant: $\sigma_\theta/\sigma_r = \tan\theta_1$, together with the strain-hardening function, defines the equations for the critical zone $c \leqslant r \leqslant d$. Finally, for the outer zone, $d \leqslant r \leqslant b$, compactant kinematics with $\dot{\varepsilon}_\theta > 0$ and $\dot{\varepsilon}_r = 0$ induce a displacement that is constant with respect to space in the entire zone, and hence equal to the displacement of the outer boundary, u_b. By imposing displacement and (radial) stress continuity at $r = c$ and in $r = d$, the following set of transcendental equations for the coupled chemo-mechanical problem is obtained.

The radial stress continuity at $r = c$ requires that

$$p_c = \frac{\tan\phi_1 - \tan\theta_1}{\tan\theta_1 + 1}\sigma^*_{01}\left\{\frac{1 - \delta K_c^j t}{1 - \tan\theta_1}\left[\left(\frac{a}{c}\right)^{1-\tan\theta_1} - 1\right] + \frac{(\tan\theta_1 - 1)(\gamma u_c c^{\tan\theta_1} + \delta\int_0^t K^j u_c c^{\tan\theta_1}\,\mathrm{d}t)}{2\tan\theta_1} \times \left[c^{-\tan\theta_1 - 1}\left(1 - \frac{a^{-2\tan\theta_1}}{c^{-2\tan\theta_1}}\right)\right]\right\} \tag{20}$$

The above condition and a one-to-one relationship between radial and circumferential stress at the critical state imply that

$$p_c\tan\phi_1 = p_c\tan\theta_1 - \frac{\tan\phi_1 - \tan\theta_1}{\tan\theta_1 + 1}\sigma^*_{01}\left\{1 + (\tan\theta_1 - 1)\left[\gamma\frac{u_c}{c} + \delta\int_0^t K^j\frac{u_c}{c}\,\mathrm{d}t\right] - \delta K_c^j t\right\} \tag{21}$$

The displacement continuity at $r = c$ requires that

$$u_c = \frac{1}{\gamma c}\left\{\begin{array}{l}\dfrac{1 - \delta K_c^j t}{2}(c^2 - d^2) \\ -\dfrac{p_c}{\sigma^*_{02}}\dfrac{\tan\theta_1}{\tan\theta_1 + 1}c^2\left[1 - \left(\dfrac{d}{c}\right)^{\tan\theta_1 + 1}\right] + \gamma u_d d\end{array}\right\} \tag{22}$$

The radial stress continuity at $r = d$ requires that

$$p_c\left(\frac{c}{d}\right)^{1-\tan\phi_1} = \frac{pb}{d} + \sigma^*_{02}\left[(1 - \delta K_c^j t)\left(1 - \frac{b}{d}\right) + \gamma\frac{u_b}{d}\ln\left(\frac{b}{d}\right)\right] \tag{23}$$

The circumferential stress continuity at $r = d$ results from a similar argument as above for $r = c$, as

$$p_c\tan\phi_1\left(\frac{c}{d}\right)^{1-\tan\phi_1} = \sigma^*_{02}\left[1 - \gamma\frac{u_b}{d} - \delta K_c^j t\right] \tag{24}$$

The displacement continuity between the critical and compactant zone and the uniform radial displacement across the compactant zone imply that

$$u_d = u_b \tag{25}$$

The enhanced dissolution due to the formation of new cracks in the critical zone is not considered in obtaining an analytical solution of the differential equation (22). The zone itself has a numerically insignificant thickness, which makes this assumption reasonable.

A parametric study of the numerical solution for equations (20)–(25) using Matlab© is presented in Figs 16–19. The constitutive parameters and geometry are listed in Tables 2–4. Fig. 16(a) presents the displacement u_a of the internal circumference, $r = a$, induced by a purely chemical process at different pH values. This displacement can be interpreted as a closure of the pore space, accompanied by a substantial weakening of the material around it. Notably, for the most acidic solution (pH = 2·8) after about 6 min of the chemical

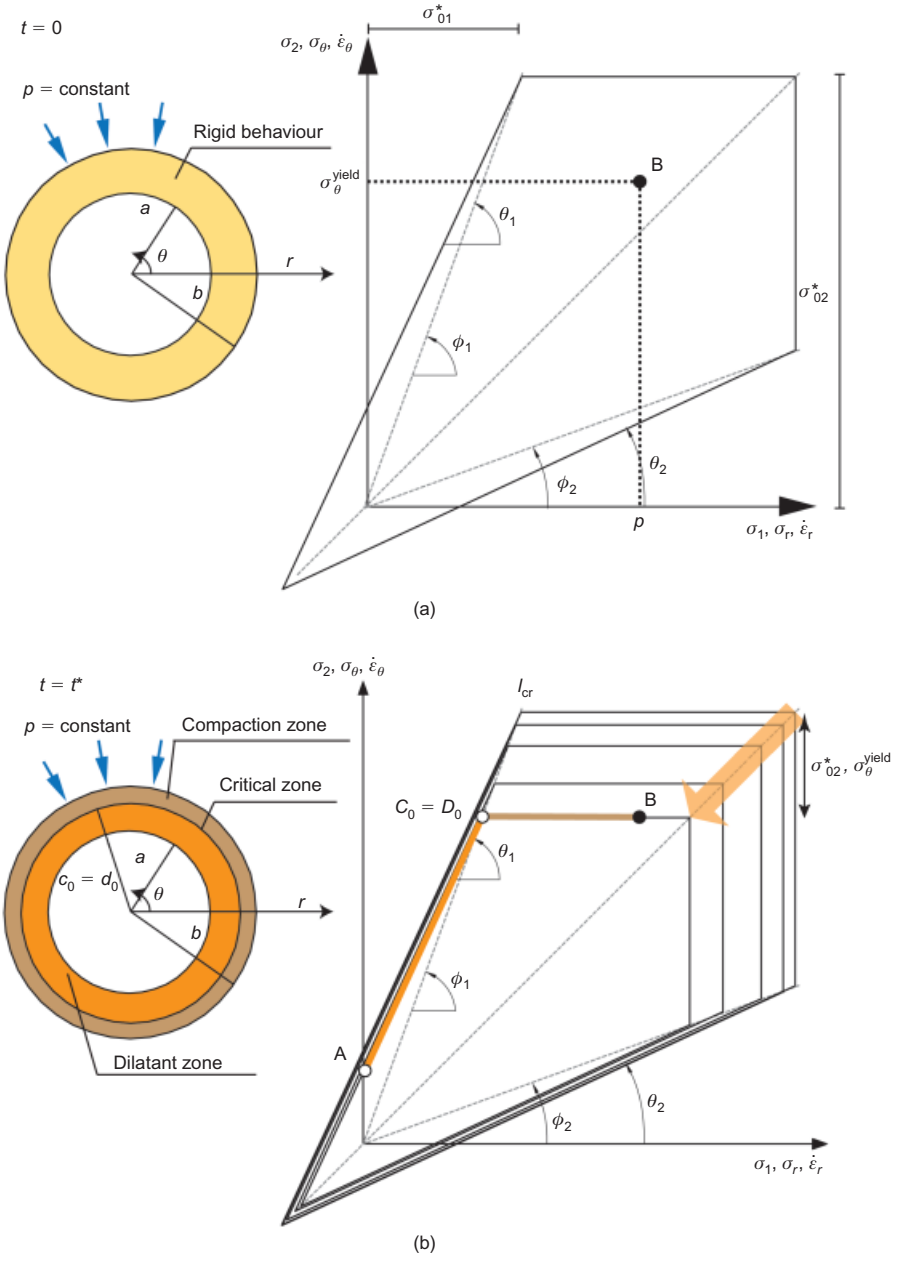

Fig. 14. Initiation of yielding due to chemical dissolution: stress state before (a) and at yielding onset (b)

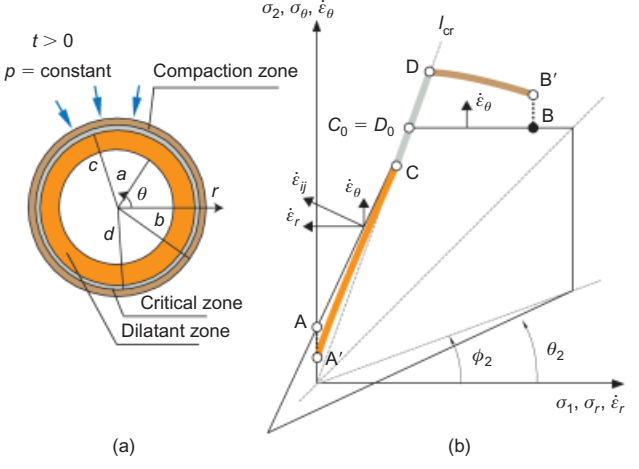

Fig. 15. Three zones of different kinematic response: (a) layout of zones; (b) stress path segments corresponding to the different zones for a generic moment

exposure, at a value of 5% of the inner radius, the inward displacement becomes uncontrollable, and the solution of equations (20)–(25) ceases to exist. Fig. 16(b) illustrates the evolution of the zones across the pore surroundings for different pH. With time, the compaction zone becomes smaller (50%), while the dilatant damage zone spreads, owing to the chemical enhancement of damage. The relative mass dissolution and volumetric strain for pH = 7·5 are depicted in Figs 17(a) and 17(b). The largest mass dissolution occurs at $r = a$, its rate being proportional to dilatancy. At the terminal moment ($t = 530$ h), the mineral dissolution at $r = a$ reaches the value 6%, 30 times higher than the pre-existing background dissolution.

As the external radial loading is constant at both $r = a$ and $r = b$, the radial stress distribution (Figs 17(c) and 18) does not change much. Spatially, the stress varies quite significantly across the radius (Fig. 17(d)). The displacement evolution for each point of the pore surroundings is depicted in Fig. 19. The closing of the internal pore accelerates with time. It is seen (Fig. 17) that in the dilatant zone the two

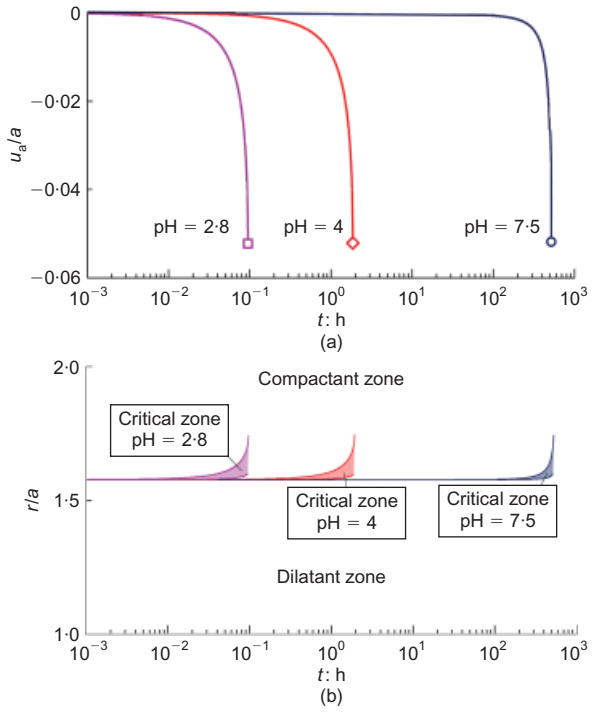

Fig. 16. (a) Closing of the pore to chemical damage; (b) propagation of zones

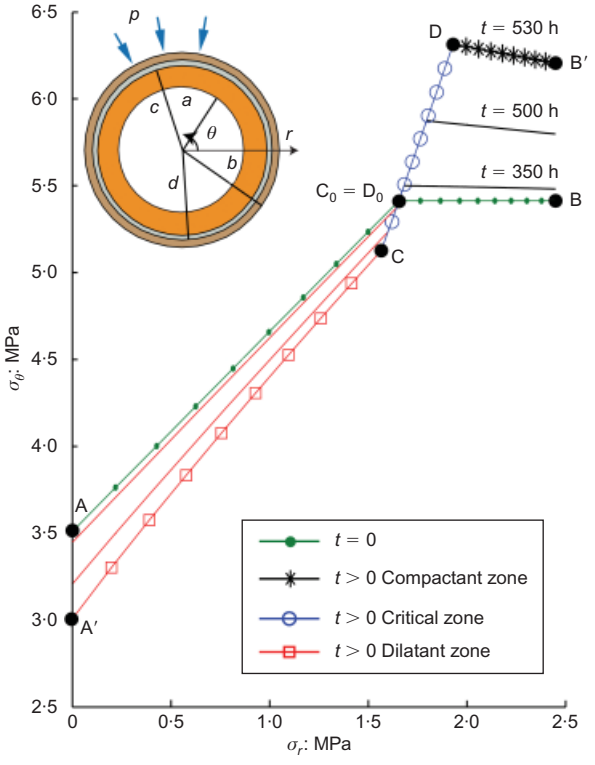

Fig. 18. Stress evolution in principal stress space

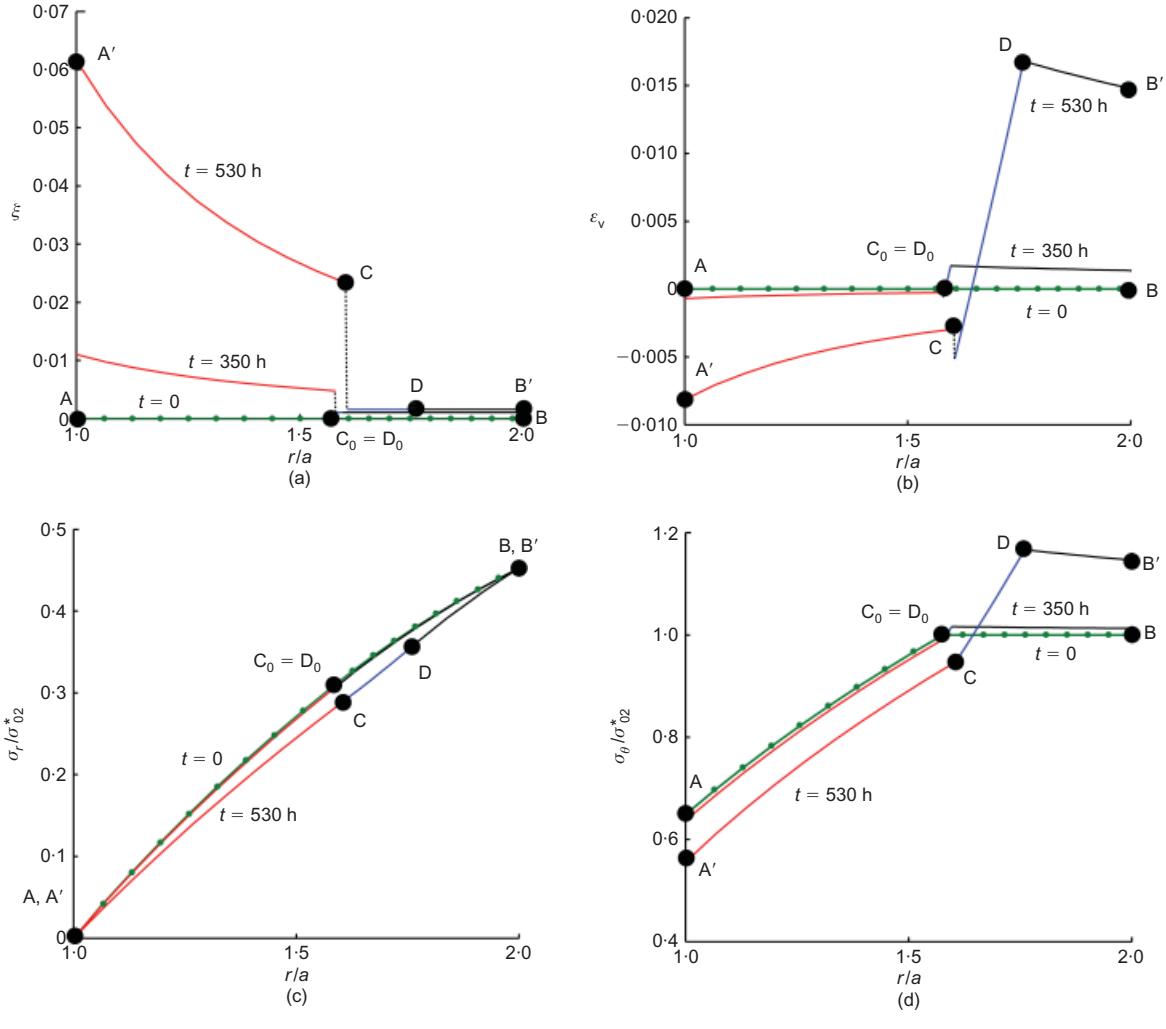

Fig. 17. Evolution of: (a) relative mass dissolution; (b) volumetric strain; (c) radial stress; (d) circumferential stress

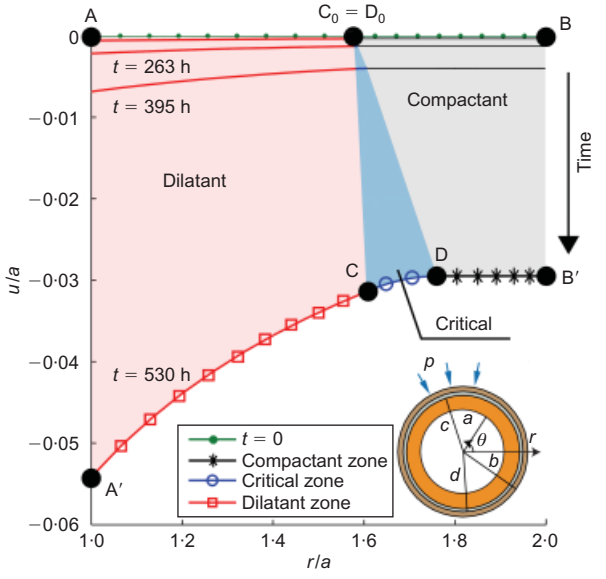

Fig. 19. Displacement evolution with time

softenings (strain-softening and chemical softening) superimpose one over the other. Plasticity consistency rules preclude a stable and unique response to unconstrained softening behaviour with an inward stress rate (e.g. Maier & Hueckel, 1979). However, even if local behaviour can be unstable, a global BVP response can be stable, if a region in a hardening, stable mode is sufficiently large for the integral of the second-order work to be positive (Hueckel & Maier, 1977). It is the same in the considered case, except that there are two sources of softening. So, physically, until there is a sufficiently large supporting mass in the hardening mode (here in the form of the external strain-hardening shell), the pore remains stable. Eventually, the shrinking external zone does not provide sufficient support, and the whole solid matrix collapses. Mathematically, this means there is no admissible solution to the system of differential equations for the evolution of the material, equilibrium, chemical process rate and kinematics. Fig. 20 shows the resulting equilibrium surface of the external perimeter pressure as a function of total dissolved mass within the cylinder and external perimeter displacement, $p(\bar{\xi}, u_b)$. Imposing a constant p across the surface of solutions with a resulting pre-critical dissolved mass–displacement relationship, it emerges that beyond a critical point A' no solution satisfying all the required conditions can be obtained. A process driven by the time-dependent, uncontrollable variable of mass removal (the dark line AA′), in order to continue (A′B′), would require a reversal of chemical reaction, $\dot{\bar{\xi}} < 0$, to satisfy the above relationships. Following an arbitrary $\delta(u_b/b)/\delta(\bar{\xi}) > 0$ path (A′B) that *does* follow the surface requires that $\dot{p} < 0$, and hence violates the set of the governing conditions. Visibly, there exists a locus (dashed line) of points of instability.

UPSCALING

To develop a quantitative simulation tool for the chemo-mechanical mechanism described, it is necessary to represent the obtained results at the macro scale, using macroscopic variables. A previously developed macroscopic chemo-plasticity theory (Hueckel, 1992, 2002), which is an extension of Cam-clay theory (Schofield & Wroth, 1968), will be used for this purpose. The macro-scale yield limit is expressed via the mean normal stress $\bar{p}$ and deviatoric stress invariant $\bar{q}$ (variables with an overbar refer to macro scale)

$$\bar{f} = \bar{q} + \bar{p}\mathrm{M}\ln\left(\frac{\bar{p}}{\bar{p}_c}\right)$$
$$\bar{q} = \left(\tfrac{1}{2}\bar{s}_{ij}\bar{s}_{ij}\right)^{1/2} \tag{26}$$

Table 2. Geometrical parameters for the meso-BVP (thick cylinder geometry)

a: μm	b: μm	$2b$: μm	V_T: μm^3	V_V: μm^3	V_S: μm^3	n	e
100	200	400	$5{\cdot}0 \times 10^7$	$2{\cdot}6 \times 10^7$	$2{\cdot}4 \times 10^7$	0·52	1·08

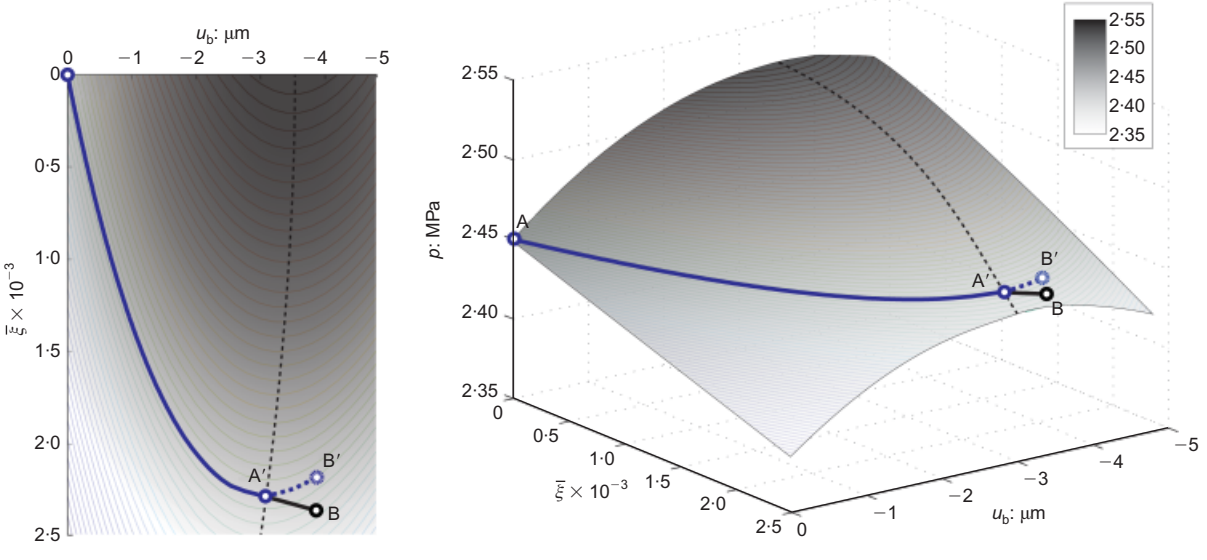

Fig. 20. Pressure as a function of reaction progress and external displacement: segment AA′ response along actual path u_b/b against dissolved mass; segment A′B, response to arbitrary path $\delta t > 0$

The hardening variable $\bar{p}_c$, describing the size of the yield locus and hence the apparent preconsolidation stress, is dependent on the macro-scale volumetric plastic strain and relative mass change according to (Hueckel *et al.*, 1999)

$$\bar{p}_c = \bar{p}_c^0 \exp\left[\frac{(1+e_0)}{\bar{\lambda}}\bar{\varepsilon}_v^{pl} + R(\bar{\xi})\right] \tag{27}$$

where $\bar{p}_c^0$ is the initial size of the yield locus, e_0 is the initial void ratio, and $\bar{\lambda}$ is the plastic bulk modulus of compressibility. To be consistent with the microscopic approach, rigid plasticity is adopted. The chemical softening term R is a function of the macroscopic relative mass loss $\bar{\xi}$, identified as the volume average of a meso-scale mass removed from the solid structure: ξ integrated over the macro-REV. The expression for this volume average is a cross-scale transfer function for the mass removal (Hu & Hueckel, 2007a).

Cross-scale functions and upscaling procedure

Macroscopic tests make it possible to observe and measure the strength decrease of calcarenite due to weathering at constant load (e.g. geostatic conditions). For a constant stress $\dot{\bar{\sigma}}_{ij} = 0$, or for $(\partial\bar{f}/\partial\dot{\bar{\sigma}}_{ij})\dot{\bar{\sigma}}_{ij} = 0$, the resulting macroscopic plastic strain rate is obtained from the extended Prager consistency condition (Hu & Hueckel, 2007b) as

$$\dot{\bar{\varepsilon}}_v^{pl} = -\frac{(\partial\bar{f}/\partial\bar{\xi})\dot{\bar{\xi}}}{\partial\bar{f}/\partial\bar{\varepsilon}_v^{pl}} \tag{28}$$

To take advantage of the quantifiable phenomena at the meso scale, the macro-scale REV is postulated as a periodic arrangement of the meso-scale REVs (Fig. 21). Then the chemical softening term $R(\bar{\xi})$ in equation (27) can be calculated using the data from the simulation of the meso-scale process of dissolution, assuming it to be a linear function $R(\bar{\xi}) = R_c\bar{\xi}$ of the macroscopic relative mass dissolution.

$$R_c = -\frac{(\partial\bar{f}/\partial\bar{\varepsilon}_v^{pl})\dot{\bar{\varepsilon}}_v^{pl}}{\dot{\bar{\xi}}} \tag{29}$$

Subsequently, the macroscopic variables $\dot{\bar{\xi}}$ and $\dot{\bar{\varepsilon}}_v^{pl}$ are substituted by their counterpart averages at the meso scale. Knowing $\partial\bar{f}/\partial\bar{\varepsilon}_v^{pl}$, and the averaged rates $\dot{\bar{\xi}}$ and $\dot{\bar{\varepsilon}}_v^{pl}$, the coefficient R_c is determined. The macroscopic strain rate can be calculated from the boundary displacement rate, $\dot{u}_i$, of the meso-scale REV (Bagi, 1996) as

$$\dot{\bar{\varepsilon}}_v^{pl} = \frac{\int_S \dot{u}_i n_i \mathrm{d}S}{V} = -\frac{2\dot{u}_b}{b} \tag{30}$$

where V is the volume of the REV with the boundary surface S, and n_i is the outward unit normal to S. The macroscopic relative mass dissolution rate $\dot{\bar{\xi}}$ is obtained as

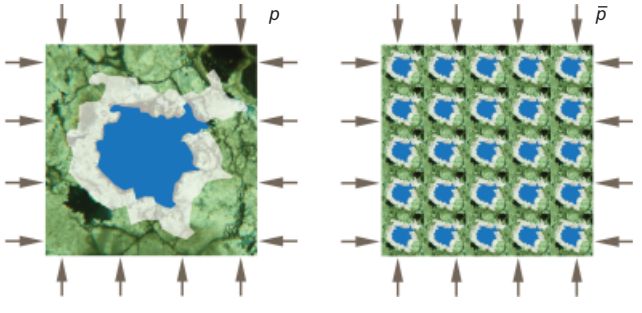

Fig. 21. Macro-REV (right) as periodic repetition of meso-REV (left)

$$\begin{aligned}\dot{\bar{\xi}} &= \frac{\int_V \dot{\xi}\mathrm{d}V}{V} \\ &= \frac{2\pi}{\pi(b^2-a^2)}\int_a^b \dot{\xi} r \mathrm{d}r \\ &= \frac{2}{b^2-a^2}\int_a^b \left(rK_c^j\langle-\varepsilon_v\rangle + rK_c^j\right)\mathrm{d}r\end{aligned} \tag{31}$$

Furthermore, substituting

$$\dot{\xi} = \begin{cases} K_c^j + K^j(\tan\theta - 1)\dfrac{u_c}{c}\left(\dfrac{r}{c}\right)^{-\tan\theta-1} & \text{for } a \leqslant r \leqslant c \\ K_c^j & \text{for } c < r \leqslant b \end{cases} \tag{32}$$

the rate of mass removal at the macro scale becomes

$$\dot{\bar{\xi}} = K_c^j + K^j\frac{2u_c}{b^2-a^2}c^{\tan\theta}(a^{1-\tan\theta} - c^{1-\tan\theta}) \tag{33}$$

while

$$\begin{aligned}R_c &= \frac{1+e_0}{\bar{\lambda}}\left(\frac{-\dot{\bar{\varepsilon}}_v^{pl}}{\dot{\bar{\xi}}}\right) \\ &= \frac{1+e_0}{\bar{\lambda}}\left\{\frac{2\dot{u}_b/b}{K_c^j + K^j[2u_c/(b^2-a^2)]c^{\tan\theta}(a^{1-\tan\theta} - c^{1-\tan\theta})}\right\}\end{aligned} \tag{34}$$

At this point, if all the mechanical meso- and macro-scale parameters of equation (34) are known, it is possible to determine R_c. The most important outcome of the upscaling procedure is deduced from the parametric study proposed in Fig. 22. A set of three different values of macroscopic plastic strain rate. and hence of $\dot{u}_b$ (equation (30)), is used as an input for the meso-BVP model (Fig. 22(a)). The corresponding upscaled results of the meso-BVP response are presented in Figs 22(b)–22(d). Notably, the upscaled macroscopic rate of mass removal is identical for the three different tests, and is a linear function of the macroscopic volumetric plastic strain (Fig. 22(d)). This means that once the meso model has been calibrated (using a suitable loading condition), and hence the linear relationship between $\dot{\bar{\xi}}$ and $\dot{\bar{\varepsilon}}_v^{pl}$ has been determined, the macroscopic hardening law can be written without the need to use the meso-scale model any more. In fact,

$$\begin{aligned}\dot{\bar{p}}_c &= \bar{p}_c\left[\frac{(1+e_0)}{\bar{\lambda}}\dot{\bar{\varepsilon}}_v^{pl} + R_c\dot{\bar{\xi}}\right] \\ &= \bar{p}_c\left\{\frac{(1+e_0)}{\bar{\lambda}}\dot{\bar{\varepsilon}}_v^{pl} + R_c[A(K_c^j) + B(K^j)\bar{\varepsilon}_v^{pl}]\right\}\end{aligned} \tag{35}$$

The calibration of the rest of the meso-scale parameters is performed using macroscopic experiments, as below.

Meso-scale model calibration: a downscaling procedure

The parameters defining the geometry of the meso-scale REV are determined by imposing that the index properties at the meso scale and macro scale are the same (Table 1), and that the meso-pore constitutes 50% of the meso-scale REV total pore volume. This percentage is derived from the pore size distribution curve (Fig. 4) showing that 50% of the pores are between 40 and 200 μm, with a mean radius of 100 μm. (Hence $a = 100$ μm was chosen.) The remaining void volume is incorporated in the rock matrix surrounding the meso-pore. The resulting geometry of the meso-scale

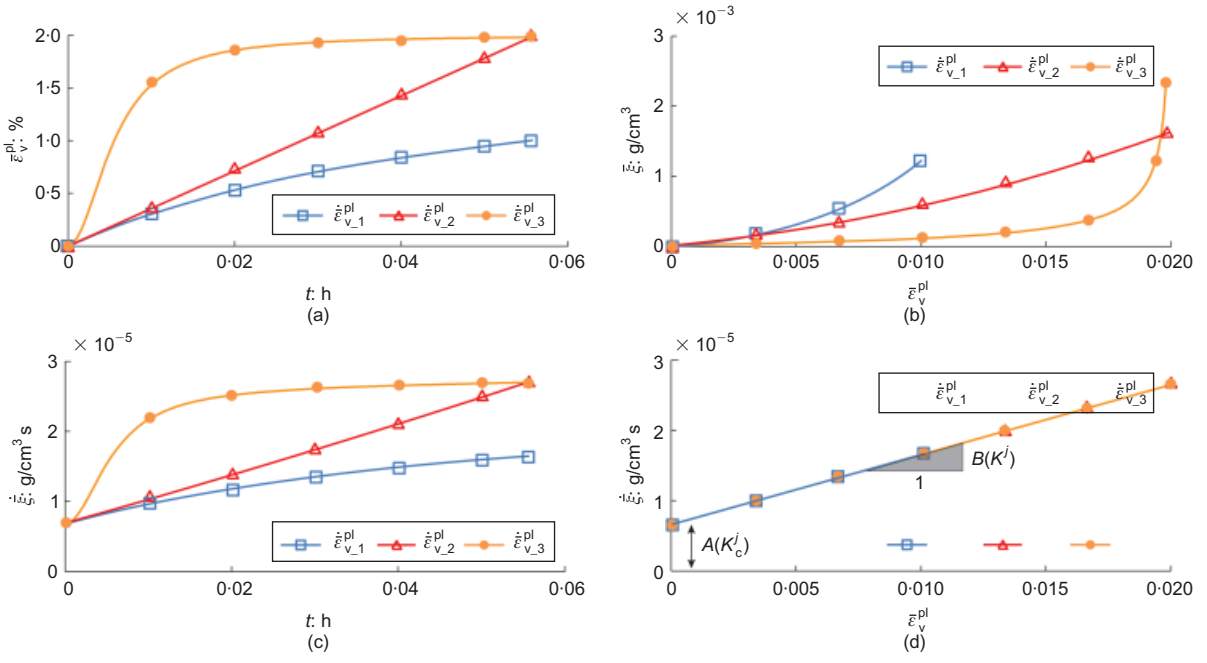

Fig. 22. Upscaled meso-BVP results for three different plastic strain histories: (a) macroscopic plastic strain with time (input to meso-BVP in terms of u_b); (b)–(d) corresponding upscaled results

REV is provided in Table 2 (the thickness in the z direction is assumed to be $2b$). The physical parameters (Table 3) are estimated using MIP, whereas the opening of the micro-cracks, Δ, is determined through SEM observations of the micro-cracked calcarenite. ϕ is calculated from the parameter Δ via equation (5). The remaining parameters (σ^*_{01}, θ_1, ϕ_1, γ, δ) of the meso model are calibrated using a down-scaling procedure. Downscaling implies using macroscopic experiments to calibrate the parameters of the meso-scale model. First, the parameters (σ^*_{01}, θ_1, ϕ_1, γ) controlling the mechanical response only are calibrated using mechanical macroscopic tests. Subsequently, the chemical parameter (δ) is calibrated, evaluating the strength loss with time due to chemical dissolution of unstressed samples. The mechanical test to calibrate the model is the isotropic compression of calcarenite performed by Lagioia & Nova (1995) (Fig. 23). The macroscopic response of the sample is elastic until it becomes unstable, forming compaction bands (Nova *et al.*, 2003). The elastic limit and the post-peak behaviour are used to calibrate the mechanical parameters of the meso-scale BVP. The p–(u_b/b) curves are presented in terms of the macroscopic variables e–$\bar{p}$ using equation (30), and the relationship between void ratio and volumetric strain, $e = e_0 - (1 + e_0)\bar{\varepsilon}_v$. The yielding point and the volumetric collapse are both well captured through the upscaled meso-scale BVP (Fig. 23(b)). The calibrated mechanical parameters are listed in Table 4.

The chemical rate constants are calculated from Fig. 10. The R_c constant is calibrated matching the macroscopic strength decrease with time due to chemical dissolution of calcarenite in acid (Fig. 24(d); Ciantia *et al.*, 2013). The specimens were immersed in acid, and pH, ΔM (change in

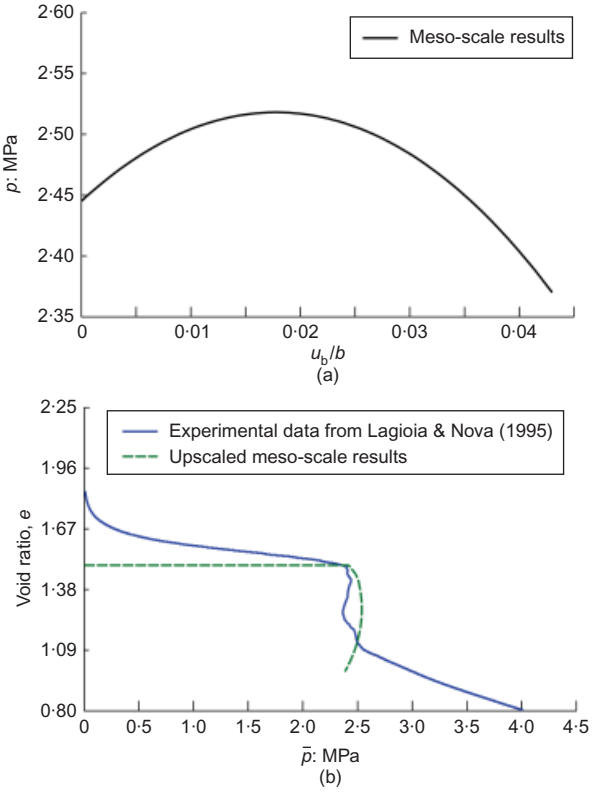

Fig. 23. (a) Meso-scale mechanical response to isotropic compression (displacement-controlled simulation); (b) macro-scale model response after calibration

Table 3. Physical properties of the meso-BVP

G_s	M: g	M^m: g/mol	S_s: m^2/g	A^*_0: cm^2/cm^3	Δ: μm	ϕ
2·73	$6{\cdot}59 \times 10^{-5}$	100	2·7	68 040	1	1847

Table 4. Mechanical parameters for the meso-BVP

σ_{01}^{*}: MPa	ϕ_1: degrees	θ_1: degrees	γ
1·65	71	49	10

mass) and (via an oedometric test) the yielding threshold were measured with time (Figs 24(a), 24(b), 24(c)). The chemical softening parameter ($\delta = 5$) was calibrated, simulating a compensatory mechanism that required the R_c constant in equation (34) and the macroscopic one to be equal.

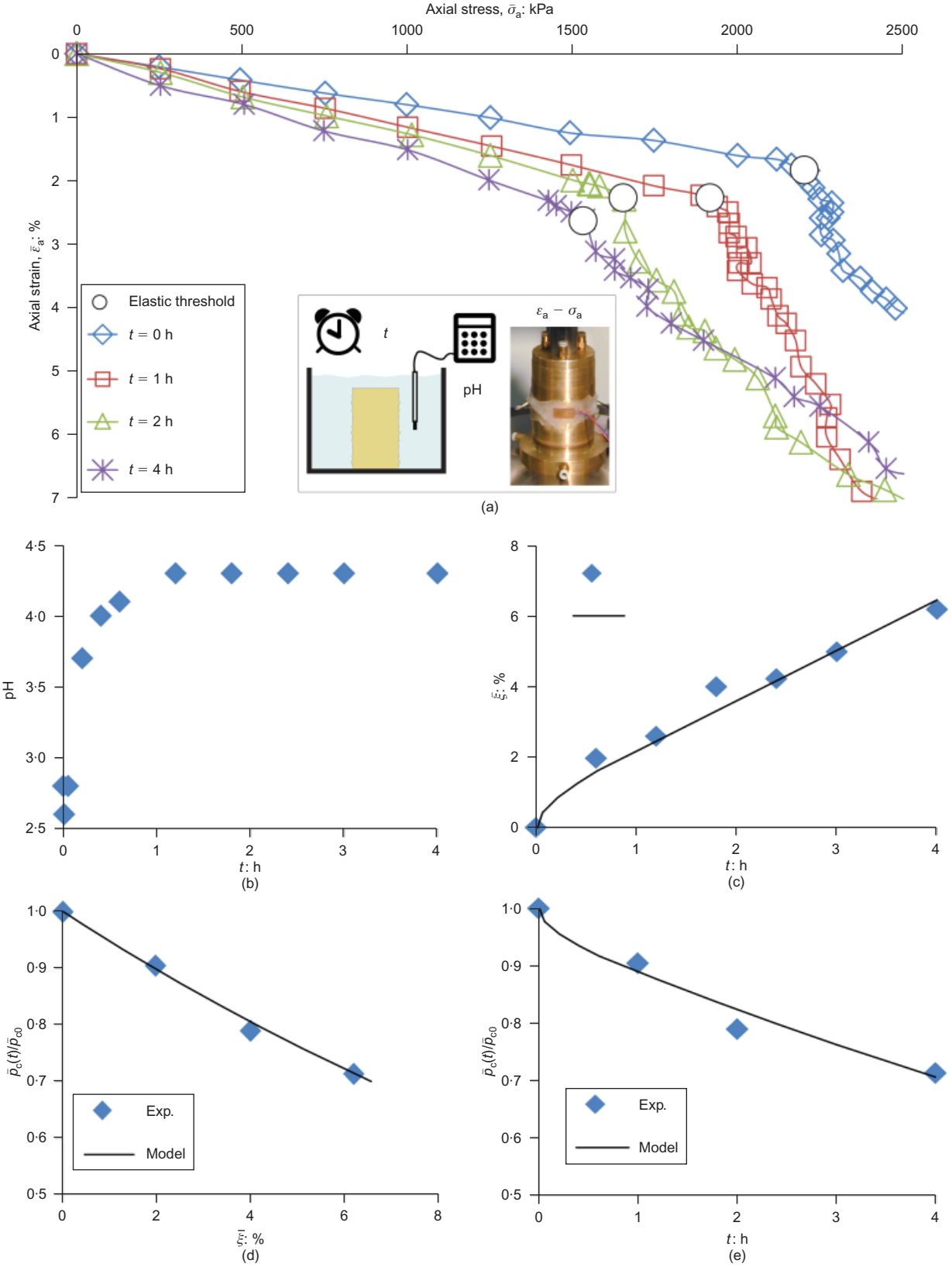

Fig. 24. Macro-calibration in acid of chemically induced dissolution damage: (a) axial stress plotted against axial strain; (b) pH evolution with time during the dissolution phase of the submerged samples; (c) macro-scale accumulated relative mass removal evolution with time; evolution of preconsolidation pressure with respect to macro-scale accumulated relative mass removal (d) and time (e)

Note that R_c is independent of pH and fairly constant with time, except in the last stages as the solution becomes unstable (Fig. 25).

The multiscale model is validated by predicting the long-term behaviour of calcarenite subject to chemical weathering in contact with water at a neutral pH (Fig. 26). The four experimental points available for comparison are placed in the context of results on other rocks (Matsukura & Hirose, 1999).

It is interesting to note that, according to the model, only 5% of mass loss can cause a 24% loss of strength in terms of $\bar{p}_c$. At pH = 4 this happens in about 3 h, whereas in water with a neutral pH for an open system scenario, the same weight loss – and hence damage – is expected in about 1·8 years.

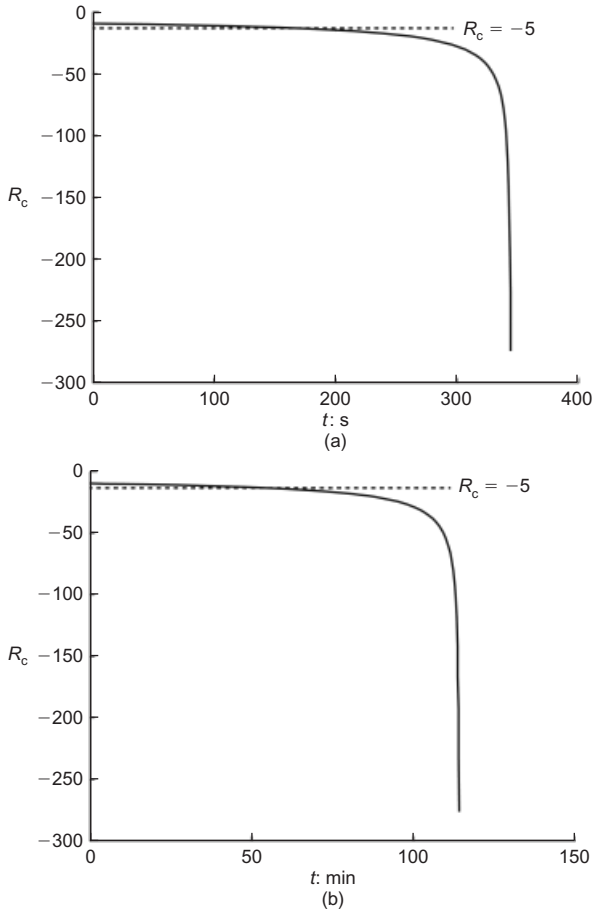

Fig. 25. Graphic representation of equation (34) for: (a) pH = 2·8; (b) pH = 4. R_c constant is independent of the bulk fluid

CONCLUSIONS

In this paper, the consequences of dissolution of calcarenite in stressed conditions for the change in the mechanical properties are investigated, quantified and modelled by means of a multiscale procedure. The mathematical model developed is effectively a three-scale model. The chemistry of the problem is simulated at the scale at which the kinetic laws of geochemical reactions are formulated (micro scale), while the chemically enhanced mechanical damage phenomena are quantified at the meso scale. Finally, a model of a reactive porous continuum at the macro scale, at which engineering large-scale computations can be performed, is produced via upscaling.

The peculiarity of this multiscale model is that the meso model is a multi-physical BVP by itself. However, by virtue of the chosen geometry of the REV, the BVP can be solved semi-analytically. The emphasis of the work is on well-defined and reproducible procedures to represent mechanisms formulated from basic geochemistry and inelastic constitutive laws at a scale at which they can be tested experimentally, and simulated for engineering purposes. Cross-scaling functions allow the variables of the meso scale to be suitably represented at the macro scale, and vice versa. The key mechanism of the model is the coupling between the rate of dissolution and the increase of the specific surface area induced by microcracking.

The available experimental data and the experiments performed ad hoc in the laboratory on calcarenite are sufficient to perform the inter-scale identification of model parameters at all scales involved. The limited predictions performed for different pH conditions of water thus far yield a very convincing scenario of the effect of weathering of calcarenites on the stability of the coast. An interesting outcome of the adopted upscaling procedure is that the upscaled macroscopic rate of mass removal is proportional to the macroscopic volumetric plastic strain. This means that, once the microstructure of the material has been determined (e.g. specific surface area and microcrack characteristic dimensions), the macroscopic hardening law can be postulated and calibrated phenomenologically without the need to use the meso-scale variables. While many of the aspects of the model require further study, a tool to answer the opening question of how quickly portions of the calcar-

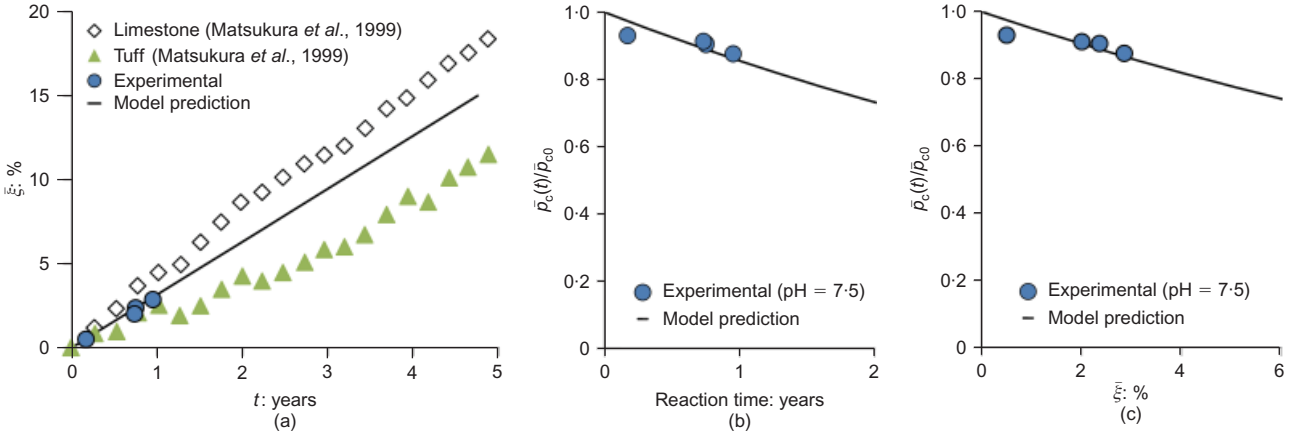

Fig. 26. Comparison of experimental and model predictions in (a) dissolved mass versus time plane, (b) normalised preconsolidation pressure versus time and (c) normalised preconsolidation pressure versus dissolved mass of chemically induced dissolution damage tests (pH = 7·5)

enite shore can become mechanically unstable, and also which portions are the most vulnerable, is available as a prototype.

ACKNOWLEDGEMENTS

The authors wish to thank Professor Claudio di Prisco, Professor Riccardo Castellanza and Ing. Stefano Langè for many helpful discussions concerning the presented work. MOC acknowledges his internship at Duke University, January–June 2010. Part of the work (by TH) has been supported by US NSF grant no. 0700294 of the Civil, Mechanical and Manufacturing Innovation Division, Geomechanics and Geomaterials programme.

NOTATION

A^* calcite specific surface area per unit reacting fluid volume
A_0^* initial specific surface area per unit reacting fluid volume
a thick cylinder inner boundary
$\tilde{a}$ scalar internal variable representing amount of added surface area
B nondimensional constant
b thick cylinder outer boundary
C equilibrium constant function of k_{sp}
$[Ca^{2+}]$ concentration of calcite ions
$[CO_3^{2-}]$ concentration of carbonate ions
c dilatant-critical boundary radius
d compactant-critical boundary radius
e void ratio
e_0 initial void ratio
f yield locus function
$\bar{f}$ macro-scale yield locus function
G_s specific gravity
$[H^+]$ concentration of hydrogen ions
h hardening function
J_2 second invariant of deviatoric stress
K^j increase in dissolution rate due to coupling effects; $j =$ a or b if in acid or base
K_c^j dissolution rate in uncoupled conditions; $j =$ a or b if in acid or base
k_a^* apparent rate constant in acid pH
k_b^* apparent rate constant in basic pH
k_{sp} thermodynamic equilibrium constant
$[M]$ mass per unit reacting fluid volume; slope of critical state line
$[M_0]$ initial mass per unit reacting fluid volume
M^m molecular mass
n porosity
n_i outward unit normal
p outer boundary radial pressure
$\bar{p}$ macro-scale isotropic effective stress
p_c radial stress at dilatant-critical boundary
$\bar{p}_c$ macro-scale hardening variable representing apparent preconsolidation stress
$\bar{p}_{c0}$ macro-scale hardening defining the initial size of the yield locus
$\bar{q}$ macro-scale deviatoric stress
R macro-scale chemical softening function
R_c macro-scale chemical softening constant
r outward radial coordinate
S REV boundary surface
S_s specific surface area
$\bar{s}_{ij}$ deviatoric component of the macro-scale stress tensor
t time
t^* time necessary to activate yielding
u radial displacement
u_i radial displacement of point i of thick cylinder (u_b represents radial displacement of point b)
V REV volume
V_S volume occupied by the solid phase
V_T total volume
V_V volume of voids
α yield locus parameter
γ strain-hardening constant
γ_s unit weight of solid phase
γ_{sat} unit weight of saturated material
Δ average crack opening at the apex
δ chemical softening constant
ε_r radial micro strain
ε_v volumetric micro strain
ε_{ij} total micro strain tensor
ε_θ circumferential micro strain
ε_{ij}^{irr} plastic strain tensor
ε_v^{irr} volumetric plastic strain
$\bar{\varepsilon}_v^{pl}$ macro-scale volumetric plastic strain
θ outward circumferential coordinate
θ_i yield locus parameter
θ_1 yield locus parameter
ξ accumulated relative mass removal
$\bar{\xi}$ macro-scale accumulated relative mass removal
$\dot{\xi}$ rate of relative dissolved mass
Λ plastic multiplier
$\bar{\lambda}$ plastic bulk modulus of compressibility
σ_{ij} stress tensor
$\bar{\sigma}_{ij}$ macro-scale stress tensor
σ_r radial stress
σ_z stress perpendicular to radial and circumferential coordinates
σ_θ circumferential stress
σ_θ^{yield} circumferential stress at the7 moment of yielding
σ_{01}^* stress related to initial strength
σ_{02}^* stress related to initial strength
ϕ proportionality constant indicating degree of chemo-mechanical coupling
ϕ_i yield locus parameter
ϕ_1 yield locus parameter

REFERENCES

Andriani, G. F. & Walsh, N. (2007a). Rocky coast geomorphology and erosional processes: a case study along the Murgia coastline South of Bari, Apulia – SE Italy. *Geomorphology* **87**, No. 3, 224–238.

Andriani, G. F. & Walsh, N. (2007b). The effects of wetting and drying, and marine salt crystallization on calcarenite rocks used as building material in historic monuments. *Geol. Soc. London Spec. Pub.* **271**, 179–188.

Bagi, K. (1996). Stress and strain in granular assemblies. *Mech. Mater.* **22**, No. 3, 165–177.

Buhmann, D. & Dreybrodt, W. (1985a). The kinetics of calcite dissolution and precipitation in geologically relevant situations of karst areas: 1. Open system. *Chem. Geol.* **48**, No. 1–4, 189–211.

Buhmann, D. & Dreybrodt, W. (1985b). The kinetics of calcite dissolution and precipitation in geologically relevant situations of karst areas: 2. Closed system. *Chem. Geol.* **53**, No. 1–2, 109–124.

Castellanza, R. (2002). *Weathering effects on the mechanical behaviour of bonded geomaterials: An experimental, theoretical and numerical study.* PhD thesis, Politecnico di Milano, Italy.

Castellanza, R. & Nova, R. (2004). Oedometric tests on artificially weathered carbonatic soft rocks. *J. Geotech. Geoenviron. Engng ASCE* **130**, No. 7, 728–739.

Castellanza, R., Parma, M., Pescatore, V. & Silvestro, G. (2009). Model footing load tests on soft rocks. *Geotech. Test. J.* **32**, No. 3, 262–272.

Ciantia, M. O., Castellanza, R., di Prisco, C. & Hueckel, T. (2013). Experimental methodology for chemo-mechanical weathering of calcarenites. In *Multiphysical testing of soils and shales* (eds L. Laloui and A. Ferrari), pp. 331–336. Berlin/Heidelberg, Germany: Springer-Verlag.

De Groot, S. R. (1966). *Thermodynamics of irreversible processes*. Amsterdam, the Netherlands: North-Holland.

Delenne, J. Y., Soulié, F., El Youssoufi, M. S. & Radjai, F. (2011). Compressive strength of an unsaturated granular material during cementation. *Powder Technol.* **208**, No. 2, 308–311.

Eslami, J., Grgic, D. & Hoxha, D. (2010). Estimation of the damage of a porous limestone from continuous (P- and S-) wave velocity

measurements under uniaxial loading and different hydrous conditions. *Geophys. J. Int*. **183**, No. 3, 1362–1375.
Ghabezloo, S. & Pouya, A. (2006). Numerical modelling of the effect of weathering on the progressive failure of underground limestone mines. *Proc. Int. Symp. Int. Soc. for Rock Mechanics (EUROCK), Liège*, 233–240.
Hill, R. (1950). *The mathematical theory of plasticity.* Oxford, UK: Clarendon Press.
Hu, L. B. & Hueckel, T. (2007a). Coupled chemo-mechanics of intergranular contact: toward a three-scale model. *Comput. Geotech*. **34**, No. 4, 306–327.
Hu, L. B. & Hueckel, T. (2007b). Creep of saturated materials as a chemically enhanced rate dependent damage process. *Int. J. Numer. Analyt. Methods Geomech*. **31**, No. 14, 1537–1565.
Hueckel, T. (1992). Water–mineral interaction in hydro-mechanics of clays exposed to environmental loads: a mixture theory approach. *Can. Geotech. J.* **29**, No. 6, 1071–1086.
Hueckel, T. (2002). Reactive plasticity for clays during dehydration and rehydration. Part I: Concepts and options. *Int. J. Plasticity* **18**, No. 3, 281–312.
Hueckel, T. & Borsetto, M. (1990). Thermoplasticity of saturated soils and shales: constitutive equations. *J. Geotech. Engng ASCE* **116**, No. 12, 1765–1777.
Hueckel, T. & Maier, G. (1977). Incremental boundary value problems in the presence of coupling of elastic and plastic deformations: a rock mechanics oriented theory. *Int. J. Solids Struct*. **13**, No. 1, 1–15.
Hueckel, T. & Mróz, Z. (1973). Some boundary value problems for variable density materials. In *Problèmes de la Rhéologie* (ed. W. K. Nowacki), pp. 173–191. Warsaw, Poland: PWN.
Hueckel, T., Pellegrini, R. & Del Olmo, C. (1998). Constitutive properties of thermo-elasto-plastic behavior of deep carbonatic clays. *Int. J. Numer. Analyt. Methods Geomech*. **22**, No. 7, 549–576.
Hueckel, T., Tao, F., Cassiani, G. & Pellegrino, A. (1999). Reactive plasticity for geological materials with a double structure evolving during aging. *Proc. 4th Int. Conf. on Constitutive Laws for Engng Mater., Troy, NY*, 383–387.
Kier, R. S. (1980). The dissolution kinetics of biogenic calcium carbonates in sea water. *Geochim. Cosmochim. Acta* **44**, No. 2, 241–252.
Krajcinovic, D. (1989). Damage mechanics. *Mech. Mater.* **8**, No. 2–3, 117–197.
Krauskopf, K. B. & Bird, D. K. (1995). *Introduction to geochemistry*, 3rd edn. New York, NY, USA: McGraw-Hill.
Lagioia, R. & Nova, R. (1995). An experimental and theoretical study of the behaviour of a calcarenite in triaxial compression. *Géotechnique* **45**, No. 4, 633–648, http://dx.doi.org/10.1680/geot.1995.45.4.633.
Lumb, P. (1962). The properties of decomposed granite. *Géotechnique* **12**, No. 3, 226–243, http://dx.doi.org/10.1680/geot.1962.12.3.226.
Maier, G. & Hueckel, T. (1979). Nonassociated and coupled flow rules of elastoplasticity for rock-like materials. *Int. J. Rock Mech. Mining Sci*. **16**, No. 2, 77–92.
Matsukura, Y. & Hirose, T. (1999). Five year measurements of rock tablet weathering on a forested hillslope in a humid temperate region. *Engng Geol*. **55**, No. 1–2, 69–76.
Moore, R. & Brunsden, D. (1996). Physico-chemical effects on the behaviour of a coastal mudslide. *Géotechnique* **46**, No. 2, 259–278, http://dx.doi.org/10.1680/geot.1996.46.2.259.
Morse, J. W., Arvidson, R. S. & Luttge, A. (2007). Calcium carbonate formation and dissolution. *Chem. Rev.* **107**, No. 2, 342–381.
Mróz, Z. (1973). *Mathematical models of inelastic material behaviour*. Waterloo, Canada: Waterloo University Press.
Mróz, Z. & Kwaszczynska, K. (1971). Certain boundary value problems for pulverized media with density hardening. *Engng Trans*. **19**, No. 1, 15–42 (in Polish).
Nova, R., Castellanza, R. & Tamagnini, C. (2003). A constitutive model for bonded geomaterials subject to mechanical and or chemical degradation. *Int. J. Numer. Analyt. Methods Geomech*. **27**, No. 9, 705–732.
Plummer, L. N. & Wigley, T. M. L. (1976). The dissolution of calcite in CO_2-saturated solutions at 25°C and 1 atmosphere total pressure. *Geochim. Cosmochim. Acta* **40**, No. 2, 191–202.
Schofield, A. N. & Wroth, C. (1968). *Critical state soil mechanics*. London, UK: McGraw-Hill.
Scholz, C. (1968). Micro fracturing and the inelastic deformation of rock in compression. *J. Geophys. Res*. **73**, No. 4, 1417–1432.
Sjöberg, E. L. (1976). A fundamental equation for calcite dissolution kinetics. *Geochim. Cosmochim. Acta* **40**, No. 4, 441–447.
Sjöberg, E. L. & Rickard, D. T. (1984). Temperature dependence of calcite dissolution kinetics between 1 and 62°C at pH 2·7 to 8·4 in aqueous solutions. *Geochim. Cosmochim. Acta* **48**, No. 3, 485–483.
Sjöberg, E. L. & Rickard, D. T. (1985). The effect of added dissolved calcium on calcite dissolution kinetics in aqueous solutions at 25°C. *Chem. Geol*. **49**, No. 4, 405–413.
Shuzui, H. (2001). Process of slip-surface development and formation of slip-surface clay in landslides in Tertiary volcanic rocks, Japan. *Engng Geol*. **61**, No. 4, 199–219.
Shuzui, H. (2002). Landsliding of ignimbrite subject to vapor-phase crystallization in the Shirakawa pyroclastic flow, northern Japan. *Engng Geol*. **66**, No. 1–2, 111–125.
Zhao, Y., Duan, X. K., Hu, L. B., Cui, P. & Hueckel, T. (2011). Multi-scale chemo-mechanical analysis of the slip surface of landslides in the Three Gorges, China. *Sci. China Technol. Sci*. **54**, No. 7, 1757–1765.

Alonso, E. E. & Ramon, A. (2013). *Géotechnique* **63**, No. 10, 857–870 [http://dx.doi.org/10.1680/geot.SIP13.P.023]

Massive sulfate attack to cement-treated railway embankments

E. E. ALONSO* and A. RAMON*

Two access embankments to a railway bridge, having a maximum height of 18 m, experienced a continuous and severe heave shortly after construction. Vertical displacements reached 120 mm in a 2-year period. The embankments were designed, by including soil–cement-treated transition wedges, to provide an increasingly rigid support as the trains approach the stiff bridge abutments. A grid of 10 m deep jet-grouting columns was also built, with the purpose of stabilising the embankments. Instead, a sustained swelling deformation, which extended to depths of 8–10 m, was activated. The compacted soil was low-plasticity clayey material, with a variable percentage of gypsum. The embankments suffered a massive ettringite–thaumasite attack, which was triggered by the simultaneous presence of cement, clay, sulfates and an external supply of water (rain). The paper describes the field extensometer and inclinometer records, the long-term laboratory tests performed, some mineralogical observations and the reactions leading to the growth of expansive crystals, and presents a model that simulates the measured heave. Forces acting against the bridge, which was seriously damaged, were estimated. Remedial measures include removal of the active upper zone of the embankments, and the construction in stages of slabs supporting the rails and founded on piles built on both sides of the embankments. The case is considered unique because of the magnitude of the reaction developed in the embankments, and its damaging action on the nearby bridge structure.

KEYWORDS: case history; chemical properties; expansive soils; field instrumentation; ground improvement; mineralogy

INTRODUCTION

Cement attack by sulfates is a well-known mechanism of degradation of concrete and mortars made of Portland cement. The phenomenon is well known in general terms. Portland cement has a dominant content (60–70%) of calcium oxide (CaO), a significant proportion (20–25%) of silica (SiO_2), a small proportion (2–6%) of aluminium and iron oxides (Al_2O_3, Fe_2O_3), and sulfate (in the form of gypsum: $CaSO_4{\cdot}2H_2O$) (1–5%). Gypsum is added to retard the paste setting.

Sulfate attack of a hardened cement paste leads to the development of ettringite, a hydrated sulfate of calcium and aluminium. This mineral crystallises in bundles of elongated filaments, which retain a high proportion of water molecules in the crystalline structure. The source of the attack is often described as being either 'internal' (when the cement itself has excessive sulfate content) or 'external' (when water carrying sulfate ions enters into contact with the hardened cement). The development of ettringite implies a destruction of the strength of the cement paste, and a substantial swelling. The external attack progresses as an advancing front from the surface exposed to the sulfated water. Aluminium oxides are reduced to a minimum in sulfate-resistant cements. In the absence of aluminium, ettringite does not develop. Another mineral, thaumasite, also develops as a consequence of sulfate attack. It is a hydrated sulfate of calcium and silicon. It may crystallise from ettringite by means of an isomorphous substitution of aluminium by silicon.

Cement- and lime-treated soils are often used to stabilise road bases and sub-bases. When the soil has some proportion of gypsum, or the treated soil is exposed to sulfated waters, a similar attack resulting in loss of strength and significant heave has often been reported (Sherwood, 1962; Mitchell & Dermatas, 1992; Snedker, 1996; Rajasekaran *et al.*, 1997; Puppala *et al.*, 2003; Rajasekaran, 2005). Some of these studies discuss the minimum sulfate content that triggers the attack. Most of the papers point out that sulfate contents in excess of 0·5–1% (concentration of soluble sulfate in water, by weight) result in ettringite formation and soil swelling.

However, lower threshold values (0·3%) have also been identified (Mitchell & Dermatas, 1992; Snedker, 1996). It appears that the loss of strength of the treated soil and associated swell is related to the sulfate content. Sherwood (1962) described an unconfined compressive strength reduction of 24% of treated soil when the sulfate content was as low as 0·25%.

Unlike 'pure' cement mixtures or concrete, treated soils usually contain a certain proportion of clay minerals, which are a source of aluminium and silicon ions. In fact, the highly basic environment (pH in excess of 12) created by the hydration of cement's calcium oxide is capable of dissolving the clay minerals and releasing Al and Si atoms, ready to be integrated into ettringite and thaumasite molecules. The implication is that sulfate-resistant cements, low in aluminium oxides, do not necessarily guarantee the prevention of sulfate attack in treated soils. However, Puppala *et al.* (2003) report the good performance of sulfate-resistant cement in stabilising soft and expansive clays with high sulfate content.

Most of the geotechnical literature on sulfate attack concerns the stabilisation of compacted road bases and sub-bases. The treatment is applied to relatively thin layers, and the sulfate attack results in surface heave and reduction of soil strength. In contrast, the case described here concerns an entire embankment. The induced swelling strains resulted not only in a surface heave but also in very high and totally unexpected forces against bridge abutments, which caused significant structural damage.

Manuscript received 5 March 2012; revised manuscript accepted 21 December 2012. Published online ahead of print 8 March 2013. Discussion on this paper closes on 1 January 2014, for further details see p. ii.

* Department of Geotechnical Engineering and Geosciences, Universitat Politècnica de Catalunya, Barcelona, Spain.

The paper first describes the two affected embankments, located on both sides of a bridge built recently for a high-speed railway line. Field measurements, once the heave was first identified, will be described, as well as the properties of the compacted material used in the construction of embankments. Sulfate attack will be described in some detail, relying on some specific tests performed and on some geochemical calculations. The embankment swelling was modelled, and an estimation of pressures developed against the bridge abutment was made. Finally, the costly remedial measures are briefly described. The case is probably an extreme case of sulfate attack to a large engineering structure, and highlights the severity of the phenomenon, which may develop when several contributory factors cooperate to create a critical and dangerous situation.

DESIGN AND CONSTRUCTION OF EMBANKMENTS

A 196 m long bridge, Pallaresos Bridge, which belongs to the high-speed railway link between Madrid and Barcelona, was built in the province of Tarragona, Spain, in 2004. Fig. 1 shows the plan view and a longitudinal section of the bridge. Each one of the seven bridge spans was structurally resolved by two parallel box girder beams resting isostatically on the pillars. A continuous, cast in situ slab was extended over prefabricated slabs placed over the girder beams. Rails were supported by a ballast layer on top of the continuous concrete slab. Fig. 2 shows a photograph of one of the embankments, the abutment and the bridge.

Bridge pillars were founded on excavated piles. The two abutments, of similar design and dimensions, were directly founded on a hard marl of Tertiary age. They limit the two embankments shown in the figure, which reached a maximum height of 18 m in the proximity of the abutments. The thickness of the approaching embankment decreased progressively away from the bridge abutments. The internal design of the embankments is shown, in longitudinal section, in Fig. 3. Transition wedges of increasing stiffness were designed to ensure a smooth transition from the compacted soil to the rigid bridge structure. The wedge closest to the abutment was specified as a cement–soil mixture. The embankment material was previously excavated in a Miocene natural formation: a sequence of claystones with some proportion of gypsum veins and interstratified sandstone layers. Some selected soil was used also as a rail track sub-base.

Fig. 2. Pallaressos embankment, Lleida side. The excavated pathway on the embankment side was made to allow access of drilling machines for installation of measuring instruments

Once the railway line was in operation, rail levelling started on a routine basis. Results of this levelling for two dates, 13 December 2005 and 3 April 2006, are shown in Fig. 4. The levelling performed in April 2006 shows two distinct swelling peaks in the position of the two abutments. No significant settlement or heave was detected along the bridge itself. Data in Fig. 4 show a maximum heave of 12–16 mm with respect to the initial levelling. Maximum heave rate, comparing the two successive levellings, is about 4·0–4·5 mm/month.

Countermeasures were adopted, and the rail tracks were levelled periodically by adjusting the thickness of the ballast layer. Since no signs of a reduction in heave rate were noticed, geotechnical investigations were commissioned. A difficulty for all the subsequent field activities was the need to keep the railway line in full operation.

Samples taken in the first borings drilled through the two embankments indicated that the cement-treated soil was rather weak, and prone to disintegration. It was also difficult to identify the expected geometry of wedges as shown in Fig. 3. These findings were probably the reason behind the

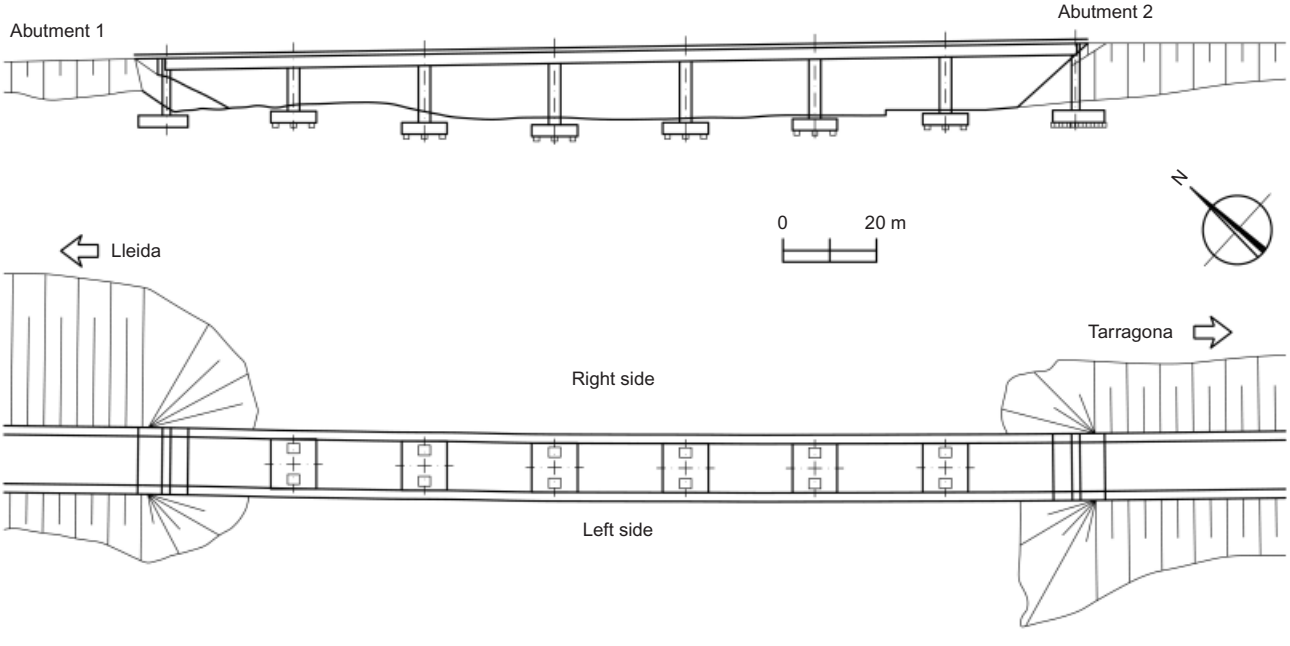

Fig. 1. Longitudinal profile and plan view of Pallaressos bridge

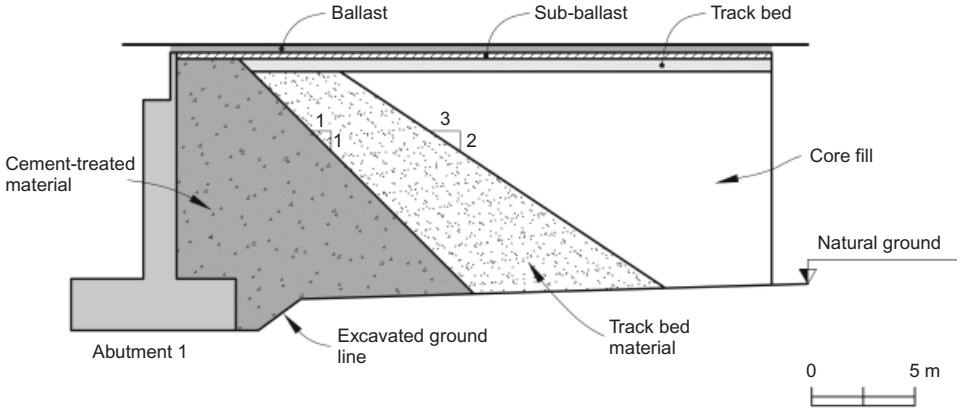

Fig. 3. Design of embankment

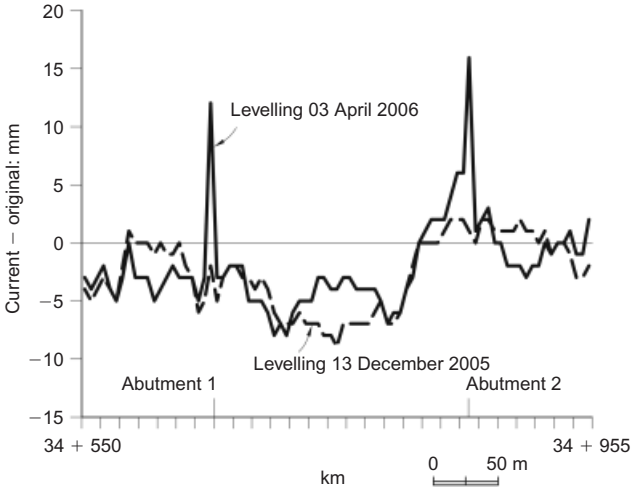

Fig. 4. Rail levelling after construction

decision to again reinforce the embankments, in October 2006, by means of 1·5 m diameter jet-grouting columns, which were arranged in the manner shown in Fig. 5.

The central part of the embankment was treated. Columns reached a depth of 10 m in the vicinity of the abutment. The length and density of the columns were reduced as the distance to the abutment increased. The transition zone was extended in both embankments to an overall length of 30 m.

One year after finishing jet-grouting treatment, at the end of 2007, embankment heave was again detected, and track profiling, by modifying the ballast cushion, had to start again. In May 2008 a surface-topographic survey provided precise information on the evolution of heave. It was found that the embankment heave had resumed, and measured heave rates (4·2 mm/month, 5·7 mm/month and 6·5 mm/month in different positions) were even higher than the values first observed when the problem was initially detected. Field monitoring and soil testing were thereafter increased.

FIELD OBSERVATIONS

Additional surface-topographic marks were installed on the top of the embankments. They covered a length of 35 m in the Lleida (1) embankment (Fig. 6) and 45 m in the Tarragona (2) embankment. Surface horizontal displacements were measured in the transverse and longitudinal embankment directions. Fig. 7 provides the measurements of horizontal and vertical surface movements in one of the abutments from 2 March 2009 to 19 April 2010. The records indicated that significant horizontal movements were developing in the transverse direction. An accumulated horizontal transverse movement of 150 mm was measured during the first 17·8 months of monitoring at topographic mark PR-1·5, located 10 m away from the Lleida abutment structure. An accumulated heave of 59 mm was measured at PR-1·5 during the same period.

The distribution of surface heave along distance is shown in Fig. 8 for Abutment 1. The maximum heave occurred at a distance of 10–13 m from the abutments. At further distances the displacement decreased progressively. At distances in excess of 30 m to the abutment no movements were detected. The transverse horizontal movements followed the same pattern. The maximum transverse horizontal movements were measured at the same points where the maximum heave was recorded.

The two embankments exhibited similar behaviour. The topographic monitoring also made it possible to measure horizontal movements along the longitudinal direction of the embankments. Points displaced towards the bridge abutment. Longitudinal displacements were substantially lower than the displacements recorded in the other two directions. However, displacements reaching 22 mm towards the abutment structure were measured during 17·8 months in topographic marks installed along the first 10 m from the abutment. The smaller displacements recorded in the longitudinal direction are explained by the confinement applied by the abutment and the bridge structure on one side, and by the rest of the embankment on the opposite side.

Topographic stations and levelling marks were also installed outside the embankments, on the natural ground, but no movements were recorded.

The evolution of vertical displacements in time at some points of both embankments is shown in Fig. 9. The rate of vertical displacements has not been constant in time. The average rates of heave, obtained by means of different measurement procedures, have been plotted in Fig. 10. The first estimation of heave rate corresponds to rail levelling that was available in 2006. Despite the variability of results, the plot shows that the heave rate has increased from values around 2–4 mm/month in 2006 to heave rates varying from 2·5 to 7·5 mm/month in 2008. Fig. 9 also provides the total accumulated rainfall. A relation between the evolution of heave and the rainfall events can be identified. Heave rate accelerates in periods immediately following significant rainfall events.

Inclinometer records showed that the horizontal movements were developing in depth. Some results are shown in Fig. 11. The horizontal displacements decreased gradually along the first 8–10 m of boring. Horizontal movements at positions deeper than 13–14 m were not significant. This

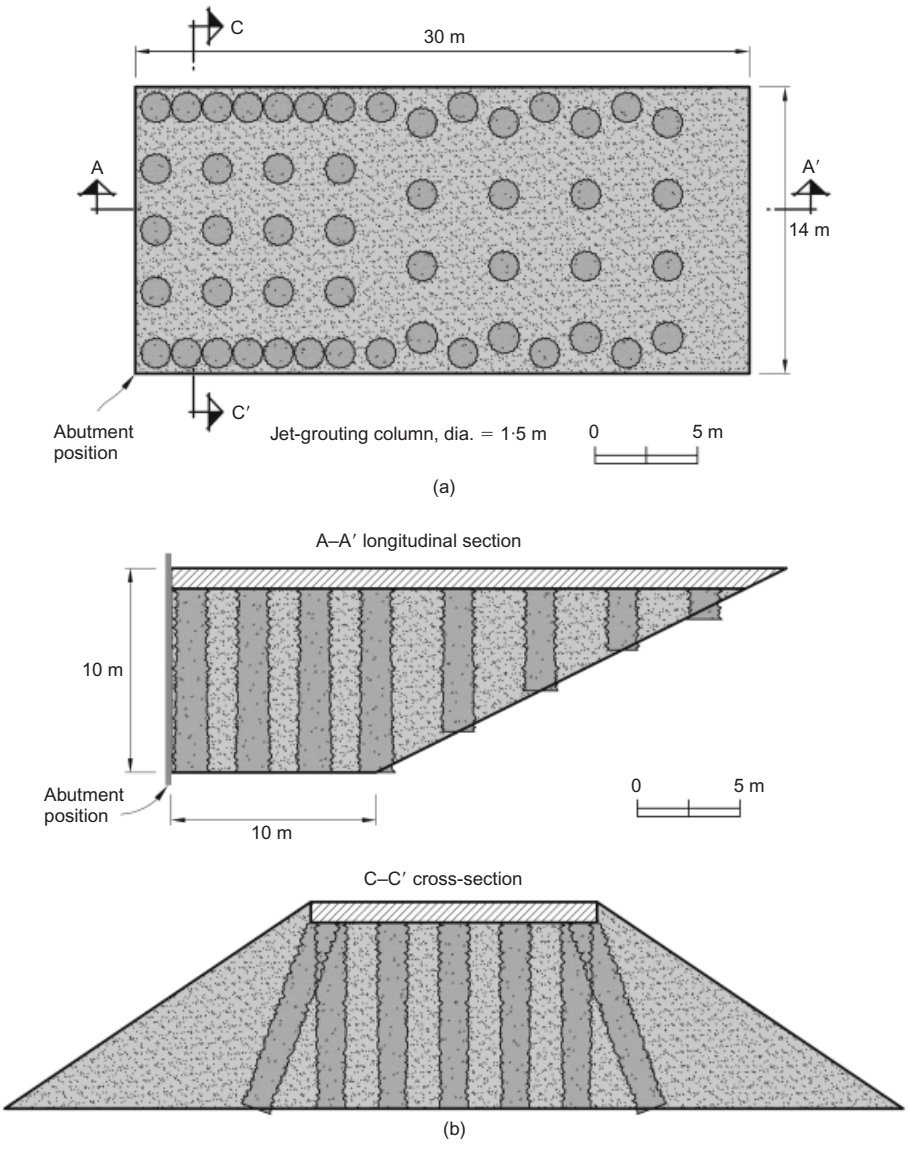

Fig. 5. Jet-grouting treatment of embankments: (a) position of columns in plan view; (b) cross-sections

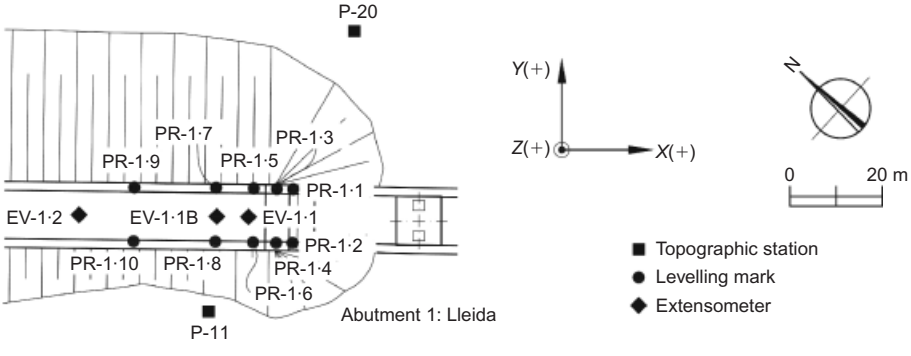

Fig. 6. Position of surveying topographic stations, levelling marks and continuous extensometers in Lleida embankment

behaviour was also observed for other inclinometers. Inclinometers measured a horizontal movement about 9–12 mm in the transverse direction from 31 October 2008 to 16 January 2009. Those horizontal movements indicated that the embankment was also swelling in a lateral direction.

Vertical deformation of embankments was investigated by means of continuous extensometers (sliding micrometers; Kovári & Amstad, 1982) installed in boreholes. Data were recorded on a monthly basis. The positions of the extensometers installed in the Lleida embankment are shown in Fig. 6. Continuous extensometers with lengths varying from 18 to 48 m were installed in each embankment at distances of 8, 13 and 40 m from the abutments. Measured swelling strains concentrated at the first 8 m. Smaller compressive

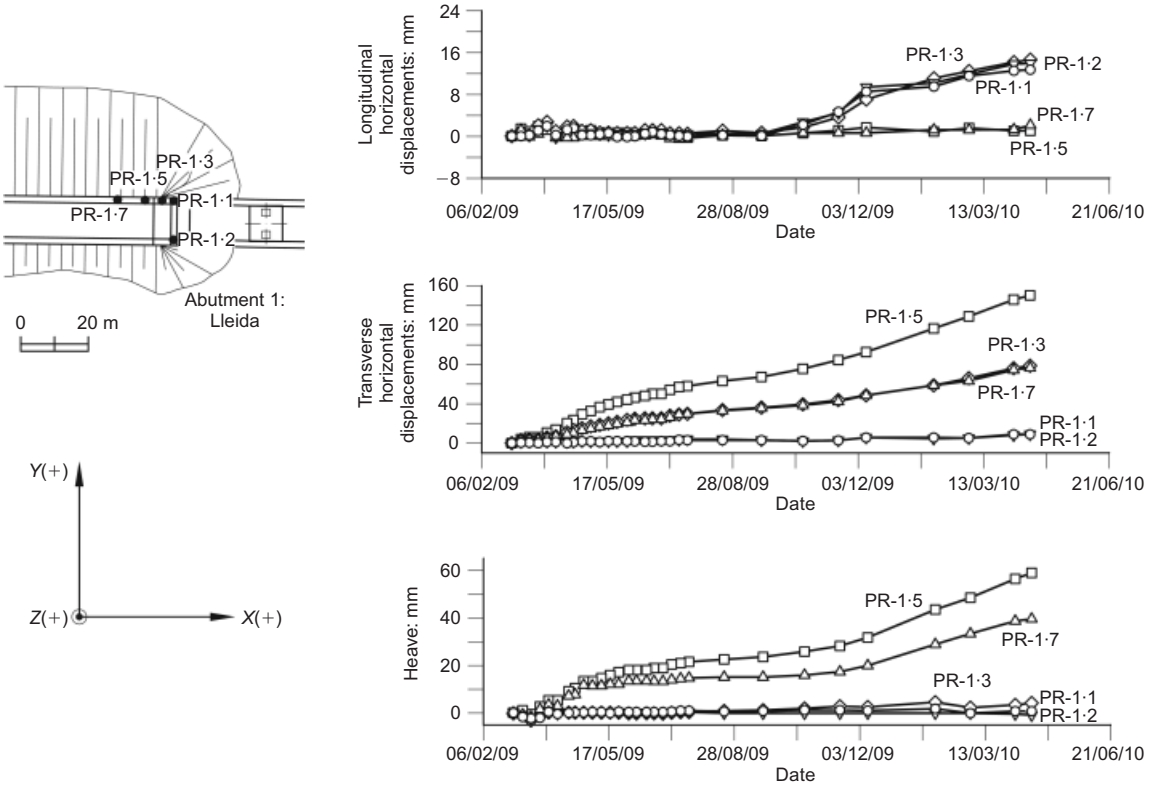

Fig. 7. Evolution over time of movements measured on embankment surface. Movements along three perpendicular directions were monitored by topographic surveillance

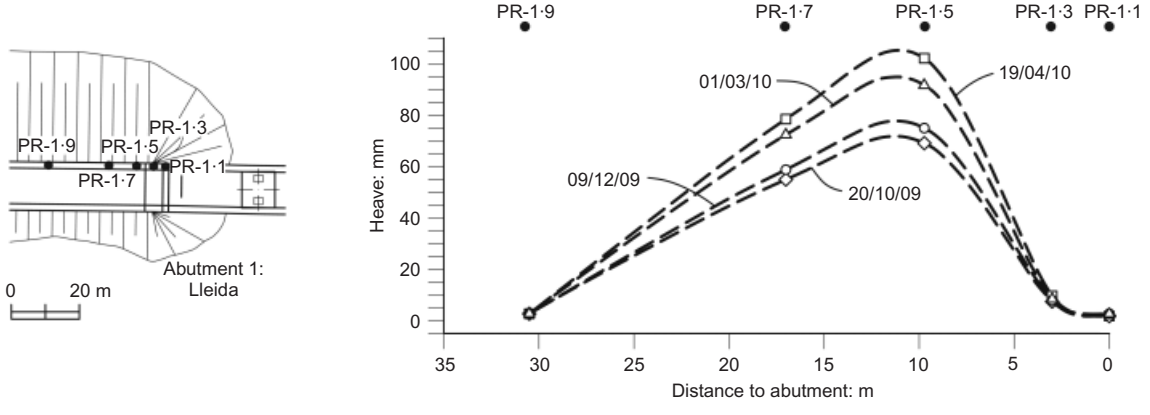

Fig. 8. Distribution of heave magnitude, measured by topographic levelling, on embankment surface plotted against distance between levelling mark and abutment. Initial measurement 26 May 2008

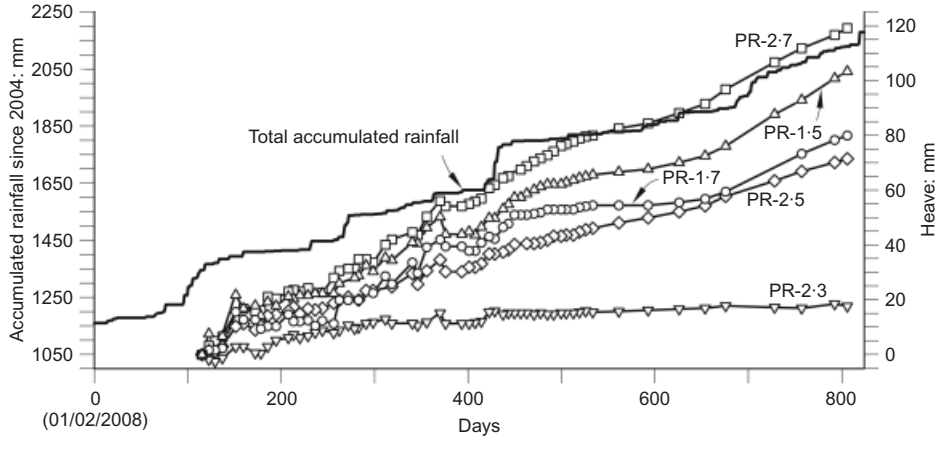

Fig. 9. Evolution of vertical displacements over time, measured at levelling marks of both embankments

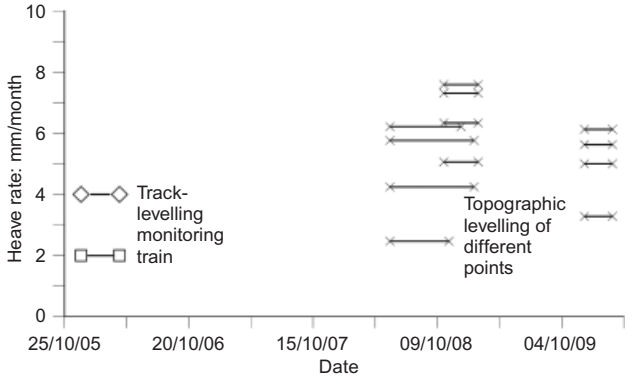

Fig. 10. Average heave rates of embankment at different periods of time

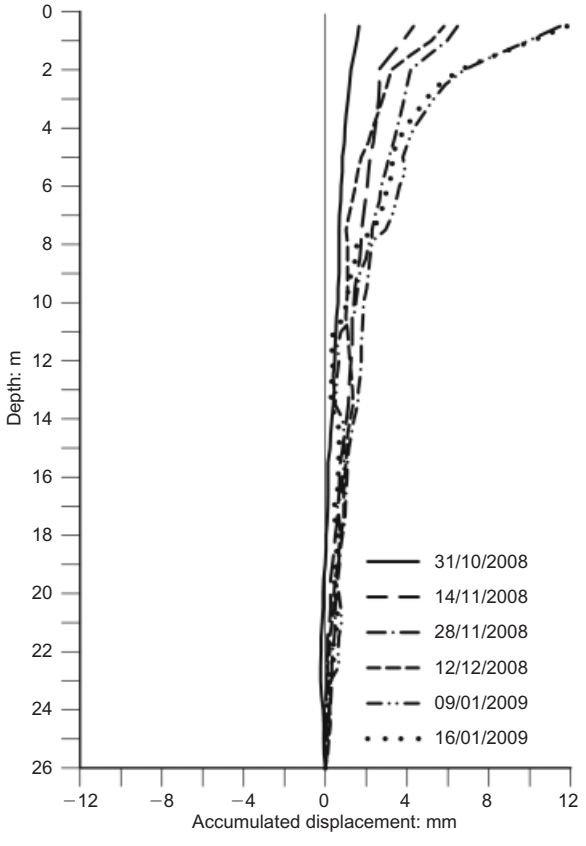

Fig. 11. Accumulated displacements measured at inclinometer I1T in Tarragona embankment

strains were recorded in the lower part of the embankments (Fig. 12). Strain records maintained the pattern of vertical variations over time (Fig. 12). The upper 'active' level did not progress downwards. Micrometers installed at a distance of 40 m from abutments recorded only a small compression.

The integral of strains along depth, measured in micrometres, was found to be consistently very close to the surface displacements measured in topographic marks. A continuous extensometer was also installed in natural ground at the centre of the valley to check whether any source of movements, other than the deformation of the embankments, was present in this case. No vertical displacements were measured by this instrument. The substratum was also shown as unstrained in all the sliding micrometers installed.

The results described indicate the three-dimensional nature of the deformation of embankments as a result of an internal volumetric swelling. A significant result was the reduced longitudinal deformation, which implied that high horizontal loads could be acting against the abutments, and therefore against the bridge itself. These forces were probably symmetrical, acting on both sides of the bridge. In fact, an inspection of the bridge structure revealed the existence of fissures and spalling damage at the contact between the abutment and bridge structural elements (Fig. 13). The development of swelling in the embankment also induced significant damage in the communications and drainage conduits on the top of the embankments, near the abutments. A displacement of the abutment structure towards the bridge was noticed 'de visu'. This unforeseen horizontal loading against the bridge prompted a thorough inspection of the structure, and the adoption of various repairs that are not described here. An interesting observation, which shows the effect of opposing forces acting on the two sides of the bridge, is the pattern of bending-induced cracking on the lower part of the pillars, which is sketched in Fig. 14.

There was also a concern about the possibility of strong passive stresses developing on the upper part of the embankments, in the longitudinal direction. A passive failure could result in a risk of rail distortions. An analysis of the stress state inside the embankments, reported below, was performed. First, the geotechnical properties of the embankment materials will be described.

GEOTECHNICAL DATA

Pallaresos Bridge crosses a small valley in the eastern part of the Ebro Basin, which is filled by Tertiary deposits of Miocene age. The substratum, a sequence of horizontally deposited reddish claystone layers and sandstones poorly cemented, appears close to the surface. Thin veins of gypsum cross the claystone at regular intervals. Limestone layers of high lateral continuity are also interbedded in the sequence of claystones and sandstones. Claystone levels dominate the sequence. When intact, it reaches unconfined compression strengths in the range 10–50 MPa. However, the claystone has a weak cementation, and it is very sensitive to changes in water content.

Compaction data taken during construction of embankments are given in Fig. 15. Dry-density–water-content pairs determined on embankment lifts are plotted in the figure. Also indicated are the determined modified Proctor optimum values. The fill reached quite high dry densities, even if the modified optimum dry densities were seldom reached. On the other hand, the compaction water content was ordinarily on the dry side of optimum. Very often, the degree of saturation was fairly low ($< 0{\cdot}7$): therefore as-compacted suction was high, and water (mainly from rainfall) would tend to progressively wet the embankment.

One of the modified Proctor optimum points in Fig. 15 shows an exceptionally high value of water content and a low dry density. This point was reported in the original 'as built' documents. It was decided to maintain it, despite the large differences with respect to the remaining points. The plot in Fig. 15 includes density and water content information on 24 construction layers. Interestingly, the field densities determined for the particular layer (a total of eight values), showing the exceptional density and water content values of the modified Proctor (MP) optimum, also exhibited abnormally low density values. It is inferred that the data are correct, and may be explained by the heterogeneous nature of the source material.

Points above the $S_r = 1$ line are explained by errors in the raw laboratory data. The tests were performed at the time of construction by a control laboratory, and it was decided to include all of them in the plot of Fig. 15.

Figure 16 shows the exposed surface of a cut through the

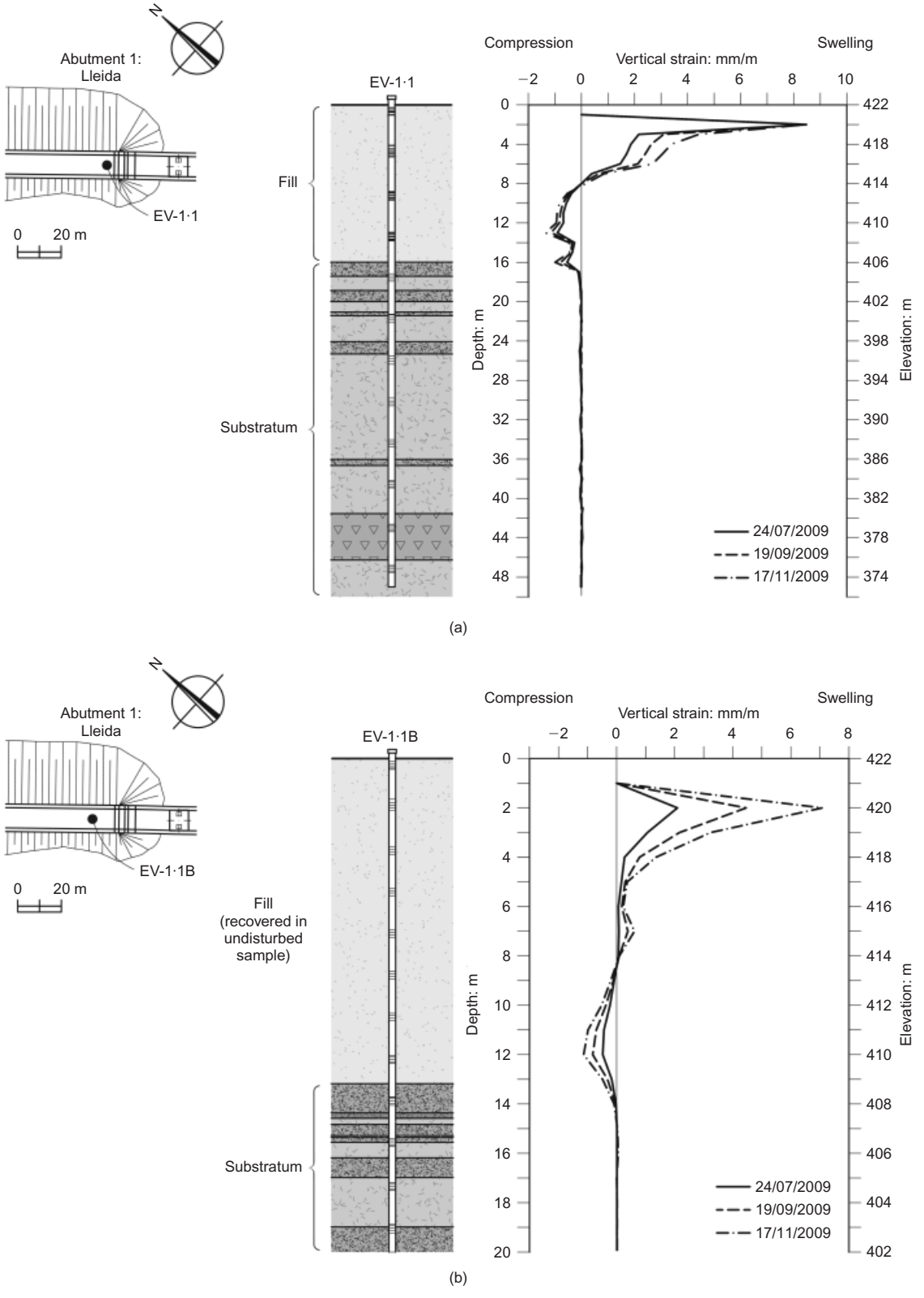

Fig. 12. Vertical displacements measured by sliding micrometer: (a) EV-1·1; (b) EV-1·1B (see positions in Fig. 6)

upper part of one of the embankments. The excavation was performed during the underpinning operations described later. The picture shows two jet-grouting columns, a cement-treated soil in the lower part, and the reddish compacted fill with an abundant presence of gravels and small boulders.

Samples taken in some borings were tested, and vertical profiles of some identification properties are given in Fig. 17. The fine fraction is low-plasticity clay. The data suggest a decrease in plasticity with depth within the embankment. Water content remains below the plastic limit, except in one of the tested specimens, which has an abnormally high value in view of the compaction data given in Fig. 15. Grain-size distribution tests provided the following fractions (average value and range): gravel 35% (62·1–18·6%); sand 21% (35·1–10·5%); and fines content 35% (69·3–7%). The mean diameter varied widely (8·0–0·0035 mm), with an average

Fig. 13. Damage observed near abutments

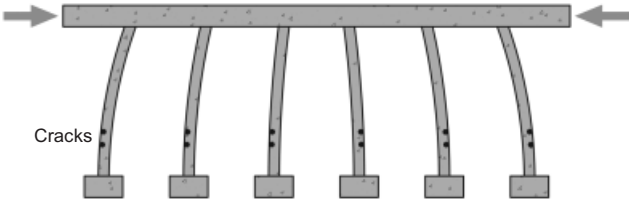

Fig. 14. Loading and deformation situation of bridge due to thrusts on abutments

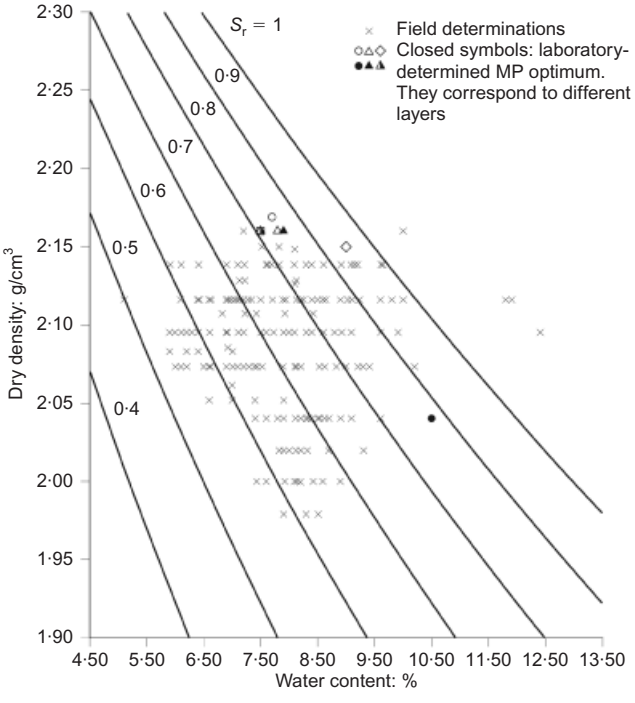

Fig. 15. Compaction data taken during construction of embankments (open symbols, field determinations; closed symbols, laboratory-determined modified Proctor (MP) optima)

value of 1·6 mm. Some boulders with sizes in excess of 100 mm were scattered inside the fill. They had sharp edges, because they were a result of blasting the Miocene formation. Smaller-size gravels, however, had rounded edges. The main minerals identified, and their approximate contents, as determined in semi-quantitative X-ray diffraction analysis,

Fig. 16. View of cut across one of the embankments made during underpinning operations. Two jet-grouting columns and a level of cement-treated material, in the lower part, are visible. Sandstone gravels and small boulders are scattered in the compacted marl matrix

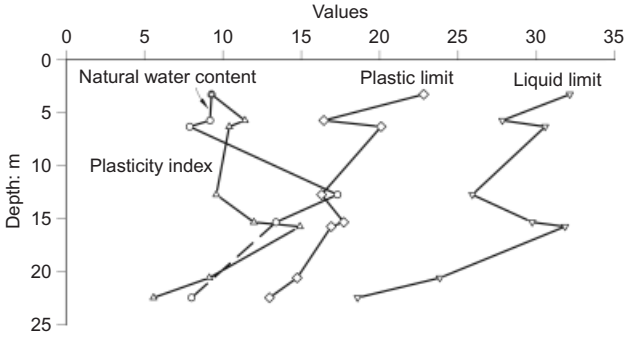

Fig. 17. Index properties determined in samples taken in boring drilled in Tarragona embankment (data from boring ST-1)

were: carbonates (calcite and dolomite) 52%; gypsum 20%; clay minerals (illite and kaolinite) 18%; and quartz 10%.

Relevant information is the variation with depth of soluble sulfates in the soil, given in Fig. 18. It reaches values in the range 2·0–2·5% in the upper 8 m. At lower levels, the sulfate content drops to less than 0·5%. Most probably this was the result of two different source areas. It reflects the natural variation of gypsum content found in the natural formation. Data given in the introduction suggest that sulfate attack of cement is likely to develop in the upper 8 m of the embankment.

Swelling tests

Samples recovered in borings were difficult to test, because of the presence of gravels. The following procedure was followed to approximate the conditions in the embankment. Gravels of limestone or sandstone were removed, and the remaining soil was homogenised. The homogenisation was carried out in disturbed samples recovered in boring lengths of approximately 1·20 m. The resulting 'soil' was compacted to standard Proctor energy and a water content of 10%. A dry density very close to 2 g/cm^3 was achieved in four tested samples that extended from the surface to a depth of 4·80 m. Samples were tested in the plastic mould used for compaction (diameter 120 mm, height 160 mm). Silicon grease was previously applied to the mould inner surface. The unloaded samples were placed in a closed chamber at a constant temperature (8°C), and the lower

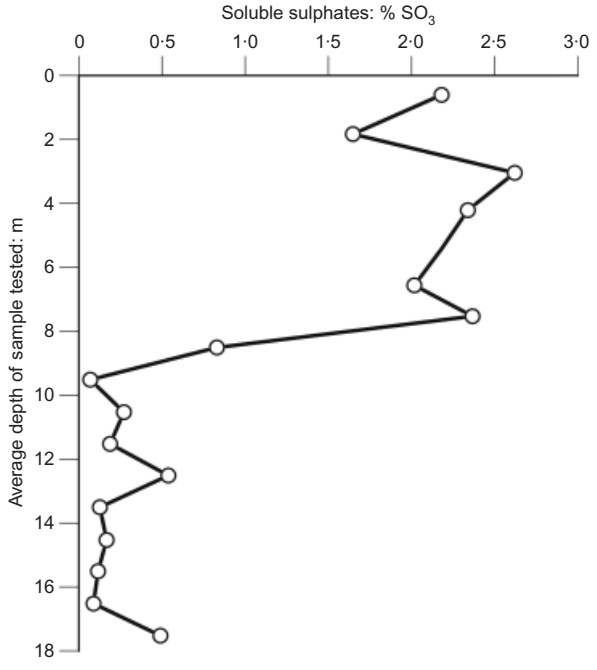

Fig. 18. Variation of sulfate content determined in samples recovered in boring S-2·1B (Tarragona embankment)

20−30 mm of each sample were kept in a bath under water. Water could migrate upwards by capillary gradients. Vertical displacements were measured on the sample top.

The results are shown in Fig. 19. The initial response reflects a 'standard' swelling associated with suction reduction and clay minerals hydration, but the long-term swelling observed in all samples cannot be explained by these mechanisms. In addition, the strong swelling measured in some samples, especially in one of them (1·20−2·40 m), is not expected in a low-plasticity soil compacted at a standard Proctor density. The mineral content of the samples before testing was not determined: therefore the measured swelling cannot be related to some particular distribution of constituents (the compaction water content and dry density were very similar in all four samples tested). The significant result is that all tests exhibited a long-term swelling that, despite variation from test to test, was very relevant. Again, these tests are an indication of the heterogeneity of fill characteristics. The sample taken from 1·20−2·40 m, which developed the strongest swelling, was dismantled after 150 days of testing, and smaller portions were subjected to X-ray diffraction and scanning electron microscopy (SEM) observations. Ettringite and thaumasite crystals were identified.

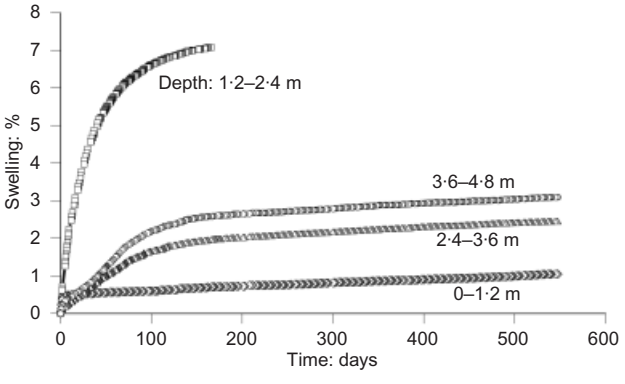

Fig. 19. Long-term swelling tests on compacted samples (boring S-2·1B)

They also provided strong peaks in the X-ray diffractograms. Samples collected in the embankments were also analysed, as described below.

MINERAL GROWTH AND CHEMICAL REACTIONS

Samples for mineralogical observations were taken from several positions in the field

(*a*) core samples from borehole instrumentation
(*b*) samples taken from the exposed soil or jet-grouting columns on the surface of embankments
(*c*) samples taken in excavations of the upper 5 m of the embankments during underpinning.

They were subjected to X-ray diffraction analysis and SEM–EDS (scanning electron microscopy–energy dispersed spectrometry) observations. An optical microscope with a 100× magnifying power was also employed. The results can be summarised as follows.

(*a*) Poorly cemented soil–cement mixtures or pure cement grout had a low apparent weight, a wet, sometimes muddy, consistency, and a whitish colour. Ettringite and, most notably, thaumasite were always found. The SEM photographs in Figs 20 and 21 are characteristic patterns.
(*b*) The following minerals were detected in the reddish clay matrix: calcite, gypsum, quartz, dolomite, illite (sericite) and kaolinite.

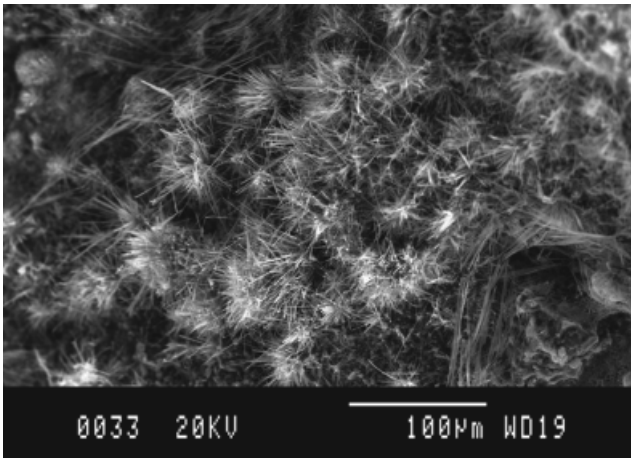

Fig. 20. Ettringite needles found in tested sample

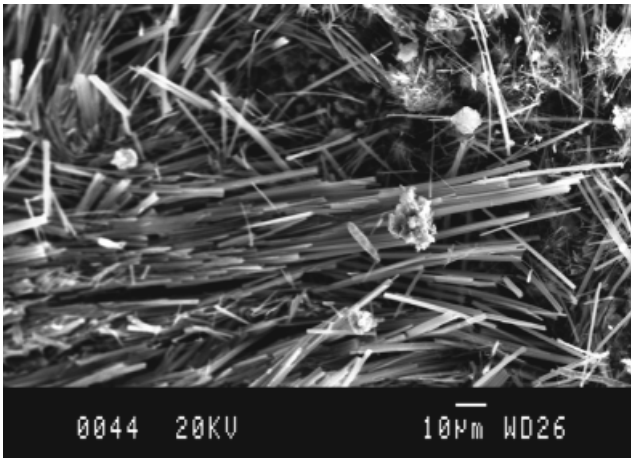

Fig. 21. Thaumasite flat crystals and ettringite needles found in tested sample

(*c*) Low-density thin flakes could be easily peeled off from the cement-treated columns, which often exhibited an advanced degradation state. A white powder was observed, especially in fissures or holes. When observed by the SEM, it was identified as thaumasite crystals.

The chemical formulae for ettringite and thaumasite are

(*a*) ettringite: $Ca_6[Al(OH)_6]_2(SO_4)_3 26H_2O$
(*b*) thaumasite: $Ca_6[Si(OH)_6]_2(CO_3)_2(SO_4)_2 24H_2O$.

In both minerals, the presence of water is remarkable. Thaumasite growth is regarded as a secondary process once ettringite has crystallised. Comparing the two atomic compositions, thaumasite implies the substitution of Al by Si, and the presence of a carbonate component. The development of both minerals follows a complex process, which has been described by Hunter (1988), Mitchell & Dermatas (1992) and Mohamed (2000). In lime- or cement-stabilised soils, the process starts by the hydration of lime and ionisation of the calcium hydroxide. The highly basic environment (pH $>$ 12) dissolves clay minerals, which provide a source for Al and Si. High pH also favours the dissolution of sulfate minerals, which provides Ca^{2+} and SO_4^{2-} ions. Ettringite precipitates when aluminium released from clays, calcium from cement or lime, and sulfates combine with water molecules. Crystals develop in the pore solution (Deng & Tang, 1994; Mohamed, 2000).

Carbonic acid, present in the pore water, and the dissolution of calcite lead to the precipitation of thaumasite, once ettringite is present. Hunter (1988) indicates that the presence of thaumasite (and the absence of ettringite) suggests that the transition of ettringite to thaumasite is complete. The dominant presence of thaumasite in the analysed samples from the embankment suggests an advanced state of sulfate attack. Bensted (2003) indicates that thaumasite can be formed by a direct reaction between calcium, sulfate, silica and carbonate ions in water solutions. However, these reactions are unlikely, or very slow (Köhler *et al.*, 2006). Additionally, it has been reported that thaumasite crystallises only at temperatures not reaching 15°C, a result that was recently challenged by Blanco-Varela *et al.* (2006), who found that thaumasite may develop at temperatures as high as 25°C. Rajasekaran (2005) reports that ettringite appears to be more stable above 15°C. Therefore, the climate in Pallaressos (a marked two-season Mediterranean environment) may explain the development of thaumasite as well as ettringite at all times throughout the year.

With the purpose of obtaining an improved understanding of the sulfate attack, a simulation of the processes taking place at the soil/cement interface was performed with the help of a general-purpose transport and chemical reactions program, Retraso (reactive transport of solutes; Saaltink *et al.*, 1998, 2005). Retraso solves the coupled hydraulic transport processes and the chemical reactions. Chemical equations provide the source or sink terms (concentrations of different species) of the mass conservation equations. The set of non-linear partial differential equations is solved simultaneously by iterative procedures. The included transport processes are advection, molecular diffusion and mechanical dispersion. The code handles mineral precipitation and dissolution reaction under a large set of experimental kinetic and equilibrium laws. Kinetic laws are included in a large database. The structure of the kinetic equations was proposed by Lasaga (1984). The code can handle a number of chemical reactions (e.g. acid–base, redox, aqueous complexation) under local equilibrium.

A simple one-dimensional problem, illustrated in Fig. 22(a), was analysed. Two porous materials, the compacted

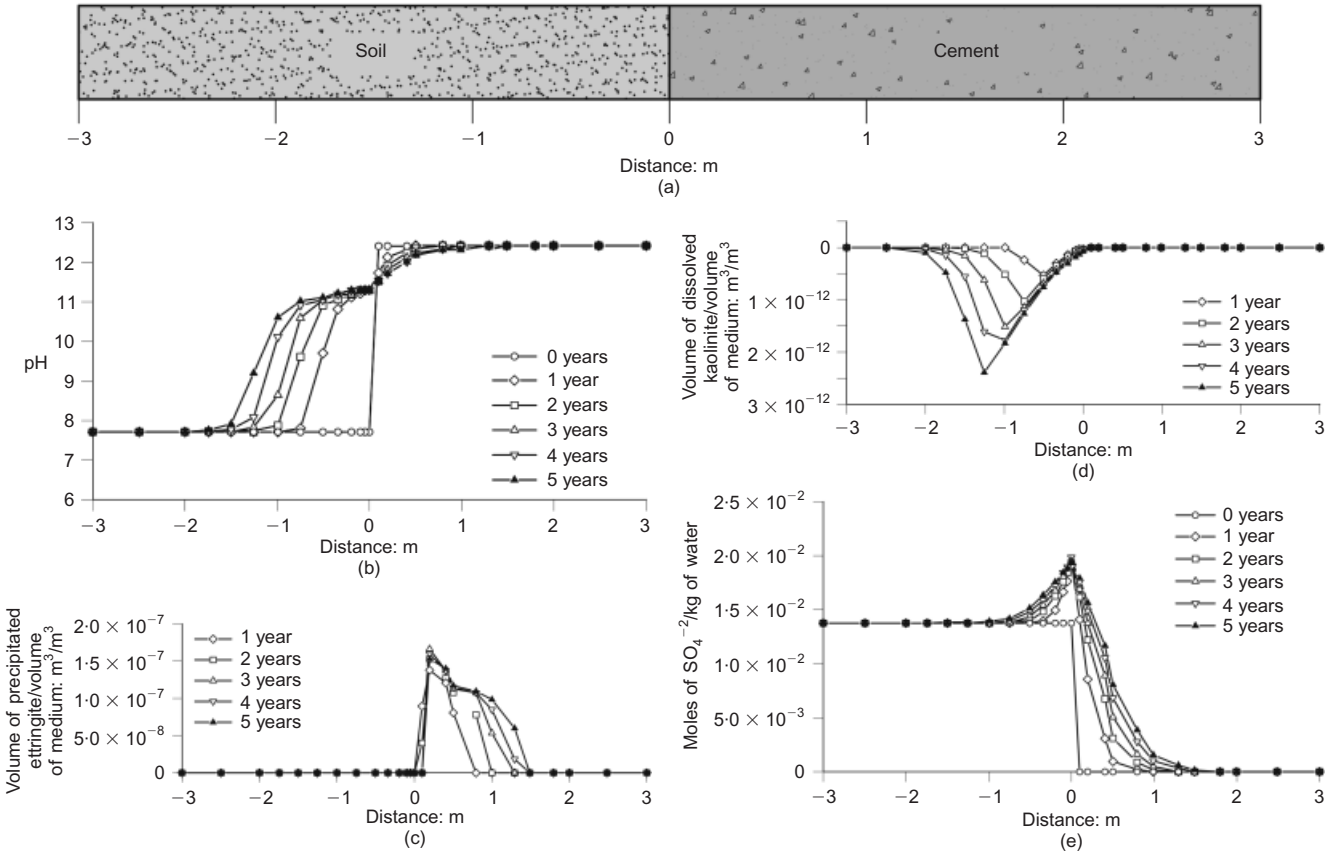

Fig. 22. Analysis of soil–cement reactions with the program Retraso: (a) geometry of problem; (b) evolution and distribution of pH; (c) volume of ettringite; (d) volume of kaolinite; (e) concentration of sulfate

soil and a cement grout, interact through a common interface. The soil–cement properties and their 'active' constituents are given in Table 1. Only diffuse processes are considered.

The idea was to check whether ettringite comes out naturally as a new species, and to follow its distribution in space (on both sides of the interface) and time. In addition, there was an interest in knowing the evolution of other constituents and the pH of the medium, a key piece of information to explain the sulphate attack.

An initial pH in equilibrium was calculated for the soil and the cement pore water with the program PHREEQC (Parkhurst, 1995; Parkhurst & Appelo, 1999), which simulates chemical reactions in aqueous solutions. Initial values of pH = 7·7 and pH = 12·4 were calculated for the soil and cement pore water respectively. Then Retraso was used to obtain the precipitated or dissolved amounts of calcite, dolomite, gypsum and ettringite. They were calculated by equilibrium equations, because they result from rapid reactions. In the case of kaolinite, quartz and portlandite (calcium hydroxide), kinetic equations were used in Retraso. Some results are given in Fig. 22 for a calculation period of 5 years.

The pH maintains a high value on the cement side of the interface. A plume of high pH values migrates progressively towards the soil (Fig. 22(b)). In parallel, an ettringite front advances in the cement medium (Fig. 22(c)). In 5 years, a deep penetration is calculated (~1·5 m). The sulfate attack started (against the treated wedge and, later, against jet-grouting columns) in 2006, soon after the end of embankment construction. The calculated depth of the ettringite front in Fig. 22(c) suggests that the attack has currently (2012) affected the whole volume of the grouted columns. In fact, in all samples recovered at different positions, ettringite and/or thaumasite was identified.

Two additional results are shown in Figs 22(d) and 22(e). Kaolinite is being progressively dissolved in the soil, starting at the interface. The consequence is the release of Al ions, necessary for ettringite precipitation. The concentration of sulfate increases at the interface and in the immediate vicinity, which induces the precipitation of ettringite.

Even if the analysis performed is quantitative, the calculated volume fraction of precipitates (or dissolved species) is not believed to be representative. The real problem is exceedingly complex: for example, the reactive surface is unknown (a small value, 0·14 m^2/m^3, was adopted in the calculation model), there are uncertainties on the validity of the kinetic equations, the pore water was probably under significant suction values for most of the time, and initial volume fractions and diffusion coefficients were estimated. Therefore, no attempt was made to couple the chemical calculations with the observed heave. The measured swelling strains and their effect on the bridge were approached in a much simpler manner, as discussed below. Nevertheless, the chemical analysis performed provided a good understanding of sulfate attack.

Table 1. Initial parameters for hydro-chemical analysis

Property	Compacted soil	Cement
Porosity	0·3	0·3
Diffusion coefficient, D: m^2/s	10^{-9}	10^{-9}
Volumetric fractions	Calcite: 0·2 Dolomite: 0·18 Gypsum: 0·05 Kaolinite: 0·05 Quartz: 0·03	Portlandite: 0·35 Quartz: 0·35
Reactive surface: m^2/m^3	0·14	0·14

MODELLING EMBANKMENT SWELLING

Measured swelling strains and surface heave provided data to perform a stress analysis of the embankment. A suspected passive state in the upper part of the embankment caused some concern, because of a possible instability disrupting the rail tracks. Also, structural engineers in charge of bridge rehabilitation were interested in estimating the existing longitudinal forces against the bridge.

A plane-strain analysis was conducted (Fig. 23). The embankment material was simulated as a Mohr–Coulomb model with parameters estimated from available design and construction data ($E = 67$ MPa, $\nu = 0{\cdot}3$, $c' = 5$ kPa, $\phi' = 30°$). Elastic moduli were measured in loading–reloading branches of plate-loading tests performed during embankment construction. Seven tests were performed, and the chosen value is close to the lower limit. Strength parameters are a conservative estimate of the compacted low-plasticity soil. A zero dilatancy angle was also imposed.

Swelling was modelled by imposing a volumetric deformation distributed in the volume indicated in Fig. 23. This active zone was divided in sectors, following the data provided by the continuous extensometers. The imposed strains were guided by two criteria: reproducing the sliding micrometer data approximately, and reproducing the measured heave at surface level.

Figure 24 shows a comparison of measured and calculated heave in the period 26 May 2008 to 9 December 2009. Swelling strains result in a substantial change in the initial geostatic distribution of stresses. Horizontal stresses become major principal stresses in the upper part of the embankment (Fig. 25). Calculated stresses against the fixed bridge abutment indicated that the essentially horizontal stresses have reached a passive state. The calculation provided an estimated total force of 2·32 MN/m in the transverse direction against the bridge abutment. A discontinuity is calculated at the boundary between the swelling layer and the lower non-active soil.

Calculated stresses and forces against the bridge are most probably a lower limit to the actual values, because of the

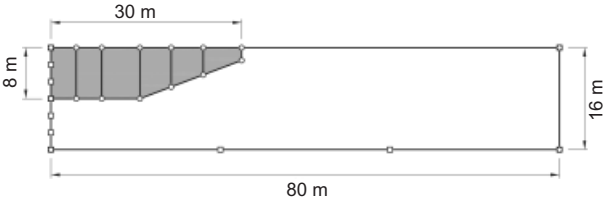

Fig. 23. Geometry of finite-element model

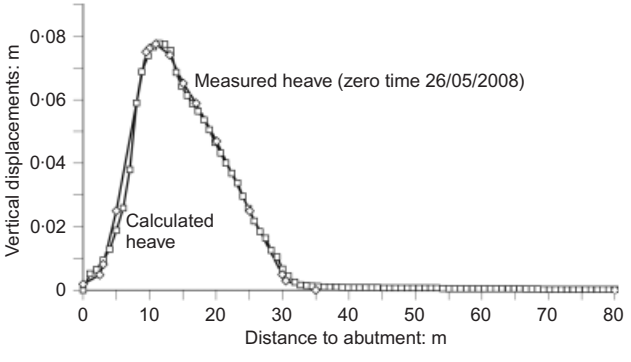

Fig. 24. Calculated and measured vertical displacements, matching recorded swelling

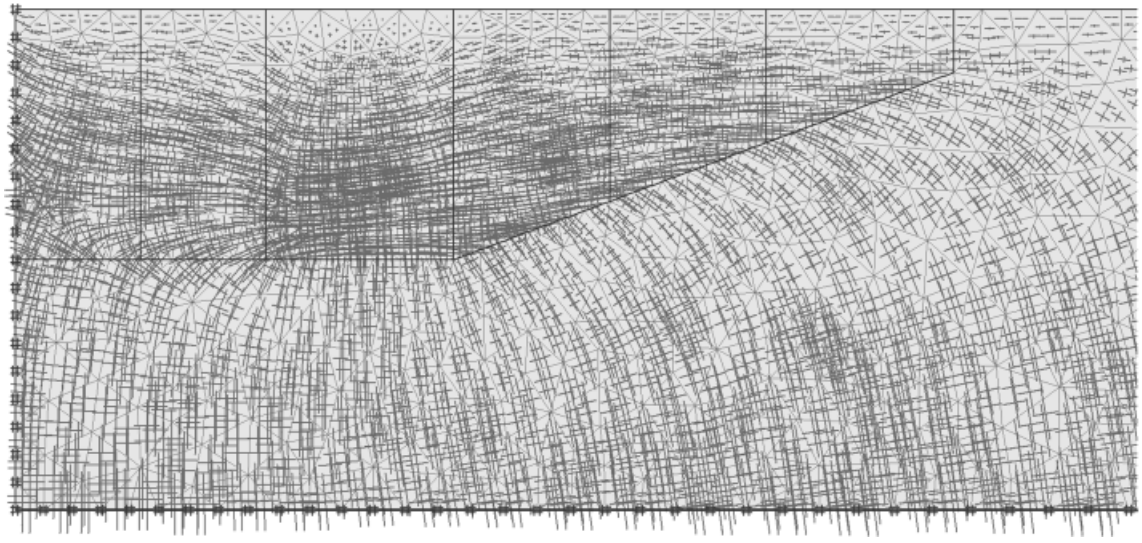

Fig. 25. Calculated principal stresses in embankments

conservative estimate of friction and effective cohesion, bearing in mind that the fill remains unsaturated. Increased strength would not prevent a passive state being reached, because the actual swelling experienced by the fill since the first warnings in 2006 is substantially higher than the modelled heave recorded in the shorter period analysed.

It was concluded that, in addition to the need to provide a new and stable support for the rails, the stresses against the bridge abutment should also be substantially reduced. On the other hand, there was no hope of a reduced swelling rate for the immediate future.

REMEDIAL MEASURES

Despite the signs of a mature state of the sulfate attack (hydrochemical calculations described; dominant presence of thaumasite), the field swelling records suggested that heave of the treated embankments could continue for years at a sustained rate. Modifying the thickness of the ballast cushion below the rail tracks could not cope with the expected medium-term heave. Forces against the abutment wall were damaging the bridge, and a passive state of stress, threatening the rail tracks, had developed in the upper part of the embankments.

It was then decided to excavate the upper 6 m of the embankments in the stretch affected by sulfate attack, and also to support the rail tracks by a structure founded on piles on both sides of the embankment. The solution is shown in Fig. 26. Supporting piles (excavated piles, which reach the substratum) were first built in the position shown in the plan view of Fig. 26(a). Then reinforced concrete slabs were built on the sides of the railway tracks, after enlarging the embankments in a lateral direction. Once the rail tracks were underpinned, the upper part of the embankments was excavated in stretches 9 m long, and the concrete slabs were slid into place. Fig. 26(b) shows a longitudinal section of the solution. An open gap, 3 m thick, will be left between the lower surface of the slabs and the new upper surface of the embankments.

CONCLUDING REMARKS

Sliding micrometer data were conclusive in showing the extent of the swelling strains within the embankment. The upper 8 m had a sulfate content (2·5%) sufficiently high to explain the attack. However, solid gypsum gravels were scattered throughout the soil mass. They constitute, *de facto*, a substantial increase in gypsum content, which is not accounted for in the chemical analysis of the fine fraction of the soil.

The potential growth of ettringite and thaumasite will continue until the exhaustion of sulfates. The availability of other chemical species (calcium, silicates, aluminium and water) seems essentially unlimited in the embankments.

The longitudinal profile of surface heave is, in part, explained by the layout of grouting columns. Friction against the abutments, enhanced by the high horizontal stresses developed in the longitudinal direction, explain the small vertical displacements measured in the vicinity of the abutment wall. The restriction to vertical heave offered by the abutment also explains, to some extent, the settlements measured by the extensometers below the upper expanding volume. But there is also the possibility of a collapse of soil as rainwater migrates downwards. The compaction data given in Fig. 15 indicate that a significant proportion of the embankments was initially under high suction. The confining stress below the 'active' upper part (vertical stresses in excess of roughly 170–180 kPa) is probably enough to explain some collapse strains. This aspect of the embankment behaviour has not been analysed in this paper, which concentrates on the chemical changes and their consequences, associated with sulfate attack on cement-treated materials in the presence of clay minerals and water.

The case history described is a case of failure of the controls expected during the execution of earthworks for bridge abutments (the Spanish Standards indicate that soils containing gypsum and other salts should not be stabilised with cement). The Standards also open the possibility of using sulfate-resistant cement in cases of sulfate content in excess of 0·5%. Many access embankments to bridges located in the very large Ebro Basin, where sulfates are widespread, have been built in recent years. However, to the authors' knowledge, no similar reaction has been reported. Nearby cases in which the embankment material was selected to avoid sulfates are also known to the authors. No damage was observed in those cases. Standards also specify that the director of works should conduct a laboratory testing plan, whose scope is also defined, before authorising the initiation of fieldworks. It seems that these controls and provisions were not followed to the extent required in the case reported.

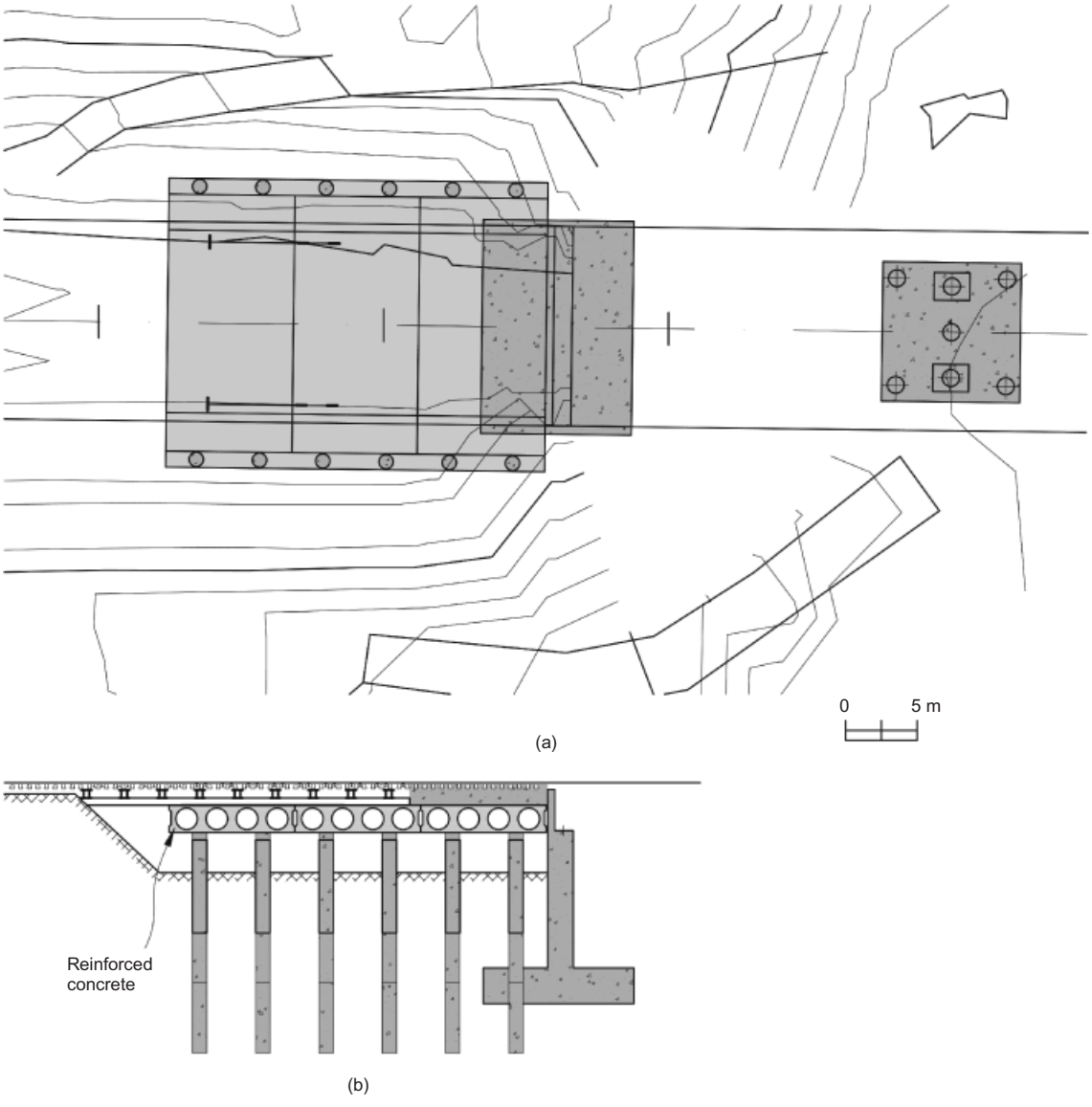

Fig. 26. Design of repair solution: (a) plan view of slabs founded on piles; (b) longitudinal section showing excavation, underpinning of rail tracks, supporting reinforced slabs and piles

ACKNOWLEDGEMENTS

The authors wish to acknowledge the technical and economic support provided by A. Alba and I. Macías, engineers of the Spanish Railway Agency, ADIF. Thanks are also extended to Dr M. Saaltink for his help on the chemical modelling and to Professor E. Vázquez, Dr M. Barrera and E. Tauler for their contribution in the identification of minerals.

REFERENCES

Bensted, J. (2003). Thaumasite: direct, woodfordite and other possible formation routes. *Cem. Concr. Compos*. **25**, No. 8, 873–877.

Blanco-Varela, M. T., Aguilera, J. & Martínez-Ramírez, S. (2006). Effect of cement C_3A content, temperature and storage medium on thaumasite formation in carbonated mortars. *Cem. Concr. Res*. **36**, No. 4, 707–715.

Deng, M. & Tang, M. (1994). Formation and expansion of ettringite crystals. *Cem. Concr. Res*. **24**, No. 1, 119–126.

Hunter, D. (1988). Lime-induced heave in sulphate-bearing clay soils. *J. Geotech. Engng, ASCE* **114**, 150–167.

Köhler, S., Heinz, D. & Urbonas, L. (2006). Effect of ettringite on thaumasite formation. *Cem. Concr. Res*. **36**, No. 4, 697–706.

Kovári, K. & Amstad, C. (1982). A new method of measuring deformations in diaphragm walls and piles. *Géotechnique* **32**, No. 4, 402–406, http://dx.doi.org/10.1680/geot.1982.32.4.402.

Lasaga, A. C. (1984). Chemical kinetics of water-rock interactions. *J. Geophys. Res*. **89**, No. B6, 4009–4025.

Mitchell, J. K. & Dermatas, D. (1992). Clay soil heave caused by lime-sulphate reactions. In *Innovations and uses for lime* (eds D. D. Walker Jr, T. B. Hardy, D. C. Hoffman and D. D. Stanley), ASTM STP 1135, pp. 41–64. West Conshohocken, PA, USA: ASTM International.

Mohamed, A. M. O. (2000). The role of clay minerals in marly soils on its stability. *Engng Geol*. **57**, No. 3–4, 193–203.

Parkhurst, D.L. (1995). *User's guide to PHREEQC-A computer program for speciation, reaction-path, advective-transport, and inverse geochemical calculations*, Water-Resources Investigations Report 95-4227. Denver, CO, USA: US Geological Survey.

Parkhurst, D. L. & Appelo, C. A. J. (1999). *User's guide to PHREEQC (version 2)-A computer program for speciation, batch-reaction, one-dimensional transport, and inverse geochemical calculations*, Water-Resources Investigations Report 99-4259. Denver, CO, USA: US Geological Survey Earth Science Information Center.

Puppala, A. J., Wattanasanticharoen, E. & Punthutaecha, K. (2003). Experimental evaluations of stabilisation methods for sulphate-rich expansive soils. *Ground Improve*. **7**, No. 1, 25–35.

Rajasekaran, G. (2005). Sulphate attack and ettringite formation in

the lime and cement stabilized marine clays. *Ocean Engng* **32**, No. 8–9, 1133–1159.
Rajasekaran, G., Murali, K. & Srinivasaragahvan, S. (1997). Effect of chlorides and sulphates on lime treated marine clays. *Soils Found*. **37**, No. 2, 105–115.
Saaltink, M. W., Ayora, C. & Carrera, J. (1998). A mathematical formulation for reactive transport that eliminates mineral concentration. *Water Resour. Res*. **34**, No. 7, 1649–1656.
Saaltink, M. I., Ayora, C. & Olivella, S. (2005). *User's guide for RetrasoCodeBright (RCB)*. Barcelona, Spain: Department of Geotechnical Engineering and Geo-Sciences, Technical University of Catalonia/Institute of Earth Sciences Jauma Almera, Spanish Research Council (CSIC).
Sherwood, P. T. (1962). Effect of sulphates on cement and lime stabilized soils. *Highway Res. Bull*., No. 353, 98–107.
Snedker, E. A. (1996). M40: lime stabilization experiences. In *Lime stabilization* (eds C. D. F. Rogers, S. Glendinning and N. Dixon), pp. 142–158. London, UK: Thomas Telford.

Chu, J. *et al.* (2013). *Géotechnique* **63**, No. 10, 871–875 [http://dx.doi.org/10.1680/geot.SIP13.P.007]

TECHNICAL NOTE

Microbial method for construction of an aquaculture pond in sand

J. CHU*†, V. IVANOV*†, V. STABNIKOV*‡ and B. LI*

A method to construct an aquaculture pond in sand using microbial biocementation is presented in this paper. The microbially induced calcium carbonate precipitation process was used to form a low-permeability layer in sand for the construction of a water pond model in the laboratory. The test results indicated that the permeability of sand was reduced from the order of 10^{-4} m/s to 10^{-7} m/s when an average 2·1 kg of calcium (Ca) per m^2 of sand surface was precipitated. The bending strengths of the walls and the base of the model pond were in the range of 90–256 kPa. The unconfined compressive strengths for the samples taken from the walls and the base of the pond were in the range of 215–932 kPa.

KEYWORDS: ground improvement; grouting; permeability; seepage

INTRODUCTION

Conventionally, compacted bentonite, geosynthetic clay liner or plastic liners are used to seal ponds, channels and reservoirs in sand. However, these methods are costly. For example, about 60 kg of bentonite is required to seal 1 m^2 of pond area according to Pillay & Kutty (2005). The technology with plastic liner is more expensive depending on the design situations (Pillay & Kutty, 2005).

Studies have shown that the microbially induced carbonate precipitation (MICP) process can be used to increase the shear strength and decrease the permeability of sand, owing to the filling of the pores with the minerals precipitated (Gollapudi *et al.*, 1995; Mitchell & Santamarina, 2005; Whiffin *et al.*, 2007; Chu *et al.*, 2009; DeJong *et al.*, 2010; Tobler *et al.*, 2011). The MICP process is catalysed by urease-producing bacteria (UPB) owing to an increase in pH to produce carbonate in the presence of calcium ions (Ferris *et al.*, 1996; Stocks-Fischer *et al.*, 1999) as shown in the following

$$CO(NH_2)_2 + 2H_2O + Ca^{2+} + UPB \rightarrow CaCO_3 + 2NH_4^+ + UPB \quad (1)$$

However, practical applications of the MICP process for soil treatment are far more complicated (Ivanov & Chu, 2008; Ivanov, 2010) because the quantity of reagents required by conventional biocementation through percolation of soil with bacterial suspension and solutions of calcium salt and urea is large. Recently, a new approach has been developed to form a low-permeability layer several centimetres thick on top of a sand surface through the MICP process (Chu *et al.*, 2012). This method has been adopted to build a laboratory-scale water pond model in sand. The method for the construction of this pond and the properties of the microbial mediated sand are discussed in this paper. Potential applications of the method presented could include the construction of runoff collection ponds in deserts' sand (Boers, 1994), aquaculture ponds (Kitto & Reginald, 2011; Lucas & Southgate, 2012) or algal biofuel production ponds (Campbell, 2008).

CONSTRUCTION OF MODEL POND

Sand and reagents

Ottawa sand with a mean grain size of 0·42 mm was used for the construction of the water pond model. The sand was deposited dry in a box and the density achieved was 1600 kg/m^3.

The reagents used for creating a low-permeability layer in sand included

(*a*) a suspension of bacterial cells of *Bacillus* sp. VS1 with urease activity 2·7 mM hydrolysed urea/min (9·7 g urea/l·h)
(*b*) a solution containing 82·5 g/l (0·75 M) calcium chloride and 90 g/l (1·5 M) urea. The strain of UPB *Bacillus* sp. VS1 was used as a bioagent inducing formation of calcite from calcium chloride and urea (Stabnikov *et al.*, 2011; Chu *et al.*, 2012).

Urease-producing bacteria were grown in a liquid medium of the following composition: Tryptic soy broth DIFCO™, 30 g/l; urea, 20 g/l; $MnSO_4 \cdot H_2O$, 12 mg/l; $NiCl_2 \cdot 6H_20$, 24 mg/l; conductivity of the prepared medium was 1400 mS/m. All components of this medium, with the exemption of urea, were sterilised at 121°C for 15 min. The stock solution of urea, 100 g/l, was prepared and sterilised by filtration through Whatman™ nitrocellulose membrane with 0·2 μm pores to prevent urea being lost during autoclaving. Cultivation was conducted in a B. Braun biostat fermentor (International Equipment Trading Ltd., Vernon Hills, Illinois, USA) with working volume 1·5 l at temperature 30°C under aeration rate 3 l/min. Palm oil was used as an antifoaming agent in quantity 0·2% (v/v). Duration of cultivation was 4 days. The pH value of the culture liquid, with a concentration of bacterial cells of about 8 g of dry biomass/l, was adjusted to pH 7 by 1 N HCl.

Manuscript received 28 February 2012; revised manuscript accepted 22 October 2012. Published online ahead of print 31 January 2013. Discussion on this paper closes on 1 January 2014, for further details see p. ii.
* School of Civil and Environmental Engineering, Nanyang Technological University, Singapore.
† Department of Civil, Construction & Environmental Engineering, Iowa State University, USA.
‡ Department of Microbiology and Biotechnology, Ukrainian National University of Food Technologies, Kiev, Ukraine.

Formation of low-permeability layer in sand

The model pond was built within a rectangle glass tank of 48 cm × 38 cm × 20 cm (length × width × height) filled with 28 kg of sand, in which a rectangular hole of 34 cm × 26 cm × 5 cm (length × width × height) was excavated manually as shown in Fig. 1(a). A plastic board was used to support the stability of the walls of the excavated hole.

The following five steps were used to treat the surface of the model pond

(*a*) spray with bacterial suspension
(*b*) spray with calcium chloride and urea solution
(*c*) spray with bacterial suspension for a second time
(*d*) cover the sand surface with calcium chloride and urea solution
(*e*) dry the model pond outdoors under sunlight for 2 days.

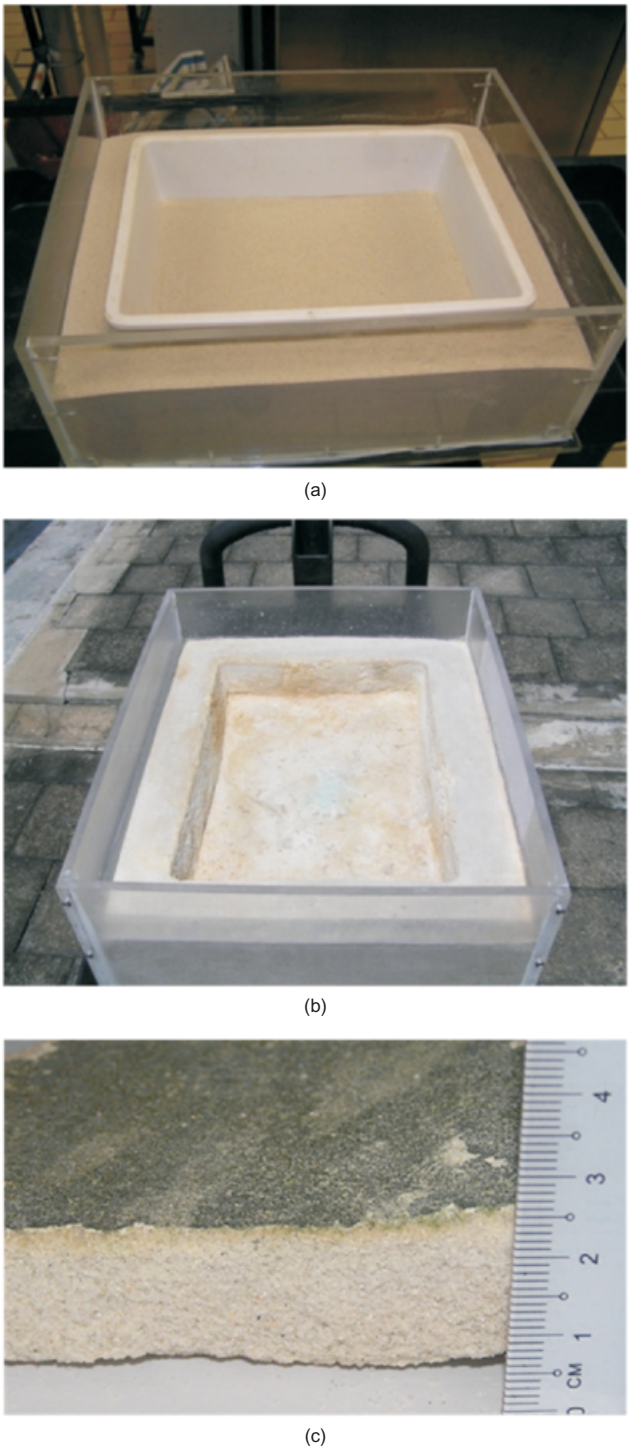

Fig. 1. Formation of a water pond model in sand: (a) before treatment; (b) after treatment; (c) cross-sectional view of the bottom of the pond after cultivation of algae

The first spray (first treatment) of the bacterial suspension on the bottom and four walls of the pond supplied a dosage of about 1·35 ml/cm^2 (or 0·11 kg/m^2) of dry biomass and the average supply rate was 0·7 ml/cm^2 per h (or 7 l/m^2 per h). The spray of the solution containing calcium chloride and urea on the bottom and four walls provided a dosage of approximately 2·3 ml/cm^2 (or 23 l/m^2) of calcium (Ca) and the average supply rate was 0·7 ml/cm^2 per h (or 7 l/m^2 per h). The supply rate and time of the treatment were adjusted so that there was no liquid above the sand surface. The second spray (second treatment) of the bacterial suspension on the bottom and the four walls provided a dosage of 0·7 ml/cm^2 (0·05 kg/m^2) of dry biomass and the average supply rate was approximately 0·7 ml/cm^2 per h (7 l/m^2 per h). The supply rate and time of the treatment were adjusted so that there was no liquid above the sand surface. Then, the model pond was filled with calcium chloride and urea solution so that the level of liquid was 5 mm above the sand surface for 2 days. This third treatment enhanced the biocementation of the surface layer (Chu *et al.*, 2012) but is not mandatory for real construction technology. Subsequently, the liquid was drained off from the tank and the model pond was left to dry outdoors for 2 days. The water pond formed is shown in Fig. 1. A cross-sectional view of the model pond after it had been used for cultivation of algae is shown in Fig. 1(c). It can be seen that the water pond is formed by a low-permeability layer surrounding the boundary of the pond. The sand below the low-permeability layer was not treated. In this way, the biotreatment was localised and thus the cost of treatment was reduced.

Design of the biocemented layer of sand

The formation of the biocemented layer of sand during the construction of the pond can be calculated using the following model. The maximum deposition of calcium (Q, kg) in the biocemented layer of sand is

$$Q = CV_p + CV_s \tag{2}$$

or

$$Q = CA(H_p n + H_s) \tag{3}$$

where C is calcium concentration (kg/m^3); V_p is volume of pores in the soil (m^3); V_s is volume of calcium salt solution (m^3); A is treated area (m^2); H_p is height of the treated sand (m); n is sand porosity; H_s is height of the calcium salt solution above soil surface (m). The calculated ratio of the quantities of precipitated calcium in the biocemented crust and in the bulk of sand for the model pond was 0·83, which was almost the same as the experimental value of 0·80. This ratio could be diminished by the formation of a low-permeability layer on top of the sand by sequential spraying of biocementing solution performed before major precipitation of calcium from solution above the surface of the sand.

The thickness of the biocemented layer, H_p, of sand can be calculated as follows

$$H_p = (V_b/A)n \tag{4}$$

where V_b is volume of bacterial suspension and solution of calcium chloride and urea, which was used for spraying the sand surface. The thickness of the biocemented layer was from 20 to 30 mm for the bottom and from 15 to 20 mm for the walls (Fig. 1(c)).

A field emission scanning electron microscope (FE-SEM)

JSM-7600 (Jeol, Japan) was used to study the dry, platinum (Pt)-coated samples of bio-treated sand. From the SEM image, it can be seen that the pores between sand grains were filled by the minerals precipitated. According to the energy dispersive X-ray spectroscopy (EDS) spectrum, the fill material between the sand grains had the following contents, in atomic %: C, 19·9; O, 31·1; Ca, 49·0, whereas the sand grains had: C, 8·7; O, 60·8; Al, 1·3; Si, 23·9; Ca, 0·5; Zr, 4·8. The higher contents of calcium and carbon in the fill material could be an indication of the formation of calcium carbonate ($CaCO_3$).

GEOTECHNICAL PARAMETERS OF MODEL POND

Water leakage tests

The average leakage rate from the bio-treated model pond was determined roughly by the change of water table over a given time interval. The water level change was monitored after the pond was filled with 5 l of tap water. This was done at the end of every treatment. For every measurement, the time taken for 25 mm of water drop to occur was recorded. The leakage rate calculated after each treatment is shown in Fig. 2. It can be seen that the leakage rate reduced with each additional treatment. The leakage rate after the fourth treatment was 3×10^{-7} m/s. It is possible to reduce the leakage rate further by using one or two additional treatments. However, a leakage rage in the order of 10^{-7} m/s was comparable with the leakage rate required for tropical fish ponds, aquaculture ponds (Teichert-Coddington *et al.*, 1989) or for shrimp mariculture ponds (Weisburd & Laws, 1990). Therefore, the leakage rate was considered adequate for aquaculture or fish ponds.

Permeability tests

The engineering properties of the soil in the bio-treated low-permeability layer were measured using different laboratory tests. Samples taken from the walls and the bottom of the pond were tested separately. Permeability tests were conducted using a triaxial cell by following the constant head method (Head, 1986). As the bio-treated sand was hard and brittle, it was difficult to trim a sample into a perfect cylinder. Small cracks could also occur on the surface of the sample. To overcome these problems, model clay was used to seal the cylindrical surface of a 38 mm dia. specimen, as shown in Fig. 3. The specimen was then installed into a triaxial cell and sealed using a membrane. A confining pressure of 50 kPa was used. Two GDS pressure volume controllers that could apply a pressure and measure the volume at the same time (Chu *et al.*, 1992) were used to apply pressures of 45 and 40 kPa to the bottom and top of the specimen respectively. Once steady-state flow conditions were obtained, the quantity of flow over a time interval was measured to calculate the permeability. Two permeability tests each were conducted on samples taken from the walls and the bottom of the pond. The results are presented in Fig. 4. It can be seen that the permeability of the bio-treated sand taken from both the walls and the bottom of the pond had been reduced from the initial $4{\cdot}0 \times 10^{-4}$ to $3{\cdot}5 \times 10^{-7}$ m/s, on average. This permeability value was still not low enough to make a leakage-free water pond. However, it was adequate for building aquaculture ponds.

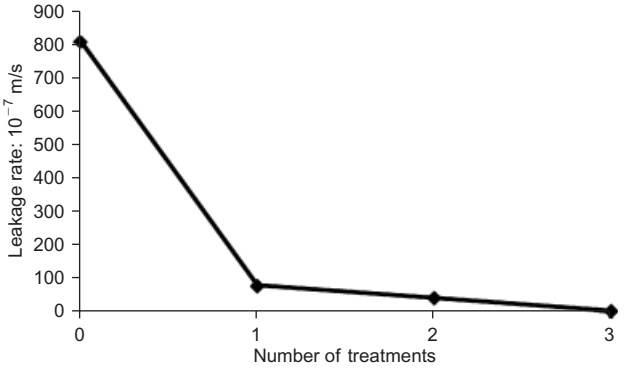

Fig. 2. The leakage rate measured after each treatment

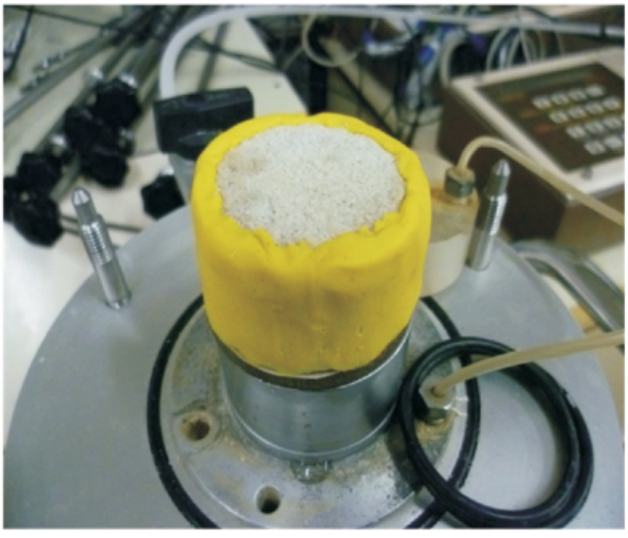

Fig. 3. Specimen for permeability test

Four-point bending tests

The MICP process not only reduced the permeability of sand substantially, but also increased the stiffness and shear strength of the soil. By observation, it can be seen that the bio-treated soil cemented together like sandstone. The cementation effect was likely to have been created by the minerals produced through the MICP process. The cementation effect not only increased the shear strength, but also created cohesion or tensile strength in the soil. To assess the tensile strength of the bio-treated soil, some four-point bending tests were carried out by following a procedure detailed in ASTM standard D6272-10 (ASTM, 2010). One

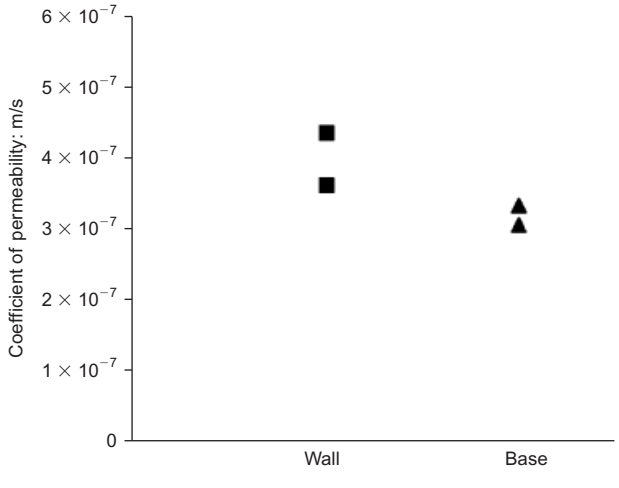

Fig. 4. Results of permeability tests

reason for doing the four-point bending tests was that the samples were only suitable for this type of test. The test set-up is shown schematically in Fig. 5. The support span was 80 mm. The dimensions of the specimen were 5 mm thick, 100 mm long and 20 mm wide, which did not exceed one-quarter of the support span. The loading span was 26·7 mm, which was one-third of the length of the supported span. The diameter of the round loading noses was 6 mm. The maximum bending stress S for a load span of one-third of the support span is calculated as follows (ASTM D6272-10 (ASTM, 2010))

$$S = P\frac{L}{t}d^2 \tag{5}$$

where S is the bending strength in the outer fibre throughout the load span (MPa); P is the load at a given point on the load–deflection curve (N); L is the support span (mm); t is the thickness of the beam (mm); and d is the depth of the beam (mm).

The bending strengths measured by the four-point bending tests for samples taken from the walls and base are shown in Fig. 6. It can be seen that the bending strengths measured are in the range of 90–256 kPa. These bending strengths were still much smaller compared with those of rocks. However, as the untreated sand had no cohesion or tensile strength at all, the measured bending strength is a good indication of the cementation effect due to bio-treatment. This bending strength of the soil will enhance the stability of the pond and all steeper slopes or even walls to be used for the pond. This will help to cut down further the construction cost for the pond.

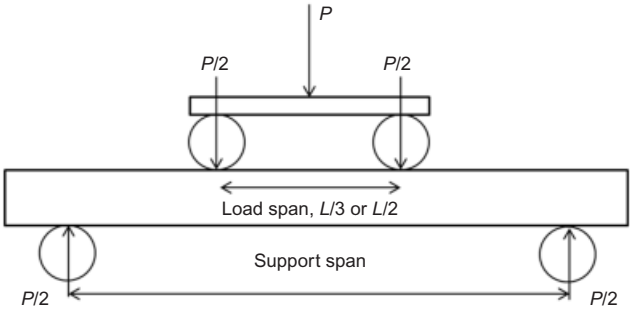

Fig. 5. Set-up for four-point bending tests

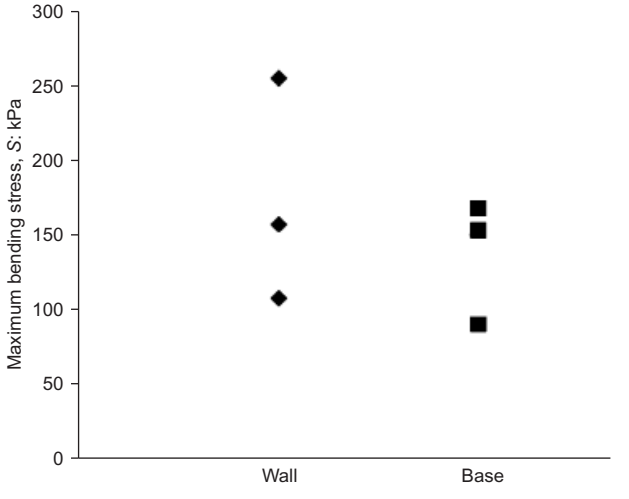

Fig. 6. Results of four-point bending tests on samples taken from the wall and the base

Unconfined compression tests

Unconfined compression (UC) tests were also conducted on specimens 10 mm in diameter and 20 mm high. Small-diameter samples had to be used as the cementation zone was only 15–30 mm thick. Nevertheless, the UC test provided a way to assess the degree of improvement of the sand given the fact that clean sand would not even stand as a column. A loading rate of 0·4 mm/min (or 2% strain) was used in the tests. The UC strengths obtained for samples taken from both the walls and the base were in the range 215–932 kPa (Fig. 7). There was a large variation in the UC strength even for samples taken from the same zone. This could be partially attributed to the non-uniformity in the treatment of the soil and the disturbance to the samples during sample preparation. Similar to the bending strength obtained from the four-point tests, the strength of the sample at the bottom of the pond is slightly lower than that of the sample at the wall. This could be because the walls had a larger surface area than the base for the application of biocementation solution. Additionally, sample size may have a significant effect on the absolute value and variations of the unconfined compressive strength.

CONCLUSIONS

A method to construct a water pond in sand based on an MICP approach is presented in this paper. The calcite formed through the MICP process filled the pores in sand and resulted in a substantial reduction in the permeability as well as an increase in the stiffness and shear strength of sand. A water pond model was built in the laboratory using this method. The test results indicated that the permeability of sand was reduced from the order of 10^{-4} m/s to 10^{-7} m/s when an average 2·1 kg/m^2 of calcium was precipitated in sand. Although clean sand has no tensile or unconfined compressive strength, the bio-treated soil had a bending strength of up to 256 kPa, as measured by four-point bending tests, and an unconfined compressive strength of up to 932 kPa.

ACKNOWLEDGEMENT

This research was supported by a grant from the Agency for Science, Technology and Research (A*STAR), Singapore.

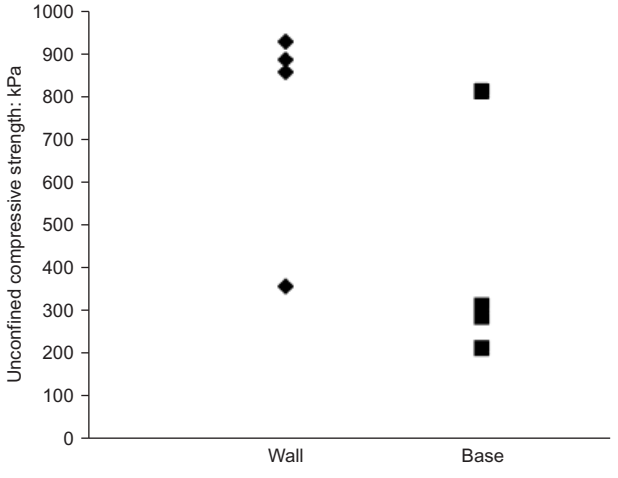

Fig. 7. Unconfined compressive strength measured on samples taken from the wall and the base

NOTATION

A treated area (m^2)
C calcium concentration (kg/m^3)
d depth of beam (mm)
H_p height of the treated sand (m)
H_s height of the calcium salt solution above soil surface (m)
L support span (mm)
n sand porosity
P load at a given point on the load–deflection curve (N)
Q maximum deposition of calcium in biocemented layer of sand (kg)
S bending strength in outer fibre throughout load span (MPa)
t thickness of beam (mm)
V_b volume of bacterial suspension and solution of calcium chloride and urea, used for spraying sand surface (m^3)
V_p volume of pores in the soil (m^3)
V_s volume of calcium salt solution (m^3)

REFERENCES

ASTM (2010). *ASTM D6272-10: Standard test method for flexural properties of unreinforced and reinforced plastics and electrical insulating materials by four-point bending*. West Conshohocken, PA, USA: Committee D20 on Plastics, ASTM.

Boers, T. M. (1994). *Rainwater harvesting in arid and semi-arid zones*. Wageningen, the Netherlands: International Institute for Land Reclamation and Improvement.

Campbell, M. N. (2008). Biodiesel: algae as a renewable source for liquid fuel. *Guelph Engng J.* **1**, No. 1, 2–7.

Chu, J., Lo, S.-C. R. & Lee, I. K. (1992). Strain softening behavior of granular soil in strain path testing. *J. Geotech. Engng, ASCE* **118**, No. 2, 191–288.

Chu, J., Ivanov, V., Lee, M. F., Oh, X. M. & He, J. (2009). Soil and waste treatment using biocement. In *Ground improvement technologies and case histories* (eds C. F. Leung, J. Chu and R. F. Shen), pp. 160–166. Singapore: Research Publishing.

Chu, J., Ivanov, V. & Stabnikov, V. (2012). Microbially induced calcium carbonate precipitation on surface or in the bulk of soil. *Geomicrobiol. J.* **29**, No. 6, 544–549.

DeJong, J. T., Mortensen, B. M., Martinez, B. C. & Nelson, D. C. (2010). Bio-mediated soil improvement. *Ecol. Engng* **36**, No. 2, 197–210.

Ferris, F. G., Stehmeier, L. G., Kantzas, A. & Mourits, F. M. (1996). Bacteriogenic mineral plugging. *Can. J. Petroleum Technol.* **35**, No. 9, 56–61.

Gollapudi, U. K., Knutson, C. L., Bang, S. S. & Islam, M. R. (1995). A new method for controlling leaching through permeable channels. *Chemosphere* **30**, No. 4, 695–705.

Harkes, M. P., van Paassen, L. A., Booster, J. L., Whiffin, V. S. & van Loosdrecht, M. C. M. (2010). Fixation and distribution of bacterial activity in sand to induce carbonate precipitation for ground reinforcement. *Ecol. Engng* **36**, No. 2, 112–117.

Head, K. H. (1986). *Manual of soil laboratory testing*, vol. 3. London, UK: Pentech Press.

Ivanov, V. (2010). *Environmental microbiology for engineers*. Boca Raton, FL, USA: CRC Press.

Ivanov, V. & Chu, J. (2008). Applications of microorganisms to geotechnical engineering for bioclogging and biocementation of soil in situ. *Rev. Environ. Sci. Biotechnol.* **7**, No. 2, 139–153.

Kitto, M. R. & Reginald, M. (2011). Effect of summer/winter light intensity and salt on growth kinetics and beta carotene accumulation by *Dunaliella* in open outdoor earthern ponds in a desert island, off UAE coast. *J. Algal Biomass Utilization* **2**, No. 4, 14–21.

Lucas, J. S. & Southgate, P. C. (2012). *Aquaculture: farming aquatic animals and plants*, 2nd edn. Chichester, UK: Wiley.

Mitchell, J. K. & Santamarina, J. C. (2005). Biological considerations in geotechnical engineering. *ASCE J. Geotech. Geoenviron. Engng* **131**, No. 10, 1222–1233.

Pillay, T. V. R. & Kutty, M. N. (2005). *Aquaculture: principles and practices*. Oxford, UK: Wiley-Blackwell.

Stabnikov, V., Naemi, M., Ivanov, V. & Chu, J. (2011). Formation of water-impermeable crust on sand surface using biocement. *Cement and Concrete Research* **41**, No. 11, 1143–1149.

Stocks-Fischer, S., Galinat, J. K. & Bang, S. S. (1999). Microbiological precipitation of $CaCO_3$. *Soil Biol. Biochem.* **31**, No. 11, 1563–1571.

Teichert-Coddington, D. R., Peralta, M. & Phelps, R. P. (1989). Seepage reduction in tropical fish ponds using chicken litter. *Aquacultural Engng* **8**, No. 3, 147–154.

Tobler, D. J., Cuthbert, M. O., Greswell, R. B., Riley, M. S, Renshaw, J. C., Handley-Sidhu, S. & Phoenix, V. R. (2011). Comparison of rates of ureolysis between *Sporosarcina pasteurii* and an indigenous groundwater community under conditions required to precipitate large volumes of calcite. *Geochim. Cosmochim. Acta* **75**, No. 11, 3290–3301.

Weisburd, R. S. J. & Laws, E. A. (1990). Free water productivity measurements in leaky multiculture ponds. *Aquacultural Engng* **9**, No. 6, 377–403.

Whiffin, V. S., van Paassen, L. A. & Harkes, M. P. (2007). Microbial carbonate precipitation as a soil improvement technique. *Geomicrobiol. J.* **24**, No. 5, 417–423.